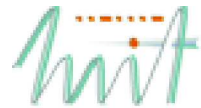




TECHNISCHE UNIVERSITÄT ILMENAU



Fakultät für Elektrotechnik und Informationstechnik  
der Technischen Universität Ilmenau

## LIMITATIONS OF EXPERIMENTAL CHANNEL CHARACTERISATION

*Markus Landmann*

Dissertation zur Erlangung des  
akademischen Grades Doktor-Ingenieur (Dr.-Ing)

Anfertigung im:	Fachgebiet Elektronische Messtechnik Institut für Informationstechnik Fakultät für Elektrotechnik und Informationstechnik
Gutachter:	Univ.-Prof. Dr.-Ing. habil. Reiner S. Thomä Univ.-Prof. Dr. rer. nat. habil. Matthias Hein o.Univ.-Prof. Jun-ichi Takada
Vorgelegt am:	11.12.07
Verteidigt am:	28.03.08



# ABSTRACT

This thesis deals with *Experimental Channel Characterisation* and its performance limits in real propagation environments. This includes recording of the multidimensional wideband channel matrix by using a Multiple-Input Multiple-Output (MIMO) channel sounder and antenna arrays at both sides of the link. *High-resolution* parameter estimation is finally applied to characterise the channel in terms of Direction of Departure (DoD), Direction of Arrival (DoA), Time Delay of Arrival (TDoA), and complex polarimetric path weights. The quality of these estimates in “real world” scenarios is degraded by several impairments of the *practical* antenna arrays and the measurement system used. The resulting estimation quality limits are investigated in detail by simulations and measurements. The entire processing chain is analysed in terms of possible error sources. To this end, measurement system impairments, antenna array calibration errors as well as limitations of the radio channel model applied by the *high-resolution* parameter estimation procedure are investigated. Moreover, consequences of using these results to deduce and parameterise geometry based channel models are demonstrated.

Propagation measurements give us an antenna dependent description of the radio channel. For the antenna independent characterisation of the radio channel, *high-resolution* parameter estimation algorithms are applied to determine the DoD and DoA of the specular paths at the transmit and receive side respectively. The gradient based Maximum Likelihood (ML) parameter estimation framework RIMAX, which is reviewed in this thesis uses a data model that describes the radio channel and the measurement system including the antenna arrays. Contrary to other ML parameter estimation algorithms, the model of the radio channel comprises two parts: specular like reflections and distributed diffuse scattering. For the model of the measurement system, an efficient and accurate description of the measured polarimetric antenna array radiation patterns is required. The proposed analytic description of antenna array radiation patterns, which is called Effective Aperture Distribution Function (EADF), is essentially a two dimensional (2D) Fourier transformation of the periodic radiation patterns. As opposed to other models, radiation patterns and its derivatives can be easily calculated analytically from the EADF with low computational burden and high accuracy. A full polarimetric 2D array calibration procedure for the accurate measurement of the radiation patterns of antenna arrays is proposed. This procedure contains the calibration of the entire measurement setup including the MIMO channel sounder, the dual polarised reference horn antenna, and all devices in the Radio Frequency signal path. In this context, a new gradient based ML estimation algorithm is proposed to correct the measured radiation patterns for a phase offset, which occurs during the calibration measurement.

A powerful framework for the performance evaluation of *practical* antenna arrays in terms of angular resolution limits in the presence of additive independent and identically distributed (i.i.d.) Gaussian measurement noise is presented. It is based on the EADFs of measured radiation patterns, which allow us to calculate the Cramér-Rao Lower Bounds of the angular parameters of the specular like reflections. The benefits of using the EADF to describe the radiation patterns including all “imperfections” of the measured antenna array is hereby exploited. The proposed antenna array performance evaluation framework is verified based on measurements in an anechoic chamber.

The derived model of the measurement system including the antenna arrays can only be determined within certain accuracy. A mismatch between the real measurement system and its model used

for parameter estimation always exists. From the analysis of several estimation results of a wide range of measurements it was found that such a model mismatch partially may cause significant errors in the estimation results. In this thesis a distinction is made between antenna array related model mismatch and measurement system related model mismatch. Antenna array related model mismatch caused by systematic errors depending on the quality of antenna array calibration and systematic errors due to the usage of incomplete data models (e.g. ignoring polarisation characteristic of the antenna elements) are investigated. The consequence of phase noise and unsuitable calibrated measurement systems are presented in the context of model mismatch related to the measurement system. It is shown that the use of an inaccurate model of the measurement system inherently will result in biased and/or artificially spread angular estimates of the parameters of the specular reflections. Methods are proposed to correct/avoid model mismatch and to reduce the consequence of inaccurate/simplified models, whereas it is emphasised that some errors are unavoidable.

The consequences of all unavoidable errors on *Experimental Channel Characterisation* in complex propagation environments are investigated in the last part of this work. It is clearly shown under which circumstances the estimated specular reflections and distributed diffuse scattering are reliable and relevant. The investigations are based on realistic simulations of the radio channel (ray-tracing) and macro-cell propagation measurements. This synthesis of ray-tracing simulations and measurements guarantees the correctness and reliability of the accomplished results.

The contributions of this thesis are of interest for researchers dealing with *high-resolution* parameter estimation and channel modelling and can be summarised as follows:

- the efficient and accurate radiation pattern modelling of antenna arrays,
- the powerful performance evaluation framework for *practical* antenna arrays,
- the exposure of consequence of modelling errors on parameter estimation,
- and the demonstration of overall limitations of *Experimental Channel Characterisation*.



## KURZFASSUNG

In dieser Dissertation wird die *Experimentelle Kanalcharakterisierung* und deren Grenzen in realen Ausbreitungsbedingungen untersucht. Dies beinhaltet die Aufzeichnung der mehrdimensionalen breitbandigen Kanalmatrix mit einem Multiple-Input Multiple-Output (MIMO) Channel-Sounder unter Verwendung von Antennenarrays auf der Sende- und Empfangsseite. Um den Funkkanal mit Hilfe der Parameter *Sendewinkel (DoD)*, *Empfangswinkel (DoA)*, *Laufzeit (TDoA)* und den komplexen polarimetrischen Pfadgewichten zu charakterisieren, werden *hochauflösende* Parameterschätzverfahren verwendet. Die Genauigkeit dieser Parameterschätzergebnisse in „realen“ Messumgebungen wird durch eine Vielzahl von Fehlerquellen begrenzt. Diese Genauigkeitsgrenzen der Parameterschätzung werden anhand zahlreicher Simulationen und Messungen analysiert. Fehlerquellen im gesamten Verarbeitungsablauf werden untersucht. Dazu gehören die Einschränkungen durch das Messsystem, systematische Fehler bei der Kalibrierung *praktischer* Antennenarrays sowie Unzulänglichkeiten des Funkkanalmodells des *hochauflösenden* Parameterschätzers. Darüber hinaus werden die Auswirkungen der Parametrierung bzw. Ableitung geometrisch basierter Kanalmodelle auf der Grundlage von Parameterschätzergebnissen mit begrenzter Genauigkeit aufgezeigt.

Mit Messungen in typischen Ausbreitungsbedingungen kann der Funkkanal immer nur in Abhängigkeit der Messantennen beschrieben werden. Als Ziel wird jedoch eine antennenunabhängige Beschreibung des Funkkanals angestrebt. Daher ist es notwendig, die Sende- und Empfangswinkel der spekularen Ausbreitungspfade mittels *hochauflösender* Parameterschätzverfahren zu bestimmen. Der gradientenbasierte Maximum Likelihood (ML) Parameterschätzer RIMAX, auf dem diese Arbeit aufbaut, verwendet ein Datenmodell, das den Funkkanal und das Messsystem inklusive der Antennenarrays beschreibt. Im Gegensatz zu anderen ML-Parameterschätzern wird ein Funkkanalmodell angewendet, welches spekulare Reflektionen und verteilte diffuse Streuungen berücksichtigt. Für die Modellierung des Messsystems wird ein effizientes und exaktes Modell der gemessenen polarimetrischen Richtcharakteristika benötigt. Das hier vorgeschlagene Modell, die so genannte Effective Aperture Distribution Function (EADF), beschreibt die Antennenrichtcharakteristika analytisch und basiert im Wesentlichen auf der zweidimensionalen (2D) Fouriertransformation der periodischen Richtcharakteristika. Im Gegensatz zu anderen Verfahren können auf der Grundlage der EADF die Antennencharakteristika und ihre Ableitungen mit geringem Aufwand und hoher Genauigkeit berechnet werden. Für eine exakte Messung der Richtcharakteristika eines Antennenarrays wird ein vollpolarimetrisches 2D-Kalibrierverfahren vorgeschlagen. Mit diesem Verfahren wird der komplette Messaufbau kalibriert. Dazu gehören der MIMO Channel-Sounder, die dual polarisierte Referenzhornantenne und alle Hochfrequenzkomponenten außer dem zu untersuchenden Antennenarray. Im Zusammenhang mit der Arraykalibrierung wird ein gradientenbasierter ML-Parameterschätzer entwickelt, mit dem eine bei der Kalibrierung auftretende Phasenabweichung korrigiert wird.

Des Weiteren wird ein leistungsstarkes Verfahren zur Bewertung *praktischer* Antennenarrays auf der Basis der EADFs gemessener Richtcharakteristika vorgeschlagen. Die Cramér-Rao-Schranken der Winkelparameter in Abhängigkeit des Signal-Rausch-Verhältnisses werden mit dem EADF-Modell analytisch berechnet. Der Vorteil des EADF-Modells besteht darin, dass die Richtcharakteristika eines realen Antennenarrays unter Einbeziehung aller störenden Einflussgrößen beschrieben werden. Das vorgeschlagene Bewertungsverfahren wird anhand von Messungen im Antennenmessraum

verifiziert.

Das Modell des Messsystems inklusive der Antennenarrays, welches für die Parameterschätzung verwendet wird, kann das reale System nur begrenzt beschreiben. Es wurden Schätzergebnisse von zahlreichen Messungen analysiert. Hierbei musste festgestellt werden, dass Fehler bei der Modellierung zu teilweise unglaublichen Schätzergebnissen führen. Genauer untersucht werden Fehler in Bezug auf die Antennenarrays und das Messsystem. Erstere werden hervorgerufen durch systematische Fehler bei der Arraykalibrierung und durch die Verwendung unvollständiger Datenmodelle (z.B. Nichtberücksichtigung der polarimetrischen Eigenschaften der Antennen). Letztere entstehen einerseits durch Phasenrauschen und andererseits durch ungeeignete Kalibrierung. Es wird nachgewiesen, dass die Verwendung ungenauer Modelle zur Schätzung von Artefakten führt. Diese Schätzfehler äußern sich in Abweichungen und/oder in einer künstlichen Aufspreizung der Winkelschätzungen der spekularen Anteile. Es werden geeignete Methoden vorgeschlagen, um die Auswirkungen von Modellfehlern weitestgehend zu vermeiden bzw. zu korrigieren. Betont werden muss jedoch, dass einige Fehler unvermeidbar sind.

Die Auswirkungen aller unvermeidbaren Fehler auf die *Experimentelle Kanalcharakterisierung* in komplexen Ausbreitungsumgebungen werden im letzten Teil dieser Arbeit dargestellt. Es wird gezeigt, unter welchen Bedingungen die geschätzten spekularen Anteile sowie die geschätzten verteilten diffusen Streuanteile glaubwürdig und physikalisch relevant sind. Die Untersuchungen basieren auf „realistischen“ Simulationen des Funkkanals (Ray-Tracing) und auf Messungen. Diese Synthese garantiert Glaubwürdigkeit und Aussagefähigkeit der in der Arbeit gewonnenen Ergebnisse.

Die Resultate dieser Dissertation sind speziell für Wissenschaftler auf dem Gebiet der Parameterschätzung sowie Funkkanalmodellierung von Interesse und können wie folgt zusammengefasst werden:

- die Entwicklung eines Modells zur exakten und effizienten Beschreibung der Richtcharakteristika von Antennenarrays,
- ein Verfahren zur Bewertung *praktischer* Antennenarrays,
- die Sensibilisierung für Modellfehler und deren Auswirkungen auf die Parameterschätzergebnisse und
- die Bestimmung der Grenzen *Experimenteller Kanalcharakterisierung* unter Berücksichtigung aller unvermeidbarer Fehlerquellen.

# ACKNOWLEDGEMENTS

The discussion with various people has made this thesis possible or complete. First, I want to thank Prof. Reiner Thomä for his continuous support and encouragement, both as a supervisor and as a colleague. Further, I thank all the colleagues in the department Elektronische Messtechnik at Technische Universität Ilmenau. I like to mention especially Gerd Sommerkorn, Milan Narandžić, Vadim Algeier, Christian Schneider, Karl Borkowski, Gitta Weber and Dr. Wim Kotterman who helped me in practical and scientific matters. I am very grateful for the fruitful cooperation with Dr. Andreas Richter during the time we developed the [RIMAX](#) parameter estimation framework.

I feel a special gratitude for Prof. Jun-ichi Takada, for his support during my time as visiting researcher at the Tokyo Institute of Technology and for the discussion with respect to my research.

The measurement campaign in Section 8.3 is supported by the National Institute of Information and Communications Technology (NICT) of Japan. Furthermore, I would like to thank the members of the Takada Laboratory for their support during these measurements, especially Kriangsak Sivasondhivat, Mir Ghoraiishi, Gilbert Siy Ching and Navarat Lertsirisopon.

I am very grateful for the help of Gilbert Siy Ching of the Takada Laboratory who was proofreading this work several times.

Furthermore, I thank Prof. Matthias Hein for reviewing my thesis.

The cooperation with MEDAV GmbH, Uttenreuth in the field of channel sounding was of crucial importance for this work. Special thanks go to the colleagues Dirk Brückner, Steffen Warzügel, Johannes Schramm, and Walter Wirnitzer for their continuous support.

The applied ray-tracer and its description in Section 8.2 was provided from Thomas Fügen and Jürgen Maurer of the Institut für Höchsthfrequenztechnik und Elektronik of the University of Karlsruhe.

A longer list of fellow researchers, not directly mentioned, of Bristol University, Lund University, Wien University of Technology and Helsinki University of Technology deserve my gratitude for the successful collaborations and interesting discussions.

Furthermore, I would like to thank Giovanni Del Galdo and Jörg Lotze for the research cooperation when comparing the radiation pattern descriptors [EADF](#) and [VSH](#). I also would like to thank both for many useful tips in terms of applying  $\text{\LaTeX}$  to write this thesis.

*My biggest gratitude goes indeed to my parents who always showed and allowed me to see the world from many different perspectives. My grandmother deserves special thanks for her continuous support, power and years of serving the best food. Furthermore, I have to thank my girlfriend Kotomi who encouraged me indirectly to finish my thesis.*

Finally, I would like to thank all my friends who are a very important part of my life.



# CONTENTS

<b>Title</b> . . . . .	i
<b>Abstract</b> . . . . .	iii
<b>Kurzfassung</b> . . . . .	v
<b>Acknowledgements</b> . . . . .	vii
<b>Contents</b> . . . . .	ix
<b>List of Figures</b> . . . . .	xv
<b>List of Tables</b> . . . . .	xix
<b>1. Introduction</b> . . . . .	1
1.1 Channel Modelling and Experimental Channel Characterisation . . . . .	1
1.2 Drawbacks of the Experimental Channel Characterisation and Motivation . . . . .	4
1.3 Overview and Contributions . . . . .	5
<b>2. Channel Measurement</b> . . . . .	9
2.1 Channel Measurement Techniques . . . . .	9
2.2 MIMO Channel Sounding Measurement Technique . . . . .	12
2.3 Detailed Configuration of the Applied MIMO Sounder Systems . . . . .	13
2.3.1 Tx/Rx Synchronisation in Remote Operation . . . . .	16
2.3.2 Back-to-Back Calibration . . . . .	16
2.3.3 Receiver Sensitivity . . . . .	18
2.3.4 Phase Noise . . . . .	20
2.3.5 Arrangement of External Amplifiers in the RF Signal Path . . . . .	22
2.4 Antenna Arrays . . . . .	26
<b>3. Antenna Array Data Model</b> . . . . .	33
3.1 Broadband Model of a Single Antenna Element . . . . .	34
3.2 Narrow Band Model of the Measured Radiation Pattern . . . . .	36
3.3 The Effective Aperture Distribution Function . . . . .	38
3.3.1 The Idea behind the EADF . . . . .	38
3.3.2 Construction of the 2D Periodic Radiation Pattern . . . . .	38
3.3.3 EADF calculated from the 2D Periodic Radiation Pattern . . . . .	40

---

3.3.4	Analytic Expression for Radiation Patterns and Derivatives of an Antenna Array . . . . .	41
3.3.5	Model Error Dependent on the Number of Relevant Samples Used for the EADF . . . . .	43
3.4	Performance and Accuracy Comparison Between Different Interpolation Methods . .	44
3.5	Minimum Angular Sampling Grid for Antenna Array Radiation Patterns . . . . .	45
<b>4.</b>	<b>Antenna Array Calibration . . . . .</b>	<b>51</b>
4.1	Obtaining the Antenna Array Radiation Patterns from Measurement . . . . .	51
4.1.1	Measurement System Setup . . . . .	52
4.1.2	2D Antenna Positioning System . . . . .	52
4.1.3	Back-to-Back Calibration of the Measurement System . . . . .	53
4.1.4	Calibration of the Dual Polarised Reference Horn Antenna . . . . .	55
4.1.5	Calibration of Channel Measurement Antenna Arrays . . . . .	57
4.2	Estimation of EADFs from Measured Radiation Patterns . . . . .	58
4.2.1	Data Model of the Measured Radiation Patterns Including a Collective Phase Change . . . . .	58
4.2.2	EADF Estimation Algorithm . . . . .	60
4.2.3	Algorithm performance dependent on SNR and number of elements . . . . .	62
4.2.4	Measurement Example . . . . .	62
4.2.5	Conclusion on EADF Estimation Algorithm . . . . .	64
4.3	Measured Radiation Patterns and EADFs of Different Array Types . . . . .	65
4.3.1	“Single Polarised” Antenna Array UCAx1x1x16 . . . . .	65
4.3.2	Polarimetric Antenna Array SPUCPAx2x4x24 . . . . .	68
4.3.3	Polarimetric Antenna Array PULPAx2x1x8 . . . . .	68
<b>5.</b>	<b>Channel Modelling and Parameter Estimation . . . . .</b>	<b>73</b>
5.1	Radio Channel Model . . . . .	73
5.1.1	The Specular Path Model (SC) . . . . .	74
5.1.2	The Dense Multipath Model (DMC) . . . . .	77
5.2	Maximum Likelihood Parameter Estimator RIMAX . . . . .	78
5.2.1	Formulation of the Estimation Problem . . . . .	79
5.2.2	Global Search for New Paths . . . . .	81
5.2.3	Local Search and Discussion of the Algorithm’s Convergence . . . . .	84
5.2.4	Estimation example . . . . .	87
5.3	Discussion about the Limitations of the Estimator and its Model . . . . .	87
<b>6.</b>	<b>Performance Evaluation of Practical Antenna Arrays . . . . .</b>	<b>89</b>
6.1	CRLB Based Evaluation Framework for Practical Antenna Arrays . . . . .	89
6.1.1	Example: Comparison of a Theoretical and Measured CUBA . . . . .	91
6.2	Verification of the Antenna Array Performance Evaluation Framework . . . . .	94
6.2.1	Single Path Scenario . . . . .	95
6.2.2	Coherent two path scenario . . . . .	96

---

6.3	Conclusion Chapter 6	100
<b>7.</b>	<b>Consequences of Modelling Errors in Channel Parameter Estimation</b>	<b>101</b>
7.1	Analysis Procedure and Definition of Basic Parameters Used in this Chapter	101
7.2	Antenna Array Related Model Mismatch	103
7.2.1	Systematic Error Related to the Quality of the Calibration Measurement and to the Narrow Band Model	103
7.2.1.1	Accuracy of the Narrow Band Model derived from Anechoic Chamber Measurements (Angular Domain)	105
7.2.1.2	Consequences of distorted Radiation Patterns on the Calculated EADFs	110
7.2.1.3	Simplified Reflection Model of the Positioning System and Distorted EADFs	115
7.2.1.4	Systematic Error of the Estimation Result Caused by Distorted EADFs	118
7.2.1.5	Concluding Remarks on Systematic Error Related to the Quality of the Calibration Measurement and to the Narrow Band Model	120
7.2.2	Systematic Error Due to Incomplete Data Models	121
7.2.2.1	Effect of Ignoring Elevation Characteristics	123
7.2.2.2	Ignoring Polarisation Characteristic	131
7.2.2.3	Consequences of the “Plane Wave Assumption”	135
7.2.2.4	Concluding Remarks on Systematic Error Due to Incomplete Data Models	145
7.3	System Related Consequences	146
7.3.1	Consequence of Phase Noise on the DoD/DoA Estimation	146
7.3.1.1	Long Term Phase Drift	146
7.3.1.2	Phase Noise	150
7.3.1.3	Estimation of Artefacts as Consequence of Phase Noise	155
7.3.2	Consequence of an Unsuitable Calibrated External LNA	157
7.3.3	Concluding Remarks on System Related Consequences	160
7.4	Conclusions Chapter 7 and Array Error Chart	160
<b>8.</b>	<b>Overall Limitations of Experimental Channel Characterisation</b>	<b>163</b>
8.1	Definition of Metrics	163
8.1.1	Antenna Independent Metrics	164
8.1.2	Antenna Dependent Metrics	166
8.1.2.1	Relative Error of the MIMO Channel Diversity Metrics	168
8.2	Error Analysis Based on Ray-tracing	169
8.2.1	Description of the 3D Ray-tracer	169
8.2.2	Ray-tracing Based Analysis Procedure	171
8.2.3	Consequences of an Overall Model Accuracy Lower than the Maximum SNR in the CIR	174
8.2.3.1	Relevance of the Estimated DMC	175

8.2.3.2	Angular Power Spectrum of the SC . . . . .	175
8.2.3.3	ECM Mismatch of the SC . . . . .	176
8.2.3.4	MIMO Capacity Error . . . . .	178
8.2.3.5	NPCG Error . . . . .	179
8.2.4	Consequences of an Overall Model Accuracy Higher than the Maximum SNR in the CIR . . . . .	180
8.2.4.1	Relevance of the Estimated DMC . . . . .	181
8.2.4.2	Angular Power Spectrum of the SC . . . . .	181
8.2.4.3	ECM Mismatch of the SC . . . . .	184
8.2.4.4	MIMO Capacity Error . . . . .	184
8.2.4.5	NPCG Error . . . . .	185
8.3	Error Analysis Based on Measurements . . . . .	186
8.3.1	Description of the Measurement . . . . .	186
8.3.2	Measurement Based Analysis Procedure . . . . .	188
8.3.3	Consequences of an Overall Model Accuracy Lower or Higher than the SNR in the CIR . . . . .	191
8.3.3.1	Relevance of the Estimated DMC . . . . .	191
8.3.3.2	MIMO Capacity Error . . . . .	192
8.4	Conclusion Chapter 8 . . . . .	195
<b>9.</b>	<b>Conclusions and Future Prospects . . . . .</b>	<b>197</b>
<b>Appendix A.</b>	<b>Channel Measurement . . . . .</b>	<b>201</b>
A.1	Estimation of the Phase Noise Properties of the MIMO Sounders Used . . . . .	201
A.2	Correction for the Switched Reference Attenuator . . . . .	202
<b>Appendix B.</b>	<b>Antenna Array Data Model . . . . .</b>	<b>205</b>
B.1	Efficient Antenna Array Data Format . . . . .	205
B.1.1	Compressed EADF for Single Antenna Element . . . . .	205
B.1.2	Efficient Matrix Notation for Joint Description of All Antenna Elements . . . . .	207
<b>Appendix C.</b>	<b>A General Characterisation of the Antenna Arrays Used . . . . .</b>	<b>211</b>
C.1	Definition of Mean Antenna Array Element Parameters . . . . .	211
C.1.1	Maximum Gain and Mean Gain of All Antennas . . . . .	211
C.1.2	Mean XPD of All Antennas of the Array . . . . .	212
C.1.3	3 dB beam width in azimuth and co-elevation . . . . .	212
C.2	Overview of All Arrays . . . . .	212
<b>Appendix D.</b>	<b>Performance Comparison of Practical Antenna Arrays . . . . .</b>	<b>215</b>
D.1	Settings for the Analysis . . . . .	216
D.2	Constant SNR . . . . .	217
D.3	Constant transmit power and receiver sensitivity . . . . .	218
D.3.1	Single path scenario . . . . .	220
D.3.2	Coherent two path scenario . . . . .	223

---



---

D.3.2.1	Settings and Parameter Definition . . . . .	223
D.3.2.2	Azimuth Results for Constant Co-Elevation . . . . .	227
D.3.2.3	Co-elevation Results for Constant Azimuth . . . . .	229
<b>Appendix E.</b>	<b>Glossary of Notations, Operators, Matrices, Symbols, and Acronyms . . . . .</b>	<b>233</b>
E.1	Notations . . . . .	233
E.2	Mathematical operators . . . . .	233
E.3	Special matrices . . . . .	234
E.3.1	Fourier matrix . . . . .	234
E.3.2	Noise matrix or vector . . . . .	234
E.3.3	Reflection and Selection matrices . . . . .	234
E.4	List of Frequently Used Symbols . . . . .	236
E.5	Acronyms . . . . .	238
<b>Bibliography</b>	. . . . .	<b>241</b>
<b>Theses</b>	. . . . .	<b>253</b>

---



## LIST OF FIGURES

1.1	Double directional Direction of Departure (DoD)/Direction of Arrival (DoA) structure of a multipath radio channel. . . . .	3
2.1	Multi-carrier spread spectrum signal in the time and frequency . . . . .	11
2.2	MIMO sounder block diagram . . . . .	13
2.3	MIMO sounder switching time frame . . . . .	14
2.4	Key Features of the sounders used . . . . .	14
2.5	Block diagram of the MIMO sounder . . . . .	16
2.6	Back-to-back calibration setup . . . . .	17
2.7	Characterisation of all RF parts dependent on the AGC level . . . . .	17
2.8	Characterisation of the switched reference attenuator . . . . .	18
2.9	Frequency bin SNR versus Delay bin SNR . . . . .	19
2.10	Maximum achievable signal power and mean noise power ATM vs. HyEff . . . . .	20
2.11	Random walk phase and phase noise correlation . . . . .	22
2.12	Back-to-back calibration setup including external PA and LNA . . . . .	24
2.13	Exemplary LNA characteristic for different input power levels . . . . .	24
2.14	1D circular measurement antenna arrays . . . . .	25
2.15	Reference and application antenna arrays/antennas . . . . .	26
2.16	Planar measurement antenna arrays . . . . .	30
2.17	2D circular measurement antenna arrays . . . . .	30
2.18	Block diagram of an antenna array . . . . .	31
3.1	Spherical coordinate system . . . . .	35
3.2	Geometrical description of the $m$ -th antenna element . . . . .	36
3.3	Simulation layout of a dual polarised patch . . . . .	40
3.4	Periodic radiation pattern . . . . .	40
3.5	Fourier transform of the over-sampled radiation pattern . . . . .	41
3.6	Mean interpolation error of a radiation pattern . . . . .	44
3.7	Radiation pattern interpolation accuracy and time . . . . .	45
3.8	Derivation of the minimum sampling grid <b>UCA<math>1 \times 1 \times 16</math></b> . . . . .	46
3.9	Derivation of the minimum sampling grid <b>PUCPA<math>2 \times 1 \times 24</math></b> . . . . .	47
3.10	Sampling grids for <b>PUCPA<math>2 \times 1 \times 24</math></b> , <b>UCA<math>1 \times 1 \times 16</math></b> and <b>SPUCPA<math>2 \times 4 \times 24</math></b> . . . . .	49
4.1	Block diagram of the antenna array calibration measurement setup . . . . .	53
4.2	Positioning system . . . . .	54

4.3	Dual polarised reference horn antenna . . . . .	55
4.4	Gains of the dual polarised reference horn antenna . . . . .	56
4.5	Cross polarisation discrimination reference horn antenna . . . . .	57
4.6	Frequency dependent gain of the dual polarised reference horn antenna . . . . .	57
4.7	Simulated phase drift over azimuthal scan and 1D EADF . . . . .	60
4.8	Flow chart of the estimation algorithm . . . . .	63
4.9	Radiation pattern reconstruction error and error of estimated phases . . . . .	64
4.10	Standard deviation of the estimated phase . . . . .	64
4.11	Reconstruction error, corrected and uncorrected EADFs of a practical antenna array	65
4.12	Radiation patterns, EADFs, and XPD <b>UCAx1x1x16</b> . . . . .	67
4.13	Cross polarisation discrimination <b>SPUCPAx2x4x24</b> . . . . .	68
4.14	Cross polarisation discrimination <b>PULPAx2x1x8</b> . . . . .	69
4.15	Radiation pattern and EADF <b>SPUCPAx2x4x24</b> . . . . .	70
4.16	Radiation pattern and EADF <b>PULPAx2x1x8</b> . . . . .	71
5.1	Multidimensional specular components data model. . . . .	76
5.2	Dense multipath model in the delay time domain . . . . .	78
5.3	RIMAX block diagram . . . . .	82
5.4	Correlation function for global search applying the minimum sampling grid N95 . . .	84
5.5	Convergence behaviour of SAGE and RIMAX . . . . .	85
5.6	Convergence behaviour of SAGE and RIMAX shown in a cost function . . . . .	86
5.7	Convergence rate SAGE and RIMAX . . . . .	86
5.8	CIR measurement example and parameter estimates . . . . .	87
6.1	Pattern of inverse FIM of a single path and a coherent two path scenario . . . . .	92
6.2	EADFs of of a theoretical and measured CUBA . . . . .	92
6.3	Radiation patterns of a theoretical and measured CUBA . . . . .	93
6.4	CRLB comparison of of a theoretical and measured CUBA for SNR of 25 dB . . . . .	95
6.5	Estimated azimuth variance vs. calculated CRLB . . . . .	96
6.6	Ratio between estimated variance and calculated CRLB . . . . .	97
6.7	Coherent two path scenario measurement setup . . . . .	98
6.8	Azimuth CRLB vs. estimated azimuth variance in a two path scenario . . . . .	99
6.9	Distribution of the ratios $r_q$ in azimuth for a two path scenario . . . . .	99
7.1	Parasitic reflections in the anechoic chamber lateral view . . . . .	105
7.2	Parasitic reflections in the anechoic chamber top view . . . . .	106
7.3	Measured IR and error IR anechoic chamber <b>UCAx1x1x16</b> . . . . .	108
7.4	Illustration of the parameter model accuracy . . . . .	109
7.5	Model accuracy <b>UCAx1x1x6</b> and <b>PULPAx2x1x8</b> . . . . .	111
7.6	Maximum measurable co-elevation angle . . . . .	112
7.7	Positioning system verification measurement setups . . . . .	113
7.8	Radiation patterns and 1D EADFs for positioning system verification measurements	114
7.9	Illustration of the simplified scattering and diffraction model of the positioning system	117

7.10	Undistorted, distorted and measured EADFs PUCPAx2x1x24 . . . . .	118
7.11	Estimated artefacts using the distorted complete or windowed EADFs . . . . .	120
7.12	SRR in case of using the distorted complete or windowed EADFs . . . . .	121
7.13	DoA ambiguity in case of using an ideal ULA . . . . .	124
7.14	Phase over 16 element UCA . . . . .	124
7.15	Estimation results ignoring elevation characteristic PULPAx2x1x8 . . . . .	126
7.16	Estimated artefacts ignoring elevation characteristic PULPAx2x1x8 . . . . .	128
7.17	Estimation results ignoring elevation characteristic UCAx1x1x16 . . . . .	129
7.18	Error of the estimated azimuth and its standard deviation ignoring elevation characteristic UCAx1x1x16 . . . . .	131
7.19	Estimation results ignoring polarisation characteristic of the UCAx1x1x16 . . . . .	133
7.20	Estimated artefacts ignoring polarisation characteristic of the UCAx1x1x16 . . . . .	134
7.21	Wave front curvature for different source distances . . . . .	137
7.22	Antenna position dependent model error for different wave front curvatures . . . . .	139
7.23	Estimation results for different wave front curvatures simulated PUCPA and ULA . . . . .	140
7.24	Estimated artefacts for different wave front curvatures . . . . .	142
7.25	Estimated artefacts when considering wave front curvature during estimation . . . . .	144
7.26	Consequences of long term phase drift with respect to the number of antennas . . . . .	149
7.27	Consequences of long term phase drift for a set of practical antenna arrays . . . . .	150
7.28	Consequences of uncorrelated phase noise for a simulated ULA, UCA, PUCPA . . . . .	151
7.29	Consequences of correlated phase noise in comparison to uncorrelated phase noise . . . . .	152
7.30	Consequences of uncorrelated phase noise for practical antenna arrays dependent on the phase noise standard deviation . . . . .	153
7.31	Consequences of uncorrelated phase noise for a set of practical antenna arrays and the HyEff system as function of azimuth . . . . .	154
7.32	Consequences of uncorrelated phase noise for a set of practical antenna arrays and the HyEff system as function of co-elevation . . . . .	155
7.33	Estimated artefacts as consequence of uncorrelated and correlated phase noise, ATM system . . . . .	156
7.34	Estimated artefacts as consequence of uncorrelated phase noise, HyEff system . . . . .	157
7.35	Consequences of an unsuitable calibrated LNA and system . . . . .	159
7.36	UCAx1x1x16 error chart . . . . .	162
8.1	Illustration of the $\text{SNR}_{\text{IR}}$ of the SC and DMC . . . . .	165
8.2	CDF of relative error in terms of NPCG for an example measurement route . . . . .	168
8.3	3D ray-tracer environment and exemplary impulse response . . . . .	170
8.4	Procedure for the ray-tracing based error analysis . . . . .	172
8.5	Alignment of the application antenna array <b>PPDA</b> related to the Rx moving direction . . . . .	174
8.6	Simulation route and SNR MT12 to MT14 . . . . .	174
8.7	Estimated $\text{SNR}_{\text{IR}}$ of SC and DMC for the measurement route MT12 to MT14 . . . . .	176
8.8	“True” and estimated Rx azimuth power spectra route MT12 to MT14 . . . . .	177
8.9	ECM mismatch of four different estimation setups route MT12 to MT14 . . . . .	178

8.10	Error in terms of capacity for the route MT12 to MT14 . . . . .	180
8.11	Error in terms of NPCG for the route MT12 to MT14 . . . . .	180
8.12	Simulation route and SNR MT59 to MT34 . . . . .	181
8.13	Estimated $\text{SNR}_{\text{IR}}$ of SC and DMC for the measurement route MT59 to MT34 . . . . .	182
8.14	“True” and estimated Rx azimuth power spectra route MT59 to MT34 . . . . .	183
8.15	ECM mismatch of four different estimation setups route MT59 to MT34 . . . . .	184
8.16	Error in terms of capacity for the route MT59 to MT34 . . . . .	185
8.17	Error in terms of NPCG for the route MT59 to MT34 . . . . .	186
8.18	Measurement scenario . . . . .	187
8.19	Portion of SC power . . . . .	188
8.20	Block diagram of the analysis procedure in case of measurements . . . . .	189
8.21	Antenna subset selection from the measurement antenna array . . . . .	190
8.22	Comparison of the $\text{SNR}_{\text{IR}}$ of the SC and DMC in case of measurements . . . . .	192
8.23	Mean capacity error and its standard deviation <b>SC+DMC+Noise</b> . . . . .	193
8.24	Mean capacity error and its standard deviation <b>SC+Noise</b> . . . . .	194
A.1	Phase noise estimation for the ATM and HyEff system . . . . .	203
A.2	Magnitude and phase offset dependent on the Tx power attenuation level for the corrected and uncorrected data . . . . .	204
B.1	Illustration of the calculation of $\mathbf{G}_{\text{K1}}$ to $\mathbf{G}_{\text{K4}}$ . . . . .	206
B.2	Matrices $\Gamma_{13}$ and $\Gamma_{24}$ of antenna array data format . . . . .	209
D.1	Comparison of azimuth standard deviation and relative variance of the path weights for a single path and constant SNR for different arrays . . . . .	219
D.2	Array comparison in case of single path for constant co-elevation and constant transmit power . . . . .	221
D.3	Array comparison in case of single path for constant azimuth and constant transmit power . . . . .	223
D.4	Performance comparison <b>SPUCPAx2x4x24</b> and <b>UCAx1x1x16</b> in terms of azimuth resolution . . . . .	225
D.5	Performance comparison between <b>SPUCPAx2x4x24</b> and <b>UCAx1x1x16</b> in terms of azimuth resolution for different path lengths . . . . .	226
D.6	Array comparison in terms of resolution capability in azimuth . . . . .	228
D.7	Relation between maximum separation error and relative variances . . . . .	229
D.8	Array comparison in terms of resolution capability in co-elevation . . . . .	231
D.9	Relation between $E_{\Delta\phi}$ and $\bar{\sigma}_{\text{Rel}\gamma}$ in the best case in co-elevation . . . . .	232

---

## LIST OF TABLES

2.1	Receiver sensitivity of the HyEff and ATM system . . . . .	20
7.1	Mean model accuracy $\bar{\xi}_{120\text{MHz}}$ in dB for different polarisation combinations and antenna arrays . . . . .	110
8.1	Observation model vs. Estimation model . . . . .	173
C.1	Array Characterisation . . . . .	213

---





# 1. INTRODUCTION

The design of future mobile radio networks (i.e., beyond third generation (3G)) requires research towards new air interfaces which are characterised by highest bandwidth efficiency and unprecedented flexibility. It is commonly understood that radio systems equipped with multiple antennas at both the Mobile Station (MS) and the Base Station (BS) have a huge potential to increase the bit-rates of wireless links. This is possible thanks to a simultaneous transmission of multiple data streams [35]. This multi-antenna technique is called Multiple-Input Multiple-Output (MIMO) and can optimally exploit the spatial diversity of the multiple propagation paths existing in a rich scattering environment. Conceptually, the multipath propagation of the radio channel gives rise to different spatio-temporal signatures for the different transmit data streams, which permits a receiver equipped with multiple antennas to separate those data streams that are otherwise not orthogonal in any of the conventional communication signal dimensions, i.e., in time, frequency, or code. Keeping this in mind, it is not really surprising that the performance of a MIMO system will strongly depend on the radio channel conditions. A key question for a system design and implementation is therefore, whether it is possible to find practically feasible schemes which are sufficiently robust for this task. Another related issue is determining what specific features are required for a practical MIMO system to work reliably under a wealth of various propagation conditions.

## 1.1 State of the Art Channel Modelling and Experimental Channel Characterisation

The thorough investigation of the multidimensional wave propagation mechanisms is a prerequisite for understanding the spatial and temporal structure of the channel transfer function, and thus, for optimum design and realistic performance evaluation of multiple antenna systems. There are many ways to simulate the input-output behaviour of the radio channel. Basically, channel modelling activities can be divided into deterministic and stochastic approaches.

Examples of deterministic modelling are Finite-Difference Time-Domain (FDTD) and ray-tracing. Ray-tracing is a physically motivated approach and is based on electromagnetic wave propagation analysis (e.g. Uniform Geometrical Theory of Diffraction (UTD)) and uses ray-optical models [36–38]. These models can be very exact and can also describe the time variant channel in certain propagation environments [39, 40]. In case of ray-tracing or ray-launching, a detailed database (i.e., a precise description of the environment) and high computation times are required. To balance the complexity of ray-tracing, stochastic modelling approaches for diffuse scattering are proposed in [41–45].

There are also completely statistical models trying to reproduce the input/output behaviour in a statistical sense by formal assumptions of correlation coefficients and distributions resulting at

---

the transmit antenna and receive antenna ports disregarding the geometrical distribution of the reflectors. A disadvantage of these non-geometric models is that they are inherently specific for a certain antenna characteristic.

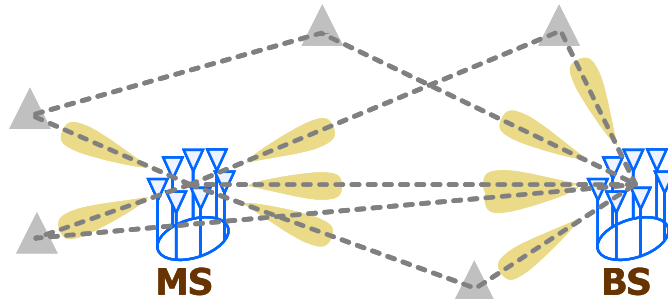
For antenna independent modelling (which allows antenna de-embedding and embedding), geometry based channel models are a must [46]. Hereby, the position and the distribution of the scattering areas are generated according to statistical assumptions. In the European forum for cooperative scientific research COST 259 [47], COST 273 [48], and in standardisation bodies (e.g. 3GPP [49], WINNER [50]) Geometry-Based Stochastic Channel Models (**GBSCM**) were extensively discussed. These models are parametrised based on measurements in typical mobile radio environments. Since the geometry of the propagation environment is taken into account, the influence of the characteristic of the antenna system, such as inter element coupling and polarisation dependent radiation patterns can be included in **GBSCM** based system simulations. Hereby, the directions of the transmitted and received waves need to be considered ([51, 52], Double Directional Channel Model).

Since the complexity of wave reflection, scattering, diffraction, etc. in real propagation environments can never be completely reproduced by electromagnetic simulation and due to the strong simplifications of the statistical approaches, all models have to be verified and/or parametrised by propagation measurements. So called *real-time* channel sounders [53, 54] with huge memory capacity and flexibility in using various antenna arrays are employed for such measurements. Directional channel models can be deduced directly from measurements in real propagation environments estimating the geometric parameters of the paths from the recorded data. Given a ray-optical path model, the parameters normally used to model a propagation path are Direction of Arrival (**DoA**) at the receiver array, Direction of Departure (**DoD**) at the transmitter array, Time Delay of Arrival (**TDoA**), Doppler shift, and the complex polarimetric path weight matrix. Figure 1.1 highlights the double directional structure of the multipath channel. Specifically, a double directional measurement, which includes joint **DoD/DoA** estimation, allows the separation of the directional and polarisation dependent influence of the antennas from the measurements which is a prerequisite of antenna independent channel characterisation. This approach, which has the potential to characterise the radio channel in an antenna independent fashion based on measurements, will be called *Experimental Channel Characterisation*.

A channel modelling approach that is directly based on the results of *Experimental Channel Characterisation* is proposed in [1]. This so called Measurement Based Parametric Channel Modelling (**MBPCM**) is essentially a two-step procedure with an *Experimental Channel Characterisation* step and a follow-up synthesis step. With the estimated path parameters from *Experimental Channel Characterisation* an antenna independent description of the radio channel is given. The synthesis step gives us the flexibility to generate realistic **MIMO** channel transfer functions employing arbitrary application antenna arrays based on the estimated path parameters. However, the estimated path parameters are only valid in a limited area around the original antenna position (during measurement). To cope with this problem the **MBPCM** approach is extended in [55] and additionally to the path parameters (described before), the reflection points of each path are estimated from the results of *Experimental Channel Characterisation*. With the knowledge of the reflection points it is possible to extend the valid area around the original antenna position for the syntheses step

of the MBPCM approach.

Note that ray-tracing, GBSCM, and MBPCM are mainly verified or parametrised via *Experimental Channel Characterisation*. Consequently, the accuracy of these modelling approaches are limited to the accuracy of the *Experimental Channel Characterisation* itself.



**Fig. 1.1:** Double directional DoD/DoA structure of a multipath radio channel.

The radio channel responses can, in general, be observed only within a limited aperture volume which is defined by the array size, frequency bandwidth and temporal observation window. This strictly limits the achievable resolution and accuracy with respect to the angular, delay, and Doppler domain, respectively, when classical non-parametric estimation algorithms are applied. Therefore, *high-resolution* parameter estimation algorithms have to be envisaged to enhance the resolution by fitting an appropriate data model of the radio channel and measurement system to the measured data. Mainly two different methods are discussed in literature [56]: subspace methods like Estimation of Signal Parameters via Rotational Invariance Techniques (ESPRIT) [57, 58], Root-Multiple Signal Classification (MUSIC) [59] and Maximum Likelihood (ML) methods like Space Alternating Generalized Expectation Maximisation (SAGE) [60, 61]. In these cases the radio channel is modelled by a number of specular propagation paths (Specular Components (SC)) that are described by the parameters DoA, DoD, TDoA, Doppler shift, and the complex polarimetric path weights, which are independent from the antennas used during the measurement. The resolution of these parameters is limited by the measurement Signal to Noise Ratio (SNR), antenna and device imperfections, calibration quality, and the limited validity of the model of the measurement system. The angular resolution performance mainly depends on the antenna array architecture and its manufacturing quality, which includes low electromagnetic coupling, high electrical and mechanical stability. In this context, also the definition of the data model is crucial. It has to be accurate enough to represent the wave propagation and the influence of the measurement system. On the other hand, the radio channel model must not be excessively detailed since the amount of information gathered by the MIMO sounder is always limited and may not be enough to estimate all model parameters precisely. A proper choice of the model structure and order can dramatically reduce the algorithmic complexity and enhance the accuracy and resolution as well as the reliability of the results. It was observed that with the specular paths only 20% to 80% of the received channel sounding signal power can be described. To solve this, the ML algorithm RIMAX [2] using a *hybrid* radio channel model was proposed. The word *hybrid* is used to indicate that the radio channel is described by a superposition of SC that result from specular-like reflection and Dense Multipath

Components (**DMC**). Up to now (see [62]) it is assumed that only **SC** which could not be estimated (unresolved **SC**) and distributed diffuse scattering are contributing to the **DMC**. The **DMC** can be described by a few parameters that essentially parameterise an exponential decaying function in the delay domain. Other causes for the **DMC** such as model errors related to the measurement system and *practical* antenna arrays were not considered up to the present.

## 1.2 Drawbacks of the Experimental Channel Characterisation and Motivation

The accuracy and limits of *high-resolution* parameter estimation techniques are commonly evaluated theoretically by computing the Cramér-Rao Lower Bound (**CRLB**), which defines the fundamental limitations on the achievable parameter variance. In most publications (e.g. in [60, 63, 64]), *high-resolution* parameter estimation techniques are verified based on the **CRLBs**, simulated antenna arrays, and synthetic radio channels. It is assumed that white Gaussian measurement noise is the only error source. Furthermore, it is assumed that the model of the antenna arrays and the radio channel data model matches reality exactly. Based on this verification, most of the parameter estimation techniques that are well known from theory are applied in practice in a straightforward manner without further considerations (e.g. in [57, 60, 65–71]). Partially unsustainable assumptions are intentionally or unintentionally made with respect to the measurement systems and parameter estimation models applied. For the measurement systems, e.g., the impact of phase noise or improper calibrated systems are often ignored. For the data models, a common approach is to use incomplete data models (e.g. ignoring full polarisation characteristic and/or elevational characteristic of antenna elements) or to ignore the finite accuracy of the antenna array calibration measurements. Nevertheless, the results of parameter estimation with unsustainable assumptions are used for further processing such as clustering algorithms, channel capacity calculations and parametrisation of **GBSCMs**. Contrary to the above mentioned publications only a few publications are found that at least try to avoid unsustainable assumptions while estimating the radio channel parameters [3, 4, 72, 73] or try to evaluate *practical* antenna arrays based on measurements [74–76]. From the above discussion and from a significant experience with measurement analysis [1–3, 5–20] we observed that the reliability, the accuracy, and the limitations of *Experimental Channel Characterisation* using *high-resolution* parameter estimation techniques are not clearly defined.

This work deals in detail with the limitations of *Experimental Channel Characterisation*. Methods for accurate and efficient modelling and performance evaluation of *practical* antenna arrays are proposed. The entire processing chain is analysed in terms of possible error sources. To this end, measurement system impairments, antenna array calibration errors as well as limitations of the radio channel model applied by the *high-resolution* parameter estimation procedures are investigated. The resulting estimation quality limits are analysed in detail by simulations and measurements. Finally, the impact of parametrisation of the geometry based channel modelling approach **MBPCM** with the results of *Experimental Channel Characterisation* is shown.

The major contribution of the work is a clear answer to five crucial questions:

1. What are the resolution limits of *practical* antenna arrays?
2. How can we obtain reliable estimates of the radio channel parameters from propagation measurements?
3. What are the fundamental limitations of *Experimental Channel Characterisation*?
4. Do the **DMC** result only from unresolved **SC** and distributed diffuse scattering, strictly speaking are they related to the real propagation conditions only?
5. What is the consequence when parametrising geometry based channel modelling approaches in particular **MBPCM** with the results of *Experimental Channel Characterisation*?

The following section illustrates the outline of the work.

### 1.3 Overview and Contributions

**Chapter 2** reviews the most commonly used measurement techniques to characterise a radio channel. Furthermore, it briefly introduces the functionality of the **MIMO** channel sounding systems applied in the measurements discussed in this thesis. The major sources of error when using such measurement systems are emphasised. Measurement setups are proposed for accurate calibration of the applied measurement systems. System parameters such as phase noise, phase drift, and receiver sensitivity are obtained from measurements. These system parameters are especially relevant in terms of reliability and accuracy of the measurement data and define the limits of the *Experimental Channel Characterisation*. The purpose and some basic design considerations of *high-resolution* antenna arrays are discussed. The *practical* antenna arrays used in this work are presented.

**Chapter 3** deals in detail with the efficient and the accurate modelling of measured polarimetric antenna array radiation patterns, which is a prerequisite for an antenna independent description of the radio channel and performance evaluation of *practical* antenna arrays. A novel and analytic description of measured antenna array radiation patterns by means of the Effective Aperture Distribution Function (**EADF**) is proposed. As opposed to other methods, the derivatives of the radiation patterns dependent on the **DoD/DoA** can be easily calculated analytically based on the **EADFs**. It is shown that the proposed **EADF** outperforms the Spline interpolation method as well as the vector spherical harmonics (Vector Spherical Harmonics (**VSH**), [21]) in terms of calculation time by achieving the same interpolation accuracy. The **EADF**'s low computational complexity, the analytic description of the radiation patterns and its derivatives, and the performance advantage is already exploited in several applications such as the IST-WINNER Channel Model [22], IlmProp (geometry-based Multi-User MIMO Channel Modelling tool) [55, 77]) and the **RIMAX** parameter estimation framework [53].

An angular sampling grid with a minimum number of samples for the efficient calculation of the radiation patterns of *practical* antenna arrays is proposed since it is often required for *Experimental Channel Characterisation*. This grid is based on the idea of the **EADF** and fulfils the Nyquist

---

theorem in the angular domain.

Parts of the material dealt in this chapter have been published in [13, 21, 23–28].

**Chapter 4** proposes a full polarimetric two dimensional (2D) array calibration procedure for the accurate measurement of the radiation patterns of *practical* antenna arrays. The procedure involves the calibration of the entire measurement setup by means of the MIMO channel sounder, the dual polarised reference horn antenna, and all devices in the Radio Frequency (RF) signal path that do not correspond to the antenna array under test.

Due to the employment of a MIMO channel sounder, we have to cope with a varying phase offset during the 2D antenna array calibration measurement time of several hours (with a Network Analyser (NWA) it would be several days!). These phase offsets prohibit the direct derivation of the EADF model from measurements. A novel gradient based ML estimation algorithm is proposed to correct the measured radiation patterns for the collective phase offset, which consequently allows the accurate derivation of the EADF model.

Applying both the array calibration procedure and the correction for the phase offset the radiation patterns and their EADFs for three different array types are discussed. With this discussion the necessity of accurate full-polarimetric 2D array calibration for *Experimental Channel Characterisation* and channel modelling is emphasised.

The authors’s contribution related to some of the topics of this chapter has been published in [29].

**Chapter 5** reviews the radio channel model applied for the gradient based ML parameter estimation framework RIMAX. The theory of this framework was developed in cooperation with Andreas Richter [62]. In this work the practical implementation of the RIMAX for arbitrary *practical* antenna arrays and measurement environments was carried out. For the RIMAX implementation, a deep knowledge in estimation theory and handling of measurement data was required.

The radio channel model of the RIMAX comprises two components, the specular (SC) and the dense multipath components (DMC). The SC result mainly from specular-like reflections and the DMC are assumed as unresolved SC and distributed diffuse scattering. As opposed to other parameter estimation algorithms this *hybrid* model preserves the balance between the maximum information we can gather from measurements and the number of estimated parameters. Further advantages of the RIMAX e.g. the convergence also in the presence of closely spaced propagation paths and the internal reliability check of the estimated paths during the iterative estimation process are highlighted.

However, the drawback of most parameter estimation frameworks is that the impact of error sources other than additive Gaussian measurement noise are neglected. The fundamental limitations of the data model used for parameter estimation with respect to the *practical* measurement system and *practical* antenna arrays is briefly introduced.

Own contributions related to the topics of this chapter have been published in [2, 8, 9, 13, 30, 31].

**Chapter 6** deals in detail with a powerful framework for the performance evaluation of *practical* antenna arrays with respect to their angular resolution limits. The framework is based on



the calculation of the **CRLB** of the parameters of the **SC**. The method can provide information about the **DoD/DoA** resolution limits of multiple propagation paths and its parameter variances. As opposed to other publications the framework is applicable to any *practical* antenna array. The advantage of the **EADF** model using the measured radiation patterns including all imperfections of the antenna array is hereby exploited. Time consuming performance evaluation measurements other than the antenna array calibration become unnecessary with the proposed framework.

For the verification of the proposed antenna array performance evaluation framework, the *simple single path* and *coherent two paths scenario* (considering worst and best case phase constellations between the two paths) are measured with a *practical* antenna array in the anechoic chamber. The results of the measurement and parameter estimation are compared with the theoretical calculated **CRLB** of the applied *practical* antenna array. With this verification the capability of the proposed performance evaluation framework is clearly shown.

Parts of the material dealt in this chapter have been published in [23, 24, 26–28].

**Chapter 7** explores the major causes of mismatch between the model of the **SC** applied by the parameter estimator and the “real” radio channel. The investigations were initiated by the observation of partially implausible estimation results that were found analysing a wide range of measurements.

A distinction is made between model mismatch related to the antenna arrays:

- bias related to quality of antenna array calibration,
- bias related to incomplete data models

and model mismatch related to the measurement system:

- consequences of phase noise,
- consequences of a unsuitable calibrated measurement system.

The proprietary parameter estimator **RIMAX** is used to demonstrate the consequences of the different error sources in case of the *simple single path scenario*. Notice that the results can be generalised, as any **ML** parameter estimator using the same data models would render similar results.

It is shown that the use of an inaccurate/simplified data model inherently will result in biased and/or artificially spread angular estimates. It is not inconceivable that the popular approach of clustering multi-paths components for channel modelling is spurred by the artefacts resulting from data model choices as described in this chapter.

For some antenna array types and error sources, estimation bias is even unavoidable, irrespective of the used data model. But for some error sources solutions are highlighted to correct/avoid model mismatch and to reduce the consequences of inaccurate/simplified data models.

Parts of the author’s contribution given in this chapter have been published in [18, 32, 33].

**Chapter 8** deals with the overall consequences of *practical* measurement systems, *practical* an-

---

tenna arrays, and unavoidable model errors on *Experimental Channel Characterisation* in complex propagation environments. It is shown that the estimated **SC** are most reliable (in well defined limits) if the **DMC** estimation is incorporated in the estimation framework. As opposed to the estimated **SC**, the estimated **DMC** are partially unreliable or can not be considered as feature of the radio channel. Especially for measurements with a maximum **SNR** of the impulse response higher than the overall accuracy of the model of the measurement system and antenna arrays, the estimated **DMC** describe mainly model error. Thus, the **DMC** can not be assumed as unresolved **SC** or distributed diffuse scattering only. In this case they are not related to the propagation conditions of the measured environment. Nevertheless it is shown that the estimated **DMC** are reasonable if the maximum **SNR** is lower or equal to the overall model accuracy. In this case the estimated **DMC** are related to the “real” propagation.

The results are of crucial importance when parametrising **GBSCMs** with the estimated **SC** and **DMC** of *Experimental Channel Characterisation*. Based on the **MBPCM** approach and the calculation of the error of **MIMO** channel diversity metrics it is shown that:

- in case of measurement **SNRs** higher than the overall model accuracy, the error increases drastically if additionally to the **SC**, the **DMC** are assumed as feature of the measured channel, consequently the **DMC** have to be discarded when parameterising the **MBPCM** approach,
- in case of measurement **SNRs** lower or equal to the overall model accuracy, the error is acceptable if both the **SC** and the **DMC** are assumed as feature of the measured channel.

Some topics dealt in this chapter have been published in [4].

**Chapter 9** summarises the key issues covered in this work, emphasising their impact on the international scientific community.

---



## 2. CHANNEL MEASUREMENT

Several techniques exist to characterise the mobile radio channel based on measurements. In Section 2.1 an overview of existing measurement techniques are given, discussing their advantages and disadvantages. The preferred measurement method of this thesis is based on the MIMO channel sounding technique, which is discussed in Section 2.2. The measurement systems that were used for channel measurements presented in this work are introduced in Section 2.3. General and also system specific properties of these kind of measurement devices are discussed. As the results of any measurement analysis procedure will be affected by the analysed system properties, such as measurement noise, phase noise, etc., this discussion is of major importance in this thesis. The purpose and the basic construction of the high resolution antenna arrays used in this thesis are presented in Section 2.4.

### 2.1 Channel Measurement Techniques

From a historical perspective, the first sounding experiments have been carried out using single tone Continuous Wave (CW) signals [78]. This was appropriate as long as only the narrow-band channel behaviour was of interest. Single tone CW sounding, however, gives us no information to resolve path time delays. To this end, we need a frequency domain bandwidth, which is roughly the inverse of the desired delay resolution. Sequential sounding at a number of different frequencies is the easiest approach to achieve even very high delay resolution, since standard vector network analyser techniques can be applied. The drawback is the resulting huge measurement time, which precludes mobile measurements. The only solution to this problem is to keep the environment fixed during one series of frequency sampling measurements. This actually has its equivalent in sequential sampling of the antenna array geometry and may be considered as an equivalent to the synthetic antenna aperture approach in the frequency domain. Sustained measurement along some longer trajectory is clearly prohibitive. Network analyser application also requires a direct cable connection between Transmitter (Tx) and Receiver (Rx) sites.

Short duration repetitive pulses together with envelope detectors have been used in early broadband real-time sounding experiments [78]. The main drawback of this method is the high peak-to-mean power ratio at the transmitter and only power delay profiles can be measured. To achieve the maximum SNR at the receiver, excitation signals with a minimum crest factor are required. The crest factor is given by the ratio of the peak value of the signal to its root mean square (r.m.s.) amplitude. Minimum crest factor signals are distinguished by a constant magnitude envelope in the time domain. At the same time, they must have a constant spectrum, which leads to a short autocorrelation function. This pulse compression approach is well known from spread spectrum technology and makes these signals very useful for real-time identification of time delay systems

---

since all frequencies are instantaneously excited and a considerable SNR processing gain is achieved in the time domain by correlation processing.

Pulse compression requires noise-like structured signals. Periodic pseudo-random excitation signals are of special importance since they can be processed in integer periods. The time-period must be at least as long as the maximum path excess time-delay  $\tau_{\max}$  to avoid TDoA ambiguities. With a maximum delay-Doppler spreading factor  $S = \tau_{\max}B_{\max}$  of a typical mobile radio channel well below 0.01, the period of the received time-variant channel response signal is still almost the same as of the excitation signal. This presumes that the minimum signal period time is chosen. Then, the channel output can be transformed to the frequency domain by Discrete Fourier Transformation (DFT)/Fast Fourier Transformation (FFT) processing without any significant leakage variance.

Probably, the most well known examples of these excitation signals are periodic Pseudo Random Bit Sequence (PRBS) [79]. PRBS can be very easily generated by a shift register since only digital circuits are required. This makes it possible to generate broadband excitation signals, even suitable for ultra-wideband sounding [80]. Another advantage of PRBS is that they can be repeated in the receiver with a slightly slower clock rate. This is applied in the classical swept time-delay cross-correlation sounder implementation as originally proposed by Cox [78]. This “sliding correlation” sounder requires only slow AD converters. The disadvantage of this principle, working sequentially in delay, is again the long measurement time which prohibits real-time operation.

The shape of the power spectrum of PRBS follows a  $[\text{sinc}(\cdot)]^2$  function. For system identification purposes it can only be used up to a frequency of about  $0.4f_c$ ,  $f_c$  being the clock rate [81]. Even though the spectrum decays rather slowly, a very high sampling rate or a suitable anti-aliasing filter at the receiver are required to avoid aliasing. Moreover, the system under test is excited in a frequency band which is not used. This effectively wastes transmit power. Most experimental transmit spectrum permissions given by regulation authorities will require strict band-limited spectra. Then, the signal must be filtered at the transmitter to remain within a finite bandwidth. Any filtering and phase slope modification, however, will increase the crest factor of the PRBS, which is supposed to be unity in the ideal case.

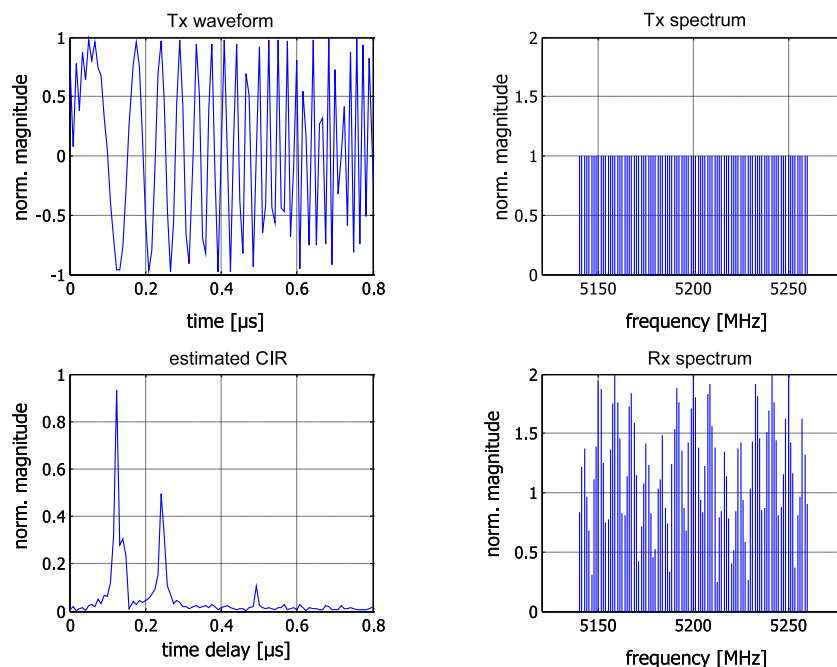
A much more flexible excitation signal concept is known as the *periodic multi-sine signal*. This approach is well known from frequency domain system identification in measurement engineering [81]. In communication engineering this signal may be called a Multi-Carrier Spread Spectrum Signal (MCSSS). The MCSSS is defined by its complex Fourier coefficients  $X(\mu\Delta f)$ :

$$x(nt_0) = \sum_{\mu=0}^{N-1} X(\mu\Delta f)e^{j2\pi\mu n/N}, \quad (2.1)$$

with  $t_p = Nt_0 = 1/\Delta f$ . Once designed in the frequency domain, the corresponding time domain waveform  $x(nt_0)$  is stored in an arbitrary waveform generator memory and periodically transmitted at the Tx. Therefore, it includes all the advantages which are discussed above for periodic signals. The difference in comparison to PRBS is that phases and magnitudes of  $X(\mu\Delta f)$  can be arbitrarily chosen in order to optimize the system performance. As an example, in Fig. 2.1 a MCSSS excitation signal with uniform power spectrum is shown. The phases of the Fourier coefficients are chosen

to minimize the crest factor of the signal waveform. Although a quadratic phase slope typically results in a crest factor below 2, numerical optimization can even further reduce the crest factor to about 1.4. Another advantage of this signal design is that analogue hardware phase distortion (e.g. from the filters) and even non-linear distortion (from the power amplifier) can be mitigated. This means that a predefined ideal transmit signal is iteratively pre-distorted throughout a calibration procedure where the real output signal is measured and optimised.

Regarding the overall spectral shape, the main advantage of MCSSS is its “brickwall-type” shape, which allows us to concentrate the signal energy precisely into the band of interest. This is also possible for multiple bands. One exemplary application is FDD sounding which means that the sounder simultaneously excites both the up-link and the down-link band. Note that the desired full flexibility of the excitation signal requires quadrature up-conversion at the transmitter. At the



**Fig. 2.1:** Broadband multi-carrier spread spectrum signal (MCSSS) in the time and frequency domain (top row) and estimated CIR and received signal spectrum (bottom row)

receiver side the signal is filtered, down converted, and demodulated via a quadrature demodulator. An efficient architecture is based on low IF analogue down conversion, IF sampling and final digital down conversion. For example for a bandwidth of 240 MHz, 160 MHz IF frequency and 640 MHz ADC sampling rate is adequate. For real-time processing, Nyquist sampling at the receiver in most cases is a must. One integer period of the received time-variant channel response  $y(t, nt_0)$  is sampled and transformed into the frequency domain by FFT processing. The final quadrature down conversion is accomplished by cyclic FFT-shifting of the result, which finally gives the baseband representation  $Y(t, \mu\Delta f)$  of the received signal. In case of multipath transmission, frequency selective fading as shown for example in Fig. 2.1(bottom row, right) shapes the power spectrum of the received signal. An estimate of the time-variant channel frequency response is calculated from

input-output cross correlation as:

$$\mathbf{H}(t, \mu\Delta f) = \frac{\mathbf{Y}(t, \mu\Delta f)\mathbf{X}^*(\mu\Delta f)}{|\mathbf{X}(\mu\Delta f)|^2} = \frac{\mathbf{Y}(t, \mu\Delta f)}{\mathbf{X}(\mu\Delta f)}. \quad (2.2)$$

The uniform shape of the excitation signal spectrum and its low crest factor at the transmitter maximises the SNR. With integer period data acquisition there is no additional estimation variance resulting from leakage noise [81]. Therefore, the required data acquisition time is minimal and the estimation variance is as small as possible. With Nyquist sampling at the receiver, the highest possible measurement repetition rate for a channel with a maximum excess time-delay  $\tau_{\max}$  can be achieved, namely  $1/\tau_{\max}$ . The lower limit is given by the Doppler bandwidth  $B_{\max}$ . It results from the Nyquist sampling criterion of the fast fading channel response. However, since the delay-Doppler spreading factor  $S = \tau_{\max} \cdot B_{\max}$  of a typical mobile radio channel is well below 0.01, there are large gaps allowed between successive measured channel response functions without sacrificing the Nyquist criterion. Normally, there is no need to measure faster since additional CIRs (which may be required for link level simulation) can always be calculated via bandlimited interpolation. Nevertheless, faster measurement speed may be desirable if we aim at further noise reduction by synchronous averaging of a temporal sequence  $\mathbf{y}(t, nt_0)$ . Only when the averaging window approaches or exceeds  $1/B_{\max}$  would this act as a Doppler low-pass filter and potentially suppress fast fading.

Fig. 2.1 shows the impulse response which would result from an inverse Fourier transform of  $\mathbf{H}(t, \mu\Delta f)$ . Calculating the impulse response in this way requires a tapering window function in the frequency domain, which effectively wastes measured data and, hence, reduces the SNR and limits the resolution. A better choice is to use  $\mathbf{H}(t, \mu\Delta f)$  as an observation vector in the frequency domain for *high-resolution TDoA* parameter estimation described in Section 5.  $\mathbf{H}(t, \mu\Delta f)$  represents the sum-of-exponentials model describing the delay spectrum. A second frequency domain dimension can be constructed from time-limited sections of the observed sequence  $\mathbf{H}(t, \mu\Delta f)$  with the sum-of-exponentials in  $t$  describing the Doppler spectrum. The 2D Fourier transform approximates the joint delay-Doppler frequency response. A Single-Input Single-Output (SISO) sounder just relies on this principle.

## 2.2 MIMO Channel Sounding Measurement Technique

A MIMO channel sounder measures the channel response matrix between all  $M_{\text{Tx}}$  antennas at the transmit side and all  $M_{\text{Rx}}$  antennas at the receiver side. This could be carried out by applying a parallel multiple channel transmitter and receiver. True parallel systems are not only extremely expensive, they lack also of versatility (when considering changing the number of antenna channels) and are susceptible to phase drift errors. Moreover, parallel operation of the transmitter channels would cause additional problems, as the  $M_{\text{Tx}}$  transmitted signals have to be separated at the receiver. A much more suitable sounder architecture is based on switched antenna access. A switched antenna sounder contains only one physical transmitter and receiver channel. Only the antennas and the

switching channels are parallel. This reduces the sensitivity to channel imbalance. As an example for such a sounder architecture the simplified block diagram of the sounders used in this thesis is given in Fig. 2.2.

Fig. 2.3 shows the switching time frame [78] of the sequential MIMO sounders used, where antenna arrays at both sides of the link are present. Any rectangular block in the figure represents one period of the transmit/receive signal. Synchronous switching at the Rx and Tx is required in order to clearly assign the received signal periods to any input-output combination of the channel matrix. Timing and switching frame synchronisation is established during an initial synchronisation process prior to measurement data recording and must be maintained over the complete measurement time even in the case of remote operation of Tx and Rx. This is accomplished by rubidium or caesium reference oscillators at both Rx and Tx. The total snapshot time length is now given by  $t_s = 2\tau_{\max}M_{Tx}M_{Rx}$ , where  $M_{Tx}$  and  $M_{Rx}$  are the number of antennas at the Tx and the Rx site, respectively. The factor two comes from the blank period inserted at the receiver after every period acting as a guard interval to avoid switching transients. Similar to Orthogonal Frequency Division Multiplex (OFDM), this Complex Impulse Response (CIR) estimation principle relies on a periodic signal model for excitation and reception. Therefore, the guard interval has to cope with the channel and the device response. For some signal processing operations based upon the recorded data, it may be a disadvantage that the antenna channels are not sampled at strictly the same time instant. If the maximum Doppler bandwidth for real-time sounding is less than  $1/t_s$ , the antenna channels can be individually interpolated resulting in MIMO channel responses with aligned sampling time for all channels.

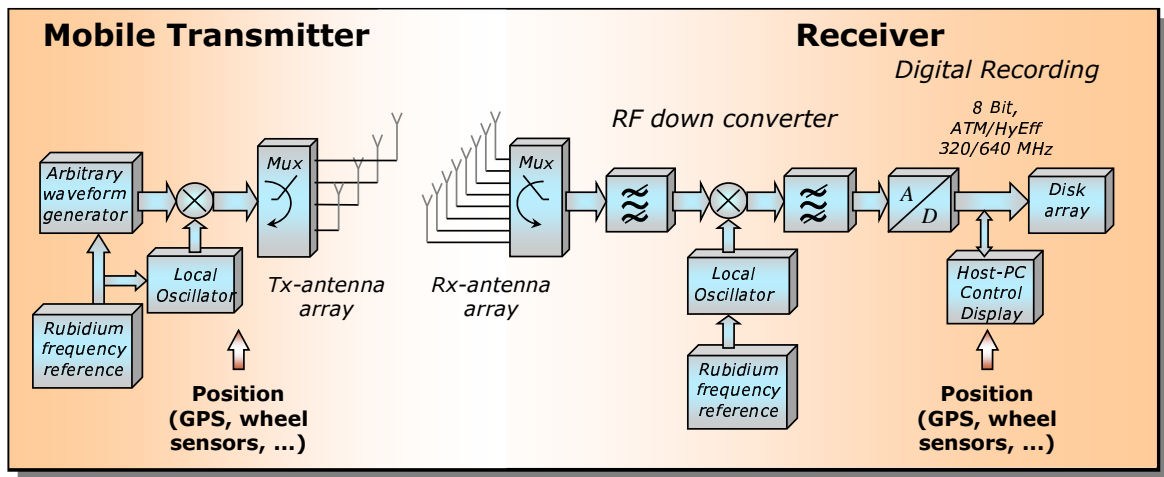


Fig. 2.2: MIMO sounder block diagram

### 2.3 Detailed Configuration of the Applied MIMO Sounder Systems

In this subsection, the two MIMO sounders used are described. The sounders were developed in cooperation with the company MEDAV GmbH [53] under the BMBF (Federal Ministry of Education and Research) projects ATMmobile (Broadband Mobile Multimedia Communication using ATM) and HyEff (High Spectral Efficiency Mobile Networks). Therefore, in the following discussion the

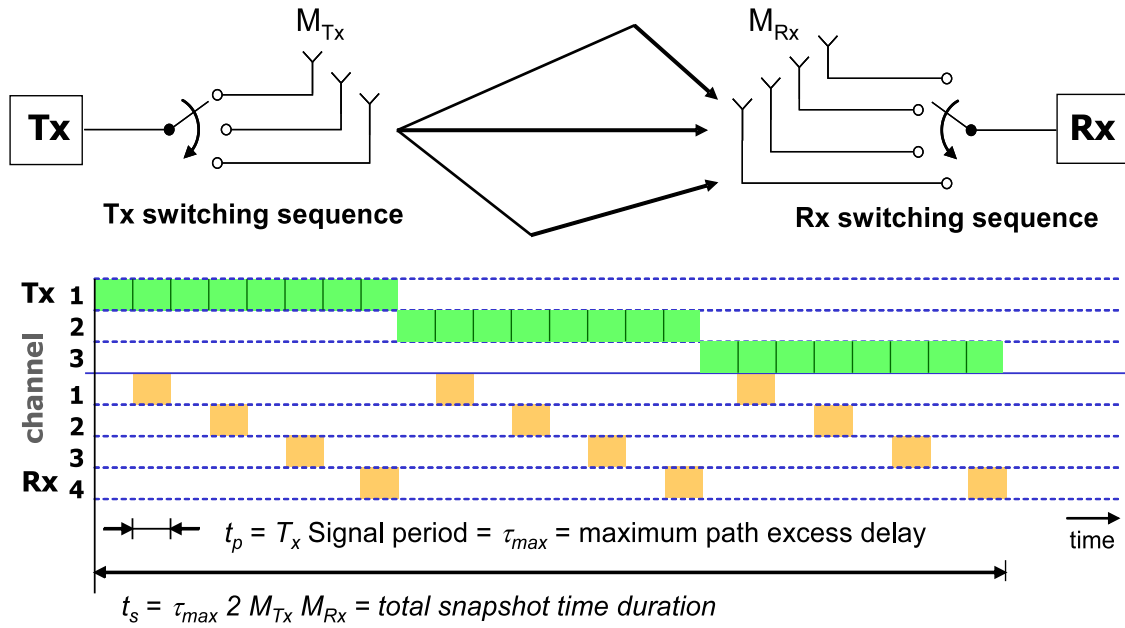


Fig. 2.3: MIMO sounder switching time frame

sounders will be called ATM and HyEff, respectively. Both systems are based on the MIMO channel sounding technique described in the previous section. However, they differ in terms of the practical realisation. The resulting key features of the two sounders are compared in Fig. 2.4. In Fig. 2.5, a

Sounder Name	Carrier frequency [GHz]	Bandwidth [MHz]	Maximum multipath delay [μs]	Tx power [W]	Repetition time [ms] at 6.4μs IR length	AGC switching per Antenna Channel & AGC dependent back-to-back System Calibration available	Internal LNA permanently connected	Tx picture	Rx picture
HyEff	5.2	240	$\Lambda^*0.8$ with $N_{max}=16$	2	.0128	Yes	No		
ATM	4.5 / 5.2	120	$\Lambda^*0.8$ with $N_{max}=16$	0.5 / 2 / 10	24.58	No	Yes		

Fig. 2.4: Key Features of the sounders used

block diagram of the **MIMO** sounders used is shown. The **RF** parts are indicated with black colour and the **RF** signal flow is indicated by black arrows. The **RF** signal path includes the up converter at **Tx**, the **Tx** Power Amplifier (**PA**), the internal Low Noise Amplifier (**LNA**) at the **Rx**, and the Radio Frequency Tuner (**RFT**) at the **Rx**. The **RFT** is a complicated system of multi-level down converters, controllable attenuators, and amplifiers. The attenuators and amplifiers at the receiver are controlled by the Automatic Gain Control (**AGC**) to ensure maximum signal level throughout the receiver chain from the antenna to the analogue digital converter (**ADC**) input. At the same time it avoids overloading. The **AGC** covers a range of 0 dB to 51 dB in steps of 3 dB. The **AGC** setting is implemented on the basis of instantaneous peak value estimation. To avoid uncontrolled transients, the **AGC** timing control is synchronised to the **MIMO** switching time frame (Fig. 2.3). If low received signal power is expected, the internal **LNA** can be used (**RF** switch setting ①). Note that in case of the ATM system, the internal **LNA** is always included in the **RF** signal path. In case of the HyEff system the internal **LNA** can be excluded by selecting the input **RF In** (**RF** switch setting ②). The input **RF In** can handle a larger input power than the input **RF In LNA**. This means that additional external **LNAs** may be used, when connected to the input **RF In**.

The golden parts in Fig. 2.5 are related to the 10 MHz clock signal distribution, which is provided from the rubidium references included in the **Tx** and **Rx**. The transmission of the *periodic multi-sine signal* (arbitrary wave form generator), the MUX switching control at **Tx** and **Rx**, the **AGC** at the receiver, and the **ADC** are synchronised to the 10 MHz clock signals. Consequently, the synchronisation of the **Tx** and **Rx** clock signals in remote operation mode are an important issue and will be discussed in Section 2.3.1.

Section 2.3.2 is related to back-to-back calibration. Back-to-back calibration means, that the overall system frequency response is measured and stored for equalisation purposes. The **Tx** and **Rx** are directly connected via a reference attenuator. The calibration includes the absolute device power gain as well. This is achieved throughout the back-to-back calibration when operating the transmitter with its nominal output power to the reference attenuator. For a calibration of the system for a certain **AGC** level, the input power at the receiver is adjusted by the reference attenuator. Therefore, the reference attenuator is a switched reference attenuator. The attenuation can be varied in the range of 0 dB to 120 dB. In case of the HyEff system, the attenuation settings are software controllable, whereas it is only manually adjustable in case of the ATM system. Based on the given system designs, two back-to-back calibration procedures will be considered: a back-to-back calibration for only one **AGC** level (ATM) and an **AGC** dependent back-to-back calibration (HyEff). **AGC** dependent back-to-back calibration indicates the measurement and storage of the overall system frequency responses for all possible **AGC** levels.

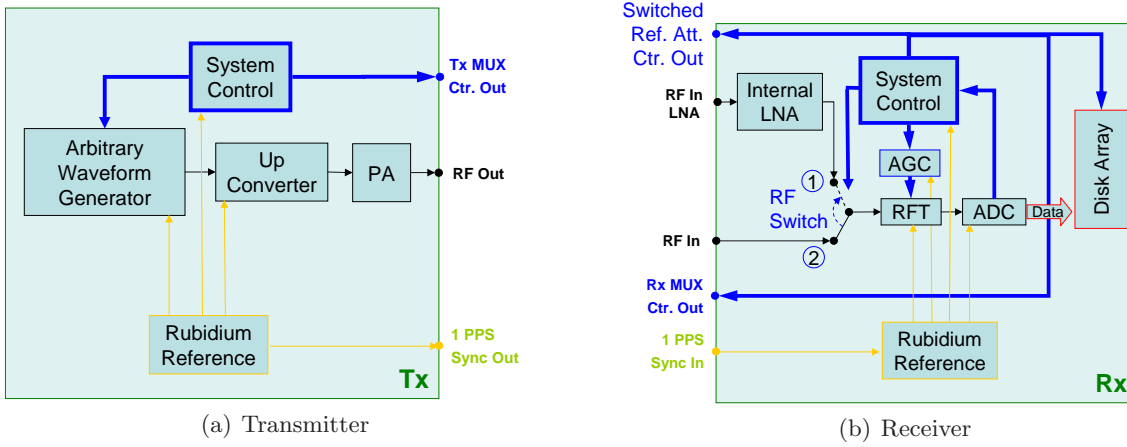
Further considerations concerning the hardware operation of the sounder systems refer to receiver sensitivity (Section 2.3.3) and phase noise (Section 2.3.4).

If external amplifiers are used, their arrangement in the **RF** signal path is crucial for the back-to-back calibration and measurement. Therefore, different arrangements are discussed in Section 2.3.5.

Note that all topics discussed here are directly related to the achievable quality of measurement



based channel characterisation using parameter estimation schemes and are therefore of crucial importance in most chapters of this thesis.



**Fig. 2.5:** Block diagram of the transmitter and receiver of the MIMO sounders used. Control units are in blue, RF parts in black, and golden parts are related to the 10 MHz clock signal distribution.

### 2.3.1 Tx/Rx Synchronisation in Remote Operation

Remote operation means that there is no synchronisation link applied between **Tx** and **Rx**. In this case, distinct rubidium reference sources at both **Tx** and **Rx** are required and the Local Oscillator (LO) signals have to be generated at both sides. This makes a sounder fundamentally different from a standard network analyser. The synchronisation of the **Tx** and **Rx** clock signals is achieved by manual or automatic (1 PPS synchronisation signal) adjustment of the two separate rubidium frequency references. This synchronisation normally takes place before the back-to-back system calibration is carried out. The synchronisation has to be maintained throughout the whole measurement cycle. For **DoD/DoA** estimation, full coherent operation is necessary during the snapshot period  $t_s$ . If we aim at Doppler estimation or if a sequence of snapshots is to be averaged for **SNR** enhancement, the period of coherent operation must be extended to multiples of  $t_s$ . This sets the limits for phase noise parts (see also Section 2.3.4) having a coherence time below this time interval. However, a long term phase drift can normally be accepted as long as the reference offset is smaller than the specified Doppler bandwidth. A small reference frequency offset would be measured as a respective Doppler shift. Note that for specific measurements, such as antenna array calibration measurements, a coherent operation period of several hours is necessary, which may require a direct **Tx/Rx** synchronisation by cable (Section 4.1).

### 2.3.2 Back-to-Back Calibration

As already mentioned in the previous section, two calibration procedures will be considered: 1. the back-to-back calibration for only one **AGC** level and 2. the **AGC** dependent back-to-back calibration. In Fig. 2.6 the back-to-back calibration setup for both procedures is shown. Note that for the HyEff system both procedures can be applied, whereas the ATM system is limited to the



first one. For the first back-to-back calibration procedure, all frequency responses of a measurement

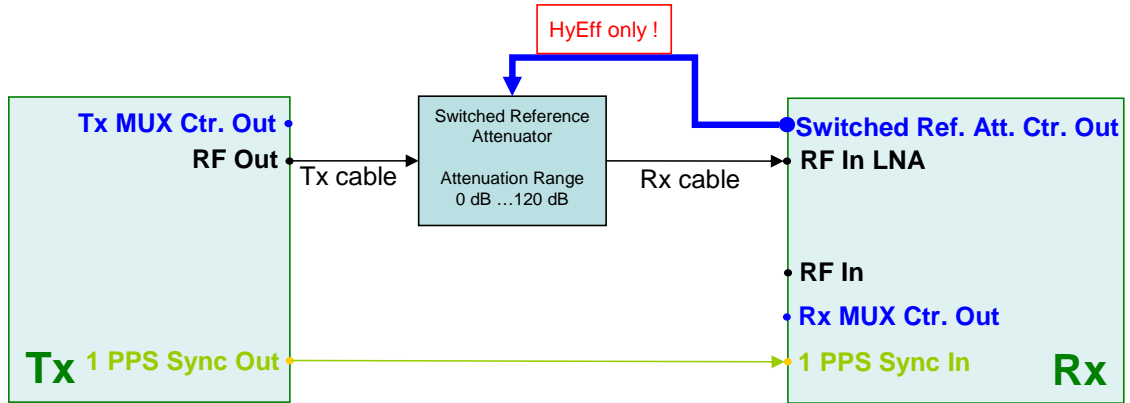
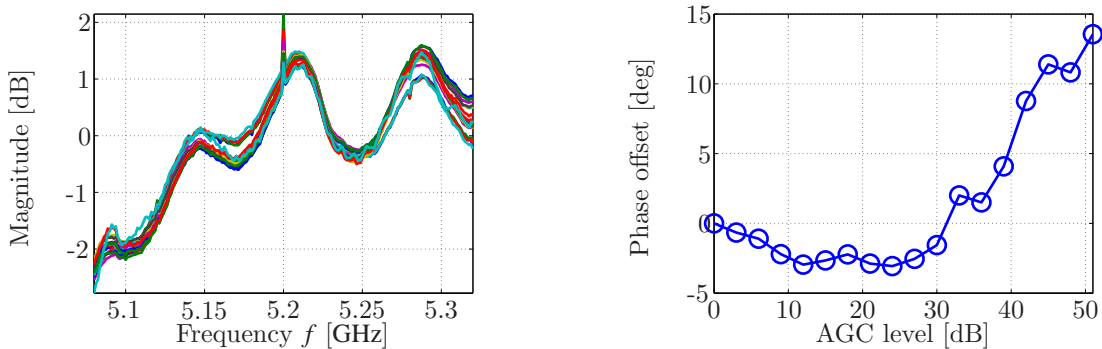


Fig. 2.6: Back-to-back calibration setup

campaign will be equalised with the same system frequency response, because from the calibration only a single frequency response for a fixed **AGC** level is available. The magnitude is corrected with the nominal **AGC** level which is set during measurement, but the system frequency characteristic in terms of phase and magnitude changes between the different **AGC** levels is ignored.

If the second procedure is applied, then each frequency response measured is equalised with the corresponding system frequency response for **AGC** level set.

Let us discuss the consequence of each calibration procedure by analysing the system frequency responses for the different **AGC** levels. For each **AGC** level, a unique chain of amplifiers and attenuators in the RFT are linked by the **AGC**. Therefore, the frequency response depends on the **AGC** level. In Fig. 2.7(a) the magnitude of the frequency responses normalised to the corresponding nominal **AGC** levels are shown. The differences in magnitude for different **AGC** levels are almost negligible. On the contrary, the combination of the attenuators for different **AGC** levels results in a different electrical length of the receiver chain, the phase offset between the different **AGC** levels is significant (see Fig. 2.7(b)). For **DoD/DoA** estimation, the phase differences between the different

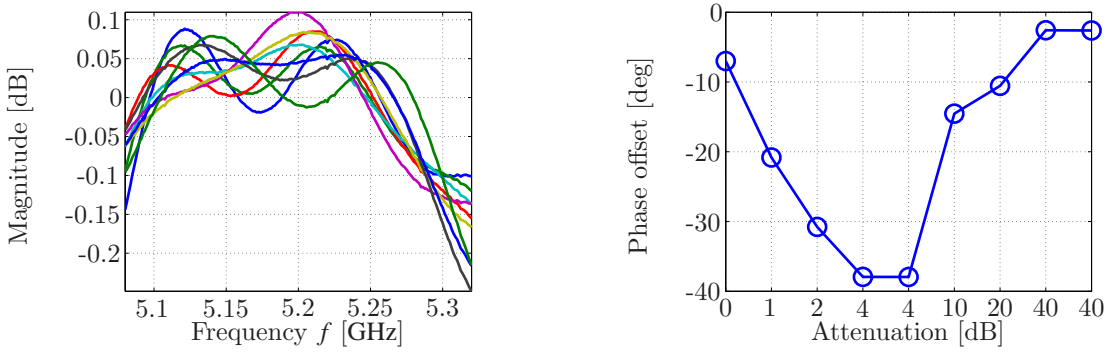


(a) Magnitude of the system frequency responses for different **AGC** levels normalised to their nominal **AGC** levels (denoted by different colours).

(b) Phase offset dependent on the **AGC** level

Fig. 2.7: Joint characterisation of all RF parts dependent on the **AGC** level set (HyEff system)

antenna channels are used. Consequently, the first calibration procedure calibrating only one **AGC** level is acceptable only when the **AGC** level is fixed while measuring all antenna channels in one snapshot. Thus, the phase offset is the same for all antenna channels and the **DoD/DoA** can be estimated correctly. The disadvantage of the fixed **AGC** setting becomes obvious especially when the received power strongly varies depending on the measured antenna channels. As the **AGC** level is adjusted to the peak power over all channels, the channels with a lower received power will be measured with a significantly worse **SNR**. On the other hand, if the **AGC** level is set for each channel and the stored complex frequency responses of the **AGC** dependent back-to-back calibration are used for equalisation, then all channels are measured with the same **SNR**. Consequently, the second calibration procedure is preferable. Nevertheless, if the back-to-back calibration setup described in



(a) Magnitude of the frequency responses of the switched reference attenuator normalised to the set nominal attenuation

(b) Phase offset dependent on the set attenuation of the switched reference attenuator

**Fig. 2.8:** Characterisation of the switched reference attenuator

Fig. 2.6 is used to obtain the system frequency responses for each **AGC** level, then it has to be taken into account that also the switched reference attenuator has different electrical lengths dependent on the attenuation set. Therefore, the measured system frequency responses have to be corrected accordingly. Appendix A.2 shows the characteristics of the switched reference attenuator and the consequence of ignoring them in the **AGC** dependent back-to-back calibration.

### 2.3.3 Receiver Sensitivity

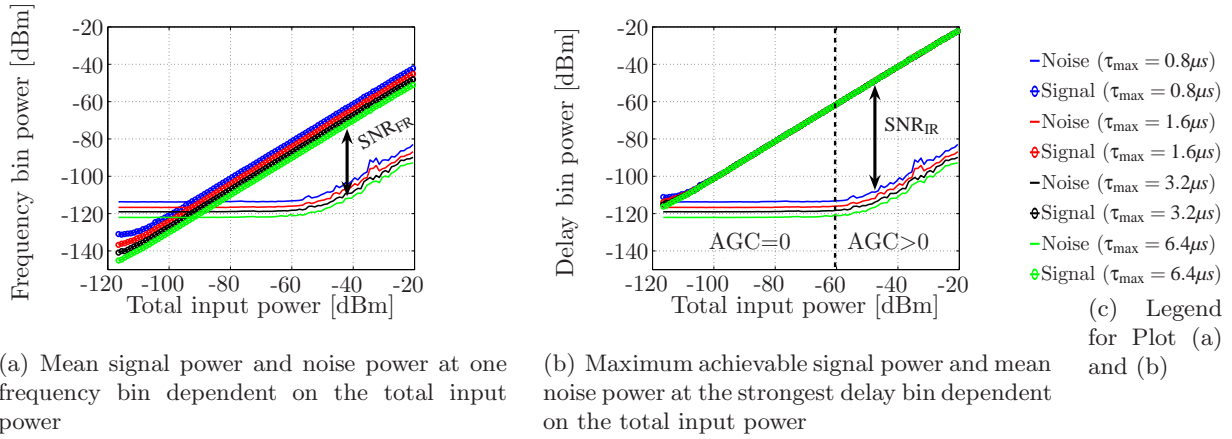
The sensitivity  $S$  in a receiver is normally defined as the minimum input signal power required to produce a specified output signal having a certain signal-to-noise ratio ( $\text{SNR}_{\min}$ ):

$$S = P_{\text{N}} \cdot \text{SNR}_{\min} \cdot F, \quad (2.3)$$

where  $F$  is the noise figure of the receiver and  $P_{\text{N}}$  the measurement noise power at the input of the receiver (related to the thermal noise of the source resistor). The noise power is defined as:

$$P_{\text{N}} = k_{\text{B}} \cdot T \cdot B \quad (2.4)$$

where  $k_B = 1.3806505 \cdot 10^{-23} \text{ J/K}$  is the Boltzmann's constant,  $T$  is the resistor's absolute temperature in Kelvin and  $B$  is the bandwidth in Hz. In case of the MIMO channel sounder different definitions of the desired SNR can be applied. One could ask for a certain  $\text{SNR}_{\text{FR},\text{min}}$  at one frequency bin or alternatively, for the  $\text{SNR}_{\text{IR},\text{min}}$  in the delay domain. The latter can be defined as the ratio between the peak power and mean noise power in the Impulse Response (IR). Note that the  $\text{SNR}_{\text{IR},\text{min}}$  also includes the correlation gain, which is related to the number of frequency bins  $M_f$  used during the measurement. Using the back-to-back calibration setup shown in Fig. 2.6, the receiver sensitivity of



**Fig. 2.9:** Mean signal and noise power at one frequency bin (a) in comparison to the maximum achievable signal power and noise power at one delay bin (b) for different impulse response lengths  $\tau_{\text{max}}$  (Hyeff system using internal LNA)

the Hyeff system (including and excluding the internal LNA) can be determined. This means that the switched reference attenuator is used to vary the total input power at the receiver. For both MIMO channel sounders used, the total transmitted power in the fixed frequency band of 120 MHz is constant, even when the number of used frequency bins  $M_f$  in this band is changed to adjust the maximum length of the impulse response  $\tau_{\text{max}}$ . Consequently, the mean signal power at one frequency bin for a small  $M_f$  is higher than in case of a larger  $M_f$ . However, with a decreasing  $M_f$  (decreasing  $\tau_{\text{max}}$ ) in the fixed band of 120 MHz the mean noise power at one frequency bin increases as the noise bandwidth which is related to the distance between two frequency bins increases. Thus, the mean  $\text{SNR}_{\text{FR}}$  defined at one frequency bin for a certain total input power is independent of the impulse response length (number of frequency bins  $M_f$ ) used. This leads us to a sensitivity definition for one frequency bin independent of the total number of frequency bins used:

$$S_{\text{FR,system}} = 10 \cdot \log_{10}(k_B \cdot B \cdot T \cdot F_{\text{System}}) + 10 \cdot \log_{10}(\text{SNR}_{\text{FR},\text{min}}) \quad [\text{dBm}]. \quad (2.5)$$

In case of the delay domain we define the minimum detectable signal after impulse compression by means of applying the inverse Fourier transformation to the measured data in the frequency domain. As the Tx and Rx are directly connected, in the calibration setup used, all signal power will be concentrated in one delay bin, where the noise power at one delay bin is equal to the noise power at one frequency bin. With an increasing length  $\tau_{\text{max}}$  of the *periodic multi-sine signal* (increasing  $M_f$ ) the  $\text{SNR}_{\text{IR}}$  of the strongest delay bin (peak) increases (see Fig. 2.9(b)). The achievable *SNR gain* of  $10 \cdot \log_{10}(M_f)$  dB is commonly called *correlation gain* in other publications. Thus, the receiver

sensitivity seen in the delay domain is dependent on the number of frequency bins used:

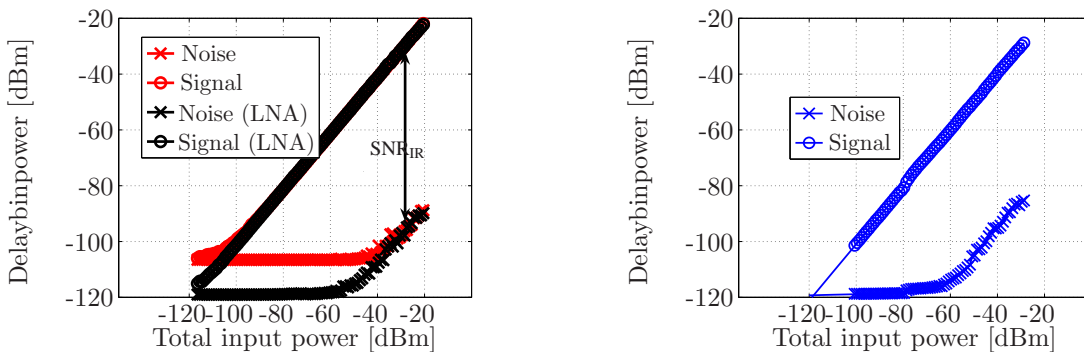
$$S_{\text{IR, System}} = 10 \cdot \log_{10}(k_B \cdot B \cdot T \cdot F_{\text{System}}) - 10 \cdot \log_{10}(M_f) + 10 \cdot \log_{10}(\text{SNR}_{\text{FR, min}}) \quad [\text{dBm}]. \quad (2.6)$$

In Table 2.1, the system specific measured values of  $10 \cdot \log_{10}(k_B \cdot B \cdot T \cdot F_{\text{System}})$  for room temperature and a bandwidth of  $B = 120$  MHz are listed for the HyEff and the ATM system. The difference of the measured values between the HyEff system with and without the internal LNA are related to the resulting noise figure  $F$  of the amplifier chain used. From this table and from Fig. 2.10 it can be seen that the ATM system has the same performance as the HyEff system using internal LNA. It

**Tab. 2.1:** System dependent measured values of  $10 \cdot \log_{10}(k_B \cdot B \cdot T \cdot F_{\text{System}})$  [dBm] for room temperature and bandwidth of  $B = 120$  MHz, the variation being related to the resulting noise figures  $F$ , when using the different inputs at the receiver.

System	$10 \cdot \log_{10}(k_B \cdot B \cdot T \cdot F_{\text{System}})$ [dBm]
HyEff (input <b>RF In LNA</b> )	-92
HyEff (input <b>RF In</b> )	-80
ATM (input <b>RF In LNA</b> )	-92

should be noted that the  $\text{SNR}_{\text{IR}}$  remains constant for a larger total input power (see Fig. 2.9). This effect is related to the **AGC**, which adds attenuation to avoid overloading of the receiver amplifiers and keep the input signal at the analogue digital converter (ADC) in its dynamic range. However, the noise figure  $F$  of the receiver is consequently increased by the additional attenuation of the **AGC**. Figure 2.9(b) is divided by a dashed line into two parts to specify the range where the **AGC** attenuation level is higher than 0 dB.



(a) Maximum achievable signal power and mean noise power at one delay bin w.r.t. the total input power with and without using the internal LNA of the Hyeff system

(b) Maximum achievable signal power and mean noise power at one delay bin w.r.t. the total input power (ATM system)

**Fig. 2.10:** Maximum achievable signal power and mean noise power at one delay bin Hyeff system (a) and ATM system (b)

### 2.3.4 Phase Noise

In principle, the phase noise (**pn**) depends on the characteristics of the Phase Locked Loop (**PLL**) used at the transmit and receive side. The output signals of the separate local oscillators at the

transmitter and receiver, denoted by  $O_{Tx}$  and  $O_{Rx}$  respectively, for the desired local frequency  $f_{LO}$  are given by:

$$O_{Tx}(t) = e^{j2\pi f_{LO}t + \varphi_{Tx}(t)} \quad (2.7)$$

and

$$O_{Rx}(t) = e^{j2\pi f_{LO}t + \varphi_{Rx}(t)} \quad (2.8)$$

where  $\varphi_{Tx}(t)$  and  $\varphi_{Rx}(t)$  are the phase noises at the **Tx** and **Rx** local oscillators, respectively. For the modelling of the phase-distorted channel matrix it is assumed that the phase noise affects all frequency sub-channels of the multi-carrier spread spectrum test signal equally. This means that the coherence time of the phase noise is assumed to be larger than the cycle duration of the *periodic multi-sine* test signal. Herewith, the phase noise affected and time-variant channel frequency response can be written as:

$$\begin{aligned} \mathbf{H}_{pn}(t, \mu \cdot \Delta f) &= \mathbf{H}(t, \mu \cdot \Delta f) \cdot e^{j(\varphi_{Tx}(t) - \varphi_{Rx}(t))} \\ &= \mathbf{H}(t, \mu \cdot \Delta f) \cdot e^{j\varphi_{pn}(t)} \end{aligned} \quad (2.9)$$

The phase noise is commonly modelled as an uncorrelated stationary Gaussian process with zero mean and  $\sigma^2$  variance ([82–84]). Additionally, long term phase drift affects (random walk phase [85]) and correlated phase noise dependent on the characteristics of the PLLs have been reported [86]. Therefore, the phase noise is assumed here as a superposition of a long term phase drift  $\varphi_{pnL}(t)$  and phase noise  $\varphi_{pnS}(t)$  modelled as a correlated Gaussian process with zero mean and  $\sigma_{pnS}^2$  variance, which leads us to:

$$\varphi_{pn}(t) = \varphi_{pnS}(t) + \varphi_{pnL}(t). \quad (2.10)$$

We assume that for the period  $t_s = 2 \cdot \tau_{max} \cdot M_{Rx} \cdot M_{Tx}$  of one snapshot the long term phase drift  $\varphi_{pnL}(t)$  can be approximated by a linear function. Thus, it can be written as:

$$\varphi_{pnL}(t) = \Delta\varphi_{pnL}(t_s, t) \cdot t + \varphi_{pn0} \quad ; \text{for } t_0 \leq t \leq t_0 + t_s, \quad (2.11)$$

where  $\Delta\varphi_{pnL}(t_s, t)$  is the phase gradient. For the long term phase drift basically two cases can be considered:

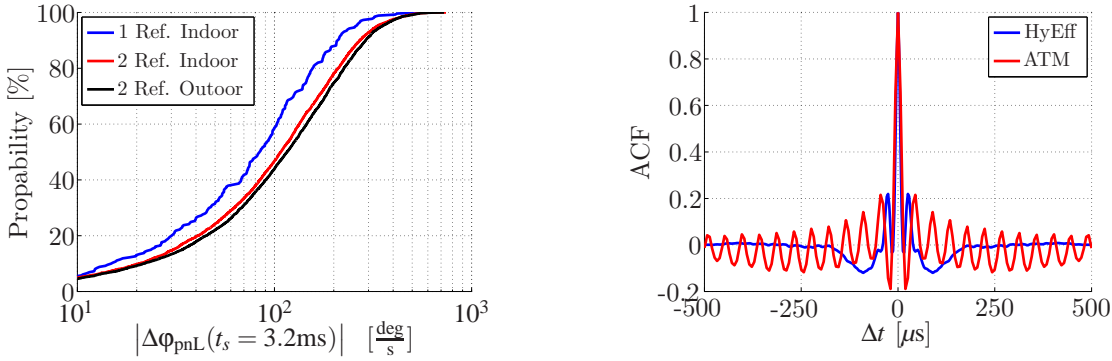
- if the system is phase-locked (e.g., transmitter and receiver are connected and use a common reference (denoted by **1 Ref.**)) the resulting gradient  $\Delta\varphi_{pnL}(t_s, t)$  is expected to be small (basically depends on the temperature stability of the rubidium reference),
- if the system is in remote operation, which means that the system is only frequency-locked and 2 references are used (**2 Ref.**).

In the second case, the gradient  $\Delta\varphi_{pnL}(t_s, t)$  can be larger, which is mainly dependent on the quality of synchronisation of the 2 rubidium references. Here, the temperature stability of the references

---

used plays a major role, as a constant temperature of the surrounding area can not always be guaranteed, especially in case of outdoor measurements. Figure 2.11(a) shows a CDF, estimated from measurement results, of the magnitude of the gradient  $\Delta\phi_{\text{pnL}}(t_s = 3.2\text{ms})$  using one or two separate rubidium references for an indoor and outdoor measurement. Note that these results only refer to the phase gradient for a specific test measurement, whereas it is not necessarily guaranteed that in an outdoor measurement the phase gradient is always smaller than  $10^3 \text{ [deg/s]}$ . This basically depends on how much time is spent for a proper synchronisation and how constant the temperature of the references can be kept. Nevertheless, the results illustrate in which range the phase gradient can be expected.

The phase noise standard deviation  $\sigma_{\text{pnS}}$  and the phase noise covariance matrix  $\Sigma$  of the correlated Gaussian phase noise process are obtained from measurements. The analysis procedure is discussed in appendix A.1. Finally, the phase noise standard deviation  $\sigma_{\text{pnS}}$  is  $5.69^\circ$  for the ATM system and  $2.94^\circ$  for HyEff system. The estimated auto correlation functions of the phase noise process of both MIMO sounders are shown in Fig. 2.11(b).



(a) CDF of the gradient  $\Delta\phi_{\text{pnL}}(t_s = 3.2\text{ms})$  for using only 1 (1Ref.) or 2 (2Ref.) rubidium reference indoor and outdoor

(b) Estimated auto correlation function of the correlated phase noise process

**Fig. 2.11:** CDF of the random walk phase gradient  $|\Delta\phi_{\text{pnL}}(t_s = 3.2\text{ms})|$  using 1 or 2 rubidium references in different environments (a) and auto correlation function (ACF) of the Gaussian phase noise process for the HyEff and ATM system (b)

### 2.3.5 Arrangement of External Amplifiers in the RF Signal Path

Regarding the arrangement of antenna switches and amplifiers in the RF signal path, a trade-off always exists between sensitivity and phase stability. Separate LNAs after each Rx antenna and/or separate PAs before each Tx antenna are mostly inadequate because of the increase in phase drift between antenna channels. Also, the usage of separate filters in each antenna channel is not appropriate, as the phase drift between the antenna channels increases due to the differences between the filters. Differences are related to the manufacturing and also to the ageing process stage of each filter.

To avoid such differences it is better to use a single PA and LNA before the Tx antenna switch and after the Rx antenna switch respectively. Consequently, all antenna channels are collectively

biased with the same phase drift. This phase offset that is equal for all channels will not affect the quality of the DoD/DoA estimation. The corresponding back-to-back calibration setup is shown in Fig. 2.12.

The external PA or LNA is required to compensate for the attenuation of the RF cables between the transmitter and the Tx array (Tx cable 1) or between the Rx array and the receiver (Rx cable 1). This is especially the case if RF cables with a larger attenuation need to be used. To minimise the signal attenuation which can not be compensated, the cable between the output of the external PA and the Tx antenna switch (Tx cable 2) and the cable between the output of the Rx antenna switch and the input of the LNA (Rx cable 2) should be as short as possible (see Fig. 2.12). Furthermore, the amplification of the external LNA should be in the range of the attenuation of the Rx cable 1. If a LNA with a large amplification or a LNA with a better noise figure than the internal LNA is used, the input RF In that is less sensitive against non-linear distortions should be selected. For the single PA at the Tx, the corresponding Tx antenna switch has to handle the full output power which may exceed 2...10 W for broadband urban measurements. Using the proposed arrangement of the PA and LNA in the RF signal path, it is necessary to include them in the back-to-back system frequency response calibration, as these kind of amplifiers (which may also include filters) are normally frequency dependent. Furthermore, the frequency responses of LNAs or PAs depend on the input power level. As an example, the magnitude and phase of the normalised frequency responses of an LNA used in this thesis are shown in Fig. 2.13, the colour indicating the different input power levels in dBm. It is clear that the frequency responses differ with respect to the different input power levels. Even though the magnitude differences seem to be small (0.5 ... 3dB), the differences of the phase are not negligible. Therefore, the appropriate arrangement of the LNA or PA in the RF signal path during back-to-back calibration is an important issue. As the output power of the transmitter does not change, the PA is always used at the same input power. Consequently, the PA needs to be calibrated only for one power input level and the frequency response remains stable (except phase drift) during the whole measurement time. For the LNA a constant power input level is not given. Therefore, the frequency response of the LNA has to be determined dependent on the input power level (LNA calibration). Using the back-to-back calibration setup shown in Fig. 2.12 the LNA and the different AGC levels can be jointly calibrated. To avoid that the receiver amplifiers are used in their non-linear region, it is important that the input power at the receiver is within the specified dynamic range. Note that in case of the ATM system the LNA can not be calibrated dependent on the power input level. Therefore, it has to be decided before the measurement at which power input level the system should be calibrated. This assumes that the power which will be received in a measurement is already known in advance. Since it is an often made mistake that the LNA is calibrated for a inappropriate power input level, the consequences of an unsuitable calibrated external LNA on the parameter estimation results will be discussed in Section 7.3.2 of Chapter 7.



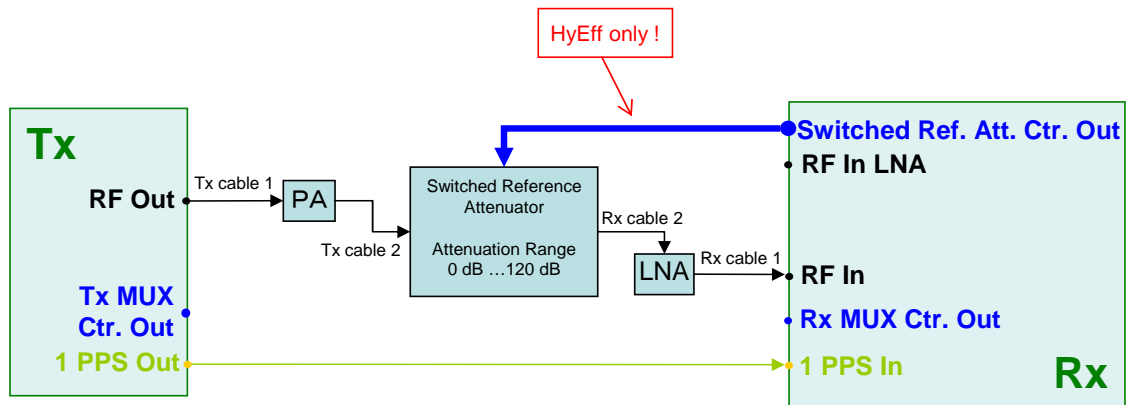


Fig. 2.12: Back-to-back calibration setup including external PA and LNA

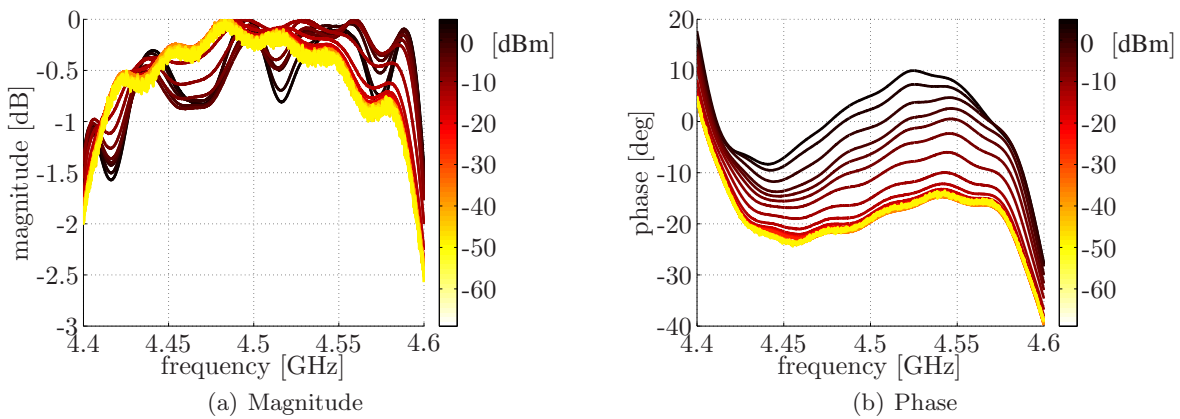


Fig. 2.13: Magnitude (a) and phase (b) of the normalised frequency response of an exemplary LNA for different input power levels (denoted with different colour).




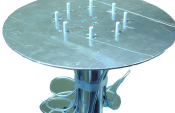


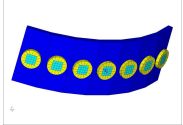

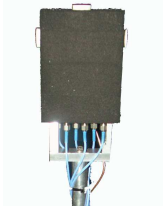


	Vendor	Antenna Type & Polarisation	MUX Type	MUX Att. [dB]	Max. Ap. zy [λ]	Max. Ap. xy [λ]	Max. Power [W]	picture
<b>1D Circular Arrays</b>								
CUBAx1x1x8	TUI/IHE	Biconical v	8→1	ca.4	0	0	.5	
UCAx1x1x8	BRI	Monopol v	8→1	ca.4	1.3	1.3	.5	
PUCPAx2x1x8	BRI	Patch v/h	8→1	ca.4	1.3	1.3	.5	
UCAx1x1x16	TUI	Conical Monopol v	8→2→1	ca.7	1.7	1.7	.5	
PUCPASIMx2x1x24	TUI/IRK	Patch v/h	No MUX	ca.12	3.4	3.4	x	
PUCPAx2x1x24	TUI/IRK	Patch v/h	Cascade of 6 2→1 switches	ca.12	3.4	3.4	.25	

Fig. 2.14: 1D circular measurement antenna arrays

## 2.4 Antenna Arrays

The spatial dimension of the channel response is accessed by antenna arrays. The angular resolution capability of an array depends on the effective aperture size as seen from the respective wave direction. Therefore, the spatial arrangement of the antenna elements has a major influence.

	Vendor	Antenna Type & Polarisation	MUX Type	MUX Att. [dB]	Max. Power [W]	picture
<b>Special Arrays and Antennas</b>						
PPDA	TUI	Patch v/h	8→1	ca. 3	.5	
PHORN	IRK	Slot v/h	x	x	x	
OMNI	TUI	Conical Monopol v	x	x	x	

**Fig. 2.15:** Reference and application antenna arrays/antennas

Sophisticated antenna array architecture design is required to achieve high DoD/DoA resolution. This has to go along with mechanically and electrically stable construction and precise calibration. Since there is always a trade-off between various specifications including resolution, measurement time, availability, and costs, there is a wide variety of useful antenna array architectures. In the sequel, some basic design considerations are summarised.

- Planar antenna arrays such as Uniform Linear Array (ULA) or Uniform Rectangular Array (URA) always have a limited viewing angle and inherent forward/backward ambiguity. They are useful to represent a BS assuring that scatterers are only in front of the array. The effective array aperture depends on the DoD/DoA and the resolution capability is not uniform.
- Circular antenna arrays, on the other hand, cover the entire azimuth range of 360°. They have to be used to represent the MS. Their angular resolution capability is fairly uniform.
- Double directional estimation requires arrays at both sides of the link and MIMO operation

of the sounder. For cellular system consideration, a combination of planar and circular arrays is adequate, whereas for ad-hoc peer-to-peer networks identical circular arrays are most preferable.

- Mainly for micro- and pico-cell scenarios, estimation of the co-elevation is desired in addition to the azimuth. This requires application of uniform rectangular, cylindrical or spherical arrays. However, two dimensional wave analysis (which includes azimuth and elevation) is not only necessary to derive two dimensional spatial propagation models. It is also required for the removal of the influence of the complex radiation pattern of the measurement antennas from the data. Moreover, this must also include polarisation resolution.
- Spherical antenna arrays may be applied for full azimuth and co-elevation coverage. However, there exists no geometric solution to arrange more than 20 patch antenna elements on a spherical surface with identical inter-element distances (check the 5 platonic bodies). Therefore, non-uniform inter-element distances and various relative polarisation orientations of adjacent elements will complicate the design of spherical arrays.
- Moreover, optimisation of the inter-element distance for circular and spherical arrays (or of the array diameter in case of a fixed number of antenna elements, respectively) is required to minimise the side lobes of the angular correlation function to reduce the probability of outliers in the iterative parameters search. This typically leads to inter-element distances smaller than half of the wavelength [5, 9].
- Full polarimetric analysis of the radio channel requires not only polarimetric reception but also polarimetric excitation of the channel.
- High and reliable resolution in terms of separation capability of closely spaced paths and low probability of outliers requires an antenna architecture which offers a minimum of antenna array aperture size in the respective spatial dimension, including a minimum number of antenna elements, low antenna element coupling, and precise calibration. This has also to include the antenna switches and feeder cables.
- The characteristics of the antenna elements depend on the basic element design (dipoles, patches, slots, etc.). It has a strong influence to *high-resolution* performance, estimation ambiguities, probability of outliers, and polarisation resolution capability, gain, bandwidth et cetera.

The antenna arrays used in this thesis are characterised in the following. The antenna arrays are designed for the use with the described channel sounder systems. The use with other measurement systems like a [NWA](#) in combination with additional control units is in general possible but not practical in terms of the necessary measurement time. Most of the antenna arrays are developed and designed in the Electronic Measurement Research Lab of the department of Electrical Engineering and Information Technology at Ilmenau University of Technology ([TUI](#)). The design rules for the circular antenna arrays with respect to the use in parameter estimation algorithm is partly done in [5]. Especially, the circular polarimetric patch antenna arrays are developed in

---

cooperation with IRK-Dresden (**IRK**) [87], where the electrical, mechanical design, and the corresponding antenna field simulations were carried out. Furthermore, some of the antenna arrays come from a cooperation with other universities like University of Bristol - Department of Electrical and Electronic Engineering (**BRI**) and University of Karlsruhe - Institut für Höchstfrequenztechnik und Elektronik (**IHE**). The above introduced abbreviations are used to indicate the **Vendor** of the antenna arrays.

**Definition 2.4.1.** The term *practical antenna array* is used for antenna arrays that can be employed for propagation measurements.

**Definition 2.4.2.** The term *measurement antenna array* is used for antenna arrays that are suitable for *high-resolution* parameter estimation, but can be *practical antenna arrays* as well as a simulated antenna arrays.

Three different classes of *measurement antenna arrays* are used, **Planar arrays** listed in Fig. 2.16, **1D Circular Arrays** listed in Fig. 2.14, **2D Circular Arrays** listed in Fig. 2.17.

**Definition 2.4.3.** The term *reference antenna* is used for antennas that are used for the calibration of *practical antenna arrays*.

**Definition 2.4.4.** The term *application antenna array* is used for arrays that are suitable only for a application but not for *high-resolution* parameter estimation.

*Reference antennas* and one *application antenna array* are listed in Fig. 2.15. The four lists include the basic parameters of the antenna arrays, which are explained in the following. Here, the electromagnetic design of the single antenna elements is not discussed, since most of the elements are commonly used in antenna theory and measurement. Arrays with special antenna types are cited. Each array is identified by a unique name with the abbreviations:

- CUBA - Circular Uniform Beam Array [88]
- PHorn - Polarimetric Horn (Antenna)
- PPDA - Polarimetric Personal Digital Assistant
- PUCPA - Polarimetric Uniform Circular Patch Array
- PULPA - Polarimetric Uniform Linear Patch Array
- PURPA - Polarimetric Uniform Rectangular Patch Array
- SPUCPA - Stacked Polarimetric Uniform Circular Patch Array
- UCA - Uniform Circular Array,

followed by 3 numbers  $pol \times ZDIM \times XYDIM$ . The variable *pol* specifies the number of supported polarisations (e.g. 1  $\Rightarrow$  vertical polarisation only, 2  $\Rightarrow$  vertical and horizontal polarisation), *XYDIM* is the number of elements in a plane parallel to the xy-plane and *ZDIM* specifies the number of planes, where all planes have the same layout. The spacing between the planes is chosen to be

---

0.4943 of the wavelength at the upper frequency in the band thus satisfying the sampling theorem in space, where the radius in case of circular arrays was individually optimised [9]. The resulting maximum aperture sizes in the xy and zy plane are listed in the columns **Max. Ap. xy** [ $\lambda$ ] and **Max. Ap. zy** [ $\lambda$ ] respectively. The column **Antenna Type & Polarisation** indicate the type of the antenna elements:

- Biconical antenna
- Conical monopol
- Monopol
- Patch, (all polarimetric arrays use patch antennas with two ports, where one is more sensitive for the vertical polarised wave and the other one for horizontal polarised wave)

and the preferred polarisations received by the elements. In Fig. 2.18 a simplified internal electrical design for all arrays is drawn in a block diagram. Nevertheless, there are differences especially in the design of the multiplexer (**MUX**), which sequentially switches the **RF** signal from the antenna element  $m = 1$  up to  $m = M$  to the **RF** Output. Internally, Positive Intrinsic Negative (**PIN**) diode switches with a switching speed between 30 ns and 300 ns are used, which is required when choosing the shortest possible impulse response length of 0.8  $\mu$ s of the channel sounder systems applied. The main difference between the multiplexers of the listed arrays is found in the **MUX Type** that specifies what kind of multiplexers are combined in a certain cascade depth  $C$ . The notation  $8 \rightarrow 2 \rightarrow 1$  specifies a multiplexer cascade with depth  $C = 2$ , where in the first level a  $8 \rightarrow 1$  and in the second level a  $2 \rightarrow 1$  multiplexer is used. The **MUX Type** defines the overall attenuation **MUX Att.** [dB] between the antenna element  $m$  and the **RF Out**, which has a major influence on the performance of the antenna array (see Appendix D). Some of the **Rx** antenna arrays are equipped with a **LNA** that is used to improve the **SNR** at the receiver of the channel sounder. In some cases, an additional multiplexer port is reserved for a **RF** reference signal (**RF Ref. In**). This input can be used to track the phase drift between **Tx** and **Rx** (for further explanation, see Section 4.1.1) or to measure the system frequency response (back-to-back calibration) including the characteristic of the **LNA**, the band pass filter and at least one multiplex channel. Since an additional multiplex channel is more costly, some of the arrays are equipped with a calibration input (**RF Calib. In**). For the back-to-back calibration, the relay (see Fig. 2.18) is switched to the **RF Calib. In** signal instead of the signal of the first antenna element  $m = 1$ . Because of the much higher switching time of a relay (around 15 to 20 ms) the **RF Calib. In** can not be used during the normal measurement in contrast to the **RF Ref. In**. All of the described antennas are designed for a center frequency of 5.2 GHz, except for the **PURAx2x2x4** and the **SPUCPAx2x2x24** operating at 4.5 GHz. The bandwidth of the antenna elements of all arrays are at least 120 MHz.

Note that the PUCPA with 24 dual polarised elements, which is listed as **PUCPASIMx2x1x24** is a preliminary design step for the **PUCPAx2x1x24** and is not a *practical antenna array*.



	Vendor	Antenna Type & Polarisation	MUX Type	MUX Att. [dB]	Max. Power [W]	Max. Ap. zy [λ]	Max. Ap. xy [λ]	picture
<b>Planar Arrays</b>								
PULPAx2x1x8	TUI/IRK	Patch v/h	8→2→1	ca. 7	.5 / 10	0	3.5	
PURPAx2x2x4	TUI/IRK	Patch v/h	8→2→1	ca. 5	10	0.5	1.5	

Fig. 2.16: Planar measurement antenna arrays



	Vendor	Antenna Type & Polarisation	MUX Type	MUX Att. [dB]	Max. Power [W]	Max. Ap. zy [λ]	Max. Ap. xy [λ]	picture
<b>2D Circular Arrays</b>								
SPUCPAx2x2x24	TUI/IRK	Patch v/h	Cascade of 7 2→1 switches	ca. 17	.25	3.5	3.5	
SPUCPAx2x4x24	TUI/IRK	Patch v/h	Cascade of 9 2→1 switches	ca. 23	.25	3.8	3.5	

Fig. 2.17: 2D circular measurement antenna arrays

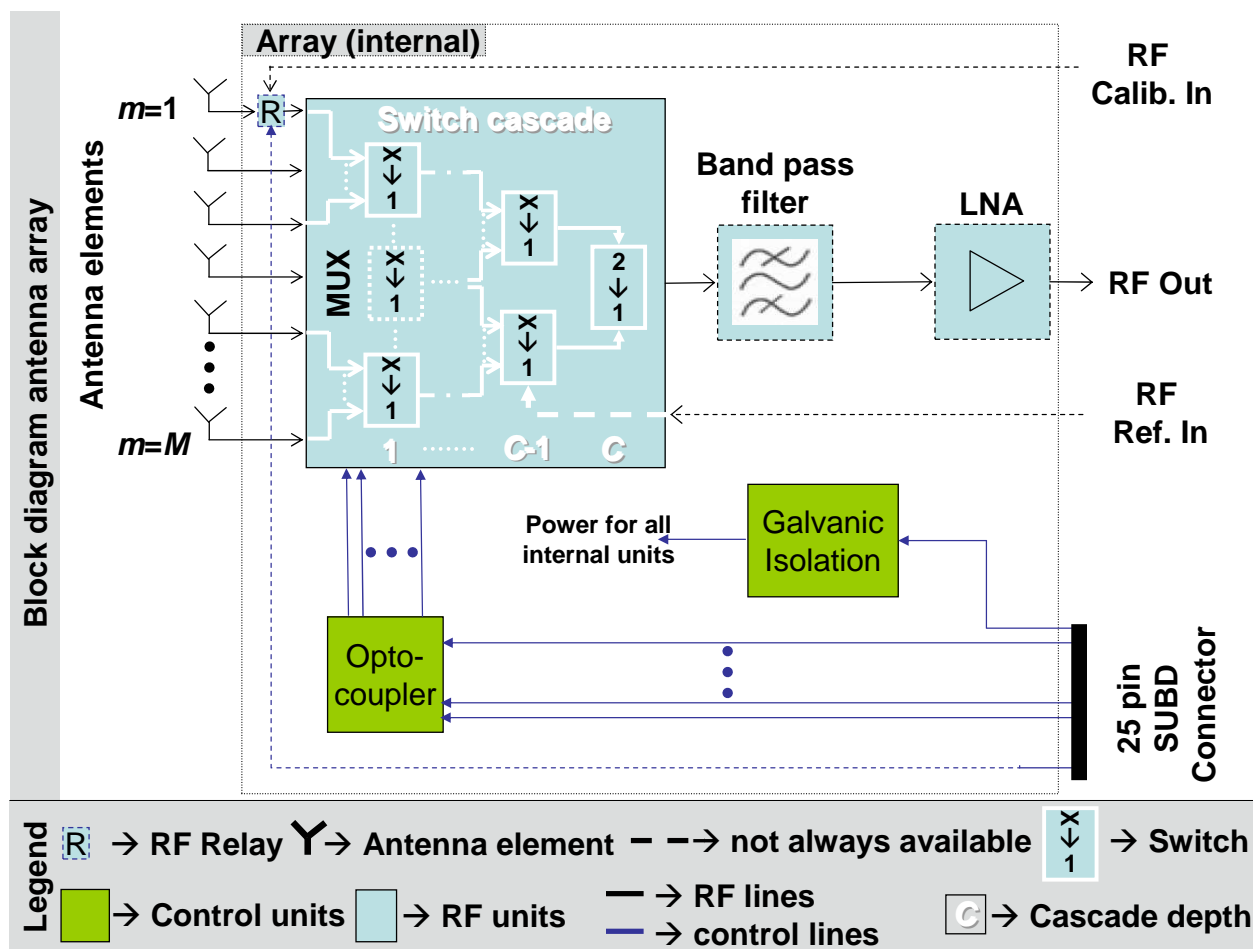


Fig. 2.18: Block diagram of an antenna array





### 3. ANTENNA ARRAY DATA MODEL

The spatial dimension of the channel response is accessed by antenna arrays. Consequently, a precise description of the antenna array radiation patterns in magnitude and phase is required in the description, modelling, and estimation of wireless channels ([62, 89, 90]). Thus, the antenna independent description of the mobile radio channel is of major importance for measurement based channel characterisation via parameter estimation algorithms. The antenna influence has to be separated from the measured channel, otherwise, the channel description can only be given including the influence of the specific antennas used throughout the measurement.

For low computational complexity of the estimation algorithm, the frequency dependent description of an antenna element (dealt in Section 3.1) is normally not used. The estimation algorithms commonly rely on narrow band models (Section 3.2) derived from antenna array calibration measurement with a bandwidth up to 200 MHz. From this measurements only sampled narrow band radiation patterns can be obtained. It was found that using these sampled representations for parameter estimation is inappropriate [5, 31]. The usage of the Spline interpolation method (e.g. used in [89]) is popular to interpolate the measured radiation patterns. However, with this method an analytic description of the radiation patterns is not given. Therefore, an efficient analytic antenna array data model based on the Effective Aperture Distribution Function (EADF, first published in [23]) is proposed in Section 3.3. As opposed to other methods, the derivatives of the narrow band radiation patterns dependent on the azimuth and co-elevation angle can be analytically calculated. These derivatives are required when using gradient based parameter estimation methods as described in [30] and Chapter 5. Furthermore, the performance of practical antenna arrays can be evaluated based on this method (Chapter 6, [13, 26–28]), as it can be obtained from calibration measurements.

In Section 3.4 it will be shown, that the proposed antenna array data model outperforms the Spline interpolation method as well as the vector spherical harmonics (VSH, [21]) in terms of calculation time by achieving the same interpolation accuracy.

A further important issue is the definition of a sampling grid for a function (e.g. radiation pattern) on the sphere. As equidistant grids in azimuth and/or co-elevation (Chebyshev angular grid or Gauss-Legendre angular grid) lead to a non equidistant distribution of the sampling points on the sphere, a function on the sphere will be normally oversampled towards the poles of the spherical coordinate system. Therefore, Lebedev angular grids [91, 92] were proposed to distribute the sampling points as equidistant as possible on the sphere. These grids are most efficient, but are not available for an arbitrary number of sampling points. As for parameter estimation an efficient calculation of the radiation patterns on the sphere is required, a minimum sampling grid for the radiation patterns of practical antenna arrays is proposed in Section 3.5. This grid is based on the

---

EADF and fulfils the Nyquist theorem in the angular domain.

### 3.1 Broadband Model of a Single Antenna Element

For parameter estimation, the complex radiation pattern of an antenna  $\mathbf{b}(f, \boldsymbol{\varphi}, \vartheta, q)$  in the far field is traditionally described with respect to the frequency  $f$ , azimuth  $\boldsymbol{\varphi}$ , co-elevation  $\vartheta$  (or elevation  $\theta$ ), and polarisation  $q$  in a spherical coordinate system. The polarisation  $q$  can either be horizontal (h) or vertical (v). In case of vertical polarisation the vector of the transmitted/received electrical field  $E$  is parallel to  $\vec{e}_\theta$ , whereas in case of horizontal polarisation the vector of the electrical field  $E$  is parallel to  $\vec{e}_\varphi$ . The vectors  $\vec{e}_\theta$  and  $\vec{e}_\varphi$  are defined in the spherical coordinate system, as shown in Fig. 3.1. Note that this definition of the vertical and horizontal polarisation is used throughout the entire thesis and is commonly used in channel modelling.

For comparison to antenna theory, the gain function of an antenna can be written as:

$$g(f, \boldsymbol{\varphi}, \vartheta) = \left\| \mathbf{b}(f, \boldsymbol{\varphi}, \vartheta, q = \text{h}) \cdot \vec{e}_\varphi + \mathbf{b}(f, \boldsymbol{\varphi}, \vartheta, q = \text{v}) \cdot \vec{e}_\theta \right\|^2 \quad (3.1)$$

In the following, the  $m$ -th antenna element of an antenna array with  $M$  antennas is described (see also Fig. 3.2). The position of a single antenna element is given relative to the centre of the antenna array, which is equivalent to the origin of the coordinate system. Therefore, the radiation pattern of the  $m$ -th antenna element (3.2) is composed of two parts: the radiation pattern  $\mathbf{b}_A(f, \boldsymbol{\varphi}, \vartheta, q, m)$  of the antenna relative to its centre and the phase term  $\mathbf{b}_{\text{ph}}(f, \boldsymbol{\varphi}, \vartheta, m)$ , which depends on the position of the  $m$ -th element.

$$\mathbf{b}(f, \boldsymbol{\varphi}, \vartheta, q, m) = \mathbf{b}_A(f, \boldsymbol{\varphi}, \vartheta, q, m) \cdot \mathbf{b}_{\text{ph}}(f, \boldsymbol{\varphi}, \vartheta, m) \quad (3.2)$$

The phase term is defined as:

$$\mathbf{b}_{\text{ph}}(f, \boldsymbol{\varphi}, \vartheta, m) = e^{\frac{-j \cdot 2\pi \cdot f \cdot \left\| \vec{\mathbf{k}}(\boldsymbol{\varphi}, \vartheta) - \vec{\mathbf{r}}_m \right\|}{c}}, \quad (3.3)$$

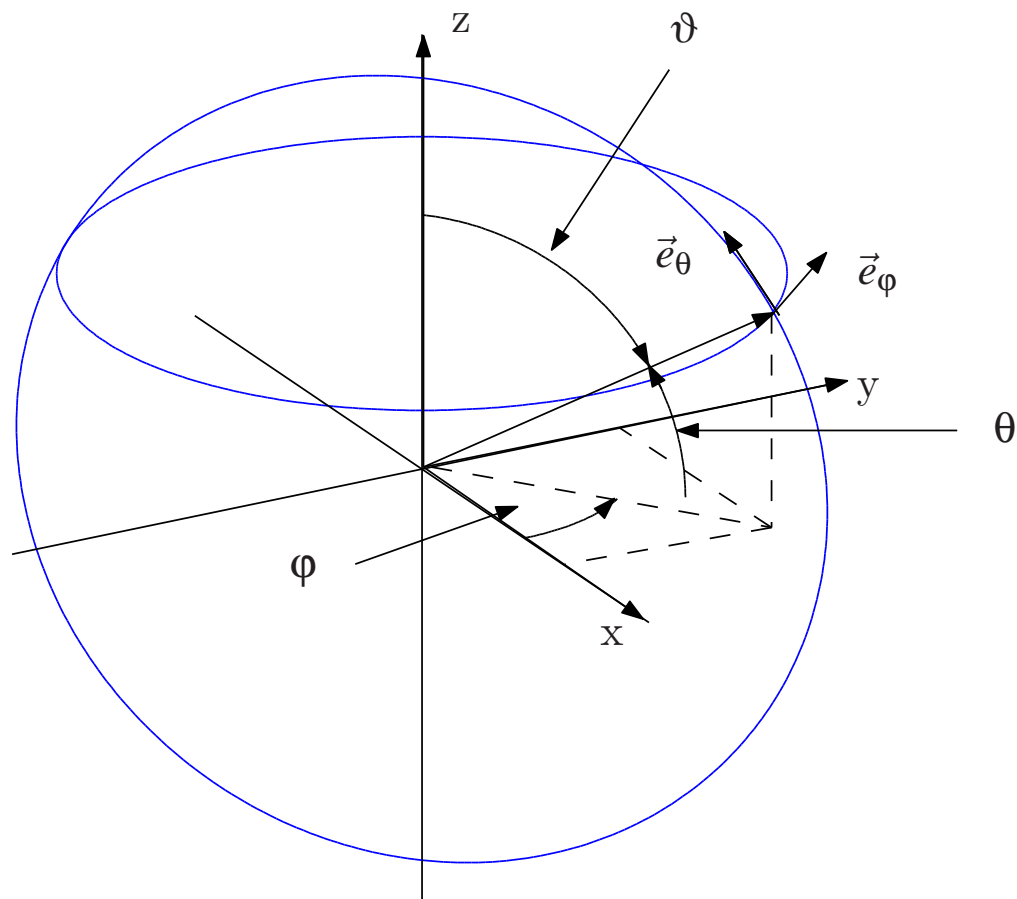
where  $\vec{\mathbf{k}}$  is a vector pointing to the source of the electrical field,  $\vec{\mathbf{r}}_m$  is the position vector of the  $m$ -th element and  $c$  the speed of light in free space. If a plane wavefront can be assumed the phase term is defined as:

$$\mathbf{b}_{\text{ph}}(f, \boldsymbol{\varphi}, \vartheta, m) = e^{\frac{-j \cdot 2\pi \cdot f \cdot \vec{\mathbf{k}}(\boldsymbol{\varphi}, \vartheta) \cdot \vec{\mathbf{r}}_m}{c \cdot \left\| \vec{\mathbf{k}} \right\|}}. \quad (3.4)$$

This plane wave assumption is valid under the ‘‘far field’’ condition. From antenna theory several definitions for the term ‘‘far field’’ are known. One commonly used is the so called Rayleigh distance [93] with:

$$l = \frac{2D^2}{\lambda}, \quad (3.5)$$

where  $D$  is the cross-section dimension of the antenna. This distance is related to a maximum phase error of  $22.5^\circ$  at the edge of the antenna, which results in a magnitude error of ca.  $-8\text{dB}$ . In general, this condition is related to a single antenna element. As equation (3.4) is related to the position within an antenna array,  $D$  has to be defined at least as the maximum aperture size of the entire antenna array.



**Fig. 3.1:** Spherical coordinate system

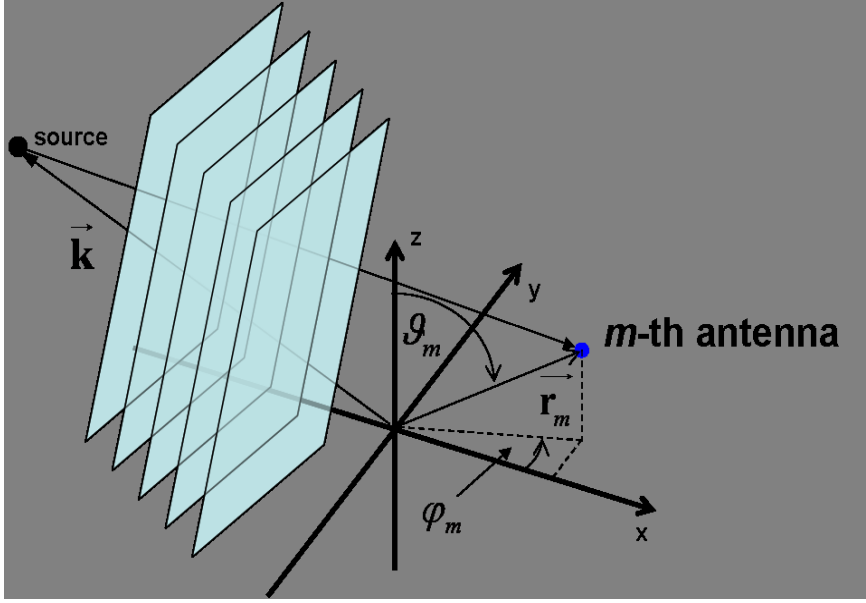


Fig. 3.2: Geometrical description of the  $m$ -th antenna element

### 3.2 Narrow Band Model of the Measured Radiation Pattern

The complex polarimetric radiation patterns of an antenna array are measured in a well defined propagation environment. This should be an anechoic chamber and the pivot point of the antenna array is located at the origin of the spherical coordinate system. The radiation patterns are measured with respect to the fixed distance  $r = |\vec{\mathbf{k}}|$ , as function of frequency  $f$ , azimuth  $\varphi$ , co-elevation  $\vartheta$ , and polarisation  $q$ . From the antenna calibration measurement a sampled version of the following function can be obtained:

$$y(f, \varphi, \vartheta, q, m) = \mathbf{b}_{\text{Ref}}(q, f) \cdot \mathbf{H}(f) \cdot \mathbf{G}_{\text{Sys}}(f) \cdot \mathbf{b}(f, \varphi, \vartheta, q, m), \quad (3.6)$$

which is a product of the frequency responses of the reference antenna  $\mathbf{b}_{\text{Ref}}$  in its main beam direction, the channel  $\mathbf{H}$ , the measurement system  $\mathbf{G}_{\text{Sys}}$  and the radiation pattern of the antenna under test  $\mathbf{b}(f, \varphi, \vartheta, q, m)$ . As in an anechoic chamber only the direct path exists, the frequency response  $\mathbf{H}$  of the channel can be written as (see also the *Friis's formula* [94]):

$$\mathbf{H}(f) = \frac{1}{4\pi \cdot f \cdot \tau(r)} e^{-j \cdot 2\pi \cdot f \cdot \tau(r)}, \quad (3.7)$$

where  $\tau$  is the delay corresponding to the distance  $r$  between the reference antenna and the pivot point of the antenna array under test. This means that the frequency dependent radiation pattern is given by:

$$\mathbf{b}(f, \varphi, \vartheta, q, m) = \frac{y(f, \varphi, \vartheta, q, m) \cdot 4\pi \cdot f \cdot \tau(r) \cdot e^{j \cdot 2\pi \cdot f \cdot \tau(r)}}{\mathbf{b}_{\text{Ref}}(f, q) \cdot \mathbf{G}_{\text{Sys}}(f)}. \quad (3.8)$$

To simplify the antenna array data model, most parameter estimation algorithms described in the literature (for a centre frequency  $f_0$  between 2 GHz to 6 GHz and a bandwidth  $B$  between 100 MHz to 200 MHz) assume that the antenna is frequency independent (“narrow band assumption”). This assumes that the antenna frequency responses are constant in magnitude and phase in the range between  $f_0 - B/2$  and  $f_0 + B/2$ . However, the phase term of the  $m$ -th antenna in an array (eqn. (3.3), (3.4)) is frequency dependent. This means, that the narrow band model has a limited accuracy defined by the applied bandwidth  $B$ . The consequence of the “narrow band assumption” on the model accuracy will be discussed in detail in Chapter 7.

Assuming that the resulting model accuracy is sufficient, the narrow band radiation pattern can be defined as:

$$\mathbf{b}(\boldsymbol{\varphi}, \vartheta, q, m) = \frac{1}{B} \int_{f_0 - B/2}^{f_0 + B/2} \mathbf{b}(f, \boldsymbol{\varphi}, \vartheta, q, m) df. \quad (3.9)$$

However, from calibration measurements only a noisy sampled radiation pattern can be obtained. The vector valued frequency responses with  $M_f$  frequency samples are normally measured in the range of  $\boldsymbol{\varphi} = (-\pi \dots \pi - \Delta\boldsymbol{\varphi})$  in azimuth and  $\vartheta = (0 \dots \pi)$  in co-elevation. An equidistant grid in azimuth  $\Delta\boldsymbol{\varphi} = \frac{2\pi}{N_\varphi}$  and co-elevation  $\Delta\vartheta = \frac{\pi}{(N_\vartheta - 1)}$ , with  $N_\varphi$  and  $N_\vartheta$  samples in azimuth and co-elevation respectively is used. Herewith, the measured antenna frequency response for the measurement position  $\{n_\varphi, n_\vartheta\}$  can be written as:

$$\tilde{\mathbf{b}}_f^{[M_f \times 1]}(\boldsymbol{\varphi}_{n_\varphi}, \vartheta_{n_\vartheta}, q, m) = \mathbf{b}(\boldsymbol{\varphi}_{n_\varphi}, \vartheta_{n_\vartheta}, q, m) + \mathbf{n}. \quad (3.10)$$

where  $\mathbf{n}$  corresponds to the measurement noise vector. By applying the discrete Fourier transform on the vector  $\tilde{\mathbf{b}}_f$ , the vector valued impulse response  $\tilde{\mathbf{b}}_d^{[M_f \times 1]}$  of the antenna can be calculated with:

$$\tilde{\mathbf{b}}_d^{[M_f \times 1]}(\boldsymbol{\varphi}_{n_\varphi}, \vartheta_{n_\vartheta}, q, m) = \frac{1}{\sqrt{M_f}} \cdot \mathbf{F} \cdot \tilde{\mathbf{b}}_f^{[M_f \times 1]}(\boldsymbol{\varphi}_{n_\varphi}, \vartheta_{n_\vartheta}, q, m), \quad (3.11)$$

where  $\mathbf{F}$  corresponds to the Fourier matrix of size  $M_f$ . The strongest delay bin (maximum power) of this vector valued impulse response corresponds to the narrow band radiation pattern (eqn. (3.9)) for the angles  $\{\boldsymbol{\varphi}_{n_\varphi}, \vartheta_{n_\vartheta}\}$ . Note that the SNR of this narrow band radiation pattern is improved about  $10 \cdot \log_{10}(M_f)$  dB (correlation gain) compared to the SNR of the single frequency bin.

Finally, the measured narrow band radiation pattern can be written in matrix notation as:

$$\tilde{\mathbf{B}}^{[N_\vartheta \times N_\varphi]}(q, m) = \mathbf{B}^{[N_\vartheta \times N_\varphi]}(q, m) + \mathbf{N}^{[N_\vartheta \times N_\varphi]}, \quad (3.12)$$

where  $\mathbf{B}(q, m)$  is the matrix with the sampled version of the function  $\mathbf{b}(\boldsymbol{\varphi}, \vartheta, q, m)$  and  $\mathbf{N}$  is the measurement noise matrix. The single elements of  $\mathbf{N}$  are defined as described in eqn. (E.3) with standard deviation  $\sigma$ .

### 3.3 The Effective Aperture Distribution Function

As for signal processing or parameter estimation algorithms a continuous or analytic description of the radiation patterns of an antenna array are required, an interpolation of the radiation pattern  $\tilde{\mathbf{B}}(q,m)$  becomes necessary. Unfortunately, most of these interpolation methods can not provide an efficient analytic description of the radiation pattern. Furthermore, an analytic description of the derivatives of the radiation patterns dependent on azimuth and co-elevation is not given. Nevertheless, these derivatives are necessary for gradient based parameter estimation algorithms or for the performance evaluation of practical antenna arrays, as described in Chapter 6.

This section addresses an efficient analytic description of the polarimetric radiation patterns and their derivatives of an antenna array dependent on the azimuth and co-elevation angles. The proposed analytic data model for the antenna radiation pattern will be called Effective Aperture Distribution Function and was first published in [23] and resumed in several publications and applications in the field of parameter estimation, channel modelling, and antenna array performance evaluation ([13, 22, 24–29, 55, 77, 95–97]).

#### 3.3.1 The Idea behind the EADF

The two-dimensional Discrete Fourier Transformation can easily be applied to a sampled antenna radiation pattern, as the constraint of a periodic function is naturally given for any radiation pattern with respect to the azimuth and co-elevation angles. The transformation results in a projection of the 2D far field radiation pattern into a near field distribution in a 2D plane. The inverse transformation is commonly known from antenna theory [98] and refers to “Near Field to Far Field Transformation” methods using the Fourier transformation. The electrical field is measured in the near field with a probe antenna and then the far field radiation pattern is obtained by Fourier transform of the measured data.

The electrical field in the near field is normally concentrated in a limited area. Consequently, also the energy in the aperture domain, by means of the Fourier transform of the measured far field radiation pattern, is also concentrated in a limited area. The size of the area is related to the aperture size of the antenna. This property can be used to compress the measured data of a radiation pattern. The relevant samples in the aperture domain will be called effective aperture distribution function EADF. All samples containing signal energy are relevant. Samples with noise only are not taken into account.

Using the EADF, the radiation pattern and its derivatives can be analytically calculated dependent on azimuth and co-elevation (Section 3.3.4).

#### 3.3.2 Construction of the 2D Periodic Radiation Pattern

As aforementioned the radiation patterns are naturally periodic in azimuth and co-elevation, but due to the redundancy of the spherical coordinate system it is enough to measure the radiation patterns in the range of  $\varphi = (-\pi \dots \pi - \Delta\varphi)$  in azimuth and  $\vartheta = (0 \dots \pi)$  in co-elevation for a complete

---

description. This reduces drastically the total antenna calibration measurement time, which may exceed several hours. The measurements in the range of  $\vartheta = (\pi \dots 2\pi - \Delta\vartheta)$  in co-elevation are not necessary, but for the calculation of the EADF the periodic description of the radiation pattern is required. Therefore we describe in the following, how the fully 2D-periodic data structure can be obtained by periodic extension of  $\tilde{\mathbf{B}}(q, m)$ .

The 2D-periodic radiation pattern  $\tilde{\mathbf{B}}_{\mathbf{p}}^{[N'_{\vartheta} \times N_{\varphi}]}$  is defined as:

$$\tilde{\mathbf{B}}_{\mathbf{p}}^{[N'_{\vartheta} \times N_{\varphi}]}(q, m) = \begin{bmatrix} \tilde{\mathbf{B}}(q, m) \\ \tilde{\mathbf{B}}_{\mathbf{r}}(q, m) \end{bmatrix}, \quad (3.13)$$

with

$$N'_{\vartheta} = 2 \cdot (N_{\vartheta} - 1). \quad (3.14)$$

The periodic extension is given by:

$$\tilde{\mathbf{B}}_{\mathbf{r}}^{[N_{\vartheta}-2 \times N_{\varphi}]}(q, m) = \begin{bmatrix} -\tilde{\mathbf{B}}_1(q, m) & -\tilde{\mathbf{B}}_2(q, m) \end{bmatrix}, \quad (3.15)$$

with the matrices  $\tilde{\mathbf{B}}_1$  and  $\tilde{\mathbf{B}}_2$  as follows:

$$\tilde{\mathbf{B}}_1^{[N_{\vartheta}-2 \times N_{\varphi}/2]}(q, m) = \begin{bmatrix} \mathbf{0} & \mathbf{\Pi}^{[N_{\vartheta}-2 \times N_{\varphi}-2]} & \mathbf{0} \end{bmatrix} \cdot \tilde{\mathbf{B}}^{[N_{\vartheta} \times N_{\varphi}]}(q, m) \cdot \begin{bmatrix} \mathbf{0}^{[N_{\varphi}/2 \times N_{\varphi}/2]} \\ \mathbf{I}^{[N_{\varphi}/2 \times N_{\varphi}/2]} \end{bmatrix} \quad (3.16)$$

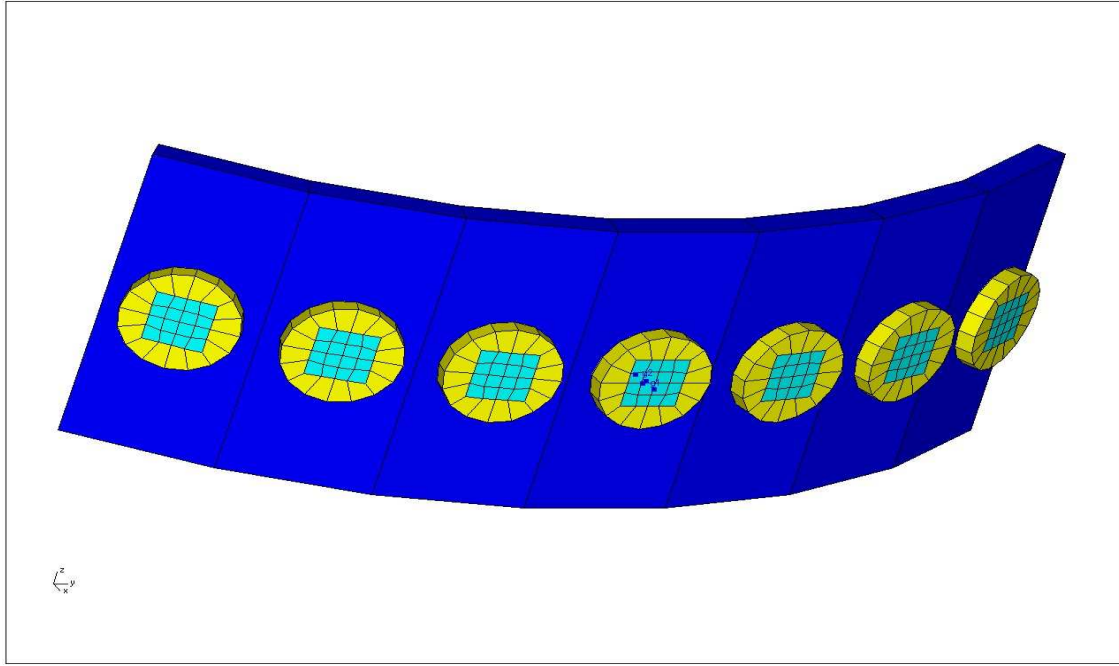
$$\tilde{\mathbf{B}}_2^{[N_{\vartheta}-2 \times N_{\varphi}/2]}(q, m) = \begin{bmatrix} \mathbf{0} & \mathbf{\Pi}^{[N_{\vartheta}-2 \times N_{\varphi}-2]} & \mathbf{0} \end{bmatrix} \cdot \tilde{\mathbf{B}}^{[N_{\vartheta} \times N_{\varphi}]}(q, m) \cdot \begin{bmatrix} \mathbf{I}^{[N_{\varphi}/2 \times N_{\varphi}/2]} \\ \mathbf{0}^{[N_{\varphi}/2 \times N_{\varphi}/2]} \end{bmatrix}, \quad (3.17)$$

where  $\mathbf{\Pi}$  is a reflection matrix (see Appendix E.3 eqn. (E.4)). In essence this extension follows from  $-\tilde{\mathbf{B}}(q, m)$  shifted about  $180^\circ$  in azimuth and flipped in co-elevation direction. The negation of  $\tilde{\mathbf{B}}(q, m)$  results from the rotation of the polarisation vector by  $180^\circ$ .

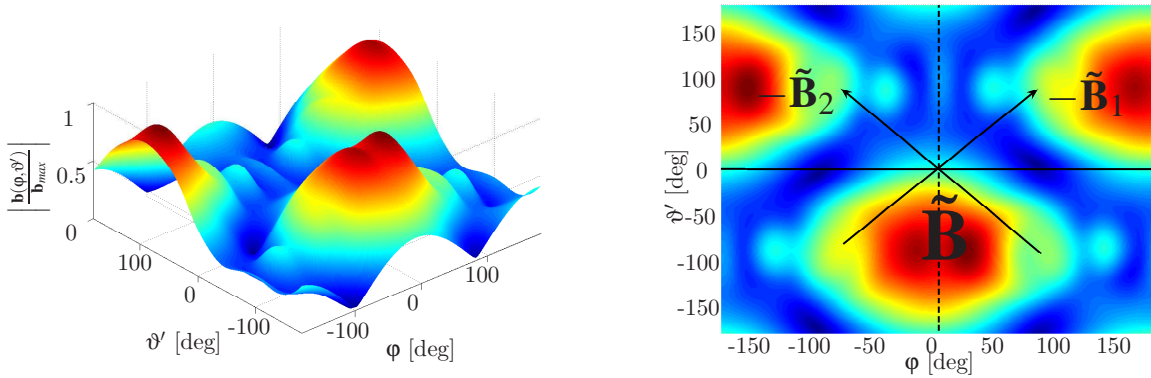
The 2D radiation pattern of the resulting matrix structure can be seen in Fig. 3.4. Within this chapter, a simulated radiation pattern<sup>1</sup> of the polarimetric uniform circular patch array (PUC-PAx2x1x24) (see Fig. 3.3) with 24 dual polarised patch antennas is used. The radiation pattern is simulated in the presence of adjacent antenna elements and is consequently affected by mutual coupling. The radiation pattern shown is related to the generator g1 (or port g1 which is in this thesis equivalent to an antenna element) for vertical excitation  $q = v$ . The patch antenna itself is located in the origin of the coordinate system, which means that  $\mathbf{b}(\varphi, \vartheta, q, m)$  is equal to  $\mathbf{b}_A(\varphi, \vartheta, m)$  of the single antenna element.

---

<sup>1</sup> The antenna simulation is carried out by IRK-Dresden [87] with the software WIPL-D [99].



**Fig. 3.3:** Simulation layout [87] of a dual polarised patch with adjacent elements in a PUCPA with 24 elements



**Fig. 3.4:** Radiation pattern  $\tilde{\mathbf{B}}_p$  (periodic in azimuth and co-elevation) with  $\vartheta' = \vartheta - \pi$

### 3.3.3 EADF calculated from the 2D Periodic Radiation Pattern

To calculate the 2D Fourier transform of the radiation pattern  $\tilde{\mathbf{B}}_p(q, m)$ , one could multiply  $\tilde{\mathbf{B}}_p(q, m)$  from the right and the left with the conventional Fourier matrix of size  $N_\phi$  and  $N'_\vartheta$  respectively. As the EADF considers only the relevant samples  $L_\vartheta \times L_\phi$  of the 2D Fourier transform, a reduced version of the full Fourier matrix is used for transformation. Herewith, the elevation transformation matrix is defined as:

$$\mathbf{D}_\vartheta = e^{-j2\pi \cdot \vartheta' \cdot \mathbf{f}_\vartheta} = e^{-j2\pi \mu_\vartheta \Delta f_\vartheta \cdot \mathbf{n}_\vartheta \Delta \vartheta'} = e^{-j2\pi \cdot \mu_\vartheta \mathbf{n}_\vartheta / N'_\vartheta}; \quad \Delta \vartheta' = \frac{2\pi}{N'_\vartheta}; \quad \Delta f_\vartheta = \frac{1}{2\pi} \quad (3.18)$$

with:

$$\mathbf{n}_\vartheta = \left[ \begin{array}{c} -\frac{N'_\vartheta}{2} \quad \dots \quad \frac{N'_\vartheta}{2} - 1 \end{array} \right]; \quad \vartheta' = \vartheta - \pi \quad (3.19)$$



and the vector for the selection of the  $L_\vartheta$  relevant co-elevation aperture samples:

$$\boldsymbol{\mu}_\vartheta^T = \left[ \frac{-(L_\vartheta-1)}{2} \quad \dots \quad \frac{(L_\vartheta-1)}{2} \right]. \quad (3.20)$$

The azimuth transformation matrix is defined as:

$$\mathbf{D}_\varphi = e^{-j2\pi \cdot \boldsymbol{\varphi} \cdot \mathbf{f}_\varphi} = e^{-j2\pi \mu_\varphi \Delta f_\varphi \cdot \mathbf{n}_\varphi \Delta \varphi} = e^{-j2\pi \cdot \mu_\varphi \mathbf{n}_\varphi / N_\varphi}; \quad \Delta \varphi = \frac{2\pi}{N_\varphi}; \quad \Delta f_\varphi = \frac{1}{2\pi}, \quad (3.21)$$

with:

$$\mathbf{n}_\varphi^T = \boldsymbol{\mu}_\varphi = \left[ -\frac{N_\varphi}{2} \quad \dots \quad \frac{N_\varphi}{2} - 1 \right] \quad (3.22)$$

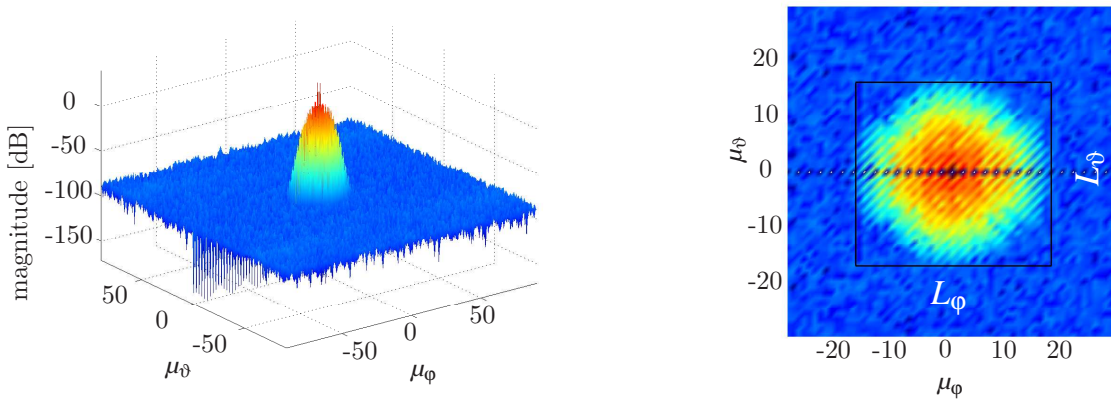
and the vector for the selection of the  $L_\varphi$  relevant azimuth aperture samples:

$$\boldsymbol{\mu}_\varphi = \left[ -\frac{(L_\varphi-1)}{2} \quad \dots \quad \frac{(L_\varphi-1)}{2} \right]. \quad (3.23)$$

With  $\mathbf{f}_\vartheta$ ,  $\mathbf{f}_\varphi$  being the frequencies in aperture domain. Finally, the EADF of the  $m$ -th antenna element is:

$$\mathbf{G}(q, m) = \frac{1}{N_\varphi \cdot N_\vartheta'} \mathbf{D}_\vartheta \cdot \tilde{\mathbf{B}}_p(q, m) \cdot \mathbf{D}_\varphi. \quad (3.24)$$

On the left side of Fig. 3.5 the magnitude of the 2D Fourier transform of the used example radiation pattern is shown, on the right side the relevant samples for the EADF are pointed out. In case of an over-sampling in the angular domain, this transformation maybe used to achieve a data compression Fig. 3.5 (right).



**Fig. 3.5:** Fourier transform of the over-sampled radiation pattern (left), relevant samples  $L_\varphi$  and  $L_\vartheta$  for the EADF (right)

### 3.3.4 Analytic Expression for Radiation Patterns and Derivatives of an Antenna Array

In the previous section it was described how the discrete EADF can be obtained from the discrete measured radiation pattern. In principle, the inverse transformation from the EADF to the radi-

tion pattern is similar, but different in the way that an analytic expression for the radiation patterns and their derivatives is desired. For this purpose, the complex exponentials for the co-elevation and azimuth are used:

$$\mathbf{d}_{\vartheta}(\vartheta') = e^{j\vartheta' \cdot \boldsymbol{\mu}_{\vartheta}^T} \quad (3.25)$$

$$\mathbf{d}_{\varphi}(\varphi) = e^{j\mu_{\varphi} \cdot \varphi}. \quad (3.26)$$

This allows us to calculate the radiation pattern and its derivatives for an arbitrary azimuth/co-elevation angle pair  $\varphi, \vartheta$  as follows:

$$\mathbf{b}(\varphi, \vartheta, q, m) = \mathbf{d}_{\vartheta} \cdot \mathbf{G}(q, m) \cdot \mathbf{d}_{\varphi} \quad (3.27)$$

$$\frac{\partial \mathbf{b}(\varphi, \vartheta, q, m)}{\partial \vartheta} = j \cdot \mathbf{d}_{\vartheta} \cdot \text{diag} \{ \boldsymbol{\mu}_{\vartheta}^T \} \cdot \mathbf{G}(q, m) \cdot \mathbf{d}_{\varphi} \quad (3.28)$$

$$\frac{\partial \mathbf{b}(\varphi, \vartheta, q, m)}{\partial \varphi} = j \cdot \mathbf{d}_{\vartheta} \cdot \mathbf{G}(q, m) \cdot \text{diag} \{ \mu_{\varphi}^T \} \cdot \mathbf{d}_{\varphi}. \quad (3.29)$$

In the following, the joint calculation of the  $M$  radiation patterns and their derivatives of an antenna array are introduced. The equations can be used for an analytic calculation of the vector valued function of the radiation patterns:

$$\mathbf{b}(\varphi, \vartheta, q)^{[M \times 1]} = \begin{bmatrix} \text{vec} \{ \mathbf{G}(q, m = 1) \}^T \\ \vdots \\ \text{vec} \{ \mathbf{G}(q, m = M) \}^T \end{bmatrix} \cdot \text{vec} \{ \mathbf{d}_{\vartheta}^T(\vartheta) \cdot \mathbf{d}_{\varphi}^T(\varphi) \} \quad (3.30)$$

$$\mathbf{b}(\varphi, \vartheta, q)^{[M \times 1]} = \Gamma^{[M \times L_{\vartheta} \cdot L_{\varphi}]}(q) \cdot \mathbf{d}^{[L_{\vartheta} \cdot L_{\varphi} \times 1]}(\vartheta, \varphi). \quad (3.31)$$

and their derivatives dependent on azimuth  $\varphi$  and co-elevation  $\vartheta$ :

$$\frac{\partial \mathbf{b}(\varphi, \vartheta, q)^{[M \times 1]}}{\partial \varphi} = \mathbf{\blacksquare}^{[M \times L_{\vartheta} \cdot L_{\varphi}]}(q) \cdot \frac{\partial \mathbf{d}^{[L_{\vartheta} \cdot L_{\varphi} \times 1]}(\varphi, \vartheta)}{\partial \varphi} \quad (3.32)$$

$$\frac{\partial \mathbf{b}(\varphi, \vartheta, q)^{[M \times 1]}}{\partial \vartheta} = \mathbf{\blacksquare}^{[M \times L_{\vartheta} \cdot L_{\varphi}]}(q) \cdot \frac{\partial \mathbf{d}^{[L_{\vartheta} \cdot L_{\varphi} \times 1]}(\varphi, \vartheta)}{\partial \vartheta}. \quad (3.33)$$

The derivatives of the combined complex exponentials  $\frac{\partial \mathbf{d}(\vartheta, \varphi)}{\partial \vartheta}$  and  $\frac{\partial \mathbf{d}(\vartheta, \varphi)}{\partial \varphi}$  for co-elevation and azimuth are applied.

Notice, that using these equations ((3.31), (3.32), and (3.33)) the number of real multiplications increases to  $8 \cdot L_{\vartheta} \cdot L_{\varphi}$  instead of  $4(L_{\vartheta} \cdot L_{\varphi} + L_{\varphi})$  when using equation (3.27) to calculate the radiation

pattern and derivatives with respect to one angle pair  $\boldsymbol{\varphi}$ ,  $\boldsymbol{\vartheta}$ .

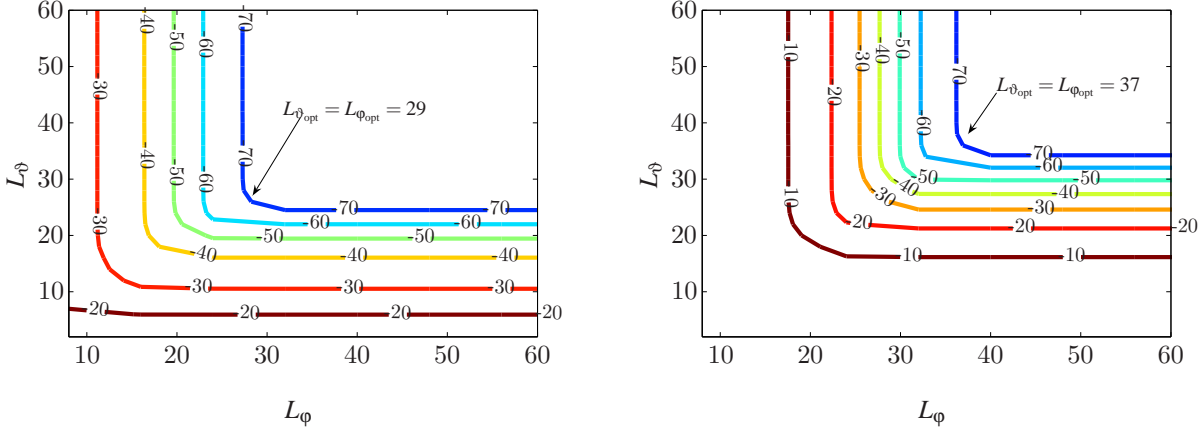
The efficient computation of the  $M$  radiation patterns of an antenna array dependent on a set of angle pairs (azimuth, co-elevation) and both polarisations is an important issue for most parameter estimation algorithms (Chapter 5) and for channel modelling (e.g. IST-WINNER Channel Model [22], IlmProp (geometry-based Multi-User MIMO Channel Modelling tool) [77]). Both the WINNER channel model and the IlmProp channel modelling tool use the previously described EADF framework for the calculation of the radiation patterns. However, for the commercially available RIMAX algorithm ([53]) and for this thesis a more efficient antenna array data format for a joint calculation of the  $M$  radiation patterns and their derivatives is developed. The inherent redundancy of the EADF is removed and an efficient matrix notation for the joint calculation of all radiation patterns and derivatives in one step is found. For the reader's convenience this implementation is discussed in Appendix B.1.

### 3.3.5 Model Error Dependent on the Number of Relevant Samples Used for the EADF

The model error of the previously described analytic description of the radiation patterns can be expressed as the mean interpolation error  $\zeta$ :

$$\zeta(L_\varphi, L_\vartheta, q, m) = \sqrt{\frac{1}{N'_\vartheta \cdot N_\varphi} \frac{\left\| \text{vec} \{ \tilde{\mathbf{B}}_p \} - \text{vec} \{ \mathbf{D}_\vartheta^H \cdot \mathbf{G}(q, m)^{[L_\vartheta \times L_\varphi]} \cdot \mathbf{D}_\varphi^H \} \right\|_F^2}{\text{vec} \{ \tilde{\mathbf{B}}_p \}^H \cdot \text{vec} \{ \tilde{\mathbf{B}}_p \}}} \quad (3.34)$$

dependent on the size  $L_\varphi \times L_\vartheta$  of the EADF  $\mathbf{G}(q, m)$ . The minimum achievable mean interpolation error is limited by the SNR of the measurement. Consequently, the optimum size of the EADF with  $L_{\vartheta_{\text{opt}}}$ ,  $L_{\varphi_{\text{opt}}}$  is reached, when the mean interpolation error  $\zeta(L_\varphi, L_\vartheta, q, m)$  can not be improved by a EADF size larger than  $L_{\varphi_{\text{opt}}} \times L_{\vartheta_{\text{opt}}}$ . For comparison, in Fig. 3.6 the mean interpolation error is shown for the case of a centred patch antenna and an antenna placed at a radius of  $r = 1.75 \cdot \lambda$  (related to the rotation centre). The figure clearly shows that the interpolation error is larger in case of an eccentric positioned patch antenna with respect to the same  $L_\vartheta$ ,  $L_\varphi$ . Thus, the aperture size of the eccentric positioned antenna becomes larger compared to centred positioned antenna. In other words, the EADF of the phase term  $\mathbf{b}_{\text{ph}}$  is convolved with the EADF of the radiation pattern of the antenna  $\mathbf{b}_A$ , which results in a larger number of relevant samples for the EADF of the eccentric positioned antenna to achieve the same model accuracy. The accuracy of the radiation pattern simulation used was limited to 70 dB. Analysing Fig. 3.6, the optimum size of the EADF in case of the centred antenna is  $L_{\vartheta_{\text{opt}}} = L_{\varphi_{\text{opt}}} = 29$  and  $L_{\vartheta_{\text{opt}}} = L_{\varphi_{\text{opt}}} = 37$  in case of the eccentric placement of the antenna. Thus, only the data of the finite support area with the size  $L_{\vartheta_{\text{opt}}}$  by  $L_{\varphi_{\text{opt}}}$  are kept as EADF. The mean SNR of the relevant aperture samples for the EADF is higher than the mean SNR of the samples in the angular domain in case of an oversampling in the angular domain. Consequently, a SNR enhancement can be achieved by using the EADF for the calculation of the radiation pattern.



**Fig. 3.6:** Mean interpolation error  $\zeta$  in dB in case that the patch antenna is centred (left) and in case that the patch antenna is placed at a radius of  $r = 1.75 \cdot \lambda$  (right)

### 3.4 Performance and Accuracy Comparison Between Different Interpolation Methods

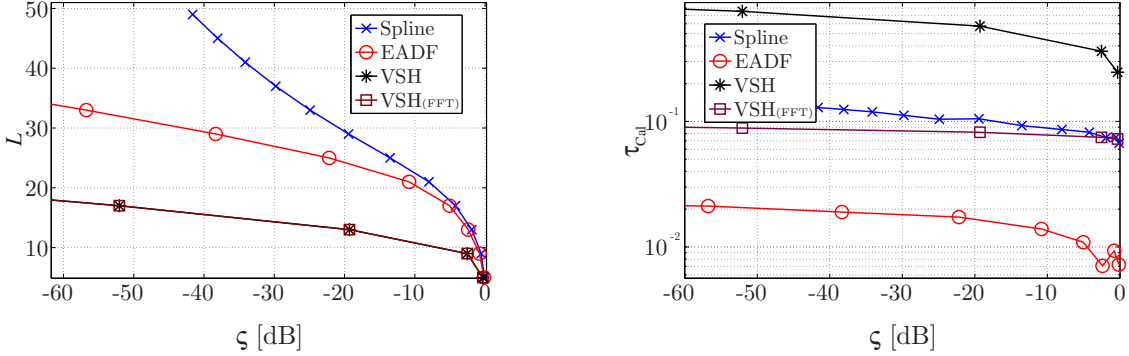
In this section the proposed data format for antenna array radiation pattern interpolation, described in Appendix B.1, will be compared with the conventional Spline interpolation and the interpolation using the vector spherical harmonics (VSH). The performance and accuracy of these algorithms will be shown.

An antenna array with 30 dual polarised patch antennas is simulated. The simulated radiation pattern of the PUCPA is used for each antenna element. The Spline interpolation is used as implemented in MATLAB, for the VSH an implementation is used as described in [21]. For the VSH, two different versions are implemented. The first version uses a FFT, which implies that the radiation pattern can only be interpolated in an equidistant grid in the azimuth angle. The second version does not use the FFT and arbitrary grids can be used. With all four interpolation methods, the radiation patterns of all 30 elements for horizontal and vertical excitation are calculated. The interpolation grid is set to  $3^\circ$  in azimuth and co-elevation. First, the accuracy is investigated by calculating the mean interpolation error  $\zeta$  depending on the total number of samples or coefficients  $L^2$  used for the interpolation of one radiation pattern. In case of the EADF, the number of samples in the azimuth aperture and co-elevation aperture are chosen to be  $L = L_\phi = L_\psi$ , in case of the Spline interpolation, an equidistant grid with  $L$  samples in azimuth and  $L$  samples in co-elevation is used and in case of the VSH the total number of coefficients is set to  $L^2$ .

Figure 3.7 (left) plots the required number of samples  $L$  that are necessary to achieve a certain mean interpolation error  $\zeta$ . The figure indicates clearly that the VSH performs best in terms of accuracy by using less samples than the EADF and the Spline interpolation. Furthermore, the calculation time vs. the mean interpolation error is computed. The radiation patterns for all 30 elements are calculated 1000 times with each method. The normalised calculation time is plotted for all 4 methods in Fig. 3.7 (right). All times are relative to the maximum calculation time of all methods. It can be seen that the EADF performs 6 to 10 times faster than VSH<sub>(FFT)</sub> or Spline by achieving the same accuracy. Compared to the Spline interpolation this performance is related to

the higher compression of the radiation pattern using the compressed **EADF** data format, which implies less multiplications. In case of **VSH (FFT)** and **VSH**, mainly the higher complexity is the reason for this performance difference.

Additionally, the first order derivatives of the radiation patterns dependent on azimuth and elevation can be calculated analytically by using the **EADF**, achieving the same performance as for the radiation patterns. In case of the Spline, the derivatives can be calculated only numerically, and in case of the **VSH** the complexity is also rather high.



**Fig. 3.7:** Number of required samples  $L$  vs. the mean interpolation error  $\zeta$  (left), normalised calculation time  $\tau_{Cal}$  vs. the mean interpolation error  $\zeta$  (right)

### 3.5 Minimum Angular Sampling Grid for Antenna Array Radiation Patterns

In the following, a minimum angular sampling grid, which is necessary for several array signal processing algorithms, is derived based on the idea of the **EADF**. The proposed grid fulfils the Nyquist theorem in space for the radiation patterns used. The usage of a minimum number of samples is of major importance, as it has direct impact on the calculation time and memory consumption of the signal processing algorithm.

One could use an equidistant grid in azimuth and co-elevation, but when analysing the distribution of the sampling points on the sphere, it is clear that the points are much denser at the poles. To calculate the integral of functions on the sphere, in which case only sampled data are available, several grids like Chebyshev angular grid (equidistant grid and same number of samples in  $\varphi$  and  $\vartheta$ ), Gauss-Legendre angular grid (equidistant grid and double number of samples in  $\varphi$  compared to  $\vartheta$ ) and Lebedev angular grid [91, 92] are proposed. The latter is the most efficient, since it distributes less samples at the poles and more around the equator. Unfortunately these grids are not available for an arbitrary number of sampling points.

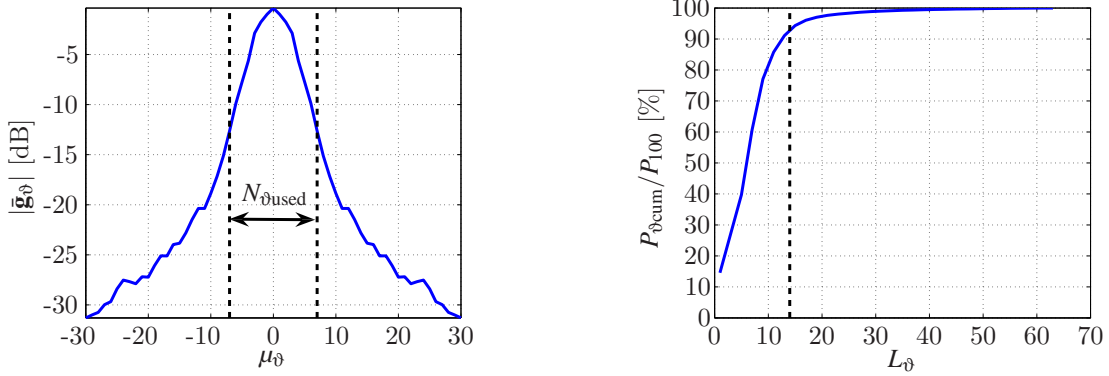
In the following it is described how to derive a grid with a minimum number of sampling points for practical antenna arrays. The method is based on the Fourier transform of the radiation patterns of all antenna elements in an array. The derivation takes place in two steps: first defining the minimum number of samples used in co-elevation  $N_{\vartheta_{used}}$  and second defining the minimum number of samples used in azimuth  $N_{\varphi_{used}}(\vartheta)$  for each co-elevation sample. Both steps are demonstrated

using the data of the **UCAx1x1x16** (see Fig. 3.8) and the **PUCPAx2x1x24** (see Fig. 3.9).

The required samples in co-elevation  $N_{\vartheta_{\text{used}}}$  are derived from the mean magnitude of the co-elevation Fourier transform over all antenna elements and azimuth angles:

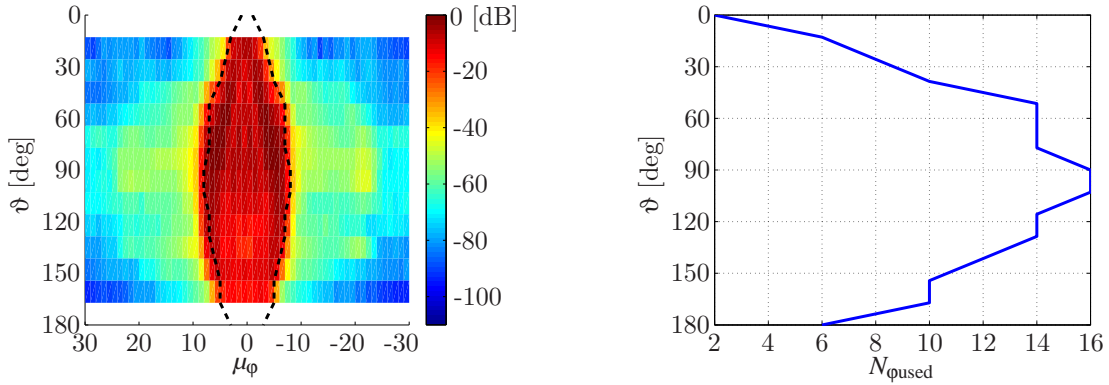
$$\bar{\mathbf{g}}_{\vartheta}^{[L_{\vartheta} \times 1]} = \sum_{m=1}^{M_{\text{Rx}}} \left| \mathbf{D}_{\vartheta}^{[L_{\vartheta} \times N'_{\vartheta}]} \cdot \mathbf{B}_{\text{p}}^{[N'_{\vartheta} \times N_{\varphi}]}(m) \right| \cdot \mathbf{1}^{[N_{\varphi} \times 1]}. \quad (3.35)$$

The range covered by  $N_{\vartheta_{\text{used}}}$  contains 95% of the signal energy of the mean co-elevation aperture (Fig. 3.8(a), Fig. 3.9(a)). The number of co-elevation samples  $N_{\vartheta_{\text{used}}}$  used for the minimum grid is determined by calculating the cumulative power sum  $P_{\text{cum}\vartheta}$  in the range of  $\mu_{\vartheta} = \pm 1$  to  $\mu_{\vartheta} = \pm \frac{L_{\vartheta}-1}{2}$ . In Fig. 3.8(b) and in Fig. 3.9(b) the relative cumulative power sum  $P_{\text{cum}\vartheta}/P_{100}$  is shown,  $P_{100}$  being the total signal power in the mean co-elevation aperture. In the second step, the number of



(a) Mean aperture in co-elevation  $\bar{\mathbf{g}}_{\vartheta}$  of the **UCAx1x1x16**

(b) Relative cumulative power vs. aperture samples  $L_{\vartheta}$  **UCAx1x1x16**

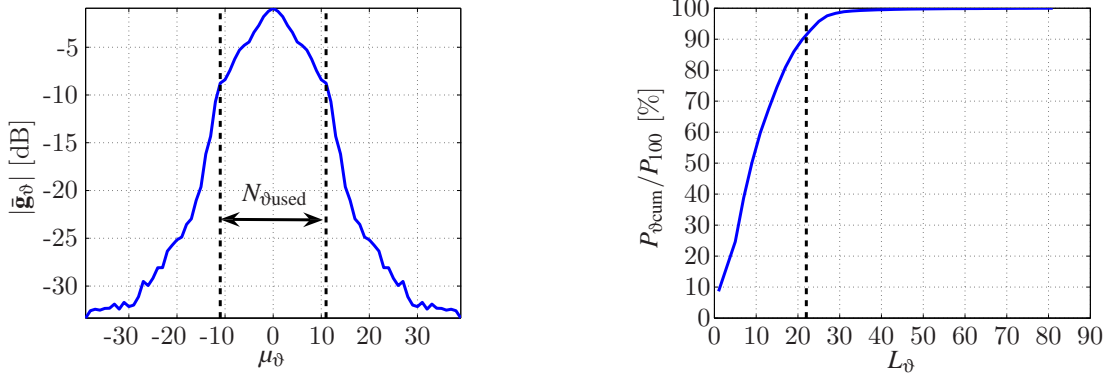


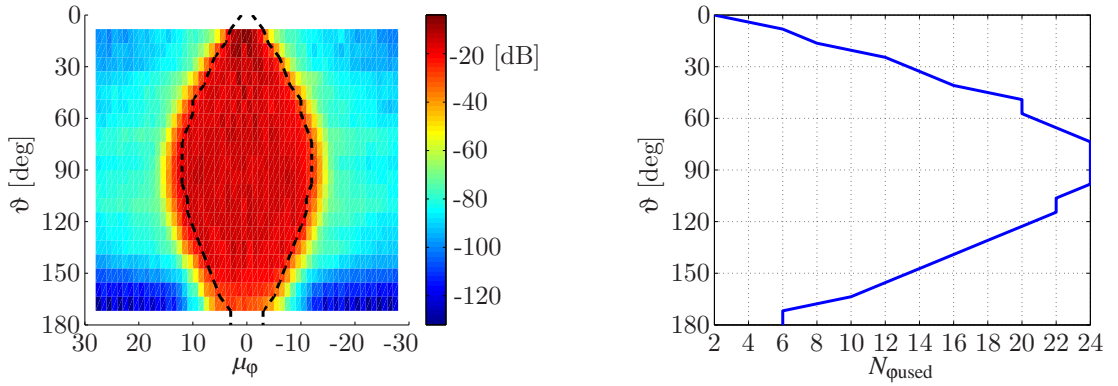
(c) Magnitude of the mean azimuth aperture  $\bar{\mathbf{G}}_{\varphi}$  of the **UCAx1x1x16** vs. co-elevation

(d) Number of used azimuth samples vs. the co-elevation level **UCAx1x1x16**

**Fig. 3.8:** Co-elevation and azimuth step in deriving the minimum sampling grid in case of the **UCAx1x1x16**

sampling points in azimuth for the  $N_{\vartheta_{\text{used}}}$  equidistant spaced co-elevation angles in the range of  $0^{\circ}$


 (a) Mean aperture in co-elevation  $\bar{\mathbf{g}}_{\vartheta}$  of the **PUC-PAx2x1x24**

 (b) Relative cumulative power w.r.t. aperture samples  $L_{\vartheta}$  **PUCPAx2x1x24**

 (c) Mean azimuth aperture  $|\bar{\mathbf{G}}_{\varphi}|$  (dB) of the **PUC-PAx2x1x24**

 (d) Number of used azimuth samples w.r.t. the co-elevation level **PUCPAx2x1x24**
**Fig. 3.9:** Co-elevation and azimuth step in deriving the minimum sampling grid in case of the **PUCPAx2x1x24**

to  $180^\circ$  are derived. The mean aperture in azimuth is calculated:

$$\bar{\mathbf{G}}_{\vartheta}^{[N_{\vartheta_{\text{used}} \times L_{\varphi}}]} = \sum_{m=1}^{M_{\text{Rx}}} \left| \mathbf{B}^{[N_{\vartheta_{\text{used}} \times N_{\varphi}}]}(m) \cdot \mathbf{D}_{\vartheta}^{[N_{\varphi} \times L_{\varphi}]} \right|, \quad (3.36)$$

where  $\mathbf{B}^{[N_{\vartheta_{\text{used}} \times N_{\varphi}}]}(m)$  is the  $m$ -th radiation pattern oversampled in azimuth with  $N_{\varphi}$  samples and with  $N_{\vartheta_{\text{used}}}$  samples in co-elevation, as derived above. In Fig. 3.8(c) and Fig. 3.9(c) it becomes clear that the number of required samples in azimuth decreases towards the poles of the spherical coordinate system. Calculating the cumulative power sum at the  $N_{\vartheta_{\text{used}}}$  co-elevation samples  $\vartheta_{\text{used}} = [0 \dots \frac{\pi}{N_{\vartheta_{\text{used}}-1}} \dots \pi]$  the number of required samples  $N_{\varphi_{\text{used}}}(\vartheta_{\text{used}})$  can be derived (assuming 95% of the total power). In the figures of the mean azimuth aperture the range  $N_{\varphi_{\text{used}}}(\vartheta)$  is specified by the dashed black lines. Furthermore, in Fig. 3.8(d) and 3.9(d)  $N_{\varphi_{\text{used}}}(\vartheta_{\text{used}})$  is plotted vs. the co-elevation samples  $\vartheta_{\text{used}}$ . As the parameters  $N_{\vartheta_{\text{used}}}$  and  $N_{\varphi_{\text{used}}}(\vartheta_{\text{used}})$  are directly related to the aperture size of the antenna array, as seen comparing the results of the **UCAx1x1x16** and **PUCPAx2x1x24**, an optimum sampling grid can be derived for each antenna array (see Fig. 3.10). For demonstration,

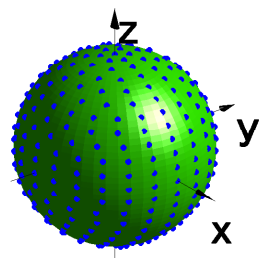
the derived sampling grid for the **PUCPAx2x1x24** with a total number of  $N_{95} = 363$  sampling points at the sphere is shown in the spherical coordinate system (Fig. 3.10(a), Fig. 3.10(d)) and in the Cartesian coordinate system (Fig. 3.10(b)). In comparison, an equidistant sampling grid in azimuth and co-elevation with the same resolution at the equator requires 1225 points (Fig. 3.10(c)). This is approximately a factor of four more sampling points compared to the proposed grid. In the following chapters this grid is called **N95** grid:

$$\zeta^{N_{95}} = \{(\varphi_{n_{95}}, \vartheta_{n_{95}}); n_{95} \in Z; n_{95} \in [1, N_{95}]\} \quad (3.37)$$

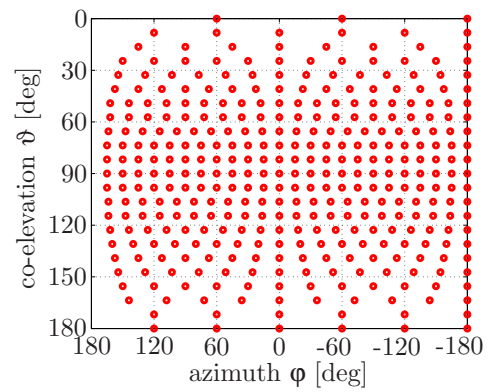
with a total number of  $N_{95}$  sampling points, each sampling point consisting of a pair of angles  $\langle \varphi_{n_{95}}, \vartheta_{n_{95}} \rangle$ . Observing the grids of different arrays (Fig. 3.10(d), 3.10(e), Fig. 3.10(f)), the direct relation to the aperture size of the antenna array becomes obvious again. Furthermore, the grid seems to be almost uniformly distributed at the sphere.

Note that this grid is mainly developed to speed up the parameter estimation process in the **RI-MAX** algorithm. A further possible application would be a time efficient antenna array calibration measurement with a minimum number of sampling points.

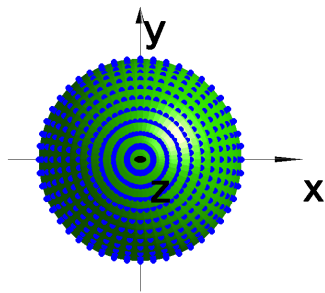




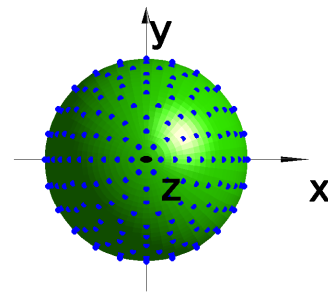
(a) Minimum grid of the **PUCPA<sub>x2x1x24</sub>** with 363 points, lateral view



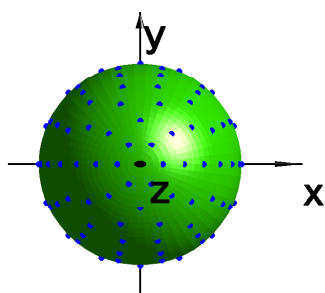
(b) Minimum grid of the **PUCPA<sub>x2x1x24</sub>** with 363 points in Cartesian coordinate system



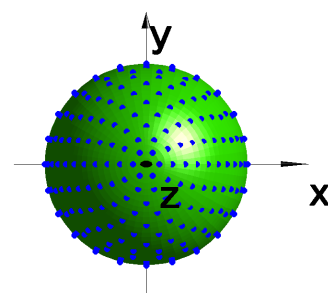
(c) Equidistant grid in azimuth and co-elevation of the **PUCPA<sub>x2x1x24</sub>** with 1225 points top view



(d) Minimum grid with 363 points of the **PUCPA<sub>x2x1x24</sub>** top view



(e) Minimum grid of the **UCA<sub>x1x1x16</sub>** with 167 points, top view



(f) Minimum grid of the **SPUCPA<sub>x2x4x24</sub>** with 437 points, top view

**Fig. 3.10:** Sampling grids in the angular domain in case of the **PUCPA<sub>2x1x24</sub>**, **UCA<sub>1x1x16</sub>** and the **SPUCPA<sub>2x4x24</sub>**



## 4. ANTENNA ARRAY CALIBRATION

This chapter addresses the practical issues of antenna array calibration. The radiation patterns and their **EADFs** as described in the previous chapter are derived from measurements with a novel estimation algorithm.

In Section 4.1 it is discussed, how the antenna array radiation patterns are obtained from calibration measurements. The measurement setup using a channel sounder is introduced in Section 4.1.1. The calibration of the **RF** signal path and the **Tx** reference horn antenna of the measurement system is presented in Section 4.1.3 and in Section 4.1.4 respectively. With the calibrated system we are capable of obtaining the antenna array radiation patterns in absolute gain and phase, as it will be discussed in Section 4.1.5.

The estimation of the **EADFs** from the measured radiation patterns in the presence of a varying collective phase offset during calibration measurement is presented in Section 4.2. In Section 4.2.1 a measurement data model that incorporates a collective phase offset dependent on the measurement position is introduced. An estimation algorithm (first published in [29]) that estimates both: the **EADFs** and the phase offsets is proposed in Section 4.2.2. The algorithm performance is shown in simulations and measurements in Sections 4.2.3 and 4.2.4 respectively.

For three different types of antenna arrays, the **2D** radiation patterns and **EADFs** obtained from measurement are shown and discussed in Section 4.3.

### 4.1 Obtaining the Antenna Array Radiation Patterns from Measurement

Traditionally a network analyser together with a positioning system is used to measure the frequency response of the antenna vs. the angle of arrival and vs. polarisation. A set of measurement points in azimuth and elevation are recorded in one measurement cycle for horizontal polarisation ( $\vec{e}_\phi$ ) and in a second cycle for vertical polarisation ( $\vec{e}_\theta$ ). Demanding a high accuracy of the measured radiation pattern increases the measurement time drastically. Furthermore, the calibration measurement time for antenna arrays increases with the number of antenna elements. As a **MIMO** channel sounder is based on a different measurement principle, as described in Chapter 2, the frequency responses of all antenna elements can be obtained much faster. Consequently, the sounders described in Section 2.3 will be used in the following.

The calibration of the radiation patterns in absolute gain and phase is of major importance, as already mentioned in Chapter 3. Therefore, the calibration of the system including the polarimetric reference horn antenna is required and will be discussed after introducing the measurement system setup. Finally, the narrow band radiation patterns are obtained from the measurements of the well calibrated measurement system.

---

### 4.1.1 Measurement System Setup

The device components that are needed for the calibration are shown in Fig. 4.1. The RF signal path is indicated by black lines and the control paths are indicated by blue and red lines. The entire measurement system is controlled by a personal computer (PC). The receiver (Rx) is controlled by Rx Ctr. and the transmitter (Tx) is controlled by Tx Ctr.. Furthermore, the PC controls the positioning system (Section 4.1.2) and the switching of the Tx multiplexer (Tx Multiplexer (MUX)), the Rx multiplexer (Rx MUX) and the multiplexer that is included in the antenna array to switch between antennas 1 to  $M_{Rx}$ . To allow the measurement of both polarisations in one positioning cycle, a dual polarised reference horn antenna is used. The Tx switching takes place between horizontal polarisation (Tx1) and the vertical polarisation (Tx2).

To record the long term phase drift dependent on the measurement time, as observed in Section 2.3.4 (see also Appendix A.1), a reference channel between Tx3 and Rx2 is measured. Therefore, an additional multiplexer at the Rx side (Rx MUX) that switches between the antenna array and the reference channel is necessary. The cable used for the reference channel is a RF cable with high phase stability. If such a reference channel does not exist an algorithmic solution for phase correction is necessary (see Section 4.2).

At the receiver, the RF signal passes through the switched reference attenuator before the radio frequency input (RF In). This controllable switched reference attenuator is used for the AGC dependent back-to-back calibration (see Section 2.3.2) to measure the AGC dependent frequency responses of the measurement system including all cables and multiplexers that are independent of the antenna array under test. During the antenna array calibration measurement the switched reference attenuator is set to 0 dB attenuation.

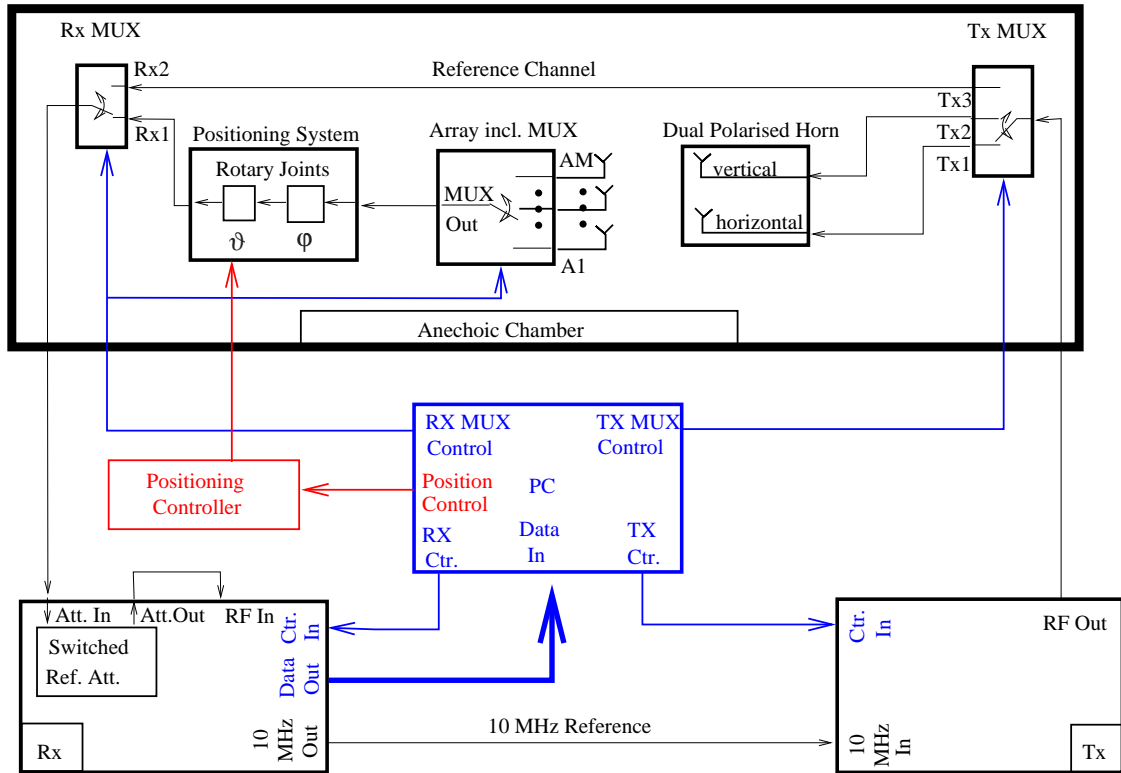
### 4.1.2 2D Antenna Positioning System

In most anechoic chambers two axis positioning systems are used to rotate the antenna under test with respect to the angles  $\varphi$  and  $\vartheta$  of the spherical coordinate system. The vertical rotation axis seen in Fig. 4.2 (left) assures the rotation in co-elevation  $\vartheta$  between  $0^\circ$  and  $180^\circ$ , whereas the horizontal axis assures the rotation in the azimuth  $\varphi$  between  $-180^\circ$  and  $180^\circ$ . The distance  $l_c$  is variable and has to be adjusted for every antenna array to place the centre of the antenna array in the pivot point of the positioning system. The pivot point is characterised by the intersection between the  $\varphi$ -rotation axis and the  $\vartheta$ -rotation axis.

If the radiation pattern of a single antenna is measured, the direction of the main beam normally corresponds to the direction of the  $\varphi$ -rotation axis. In this setup, the positioning system is in the rear direction of the main beam to minimise the influence of parasitic reflections. For antenna arrays, the alignment of the main beam of all radiation patterns in the same direction is normally impossible. Especially in the case of circular or spherical antenna arrays, each antenna has a different alignment. For example, calibrating a circular antenna usually means that the main beam direction of the antenna is orthogonal to the  $\varphi$ -rotation axis.

In the previous section it was already mentioned that the phase stability of the entire RF system

---



**Fig. 4.1:** Block diagram of the antenna array calibration measurement setup. The blue and red lines indicate the control lines and black lines indicate the RF signal path.

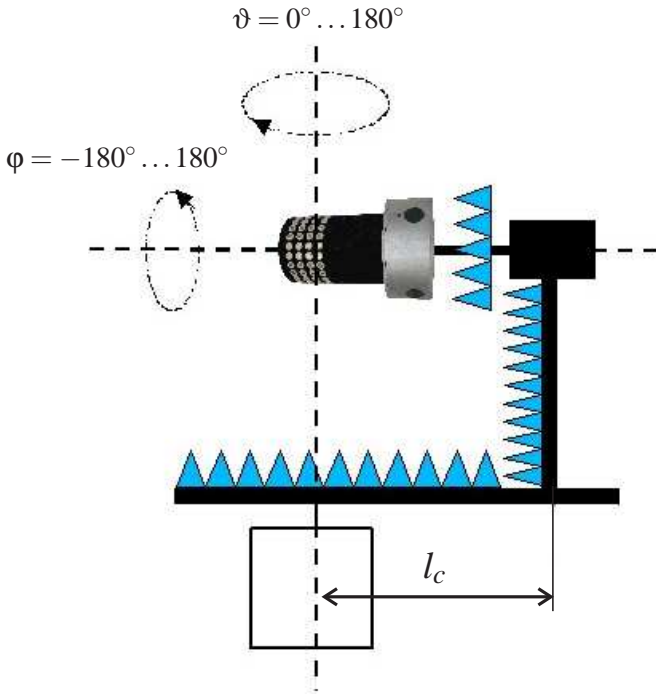
is an important issue. As a bending of a RF cable always causes a change in phase, the cables with high phase stability are fixed at the positioning system. At the rotation points of the positioning system the RF cables are connected to RF rotary joints, which ensure a high phase stability during rotation (see also Fig. 4.1).

### 4.1.3 Back-to-Back Calibration of the Measurement System

The back-to-back frequency response calibration procedure as described in Section 2.3.2 is applied. The frequency responses of all cables and devices in the RF signal path, which are independent of the antenna array under test have to be included in the back-to-back calibration. Two kinds of back-to-back calibration setups are considered, in which the MUX is either included or excluded.

The first setup will be applied to determine the antenna radiation patterns of the reference horn antenna (see Section 4.1.4). The multiplexer (MUX) used to switch between the horizontal and vertical port is not part of the antenna module. Therefore, the radiation patterns of each antenna port will be determined without any influence of RF cables or multiplexers, which are connected after the antenna output. Using the dual polarised reference horn antenna at the Tx side this setup results in  $M = 4$  measured system frequency responses  $G_{\text{Sys}}(f, m_{\text{Rx}}, m_{\text{Tx}})$ .

The second setup is used for measurement antenna arrays. As for measurement antenna arrays the MUX is permanently connected to the antennas, the MUX of the antenna array under test is not included in the back-to-back calibration. This means, the frequency responses of the MUX and all



(a) Schematic of the 2D positioning system



(b) Picture of the 2D positioning system

**Fig. 4.2:** Positioning system

RF cables until the MUX Out port of the antenna array will be a part of the frequency dependent radiation patterns of the array under test. Consequently, only  $M = 2$  back-to-back calibration frequency responses will be obtained. For the vertical excitation at the Tx, the back-to-back calibration data:

$$G_{\text{Sys}}(f, q = v) = G_{\text{Sys}}(f, m_{\text{Tx}} = 1) \quad (4.1)$$

is obtained by connecting the cable from the vertical input of the Tx reference horn antenna with the cable that is normally connected to the MUX Out of the Rx antenna array. For the horizontal excitation at the Tx, the back-to-back calibration data:

$$G_{\text{Sys}}(f, q = h) = G_{\text{Sys}}(f, m_{\text{Tx}} = 2) \quad (4.2)$$

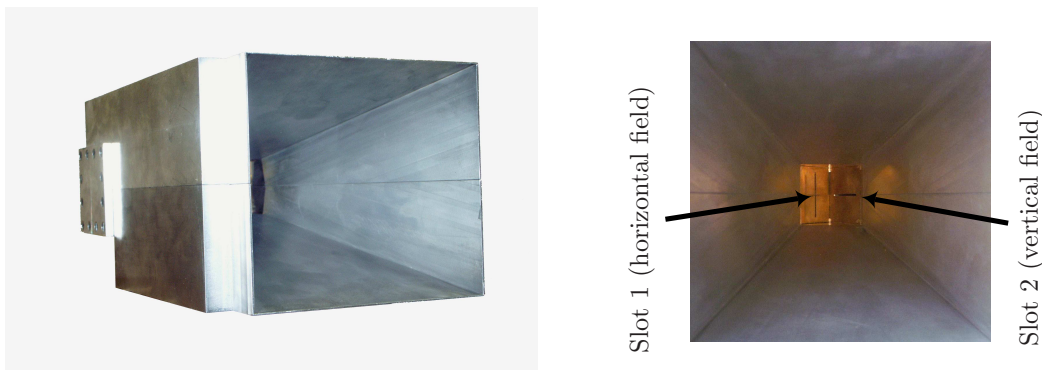
is obtained by connecting the cable from the horizontal input of the Tx reference horn antenna with the cable that is normally connected to the MUX Out of the Tx antenna array. This calibration setup is used to determine the radiation patterns of measurement antenna arrays (see Section 4.1.5). Note that Rx filter and Rx LNA characteristics, which may be included in the antenna array under test should be included in the back-to-back calibration. The reason for this is that the filters and LNAs are normally strongly frequency dependent. That means the narrow band radiation pattern can not be deduced from measurement data that includes the LNA or filter characteristics.

#### 4.1.4 Calibration of the Dual Polarised Reference Horn Antenna

For the radiation pattern measurement of an antenna array under test, a reference antenna is needed. The reference antenna should fulfil the following requirements:

1. two ports for the excitation of the vertical and horizontal electrical field
2. high cross polarisation discrimination (XPD) in the far field of the antenna for both excitations ( $XPD \geq 40$  dB)
3. same phase centre for both excitations
4. high gain in the main beam direction
5. low frequency dependence in the desired frequency band

To fulfil all these requirements a dual polarised horn antenna with a squared aperture is chosen (see Fig. 4.3 (left)). Inside the horn, two slot antennas Fig. 4.3 (right) are used: slot 1 (S1) to excite the horizontal electrical field and slot 2 (S2) to excite the vertical electrical field. To use this



**Fig. 4.3:** Dual polarised reference horn antenna (produced by IRK Dresden) (left), Aperture of the dual polarised horn antenna (right)

horn antenna as a reference antenna in the calibration of arbitrary antenna arrays, the complex frequency responses in absolute gain and phase for both ports are required. To determine these two frequency responses, the “two antenna method”, which requires two identical antennas will be used. One horn is used as transmit antenna and one as receive antenna that is placed at the positioning system. Both antennas are placed at the same height and aligned with a water meter. The direction where the two apertures are in parallel is defined as  $\varphi = 0^\circ$  and  $\vartheta = 90^\circ$ . After this alignment the two dimensional measurement of the Rx horn antenna is performed, which leads to  $\mathbf{y}_{S1S1}(f, \varphi, \vartheta)$ ,  $\mathbf{y}_{S1S2}(f, \varphi, \vartheta)$ ,  $\mathbf{y}_{S2S1}(f, \varphi, \vartheta)$  and  $\mathbf{y}_{S2S2}(f, \varphi, \vartheta)$ .

Let us first discuss the general behaviour of the dual polarised horn antenna. In Fig. 4.4 (left) the narrow band radiation pattern (using equation 3.9) with respect to the azimuth angle ( $\vartheta = 90^\circ$ ) is plotted, whereas in Fig. 4.4 (right) the radiation pattern with respect to the co-elevation angle ( $\varphi = 0^\circ$ ) is plotted. Furthermore, the XPD, which is defined as the ratio between the power of

the co-polarised radiation pattern with polarisation  $q$  to the power of the radiation pattern with cross-polarisation  $q_x$  (e.g.  $q$  is horizontal and  $q_x$  is vertical):

$$\text{XPD}(\varphi, \vartheta, m) = 10 \cdot \log_{10} \left( \frac{|\mathbf{b}(\varphi, \vartheta, q = q, m)|^2}{|\mathbf{b}(\varphi, \vartheta, q = q_x, m)|^2} \right) \quad [\text{dB}], \quad (4.3)$$

is calculated for both slot antennas from the 2D measurement data. In Fig. 4.5 the XPDs of slot 1 (left) and slot 2 (right) are shown with respect to azimuth and co-elevation. The polarisation characteristics of both slots are different. The maximum XPD in both cases is around 60 dB, but can not be achieved for the same direction for both slots. Therefore, the direction  $\varphi = 0^\circ$  and  $\vartheta = 90^\circ$  is chosen as the reference direction. For this direction the XPD of slot 1 (horizontal) is around 43 dB, whereas the XPD of slot 2 (vertical) is around 41 dB.

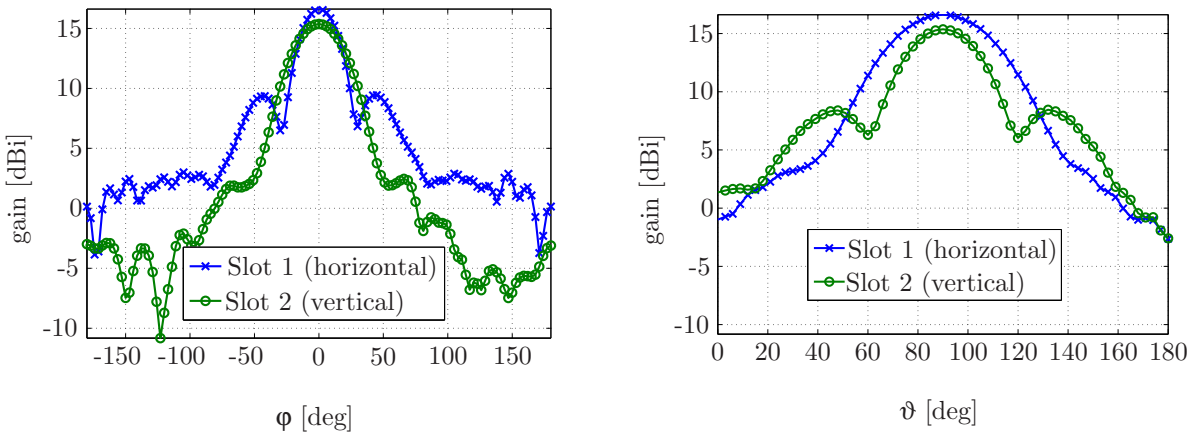
Finally, for the calibration of channel measurement antenna arrays one of these horn antennas is used as a reference antenna. The antenna array under test is placed in the direction  $\varphi = 0^\circ$ ,  $\vartheta = 90^\circ$  of the horn antenna. To exclude the characteristic of the reference antenna, the two frequency responses  $\mathbf{b}_{\text{Ref}}(f, q = h) = \mathbf{b}(f, \varphi = 0^\circ, \vartheta = 90^\circ)_{S1}$  and  $\mathbf{b}_{\text{Ref}}(f, q = v) = \mathbf{b}(f, \varphi = 0^\circ, \vartheta = 90^\circ)_{S2}$  are required. Applying the “two antenna method”, the frequency responses of slot 1 and slot 2 are defined as:

$$\mathbf{b}(f, \varphi = 0^\circ, \vartheta = 90^\circ)_{S1} = \sqrt{\frac{y(f)_{S1S1} \cdot 4\pi \cdot \tau \cdot f \cdot e^{j \cdot 2\pi \cdot f \cdot \tau}}{G_{\text{Sys}}(f, m_{\text{Rx}} = 1, m_{\text{Tx}} = 1)}} \quad (4.4)$$

and

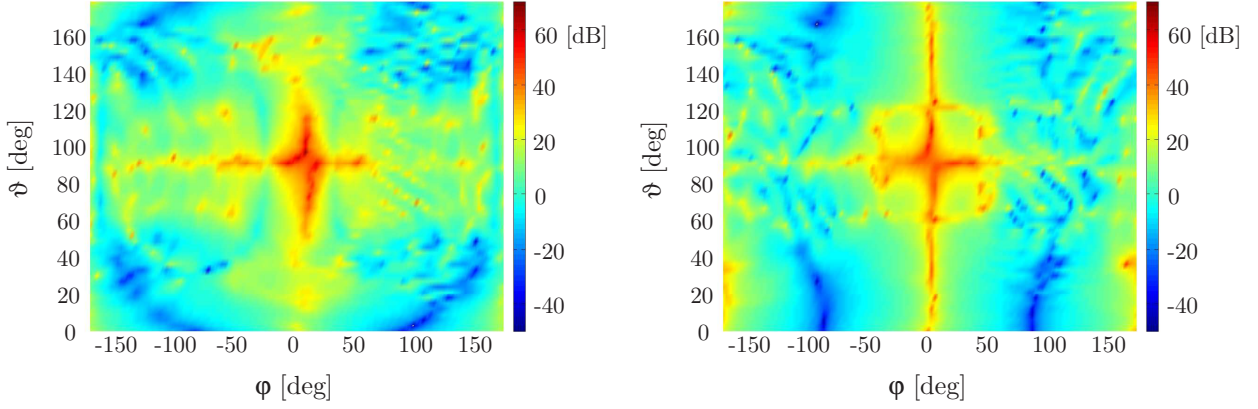
$$\mathbf{b}(f, \varphi = 0^\circ, \vartheta = 90^\circ)_{S2} = \sqrt{\frac{y(f)_{S2S2} \cdot 4\pi \cdot \tau \cdot f \cdot e^{j \cdot 2\pi \cdot f \cdot \tau}}{G_{\text{Sys}}(f, m_{\text{Rx}} = 2, m_{\text{Tx}} = 2)}}, \quad (4.5)$$

where  $\tau$  is the delay due to the distance between Tx horn antenna and Rx horn antenna. In Fig. 4.6 (left) the magnitudes of  $\mathbf{b}(f, \varphi = 0^\circ, \vartheta = 90^\circ)_{S1}$  and  $\mathbf{b}(f, \varphi = 0^\circ, \vartheta = 90^\circ)_{S2}$  are shown in dBi. Due to the design of the dual polarised horn a gain difference of almost 2 dB can be observed. Furthermore, a difference in phase exists, since the feeds of the two slot antennas are of different lengths.

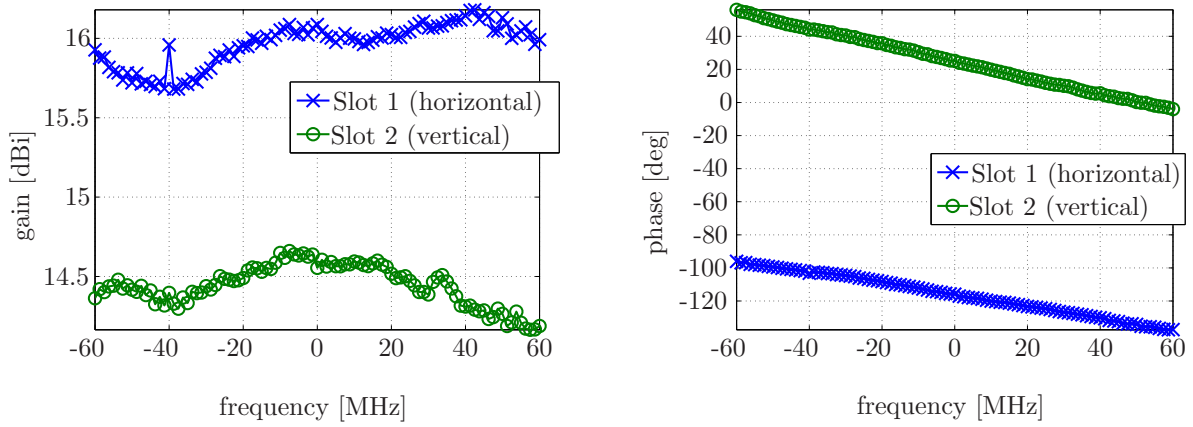


**Fig. 4.4:** Gains of the dual polarised reference horn antenna in azimuth (left), gains of the dual polarised reference horn antenna in co-elevation (right)





**Fig. 4.5:** XPD of Slot 1 (horizontal field) (left), XPD of Slot 2 (vertical field) (right)



**Fig. 4.6:** Gains of the dual polarised reference horn antenna vs. the frequency around the centre frequency of 5.2 GHz (left), Phases of the dual polarised horn antenna vs. the frequency around the centre frequency of 5.2 GHz (right)

#### 4.1.5 Calibration of Channel Measurement Antenna Arrays

The measurement setup described in Section 4.1.1 will be applied. The reference horn antenna that is calibrated as described in the previous section is used. To calculate the narrow band radiation patterns, the measurements  $y(f, \varphi, \vartheta, q, m)$  are corrected by the system frequency responses of the corresponding Tx channel  $G_{\text{Sys}}(f, q = h)$  or  $G_{\text{Sys}}(f, q = v)$ , the frequency responses of the horn antenna for horizontal or vertical polarisation  $b_{\text{Ref}}(f, q)$ , and the normalised frequency response of the reference channel between Tx3 and Rx2. The normalised frequency response of the reference channel is defined as the ratio between the measured frequency response of the reference channel  $y(f, \varphi, \vartheta)_{\text{Tx3Rx2}}$  at the first measurement position ( $\varphi = \varphi_1, \vartheta = \vartheta_1$ ) and the frequency response of the reference channel at the measurement position to correct ( $\varphi, \vartheta$ ). Based on the equations (3.9) and (3.8), the narrow band radiation patterns are defined as:

$$b(\varphi, \vartheta, q, m) = \frac{1}{B} \int_{f_0 - B/2}^{f_0 + B/2} \frac{y(f, \varphi, \vartheta, q, m) \cdot 4\pi \cdot f \cdot \tau(l) \cdot e^{j \cdot 2\pi \cdot f \cdot \tau(l)}}{G_{\text{Sys}}(f, q) \cdot b_{\text{Ref}}(f, q)} \cdot \frac{y(f, \varphi_1, \vartheta_1)_{\text{Tx3Rx2}}}{y(f, \varphi, \vartheta)_{\text{Tx3Rx2}}} df. \quad (4.6)$$

## 4.2 Estimation of EADFs from Measured Radiation Patterns

For a precise determination of the EADFs from measured radiation patterns, phase and amplitude of the measurement system have to be stable in all required measurement positions in azimuth and co-elevation over the entire measurement time. Therefore, in the previous section the recorded data of a reference channel was used to correct the measured radiation patterns for the long term phase drift of the channel sounder.

The measurement of a reference channel is in some cases not possible with channel sounding, since transmitter and receiver of the sounder are not necessarily positioned close to each other (e.g. free field calibration). Apart from the long term phase drift of the measurement system (see Section 2.3.4), cable bending and eccentric antenna positioning may result in a collective phase change for all measured antennas dependent on the measurement position. The collective phase change over the calibration measurement time is a major source of error in the estimation of the EADFs from measurement data. Consequently, an algorithm is needed to estimate both the EADFs and the collective phase change.

### 4.2.1 Data Model of the Measured Radiation Patterns Including a Collective Phase Change

The data model of the narrow band radiation patterns of an antenna array as described in Chapter 3 will be extended in the following. Furthermore, the influence of the collective phase change on the EADFs, which are directly calculated from measurement data, is shown. An Uniform Circular Array (UCA) with 8 antenna elements is used as an example.

Only the one-dimensional (1D) radiation patterns dependent on the azimuth angle  $\varphi$  for a constant co-elevation  $\vartheta = 90^\circ$  are taken into account, but model and algorithm can be extended to the two dimensional case (azimuth and co-elevation).

In equation (3.12) the sampled narrow band radiation patterns derived from measurement are only affected by the measurement noise. Additionally to the measurement noise the error free radiation patterns  $\mathbf{b}^{[M \times 1]}(\varphi_{n_\varphi})$  are affected by the collective phase offset  $\varepsilon_{n_\varphi}$  at the measurement position  $n_\varphi$ . This gives the extended model of the  $M$  narrow band radiation patterns:

$$\tilde{\mathbf{b}}(\varphi_{n_\varphi}) = e^{j \cdot \varepsilon_{n_\varphi}} \cdot \mathbf{b}(\varphi_{n_\varphi}) + \mathbf{n}, \quad (4.7)$$

where the vector  $\mathbf{n}^{[M \times 1]}$  denotes the measurement noise vector (independent and identically distributed (i.i.d.) Gaussian in real and imaginary part (eqn. (E.3))). From eqn. (4.7) it can be seen that the phase term  $e^{j \cdot \varepsilon_{n_\varphi}}$  is assumed to be constant for all antennas  $M$  at one position  $n_\varphi$ . This assumption is acceptable due to the fact that the long term phase drift is a slow process compared to the much shorter switching time. Also the cable bending and the eccentric positioning results in collective phase offset only.

Again, the radiation pattern is measured in the range between  $\varphi_1 = -\frac{N_\varphi}{2} \cdot \Delta\varphi$  and  $\varphi_{N_\varphi} = (\frac{N_\varphi}{2} - 1) \cdot \Delta\varphi$ .  $N_\varphi$  is the total number of measurement points and  $\Delta\varphi = \frac{2\pi}{N_\varphi}$  is the measurement grid in azimuth.

This gives the matrix of the measured radiation patterns  $\tilde{\mathbf{B}}^{[M \times N_\phi]}$  and the matrix of the error free radiation patterns  $\mathbf{B}^{[M \times N_\phi]}$ . Using the definition of the **EADF**,  $\mathbf{B}$  can be expressed as:

$$\mathbf{B} = \Gamma^{[M \times L_\phi]} \cdot \mathbf{D}_\phi^H, \quad (4.8)$$

where  $\Gamma$  includes the **EADFs** of all antenna elements,  $\mathbf{D}_\phi$  (equation (3.21)) is the transformation matrix in azimuth, and  $L_\phi$  is the effective number of samples in the aperture domain. To include the phase drift in the model, the phase drift matrix is defined as:

$$\mathbf{P}^{[N_\phi \times N_\phi]} = \begin{pmatrix} e^{j\varepsilon_1} & 0 & 0 \\ 0 & \ddots & 0 \\ 0 & 0 & e^{j\varepsilon_{N_\phi}} \end{pmatrix}, \quad (4.9)$$

which gives:

$$\tilde{\mathbf{B}} = \Gamma \cdot \mathbf{D}_\phi^H \cdot \mathbf{P} + \mathbf{N}, \quad (4.10)$$

where  $\mathbf{N}$  is the noise matrix.

In the following an **UCA** with  $M = 8$  omni directional elements is used to demonstrate the influence of collective phase change on the calculated **EADF** without correction. The radius of the array is chosen as  $r_{opt}$  as described in [9]. Assuming antennas with a gain of 1 in all directions, the radiation pattern of the single element  $m$  is defined as:

$$b(\varphi, m) = e^{-j2\pi \cdot \frac{r_{opt}}{\lambda} \cdot \cos(\varphi - m \cdot \varphi_0)}, \quad (4.11)$$

where  $\varphi_0 = \frac{2\pi}{M}$  is the angular distance between two elements of a circular array. The measurement grid in azimuth  $\Delta\varphi$  is set to 1 degree. Further, the **SNR** is defined as the ratio between the mean power over all antennas and measurement positions in  $\mathbf{B}$ , and the variance  $\sigma^2$ .

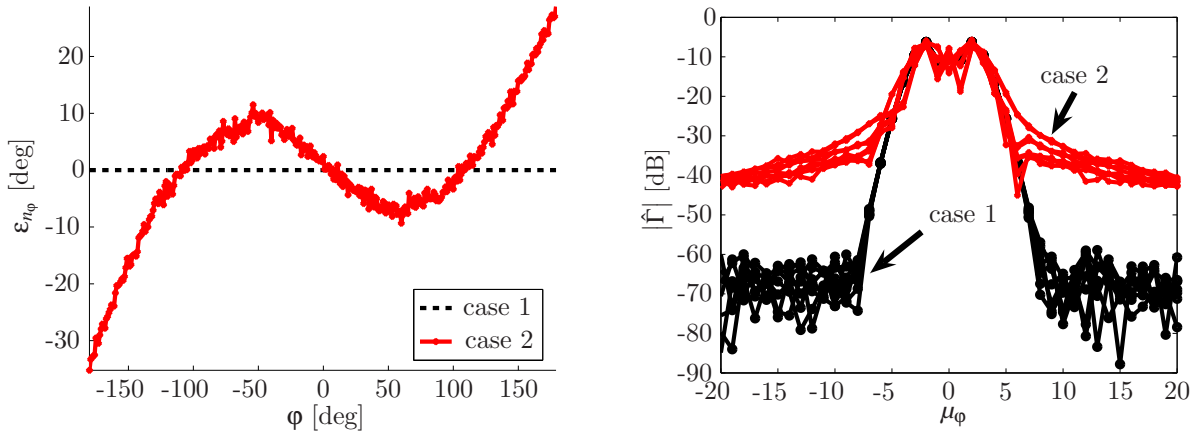
In the following, two cases are shown, assuming a **SNR** of 40 dB. In case 1, the radiation patterns are only effected by measurement noise while the collective phase offset was set to zero for all angles. In case 2, realistic collective phase offsets are applied (see Fig. 4.7 (left)). The collective phase offsets in case 2 are a superposition of a measured long term phase drift (from a calibration measurement using a reference channel) and a sinusoidal phase with an amplitude of 20 degree caused by an eccentric positioning of the antenna array (at 5.2 GHz about 3 mm). Direct application of the transformation to the measurement data gives the following estimates of the **EADFs**:

$$\hat{\mathbf{B}} = \frac{1}{N_\phi} \cdot \tilde{\mathbf{B}} \cdot \mathbf{D}_\phi. \quad (4.12)$$

In Fig. 4.7 (right) the absolute values of all **EADFs** of both cases are shown. In case 2, the **EADFs** are distorted by the collective phase offsets. By applying the inverse transformation (eqn. (3.31)) to these **EADFs** (eqn. 4.12), the accuracy of the reconstructed radiation patterns is 20 dB less than for case 1.

These results show that it is necessary to determine the collective and unknown phase offsets

by direct measurement or by an estimation algorithm for a correction of the measured radiation patterns.



**Fig. 4.7:** Simulated phase drift over azimuthal scan (left),  $|\hat{\Gamma}|$  of case 1 and case 2 (right)

#### 4.2.2 EADF Estimation Algorithm

In the following an iterative algorithm is presented that is based on a non linear least squares algorithm (Levenberg-Marquardt [100]). The fundamental assumption of this algorithm is that the phase does not change during the measurement of all antennas  $M$  at the measurement position  $n_\varphi$ . If this assumption is not applicable, application of the algorithm will lead to an ill-posed estimation problem due to the large number of unknown values.

Based on (4.10) the following cost function has to be minimised:

$$\chi(\tilde{\mathbf{B}}, \Phi) = \|\text{vec}\{\tilde{\mathbf{B}}\} - \mathbf{s}(\Phi)\|_{\text{F}}^2 \quad (4.13)$$

with the estimation:

$$\mathbf{s}(\Phi) = \text{vec}\{\hat{\mathbf{H}} \cdot \mathbf{D}_\varphi^{\text{H}} \cdot \hat{\mathbf{P}}\}, \quad (4.14)$$

where  $\Phi$  is the vector which includes the parameters that have to be optimised. This vector is composed of two parts, the first is the parameter vector of the non linear part of the model i.e. the unknown phase terms  $\Psi = [\varepsilon_1 \dots \varepsilon_{N_\varphi}]$  and the second is the parameter vector of the linear part of the model. These are the real and imaginary part of the EADFs  $\Gamma$ . This means  $\Phi$  is defined as:

$$\Phi^{[1 \times (N_\varphi + 2 \cdot L_\varphi \cdot A)]} = \left[ \Psi \quad \text{vec}\{\Re\{\mathbf{H}\}\}^{\text{T}} \quad \text{vec}\{\Im\{\mathbf{H}\}\}^{\text{T}} \right]. \quad (4.15)$$

The algorithm that estimates the parameters of (4.15) is explained in the following. The flow chart of the algorithm is shown in Fig. 4.8. In the flow chart two iterative processes can be distinguished. In the outer, the width  $L_\varphi$  in the aperture domain is changed. Here the initial value  $L_{\varphi\text{ini}}$  is set to half of the 20 dB width of the mean magnitude of the EADFs (4.12) of all antennas  $M$ . In the inner iterative process the estimation result of (4.15) is improved with every iteration  $i$  by using the

Levenberg-Marquardt algorithm for a fixed number  $L_\varphi$ . The unknown phases  $\Psi$  are initialised with zero at the beginning of the estimation process. For every new width  $L_\varphi$  the EADFs are initialised with:

$$\hat{\Gamma}_{L_\varphi,1} = \frac{1}{N_\varphi} \cdot \tilde{\mathbf{B}}_{R1} \cdot \mathbf{P}^H(\Psi_{L_\varphi,1}) \cdot \mathbf{D}_\varphi, \quad (4.16)$$

where  $\tilde{\mathbf{B}}_{R1}$  is one realisation of the measured radiation patterns. For  $i$  larger than one, the EADFs are optimised by the Levenberg-Marquardt algorithm. To calculate the parameter vector  $\Phi_{L_\varphi,i+1}$  that will minimise the cost function in the iteration  $i+1$ , the following matrices must be calculated: the Jacobian matrix with the first derivatives:

$$\mathbf{J}_{L_\varphi,i} = \frac{\partial \mathbf{s}}{\partial \Phi}, \quad (4.17)$$

and the approximation of the second derivatives, the Hessian:

$$\mathbf{H}_{L_\varphi,i} = 2 \cdot \Re \left\{ \mathbf{J}_{L_\varphi,i}^H \cdot \mathbf{J}_{L_\varphi,i} \right\}. \quad (4.18)$$

With the residual after subtraction of the current estimation  $\mathbf{s}(\Phi_{L_\varphi,i})$ :

$$\mathbf{r}_{L_\varphi,i} = \text{vec} \left\{ \tilde{\mathbf{B}}_{R1} \right\} - \mathbf{s}(\Phi_{L_\varphi,i}) \quad (4.19)$$

the gradient is given by:

$$\mathbf{g}_{L_\varphi,i} = 2 \cdot \Re \left\{ \mathbf{J}_{L_\varphi,i}^H \cdot \mathbf{r}_{L_\varphi,i} \right\}. \quad (4.20)$$

The gradient is used to calculate the change  $\Delta\Phi$  (see Fig. 4.8), which is necessary to reach the minimum of the cost function. For  $\lambda_{L_\varphi,i}$  equal to zero the algorithm is identical to the Gauss-Newton algorithm, which converges faster close to the minimum of the cost function. For values of  $\lambda_{L_\varphi,i}$  larger than zero the step size will be reduced (Steepest descent algorithm). For the iteration  $i=1$ ,  $\lambda_{L_\varphi,i=1}$  is set to the maximum in the hessian matrix, since the convergence radius of the Gauss-Newton algorithm is possibly not reached. To decide whether or not the algorithm did find the direction to the minimum, the error of the current estimation result is defined as:

$$\zeta_{L_\varphi,i} = \chi(\tilde{\mathbf{B}}_{R2}, \Phi_{L_\varphi,i}), \quad (4.21)$$

where  $\tilde{\mathbf{B}}_{R2}$  is a second realisation of the measured radiation pattern, which is used here to make sure that the algorithm does not fit the parameters to the noise. If the error (4.21) is decreasing in the course of the iteration process, the  $\lambda_{L_\varphi,i}$  will be reduced by a factor of four for the next iteration  $i+1$ . Furthermore, Jacobian, Hessian and gradient will be updated with the improved  $\Phi_{L_\varphi,i+1}$ . If the error (4.21) increases,  $\lambda_{L_\varphi,i}$  is multiplied with 8 for the next iteration and an update of the Jacobian, Hessian, and the gradient is not necessary. The iteration in the Levenberg-Marquardt algorithm is aborted, if consecutive 15 iterations (Steepest Descent) did not improve the estimation result. From the result of the  $L_\varphi$ th Levenberg-Marquardt step, the reconstruction error  $\eta_{L_\varphi}$  (see Fig. 4.8) is calculated and the next iteration with the width  $L_\varphi+2$  is initialised with estimated

phases  $\Psi_{L_\phi, i}$ . The convergence of the outer loop is reached at the first point of inflexion of  $\eta$ .

Now the algorithm is applied to the example described in Section 4.2.1. In Fig. 4.9 (left) the reconstruction error  $\eta_{\text{Uncorrected}}$  of the uncorrected measurement data using equation 4.12, the error  $\eta_{\text{Est}}$  of the described algorithm is plotted. Additionally, the error of the corrected measurement data  $\eta_{\text{Corrected}}$ , using the estimation result  $\hat{\Psi}$  to correct the measurement data  $\tilde{\mathbf{B}}_1$ , with respect to the aperture size  $L_\phi$  is shown. Since the SNR of samples in the aperture domain is decreasing with increasing frequency  $|\mu_\phi|$ , the error of the estimated phases is increasing with a larger width  $L_\phi$  (see Fig. 4.9 (right)). The estimation result of the outer loop with  $L_{\phi_{\text{fin}}} - 2$  is considered as the final result, since at the point of inflexion with aperture size  $L_{\phi_{\text{fin}}}$  the estimation results are already degraded. In most cases the minimum of the standard deviation  $\sigma_{\Psi_{L_\phi} - \Psi}$  of the estimation error  $\Psi_{L_\phi} - \Psi$  with respect to  $L_\phi$ , where  $\Psi$  is the simulated collective phase offsets, was also found with  $L_{\phi_{\text{fin}}} - 2$ .

### 4.2.3 Algorithm performance dependent on SNR and number of elements

In the following, the influence of the measurement SNR and the number of antenna elements  $M$  on the performance of the proposed EADF estimation algorithm is discussed. The simulated phases  $\Psi$  are the same as in the previous sections. In Section 4.2.1 and Section 4.2.2, an antenna array with  $M = 8$  omni directional antennas was used and the SNR was set to 40 dB. As the estimation result is dependent on the SNR, the algorithm is applied to SNRs between 10 and 40 dB, using the same 8-element UCA. Figure 4.10 (left) shows the standard deviation of the error of the estimated phase drift vs.  $L_\phi$ . Parameter is the SNR. In the figure the line with black crosses indicates the aperture sizes  $L_{\phi_{\text{fin}}} - 2$  with the most reliable estimation result of the phase drift dependent on the simulated SNRs. With an increasing SNR more samples in the aperture domain are taken into account for a reliable estimation result with a lower standard deviation of the estimation error.

Furthermore, four different UCAs (4.11) with 2, 4, 6, and 8 antenna elements are simulated. In Fig. 4.10 (right) the standard deviation of the error of the estimated phase drift  $\sigma_{\hat{\Psi} - \Psi}$  is plotted. For low SNRs the best performance can be achieved with a higher number of elements, whereas for high SNRs the standard deviation is almost independent from the number of antenna elements.

### 4.2.4 Measurement Example

In the following the algorithm is applied to antenna array calibration measurement data. The used antenna array is the PUCPAx2x1x24. From the calibration measurement also the recorded data of a reference channel is available.

Figure 4.11 (left) shows the reconstruction error  $\eta$  as function of  $L_\phi$  when applying the EADF estimation algorithm for correction (**Corrected Est.**), when calculating the EADF directly from the measured radiation patterns without correction (**Uncorrected**), and when using the data of the measured reference channel for correction (**Reference Channel**). In case that the EADF estimation algorithm or the reference channel is used for correction the reconstruction error is around 10 dB lower than in the uncorrected case. This is also obvious from the calculated EADFs

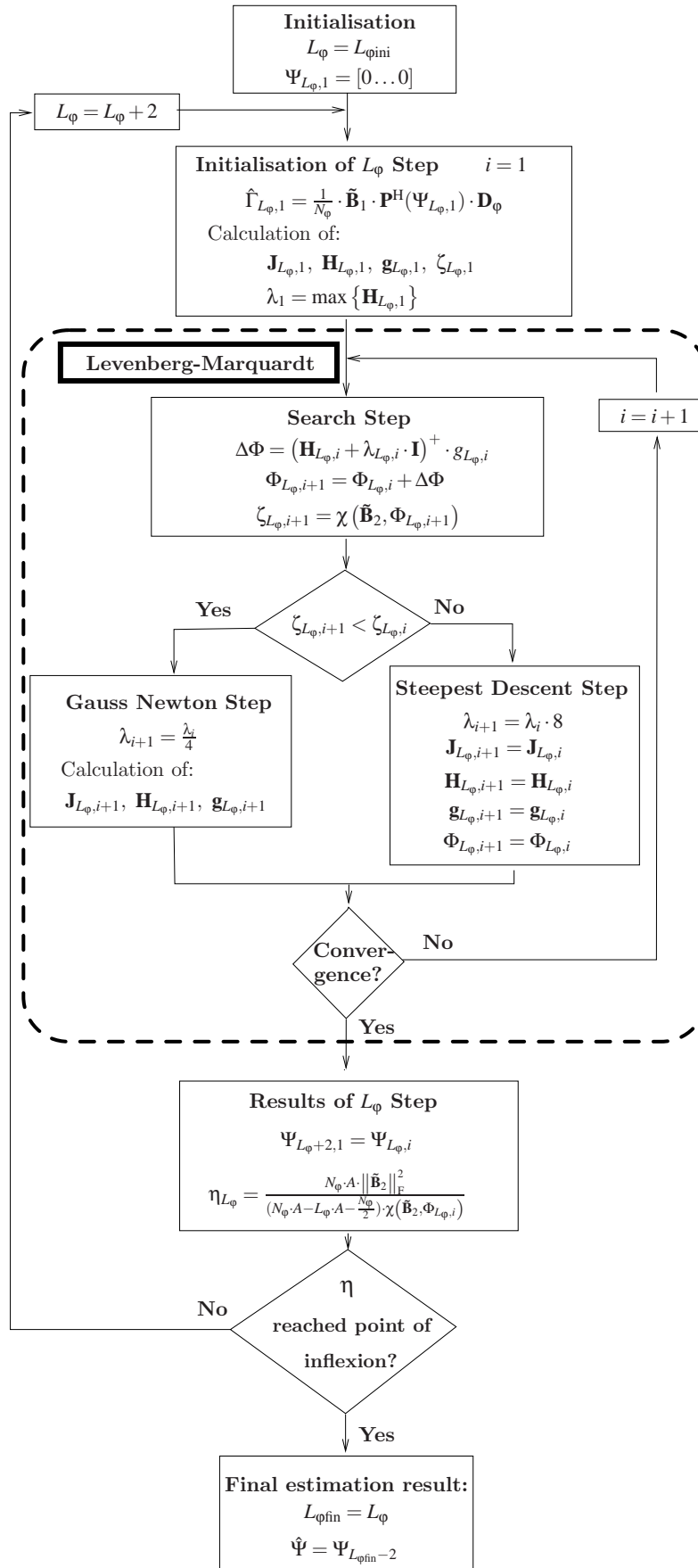
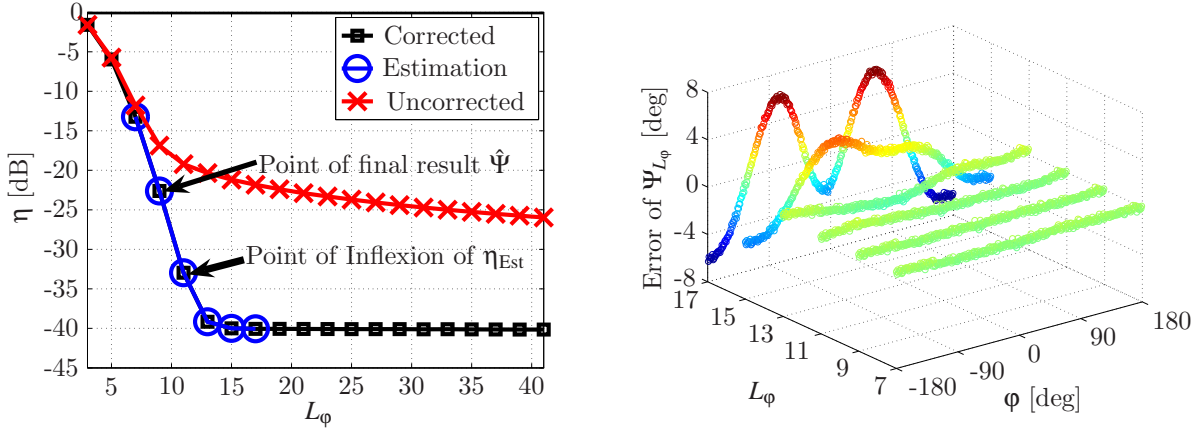
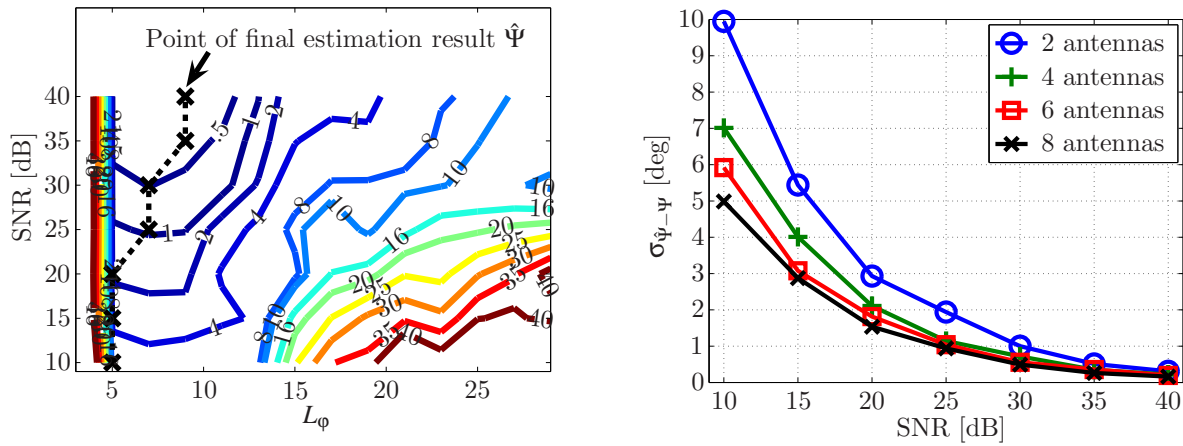


Fig. 4.8: Flow chart of the estimation algorithm





**Fig. 4.9:** Reconstruction error  $\eta$  of uncorrected  $\Gamma$ , during the estimation process, and of corrected  $\Gamma$  (left), Error of estimated  $\Psi_{L_\phi}$  (right)



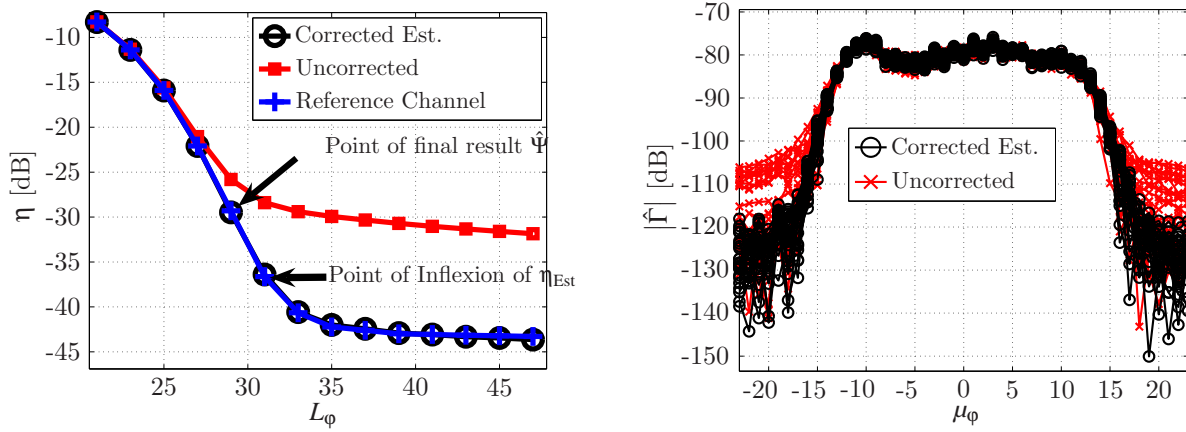
**Fig. 4.10:** Standard deviation  $\sigma_{\Psi_{L_\phi}-\hat{\Psi}}$  [deg] as function of  $L_\phi$  and SNR, using an 8 element UCA (left), Standard deviation of estimated phase drift  $\hat{\Psi}$  as function of SNR and number of antennas (right)

in Fig. 4.11 (right), the noise power in the **Corrected Est.** case being around 10 dB lower than in the **Uncorrected** case.

#### 4.2.5 Conclusion on EADF Estimation Algorithm

The proposed algorithm estimates the efficient representation of the polarimetric antenna responses of an antenna array, the **EADF**, and corrects for the collective phase offsets caused by imperfections of the measurement system. The performance of the algorithm is shown as a function of the measurement **SNR** and the number of antenna elements. Finally, the algorithm was applied to antenna array calibration measurement data. It is shown that the accuracy of the calculated antenna model (**EADFs**) is drastically improved by the proposed correction for the collective phase offsets.





**Fig. 4.11:** Reconstruction error  $\eta$  as function of  $L_\phi$  for the three different cases of correction (left), Magnitude of the Corrected and Uncorrected EADFs (right)

### 4.3 Measured Radiation Patterns and EADFs of Different Array Types

This section emphasizes that the knowledge of the full polarimetric 2D radiation patterns of all antennas of an measurement array are required for experimental channel characterisation. Note that commonly only azimuth cuts (e.g. const. co-elevation  $\vartheta = 90^\circ$ ) or co-elevation cuts (e.g. const. azimuth  $\phi = 0^\circ$ ) for a single polarisation are used in several publications related to this research field. The following results are also necessary for the interpretation of the results in Chapter 6 and 7.

The measured radiation patterns, EADFs and XPDs for one “single polarised” antenna array (UCAx1x1x16) and two polarimetric antenna arrays (SPUCPAx2x4x24, PULPAx2x1x8) are discussed. In case of the “single polarised” array, only one antenna element is chosen, whereas for the polarimetric arrays, one element with vertical preferred polarisation and one element with horizontal preferred polarisation are taken into account. The phase corrected measured horizontal radiation pattern  $\tilde{\mathbf{B}}(q = h, m)$  and vertical radiation pattern  $\tilde{\mathbf{B}}(q = v, m)$  of each antenna element will be shown. The radiation patterns and EADFs are normalised to the maximum gain of all antenna elements and all polarisations in the array. The colour in the following surface plots indicates the magnitude in dB.

Note that all antenna arrays which are used in this thesis are briefly classified based on general parameters such as maximum gain, mean gain, mean XPD, 3 dB beam width and EADF related parameters in Appendix C.

#### 4.3.1 “Single Polarised” Antenna Array UCAx1x1x16

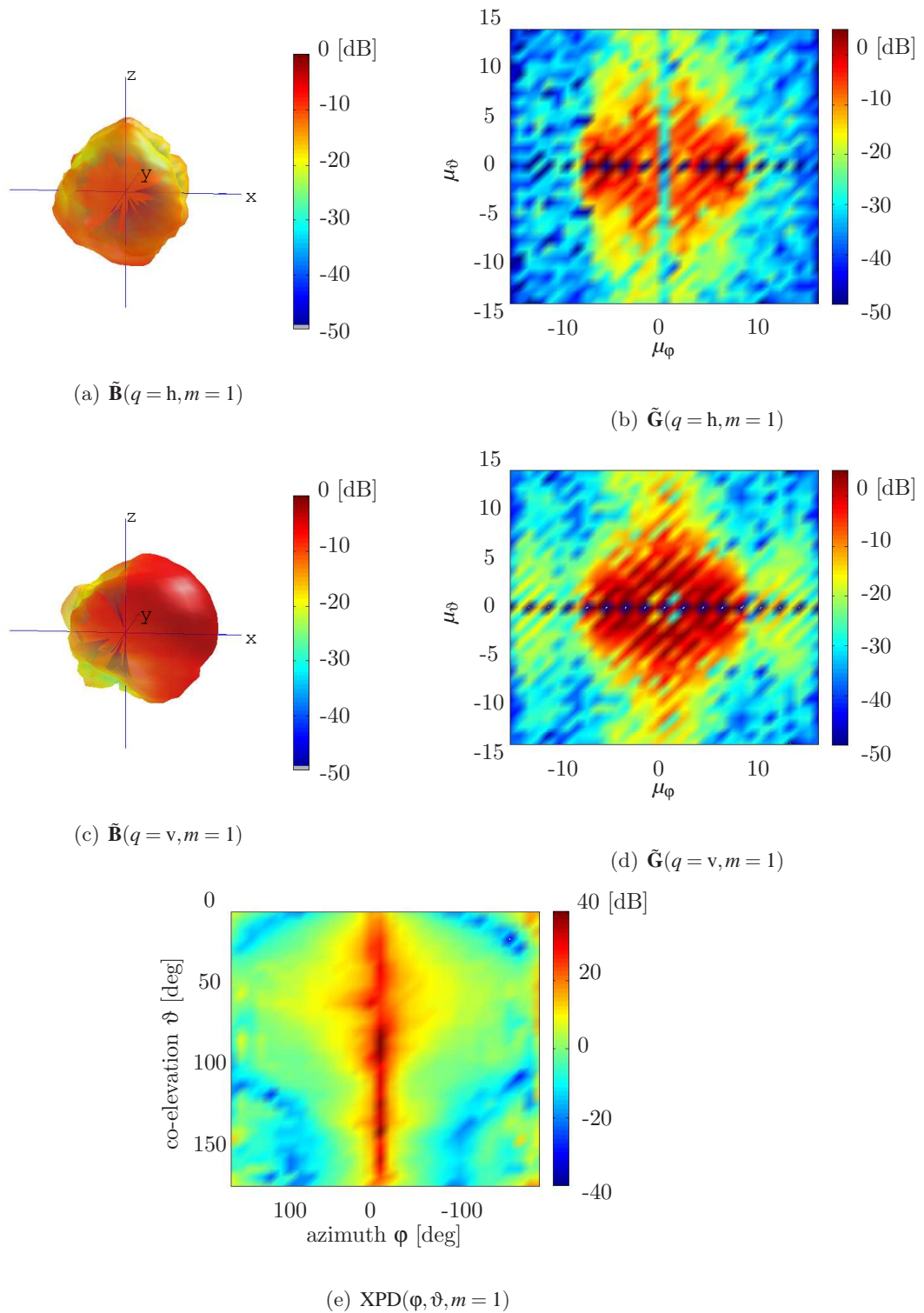
This antenna array was constructed to measure the characteristics of the mobile radio channel with respect to the vertical polarised incoming wave. The antenna elements were designed as vertical monopoles, which should only receive the power of the vertical polarised electrical field.

In Fig. 4.12 the results of the first element  $m = 1$  are shown with respect to the radiation patterns, EADFs and the XPD. The element is located in the direction of  $0^\circ$  azimuth. It is obvious that the

total received power for horizontal excitation (Fig. 4.12(a)) and vertical excitation (Fig. 4.12(c)) do not differ that much. Only in a small region around the main beam direction (x-axis) of  $\tilde{\mathbf{B}}(q = v, 1)$ , the received horizontal polarised power is low, which results in a high XPD for these directions. Analysing the XPD of the antenna element with respect to azimuth angle and co-elevation angle, it can be seen that in most cases the probability to receive both polarisation with equal power (XPD=0 dB) is rather high.

For the EADFs it can be observed that most of the signal energy is concentrated in the aperture frequency range  $|\mu_\vartheta| \leq 10$  and  $|\mu_\phi| \leq 10$  for both polarisations (Fig. 4.12(b), Fig. 4.12(d)). For the vertical case, signal energy can be identified even for higher aperture frequencies  $\mu_\phi$  in the azimuth aperture. This is basically related to the coupling to the adjacent elements, which is higher in case of the vertical polarisation. Due to parasitic reflections at the positioning system signal energy can be also found for higher aperture frequencies in the co-elevation aperture  $\mu_\vartheta$ . This energy, which is around 20 dB lower compared to the centred area, actually defines the accuracy of the measured radiation patterns. The accuracy topic is discussed in chapter 7, which analyses the different error sources during calibration measurement and the impact on the accuracy on the antenna model used.

In conclusion this antenna array can not be assumed as “vertical array”! Consequently, the radiation patterns  $\tilde{\mathbf{B}}(q = h, m)$  for horizontal excitation need to be taken into account in every signal processing algorithm, which analyses the structure of real world mobile radio channels. More details of this topic are discussed in chapter 7 Section 7.2.2.



**Fig. 4.12:** Magnitude of the radiation patterns, EADFs for the polarisation excitations  $q = h$  and  $q = v$  and XPD of the first element  $m = 1$  of the **UCAX1x1x16**

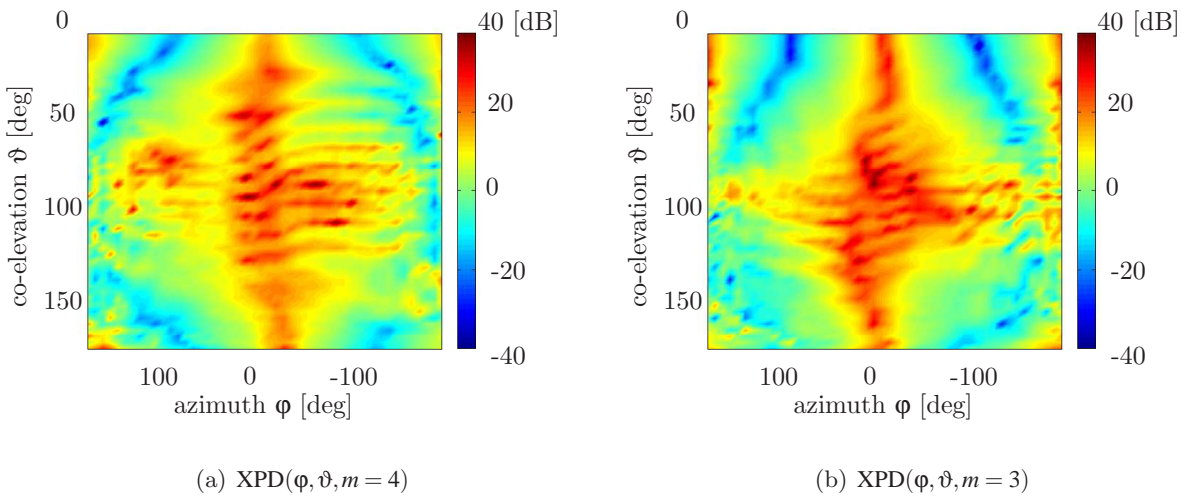
### 4.3.2 Polarimetric Antenna Array SPUCPAx2x4x24

The element  $m = 3$  for vertical preferred polarisation and the element  $m = 4$  for horizontal preferred polarisation of the **SPUCPAx2x4x24** are discussed. Both antenna elements are located in the third ring (starting from  $-z$ ) and pointing in the direction of  $0^\circ$  azimuth.

Observing the corresponding radiation patterns (Figures 4.15(a), 4.15(c), 4.15(e), 4.15(g)), it is obvious that the received power in the cross polarisation is mostly lower at least in contrast to the previous discussed monopole array. Furthermore, the radiation patterns are affected by the coupling to the elements located in the other rings. Due to constructive and de-constructive super position of the interfering wave fields of the neighbouring elements, the radiation pattern results have several ripples. The influence of the coupling seems to be higher in case of the vertical excitation. This behaviour can be also observed in the **EADFs** (Figures 4.15(b), 4.15(d), 4.15(f), 4.15(h)) of the elements, where the energy spread in the **EADFs** for vertical excitation in the co-elevation aperture is larger compared to the horizontal excitation.

Again the parasitic reflections at the positioning system result in signal energy for the higher co-elevation aperture frequencies  $|\mu_\vartheta|$ . Nevertheless, the total amount of this energy is lower compared to the monopole array.

Even if the mean **XPB** (Compare table C.1) is higher than in the case of the **UCA1x1x16**, only a limited region in azimuth and co-elevation can achieve a high **XPB** (Figures 4.13(a), 4.13(b)).



**Fig. 4.13:** Cross polarisation discrimination of the elements  $m = 4$  (horizontal preferred polarisation) and  $m = 3$  (vertical preferred polarisation) of the **SPUCPAx2x4x24**

### 4.3.3 Polarimetric Antenna Array PULPAx2x1x8

For the polarimetric uniform linear array, element  $m = 7$  for horizontal preferred polarisation and element  $m = 8$  for vertical preferred polarisation are discussed. These elements are two of the closest elements to the centre of the array.

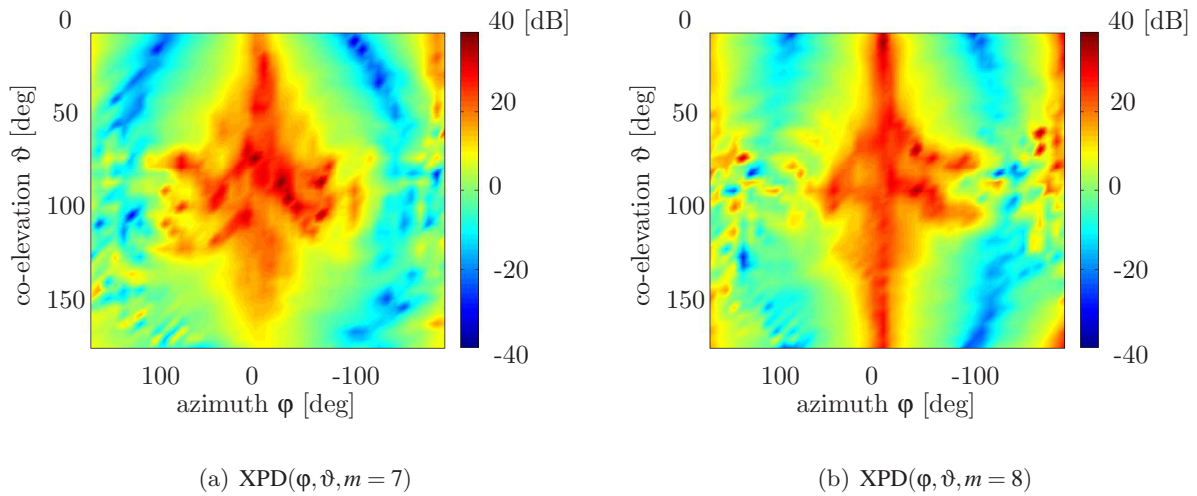
From the co-polarised radiation patterns (Figures 4.16(a), 4.16(g)) it can be seen, that the forward

to backward ratio is around -10 dB to -30 dB. This value is of major importance, since there always exist an ambiguity between the back side ( $\varphi = 90^\circ \dots 270^\circ$ ) and front side ( $\varphi = -90^\circ \dots 90^\circ$ ) in case of the array. From table C.1 and the shown radiation patterns it can be seen that the 3 dB beam width in co-elevation is around  $40^\circ$  to  $65^\circ$ . In case of the cross-polarised radiation patterns (Figures 4.16(c), 4.16(e)) it is obvious that the antenna array receives cross polarised waves mostly in the direction towards the poles of the spherical coordinate system. Only in a small range of  $\vartheta = 90^\circ \pm 15^\circ$  the received cross-polarised power is quite low and almost uniformly distributed in azimuth.

High XPD in a large azimuth range can be only achieved for co-elevation angles of  $\vartheta = 90^\circ$ .

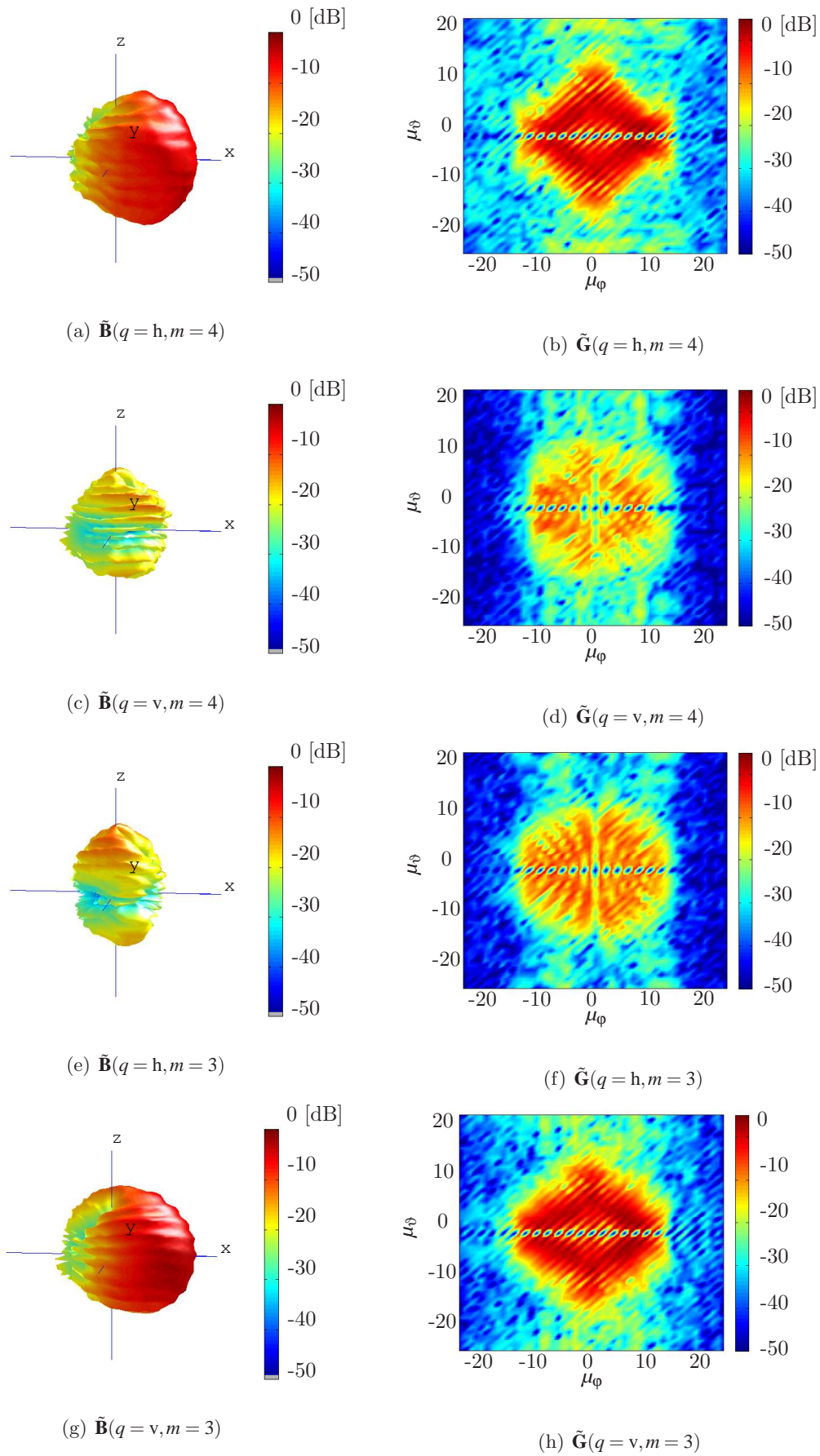
The signal energy in the EADFs (Figures 4.16(a), 4.16(c), 4.16(g), 4.16(e)) is more concentrated than in case of the other arrays (around  $\mu_\vartheta = \pm 5$  and  $\mu_\varphi = \pm 5$ ). The reason for that can be found in the position of the discussed elements ( $m = 7, m = 8$ ), which is close to the rotation centre.

From the results and discussion above, it can be concluded that the full polarimetric 2D antenna radiation patterns are required also in case of a uniform linear array. However, especially for this type of antenna array commonly only azimuth cuts of the radiation patterns are used for experimental channel characterisation. The consequences of the usage of such a simplified data model will be discussed in Chapter 7 Section 7.2.2.

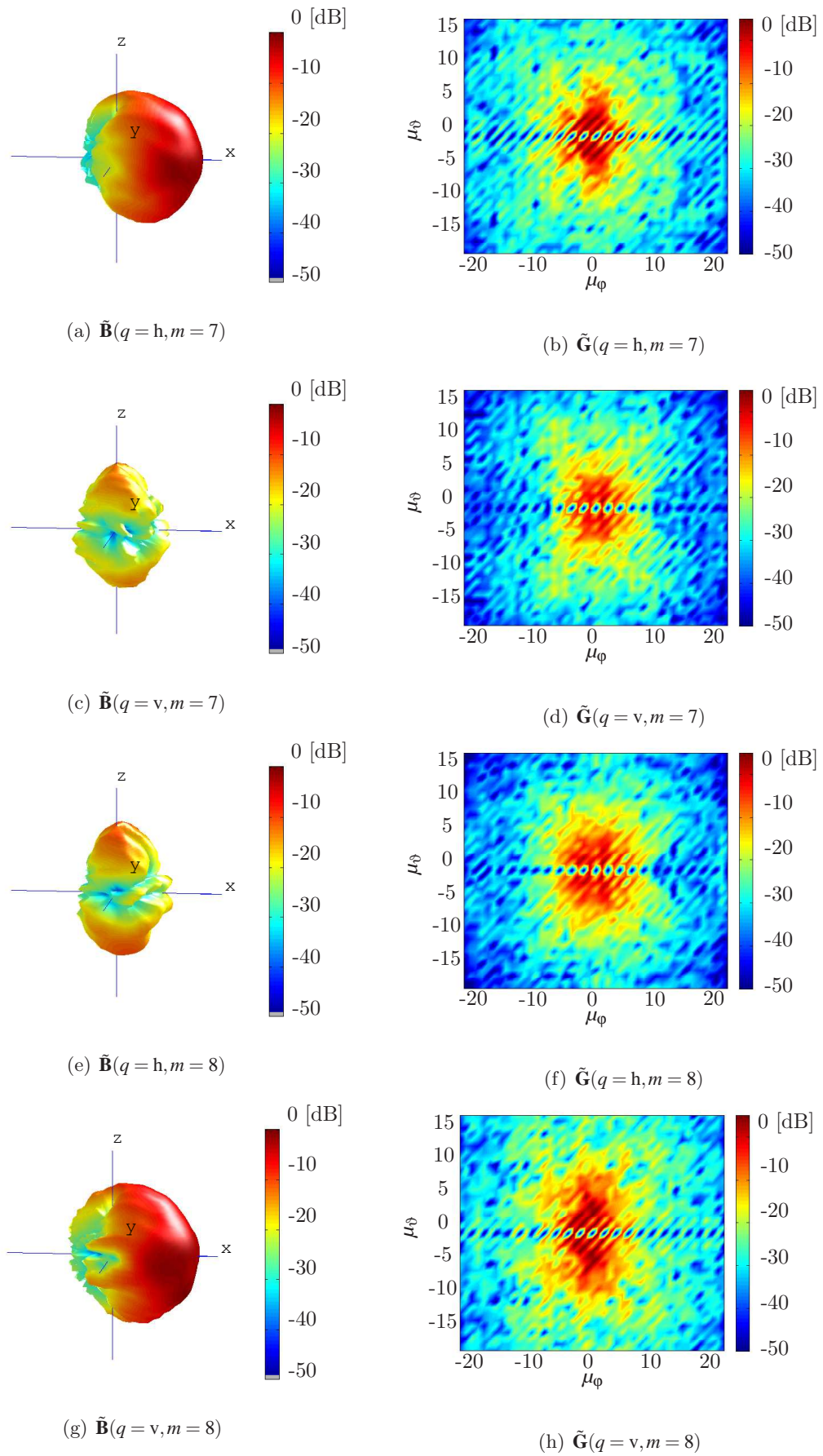


**Fig. 4.14:** Cross polarisation discrimination of the elements  $m = 7$  (horizontal preferred polarisation) and  $m = 8$  (vertical preferred polarisation) of the **PULPAx2x1x8**





**Fig. 4.15:** Magnitude of radiation patterns (left) and EADFs (right) of the elements  $m = 4$  (horizontal preferred polarisation) and  $m = 3$  (vertical preferred polarisation) of the **SPUCPAx2x4x24** for the excitations  $q = h$  and  $q = v$



**Fig. 4.16:** Magnitude of radiation patterns (left) and EADFs (right) of the elements  $m = 7$  (horizontal preferred polarisation) and  $m = 8$  (vertical preferred polarisation) of the **PULPAX2x1x8** for the excitations  $q = h$  and  $q = v$





## 5. CHANNEL MODELLING AND PARAMETER ESTIMATION

This chapter deals with the model of the wave propagation and the estimation of the model parameters applying the **RIMAX** algorithm. Furthermore, the limitations of the introduced radio channel model are briefly highlighted.

The wave propagation between transmitter and receiver is described by a simplified radio channel model. Propagation phenomena such as specular reflections and diffuse scattering is taken into account and will be described by a limited number of parameters (e.g. **DoD**, **DoA**, **TDoA**). As this simplified radio channel model is not applicable for parameter estimation a notation for the measured observations of the radio channel including the measurement system and the practical antenna arrays is presented. The estimation of the parameters of the radio channel based on measured observations with the gradient based **ML** algorithm **RIMAX** is briefly introduced. For better understanding of the algorithm and for the sake of simplicity only key aspects are presented. Since every model has its limitations, the drawbacks of the applied model are highlighted.

In Section 5.1 the model of the wave propagation in the radio channel comprising the specular (**SC**) and dense multipath components (**DMC**) is discussed. The theory of the **RIMAX** algorithm to estimate the radio channel model parameters is briefly summarised in Section 5.2. The drawbacks of the applied model are discussed in Section 5.3.

### 5.1 Radio Channel Model

The most widely accepted data model for *high-resolution* channel parameter estimation is based on a ray optical understanding of the propagation phenomena. Propagation paths are modelled by planar wave fronts. This is motivated by the idea of specular reflections at smooth surfaces, assuming frequency independent reflection coefficients in the bandwidth used. A white noise component is usually added to model the influence of receiver noise. However, the propagation in a real environment is continuous in nature and can not only be described by discrete components. It is well known that wave propagation phenomena also comprise diffuse scattered components [101]. Their contribution varies depending on the complexity of the propagation environment. Diffuse scattered components may be almost negligible in macro-cell Line of Sight (**LoS**) scenarios, but they can even dominate the propagation characteristic in complicated environments such as factory halls. While the electromagnetic background of diffuse scattering is already well understood and there are also various attempts to include diffuse scattered components into deterministic channel models [43, 45], its influence is widely neglected in *high-resolution* parameter estimation from sounding measure-

---

ments ([58, 60, 61, 72]). But, neglecting these scattered components will have a detrimental effect on the performance of the parameter estimation procedure. Therefore, a data model is introduced comprising two components, which can be handled separately throughout the estimation procedure [2, 30, 62].

The first component is considered as being deterministic and results from a limited number of specular reflections. It is also called **SC** or the structural part of the model since it has a clear geometric interpretation.

The second component, the **DMC** are assumed as dense/diffuse component that is stochastic in nature and can not be resolved as **SC** by the measurement device. It is assumed that the dense/diffuse component results from distributed diffuse scattering as it occurs in a complicated, multipath rich environment. In other words, the diffuse/dense component is considered as the contribution from multiple interactions between different reflection and scattering points. A motivation for the existence of **DMC** was given from Andreas Richter in [62] as follows: *”On every crossing between two propagation media, where the relative electric or magnetic permeability changes, a propagating wave is subdivided into parts. A part of the waves travels into the other medium, and another part is reflected or scattered. The probability that a scattered wave reaches the receiver is generally higher than the probability that a reflected wave reaches it. This is because a reflection requires a sufficiently large object with a reflecting surface, and if the reflection occurs it can only reach the receiver if the angles of incidence and the angle of reflection are appropriate to reach the next reflector or the receive antenna. Altogether the amount of specular (discrete/concentrated) propagation paths in a scenario is relatively small but their contribution to the total power transferred from the transmit antenna to the receive antenna is usually dominating the transmission. Although the contribution to the received power of a single scattered wave is small compared to the contribution of a reflected wave, the contribution of all scattered waves together reaching the receiver is significant due to their large number.”*

For example, a **MIMO** channel sounder having a measurement bandwidth of 120 MHz has a spatial resolution around 2.5 m, which corresponds to 43 wavelengths at 5.2 GHz. Thus, a big number of superimposed diffused components can be expected in each observed delay-bin. The power of the individual components reaching the receiver within the time interval between two delay-bins is strongly determined by the free space attenuation, which is approximately constant over this time interval. Thus, it can be assumed that the superimposed components in one complex delay-bin have approximately the same power. However, the phase of each component is due to the large difference in terms of the wavelength between their path lengths, approximately uniformly distributed within the time interval between two delay-bins. This means, that based on the central limit theorem it can be assumed that the contribution of the **DMC** to the observed **CIR** at one complex delay-bin can be modelled by an **i.i.d.** Gaussian process in real and imaginary part ([62]).

### 5.1.1 The Specular Path Model (SC)

The specular components are described by the  $R = 6$  structural parameters **DoD**  $\varphi_{\text{Tx}}, \vartheta_{\text{Tx}}$  (azimuth and co-elevation), **TDoA**  $\tau$ , Doppler-shift  $\alpha$ , and **DoA**  $\varphi_{\text{Rx}}, \vartheta_{\text{Rx}}$ . In the discrete angular-delay

Doppler domain the **SC** are described by a superposition of  $K$   $R$ -dimensional Dirac functions, weighted by a  $2 \times 2$  complex polarimetric path weight matrix of components  $\gamma_{xy,k}$ , where the indices  $x,y$  indicate horizontal or vertical polarisation at **Tx** and **Rx** respectively:

$$\begin{aligned} H_{\delta}(\boldsymbol{\alpha}, \boldsymbol{\tau}, \vartheta_{\text{Rx}}, \varphi_{\text{Rx}}, \vartheta_{\text{Tx}}, \varphi_{\text{Tx}}) = \\ \sum_{k=1}^K \begin{bmatrix} \gamma_{\text{hh},k} & \gamma_{\text{vh},k} \\ \gamma_{\text{hv},k} & \gamma_{\text{vv},k} \end{bmatrix} \{ \delta(\boldsymbol{\alpha} - \boldsymbol{\alpha}_k) \cdot \delta(\boldsymbol{\tau} - \boldsymbol{\tau}_k) \cdot \\ \delta(\varphi_{\text{Rx}} - \varphi_{\text{Rx},k}) \cdot \delta(\vartheta_{\text{Rx}} - \vartheta_{\text{Rx},k}) \cdot \delta(\varphi_{\text{Tx}} - \varphi_{\text{Tx},k}) \cdot \delta(\vartheta_{\text{Tx}} - \vartheta_{\text{Tx},k}) \} \end{aligned} \quad (5.1)$$

with its Fourier transformed counterpart:

$$\begin{aligned} H_e(\boldsymbol{\alpha}, \boldsymbol{\tau}, \vartheta_{\text{Rx}}, \varphi_{\text{Rx}}, \vartheta_{\text{Tx}}, \varphi_{\text{Tx}}) = \\ \sum_{k=1}^K \left\{ \begin{bmatrix} \gamma_{\text{hh},k} & \gamma_{\text{vh},k} \\ \gamma_{\text{hv},k} & \gamma_{\text{vv},k} \end{bmatrix} e^{-j2\pi\boldsymbol{\alpha}_k} \cdot e^{-j2\pi\boldsymbol{\tau}_k} \cdot \right. \\ \left. e^{-j2\pi s_{\text{Rx}} \varphi_{\text{Rx},k}} \cdot e^{-j2\pi s_{\text{Tx}} \vartheta_{\text{Rx},k}} \cdot e^{-j2\pi l_{\text{Tx}} \varphi_{\text{Tx},k}} \cdot e^{-j2\pi l_{\text{Tx}} \vartheta_{\text{Tx},k}} \right\}. \end{aligned} \quad (5.2)$$

The last equation shows that the estimation of the structural parameters is essentially a multidimensional harmonic retrieval problem. While Doppler-shift  $\boldsymbol{\alpha}$  and **TDoA**  $\boldsymbol{\tau}$  are clearly related to the observed aperture variables ( $t$  and  $f$ ) in time and frequency domain, the Fourier transform of the **DoD/DoA** parameters is not directly related to the physical antenna array aperture. For this a further geometrical transformation would be needed, which will depend on the specific array architecture. This transformation step is omitted here, since it can be avoided by relying on the proposed antenna model the **EADF** (Section 3.3) that corresponds to the Fourier transform of the angular domain. Hence, its dimensions  $s_{\text{Tx/Rx}}$ ,  $l_{\text{Tx/Rx}}$  are not uniquely defined in a physical sense but are related to the geometrical dimensions of the respective antenna array.

The geometrical definition of the specular path data model (eqn. 5.1) is illustrated in Fig. 5.1. For the sake of simplicity, the **DoD/DoA** definitions are independent and related to the local coordinate systems of the respective **Tx/Rx** arrays. Note that this specular path model has to be considered as instantaneous which means it is specific for one time instant only and may be slowly changing with time when the objects of the scenario are moving.

### Combining the Radio Channel Model with the Model of the Measurement System

The data model of eqn. (5.1) and eqn. (5.2) is not directly applicable for parameter estimation. For this a more concise vector/matrix-notation is needed. The condensed parameter vector  $\boldsymbol{\theta}_k$ :

$$\boldsymbol{\theta}_k = [\boldsymbol{\alpha}_k, \boldsymbol{\tau}_k, \varphi_{\text{Tx},k}, \vartheta_{\text{Tx},k}, \varphi_{\text{Rx},k}, \vartheta_{\text{Rx},k}, \gamma_{\text{hh},k}, \gamma_{\text{hv},k}, \gamma_{\text{vh},k}, \gamma_{\text{vv},k}] \quad (5.3)$$

contains 14 real-valued unknowns describing the six structural parameters and four complex path weight parameters of any propagation path. The observable channel response  $\mathbf{s}(\boldsymbol{\theta}_k)$  in the multidimensional aperture domain is defined by the limited observation time, finite bandwidth, and finite

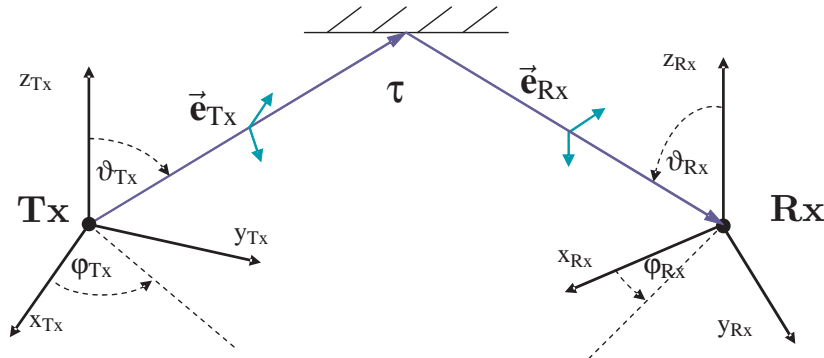
(effective) antenna apertures:

$$\begin{aligned} \mathbf{s}(\theta_k) &= \gamma_{hh,k} \cdot \mathbf{G}_{hh} \cdot \mathbf{a}(\mu_k) + \gamma_{hv,k} \cdot \mathbf{G}_{hv} \cdot \mathbf{a}(\mu_k) \\ &+ \gamma_{vh,k} \cdot \mathbf{G}_{vh} \cdot \mathbf{a}(\mu_k) + \gamma_{vv,k} \cdot \mathbf{G}_{vv} \cdot \mathbf{a}(\mu_k) \end{aligned} \quad (5.4)$$

The sampled channel response is arranged in vectors as:

$$\mathbf{a}(\mu_k) = \mathbf{a}(\mu_k^{(R)}) \otimes \mathbf{a}(\mu_k^{(R-1)}) \otimes \cdots \otimes \mathbf{a}(\mu_k^{(1)}) \quad (5.5)$$

where the  $\mathbf{a}(\mu_k^{(i)})$  are complex exponentials resulting from Fourier transform of (eqn. 5.1) and the  $\mu_k^{(i)}$  are the normalised structural path parameters, which are related to their physical counterparts by a unique projection  $\mu^{(1)} = f(\alpha)$ ,  $\mu^{(2)} = f(\tau)$ ,  $\mu^{(3)} = f(\varphi_{Tx})$ ,  $\mu^{(4)} = f(\vartheta_{Tx})$ ,  $\mu^{(5)} = f(\varphi_{Rx})$ ,  $\mu^{(6)} = f(\vartheta_{Rx})$  and a proper normalisation to the respective aperture size, e.g. frequency bandwidth in case of  $\mu^{(2)}$ . The linear projector matrices  $\mathbf{G}_{xy}$  for the transmit polarisation  $x$  and receive polarisation  $y$  describe the measurement system response, which is composed of the Kronecker products of Doppler  $\mathbf{G}^{(1)} = \mathbf{G}_t$ , frequency  $\mathbf{G}^{(2)} = \mathbf{G}_f$  and spatial responses  $\mathbf{G}^{(3,4)} = \mathbf{G}_x$  and  $\mathbf{G}^{(5,6)} = \mathbf{G}_y$ , respectively.



**Fig. 5.1:** Multidimensional specular components data model.

While the frequency response is represented by a diagonal matrix and the Doppler response is simply an identity matrix, the spatial responses are described by the EADFs of the antenna array elements. The corresponding data dimensions  $d = 1 \dots 4$  are spanned by the  $M_t$  Doppler samples,  $M_f$  frequency samples,  $M_{Tx}$  transmit antennas (spatial samples at Tx), and  $M_{Rx}$  receive antennas (spatial samples at Rx).

Reconsidering eqn. (3.31), the matrix  $\Gamma(q)$  corresponds to  $\mathbf{G}_x$  or  $\mathbf{G}_y$  at Tx or Rx respectively. Note that these spatial responses  $\mathbf{G}_x$  and  $\mathbf{G}_y$  are related to one data dimension  $d$ , while depending on two structural parameters  $(\varphi, \vartheta)$ . The matrices  $\mathbf{G}_x$  or  $\mathbf{G}_y$  can not be written as the Kronecker product of two linear projection matrices  $\mathbf{G}_{x\varphi}$  and  $\mathbf{G}_{x\vartheta}$  (see equations (3.30) and (3.31)). This means the parameter dimensions corresponding to azimuth  $\varphi$  and co-elevation  $\vartheta$  at Tx or Rx can not be handled separately.

For parameter estimation another notation of  $\mathbf{s}(\theta_k)$  applying the basis functions  $\mathbf{B}_d$  of the data dimensions Doppler  $d = 1$  with  $M_t$  samples:

$$\mathbf{B}_1(\mu_k^{(1)})^{[M_t \times 1]} = \mathbf{B}_t(\alpha_k) = \mathbf{G}^{(1)} \cdot \mathbf{a}(\mu_k^{(1)}) \quad (5.6)$$

frequency  $d = 2$  with  $M_f$  samples:

$$\mathbf{B}_2^{[M_f \times 1]}(\mu_k^{(2)}) = \mathbf{B}_f(\tau_k) = \mathbf{G}^{(2)} \cdot \mathbf{a}(\mu_k^{(2)}) \quad (5.7)$$

**Tx** antenna ports  $d = 3$  with  $M_{\text{Tx}}$  samples:

$$\begin{aligned} \mathbf{B}_3^{[M_{\text{Tx}} \times 2]}(\mu_k^{(3,4)}) &= \mathbf{B}_{\text{Tx}}(\varphi_{\text{Tx},k}, \vartheta_{\text{Rx},k}) = [\mathbf{G}_h^{(3,4)} \cdot \mathbf{a}(\mu_k^{(3,4)}) \quad \mathbf{G}_v^{(3,4)} \cdot \mathbf{a}(\mu_k^{(3,4)})] \\ &\text{with } \mathbf{a}(\mu_k^{(3,4)}) = \mathbf{a}(\mu_k^{(4)}) \otimes \mathbf{a}(\mu_k^{(3)}) \end{aligned} \quad (5.8)$$

and **Rx** antenna ports  $d = 4$  with  $M_{\text{Rx}}$  samples:

$$\begin{aligned} \mathbf{B}_4^{[M_{\text{Rx}} \times 2]}(\mu_k^{(5,6)}) &= \mathbf{B}_{\text{Rx}}(\varphi_{\text{Rx},k}, \vartheta_{\text{Rx},k}) = [\mathbf{G}_h^{(5,6)} \cdot \mathbf{a}(\mu_k^{(5,6)}) \quad \mathbf{G}_v^{(5,6)} \cdot \mathbf{a}(\mu_k^{(5,6)})] \\ &\text{with } \mathbf{a}(\mu_k^{(5,6)}) = \mathbf{a}(\mu_k^{(6)}) \otimes \mathbf{a}(\mu_k^{(5)}) \end{aligned} \quad (5.9)$$

will be used as follows:

$$\begin{aligned} \mathbf{s}(\theta_k) &= [\mathbf{B}_4(\mu_k^{(5,6)}) \otimes \mathbf{B}_3(\mu_k^{(3,4)}) \otimes \mathbf{B}_2(\mu_k^{(2)}) \otimes \mathbf{B}_1(\mu_k^{(1)})] \cdot [\gamma_{\text{hh},k} \quad \gamma_{\text{hv},k} \quad \gamma_{\text{vh},k} \quad \gamma_{\text{vv},k}]^T \\ &= [\mathbf{B}_{\text{Rx}}(\varphi_{\text{Rx},k}, \vartheta_{\text{Rx},k}) \otimes \mathbf{B}_{\text{Tx}}(\varphi_{\text{Tx},k}, \vartheta_{\text{Tx},k}) \otimes \mathbf{B}_f(\tau_k) \otimes \mathbf{B}_t(\alpha_k)] \cdot [\gamma_{\text{hh},k} \quad \gamma_{\text{hv},k} \quad \gamma_{\text{vh},k} \quad \gamma_{\text{vv},k}]^T \\ &= \mathbf{B}(\mu_k) \cdot \gamma_k. \end{aligned} \quad (5.10)$$

The basis functions in case of the spatial dimensions correspond to the complex polarimetric radiation patterns of the antenna arrays. Finally, the contribution of all specular paths  $K$  with the parameters:

$$\theta_{\text{SC}} = [\theta_1 \quad \dots \quad \theta_K] \quad (5.11)$$

can be written as:

$$\mathbf{s}(\theta_{\text{SC}}) = \sum_{k=1}^K \mathbf{s}(\theta_k). \quad (5.12)$$

### 5.1.2 The Dense Multipath Model (DMC)

From many observations of measured channel responses, an exponential decaying data model is defined to represent the dense multipath components in the delay (correlation) domain  $\Psi(\tau)$  with its corresponding power density function  $\Psi(f)$  in the frequency domain. The parameter vector  $\theta_{\text{DMC}}$  is composed of the parameters  $B_d, \tau_d, \alpha_1$ , which are the coherence bandwidth, base delay and

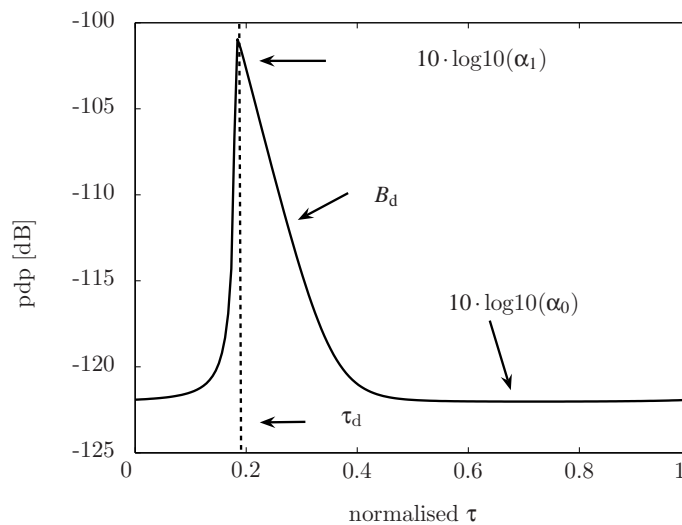
maximum power respectively:

$$\Psi(\tau) = E\{|h(\tau)|^2\} = \begin{cases} 0 & \tau < \tau_d \\ \alpha_1 \cdot \frac{1}{2} & \tau = \tau_d \\ \alpha_1 \cdot e^{-B_d(\tau-\tau_d)} & \tau > \tau_d \end{cases}$$

$$\mathcal{F} \downarrow$$

$$\Psi(f) = \frac{\alpha_1}{(B_d + j2\pi f)} \cdot e^{-j2\pi f \tau_d} \quad (5.13)$$

where  $E\{|h(\tau)|^2\}$  corresponds to the expectation value of the **DMC** channel impulse responses. At the first glance, this model implies infinite bandwidth. However, the data are observed only within the finite bandwidth of the measurement system used. This is actually a very important issue since it warrants the dense multipath model as discussed above. This modelling approach requires that the contribution to any delay-bin consist of a superposition of a reasonable number of dense components. That can be justified only by a limited bandwidth. The finite bandwidth influence and additional stationary noise component  $\alpha_0$  is also shown in Fig. 5.2 by using an example.



**Fig. 5.2:** Dense multipath model in the delay time domain

## 5.2 Maximum Likelihood Parameter Estimator RIMAX

Various algorithms have been proposed for *high-resolution* multidimensional parameter estimation in channel sounding including the multidimensional Unitary **ESPRIT** algorithm [90], and an application of the **SAGE** algorithm [60], which is essentially an Expectation Maximisation (**EM**)-based simplified **ML** parameter estimation procedure [102]. The algorithm proposed in [60] can also be understood as an application of the alternating projection algorithm [103], since the multidimensional search is broken down into sequential one-dimensional coordinate wise searches. Both classes

of algorithm are subjected to different model assumptions and underlying conceptual restrictions including applicability to certain antenna array architectures, calculation time in terms of convergence speed and statistical efficiency.

It is well known that ESPRIT is an unbiased DoD/DoA estimator only if the antenna arrays used for the measurements show the so-called shift invariant structure. Assuming identical antenna elements, this shift invariant structure is given for uniform linear and planar arrays (ULA, URA) and circular uniform beam arrays Circular Uniform Beam Array (CUBA) [90]. For other usual antenna array architectures including UCAs, and Uniform Circular Patch Array (UCPA)s or a spherical array, ESPRIT application to DoD/DoA estimation is not possible or will at least result in biased estimates.

Other drawbacks may arise if we ask for a statistically efficient estimator and/or for the parameter estimation in a more complicated context such as coloured measurement noise, non-ideal antenna-array-characteristics and arbitrary antenna array structures. In general, ML parameter estimation procedures are more flexible to cope with these requirements, as the antenna array models used can easily be applied to a large variety of antenna array architectures. The drawback of the EM or SAGE based parameter estimation algorithms, is their inefficiency and slow convergence rate if closely spaced coherent propagation paths exist in the multi-path propagation scenario (see [30]). Clearly, since only one transmitting source is used, all received paths at a fixed time stamp have to be considered as coherent. This may result in a strong coupling between the path parameters to estimate as shown in [26] and [62]. In this case, the gradient-based multidimensional ML channel parameter estimation framework RIMAX outperforms independent parameter search strategies such as SAGE.

In the following the gradient based parameter estimation algorithm RIMAX is briefly introduced. The estimation problem is formulated in Section 5.2.1. The estimation procedure is subdivided into two parts: the global search (Section 5.2.2), finding the initial parameters  $\theta_k$  of the  $k$ th path and the local gradient based search (Section 5.2.3) that optimises the parameters of all  $K$  paths.

### 5.2.1 Formulation of the Estimation Problem

With the stationary measurement noise  $\mathbf{n}$  (see eqn. (E.3)) and the dense multipath and specular components  $\mathbf{d}$  and  $\mathbf{s}$  respectively, the total observed signal vector  $\mathbf{x}$  (also called snapshot or observation at a fixed time stamp) is modelled as follows:

$$\mathbf{x}^{[M_{\text{Rx}} \cdot M_{\text{Tx}} \cdot M_f \cdot M_t \times 1]} = \mathbf{n} + \mathbf{d}(\theta_{\text{DMC}}) + \sum_{k=1}^K \mathbf{s}(\theta_k) = \mathbf{n} + \mathbf{d}(\theta_{\text{DMC}}) + \mathbf{s}(\theta_{\text{SC}}) \quad (5.14)$$

having a conditional probability density of:

$$\text{pdf}(\mathbf{x} | \theta_{\text{SC}}, \theta_{\text{DMC}}) = \frac{1}{\pi^M \det(\mathbf{R}(\theta_{\text{DMC}}))} e^{-(\mathbf{x} - \mathbf{s}(\theta_{\text{SC}}))^H \mathbf{R}(\theta_{\text{DMC}})^{-1} (\mathbf{x} - \mathbf{s}(\theta_{\text{SC}}))}. \quad (5.15)$$

The related log-likelihood function is:

$$\begin{aligned} L(\mathbf{x}; \boldsymbol{\theta}_{\text{SC}}, \boldsymbol{\theta}_{\text{DMC}}) &= -M \cdot \ln(\pi) - \ln(\det(\mathbf{R}(\boldsymbol{\theta}_{\text{DMC}}))) \\ &\quad - (\mathbf{x} - \mathbf{s}(\boldsymbol{\theta}_{\text{SC}}))^H \cdot \mathbf{R}(\boldsymbol{\theta}_{\text{DMC}})^{-1} \cdot (\mathbf{x} - \mathbf{s}(\boldsymbol{\theta}_{\text{SC}})). \end{aligned} \quad (5.16)$$

Because of the Gaussian nature of the probability density, the maximization of (5.16) with respect to  $\boldsymbol{\theta}_{\text{SC}}$  is essentially a non-linear weighted least squares problem. Since an exhaustive search in the multidimensional parameter space is not feasible, an iterative search framework is used which is based on both sequential parameter update and gradient methods. This procedure proceeds snapshot by snapshot and takes advantage from typical channel behaviour that is known a-priori from propagation physics and from experimental experience. So the estimated parameter set of every snapshot is used as the initial estimate for the next one. This is of specific importance for the  $\boldsymbol{\theta}_{\text{DMC}}$  vector since the statistic parameters of the dense multipath components changes only slowly as long as the “average environment” does not change completely. The  $K$  parameter vectors  $\boldsymbol{\theta}_k$ , on the other hand, change much faster since they directly comprise geometric parameters. Moreover, existing paths can temporarily be shadowed or completely disappear and new paths can suddenly show up. Paths that do not or slowly change their parameters over time can be initialised with the parameters of the previous snapshot, shadowed paths have to be discarded. Additionally, it is necessary to search for new paths. In this way the model order  $K$  is adaptively controlled throughout the sequence of snapshots.

A considerable simplification of the search procedure may be possible according to the EM principle if the parameters are independent in its influence. The parameter sets  $\boldsymbol{\theta}_{\text{SC}}$ , and  $\boldsymbol{\theta}_{\text{DMC}}$  can be assumed as independent. Consequently, an alternating search procedure can be used to maximize (5.16) with respect to  $\boldsymbol{\theta}_{\text{SC}}$ , and  $\boldsymbol{\theta}_{\text{DMC}}$ . This method allows the successive estimation of the deterministic specular paths from the observed data. For estimation of the parameters  $\boldsymbol{\theta}_{\text{DMC}}$ , a Gauss-Newton algorithm is applied. This gives us also a parametric representation of the covariance matrix:

$$\begin{aligned} \mathbf{R}(\boldsymbol{\theta}_{\text{DMC}}) &= \mathbf{R}_4 \otimes \mathbf{R}_3 \otimes \mathbf{R}_2(\boldsymbol{\theta}_{\text{DMC}}) \otimes \mathbf{R}_1 \\ &= \mathbf{R}_{\text{Rx}} \otimes \mathbf{R}_{\text{Tx}} \otimes \mathbf{R}_f \otimes \mathbf{R}_t \\ &= \mathbf{I}^{[M_{\text{Rx}} \times M_{\text{Rx}}]} \otimes \mathbf{I}^{[M_{\text{Tx}} \times M_{\text{Tx}}]} \otimes \mathbf{R}_2^{[M_f \times M_f]}(\boldsymbol{\theta}_{\text{DMC}}) \otimes \mathbf{I}^{[M_t \times M_t]} \end{aligned} \quad (5.17)$$

where the covariance matrix  $\mathbf{R}_f$ :

$$\mathbf{R}_f = \text{toep}(\boldsymbol{\kappa}(\boldsymbol{\theta}_{\text{DMC}}), \boldsymbol{\kappa}(\boldsymbol{\theta}_{\text{DMC}})^H) \quad (5.18)$$

is a toeplitz matrix defined by the sampled version of  $\Psi(f, \boldsymbol{\theta}_{\text{DMC}})$ :

$$\boldsymbol{\kappa}(\boldsymbol{\theta}_{\text{DMC}}) = \frac{\boldsymbol{\alpha}_1}{M_f} \left[ \begin{array}{cccc} \frac{1}{\beta_d} & \frac{e^{-j2\pi\tau'_d}}{\beta_d + j2\pi\frac{1}{M_f}} & \dots & \frac{e^{-j2\pi\tau'_d(M_f-1)}}{\beta_d + j2\pi\frac{1}{M_f}} \end{array} \right]^T + \boldsymbol{\alpha}_0 \cdot \mathbf{e}_0. \quad (5.19)$$



The normalised coherency bandwidth is defined as:

$$\beta_d = \frac{B_d}{B} \quad (5.20)$$

where  $B$  is the measurement bandwidth. Also the base delay  $\tau_d$  is normalised with the maximum impulse response length as follows:

$$\tau'_d = \frac{\tau_d \cdot M_f}{B}. \quad (5.21)$$

Furthermore, the i.i.d. Gaussian measurement noise with variance  $\alpha_0$  is included in the model, which  $\mathbf{e}_0^{[M_r \times 1]} = [\mathbf{1} \ \mathbf{0} \dots \mathbf{0}]^T$  being a unit vector.

The knowledge of  $\mathbf{R}(\theta_{\text{DMC}})$  is essential for the estimation of specular parameters  $\theta_{\text{SC}}$  since it provides appropriate weighting of the observed data according to the non-linear weighted least squares problem:

$$\hat{\theta}_{\text{SC}} = \arg \min_{\theta_{\text{SC}}} (\mathbf{x} - \mathbf{s}(\hat{\theta}_{\text{SC}}))^H \cdot \mathbf{R}(\hat{\theta}_{\text{DMC}})^{-1} \cdot (\mathbf{x} - \mathbf{s}(\hat{\theta}_{\text{SC}})) \quad (5.22)$$

To solve the minimisation problem of eqn. (5.22) for a single time stamp, the RIMAX procedure as shown in Fig. 5.3 will be applied. The alternating estimation of the SC and DMC is shown. In case of the SC estimation it is distinguished between *Global Search* for new paths (Section 5.2.2) and *Local Search* (Section 5.2.3). The *Global Search* uses an incoherent combing procedure and the SAGE algorithm. The *Local Search* improves the already estimated paths of the previous snapshot (Adjustment of the  $K_{\text{old}}$  paths) and the additional estimated paths applying a gradient based non-linear least square estimation procedure (Levenberg-Marquardt).

### 5.2.2 Global Search for New Paths

The global search for new paths  $k = K_{\text{old}} + 1 \dots K$  has to be carried out at each new time stamp (snapshot) after adjusting the already estimated  $K_{\text{old}}$  paths to the slightly changed propagation conditions. The adjustment of the  $K_{\text{old}}$  paths is done by the local search procedure (Section 5.2.3), which is initialised with the a priori knowledge of the parameters of the  $K_{\text{old}}$  estimated paths of the previous snapshot. For any new path  $k$  the non-linear optimisation problem has to be solved:

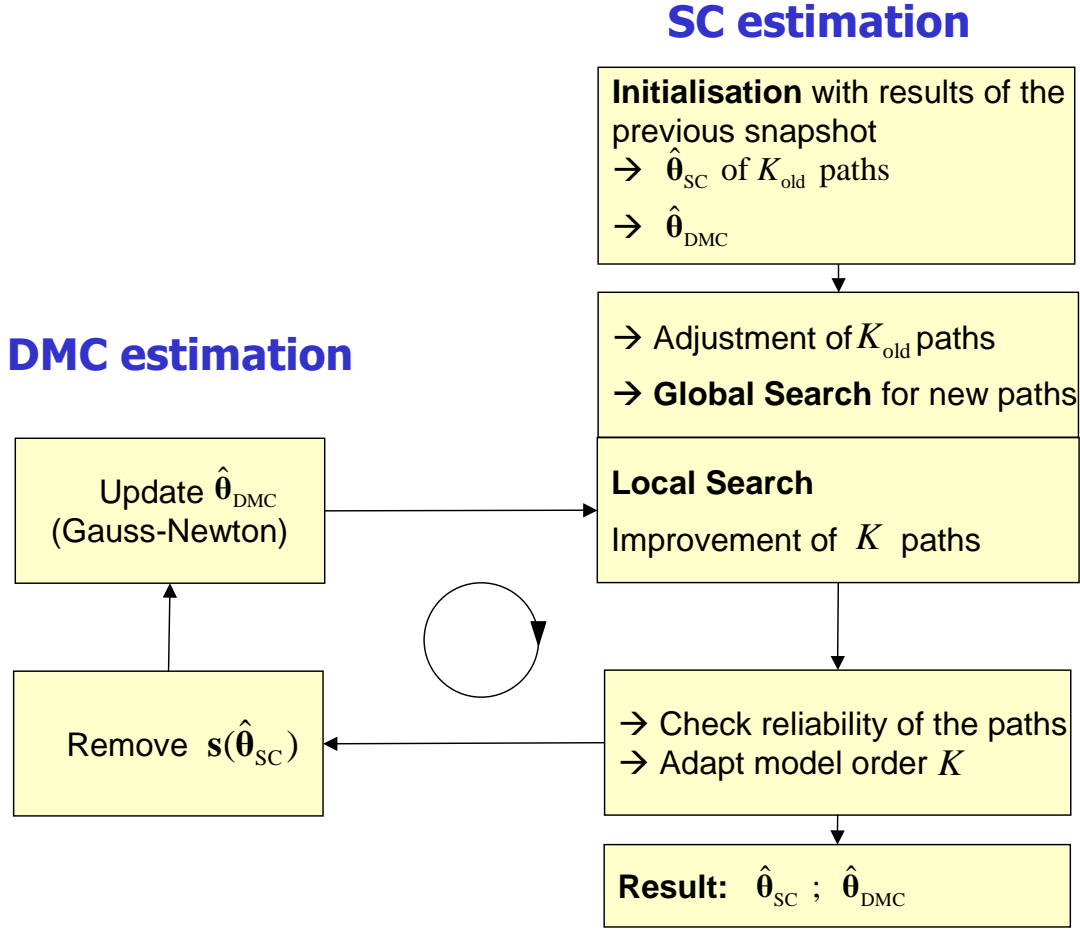
$$\hat{\mu}_k = \arg \max_{\mu_k} \{c(\tilde{\mathbf{x}}, \mu_k)\}. \quad (5.23)$$

The multidimensional correlation function  $c(\tilde{\mathbf{x}}, \mu_k)$  is defined as:

$$c(\tilde{\mathbf{x}}, \mu_k) = \tilde{\mathbf{x}}^H \cdot \mathbf{R}^{-1} \cdot \mathbf{B}(\mu_k) \cdot \left( \mathbf{B}(\mu_k)^H \cdot \mathbf{R}^{-1} \cdot \mathbf{B}(\mu_k) \right)^{-1} \cdot \mathbf{B}(\mu_k)^H \cdot \mathbf{R}^{-1} \cdot \tilde{\mathbf{x}}. \quad (5.24)$$

For notational convenience the dependence of  $\mathbf{R}$  on  $\theta_{\text{DMC}}$  is skipped in the previous equation. The remaining observation  $\tilde{\mathbf{x}}$  after removing the  $K_{\text{old}}$  adjusted paths is defined as:

$$\tilde{\mathbf{x}} = \mathbf{x} - \sum_{k=1}^{K_{\text{old}}} \mathbf{s}(\theta_k). \quad (5.25)$$



**Fig. 5.3:** Simplified RIMAX block diagram for the estimation of the parameters of the SC and DMC of a single observation (time stamp/snapshot)

The SAGE algorithm optimises the correlation function dependent only on one parameter  $\mu_k^{(l)}$ :

$$\hat{\mu}_k^{(l)} = \arg \max_{\mu_k^{(l)}} \{c(\tilde{\mathbf{x}}, \mu_k)\} \quad (5.26)$$

while all other parameters  $\mu_k^{(r)} \neq \mu_k^{(l)}$  are kept constant. In the first search step for a new path, a non-coherent combining of independent observations is used to estimate the initial values for the unknown parameters  $\mu_k^{(r)} \neq \mu_k^{(l)}$ . This strategy will be explained using the following example.

In the example only the TDoA  $\tau_k$  and DoA  $(\varphi_{\text{Rx},k}, \vartheta_{\text{Rx},k})$  will be considered. Nevertheless, the strategy can be easily extended to further parameter dimensions such as DoD and Doppler-Shift. Suppose the channel impulse response has been measured using a Polarimetric Uniform Circular Patch Array (PUCPA) with 48 ports at Rx and an omnidirectional antenna at Tx. First, the 48 individual channel impulse responses, which are equivalent to the  $m_{\text{Rx}} = 1 \dots 48$  one-dimensional correlation functions  $c_{m_{\text{Rx}}}(\tilde{\mathbf{x}}, \tau)$ , are treated as independent realisations of the same process. They are used to maximise the correlation function with respect to the time delay  $\tau$ . Non-coherent combining of this 48 impulse responses avoids any assumption on unknown DoA in this step and we get an

initial estimate  $\hat{\tau}_k$ . This reduces the maximisation problem to two concatenated “one-dimensional” problems. Any arbitrary assumption of the DoA in the example would implicitly realise coherent combining which may disregard the strong paths (in terms of power) impinging from other angles by beam-forming. This kind of non-coherent handling of the data dimension corresponding to the  $M_{R_x}$  antennas gives us a higher probability to detect the relevant paths (in terms of power) with respect to the time delay in the first step.

In the next step the correlation function is optimised dependent on the DoA and the time delay is kept fixed with the estimate  $\hat{\tau}_k$ . For the DoA which is described by the two parameters  $\phi_{R_x,k}$  and  $\vartheta_{R_x,k}$ , the two-dimensional correlation function dependent on azimuth and co-elevation is calculated. It is reasonable to calculate the two-dimensional correlation function w.r.t these two angles, since they depend only on one data dimension ( $M_{R_x}$  antenna responses) and a separate data dimension for azimuth and co-elevation for a non-coherent combining are not available. For example, calculating only the one-dimensional correlation function with respect to one of these angles  $\phi$  or  $\vartheta$ , an assumption has to be made for the second angle  $\phi_{R_x,k}$  or  $\vartheta_{R_x,k}$ . However, an assumption for this second angle  $\phi_{R_x,k}$  or  $\vartheta_{R_x,k}$  can not be made, as no a priori knowledge is available.

Practically a sampled version of the two-dimensional correlation function with respect to DoD/DoA is calculated by using the minimum sampling grid N95 ( $\zeta^{N95}$ ) (see section 3.5, eqn. (3.37)). Consequently, the initial estimates for the azimuth and co-elevation of the  $k^{th}$  path are:

$$\langle \hat{\phi}_{R_x,k}, \hat{\vartheta}_{R_x,k} \rangle = \arg \max_{\zeta_{R_x}^{N95}} \{c(\tilde{\mathbf{x}}, \hat{\tau}_k, \zeta_{R_x}^{N95})\}. \quad (5.27)$$

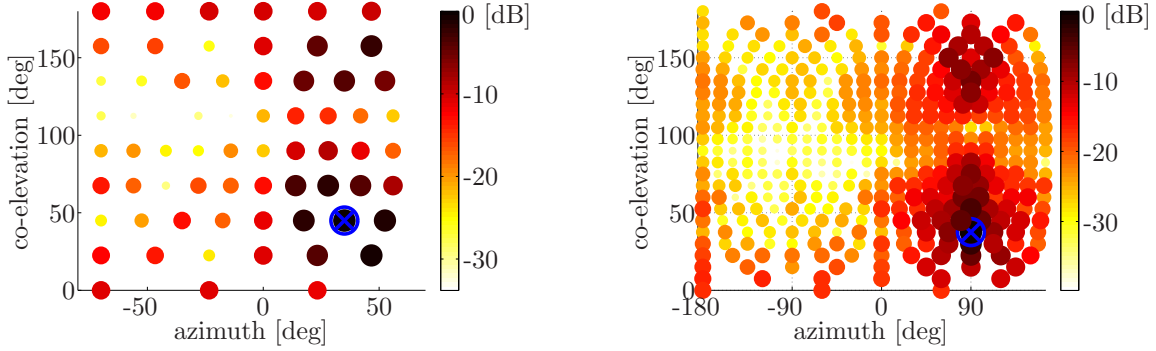
In Fig. 5.4 the sampled version of the 2D correlation functions (normalised to its maximum) by using the N95 grid  $\zeta^{N95}$  are shown for the **PURPAx2x2x4** and the **SPUCPAx2x2x24** in case of a single path scenario. The crossed blue circle indicates the maximum of the correlation function and consequently the initial estimates for  $\hat{\phi}_k$  and  $\hat{\vartheta}_k$ . Note that the number of sampling points for the 2D DoD/DoA correlation function calculation can be further reduced if additional information about the propagation environment is available. For example, using the **PURPAx2x2x4** as a base station antenna above roof top, allows us to limit the co-elevation range at least to  $\vartheta = 90^\circ \dots 180^\circ$ , since scatterers for a co-elevation smaller  $\vartheta = 90^\circ$  can not be expected.

As the initial values of TDoA and DoA found with the above described strategy only maximise the correlation function at a rough grid, all parameters  $\mu_k$  of the new path  $k$  have to be further improved by the SAGE procedure. The optimisation is done sequentially for all parameters  $\mu_k^{(1)}$  to  $\mu_k^{(R)}$ , with the correlation functions being calculated with a finer grid. Additionally, the one-dimensional correlation functions are only calculated around the initial estimate  $\mu^{(l)} = \hat{\mu}^{(l)}_k - \Delta\mu^{(l)} \dots \hat{\mu}^{(l)}_k + \Delta\mu^{(l)}$ . The range  $\Delta\mu^{(l)}$  can be defined by the Rayleigh (FFT) resolution or in case of the DoD/DoA it is defined by the angular distance to the adjacent sampling points of the N95 grid  $\zeta^{N95}$  (see Section 3.5).

After removing the new estimated path  $k$  from  $\tilde{\mathbf{x}}$  the initial values of the next path  $k+1$  will be estimated using the strategy described above. This kind of successive path estimation is also called

Serial Interference Cancellation (SIC).

Notice that the calculation of the multidimensional correlation function with respect to one data dimension  $d$  using eqn. (5.24) is computationally inefficient, therefore an efficient implementation is used, which is discussed in [8] and [62].



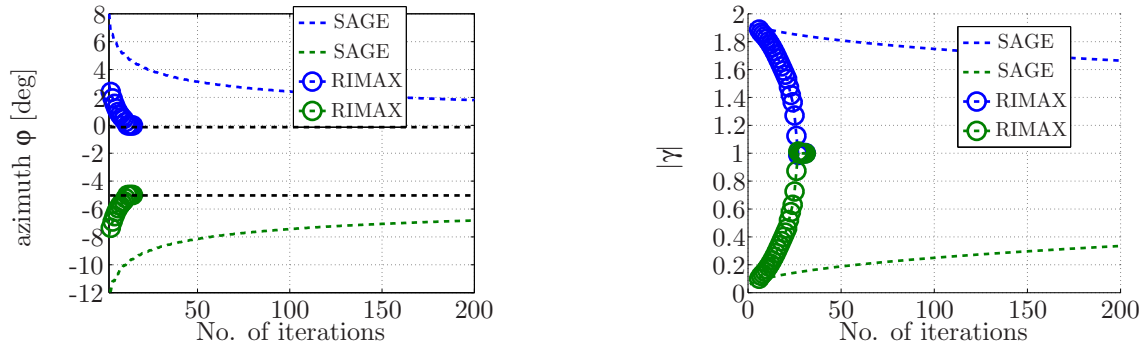
(a) Magnitude of the 2D correlation function **PURPAx2x2x4**

(b) Magnitude of the 2D correlation function **SPUCPAx2x2x24**

**Fig. 5.4:** Sampled version of the 2D correlation function using the N95 grid  $\zeta^{N95}$  assuming a single path with  $\varphi_k = 40^\circ, \vartheta_k = 40^\circ$  for the **PURPAx2x2x4** (a) and with  $\varphi_k = 90^\circ, \vartheta_k = 40^\circ$  for the **SPUCPAx2x2x24** (b)

### 5.2.3 Local Search and Discussion of the Algorithm's Convergence

The problem of local search is completely different. It is found that for closely spaced coherent paths the coordinate-wise search strategy has serious disadvantages because of its slow convergence rate which is not only time-consuming but may also end in erroneous estimates when using a quantized parameter data base [30]. This problem is related to the strong coupling of the respective parameter estimates as indicated in the Fisher Information Matrix (FIM) [62]. Since it is well known that the ML function is, under mild restrictions, quadratic at its maximum (in the local “attractor area”), a conjugate gradient search promises much better convergence performance when the parameters are coupled in its influence to the maximisation or minimisation of eqn. (5.16) or of eqn. (5.22) respectively. From the variety of available procedures for non-linear optimisation, the Levenberg-Marquardt algorithm is chosen because of its robustness. To calculate the optimum step size and direction for parameter change these algorithms require the gradient, the Jacobian matrix (matrix of the first order derivatives) and the Hessian matrix (matrix of the second order derivatives) of the log-likelihood function at the actual point in the parameter space. Fortunately, with the algebraic data model based on eqn. (5.2), the derivatives are easily available. Again the advantage of the proposed EADF (Section 3.3) is obvious since the derivatives of the radiation patterns of practical antenna arrays can be analytically calculated. The approximation of the Hessian as it is used in the Gauss-Newton / Levenberg-Marquardt algorithm is essentially an estimate of the FIM. This provides also the required information on both the variance and the mutual dependency of the parameter estimates. The following examples demonstrate the convergence performance of the RIMAX algorithm. The simulation results in Fig. 5.5 and Fig. 5.6 compare the convergence



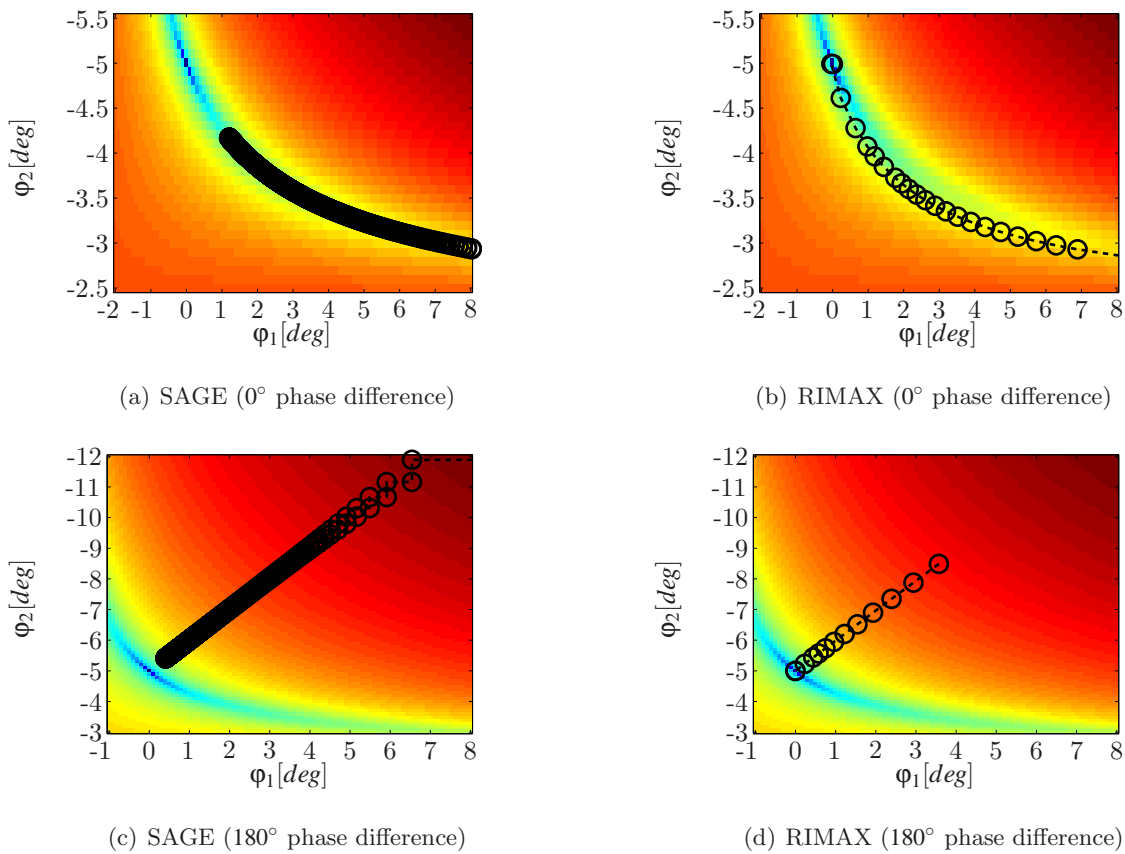
(a) Estimated azimuth angles as function of the number of iterations

(b) Estimated path weights as function of the number of iterations

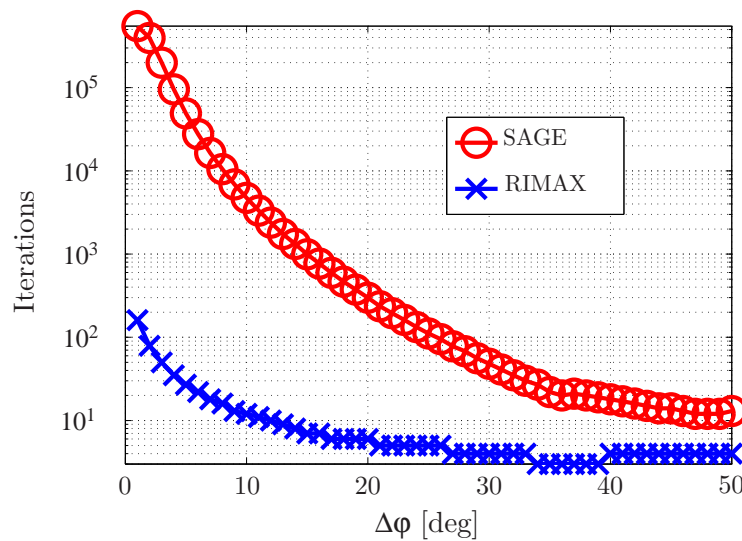
**Fig. 5.5:** Convergence behaviour of the SAGE algorithm compared to the gradient based RIMAX algorithm in case of two coherent paths (angular separation  $5^\circ$ ; phase difference  $0^\circ$ )

behaviour of the gradient based ML search to the parameter wise search of the SAGE in a noise free, closely spaced coherent path scenario. In this case, the paths differ only in DoA and they are separated by  $5^\circ$  in angle of arrival which is closer than the Rayleigh resolution of the array. The path magnitudes are equal ( $\gamma_{vv,1} = \gamma_{vv,2} = 1$ ) and the phase difference is zero for the figures 5.5(a), 5.5(b), 5.6(a), 5.6(b) and  $180^\circ$  for the figures 5.6(c), 5.6(d). Although these constellations maybe considered as worst case situations, they frequently occur in a practical propagation scenario since path length difference has to change only by 2.5 cm (for  $f_0 = 5.2$  GHz) to move from one worst case situation to the other. The applied antenna array is again the 24 element circular patch array PUCPASIMx2x1x24. Only matched vertical polarisation is considered. In Fig. 5.5 the estimated parameters of the azimuth angle and the path weights as function of the number of iterations are shown. Figure 5.6 depicts the iteration steps that are plotted on the cost function surface. Both constellations cause completely different cost function surfaces which are characterised by shaped, narrow valleys. The parameter wise search of the SAGE forces very small zigzag steps in the direction of the individual parameters which can be seen most clearly in Fig. 5.6(c). In both cases, within 2000 iterations of the SAGE procedure final convergence is still not achieved, whereas the gradient search needs only 26 and 13 steps, respectively, to reach the minimum of the cost function. Figure 5.6(c) also indicates the initial SAGE steps before starting the final gradient steps. The example shows that quantisation of the data model would be detrimental since very small steps are required by the SAGE in order to achieve some progress. This shows again that even though a quantised data model can completely describe the antenna array radiation patterns, much finer quantisation steps or an analytic description of the model is required. But irrespective from this requirement, the SAGE algorithm has to cope with the problem that such small steps maybe infeasible in the presence of measurement noise.

Figure 5.7 further compares coordinate wise (alternating) and gradient based optimisation in terms of the number of iteration vs. the angular separation of two coherent paths. It becomes clear that especially for the SAGE and paths which are closer than Rayleigh resolution, the number of the required iterations becomes prohibitive.



**Fig. 5.6:** Convergence behaviour of the SAGE algorithm compared to the gradient based RIMAX algorithm in case of two coherent paths plotted in the corresponding cost functions (angular separation 5°)



**Fig. 5.7:** Convergence rate of the SAGE algorithm in comparison to the gradient based ML algorithm RIMAX (number of iterations vs. angular separation of two coherent paths)

### 5.2.4 Estimation example

The example in Fig. 5.8 shows the estimation results in the delay domain (power delay profile (pdp)). It was calculated from measured data in a street micro cell scenario. The specular path weight magnitudes are indicated by blue dots. The reconstruction of the power delay profile within the measurement bandwidth is given by the blue curve. The green curve is the difference between the reconstructed and the measured power delay profile, thus it is an instantaneous realisation of the DMC. The expectation of the same part (which is estimated from the data) is given by the red triangular curve. The vertical red lines indicate the relative variance of the specular path weight estimates calculated from the FIM. Most reliable paths are indicated by a variance contribution that directly follows the dense multipath slope. Noise enhancement is indicated by red points above this slope (see, e.g. at 2800 ns). The outliers around 305 and 335 ns are caused by line splitting, which is characterized by two very closely spaced, excessively strong paths with opposite signs. Although those paths may very well approximate a small bin of a band-limited CIR, there is clear evidence of a wrong estimate since the relative variance is  $> 1$ . As a consequence we omit one of those paths. In the RIMAX a path is considered to be not reliable when the relative variance of the path weights is worse than -3 dB. After discarding an unreliable path, a repeated estimation step will then lead to a more accurate estimate of the remaining paths. Line splitting is a typical situation which occurs when the model is under-determined. Since the proposed procedure clearly indicates and corrects this error, it can be applied as a part of robust iterative model order control.

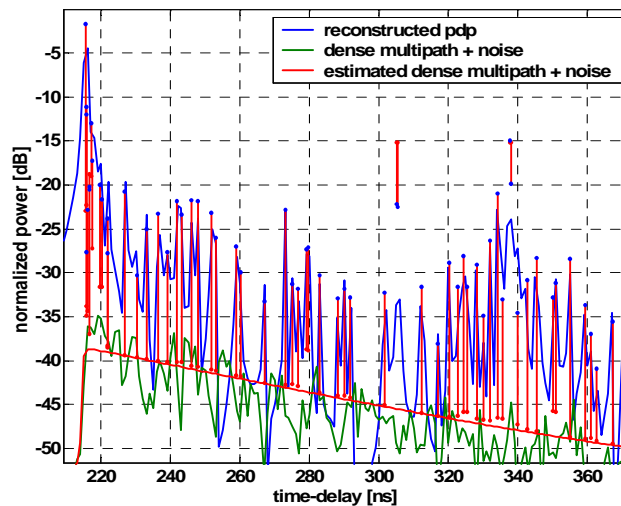


Fig. 5.8: CIR measurement example and parameter estimates

## 5.3 Discussion about the Limitations of the Estimator and its Model

Several *high-resolution* parameter estimation algorithms (such as ESPRIT, ML) have been applied to directional channel parameter estimation in channel sounding. However, the reliability of the estimation results is often not clearly defined in practical environments. From significant experience



with measurements, it has been observed, that *high-resolution* channel parameter estimators may yield results that approximates the measured data  $\mathbf{x}$  very well. That means, the model that is used for the **SC** approximates the received signal energy, but some of the estimated paths seem not to correspond to the propagation environment which was measured. This means with a so called data fitting no answer is given about the reliability of the **SC** estimation results. A verification of such physical meaningless paths in complex environments based on measurement results is almost impossible. As resolution and reliability of *high-resolution* parameter estimation has always something to do with calibration or precise knowledge of the measurement device parameters, the quality of the antenna arrays may be considered as the weakest point in the performance of *high-resolution* channel sounding.

In the literature it has been shown that an estimation algorithm can produce reliable results if the synthetic channels for evaluation are generated with the data model of the estimator. The limitations were shown in terms of the **CRLBs** of estimated **SC** parameters in the presence of measurement noise (e.g. in [60, 63, 64]). However, ideal or simulated antenna arrays and synthetic channels are used for these investigations. From a detailed literature survey we came to the conclusion that the impact of practical antenna arrays and measurement systems on the **SC** estimation results has not been completely investigated.

Also the relevance of the **DMC** from the perspective of parameter estimation has not been investigated so far. Although it could be shown with measurements (see [3, 12, 14, 104]) that the contribution of the **DMC** can contain up to 80 % of the total received signal energy, it is not clear if these estimated **DMC** are related to unresolved **SC** and distributed diffuse scattering only. So far it is not taken into account that the estimated **DMC** may also result from model error of the **SC**.

From the discussion above different issues need to be considered. The following list gives an overview of these issues and indicates in which chapter the different issues will be discussed:

1. The impact of additive measurement noise on the parameter estimation results if practical antenna arrays are used: Chapter 6. The **CRLB** of the **SC** parameters are analytically calculated for practical antenna arrays (related to **SC**).
2. Model error of the antenna array data model derived from antenna array calibration measurements: Chapter 7 Section 7.2 (related to **SC**).
3. The impact of the measurement system properties such as phase noise etc. on the estimation results: Chapter 7 Section 7.3 (related to **SC**).
4. The overall consequence of the bullet points 1. to 3. in a complex measurement environment on the estimated **SC** and the estimated **DMC**: Chapter 8 (related to **SC** and **DMC**).



## 6. PERFORMANCE EVALUATION OF PRACTICAL ANTENNA ARRAYS

This chapter presents and verifies a framework to evaluate the performance of practical antenna arrays independent on any parameter estimation algorithm that uses the specular path model.

The fundamental limitations on the achievable DoD/DoA and path weight variances dependent on the measurement SNR are defined as the CRLB [105, 106] assuming an unbiased parameter estimator. Since the CRLB indicates the minimum achievable parameter variance, the CRLB is commonly used to evaluate parameter estimation algorithms. In [60, 64, 107–109] synthetic channels and antenna arrays are used. As for the above mentioned publications, an analytic descriptions of the antenna array response is available, the CRLB can be easily derived.

However, practical antenna arrays are always susceptible to various imperfections (mutual element coupling, fabrication tolerances, etc.) that are not completely considered for simulated synthetic antenna arrays. Therefore, the evaluation of practical antenna arrays has a great relevance for *Experimental Channel Characterisation*. Based on measured antenna characteristics and the CRLB a novel framework for the performance evaluation of practical antenna arrays is presented in this chapter (first published in [23, 26, 27]). The framework can be also applied to compare simulated antenna arrays with *practical* antenna arrays.

In Section 6.1, the framework to calculate the CRLB for *practical* antenna arrays is presented and exemplarily applied to a simple *single path scenario* using a theoretical CUBA and a measured CUBA antenna array. In Section 6.2, the proposed framework is verified by anechoic measurements.

### 6.1 CRLB Based Evaluation Framework for Practical Antenna Arrays

The CRLB of the channel parameters such as DoD/DoA  $(\vartheta, \varphi)$  and of the complex path weights  $\gamma_h, \gamma_v$  are defined as the diagonal elements of the inverse FIM. The FIM is given by the covariance matrix of the  $L = K \cdot P$  first order derivatives of the observed data vector (6.2 and 6.3) with respect to the  $P$  parameters of all  $K$  paths in the given scenario:

$$\boldsymbol{\theta}^{[1 \times L]} = [\vartheta, \varphi, \Re_{\gamma_h}, \Im_{\gamma_h}, \Re_{\gamma_v}, \Im_{\gamma_v}], \quad (6.1)$$

where the vectors  $\vartheta, \varphi, \Re_{\gamma_h}, \Im_{\gamma_h}, \Re_{\gamma_v}, \Im_{\gamma_v}$  include the parameters of all  $K$  paths of the corresponding dimension. The angles co-elevation  $\vartheta$  and azimuth  $\varphi$  are defined in the spherical coordinate system

---

(see also Fig. 3.1). The observed data of the channel scenario is

$$\mathbf{x}^{[M \times 1]}(\boldsymbol{\theta}, \mathbf{n}) = \mathbf{s}^{[M \times 1]}(\boldsymbol{\theta}) + \mathbf{n}^{[M \times 1]} \quad (6.2)$$

$\mathbf{n}$  denoting the noise vector and

$$\mathbf{s}(\boldsymbol{\theta}) = \sum_{k=1}^K (\gamma_{h,k} \cdot \mathbf{b}(\boldsymbol{\varphi}_k, \boldsymbol{\vartheta}_k, q = h) + \gamma_{v,k} \cdot \mathbf{b}(\boldsymbol{\varphi}_k, \boldsymbol{\vartheta}_k, q = v)) \quad (6.3)$$

results from the superposition of all  $K$  paths and polarisation. The complex radiation patterns  $\mathbf{b}(\boldsymbol{\varphi}_k, \boldsymbol{\vartheta}_k, q = h)$  and  $\mathbf{b}(\boldsymbol{\varphi}_k, \boldsymbol{\vartheta}_k, q = v)$  are weighted with the complex path weights  $\gamma_{h,k}$  and  $\gamma_{v,k}$  for horizontal and vertical polarisation respectively. The probability density function of the described problem depending on  $\boldsymbol{\theta}$  is:

$$pdf(\mathbf{x} | (\boldsymbol{\theta}, \mathbf{R}_{mm})) = \frac{1}{\pi^M \det(\mathbf{R}_{mm})} e^{-(\mathbf{x} - \mathbf{s}(\boldsymbol{\theta}))^H \mathbf{R}_{mm}^{-1} (\mathbf{x} - \mathbf{s}(\boldsymbol{\theta}))}. \quad (6.4)$$

In the case of *i.i.d.* Gaussian noise with a standard deviation  $\sigma$  in the real and imaginary part (see eqn. (E.3)), the noise covariance matrix is defined as:

$$\mathbf{R}_{mm} = E \{ \mathbf{n}^H \cdot \mathbf{n} \} = \sigma^2 \cdot \mathbf{I} \quad (6.5)$$

The theory to determine the **CRLB** is well known (e.g. [105, 106]). For the calculation of the **CRLB**, an analytic description of the model of the observable channel response of the **SC** ( $\mathbf{s}(\boldsymbol{\Theta}_k)$ ) is required. Additionally, the analytic description of the derivatives of  $\mathbf{s}(\boldsymbol{\Theta}_k)$  dependent on the angles of arrival and the complex polarimetric path weights are needed. Consequently, an analytic description of the radiation patterns and its derivatives are necessary. Now the advantage of the **EADF** model as described in Section 3.3 becomes apparent, as the radiation patterns eqn. (3.31) and its derivatives equations (3.32), (3.33) can be easily analytically calculated for any *practical* antenna array.

The derivatives dependent on the angles of arrival are defined as:

$$\frac{\partial \mathbf{s}(\boldsymbol{\theta})}{\partial \boldsymbol{\varphi}_k} = \gamma_{h,k} \cdot \frac{\partial \mathbf{b}(\boldsymbol{\varphi}_k, \boldsymbol{\vartheta}_k, q = h)}{\partial \boldsymbol{\varphi}_k} + \gamma_{v,k} \cdot \frac{\partial \mathbf{b}(\boldsymbol{\varphi}_k, \boldsymbol{\vartheta}_k, q = v)}{\partial \boldsymbol{\varphi}_k} \quad (6.6)$$

$$\frac{\partial \mathbf{s}(\boldsymbol{\theta})}{\partial \boldsymbol{\vartheta}_k} = \gamma_{h,k} \cdot \frac{\partial \mathbf{b}(\boldsymbol{\varphi}_k, \boldsymbol{\vartheta}_k, q = h)}{\partial \boldsymbol{\vartheta}_k} + \gamma_{v,k} \cdot \frac{\partial \mathbf{b}(\boldsymbol{\varphi}_k, \boldsymbol{\vartheta}_k, q = v)}{\partial \boldsymbol{\vartheta}_k}, \quad (6.7)$$

The derivatives dependent on the real and imaginary part of the polarimetric path weights are given by:

$$\frac{\partial \mathbf{s}(\boldsymbol{\theta})}{\partial \Re \{ \gamma_{q,k} \}} = \mathbf{b}_q(\boldsymbol{\varphi}_k, \boldsymbol{\vartheta}_k) \quad (6.8)$$

$$\frac{\partial \mathbf{s}(\boldsymbol{\theta})}{\partial \Im \{ \gamma_{q,k} \}} = j \cdot \mathbf{b}_q(\boldsymbol{\varphi}_k, \boldsymbol{\vartheta}_k). \quad (6.9)$$

Thus, the matrix of the first derivatives, the Jacobian matrix is:

$$\mathbf{D}(\boldsymbol{\theta}) = \begin{bmatrix} \frac{\partial \mathbf{s}(\boldsymbol{\theta})}{\partial \theta_1} & \dots & \frac{\partial \mathbf{s}(\boldsymbol{\theta})}{\partial \theta_L} \end{bmatrix}. \quad (6.10)$$

The real part of the covariance matrix of  $\mathbf{D}$  is proportional to the Fisher-Information-Matrix:

$$\mathbf{J} = 2 \cdot \Re \{ \mathbf{D}^H \cdot \mathbf{R}_m^{-1} \cdot \mathbf{D} \}, \quad (6.11)$$

the diagonal elements of the inverse **FIM** representing the **CRLB** of the  $L$  parameters:

$$\text{CRLB}(\boldsymbol{\theta}) = \text{diag} \{ \mathbf{J}^{-1} \} = [\sigma_1^2 \dots \sigma_L^2] \quad (6.12)$$

and the non diagonal elements of the inverse **FIM** denote the co-variances.

In Fig. 6.1 the pattern of the inverse **FIM** is drawn for a simple single path and two path scenario. For a better understanding, a single polarised antenna array with only azimuth resolution and a path wise arrangement (different from the arrangement in equation (6.1)!) of the parameter dimensions in the **FIM** are chosen. In case of correlated parameters, the non-diagonal elements of the **FIM** are not zero. Basically, the parameters are correlated if mutual coupling between the antenna elements exists. Additionally, the parameters between the paths are correlated due to the limited aperture size of the antenna array.

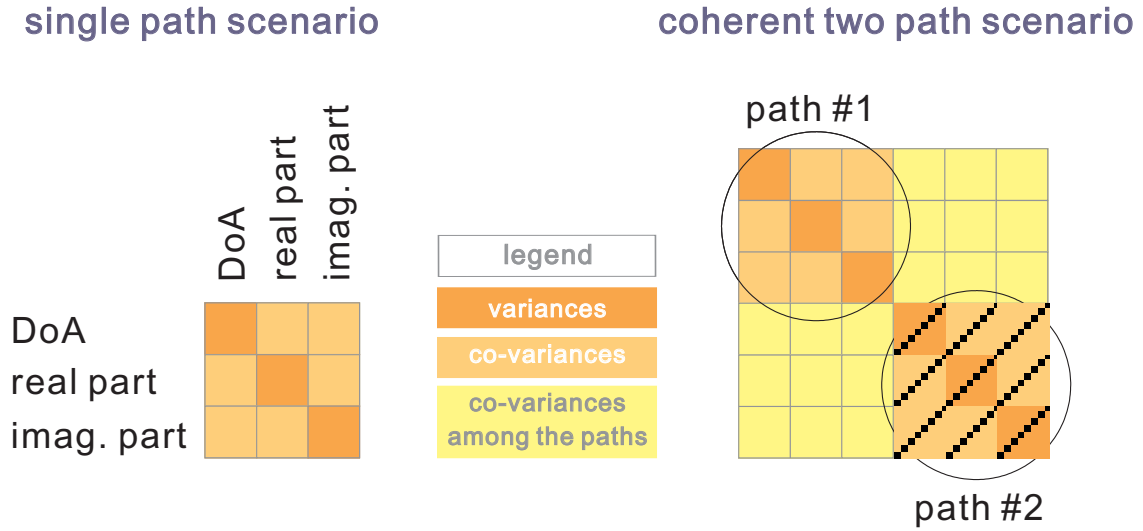
With a single path test scenario, the minimum achievable variances of all parameters of the single path dependent on a certain **SNR** can be calculated. The non diagonal elements of the **FIM** are zero if the mutual coupling between the antenna elements of the array is zero. Again, this means that the parameters are uncorrelated and the co-variances of the inverse **FIM** are zero. If mutual coupling between the antenna elements exist, the non diagonal elements of the **FIM** are not zero, the parameters are correlated, and the co-variances of the inverse **FIM** are not zero.

In more difficult scenarios with two or more coherent paths, the variances of each path can never be better than the variances of the single path scenario. Again, the non-diagonal elements in the **FIM** among two or more paths are practically not zero due to the limited aperture size of the antenna arrays. This means that the correlation between the parameters of the different paths exist and the overall variances of the path parameters increases compared to the single path scenario.

### 6.1.1 Example: Comparison of a Theoretical and Measured CUBA

The **CRLBs** of the parameters azimuth, real and imaginary part of the vertical path weight in a simple single path scenario using a theoretical **CUBA** are analytically derived. These results are compared with the **CRLBs** derived from the measured 8 element **CUBA<sub>x1x1x8</sub>** (see Section 2.4, Fig. 2.14).

The idea of using a **CUBA**, which is composed of bi-conical beam antennas [88], for **DoA** estimation was first presented in [110]. The radiation pattern function of each element is considered as a periodic  $\text{sinc}(\cdot)$  function. The main beam of the  $m_{\text{Rx}}$ -th antenna is pointing towards  $\boldsymbol{\varphi} = m_{\text{Rx}} \cdot \boldsymbol{\varphi}_0$  with  $\boldsymbol{\varphi}_0 = \frac{2\pi}{M_{\text{Rx}}}$ . As the Fourier transform of a periodic  $\text{sinc}(\cdot)$  function corresponds to a rectangular



**Fig. 6.1:** Pattern of inverse FIM of a single path and a coherent two path scenario

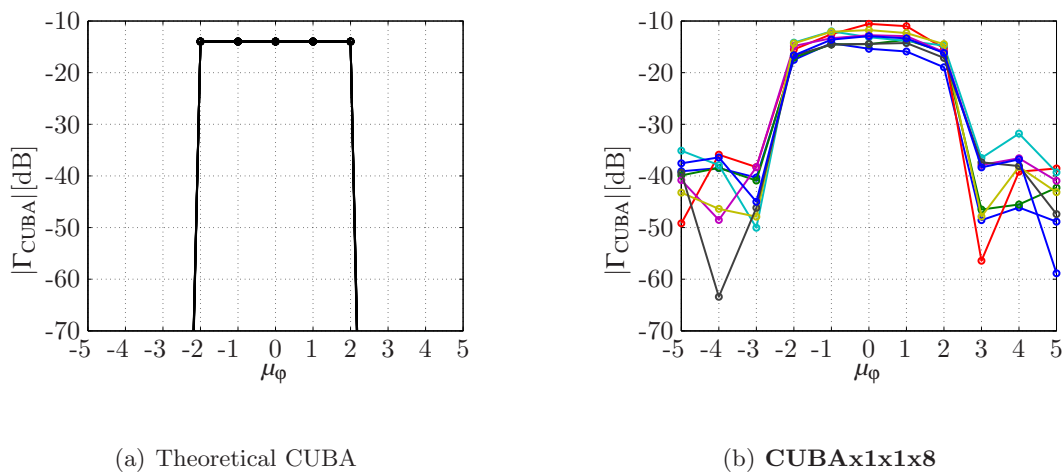
function with  $L_\varphi$  coefficients, the 1D EADF of the theoretical CUBA with  $M_{\text{Rx}}$  antennas can be written as:

$$\Gamma_{\text{CUBA}}^{[M_{\text{Rx}} \times L_\varphi]} = \frac{1}{L_\varphi} e^{-j \begin{bmatrix} 0 \\ \vdots \\ M_{\text{Rx}} - 1 \end{bmatrix} \cdot \varphi_0 \mu_\varphi^T} \quad (6.13)$$

with

$$\mu_\varphi = \left[ -\frac{L_\varphi - 1}{2} \dots \frac{L_\varphi - 1}{2} \right]. \quad (6.14)$$

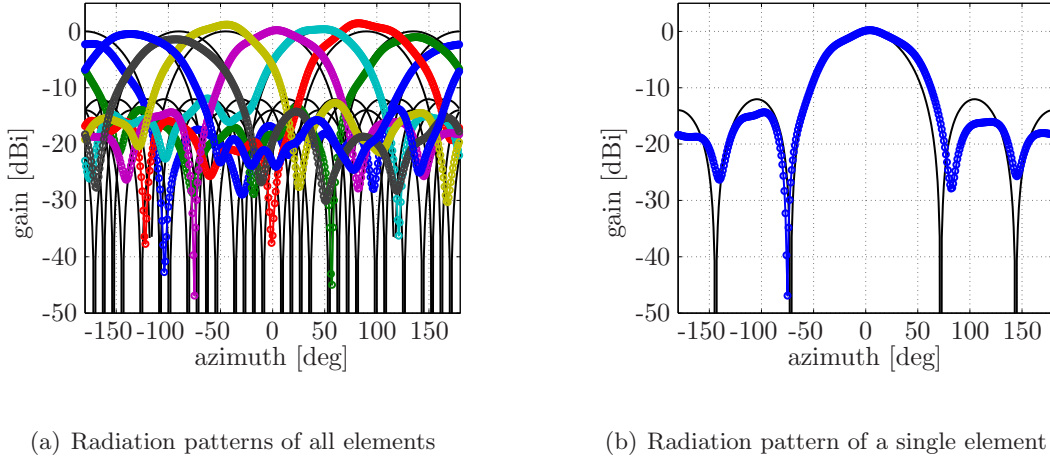
The resulting EADFs are plotted in Fig. 6.2(a). Using this EADF definition the maximum gain



**Fig. 6.2:** EADFs of the theoretical CUBA (a) and the measured CUBAx1x1x8 (b)

(see Fig. 6.3) of each element of the theoretical CUBA is 0 dBi. In order to compare the theoretical and the measured CUBAx1x1x8, the total power over the EADFs of all elements is normalised to

the same value in the theoretical and measured case. In Fig. 6.2(b) the normalised EADFs of the measured **CUBAx1x1x8** are plotted. For the radiation patterns of the measured **CUBAx1x1x8** (Fig. 6.3(b)) it can be seen, that they do not exactly match periodic sinc(.) functions. This discrepancy is related to mutual coupling and the design of the antenna array. Additionally, gain differences up to 3 dB between the elements can be observed. These differences are basically related to the different characteristics of each multiplexing channel of the *practical* array. Based on



**Fig. 6.3:** Comparison of the radiation pattern of the theoretical and measured CUBA (black graphs indicate the theoretical and the coloured graphs the measured radiation patterns)

the previous described framework, an analytic expression for the CRLB of each parameter can also be derived for the theoretical CUBA. To calculate the FIM, the first order derivatives with respect to the parameters azimuth:  $\boldsymbol{\varphi}_1$ :

$$\frac{\partial \mathbf{s}(\boldsymbol{\theta})}{\partial \boldsymbol{\varphi}_1} = \boldsymbol{\gamma}_{v,1} \cdot \mathbf{j} \cdot \boldsymbol{\Gamma}_{\text{CUBA}} \cdot \text{diag}(\boldsymbol{\mu}_\varphi) \cdot \mathbf{d}_\varphi(\boldsymbol{\varphi}_1), \quad (6.15)$$

and the real and imaginary part of the vertical complex path weight:

$$\frac{\partial \mathbf{s}(\boldsymbol{\theta})}{\partial \Re\{\boldsymbol{\gamma}_{v,1}\}} = \boldsymbol{\Gamma}_{\text{CUBA}} \cdot \mathbf{d}_\varphi(\boldsymbol{\varphi}_1) \quad (6.16)$$

$$\frac{\partial \mathbf{s}(\boldsymbol{\theta})}{\partial \Im\{\boldsymbol{\gamma}_{v,1}\}} = \mathbf{j} \cdot \boldsymbol{\Gamma}_{\text{CUBA}} \cdot \mathbf{d}_\varphi(\boldsymbol{\varphi}_1) \quad (6.17)$$

have to be determined. Assuming again i.i.d. Gaussian noise in the real and imaginary part with a standard deviation of  $\boldsymbol{\sigma}$ , a simplified expression for the necessary covariance matrix of  $\boldsymbol{\Gamma}_{\text{CUBA}}$  is:

$$\boldsymbol{\Gamma}_{\text{CUBA}}^H \cdot \boldsymbol{\Gamma}_{\text{CUBA}} = \frac{M_{\text{Rx}}}{L_\varphi^2} \cdot \mathbf{I}_{[L_\varphi \times L_\varphi]}, \quad (6.18)$$

and:

$$(\text{diag}(\boldsymbol{\mu}_\varphi) \cdot \mathbf{d}_\varphi)^H \cdot (\text{diag}(\boldsymbol{\mu}_\varphi) \cdot \mathbf{d}_\varphi) = \frac{1}{12} \cdot L_\varphi^2 \cdot (L_\varphi^2 - 1). \quad (6.19)$$

The **FIM** for the parameters of the single path scenario using the theoretical **CUBA** becomes:

$$\mathbf{J} = \frac{2}{\sigma^2} \begin{bmatrix} \frac{|\gamma_{v,1}|^2 \cdot M_{\text{Rx}} \cdot (L_\phi^2 - 1)}{12} & 0 & 0 \\ 0 & \frac{M_{\text{Rx}}}{L_\phi} & 0 \\ 0 & 0 & \frac{M_{\text{Rx}}}{L_\phi} \end{bmatrix}. \quad (6.20)$$

In this case no cross correlations between the parameters and the **CRLBs** of the parameters are found:

$$\text{CRLB}(\varphi_1) = \frac{\sigma^2}{|\gamma_{v,1}|^2} \frac{6}{M_{\text{Rx}} \cdot (L_\phi^2 - 1)} \quad (6.21)$$

$$\text{CRLB}(\Re\{\gamma_{v,1}\}) = \frac{\sigma^2 \cdot L_\phi}{2M_{\text{Rx}}} \quad (6.22)$$

$$\text{CRLB}(\Im\{\gamma_{v,1}\}) = \frac{\sigma^2 \cdot L_\phi}{2M_{\text{Rx}}}, \quad (6.23)$$

as no mutual coupling between the antenna elements is considered. Calculating the **CRLBs** in case of the measured and the theoretical **CUBA**, the array performance in this scenario can be compared as shown in Fig. 6.4. The same **SNR** of 25 dB is assumed in both cases, defining the **SNR** as the ratio between the signal power  $|\gamma_v|^2$  and the noise power  $\sigma^2$ . In Fig. 6.4(a) it can be seen, that the azimuth standard deviation of the theoretical **CUBA** (red graph) is better compared to the *practical CUBAx1x1x8* (black graphs). Due to the different characteristics of the antenna elements, especially gain differences, the relative variances of the path weights in the real (dotted line) and imaginary part (see Fig. 6.4(b)) of the *practical CUBAx1x1x8* with respect to the azimuth angle are varying about 3 dB.

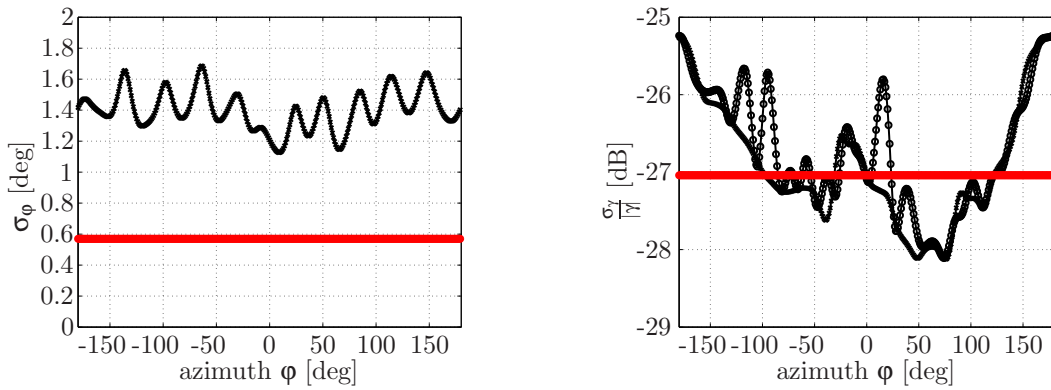
With this simple example, the advantage of the described framework is obvious, since a simulated antenna array never performs exactly like the *practical* antenna array.

Further results comparing the *practical* antenna arrays presented in Section 2.4 by using the proposed **CRLB** based evaluation framework are extensively discussed in Appendix D. The *practical* antenna arrays introduced in Section 2.4 are compared in simple single path and two path scenarios under various conditions.

## 6.2 Verification of the CRLB Based Antenna Array Performance Evaluation Framework

The verification of the described framework will be based on anechoic chamber measurements. Since the **CRLBs** essentially depend on the constellation of the impinging waves, two test scenarios are considered: the most simple *single path scenario* (Section 6.2.1) and the *coherent two path scenario* (Section 6.2.2). As transmit antennas the dual polarised reference horn antennas **PHORN** are applied (same antennas as used for antenna array calibration in Section 4.1). The *practical* antenna array under test at the receive side is the **SPUCPAx2x4x24** (Fig. 2.17).

At one hand, the fundamental limits on the parameter variances in terms of the **CRLBs** are calculated applying the described evaluation framework for both test scenarios. The **EADFs** of the



(a) standard deviation azimuth

(b) relative variances of the path weights

**Fig. 6.4:** Standard deviations of the azimuth angle (a) and relative variances of the path weights in real and imaginary part assuming a SNR of 25 dB of the theoretical (red graphs) and measured (black graphs) CUBA in case of a single path scenario

**SPUCPA<sub>x2x4x24</sub>** used are derived from calibration measurements as described in Chapter 4.

On the other hand, measurements for both test scenarios are performed in an anechoic chamber. For each path constellation (e.g. one path, two path, different **DoAs**) a fixed number of stationary observations is measured. The **DoA** and the complex polarimetric path weights are estimated for each observation with the **RIMAX** parameter estimation algorithm. Now an estimate of the variances of all parameters can be obtained from a fixed number of estimation results.

Finally, the calculated **CRLBs** are compared to the variances, which were empirically calculated from the estimated parameters of the fixed number of measurements in the well defined reference scenarios.

Since the **SPUCPA<sub>x2x4x24</sub>** is applied, the **CRLB** and the empirical variances of the azimuth angles, co-elevation angles, and of the complex polarimetric path weights (separated into real- and imaginary parts) are considered for the calculations. As similar results are found with respect to the different parameters, the following discussions will be limited to the parameter azimuth angle of the incoming waves only. Furthermore, only the case of horizontal excitation of the electrical field at the transmit side is discussed. For notational convenience, the dependence on the polarisation is skipped in the following explanations.

### 6.2.1 Single Path Scenario

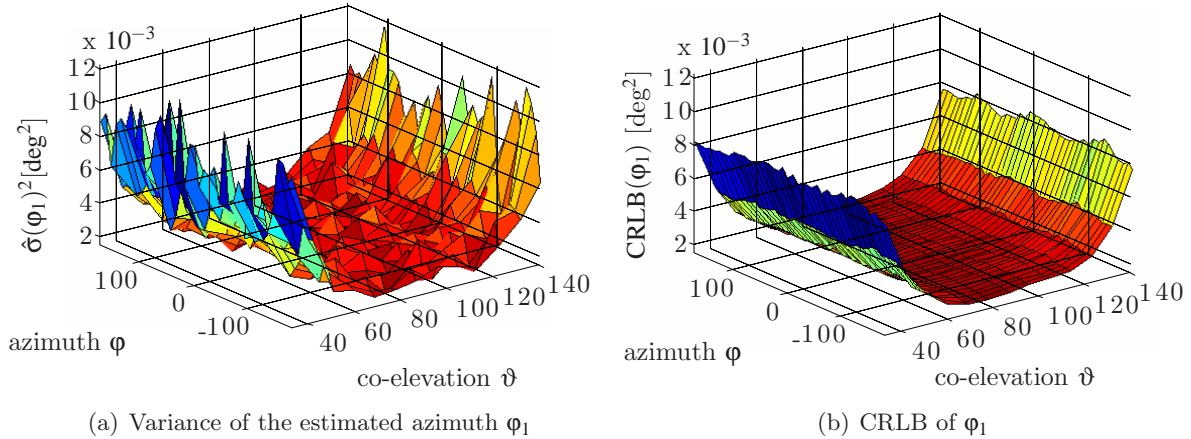
The **CRLB** and the estimated variances of the parameter azimuth for a single path with horizontal polarisation will be compared. That means the scenario is described by one **LoS** path. The direction of the impinging wave of the single path is varied between  $-180^\circ$  and  $180^\circ$  in  $10^\circ$  steps in azimuth, and between  $30^\circ$  and  $140^\circ$  in  $10^\circ$  steps in co-elevation. For the measurements, a fixed number of 64 stationary observations are recorded at each azimuth co-elevation pair. The **SNR** of the measurement was around 17 dB to 18 dB. To compare the **CRLB** with the variances of the estimated parameters, the **CRLB** is calculated for the **SNR** which was estimated from the measurements

(reliable estimate of the measurement SNR is available from RIMAX).

The estimated variance of the azimuth angle  $\varphi_1$  is shown in Fig. 6.5(a) versus the true DoAs in azimuth  $\varphi$  and co-elevation  $\vartheta$ . The CRLB results of the azimuth angle  $\varphi_1$  are depicted in Fig. 6.5(b). It can be seen that the estimated variances of the azimuth angle are similar to the calculated CRLB. Nevertheless, a stronger variation of estimated variances can be observed. This variation is basically related to the limited number of realisations, which are available to estimate the parameter variance. For a better comparison the ratio between the estimate  $\hat{\sigma}(\varphi_1)^2$  and the CRLBs of  $\varphi_1$ :

$$r_q(\varphi_1) = \frac{\hat{\sigma}^2(\varphi_1)}{\text{CRLB}(\varphi_1)} \quad (6.24)$$

are calculated and shown in Fig. 6.6(a). The histogram of this ratio over all available angle pairs are shown in Fig. 6.6(b). The standard deviation of  $r_q$  around its expectation value of one is around 18 %, which in fact matches the theoretically expected value having only 64 realisations for the estimation of the empirical variances  $\hat{\sigma}^2(\varphi_1)$ . This result shows, that the described framework to calculate the CRLB for a *practical* antenna array is valid in case of the simple single path scenario.

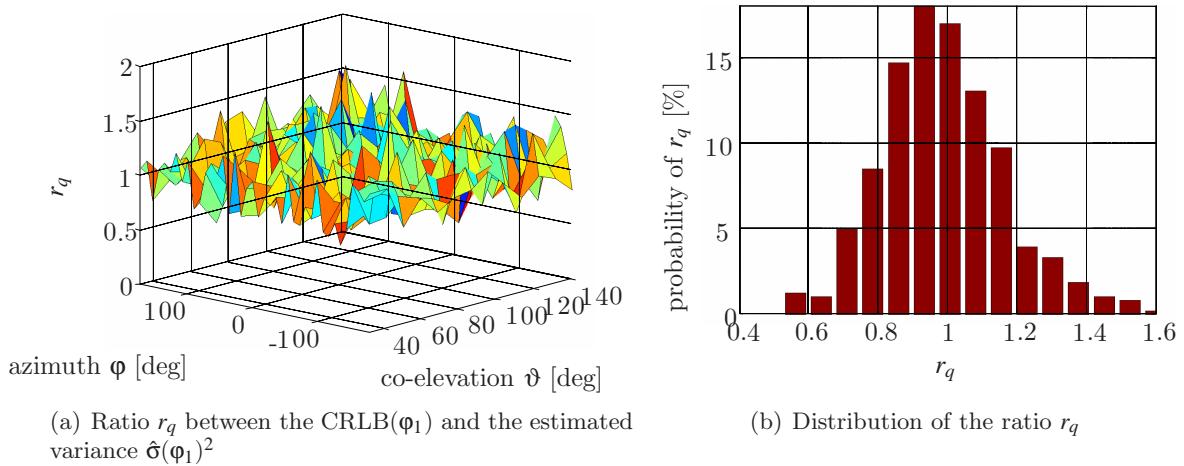


**Fig. 6.5:** Comparison of the variance of the estimated azimuth  $\varphi_1$  (a) with the calculated CRLB of  $\varphi_1$  (b)

### 6.2.2 Coherent two path scenario

The *coherent two path scenario* for the evaluation of *practical* antenna arrays was proposed in [76]. Here, the two paths are said to be coherent if they originate from the same source. Additionally, a more stringent test condition is introduced: the paths are only separated in the angular domain (DoA), whereas both paths have the same delay/path length. The separation of the two paths in the angular domain is smaller than the Rayleigh resolution of the antenna array. Because of the superposition of the two coherent wave-fronts, a static spatial pattern results with regions of constructive and destructive interference. This leads to a higher parameter variance and probably to





**Fig. 6.6:** Ratio  $r_q$  between the estimated variance  $\hat{\sigma}(\varphi_1)^2$  and  $CRLB(\varphi_1)$  dependent on azimuth and co-elevation (a) and the distribution of the ratio  $r_q$  (b)

an ill-posed parameter estimation problem [76]. In [9], it was observed that the resulting degradation depends on the phase difference between the path weights. To investigate worst case and best case path constellations, several fixed phase difference between the complex path weights of the two paths are tested. The fixed phase difference between the complex path weights can be also expressed by a path length difference of the two paths. In the following, the fixed phase difference between the two paths is varied in the range of  $\pm 2\pi$  in  $\frac{\pi}{4}$  steps.

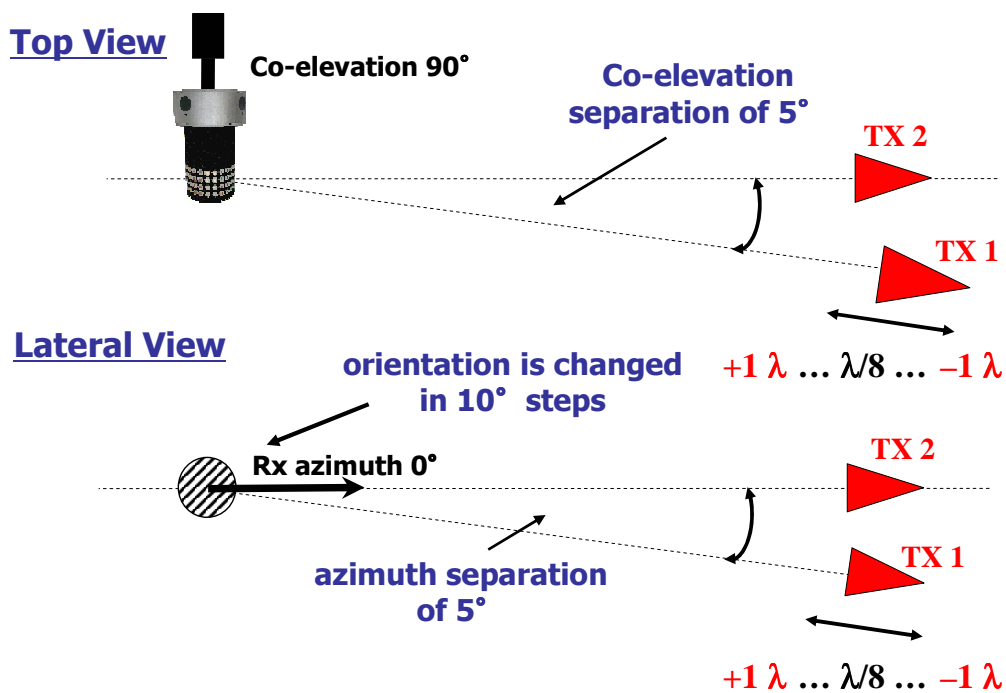
The corresponding measurement setup is shown in Fig. 6.7. The two polarimetric Horn antennas (**PHorn**) at the **Tx** side (Fig. 6.7(c), Fig. 6.7(d)) were first located at the same radial distance  $l = 6$  m to the **SPUCPA<sub>x2x4x24</sub>** (**Rx** Fig. 6.7(b)) and an angular separation in azimuth and co-elevation of  $5^\circ$ . The orientation of the **Rx** array is kept constant in co-elevation with  $\vartheta = 90^\circ$  (top view Fig. 6.7), whereas the orientation in azimuth was changed in  $10^\circ$  steps (lateral view Fig. 6.7).

As aforementioned, the radial distance  $l_1$  of the transmit antenna **Tx1** was changed in steps of  $\frac{\lambda}{8}$  from  $l_1 = l - \lambda$  to  $l_1 = l + \lambda$ , thus introducing a specific phase difference  $\leq 2\pi$  between both paths. Due to the different cables and connectors at the **Tx** side, the transmit power of both sources differed by 3 dB.

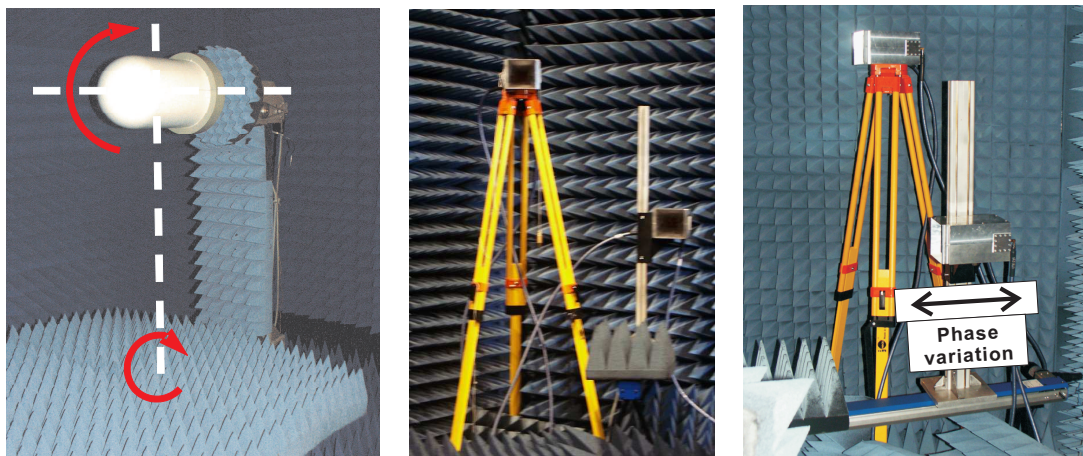
For each azimuth orientation and **Tx1** position 32 stationary observations are measured and the 32 parameter sets azimuth, co-elevation and complex polarimetric path weights of the two paths are estimated. Applying again the estimated **SNR**, the **CRLB** are calculated for exactly the same path constellation as in the measurement.

The results with respect to the parameter azimuth are plotted versus the relative **Tx1** antenna position. Exemplary only the calculated **CRLB** of the azimuth of source 2 is plotted in Fig. 6.8(a), whereas the relation between the estimated variances from the 32 azimuth results and the **CRLB** is shown as the ratio  $r_q(\varphi_2)$  in Fig. 6.8(b). The different colours in Fig. 6.8 indicate the different azimuth orientations of the **Rx** array **SPUCPA<sub>x2x4x24</sub>**.

The fixed phase difference (with its corresponding **Tx1** position) between the two complex path



(a) Measurement setup schematic

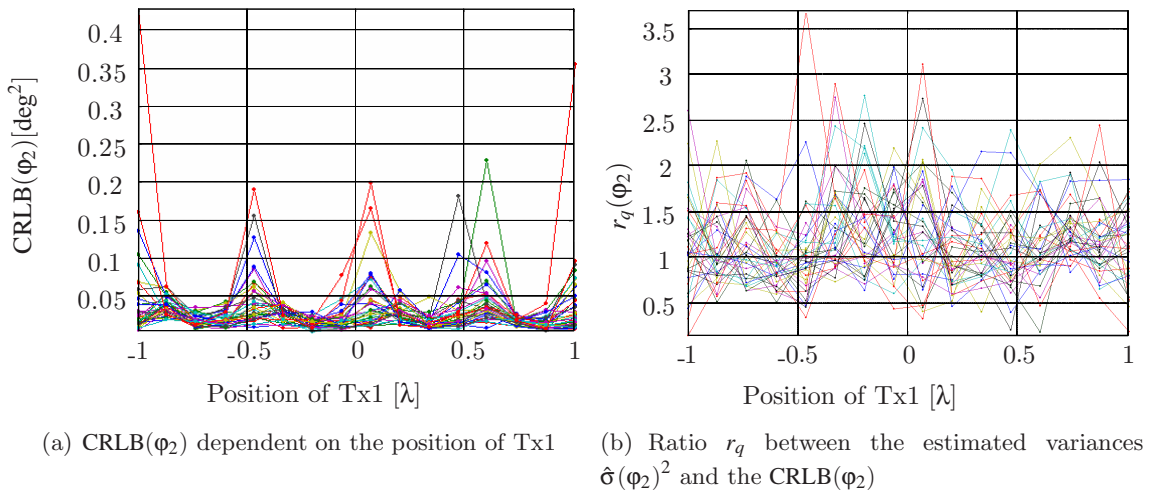


(b) Receive antenna SPUC-PA<sub>x2x4x24</sub> (c) Transmit antennas front view (d) Transmit antennas lateral view

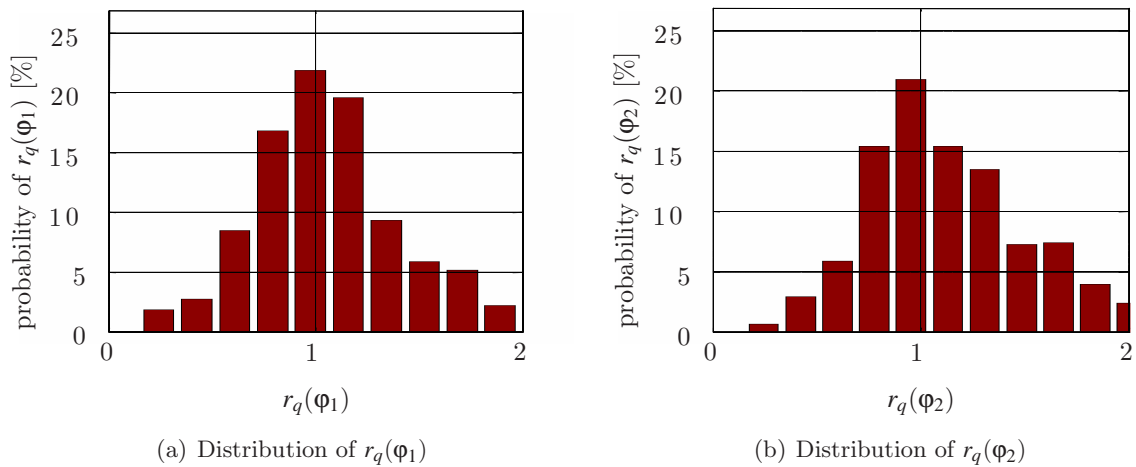
Fig. 6.7: Coherent two path scenario measurement setup

weights leads to different superposition of the two wave fronts. In case of constructive or destructive superposition the **CRLB** of the azimuth (Fig. 6.8(a)) is maximal. For phase differences of  $90^\circ$  and  $270^\circ$ , radial distance differences of  $\frac{\lambda}{4}$  and  $\frac{3\lambda}{4}$  respectively, the path weights are orthogonal and consequently the correlation between the two paths is minimal. The parameter variances by means of the **CRLB** reaches the minimum (Fig. 6.8(a)). As the element characteristics of the antennas of a *practical* array are never the same, the **Rx** array behaves not homogeneous for all azimuth orientations (indicated by colour).

From the ratio  $r_q$  (see eqn. 6.24) between the estimated variances and the **CRLB** in Fig.6.8(b) it can be again concluded that the proposed evaluation framework is reliable to calculate the **CRLB** of a *practical* antenna array. The expectation value of the ratio is again one. Its variance is related to the limited number of available observations to estimate the variance. The distributions of the ratio  $r_q$  are shown for the azimuth angle of both sources in Fig. 6.9.



**Fig. 6.8:** CRLB( $\varphi_2$ ) dependent on the position of Tx1 (a), Ratio  $r_q(\varphi_2)$  between the estimated variances from 32 observations  $\hat{\sigma}(\varphi_2)^2$  and the CRLB( $\varphi_2$ ) (b)



**Fig. 6.9:** Distribution of the ratios  $r_q$  with respect to  $\varphi_1$  (a) and  $\varphi_2$  (b)

### 6.3 Conclusion Chapter 6

In this chapter a new performance evaluation framework for *practical* antenna arrays was proposed. The framework is based on the derivation of the Cramer-Rao lower bounds of the path parameters in arbitrary test scenarios using measured or simulated antenna characteristics. Section 6.2 verifies the proposed antenna array evaluation framework by comparing the CRLB and the estimated variances derived from measurements. The results of the *single path scenario* and the *coherent two path scenario* clearly indicate the reliability of the calculated CRLB for an exemplary *practical* antenna array. Since the proposed method relies on antenna radiation pattern measurements or simulations, it can be easily applied to any antenna array. Consequently, the described framework is designed specifically for the performance evaluation of antenna arrays. Additionally, the time consuming and expensive test measurements, such as the *coherent two path scenario* or even more complicated test scenarios become unnecessary.

Since the method shows performance limits of *high-resolution DoA* estimation, the method can further be used to choose the appropriate antenna arrays for a measurement campaign. In this context the *practical* antenna arrays introduced in Section 2.4 are compared under various test conditions in Appendix D. The results are of interest especially when planning measurements and for the analysis of measurements applying *high-resolution* parameter estimation algorithms.

---

## 7. CONSEQUENCES OF MODELLING ERRORS IN CHANNEL PARAMETER ESTIMATION

Despite the popularity of the use of *high-resolution* parameter estimation for channel characterisation and modelling purposes, the influence of the system and antenna data model on the robustness and accuracy of the estimation has been often neglected. In the previous chapter, the performance of *practical* antenna arrays has been shown under the assumption that the data model perfectly matches reality. However, such an assumption is not realistic, i.e., a certain model mismatch is always present.

This chapter addresses that the use of an inaccurate data model inherently will result in biased and/or artificially spread angular estimates. For some antenna array types, estimation bias is even unavoidable, no matter what data model is chosen. It is conceivable that the popular approach of clustering multi-paths components [67, 70, 71] for channel modelling is spurred by the artefacts resulting from data model choices as described in this chapter.

The topic is dealt in two parts, antenna array related model mismatch in Section 7.2 ([18, 32]) and system related consequences in Section 7.3. For convenience, the proprietary parameter estimator **RIMAX** is used to demonstrate the consequences of the different error sources. Notice that this choice does not compromise the generality of the outcomes. In fact, any **ML** parameter estimator using the same data models would render similar results. Mainly *practical* antenna arrays, commonly used in channel measurements, are applied for demonstration. Therefore, most of the results are based on empirical analysis. However, analytic expressions are derived whenever it is possible to generalise the consequences on the parameter estimation results.

Please note that this chapter contains very detailed descriptions and analysis of various error sources, however it should be mentioned that each single source of error can lead to misinterpretations of the channel characteristic if not carefully considered planning propagation measurements.

### 7.1 Analysis Procedure and Definition of Basic Parameters Used in this Chapter

Throughout the following sections the same analysis procedure will be applied to show the consequence of the different error sources on the parameter estimation results. For classification of the own contributions, in each section a literature survey is carried out. To support further understanding, measurement and/or simulation examples will be used to investigate the consequence of each error source. The consequences of using an inaccurate data model on the parameter estimation results are demonstrated for the excitation with a single path. The direction of the incoming

---

wave is varied over the full  $4\pi$  solid angle. Based on the single path excitation the error analysis is performed in two steps:

- the single path estimation to determine the mean model accuracy of the inaccurate model,
- the estimation of a maximum number of  $K_{\max} = 10$  paths, where the 9 or even 10 paths can be wrong or so called artefacts.

First, the mean accuracy of the model used will be determined. Therefore, let  $K_{\max}$  the maximum number of paths to be estimated with the inaccurate data model be equal to one. The Signal to Remainder Ratio (SRR) eqn. (7.1) defined as the ratio between the power of the estimated specular path/paths and the remaining signal power after subtraction of the estimated specular path/paths from the measured data  $\mathbf{x}$  will be used. For the excitation with a single path and the estimation of  $K_{\max} = 1$  path, the SRR can be interpreted as the mean model accuracy of the inaccurate data model.

$$\text{SRR} = 10 \cdot \lg \left( \frac{\|\mathbf{s}(\hat{\theta}_{\text{SC}})\|_{\text{F}}}{\|\mathbf{x} - \mathbf{s}(\hat{\theta}_{\text{SC}})\|_{\text{F}} - \mathbf{M}_{\text{RX}} \cdot \mathbf{M}_{\text{TX}} \cdot \mathbf{M}_{\text{F}} \cdot \mathbf{M}_{\text{T}} \cdot \alpha_0} \right) \quad (7.1)$$

Second, an analysis is performed to show the impact of inaccurate data models on the parameter estimation results under “real world” conditions when the a priori knowledge of the number of “true paths” is unknown. The estimation algorithm can not differentiate between signal power that is related to a “true path” and the signal power that remains due to the usage of the inaccurate data model. This means for the current analysis and the single path excitation, as long as the remaining observation after the estimation of the first path:

$$\tilde{\mathbf{x}} = \mathbf{x} - \mathbf{s}(\hat{\theta}_{k=1}) \quad (7.2)$$

contains spatial information additional but wrong paths will be estimated. The maximum number of paths to estimate is set to  $K_{\max} = 10$ , even though the array was still excited with a single path. The maximum number of 9 additional paths to estimate assures in most cases that the remaining spatial information can be extracted from  $\tilde{\mathbf{x}}$ . The angular power distribution of these paths is physically meaningless and can lead to a wrong interpretation of the channel characteristics. The estimated power distributions will be shown versus the estimated centred azimuth/co-elevation and the co-elevation of the true path. The centred azimuth  $\varphi_{\text{c}}$  and co-elevation  $\vartheta_{\text{c}}$  are defined as the difference between the estimated angles  $\hat{\varphi}$ ,  $\hat{\vartheta}$  and the angles of the single “true path”  $\varphi_k$ ,  $\vartheta_k$ .

$$\begin{aligned} \varphi_{\text{c}} &= \hat{\varphi} - \varphi_k \\ \vartheta_{\text{c}} &= \hat{\vartheta} - \vartheta_k \end{aligned} \quad (7.3)$$

The centred azimuth/co-elevation can be also interpreted as angular deviation from the angles of the true path. Correct estimations correspond to  $\varphi_{\text{c}}$  and  $\vartheta_{\text{c}}$  equal to zero. Only for circular arrays, the estimated power distributions around the centred azimuth for different azimuth directions of the “true path” are averaged, which results in a single mean distribution. This is reasonable as the

---

circular arrays discussed show an almost uniform performance in the azimuth direction.

In some sections the parameter “relative power” of a path weight will be used for further discussions. This parameter describes the deviation of the estimated path weight from the path weight of the true path and is consequently defined as the power ratio between the power of the estimated path weight  $\hat{\gamma}_{k,xy}$  and the power of the true path weight  $\gamma_{k,xy}$ :

$$p_{k,xy} = \frac{|\hat{\gamma}_{k,xy}|^2}{|\gamma_{k,xy}|^2}. \quad (7.4)$$

## 7.2 Antenna Array Related Model Mismatch

There are plenty of publications dealing with estimation results from measurement campaigns employing various kinds of antenna arrays. However, in the processing chain from the calibration measurement of the antenna array to the array data model, which is finally used for estimation, several artificial assumptions are made. In most cases, the resulting systematic error of these assumptions is unknown, not discussed, or just neglected. This section addresses the whole processing chain; the consequence of the accuracy of the array calibration (Section 7.2.1) and the systematic error due to the usage of incomplete data models (Section 7.2.2) will be discussed.

### 7.2.1 Systematic Error Related to the Quality of the Calibration Measurement and to the Narrow Band Model

Concerning the impact of “calibration errors” on parameter estimation several publications can be found. However, one needs to be careful in which context the term “calibration error” is used. The discussion is often related to effects such as mutual coupling, antenna element position error, gain and phase errors [74, 76, 111–115]. The term “calibration error” is actually misused, as the mentioned effects are related to model mismatch. Only the discrepancy between the *practical* antenna array and the array data model used for parameter estimation and the consequence on the parameter estimation results are described. The **EADF** array data model described in Section 3.3 is able to model such antenna array properties. Therefore, these so called “calibration errors” or “imperfections of the antenna array” are not considered as model error in this thesis.

The accuracy of the narrow band antenna array data model (eqn. (4.6)), which is derived from the calibration measurements, will be discussed. The accuracy of the derived narrow band radiation patterns is limited by the quality of the anechoic chamber including the positioning system and the validity of the assumption of a frequency independent antenna characteristic. In Chapter 4 it is described, how to calibrate an antenna array and how to estimate the **EADF** array data model from this calibration data. However, two assumptions were made while deriving the data model. First, only the direct path between the reference horn antenna and the array to calibrate is assumed in the anechoic chamber. This means possible spurious reflections are neglected. Second, it is assumed that the array response is frequency independent. Both assumptions are only valid to some extent.

The first assumption is valid up to a certain accuracy, which depends on the properties of the



absorbing material used in the anechoic chamber and at the positioning system. For frequencies between 4 GHz and 6 GHz the reflection coefficients are between  $-10$  dB and  $-40$  dB dependent on the angle of the incoming wave and the height of the cones of the absorbing material [116]. In most cases the cones of the absorbing material in the anechoic chamber (Type I) are larger and have consequently better absorbing properties than the absorbers that cover the positioning system (Type II and Type III). Especially at the edges and intersections of the positioning system the incoming wave is reflected or diffracted and not totally absorbed. In Fig. 7.1 and Fig. 7.2, schematics of the anechoic chamber are drawn for the lateral and top view respectively. Possible parasitic reflections are drawn in the two schematics. The different types of absorbing material are specified with their reflection coefficients. Mainly the parasitic reflections at the circular absorber at the upper part of the positioning system will distort the measurement results. Unfortunately the effect of the parasitic reflections is dependent on the alignment of the positioning system. This means the angle of the incoming wave defines how much energy of the scattered wave is received from the antenna under test. Note that also the direction of the polarisation vector changes as a result of scattering. The narrow band model of the antenna arrays used are derived from impulse responses obtained from the Fourier transform of calibration measurements with a bandwidth of 120 MHz. Thus, the resulting Rayleigh resolution of the impulse response is around 8.3 ns, which corresponds to a distance of 2.5 m in free space. Consequently, the calculated radiation patterns, using eqn. (4.6), include all received parasitic reflections from the positioning system in a radius of 1.25 m.

The second assumption, a constant frequency characteristic of the antenna, which is a presumption when deriving the narrow band model, is for *practical* arrays not always valid. For example in case of the antenna arrays used, a variation of  $\pm 1.5$  dB to  $\pm 3$  dB in the band of 120 MHz was specified during the antenna design step. However, since the antenna elements are frequency dependent, the resulting model accuracy of the narrow band model is affected. Only if the antenna characteristic is constant in the considered frequency range, eqn. (4.6) leads to a constructive superposition of the desired signal energy. This is equivalent to a concentration of all signal energy in one delay bin of the impulse response after applying the Fourier transformation to the measured frequency response. In case of a frequency dependent antenna characteristic, not the total desired signal energy can be modeled with eqn. (4.6), which means that the desired signal energy is distributed in more than one delay bin.

In Section 7.2.1.1 the accuracy of the narrow band model for a single antenna is defined as a function of azimuth and co-elevation. It will be seen that the achievable accuracy is often lower than the available signal to noise ratio  $\text{SNR}_{\text{IR}}$  in the impulse response (see also Section 2.3.3). As shown in Section 3.4, for signal processing and parameter estimation the efficient antenna array data model EADF is preferable. The consequence of parasitic reflections and “radiation pattern gating” due to the positioning system on the derived EADFs will be discussed in Section 7.2.1.2. For demonstration, verification measurements using the vertical monopole antenna (OMNI see Fig. 2.15) as a reference antenna are performed. As the proposed verification measurements are inappropriate for *practical* antenna arrays (related to the antenna array mounting at the positioning system), a simplified scattering model of the positioning system is introduced in Section 7.2.1.3.

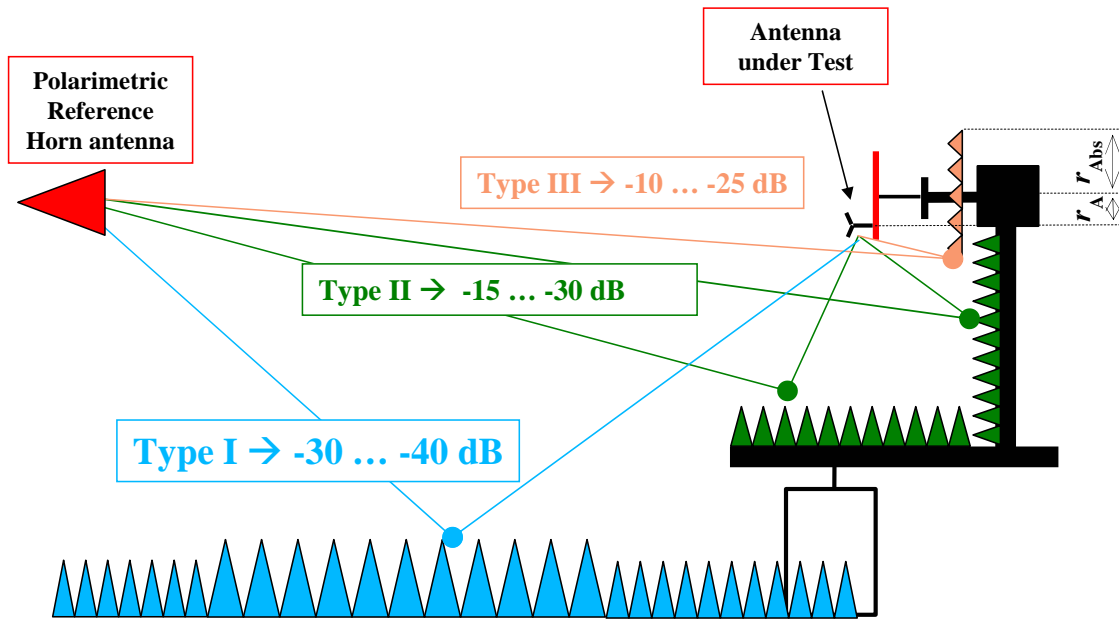


With this simplified scattering model radiation patterns and their EADFs are obtained that are distorted/imperfect due to the parasitic reflections.

**Definition 7.2.1.** The term *distorted* will be used for models that are affected by model error.

**Definition 7.2.2.** The term *undistorted* will be used for error free models.

The artificially distorted EADFs of the simulated PUCPASIMx2x1x24 are compared with the EADFs obtained from calibration measurements of the *practical* antenna array PUCPAx2x1x24. Using the artificially/measured distorted EADFs for parameter estimation will lead to estimation of artefacts. This and a EADF based method to reduce the consequences of distorted EADFs on parameter estimation are finally shown in Section 7.2.1.4.

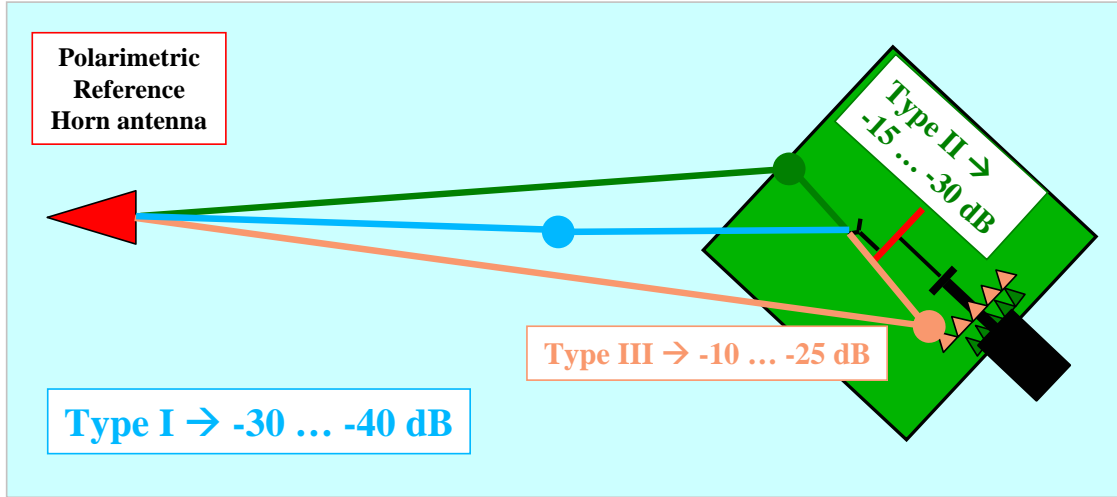


**Fig. 7.1:** Parasitic reflections and the corresponding reflection coefficients of different types of absorbing material in the anechoic chamber (Lateral View,  $\vartheta_{\text{LoS}} = 90^\circ$ )

### 7.2.1.1 Accuracy of the Narrow Band Model derived from Anechoic Chamber Measurements (Angular Domain)

The model accuracy of the narrow band model derived from anechoic chamber measurements can be defined as the closeness between the “true” frequency dependent antenna characteristic and the derived narrow band model. To support the understanding let us define a model of the calibration measurement, which considers the frequency dependence of the antenna and the parasitic reflections  $k = 1 \dots K$  in the anechoic chamber and at the positioning system. The vector valued measured frequency response for the desired excitation  $q$  and angles  $\varphi_{\text{LoS}}$ ,  $\vartheta_{\text{LoS}}$  of the  $m^{\text{th}}$  antenna with:

$$\mu = \left[ \frac{-(M_f-1)}{2} \quad \dots \quad \frac{(M_f-1)}{2} \right] \quad (7.5)$$



**Fig. 7.2:** Parasitic reflections and the corresponding reflection coefficients of different types of absorbing material in the anechoic chamber (Top View,  $\vartheta_{\text{LoS}} = 45^\circ$ )

is given by:

$$\begin{aligned}
 \mathbf{y}_f(\boldsymbol{\varphi}_{\text{LoS}}, \vartheta_{\text{LoS}}, q, m) &= \gamma_{qq, \text{LoS}} \cdot \mathbf{b}(\boldsymbol{\varphi}_{\text{LoS}}, \vartheta_{\text{LoS}}, q, m) \cdot \left( \mathbf{b}_f(\boldsymbol{\varphi}_{\text{LoS}}, \vartheta_{\text{LoS}}, q, m) \circ e^{-j2\pi\tau'_{\text{LoS}}\mu^T} \right) \\
 &+ \sum_{k=1}^K \gamma_{qh, k} \cdot \mathbf{b}(\boldsymbol{\varphi}_k, \vartheta_k, q = h, m) \cdot \left( \mathbf{b}_f(\boldsymbol{\varphi}_k, \vartheta_k, q = h, m) \circ e^{-j2\pi\tau'_k\mu^T} \right) \\
 &+ \sum_{k=1}^K \gamma_{qv, k} \cdot \mathbf{b}(\boldsymbol{\varphi}_k, \vartheta_k, q = v, m) \cdot \left( \mathbf{b}_f(\boldsymbol{\varphi}_k, \vartheta_k, q = v, m) \circ e^{-j2\pi\tau'_k\mu^T} \right) \cdot \\
 &+ \mathbf{n} \\
 &= \mathbf{y}_{f, \text{LoS}} + \mathbf{y}_{f, h} + \mathbf{y}_{f, v} + \mathbf{n}
 \end{aligned} \tag{7.6}$$

$\tau'_{\text{LoS}}$  being the normalised delay between the **Tx** reference horn antenna and the antenna under test,  $\gamma_{qq, \text{LoS}}$  is the path weight corresponding to the free space attenuation and  $\mathbf{b}_f(\boldsymbol{\varphi}, \vartheta, q, m)$  is a vector valued function expressing the frequency dependence of the antenna. In case of a frequency independent antenna, the vector  $\mathbf{b}_f(\boldsymbol{\varphi}, \vartheta, q, m)$  is filled with ones. The first term of eqn. (7.6)  $\mathbf{y}_{f, \text{LoS}}$  corresponds to the desired antenna response. The second  $\mathbf{y}_{f, h}$  and third term  $\mathbf{y}_{f, v}$  correspond to the horizontal and vertical responses of the  $K$  parasitic reflections respectively. The number of paths  $K$  depends on the direction  $\boldsymbol{\varphi}_{\text{LoS}}, \vartheta_{\text{LoS}}$ , this dependence is skipped for notational convenience in all equations. The fourth term, the measurement noise vector  $\mathbf{n}$  contains **i.i.d.** Gaussian noise (see eqn. (E.3)). Note that the frequency characteristic of the measurement system and the Tx reference horn antenna is already eliminated from  $\mathbf{y}_f$ .

To determine the model accuracy for a certain direction  $\boldsymbol{\varphi}_{\text{LoS}}, \vartheta_{\text{LoS}}$ , excitation  $q$  and antenna  $m$ , the strongest path is estimated from the vector  $\mathbf{y}_f$ :

$$\hat{\mathbf{y}}_{f, \text{LoS}} = \hat{\gamma}_{\text{LoS}} \cdot e^{-j2\pi\hat{\tau}'_{\text{LoS}}\mu^T}. \tag{7.7}$$

Here, the narrow band model with a frequency independent  $\hat{\gamma}_{\text{LoS}}$  is assumed. The error of the narrow band model  $\mathbf{y}_{f, E}$  is now defined as the difference between the measured data  $\mathbf{y}_f$  and the

frequency response of the estimated path  $\hat{\mathbf{y}}_{f,\text{LoS}}$ :

$$\begin{aligned} \mathbf{y}_{f,E}(\varphi_{\text{LoS}}, \vartheta_{\text{LoS}}, q, m) &= \underbrace{(\mathbf{y}_{f,\text{LoS}} - \hat{\mathbf{y}}_{f,\text{LoS}})}_{\mathbf{y}_{f,\text{EFreq}}} + \underbrace{(\mathbf{y}_{f,h} + \mathbf{y}_{f,v})}_{\mathbf{y}_{f,\text{ERef}}} + \mathbf{n} \\ &= \mathbf{y}_{f,\text{EFreq}} + \mathbf{y}_{f,\text{ERef}} + \mathbf{n} \end{aligned} \quad (7.8)$$

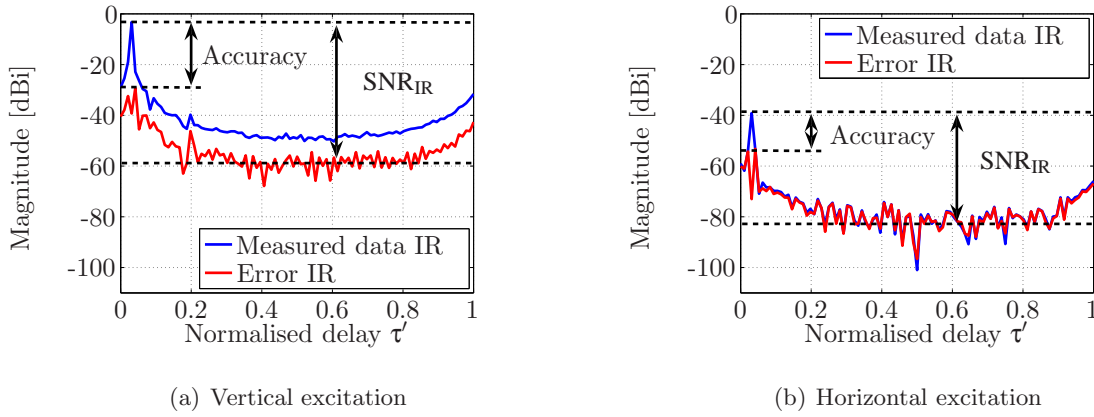
It is obvious that the error due to a frequency dependent antenna characteristic  $\mathbf{y}_{f,\text{EFreq}}$  and the error due to the parasitic reflections  $\mathbf{y}_{f,\text{ERef}}$  can not be separated. Only in case of a frequency independent antenna characteristic it would be possible to estimate a maximum number of  $K < 2 \cdot M_f$  additional paths to differentiate between the desired frequency response of the antenna and the parasitic reflections. If both effects are similar the total number of unknown parameters to estimate with  $N_{\text{unknown}} = (3 + 2 \cdot M_f) + (3 \cdot K + 2 \cdot K \cdot M_f)$  is by far larger than the number of available measurement points with  $N_{\text{known}} = 2 \cdot M_f$ . The number of calculated unknowns is related to a direction and polarisation dependent frequency dependence of the antenna. In Fig. 7.3 the normalised impulse responses of the measurement:

$$\mathbf{y}_d(\varphi_{\text{LoS}}, \vartheta_{\text{LoS}}, q, m) = \frac{\mathbf{F} \cdot \mathbf{y}_f(\varphi_{\text{LoS}}, \vartheta_{\text{LoS}}, q, m)}{\gamma_{qq,\text{LoS}}} \quad (7.9)$$

and the error impulse responses:

$$\mathbf{y}_{d,E}(\varphi_{\text{LoS}}, \vartheta_{\text{LoS}}, q, m) = \frac{\mathbf{F} \cdot \mathbf{y}_{f,E}(\varphi_{\text{LoS}}, \vartheta_{\text{LoS}}, q, m)}{\gamma_{qq,\text{LoS}}} \quad (7.10)$$

are shown for a single antenna element of the UCAx1x16 for vertical Fig. 7.3(a) and horizontal Fig. 7.3(b) excitation. The preferred polarisation of the this antenna element and for the chosen direction ( $\varphi_{\text{LoS}} = 0^\circ, \vartheta_{\text{LoS}} = 90^\circ$ ) is vertical, which can be seen by observing the peak levels of the corresponding impulse responses for both excitations. The noise floor (related to  $\mathbf{n}$ ) for vertical and horizontal excitation may vary because of the AGC, which adds attenuation depending on the input power at the receiver and thus changes the noise figure (see Section 2.3.3). For both polarisation excitations, the achievable  $\text{SNR}_{\text{IR}} \approx 40..50\text{dB}$  is larger than the achievable narrow band model accuracy. By visual inspection, the model accuracy can be seen as the power ratio between the peak power of the impulse response of the measured data and the peak power of the error impulse response (eqn. (7.10)). If the gap between the power of the parasitic reflections and the power of the measured impulse response is decreasing, the model accuracy decreases as well. As a visual inspection of the model accuracy is not feasible, let us define the model accuracy based on the IR of the measured data. Here, the following consideration is made: in case of a frequency independent antenna characteristic and a “totally echo free” anechoic chamber all signal energy is concentrated at the normalised delay  $\tau'$  in the impulse response. This delay is related to the distance between the Tx and Rx antenna. As  $\mathbf{y}_f$  is band limited and has a constant magnitude, the resulting impulse response  $\mathbf{y}_d$  can be expected as a sampled  $\text{sinc}(\cdot)$  function. The maximum of the  $\text{sinc}(\cdot)$  function is located at  $\tau'$ . If the delay of the strongest path  $\hat{\tau}'$  coincides with a multiple of the distance between two bins in the delay domain  $\Delta\tau' = \frac{1}{M_f - 1}$ , then all other delay bins are located at the zeros of the  $\text{sinc}(\cdot)$  function. Consequently, these samples should be related to the measurement noise only. In most cases  $\hat{\tau}'$  does not coincidence with a multiple of the distance  $\Delta\tau'$ . To differentiate between



**Fig. 7.3:** IR of the measured data  $\mathbf{y}_d(\varphi_{\text{LoS}}, \vartheta_{\text{LoS}}, q, m)$  and error IR  $\mathbf{y}_{d,E}(\varphi_{\text{LoS}}, \vartheta_{\text{LoS}}, q, m)$  for vertical (a) and horizontal excitation (b) of one antenna element of the UCAx1x1x16 with vertical preferred polarisation

signal energy due to the convolution with the  $\text{sinc}(\cdot)$  function and signal energy due to parasitic reflections or a frequency dependent antenna, the impulse response of the measured data will be shifted about  $-\hat{\tau}'$ . This corresponds to the following frequency domain operation:

$$\mathbf{y}_{f,\text{Shift}} = \mathbf{y}_f \circ e^{j2\pi\hat{\tau}'_{\text{LoS}}\mu^T}. \quad (7.11)$$

In consequence, the desired signal energy will be concentrated in the first delay bin of:

$$\mathbf{y}_{d,\text{Shift}} = \mathbf{F} \cdot \mathbf{y}_{f,\text{Shift}}. \quad (7.12)$$

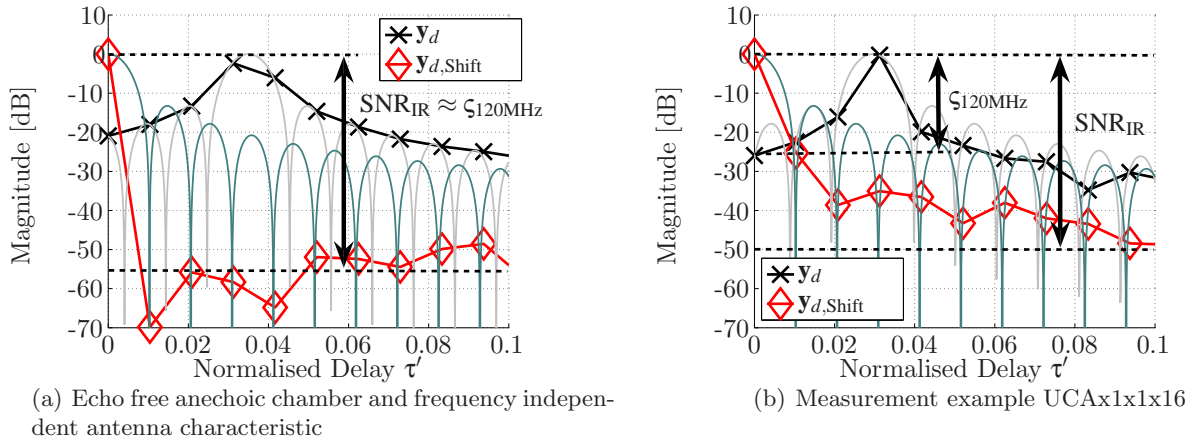
Parasitic reflections in the anechoic chamber and/or a frequency dependent antenna will lead to a signal energy especially in the second delay bin. Thus the signal energy of the second delay bin is larger than the mean noise energy. In case of parasitic reflections, most of the signal energy in the second delay bin is related to the reflections at the positioning system in a radius of 1.25 m in case of 120 MHz bandwidth. Based on the previous discussion let us define the model accuracy  $\zeta_B$  as the energy ratio between the energy of the first delay bin  $|\mathbf{y}_{d,\text{ShiftLoS}}(\tau' = 0)|^2$  and the energy of the second delay bin  $|\mathbf{y}_{d,\text{ShiftLoS}}(\tau' = \Delta\tau')|^2$ :

$$\zeta_B = \frac{|\mathbf{y}_{d,\text{Shift}}(\tau' = 0)|^2}{|\mathbf{y}_{d,\text{Shift}}(\tau' = \Delta\tau')|^2} \quad (7.13)$$

where  $B$  corresponds to the total bandwidth used.

To illustrate the previous discussion in Fig. 7.4(a) both the normalised impulse response  $\mathbf{y}_d$  and its shifted version  $\mathbf{y}_{d,\text{Shift}}$  is shown in case of a frequency independent Rx antenna and an echo free anechoic chamber for a  $\text{SNR}_{\text{IR}} \approx 50$  dB. With the fine gray lines the corresponding  $\text{sinc}(\cdot)$  function are indicated. It can be seen that in case of the shifted version, the  $\text{sinc}(\cdot)$  function is sampled at its zeros. Consequently, the  $\text{SNR}_{\text{IR}}$  can be directly derived from this shifted version. In this ideal case (no parasitic reflections and frequency independent antenna) the  $\text{SNR}_{\text{IR}}$  matches the model accuracy  $\zeta_{120\text{MHz}}$ . Based on the original version  $\mathbf{y}_d$  it would be impossible to differentiate between the impact

of the window function, the parasitic reflections and the impact of a varying antenna frequency response. In Fig. 7.4(b) the result of a measurement example using the UCAX1x1x16 is shown. In this case the achievable model accuracy  $\zeta_{120\text{MHz}}$  is lower than the maximum available  $\text{SNR}_{\text{IR}}$ . As already described, this discrepancy is related to the imperfections of the anechoic chamber and the frequency dependence of the antenna.



**Fig. 7.4:** Illustration of the parameter model accuracy  $\zeta_{120\text{MHz}}$  in case of an ideal antenna and anechoic chamber (a) and a measurement example using the UCAX1x1x16 (b)

**Narrow Band Model Accuracy of Some Example Arrays:** In the following the model accuracy will be analysed for one antenna element of the UCAX1x1x16 and for two different antenna elements with vertical and horizontal preferred polarisation of the PULPAx2x1x8 respectively (see Fig. 7.5). For the co-polarised excitation Fig. 7.5(b), Fig. 7.5(c) and Fig. 7.5(f), the model accuracy is for the majority of directions at least 25 dB or better. Exceptions are the directions where the zeros of the radiation patterns are located. At the zeros the achievable accuracy is limited due to the parasitic reflections and frequency dependence of the antenna. Unfortunately the parasitic reflections and the frequency dependent antenna have the largest impact for the directions that are close to the zeros of the radiation patterns.

As the antenna elements of the UCAX1x1x16 have a XPD around 0 dB for most directions, also the model accuracy for the cross-polarised radiation pattern Fig. 7.5(a) is as high as for co-polarised radiation pattern Fig. 7.5(b).

For the cross-polarised radiation patterns (Fig. 7.5(c), Fig. 7.5(d)) of the PULPAx2x1x8, the model accuracy is for most directions very low with 5 dB to 15 dB. This behaviour is related to a large XPD of these patch antennas. The desired signal energy is almost equal to the signal energy of the parasitic reflections at the positioning system. There are grounds for the assumption that most of the energy of the parasitic reflections is related to the reflections in which case the direction of the polarisation has changed during the scattering at the positioning system.

As seen from the previous discussion, the model accuracy is a very specific parameter of antenna, which is strongly dependent on the direction of the incoming wave and the polarisation excitation.

Generalisation in terms of the model accuracy with respect to different types of antenna arrays can not be made, as the influence of the positioning system in terms of the parasitic reflections is different for every antenna array and its elements. However, the achievable model accuracy for the positioning system and antenna arrays used in this thesis are in average not better than 25 dB to 30 dB. In Table 7.1 the mean model accuracy  $\bar{\zeta}_{120\text{MHz}}$  over all directions and elements dependent on the four different polarisation combinations are summarized for a set of selected antenna arrays. The model accuracy of the *practical* arrays are affected by the frequency dependence of the antenna elements and the parasitic reflections. In case of the simulated antenna array PUCPAx2x1x24 the model accuracy is only affected by the frequency dependence of the antenna. As already observed in Fig. 7.5, the mean model accuracy of the cross-polarised elements are smaller than in case of the co-polarised elements. The only exception is the UCAx1x1x16 with an almost equal model accuracy for cross- and co-polarised elements due to the low XPD of the elements. If the circular absorber of the positioning system (see Fig. 7.1 and Fig. 7.2) are not in the viewshed of the antenna elements, then the achievable mean model accuracy is better than for the other arrays. This is especially the case for the PULPAx2x1x8, as its elements were eccentric positioned on a radius  $r_A$  larger than the radius  $r_{\text{Abs}}$  of the circular absorber. As the positioning radius  $r_A$  of the elements in case of the circular antenna arrays used is smaller, the model accuracy is worse due to the stronger impact of the parasitic reflections at the circular absorber at the upper part of the positioning system.

An additional but very important conclusion of this section is, that even a frequency dependent antenna model will not improve the model accuracy as long as the parasitic reflections at the positioning system can not be avoided, reduced (smaller than the effect of the frequency dependence), or exactly determined.

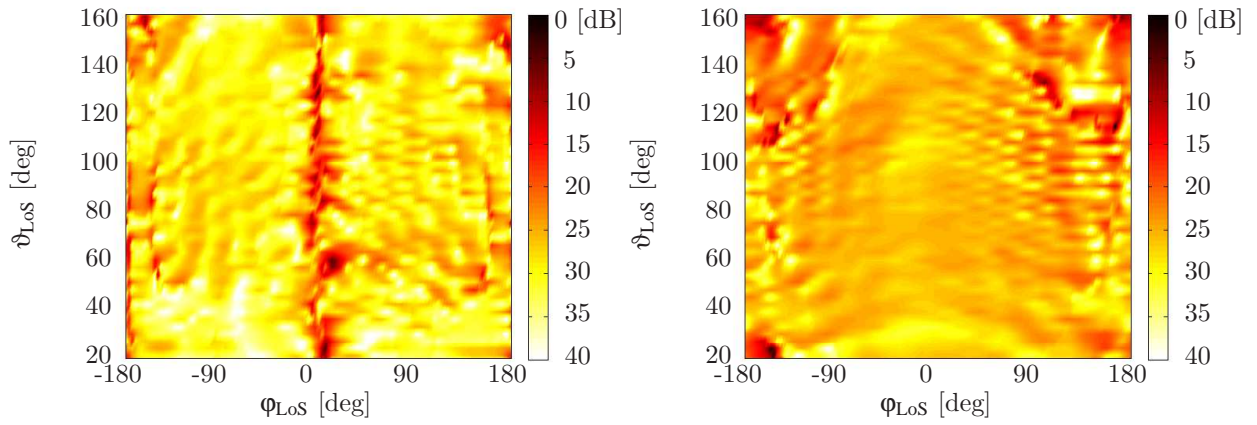
**Tab. 7.1:** Mean model accuracy  $\bar{\zeta}_{120\text{MHz}}$  in dB for different polarisation combinations and antenna arrays

Polarsation Excitation (Tx) $\Rightarrow$ Preferred Polarisation (Rx) $\Rightarrow$ Antenna Array $\Downarrow$	h	h	v	v
	h	v	h	v
OMNI	-	23.3	-	34.0
PUCPASimx2x1x24	33.4	31.1	30.8	33.5
PUCPAx2x1x24	25.9	23.7	27.0	27.6
PULPAx2x1x8 1D (only $\vartheta_{\text{LoS}} = 90^\circ$ Data)	36.5	27.9	27.6	36.9
PULPAx2x1x8 2D (full azimuth and co-elevation range)	30.7	30.7	29.3	31.3
UCAx1x1x16	-	33.2	-	32.1

### 7.2.1.2 Consequences of distorted Radiation Patterns on the Calculated EADFs

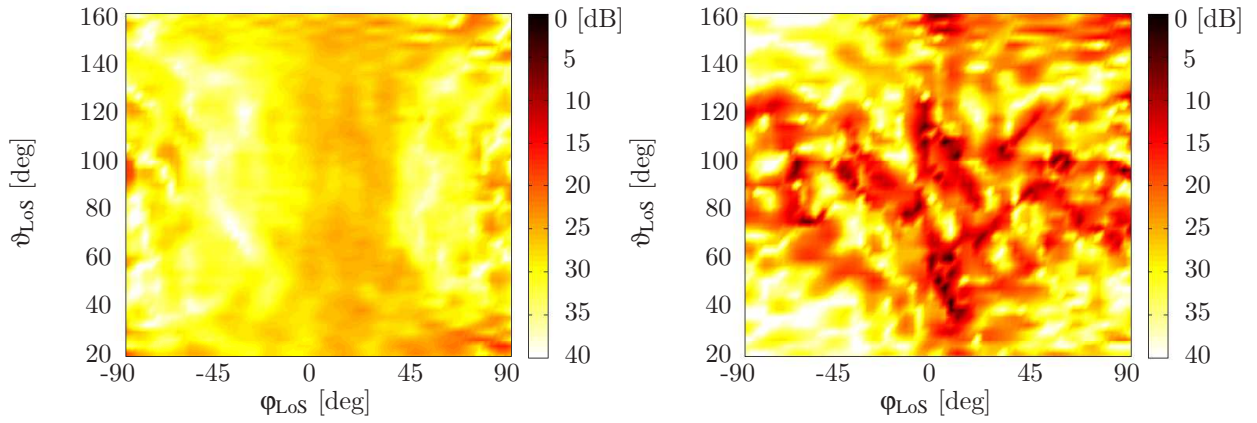
In the previous section it was described, how accurate an antenna response can be modeled by using a narrow band antenna model derived from calibration measurements. The model accuracy of the antenna was analysed in the angular-delay domain only. As the proposed antenna array data model EADF is defined in the aperture domain, the consequences of the direction dependent





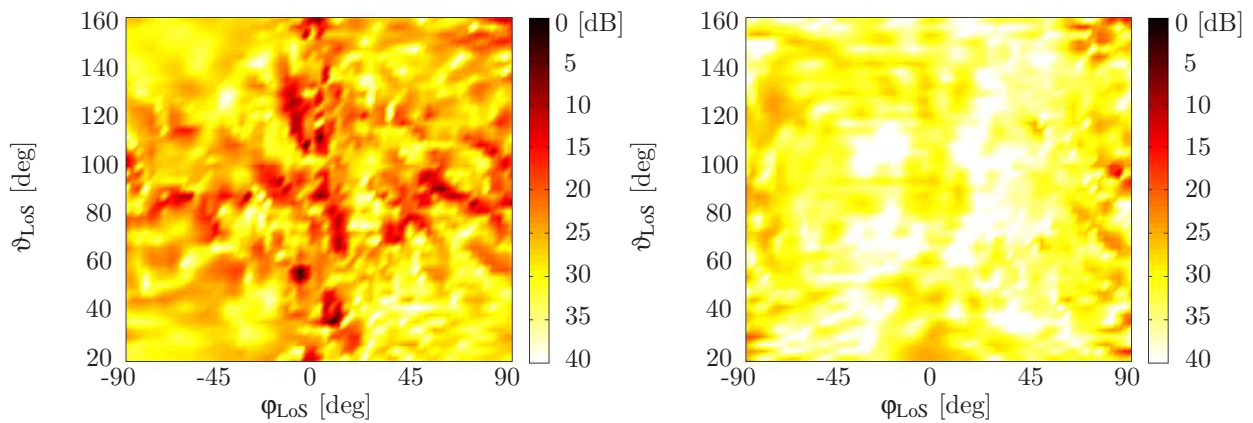
(a) First Antenna element of the UCAX1x1x16 with preferred vertical polarisation for horizontal excitation

(b) First Antenna element of the UCAX1x1x16 with preferred vertical polarisation for vertical excitation



(c) Third antenna element of the PULPAX2x1x8 with preferred horizontal polarisation for horizontal excitation

(d) Third antenna element of the PULPAX2x1x8 with preferred horizontal polarisation for vertical excitation



(e) Third antenna element of the PULPAX2x1x8 with preferred vertical polarisation for horizontal excitation

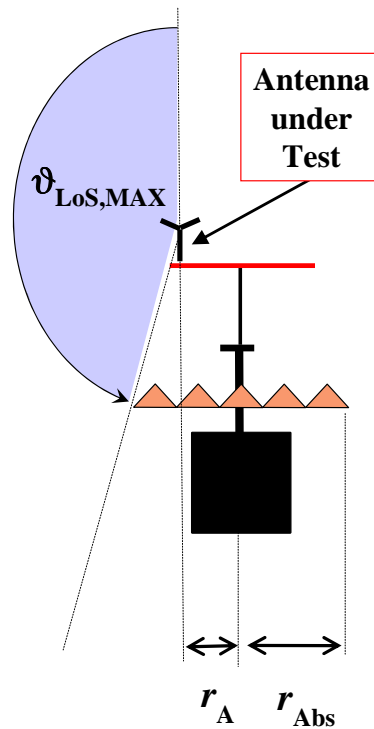
(f) Third antenna element of the PULPAX2x1x8 with preferred vertical polarisation for vertical excitation

**Fig. 7.5:** Model accuracy  $\zeta_{120\text{MHz}}$  of selected antenna elements of the UCAX1x1x6 (first row) and PULPAX2x1x8 (second and third row) for horizontal (left) and vertical excitation (right) respectively

radiation pattern distortion on the relevant samples in the aperture domain will be discussed in the following. It is differentiated between two effects: parasitic reflections and “radiation pattern gating”.

The first effect, the distortion due to the parasitic reflections results in an **EADF** that is less concentrated than the **EADF** of the corresponding undistorted radiation pattern. This means that the effective aperture of the antenna is increased by the parasitic reflections at the positioning system. The positioning system is consequently seen as part of antenna and increases the aperture size.

Second, the radiation pattern can not be measured exactly for co-elevation angles larger than  $\vartheta_{\text{LoS,MAX}}$  as the positioning system shadows the LoS path between the reference horn antenna and the antenna under test. The schematic in Fig. 7.6 shows the top view of the positioning system, with the maximum measurable co-elevation angle  $\vartheta_{\text{LoS,MAX}}$  pinpointed. The resulting “radiation pattern gating” in the angular domain is equivalent to a convolution of the undistorted **EADF** and a  $\text{sinc}(\cdot)$  function in the aperture domain. This convolution leads also to a less concentrated **EADF**, as the side lobes of the  $\text{sinc}(\cdot)$  function become apparent. The consequences of both the



**Fig. 7.6:** Maximum measurable co-elevation angle  $\vartheta_{\text{LoS,MAX}}$ , positioning system top view

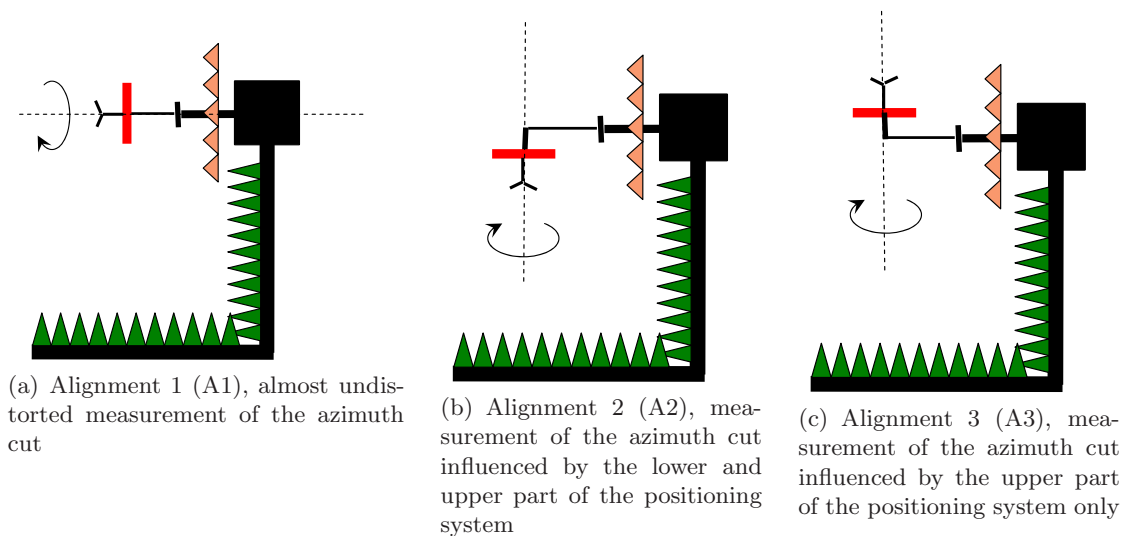
parasitic reflections and the “radiation pattern gating” on the **1D EADF** will be shown with special verification measurements. Therefore, the vertical monopole antenna (OMNI as shown in Fig. 2.15) is used as a reference antenna. The radiation pattern of the vertical monopole antenna for a co-elevation of  $\vartheta = 90^\circ$  is measured for three different alignments of the antenna at the positioning system. The different alignments are chosen in such a way that the influences of the distortions are unequally strong. In Fig. 7.7 the three different alignments and the corresponding rotation axis are



pinpointed.

In case of alignment 1 (A1) the  $\phi$ -rotation axis of the positioning system is used to measure the azimuth cut ( $\vartheta = 90^\circ$ ) almost free from parasitic reflections at the upper and closest part of the positioning system. The zeros of the radiation patterns are pointing towards the direction where most parasitic reflections are expected. Additionally, the measured azimuth cut of the radiation pattern is not gated.

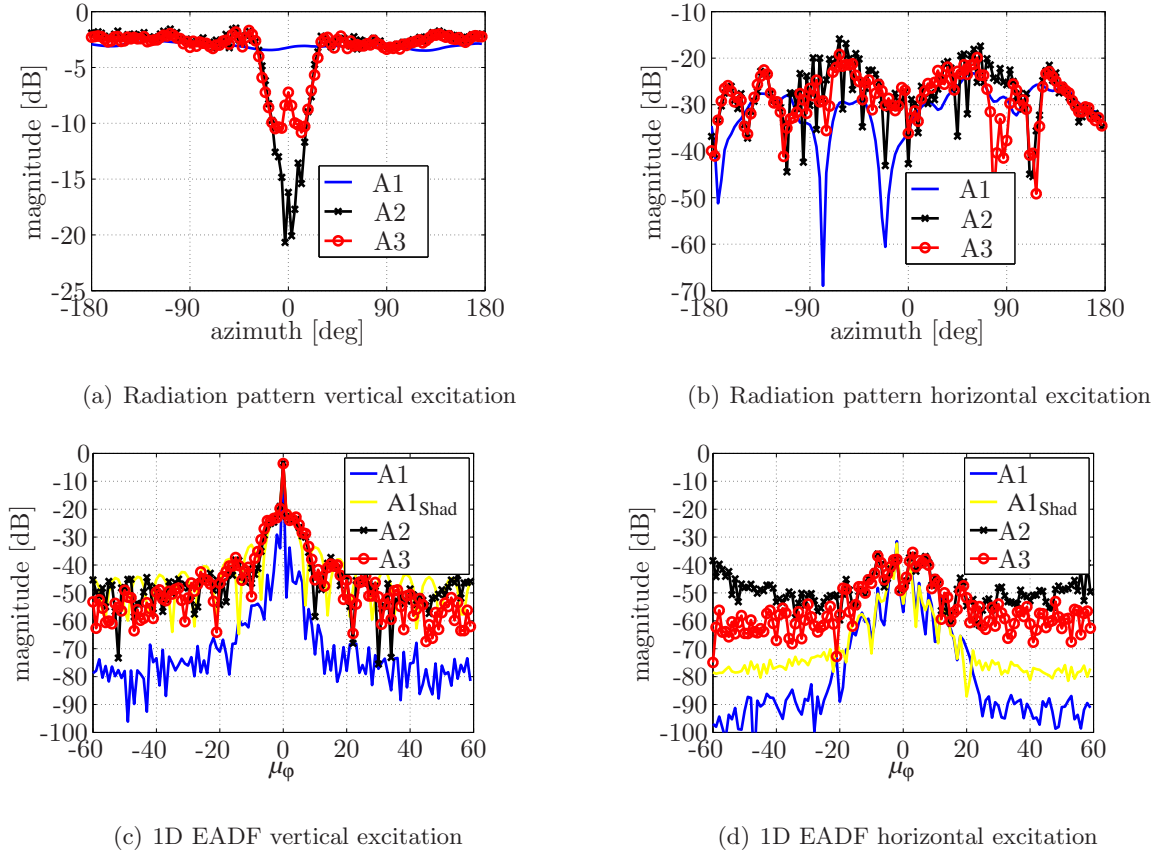
In case of the alignments 2 (A2) and 3 (A3) the  $\vartheta$ -rotation-axis of the positioning system is used to measure the same azimuth cut as in case of the alignment A1. The radiation patterns of the alignments A2 and A3 will be distorted by the parasitic reflections at the lower and upper part of the positioning system respectively. Furthermore, the azimuth cuts of the radiation patterns are gated due to the shadowing effect of the positioning system for these alignments. The measured



**Fig. 7.7:** Verification measurement setups measuring the azimuth cut ( $\vartheta = 90^\circ$ ) of the vertical monopole reference antenna (OMNI) for three different alignments at the positioning system: using the  $\phi$  rotation axis (a) and  $\vartheta$  rotation axis (b)(c).

radiation pattern for vertical excitation are shown in Fig. 7.8(a)). In case of the almost undistorted measurement A1 the radiation pattern is almost omni directional. For the alignments A2 and A3 the magnitude variation of the radiation patterns are larger due to the constructive and deconstructive superposition of the parasitic reflections dependent on the angle of the incoming wave. Additionally, the radiation patterns are gated for azimuth directions around  $\phi = 0^\circ$ , which results in a magnitude that is around 20 dB lower than in the case of A1. In the case of A3 more signal power is received in the shadowed region. The cause for the larger received signal power is the diffraction at the upper part of the positioning system. The results show that the diffraction at the circular absorber at the upper part is larger than at the pyramid absorber at the lower part (see also the picture of the positioning system in Fig. 4.2(b)). For horizontal excitation (Fig. 7.8(b)) and alignment A1, a non-omni directional radiation pattern was measured. In case of alignment A2 and A3 it can be seen, that the received power is strongly varying and larger for most directions compared to A1. Obviously, the impact of the parasitic reflections increases if the received power of the LoS path is decreasing, which is the case for this antenna and the horizontal excitation.

As the signal power of the parasitic reflections and diffractions are larger than the power of the LoS path, a gating of the radiation pattern can not be observed for horizontal excitation. Let us



**Fig. 7.8:** Azimuth cut ( $\vartheta = 90^\circ$ ) of the radiation pattern (top row) and the corresponding 1D EADF (bottom row) of the vertical monopole antenna (OMNI) for vertical (left column) and horizontal (right column) excitation and different alignments A1,A2 and A3 at the positioning system

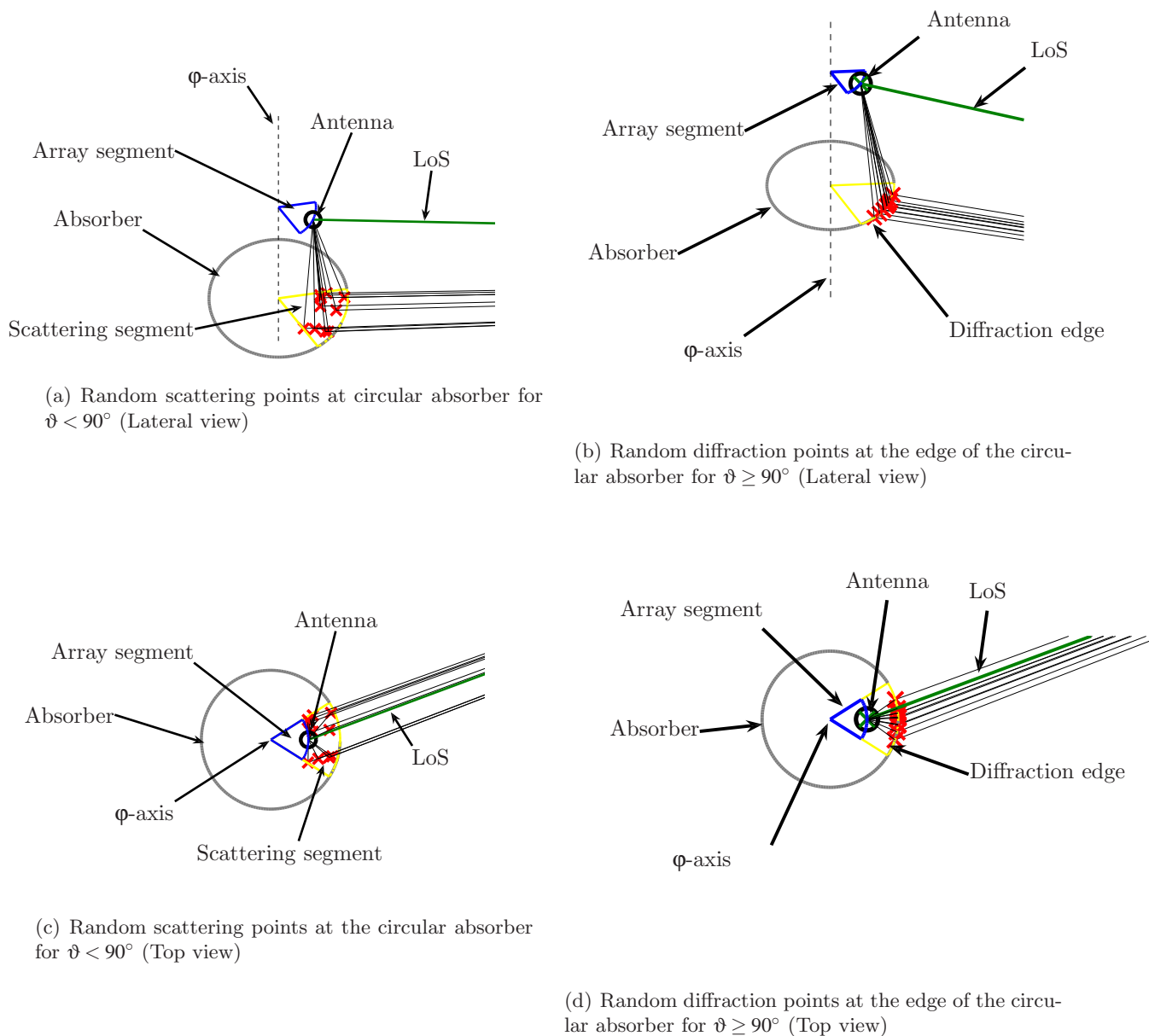
now discuss the impact of the radiation pattern gating and parasitic reflections on the EADF by comparing the 1D EADFs for the three different alignments. Additionally, the radiation pattern for alignment A1 is artificially shadowed and the corresponding 1D EADF is also calculated. The radiation pattern is set to zero in the shadowed region. For comparison the width of the shadowed region is chosen equivalent to the known shadowing width of A2 and A3. For an omni directional antenna it is expected, that the total signal power is concentrated in one sample of the 1D EADF. For vertical excitation and for the alignment A1, the 1D EADF fits almost this expectation (see Fig. 7.8(c)). As the antenna is not infinite small and the radiation pattern is not constant for all directions, the adjacent samples of  $\mu_\phi = 0$  still contain signal power, which is around 30 dB to 40 dB lower than the signal power in the main peak. For the alignment A1, the samples with  $|\mu_\phi| > 20$  contain noise power only. For the artificially shadowed radiation pattern of A1 the convolution of the original signal (EADF of A1) with the  $\text{sinc}(\cdot)$  function can be observed. The consequence of this convolution is the broadening of the main peak. Additionally, the samples  $|\mu_\phi| > 20$  contain signal power and not only noise power. Comparing the EADF of the shadowed version of A1 and the EADFs corresponding to alignment A2 and A3 a similar shape can be observed. However, due to the impact of the parasitic reflections a further broadening of the main peak can be observed.

The signal power of the adjacent samples of the main peak mainly corresponds to the power of the parasitic reflections. As already seen in Section 7.2.1.1 the power of these reflections is around 20 to 25 dB lower than the power of the designated signal in the main peak. For horizontal excitation Fig. 7.8(d) and alignment A1 it can be observed that the signal power of the desired antenna response is much lower and spread in the range of  $\mu_\phi = \pm 20$ . That means that the resulting aperture of this antenna for horizontal excitation is larger than for vertical excitation. In case of the artificially shadowed radiation pattern only a raised noise floor as a result of the convolution with the  $\text{sinc}(\cdot)$  function can be observed. Note that the noise floor for horizontal excitation is lower than for vertical excitation due to the automatic gain control (AGC) of the sounder. Observing now the EADFs for A2 and A3 for horizontal excitation it is obvious that the parasitic reflections have a larger impact on the EADFs than the radiation pattern gating shown with the shadowed version of A1. In the region where the desired signal antenna response is expected  $\mu_\phi = \pm 20$ , the signal power in case of the alignment A2 and A3 is up to 10 dB larger than for A1. This mainly corresponds to the parasitic reflections at the upper part of the positioning system. Reflections at the lower part of the positioning device have a larger distance to the antenna and lead to an increased signal power for  $|\mu_\phi| > 40$ . The impact of the parasitic reflections at the lower part of the positioning system can be only observed in case of alignment A2. In case of A3 the zeros of the antenna radiation pattern are located in the direction of the lower part of the positioning system and in consequence the impact of the corresponding reflections can not be observed.

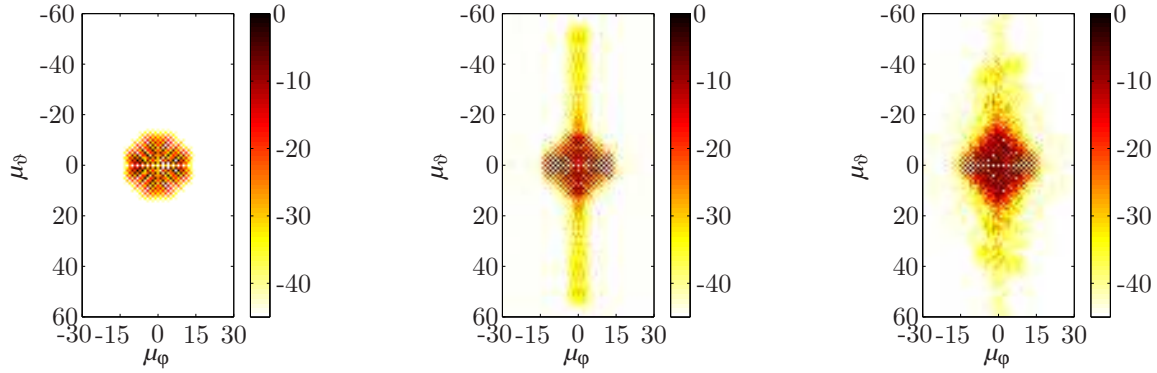
### 7.2.1.3 Simplified Reflection Model of the Positioning System and Distorted EADFs

The previous measurement example, using the validation antenna by means of the vertical monopole antenna (OMNI), clearly shows the consequences of the parasitic reflections and the “radiation pattern gating” on the calculated EADFs. However, with this measurement example using a single antenna element the consequences of distorted EADFs of an antenna array on the parameter estimation can not be demonstrated. Moreover most of the *practical* antenna arrays have only one possibility for a mounting at the positioning system and different alignments at the positioning system can not be achieved. Therefore, a simplified scattering model of the positioning system is introduced in the following. This simplified model will be used to generate distorted radiation patterns and the corresponding EADFs of the simulated PUCPASimx2x1x24. Herewith it is possible to apply the simulated distorted EADFs on simulated undistorted data during parameter estimation, which is not possible from measurements as the undistorted data is not available. For the simplified model, only parasitic reflections at the upper part of the positioning system will be considered. A difference is made between angles  $\vartheta < 90^\circ$  of the incoming wave, in which case only scattering occurs in a specified segment of the circular absorber at the upper part of the positioning system (see Fig. 7.9(a) and Fig. 7.9(c)) and angles  $\vartheta \geq 90^\circ$  of the incoming wave, in this case only diffraction at the edges of the circular absorber is considered (see Fig. 7.9(b) and Fig. 7.9(d)). In reality an absorber or every object has its own reflection pattern. For simplification this reflection pattern is not exactly modelled. For each measurement position  $\{\phi_n, \vartheta_n\}$ , a fixed number of  $K = 10$  scattering or diffraction points is randomly chosen at the specified scattering segment or diffraction edge at circular absorber respectively. The points are uniformly distributed

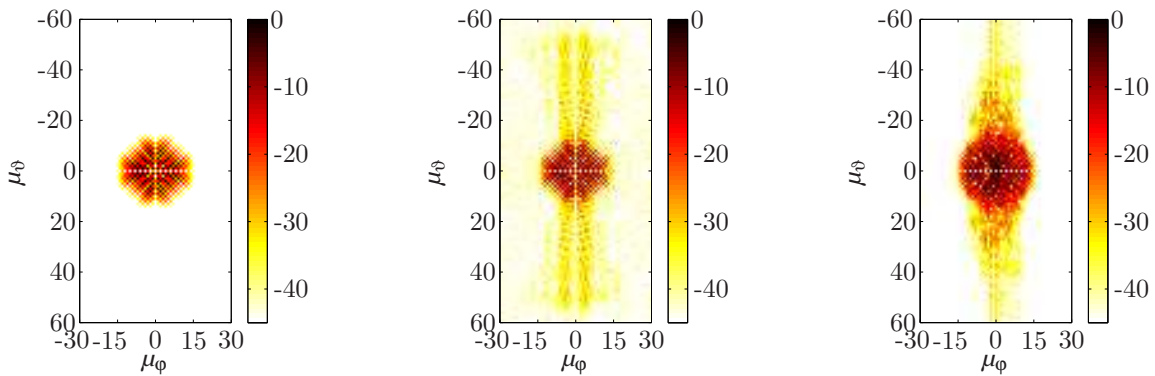
in the chosen region. For the simplified scattering model constant scattering and reflection coefficients  $a_{\text{Abs}}$  are assumed. Corresponding to the data sheets of the absorbing material the value is chosen to -25 dB. Furthermore, the scattered power is equally distributed in both polarisations, which means that the polarisation vector for horizontal and vertical excitation is turned around  $45^\circ$ . For co-elevation angles larger than  $\vartheta_{\text{LoS,MAX}}$ , it is assumed that the LoS path is totally absorbed. Using eqn. (7.6) without considering the measurement noise, the vector valued distorted frequency response of the antenna is calculated, while a distance of 5.32 m between reference horn antenna and the antenna under test is chosen. This distance is equivalent to the distance in the measurement setup described in Section 4.1. The corresponding delays  $\tau'_k$  and angles of incidence  $\{\varphi_k, \vartheta_k\}$  of all  $K$  parasitic reflections are calculated. The  $K$  path weights of the parasitic reflections for both polarisations incorporate the free space path loss and the reflection coefficient  $a_{\text{Abs}}$  of the absorbing material. Finally, the narrow band radiation patterns and EADFs are calculated using eqn. (4.6). The proposed simplified model is applied to generate distorted radiation patterns and EADFs of the simulated PUCPASIMx2x1x24. The following comparison of measured radiation EADFs and the generated distorted EADFs show that the effects of the distortion caused by the parasitic reflections and the “radiation pattern gating” can be roughly described with the proposed simplified scattering model of the positioning system. In Fig. 7.10 the normalised magnitude of the EADFs (normalised to its maximum) of the simulated PUCPASIMx2x1x24, the distorted PUCPASIMx2x1x24 and the measured PUCPAx2x1x24 from the left to the right for a vertical port only are shown. The top row corresponds to the result for vertical excitation and the bottom row for horizontal excitation. As expected, the EADFs of the simulated array are most concentrated in the range of  $\mu_\varphi = \pm 15$  and  $\mu_\vartheta = \pm 15$  for both polarisation excitations. Analysing the distorted version of the PUCPAx2x1x24 it is obvious, that the EADFs are spread in the direction of the co-elevation aperture  $\mu_\vartheta$ . This is reasonable as the simplified scattering model of the positioning system incorporates parasitic reflections in the co-elevation direction of  $\vartheta \geq \vartheta_{\text{LoS,MAX}}$ , which results in a less concentrated EADF in the direction of the co-elevation aperture  $\mu_\vartheta$ . It can be also seen that the impact on the EADF for the cross-polarised horizontal excitation is larger, as the received signal power of the LoS path is lower for this excitation. For the EADFs of the measured array it can be noticed that the region with the main signal power is slightly bigger than in case of the simulated arrays. The reason for this behaviour can be found in the stronger coupling between the antenna elements than in case of the simulation. However, the spread of the EADFs in the direction of the co-elevation aperture  $\mu_\vartheta$  is comparable to the one of the distorted simulation. As the exact reflection pattern of the positioning system could not be considered, the shape of the distortion slightly differs from the measured ones. Nevertheless, it can be concluded, that the samples in the EADF with  $|\mu_\vartheta| > 15$  in case of the distorted EADF are the result of the distortion. Consequently, it is appropriate to limit the number of samples of the EADF used for parameter estimation to  $\mu_\varphi = \pm 15$  and  $\mu_\vartheta = \pm 15$  to reduce the consequence of the radiation pattern distortion. These *windowed* EADF will be denoted with WEADF. Note that the WEADF does not completely eliminate the effect of the distortions as the remaining samples are still biased. In the following Section the impact of the distorted EADFs on the parameter estimation result will be discussed.



**Fig. 7.9:** Illustration of the simplified scattering (left column) and diffraction (right column) model of the upper part of the positioning system for  $\vartheta < 90^\circ$  and  $\vartheta \geq 90^\circ$  respectively



(a) vv EADF of the simulated PUC-PASIMx2x1x24 (b) Distorted vv EADF of the simulated PUCPASIMx2x1x24 (c) vv EADF of the measured PUC-PAx2x1x24



(d) hv EADF of the simulated PUC-PASIMx2x1x24 (e) Distorted hv EADF of the simulated PUCPASIMx2x1x24 (f) hv EADF of the measured PUC-PAx2x1x24

**Fig. 7.10:** Comparison of the normalised EADFs [dB] of a vertical port of the simulated PUC-PASIMx2x1x24 with the corresponding distorted version and the measured PUCPAx2x1x24 from left to right and from top to bottom for vertical excitation and horizontal excitation

### 7.2.1.4 Systematic Error of the Estimation Result Caused by Distorted EADFs

The consequences of distorted antenna array calibration measurements on the parameter estimation results will be discussed in the following. The distorted EADFs generated from distorted radiation patterns of the PUCPASIMx2x1x24, as described in the previous section, will be used for the parameter estimation applied to a simulated single path scenario. The undistorted EADFs are used for the generation of simulated data for the single path excitation. The path weights for horizontal and vertical polarisation are equal in magnitude. For the analysis two cases will be considered: using the distorted but complete EADFs (denoted with CEADF) with  $\mu_\phi = \pm 15$  and  $\mu_\theta = \pm 60$  and using the distorted but windowed EADFs with  $\mu_\phi = \pm 15$  and  $\mu_\theta = \pm 15$  for parameter estimation. Note that using the CEADFs is similar to the interpolation of distorted radiation patterns that is done by most of the conventional ML parameter estimation algorithms. In case of the RIMAX algorithm always the WEADFs are applied to reduce the impact of the radiation pattern distortion. First, only a single path is estimated from the simulated data to determine the mean model accuracy expressed as SRR for both versions of the distorted EADFs: CEADFs and WEADFs. In



Fig. 7.12(a) the mean **SRR** (mean over the full azimuth range) dependent on the co-elevation angle of the true path for using the **WEADF** and the **CEADF** are shown. Using the **WEADFs** that contain only the relevant but also distorted samples, the mean model accuracy for co-elevation angles between  $\vartheta = 40^\circ$  and  $\vartheta = 130^\circ$  is around 32 dB to 35 dB. The mean model accuracy when applying the **CEADFs** is around 10 dB lower for the same co-elevation angles. But in both cases a decreasing mean model accuracy can be observed for directions toward the poles of the spherical coordinate system. The undistorted/perfect radiation patterns have a lower gain in these directions, which means that the parasitic reflections are stronger compared to the desired path during calibration. Consequently, the radiation patterns and **EADFs** are more distorted for the directions towards the pole of the spherical coordinate system. Especially in the direction of the South Pole, where additionally the radiation pattern gating occurs, the model accuracy decreases most.

For the second analysis step, the maximum number of path to estimate is set to  $K_{\max} = 10$ . Consequently, the  $K \leq 9$  additional estimated paths are artefacts. In Fig. 7.11 the estimated mean power distribution around the true azimuth angle by means of the centred azimuth are shown in the top row for the case of using the **CEADFs** Fig. 7.11(a) and the **WEADFs** Fig. 7.11(b). The corresponding mean power distributions dependent on the centred co-elevation are shown in the bottom row. For both, the complete or the windowed distorted **EADFs**, an estimation of artefacts can be observed. The maximum power of the artefacts is around 25 dB lower as the power of the path in the true direction.

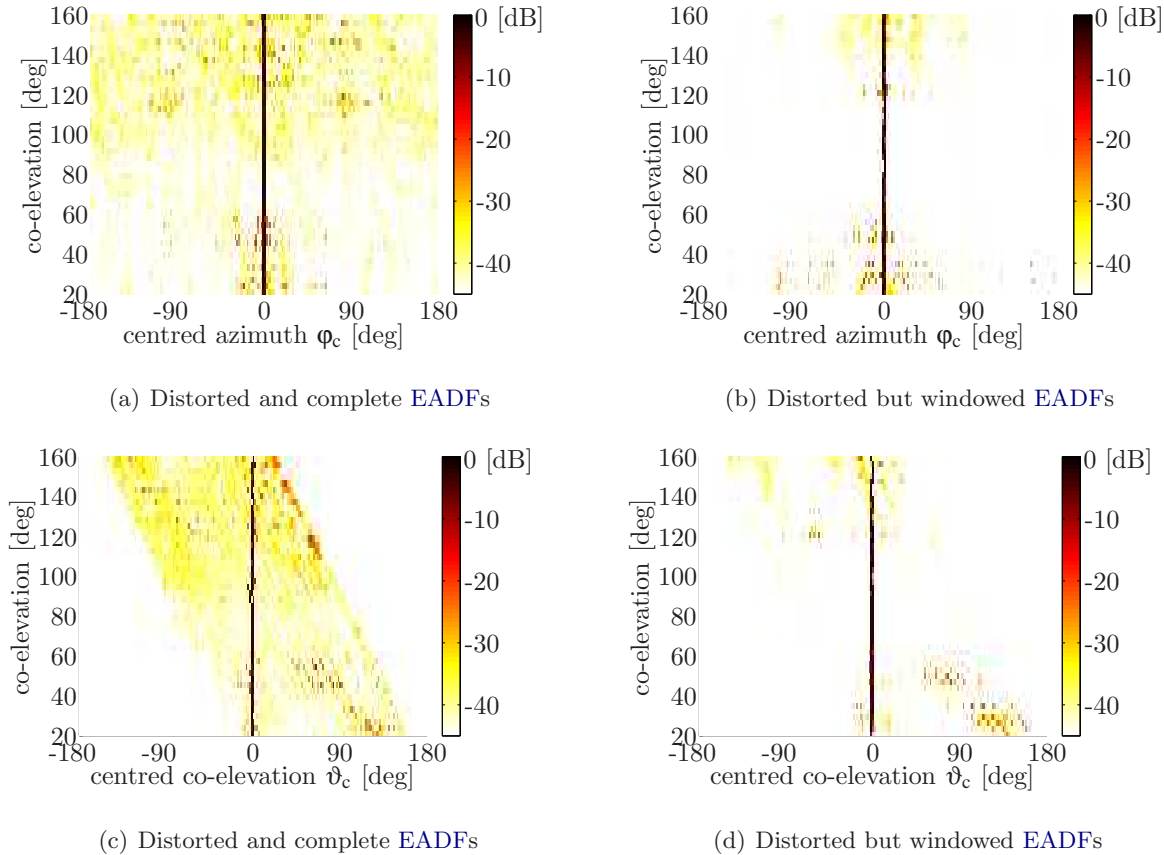
For the **CEADFs**, the artefact's power and spread in azimuth and co-elevation is larger than compared to the usage of the **WEADFs**. The spread in azimuth and co-elevation is related to the fact, that the remaining observation after subtraction of the strongest estimated paths contains almost no directional/spatial information. Even by estimating 9 additional and physical meaningless paths the **SRR** could be only improved about 6 dB (see Fig. 7.12(b)). From experience in working with measurement data, this behaviour can be quite often observed in scenarios with a large  $\text{SNR}_{\text{IR}}$  in the impulse response. In **LoS** scenarios, which often fulfil this condition, a larger number of paths with a huge spread were observed. This is especially the case when using conventional **ML** parameter estimation algorithms that interpolated distorted radiation patterns. Additionally to the estimated artefacts the computation time of the conventional **ML** estimation algorithms is increasing due to the model order overestimation which is only related to the physical meaningless artefacts.

Even so the estimation with the **WEADFs** lead also to estimation of artefacts, their power contribution is around 10 to 15 dB lower than in case of using the **CEADFs**. Lower mean model accuracy and the estimation of artefacts can be only observed for co-elevation directions towards the poles. But especially for co-elevation angles around  $\vartheta = 90^\circ$  the advantage of the **WEADFs** is obvious as the estimated artefacts are almost negligible.

It should be mentioned, that an improvement of the estimation result by the windowed **EADFs** can not be achieved in general. The quantity of the improvement is still dependent on the size of the array, their specific radiation patterns and the power contribution of the parasitic reflections during antenna array calibration.

A further possible solution to reduce the consequences of the parasitic reflections is the permanent

attachment of the circular absorber to the antenna array. This means that the circular absorber is seen as characteristic of the antenna array. The alignment and the attachment of the circular absorber can never be modified and has to be the same during antenna array calibration and a propagation measurement campaign. With this approach similar or even better results can be achieved than with the windowed EADFs. However, the disadvantage of this approach is a higher computational effort during parameter estimation, as the number of relevant EADF samples is increasing. Consequently, this will result in a higher computational burden for the parameter estimation algorithm, which is in most cases not desirable or even impracticable.

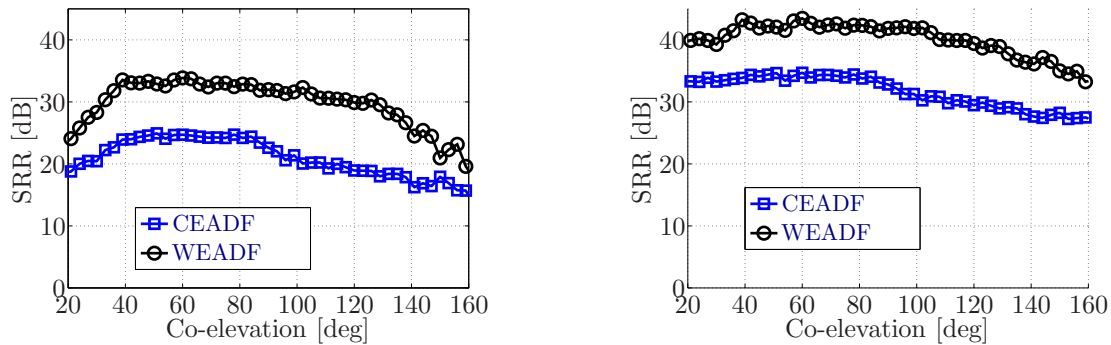


**Fig. 7.11:** Comparison between parameter estimation using the distorted and complete EADFs (CEADFs) (left) and the distorted but windowed EADFs (WEADFs) (right) for single path excitation and the PUCPASIMx2x1x24 array: Mean estimated power distribution [dB] of  $K \leq 10$  paths versus deviation from true angle in azimuth (top) or co-elevation (bottom) as function of co-elevation.

### 7.2.1.5 Concluding Remarks on Systematic Error Related to the Quality of the Calibration Measurement and to the Narrow Band Model

In the discussion of this Section 7.2.1 it has been clearly shown, that the calibration accuracy is mainly limited by the reflection properties of the positioning system. The determined mean model accuracy of the measured radiation patterns of the antenna arrays used varies between 20 to 35 dB. Better model accuracy can be achieved by antenna arrays, in which case the antenna elements





(a) SRR by means of the mean model accuracy (Single path estimation)

(b) SRR for estimation of maximum number of 10 paths (9 paths are artefacts)

**Fig. 7.12:** SRR in case of using the distorted and complete EADFs (CEADFs) and distorted but windowed EADFs (WEADFs) of the PUCPASIMx2x1x24, in case of a single path estimation (a) the SRR is equivalent to the model accuracy and in case of the estimation of 10 paths (b) the SRR specifies the signal to remainder power ratio only

can not receive the signal of the parasitic reflections. This is especially the case if the antennas are positioned on a radius  $r_A$  that is larger than the radius  $r_{Abs}$  of the circular absorber at the upper part of the positioning system. In a realistic simulation it was shown, that the distortion of the radiation pattern measurement will result in the estimation of artefacts that are almost uniformly distributed around the true path. However, with the distorted but windowed EADFs the mean model accuracy may be improved around 10 dB, which consequently result in a power reduction of the estimated artefacts.

### 7.2.2 Systematic Error Due to Incomplete Data Models

The impetus of this section stems from the following observations:

1. Parameter estimation is able to achieve high resolution by incorporating a priori knowledge.
2. Part of that a priori knowledge are the data models that describe antenna responses to particular incident wave-fields, for all possible angles of incidence and all polarisation states of fields. Obviously, the use of inadequate data models precludes high-quality estimates.
3. The fact that many arrays are composed of antenna elements that only offer one electrical input/output port is easily mistaken for insensitivity to one of the two fundamental polarisations, or for identical behaviour for both polarisations.
4. Full polarimetric calibration of antennas over  $4\pi$  space angle to make up these data models is time-consuming and cumbersome, as is storage of the calibration data and handling (interpolation of) these data during estimation.
5. Therefore, often, short-cuts are taken, resulting in using a cut through the azimuthal plane and/or calibrating for one polarisation only or even not calibrating at all but relying on theoretical patterns or only partly calibrating.

6. Linear arrays have an inherent angular response ambiguity that must lead to estimation bias.
7. A further short cut is commonly taken by assuming plane wave fronts or wave fronts with a constant curvature instead of considering the distance dependent curvature of each wave front, which is especially crucial for measurements in Indoor environments.
8. Up to now, non decent treatise has been published dealing with the consequences of particular choices for array types and data models on the estimation accuracy, as far as the author is aware of.
9. As using incomplete data models during estimation may give rise to the occurrence of clusters of multi-path components where there are none, which is of interest especially for channel modelling.

The following literature survey covering the last 20 years gives an overview of publications, incomplete data models for parameter estimation being used in simulations and measurements. Note that this list may not be complete and can be further extended.

#### **In simulations:**

- **Ignoring polarisation: 6, Ignoring elevation: 1, Ignoring polarisation & elevation: 7**
- [UCA](#) at [MS](#), ignoring polarisation [[64](#), [117–121](#)]
- [UCA](#) at [MS](#), ignoring polarisation and elevation [[97](#), [114](#), [122](#), [123](#)]
- [ULA](#) at [MS](#), ignoring polarisation and elevation [[124](#), [125](#)]
- [ULA](#) at [MS](#), ignoring elevation [[126](#)]
- Planar and Linear arrays, ignoring polarisation and partly also elevation [[58](#)]

#### **In measurements:**

- **Ignoring polarisation: 3, Ignoring elevation: 1, Ignoring polarisation & elevation: 4**
  - Micro cell environment, [UCA](#) at [MS](#) ignoring polarisation and [ULA](#) at [BS](#) (below roof top) ignoring elevation [[69](#)]
  - Micro cell environment, crossed array at [MS](#) only, ignoring polarisation [[127](#)]
  - Macro cell environment, [ULA](#) to [ULA](#) over roof top, ignoring polarisation and elevation [[68](#)]
  - Indoor environment, [UCA](#) at [MS](#) and [BS](#), ignoring polarisation [[66](#)]
  - Outdoor to Indoor, [UCA](#) at [MS](#) and [ULA](#) at [BS](#), ignoring polarisation and elevation [[70](#), [128](#)]
  - Micro cell environment, 1. [ULA](#) at [MS](#) and synthetic cross array at [BS](#), 2. [CUBA](#) at [MS](#) and [CUBA](#) at [BS](#), ignoring elevation and polarisation [[65](#)]
  - Indoor environment, synthetic volume array, ignoring polarisation [[129](#)]
-

- Micro cell environment, [URA](#) at [MS](#) and [CUBA](#) at [BS](#), ignoring polarisation and elevation [[57](#)]
- Pico cell environment, [ULA](#) at [BS](#) and synthetic [UCA](#) at [MS](#), ignoring polarisation and elevation [[60](#)]

This list shows the extent to which the topic of using appropriate data models for parameter estimation is ignored. Only a few publications can be found, where the spatial domain is fully exploited in the measurement and estimation process [[3](#), [4](#), [72](#), [73](#)].

In view of the aforementioned points, the following three major effects of incomplete data models will be discussed:

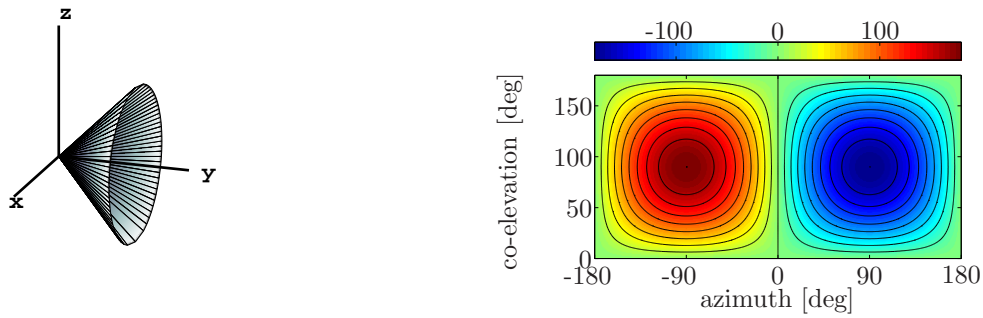
1. Inadequate treatment of the change of phase and magnitude distributions over circular and linear arrays with co-elevation in Section [7.2.2.1](#);
2. Disregarding the fact that every antenna does receive signal from both polarisation directions, by considering only array patterns for a single polarisation in Section [7.2.2.2](#);
3. Ignoring the curvature of the wave front dependent on the distance of the source in Section [7.2.2.3](#).

For the first and the second point, two popular generic types of arrays will be treated: the polarimetric uniform linear array [PULPAx2x1x8](#) and the uniform circular array [UCAx1x1x16](#) (see [Fig. 2.16](#) and [Fig. 2.14](#)). Anechoic chamber calibration measurements of a single path arriving from different co-elevation and azimuth angles for horizontal and vertical excitation are used.

### 7.2.2.1 Effect of Ignoring Elevation Characteristics

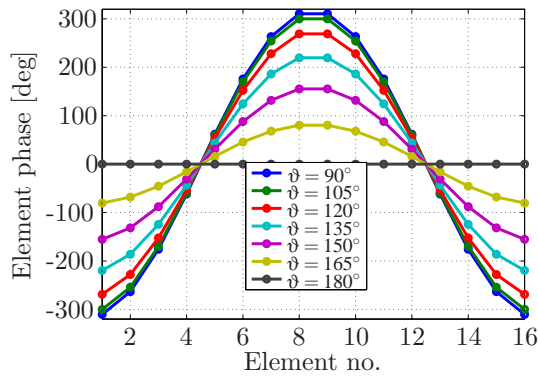
The major effect used in direction estimation with antenna arrays is the change of phase over the antenna elements with varying incident angles, both in azimuth and elevation. Additionally, amplitude effects are experienced too depending on the angular responses of the individual antenna elements of which the array is made of and on influences of the constructional parts of the array. This phase and amplitude response as function of angle of incidence is what is used by parameter estimators to match received responses to. Note that an estimator relying on element uniformity, e.g. [ESPRIT](#), is generally not able to handle non-uniform amplitude responses over array elements, be it that in some cases additional pre-processing might relieve the problem. In contrast, this non-uniformity can in some cases even be used to advantage by Maximum Likelihood ([ML](#))-estimators for resolving ambiguous responses. For example, if the non-uniformity is different for different co-elevation angles, it could be used for [ML](#)-estimation of these co-elevation angles. In this context, it is immaterial whether such non-uniformity stems from intrinsic responses from spatially differently oriented antenna elements or those differences between element responses are caused by coupling, fabrication tolerances, or influences of constructional parts of the array. Although the varying phase over the array with incidence angle is the major effect routinely used in direction estimation procedures, there is a twist to it that is often overlooked. For a linear array, the phase variation

---



(a) DoAs that result in the same phase constellation at an ideal ULA (elements placed along y-axis,  $\Delta\alpha = 45^\circ$ ) (b) Phase difference  $\Delta\alpha$  in degree between two elements of an ideal ULA dependent on azimuth and co-elevation

**Fig. 7.13:** DoA ambiguity in case of using an ideal ULA



**Fig. 7.14:** Phase over 16 element UCA,  $\varnothing$  10.5 cm at 5.2 GHz for incidence at different co-elevations  $\vartheta$ .

along the array with varying angle of incidence is inherently linear. But as the angle of incidence is defined with respect to the axis through the array, its response shows rotational symmetry around this axis. The  $M$  elements of the ULA are symmetrically placed at the y-axis, which results in the following phase term:

$$\mathbf{b}(\varphi, \vartheta, m) = e^{-j \cdot m \cdot \Delta\alpha(\varphi, \vartheta)}. \tag{7.14}$$

With  $\Delta\alpha$  being the phase difference between two elements of the ULA with:

$$\Delta\alpha(\varphi, \vartheta) = 2\pi \cdot d' \cdot \sin(\varphi) \cdot \sin(\vartheta) \tag{7.15}$$

where  $d' = 0.5$  is the distance between two adjacent elements normalised to the wavelength  $\lambda$ . Effectively, this means that different waves with their angle of incidence on the same cone around a ULA will impose the same phase gradient over the array, as shown in Fig. 7.13(a). There will be no way of telling from the array response from where on a cone an incident wave comes. An

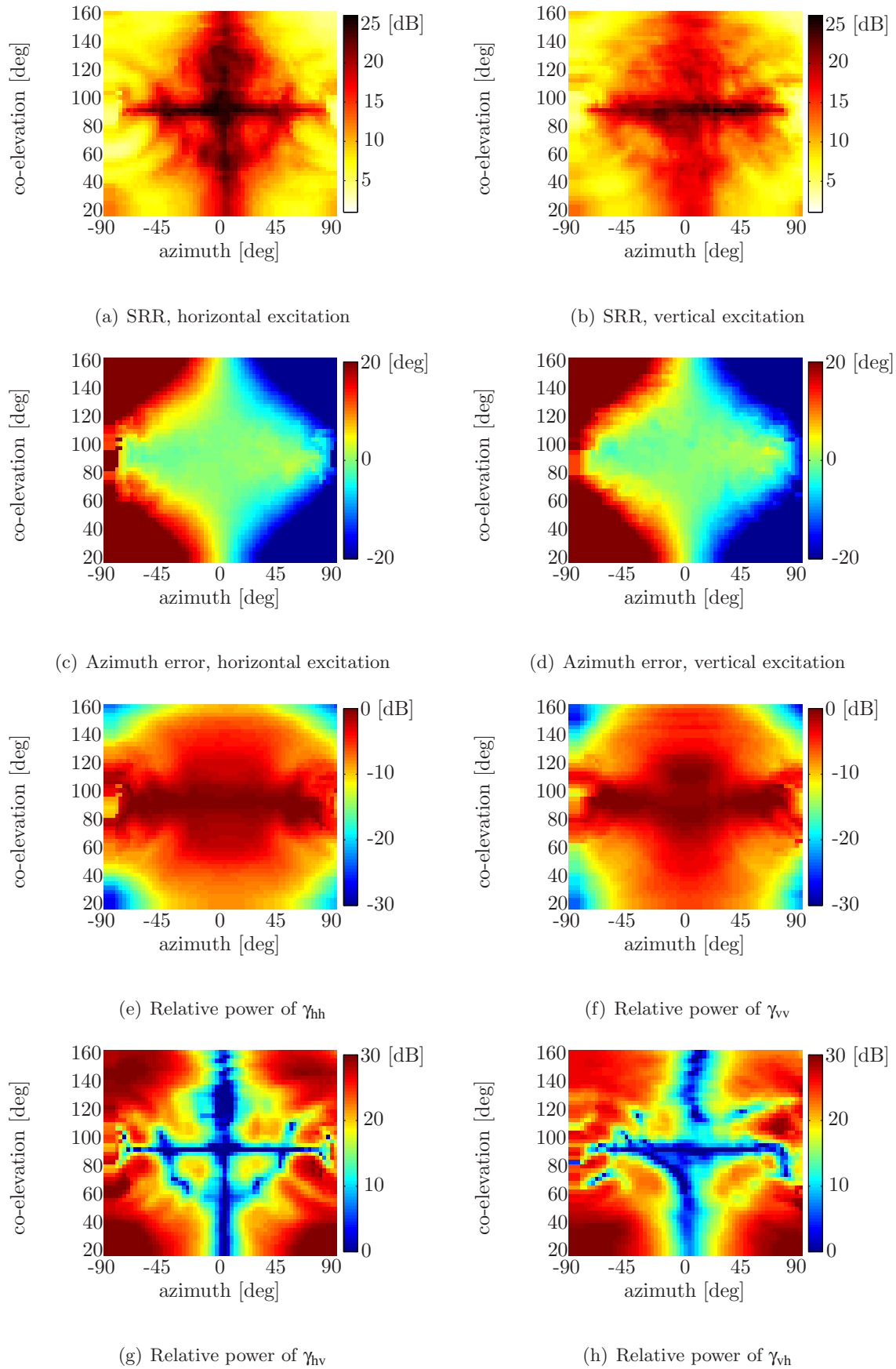
expression for the resulting azimuth error in case of planar wave fronts is given by [130]:

$$\varphi_E = \arcsin\left(\frac{\sin(\vartheta) \cdot \sin(\varphi)}{\sin(\vartheta)}\right) - \arcsin(\sin(\vartheta) \cdot \sin(\varphi)) \quad (7.16)$$

in case that the used data model or calibration is valid for  $\vartheta = 90^\circ$ . For instance, a wave with azimuthal incidence angle of  $45^\circ$  and co-elevation  $90^\circ$  is as likely as a wave with azimuth  $90^\circ$  and co-elevation  $135^\circ$ , resulting in  $45^\circ$  bias in azimuth, as illustrated in the contour plot of Fig. 7.13(b) for different angles of incidence. It is explicitly mentioned here that the directional ambiguity of linear arrays is therefore more extensive than the well-known front-back ambiguity. Intrinsically, due to the lack of aperture in the plane perpendicular to the line through the array, estimation of the co-elevation angles of incidence with linear arrays is not possible. This means that the correction of the estimated path weights for the radiation pattern dependent on the true DoD/DoA can not be achieved.

For a uniform circular array, the phase changes with varying angles of incidence along the array are typically not linear but sinusoidal. Here, there is less ambiguity as the phase gradients change with co-elevation, as shown in Fig. 7.14. However, an upper/lower ambiguity, with the azimuthal plane as plane of symmetry, still exists. For small departures from the zero-elevation plane (co-elevation equals  $90^\circ$ ), the effects are minor but the phase distribution over the array flattens progressively with increasing elevation until the field is normally incident on the array. Note that phase, being the argument of the complex amplitude, is a non-linear quantity and that complex amplitude distributions can not be transformed by a single complex scalar from one phase distribution to another; on the other hand, this exactly allows to determine the co-elevation angle, be it less accurate where the phase changes are smallest and apart from the upper/lower ambiguity. The task of a parameter estimator is to find the complex scalar that optimally matches the incoming field to the modelled amplitude distributions, that complex scalar being the “path weight” for a component with a particular angle of incidence. When for the data model, for instance, only an azimuthal cut is available, representing the phase distribution with maximum phase gradients in Fig. 7.14, a matching of lower gradient phase distributions, belonging to incidence outside this plane, to those of the azimuthal plane with just a single complex scalar will result in estimation bias and spread.

**Example PULPAx2x1x8:** The consequences of the ULA’s ambiguity for direction estimation with *practical* PULPAx2x1x8 will be illustrated in the following. In contrast to the ideal ULA, the PULPAx2x1x8 has directional dual polarised patch antennas. Also, the phase characteristics dependent on the co-elevation differ from the ideal ULA, but this information is not sufficient to estimate the co-elevation angle, as opposed to circular arrays where the asymmetry enables resolving co-elevation. Therefore, only the full polarimetric 1D data model, the azimuthal cut for a constant co-elevation of  $\vartheta = 90^\circ$ , can be used for the estimation, the consequences of which will be discussed in the following. As described in Section 7.1, in the first analysis the maximum number of paths to estimate,  $K_{\max}$ , is set to one, to demonstrate the model error made by using the 1D data model in terms of SRR, azimuth error, and error of the path weights (Fig. 7.15). In the second analysis, the impact on the azimuth power distribution is shown for horizontal and vertical excitation, when

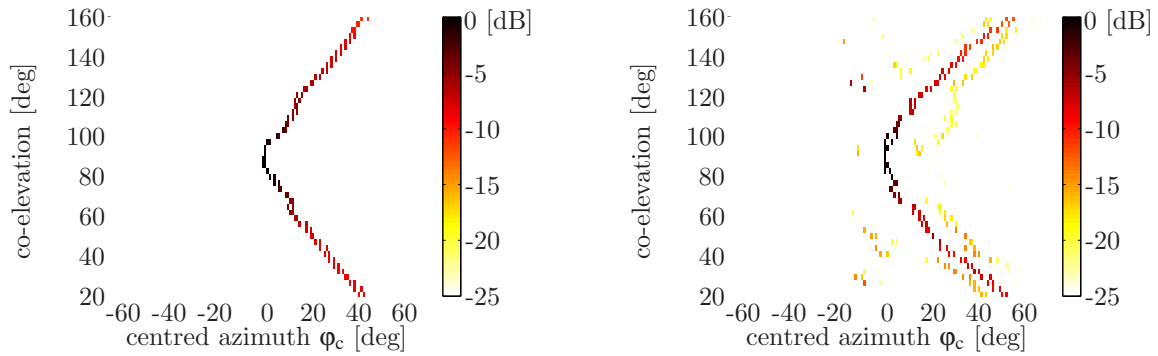
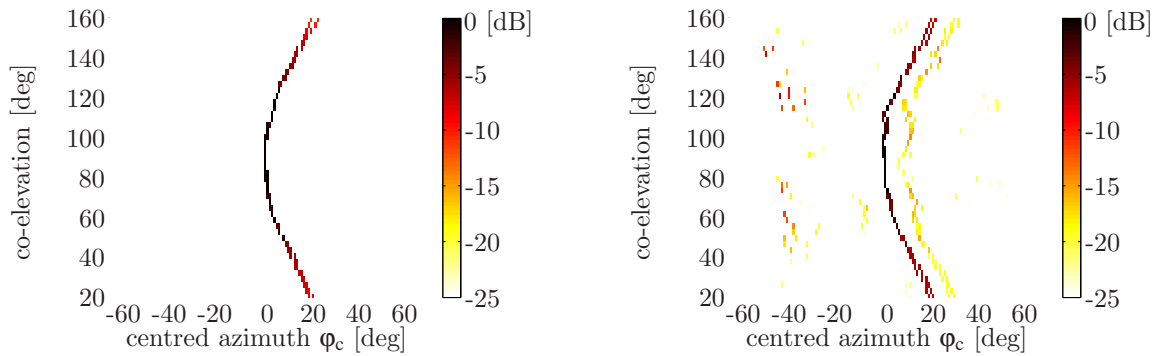
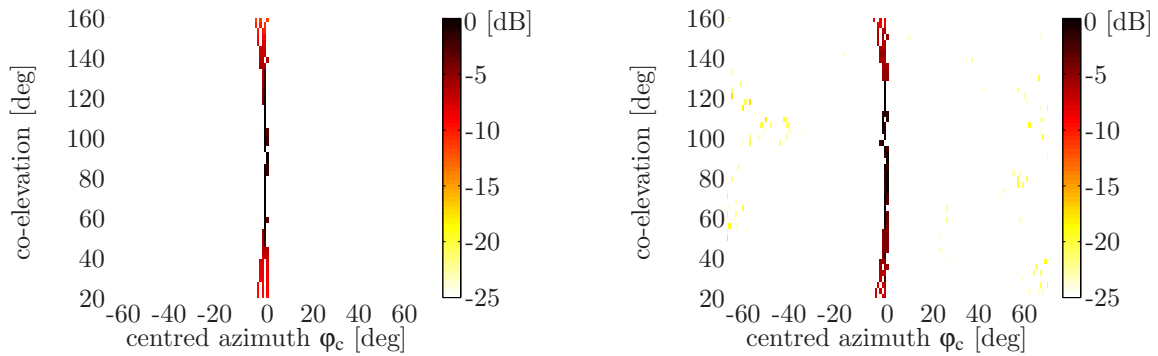


**Fig. 7.15:** Model accuracy as expressed in SRR, azimuth error, relative power of the path weights (relative to true path) using the full polarimetric 1D data model during estimation (horizontal and vertical excitation left and right side resp., PULPAx2x1x8,  $K_{\max} = 1$ )

estimation for multiple paths is allowed, upto  $K_{\max} = 10$ , as function of co-elevation and three different azimuth directions of the true paths (Fig. 7.16).

The results of the first analysis are shown as function of the azimuth and co-elevation of the true path, as the variation of the parameters to discuss is strongly dependent on the azimuth, due to the non-uniform behaviour of the array. From the SRR (top row Fig. 7.15) it can be seen that, if the highest accuracy of 25 dB (maximum accuracy of the calibration) is demanded, the 1D data model can only be used for a co-elevation range of  $\vartheta = 90^\circ \pm 5^\circ$  with azimuthal angles between  $\varphi = -70^\circ$  and  $\varphi = 70^\circ$ . For larger absolute azimuth angles and for co-elevation angles towards the poles, the model accuracy is decreasing, resulting in the estimation of additional but wrong paths. For a better visibility, the azimuth error in the second row of Fig. 7.15 is clipped to  $\pm 20^\circ$ . For SRRs better than 15 dB, the azimuth error is still small with around  $\pm 5^\circ$  (see also eqn. (7.16)). Although the azimuth angle can almost be estimated correct, the estimated path weights are strongly affected. Comparing the relative power of the co-polarised (third row) and cross-polarised path weights (fourth row), it is obvious that the power from a purely horizontal/vertical excitation will be distributed over both the co and cross-polar path weights. This means that the cross-polarised path weight becomes stronger (results in positive values of the relative power in dB), whereas the co-polarised path weight becomes weaker (results in negative values of the relative power in dB). Note that apart from being distributed over co- and cross-polar path weights, received power will also leak away into other paths due to the finite SRR. Based on Fig. 7.15, the valid azimuth range for practical purpose of the PULPAx2x1x8 is limited to approximately  $\varphi = \pm 70^\circ$ , even for a co-elevation of  $\vartheta = 90^\circ$ . With the second analysis ( $K_{\max} = 10$ ), the ambiguity with ULAs for angles symmetrically around the axis of the array can be easily demonstrated. In Fig. 7.16, the colour depicts the estimated power distributions centred around the true angle of arrival in azimuth for horizontally and for vertically polarised waves (to the left and right, respectively). Cases for three angles of incidence are shown,  $-70^\circ$ ,  $-35^\circ$ , and  $0^\circ$  in azimuth (from top to bottom) with co-elevation ranging from  $20^\circ$  to  $160^\circ$ . The picture is clipped at -25 dB, being the model accuracy as limited by calibration inaccuracies (as discussed in Section 7.2.1.2). The actually received power is normalised at 0 dB. With positive azimuth angles, mirror-imaged curves would result. The azimuthal cut for a constant co-elevation of  $\vartheta = 90^\circ$ , but full-polarimetric, was used as data model in the estimations. The effect of elevation on the bias of the angle estimation is obvious and is following eqn. (7.16). The larger spreads on the results for vertical polarisation arise from the larger non-uniformity of the array with elevation for vertical polarisation than for horizontal, caused by differences between antenna element characteristics and different influences that constructional parts of array have on the respective properties of the individual elements. From this larger non-uniformity, larger residuals in the estimation process result when the parameter estimator approximates responses from high-tilt angles with those modelled from the azimuthal plane, these residuals in turn being interpreted as separate components.

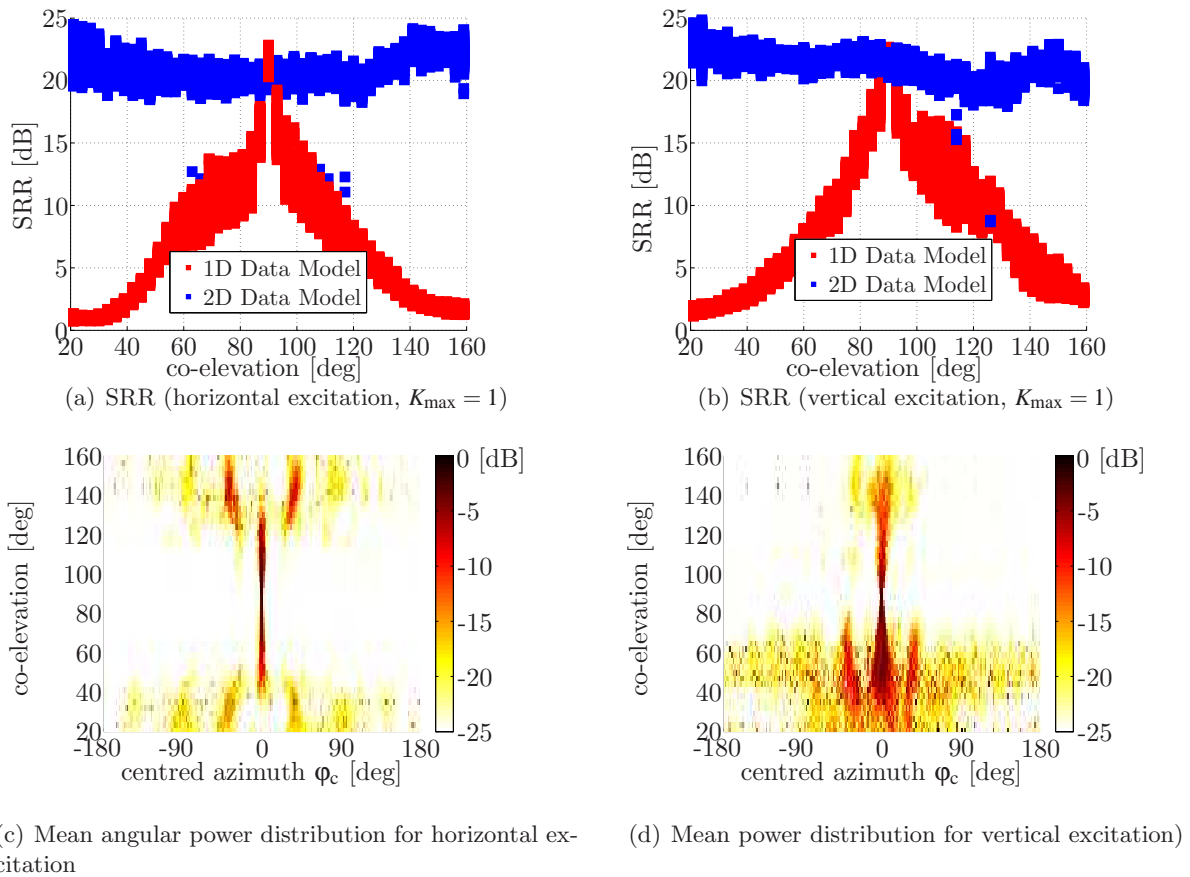
**Example UCAx1x1x16:** Earlier it was mentioned that the non-ambiguous phase variation over the array with co-elevation allows to estimate co-elevation but will on the other hand lead to estimation errors when not properly accounted for in the data model for the estimation. The following results

(a) Horizontal excitation, azimuth of the true path  $\varphi = -70^\circ$ (b) Vertical excitation, azimuth of the true path  $\varphi = -70^\circ$ (c) Horizontal excitation, azimuth of the true path  $\varphi = -35^\circ$ (d) Vertical excitation, azimuth of the true path  $\varphi = -35^\circ$ (e) Horizontal excitation, azimuth of the true path  $\varphi = 0^\circ$ (f) Vertical excitation, azimuth of the true path  $\varphi = 0^\circ$ 

**Fig. 7.16:** Power distributions of the  $K \leq 10$  estimated paths [dB] as function of the centred azimuth around the true path and co-elevation using the full polarimetric 1D data model of the PULPAx2x1x8 for  $\varphi = -70^\circ, -35^\circ, 0^\circ$  of the true path from top to bottom and for horizontal (left) and vertical excitation (right)



will illustrate this with measurements on the UCAX1x1x16. Again a single wave was received with the incidence angle ranging over full azimuth and elevation with its angle of incidence estimated on basis of a 1D data model (azimuthal cut only  $\vartheta = 90^\circ$ ). In order to preclude artefacts as to be described in the following paragraph, a full polarimetric model was used. For comparison the estimation is also performed based on the full polarimetric 2D data model. The results in terms of the mean model accuracy (SRR) from forcing the parameter estimator to estimate only one path are shown in the top row of Fig. 7.17 for using the 1D and 2D data model. Regarding the SRR, it is obvious that the model accuracy of the 1D data model drastically decreases for co-elevation angles towards the poles of the spherical coordinate system. Also the azimuth error of the single path, shown in Fig. 7.18(a), is increasing towards these co-elevation directions. The figures in the lower part of Fig. 7.17 depict the angular spectra for the case the maximum number of paths to be estimated is increased to 10. These figures are again clipped at -25 dB (being related to the



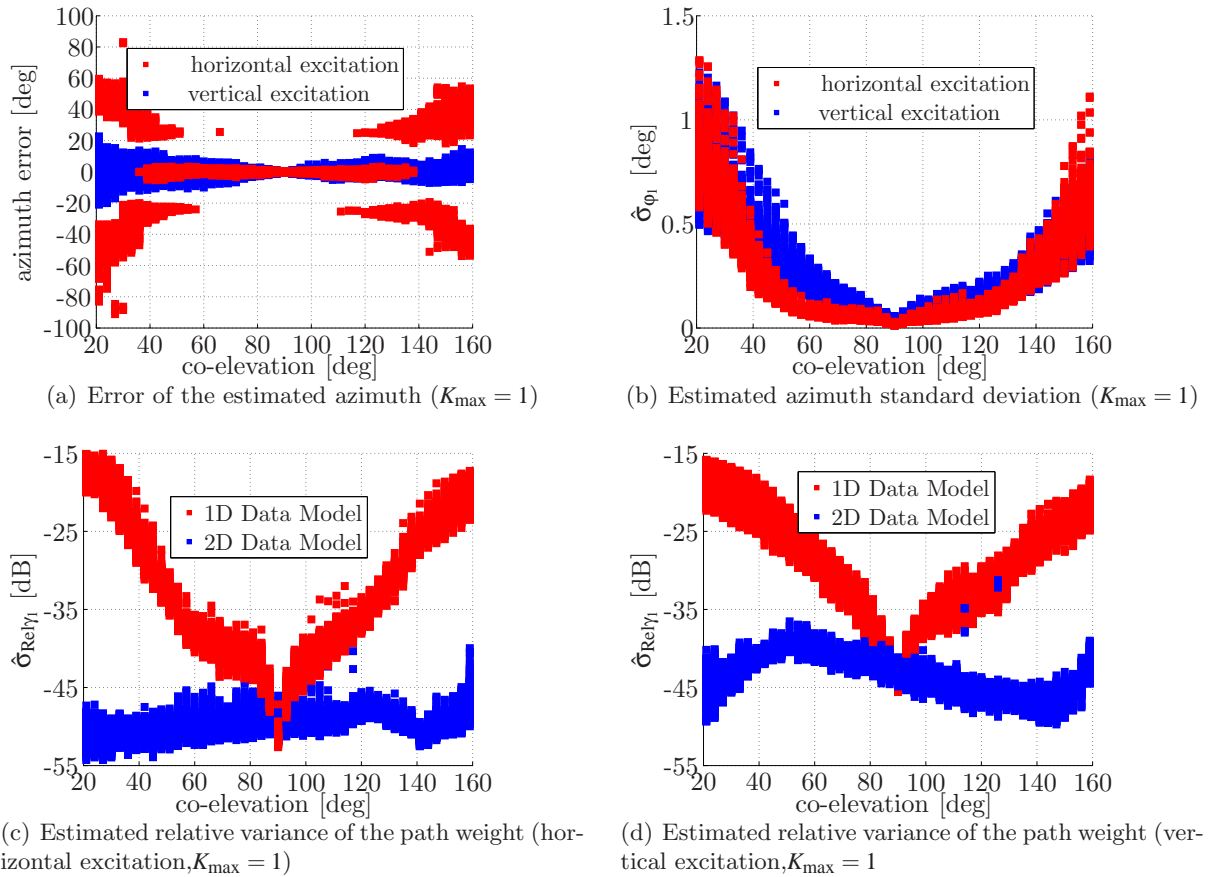
**Fig. 7.17:** Model accuracy as expressed in SRR (top) and estimated angular power distributions of  $K \leq 10$  paths (bottom) for UCAX1x1x16, using 1-D (full-polarimetric) data model (azimuthal cut). From left to right for horizontal and vertical excitation respectively.

model accuracy from antenna array calibration), with received power normalised at 0 dB. It shows that reception of a single discrete component renders a number of estimated discrete components distributed around the azimuthal angle of arrival. The larger asymmetry seen for the vertical polarisation can be understood from the interaction of the ground plate of the array with the changing direction of the electrical field with co-elevation. For horizontally polarised waves, the direction of

field does not change with co-elevation. As a conclusion, one does better not attempt to determine angular spreads, or cluster spreads for that matter, from parameters estimated with a **1D** data model, especially in fields with substantial specular power incident from higher elevational angles. Although the results are specific for this particular circular array, for instance with regard to the differences in artificial angular spreads between low elevation and high elevation incidence, it may be worthwhile to remark that the occurrence of considerable spreads itself, for small angles out of the azimuthal plane, is a generic effect for circular arrays. This effect is caused by the dissimilarity between the antenna response in the azimuthal plane ( $\vartheta = 90^\circ$ ) and the antenna responses for co-elevational incidence  $\vartheta \neq 90^\circ$ .

Although the errors are large enough to render estimation results useless, especially for the horizontal polarisation (see Fig. 7.18(a)) where large biases develop, the reliability check of the parameter estimation algorithm **RIMAX** [62] fails. The path is still considered as a valid one. The reason for that can be found in the reliability check procedure. The estimated relative variances of the path weights, as shown in the lower part of Fig. 7.18, which are derived on basis of the observation and the data model used, are taken as measure for the reliability. A path is considered to be reliable if the relative variance of the path weight is better than -3 dB. But the Figures 7.18(c) and 7.18(d) demonstrate that the estimated relative variance in case of using an incomplete data model are not an appropriate measure to check the reliability of the estimated paths. Even if the relative variance increases towards the poles of the spherical coordinate system, it still fulfils the condition of being better than -3 dB. Consequently, the path is assumed to be valid, even if the azimuth error (Fig. 7.18(a)) is rather large and the model accuracy as measured by the **SRR** is low. As Fig. 7.18(b) shows, even for a totally meaningless estimation result, the estimated variance of the estimated azimuth (Fig. 7.18(b)) is low. The estimated parameter variances (**CRLBs**), which are based on the incomplete data model, are meaningless. They are related to a model that matches the real channel only in case of  $\vartheta = 90^\circ$ . Consequently, the relative variances of the path weights are only appropriate as a reliability check, when an accurate and full polarimetric **2D** data model is used. For the sake of completeness the discussion about the reliability check was performed for the previous example. The conclusion will also apply for the other examples where incomplete data models are used. Therefore, I refrain from a explicit discussion for the other examples.

---



**Fig. 7.18:** Error of the estimated azimuth (a) and estimated azimuth standard deviation (b) for single path excitation and estimation (top row), estimated relative variance of the path weight of the single path for horizontal (c) and vertical (d) excitation where the full polarimetric 1D data model is used during estimation (UCAx1x1x16)

### 7.2.2.2 Ignoring Polarisation Characteristic

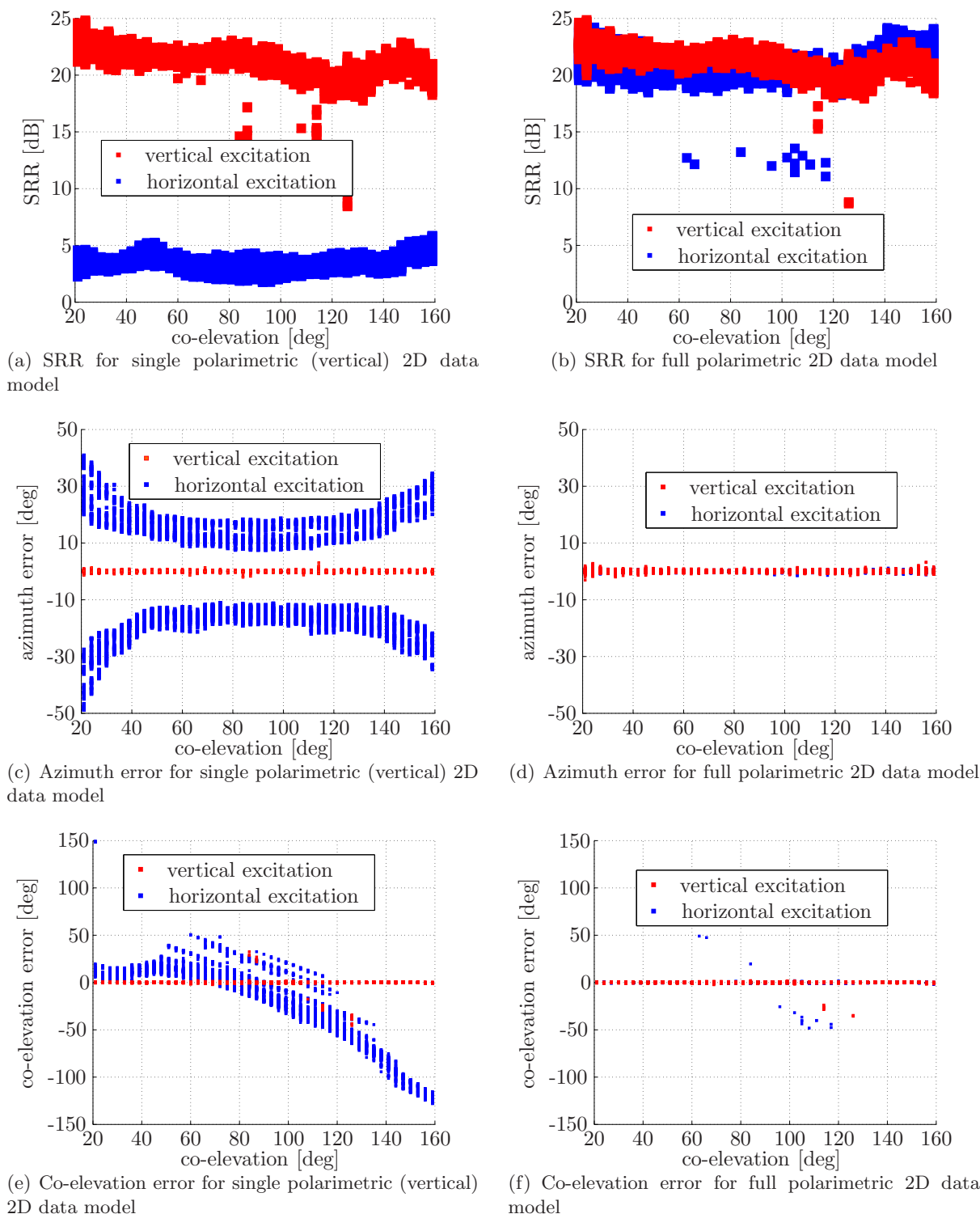
Despite the fact that radio waves are of vectorial nature, with two orthogonal polarisation components perpendicular to the propagation direction, traditionally only the vertical component has been considered in land-mobile radio communications. With the progress of technology, the mobile radio channel has changed character drastically:

1. Carrier frequency has gone up, from VHF-band to UHF and SHF, and scattering has become increasingly important. As a result:
  - the elevational range of incoming waves has enlarged, especially indoors and in case of over-rooftop propagation;
  - in many short-range communication scenarios the polarisations will be well-mixed with the power present in both polarisations of the same order of magnitude and little correlation between the fields of both polarisations.
2. With current handheld or portable mobile communication devices:

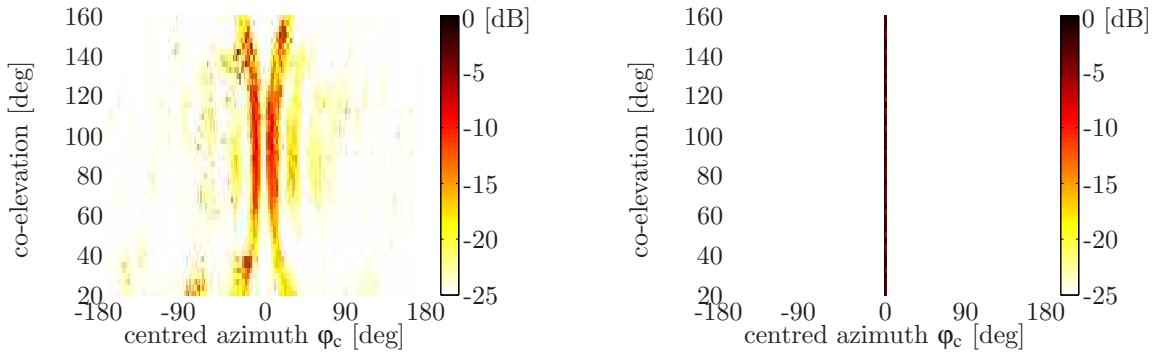
- the antennas show strong polarisation cross-talk (low cross-polar discrimination (XPD) figures), meaning these antennas will receive signal from any polarisation;
  - a fixed antenna orientation can not be guaranteed any longer.
3. For MIMO systems, the two polarisations may provide more or less independent transfers, depending on the scattering situation, offering a welcome increase of channel rank and therefore making modelling of it worthwhile.

But, all the above-mentioned points are ignored in measurements, characterisation, and modelling only a single polarisation is considered, as is often still the case (see the list of publications in the beginning of Section 7.2.2). Especially when applying parameter estimation, one should realise that for an ideal, but physically realisable antenna element, the responses to horizontally and vertically polarised fields can fundamentally never be identical. Consequently, the respective array responses can not be either and trying to estimate the direction of incidence for one of the polarisations based on a data model for the other will result in appreciable estimation errors. The next paragraph will illustrate this by a practical example.

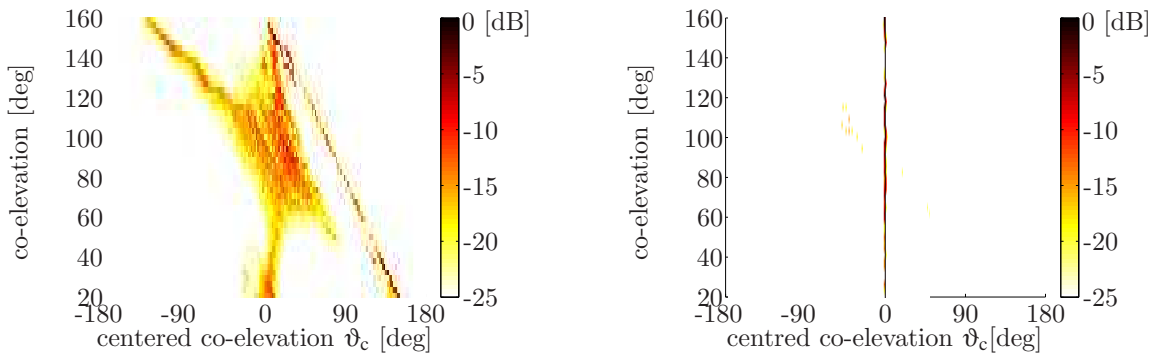
---



**Fig. 7.19:** Estimation results for UCAx1x16 with  $K_{\max} = 1$ , using the single polarimetric (vertical) 2D and full polarimetric 2D data model from left to right respectively.



(a) Single polarimetric vertical 2D data model, azimuth result (b) Full polarimetric 2D data model, azimuth result



(c) Single polarimetric vertical 2D data model, co-elevation result (d) Full polarimetric 2D data model, co-elevation result

**Fig. 7.20:** Comparison between parameter estimation using a vertical polarisation only data model (left) and a full-polarimetric data model (right) for reception of a single horizontally polarised path: mean estimated power of  $K \leq 10$  paths versus deviation from true angle in azimuth (top) or co-elevation (bottom) as function of co-elevation in dB.

**Example UCAX1x1x16:** The necessity of using a full polarimetric antenna model will become clear from the following comparison between using a full polarimetric 2D antenna model and a single polarisation 2D model during parameter estimation. By choosing 2D models, the effects described in the former paragraph are avoided. Again, the UCAX1x1x16 depicted in 2.14 with 16 monopoles was used for the comparison. Just to envision, the UCAX1x1x16 is almost equal sensitive for horizontal and vertical excitation, although the array was designed as a vertical receive array (reconsider the discussion of Section 4.3.1). In comparison to the full polarimetric 2D model in the following analysis, for the data model, vertical is chosen as the single polarisation direction, as the choice of a horizontal polarisation only model was never seen in literature, but this choice is not important. The incident field is thus chosen to be one horizontally or vertically polarised wave with its angle of incidence ranging over full azimuth and elevation. The results for the single path estimation using the single and full polarimetric 2D data model are shown on left and right side of Fig. 7.19 respectively. From the parameter SRR (top row) it is obvious, that in case of vertical excitation a single path can be estimated perfectly, within the array model accuracy of 20 dB to 25 dB, by using only the vertically 2D data model (Fig. 7.19(a)). The result of using the full polarimetric 2D data model (Fig. 7.19(b)) is almost identical. Furthermore, the azimuth and

co-elevation estimation errors for the vertical excitation are comparably low in both cases. But for a limited number of directions, a higher estimation error can be observed, caused by the ambiguity between the  $\vartheta = 0^\circ \dots 90^\circ$  range and the  $\vartheta = 90^\circ \dots 180^\circ$ . It is only due to an asymmetric behaviour of the antenna array with co-elevation that it is often possible to estimate the co-elevation angle accurately. The asymmetric behaviour is only caused by the mechanical construction of the antenna array. Note that such is not the case for an ideal UCA. From the estimation result for horizontal excitation it is obvious, that using only the vertical radiation pattern during estimation leads to a 20 dB worse SRR and model accuracy respectively. The SRR is only 5 dB, which means that using the incomplete data model allows us to subtract signal power to only -5 dB instead of up to -20 dB to -25 dB. Additionally, the estimated azimuth and co-elevation angles of the single path show biases up to  $50^\circ$  (see Fig. 7.19(c)).

Figure 7.20 shows the mean estimated angular power distributions for the  $K_{\max} \leq 10$  estimated paths. On the right-hand side, results for using the complete data model are shown (i.e. 2D full polarimetric), on the left-hand side those for using the vertical polarisation pattern only. The power distributions are given as function of the deviation from the true angle of arrival (upper row: relative in azimuth, lower row, relative in elevation), clipped at -25 dB like the earlier ones. This relative depicting (mean distributions) is possible as the variation in estimation errors over the absolute azimuth angle is small, due to the rather homogeneous response of the UCA. To the right, the estimated power is well concentrated around the true angle of arrival, both in azimuth and co-elevation with only little spurious. So, the intrinsic accuracy of the RIMAX procedure is high, when used with full-polarimetric data models. To the left, the results for using only the pattern for vertical polarisation show both a bias in azimuth (at the true azimuthal angle almost no power is found) and a large asymmetric bias in co-elevation. The asymmetry stems from the (vertically) asymmetric mechanical build-up of the UCAX1x1x16. The apparent angular spread caused by using a simplified data model, is considerable; be reminded that only a single discrete component was received. The particular shapes of the distributions in Fig. 7.20 are specific for the chosen array, the significant loss of accuracy in comparison with using a complete data model is not. One simply does not have control over the polarisation direction of incoming waves during measurements and with data models for a single polarisation at hand, estimation of components with the other polarisation is bound to yield errors of type described here. Only under restrictive conditions such estimation errors could remain small. That is, when one can be sure that the array only receives a single polarisation, either because the field has a single polarisation (corresponding with the data model) or because the XPD of the antenna elements is extremely high. The former is not so likely [3] and the latter is only true for very few antenna designs within a small range of angles of incidence.

### 7.2.2.3 Consequences of the “Plane Wave Assumption”

The plane-wave assumption has been used extensively in array signal processing, parameter estimation, and wireless channel modelling to simplify analysis. That the plane-wave assumption is not acceptable under certain circumstances has been shown in [131] based on channel capacity analysis of MIMO propagation channels. Indoor environments are discussed. The problem in such

environments stems from the short distance between the scattering points and the antenna arrays used in comparison to the wavelength.

However, parameter estimation algorithms that use specific array signal models such as **ESPRIT**, which relies on the shift invariance, assume that plane wave fronts impinging at the antenna array. Most **ML** estimation algorithms such as **EM**, **SAGE**, and **RIMAX** are more flexible in terms of the applied data models. They rely on calibration data for a fixed distance  $r_{\text{Calib}}$  (see also Chapter 4), which is limited by size of the anechoic chamber. But all algorithms have in common, that array calibrations are normally performed for a distance where the plane wave front assumption is fulfilled (considering certain accuracy). Nevertheless, in measurements it is often neglected that the plane wave front assumption is not fulfilled especially when the distance between the antenna array and the scatterer is much smaller than the calibration distance.

Only a few publications can be found (e.g. [61]), in which case the consequences of the wave curvature on estimation results by using the plane-wave model or a spherical-wave model are compared based on Ultra Wide-Band (**UWB**) anechoic chamber measurements. It is stated that with the plane wave assumption the probability of the estimation of spurious path is increasing. However, a full polarimetric radiation pattern modelling in combination with the modelling of the curvature  $r$  of the wave fronts was not given. Therefore, in [32] an antenna data model was proposed that incorporates both, the full polarimetric radiation pattern and the wave front curvature  $r$  of the incoming wave for *practical* antenna arrays. The *practical* antenna array SPUCPAx2x2x24 was used for demonstration.

**Considering the Wave Front Curvature for Simulation and Estimation:** In the previous sections only the calibration data for a fixed distance is used in simulation and estimation, as the modelling error is negligible for scatterer distances larger than the calibration distance  $r_{\text{Calib}}$ . This means that the model described in Section 3.1 was only applied for the fixed distance  $r_{\text{Calib}}$ , disregarding the true curvature  $r$  of the impinging wave front. In the following simulation and estimation, the described model will be used considering the true distance  $r$  of the scattering points or point source of the electrical field. Note that all simulations and investigations in the following are performed for a centre frequency of 5.2 GHz ( $\lambda = 5.77$  cm in free space) without further notification! Reconsidering eqn. (3.2), with the antenna response in an array being modelled by the phase term  $\mathbf{b}_{\text{ph}}$  and the radiation pattern  $\mathbf{b}_{\text{A}}$  being related to coordinate origin, shows that the error when using calibration data for a fixed distance is basically related to the phase term. The phase term eqn. (3.3) can be also written as:

$$\mathbf{b}_{\text{ph}}(\varphi, \vartheta, r, m) = e^{-j\frac{2\pi}{\lambda}\sqrt{\Delta x^2 + \Delta y^2 + \Delta z^2}} \quad (7.17)$$

$$\Delta x = r \sin(\vartheta) \cos(\varphi) - x_m \quad (7.18)$$

$$\Delta y = r \sin(\vartheta) \sin(\varphi) - y_m \quad (7.19)$$

$$\Delta z = r \cos(\vartheta) - z_m \quad (7.20)$$

where  $(x_m, y_m, z_m)$  specifies the position of the  $m$ -th element in the array compound and  $\lambda$  the wave length at the centre frequency. Consequently, this model requires the knowledge about the position

---

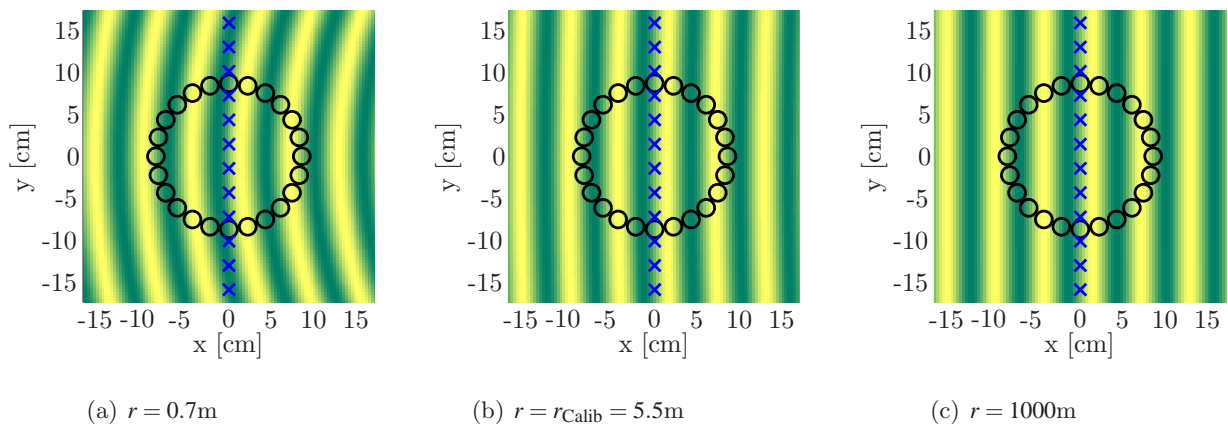


of the antenna element. For the non gradient based ML estimators such as SAGE this model is sufficient. As the gradient based estimation algorithm RIMAX is used in this thesis, the derivatives dependent on  $\varphi$ ,  $\vartheta$  and  $r$  are necessary too:

$$\begin{aligned}\frac{\partial \mathbf{b}}{\partial \varphi} &= \frac{\partial \mathbf{b}_A}{\partial \varphi} \cdot \mathbf{b}_{\text{ph}} + \frac{\partial \mathbf{b}_{\text{ph}}}{\partial \varphi} \cdot \mathbf{b}_A \\ \frac{\partial \mathbf{b}}{\partial \vartheta} &= \frac{\partial \mathbf{b}_A}{\partial \vartheta} \cdot \mathbf{b}_{\text{ph}} + \frac{\partial \mathbf{b}_{\text{ph}}}{\partial \vartheta} \cdot \mathbf{b}_A \\ \frac{\partial \mathbf{b}}{\partial r} &= \frac{\partial \mathbf{b}_{\text{ph}}}{\partial r} \cdot \mathbf{b}_{\text{ph}}.\end{aligned}\quad (7.21)$$

Note that the previous equations are based on vector valued functions  $\mathbf{b}$  for  $M_{\text{Rx}}$  or  $M_{\text{Tx}}$  antennas respectively. For notational convenience the derivatives of  $\frac{\partial \mathbf{b}_{\text{ph}}}{\partial \varphi}$  and  $\frac{\partial \mathbf{b}_{\text{ph}}}{\partial \vartheta}$  will not be given here. As for  $\mathbf{b}_A$  the EADF model is used, the corresponding derivatives can be easily calculated following the description in Section 3.3. In the following the described model will be either used to generate curvature dependent array responses, which are estimated with the fixed distance model or the model will be incorporated in the estimation algorithm.

**Wave Field and Model Error for Different Curvatures:** For a better understanding let us discuss the consequences of different source distances  $r$ , on the wave field and model error when using the fixed distance model for different angle of incidence and antenna position. In Fig. 7.21 the wave fields for 3 different distances  $r = 0.7$  m,  $r = r_{\text{Calib}} = 5.5$ m, which at the same time was used as calibration distance and  $r = 1000$ m for the DoA of  $\varphi = 0^\circ$ ,  $\vartheta = 90^\circ$  are shown. As an example, a 24 element circular array and a 12 element linear array are plotted in the wave fields. For the short distance the curvature of the wave fronts can be clearly seen, for the calibration distance and  $r = 1000$  m the wave field is quite similar and the impinging wave front is almost plane. From the shown wave field it is obvious that the phase distribution over an antenna array is changing dependent on the curvature  $r$ . For parameter estimation the resulting model error of the fixed



**Fig. 7.21:** Wave field around an exemplary 24 element circular (black) and 12 element linear antenna array (blue) for different wave front curvatures  $r$  for impinging wave from  $\varphi = 0^\circ$ ,  $\vartheta = 90^\circ$

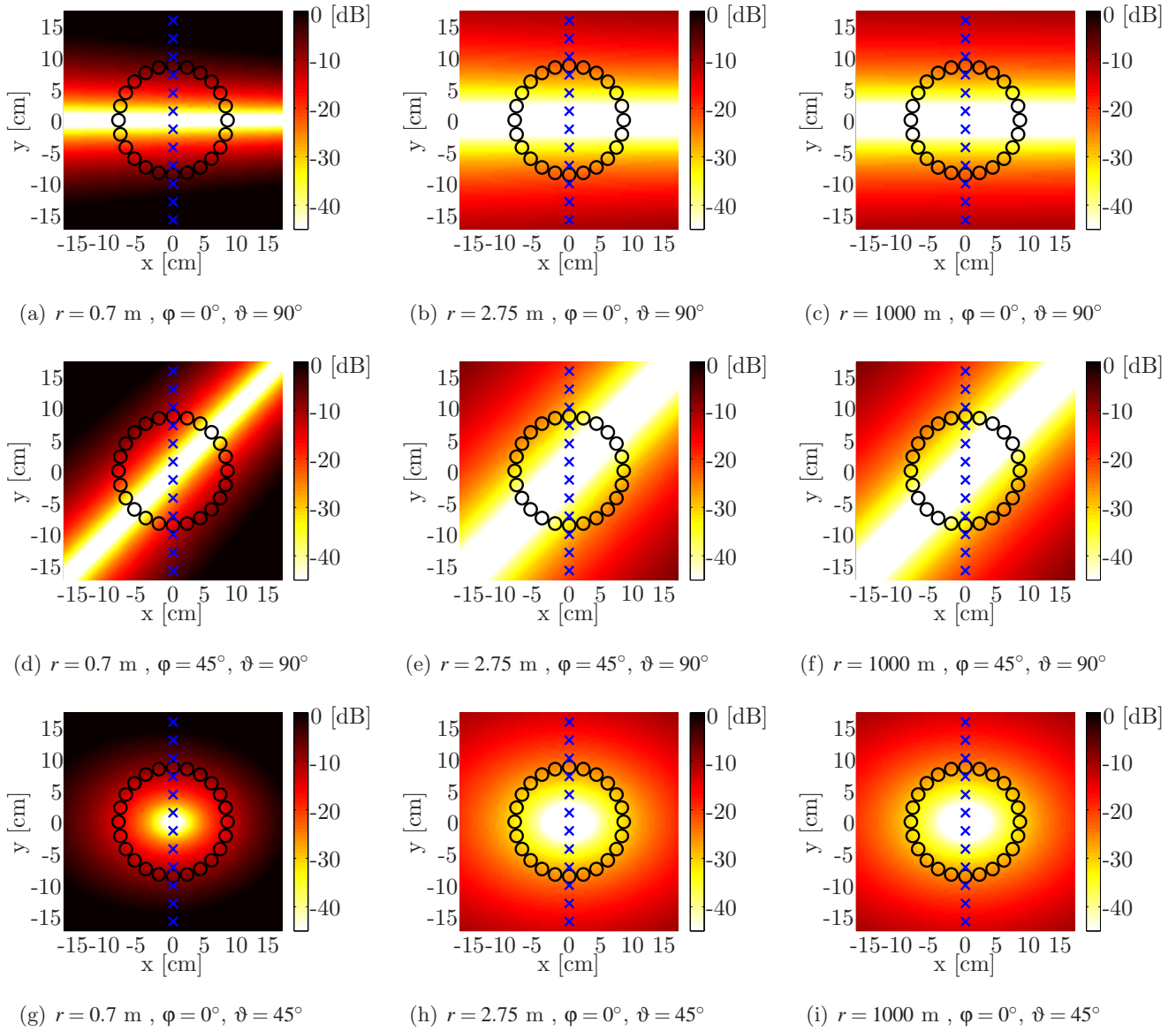
distance model for a certain antenna position:

$$\eta_{\text{Curv}}(\varphi, \vartheta, r_{\text{Calib}}, r, x_m, y_m, z_m) = \frac{b_{\text{ph}}(\varphi, \vartheta, r, x_m, y_m, z_m)}{b_{\text{ph}}(\varphi, \vartheta, r, x_0, y_0, z_0)} - \frac{b_{\text{ph}}(\varphi, \vartheta, r_{\text{Calib}}, x_m, y_m, z_m)}{b_{\text{ph}}(\varphi, \vartheta, r_{\text{Calib}}, x_0, y_0, z_0)} \quad (7.22)$$

is of major importance, as it will define the probability of estimating artefacts. The position  $x_0, y_0, z_0$  defines the centre of the antenna array used. In Fig. 7.22 the error  $\eta_{\text{Curv}}(r_{\text{Calib}} = 5.5 \text{ m})$  is shown in dB dependent on different curvatures  $r$  and DoAs. It can be seen that the error is strongly dependent on the position of the antenna element, the DoA, and the curvature  $r$  of the impinging waves. This will consequently result in the estimation of artificial paths.

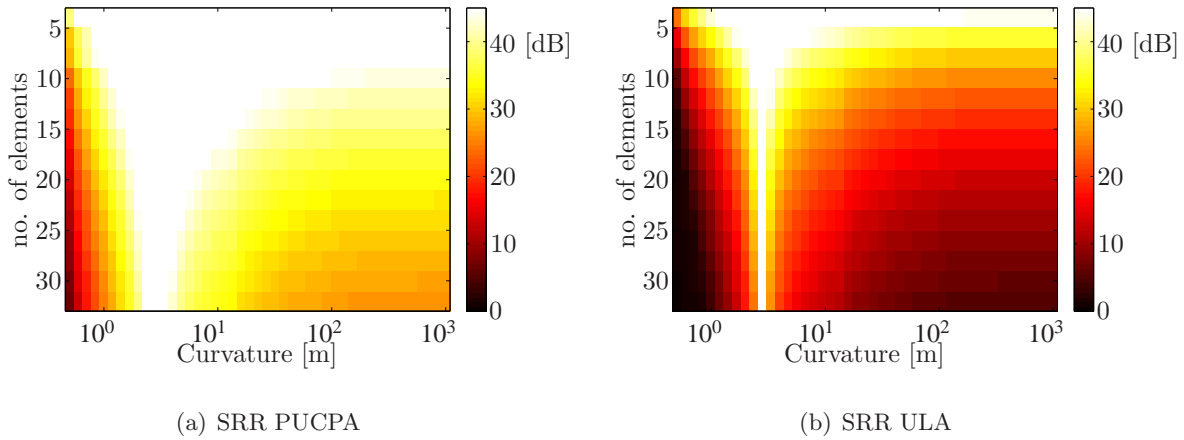
Observing the error characteristic over the antenna elements of the circular array dependent on the different azimuth angles, it can be seen that the characteristic is rotation-symmetric. Consequently, similar artificial estimated path distribution around the azimuth direction of the impinging wave can be expected for different azimuth angles for the circular array (assuming constant co-elevation angle and curvature). For the linear array, the error characteristic is not rotation-symmetric dependent on the azimuth. As opposed to the circular array, the distribution of the estimated artefacts will be strongly dependent on the azimuth angle of the impinging wave.

From the above discussion, it can be expected that the structure of the array has strong influence on the estimated distributions of artificial paths. However, from the error distribution shown it can be concluded that ignoring the curvature of the wave front is only acceptable under certain circumstances. It is dependent on the size, the structure of the antenna array, the DoAs of the incoming waves and the required model accuracy. From the error distributions it is obvious, that when neglecting the curvature for distances  $r \ll r_{\text{Calib}}$  (Example  $r = 0.7 \text{ m}$ ) the arrays need to be very small to achieve a model accuracy better than 20 dB. If the remaining curvature for the calibration distance is negligible (in terms of the model accuracy), than the curvature of the wave front for  $r > r_{\text{Calib}}$  can be neglected.



**Fig. 7.22:** Antenna position dependent model error  $\eta_{\text{Curv}}(r_{\text{Calib}} = 5.5 \text{ m})$  for different angles of incidence ( $\varphi$ ,  $\vartheta$ ) and distance  $r$  of a point source, when using a fixed distance data model with  $r_{\text{Calib}} = 5.5 \text{ m}$  during estimation. Exemplary a circular and a linear array are shown in the model error distributions.

**Consequences of Using Fixed Distance Calibration Data:** Again the simulated antenna arrays **PUCPA** and **ULA** will be used for demonstration. The consequences of using fixed distance calibration data with  $r_{\text{Calib}} = 5.5$  m for the estimation of a single path on the parameter estimation result will be discussed in the following. The **DoA** is chosen as  $\varphi = 0^\circ$  and  $\vartheta = 90^\circ$ , as this direction represents the worst case for the **PUCPA** and **ULA**. Only the parameter **SRR** as function of the number of elements and the curvature  $r$  of the impinging wave is analysed in Fig. 7.23, as the azimuth estimation error is negligible in case of the single path estimation. It can be seen that the resulting model error expressed as **SRR** is larger in case of the linear array. This stems from the fact that the maximum aperture size of the linear array with the same number of elements as a circular array is larger. Consequently, the outer elements of the array will be affected most by using the fixed distance calibration data, as the discrepancy between the assumed wave front and the true one is largest. It is obvious, that the range in which the fixed distance calibration data can be used assuming certain model accuracy is decreasing with the number of elements. Furthermore, it can be concluded that the model accuracy for curvatures larger than  $r_{\text{Calib}}$  is at least 30 dB for the antenna arrays used in this thesis (considering the size). However, it can be clearly seen that for curvatures smaller than the calibration distance the model error is increasing. For example, for measurements in indoor environments where scattering can be expected in a radius of 1 m and circular arrays larger than 25 elements or linear arrays larger than 6 elements are used, the model accuracy is below 25 dB.

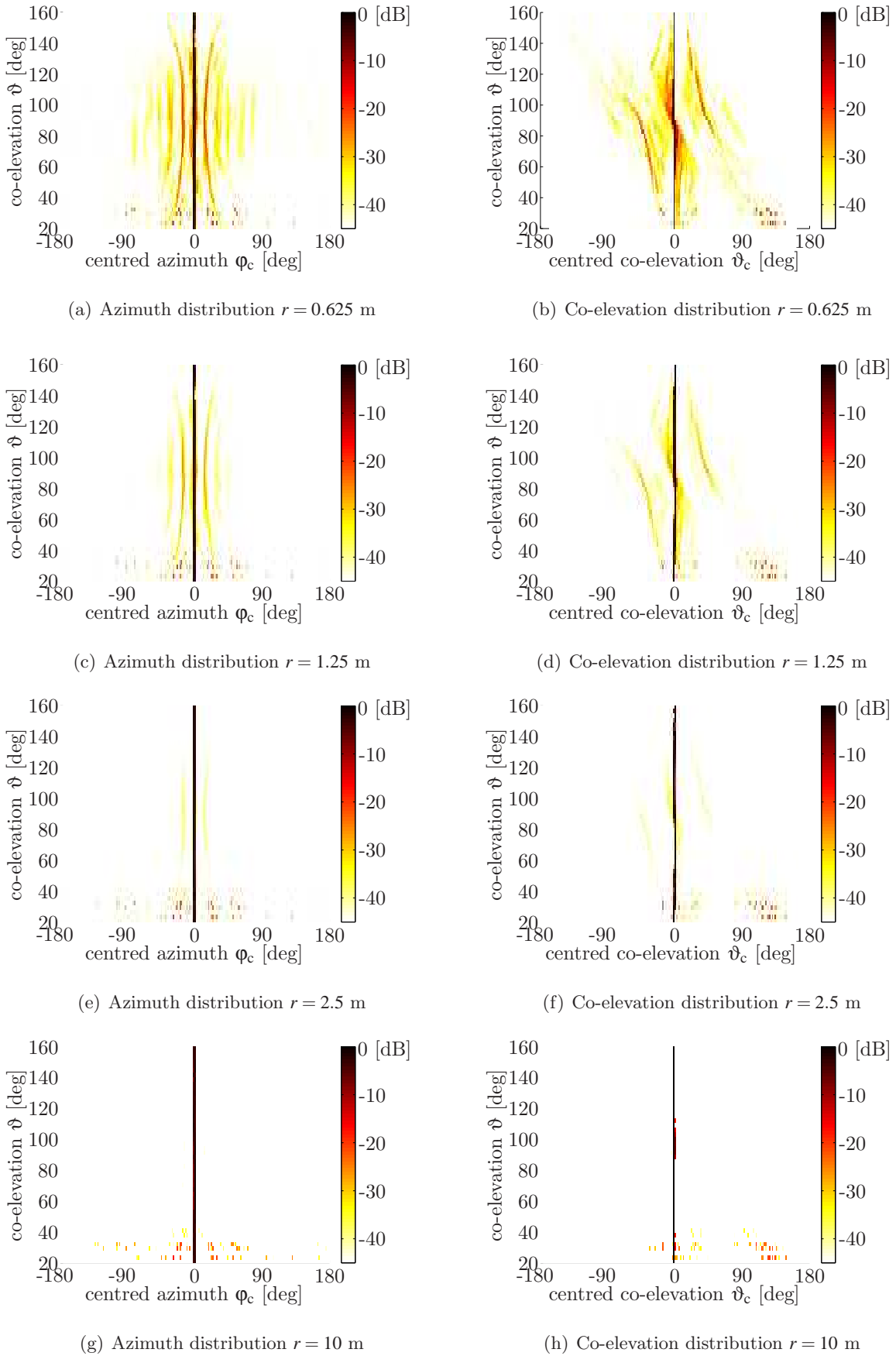


**Fig. 7.23:** SRR for single path excitation as function of the number of elements and the wave curvature  $r$ , when using a fixed distance array data model with  $r_{\text{Calib}} = 5.5$  m for the simulated arrays **PUCPA** (a) and **ULA** (b).

**Estimation of Artefacts when Using Fixed Distance Calibration Data:** As seen in the previous paragraph, the model accuracy using the fixed distance calibration data is strongly dependent on the distance  $r$  between the scattering point and the antenna array. Again with a low model accuracy artificial path distributions can be expected. The shape of the distribution is dependent on the array used, the **DoA**, and the curvature of the incoming wave. However, in the following the resulting mean angular power distributions will be shown for the circular array **PUCPASIMx2x1x24** only. Again the distributions are shown as function of centred azimuth/co-elevation and the co-

elevation of the true path. Scattering distances which will occur in a indoor measurement with  $r = 0.625, 1.25, 2.5$  m are chosen and for comparison also the results for a distance of  $r = 10$  m are shown. In Fig. 7.24 the distributions around the true angle by means of the centred azimuth (left) and centred co-elevation (right) are shown. For the curvatures 0.625 m and 1.25 m the estimated artefacts will definitely lead to a wrong interpretation of the propagation channel, whereas in the case of  $r = 2.5$  m it may be neglected for a  $\text{SNR}_{\text{IR}}$  worse than 30 dB. Note that in case of impinging multipath the probability of a constructive super position of the artefacts is increasing. Consequently, even for 2.5 m the curvature of the wave fronts should be considered during estimation to avoid the estimation of artefacts. However, for distances larger than the calibration distance  $r_{\text{Calib}} = 5.5$  m, the curvature of the wave front can be ignored (see distribution for  $r = 10$  m).

---

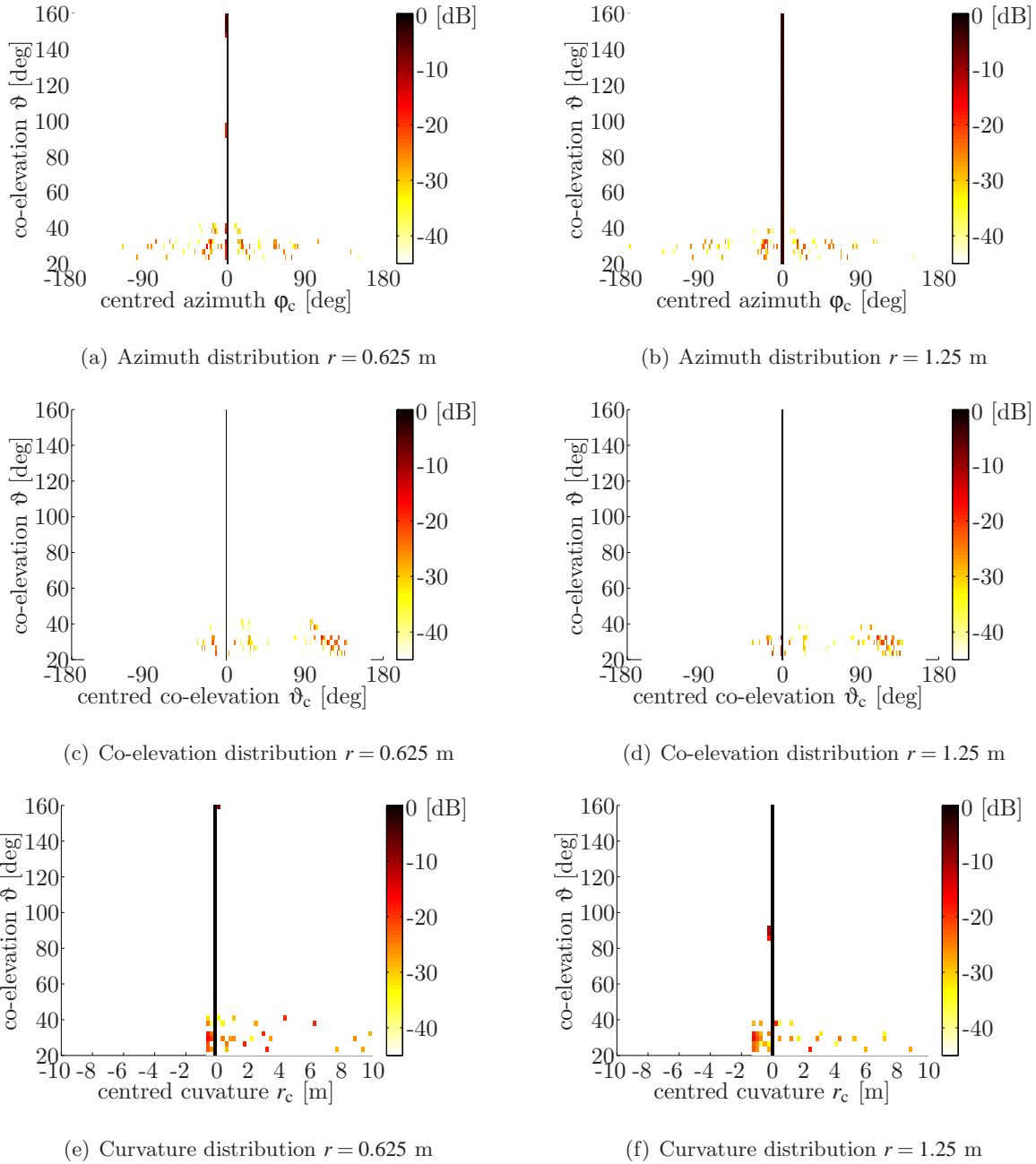


**Fig. 7.24:** Consequences of using a fixed distance data model ( $r_{\text{Calib}} = 5.5$  m): Distribution of estimated artefacts in azimuth (left) and co-elevation (right) for different curvatures  $r$  of the impinging wave on the PUCPASIM $_{2 \times 1 \times 24}$ .

**Solutions and Conclusions:** Ignoring the curvature of the wave front especially in indoor environments (for the discussed frequency!) will lead to insufficient estimation results (estimation of artefacts). For scenarios with scattering distances larger than the chosen calibration distance of  $r_{\text{Calib}} = 5.5$  m the model accuracy using the fixed distance calibration data is sufficient (30 dB to 40 dB).

To avoid the estimation of physical meaningless path distributions in indoor environments one could reduce the calibration distance, which results in an increased model accuracy when the scattering distance is similar to the calibration distance. With this approach the plane-wave front assumption for the calibration distance is not given. Consequently, the model accuracy will decrease for wave fronts with a larger curvature than the curvature of the reduced calibration distance. However, if only curvatures around  $r_{\text{Calib}}$  are expected, this would be the most appropriate choice if a low complexity and robustness of the estimation algorithm is of importance.

Another choice is to incorporate the estimation of the wave front curvature in the estimation algorithm. Therefore, the model of the radio channel for parameter estimation is extended by applying the equations (3.2), (7.20), and (7.21)). Consequently, the estimation model of the **RIMAX** is extended and the additional parameter curvature is estimate with the same approach as used for the estimation of the other parameters of the radio channel (see Section 5.2). In Fig. 7.25 the path distributions for  $r = 0.625$  m and  $r = 1.25$  m are shown when considering the wave front curvature in the **RIMAX** estimation algorithm. It can be seen that in comparison to the results of using only the fixed distance calibration data (Fig. 7.24) almost no artificial paths are estimated. Only for co-elevation angles towards the North Pole of the spherical coordinate system the power of the artificial path is increasing. The degradation is related to the existing ambiguity between co-elevation angles smaller and larger  $90^\circ$ , which becomes for this array especially apparent for co-elevation angles towards the North Pole. The performance of the **RIMAX** algorithm incorporating the estimation of the wave front curvature, has been only shown for the PUCPax2x1x24. Note, further investigations with respect to the robustness of this “extended” **RIMAX** version, for example for different array types and multipath scenarios are necessary, but will not be discussed here.



**Fig. 7.25:** Using extended data model incorporating the wave front curvature for estimation: Distribution of estimated artefacts in azimuth, co-elevation and curvature from top to bottom for  $r = 0.625$  m (left) and  $r = 1.25$  m (right) for the PUCPASIMx2x1x24.



#### 7.2.2.4 Concluding Remarks on Systematic Error Due to Incomplete Data Models

The use of linear arrays in measurements for channel characterisation poses a problem due to the inherent directional ambiguity of its response to which no solution exists. Only in cases of fields with angles of incidence confined to or close to the azimuthal plane (respectively a particular reference plane through the array line) estimation results can be trusted. The main effect will be an elevation-dependent bias.

The front-back ambiguity can be partially remedied by shaping antenna element patterns such that the sensitivity for one half-plane is greatly reduced. With patch elements, only 10 to 20 dB front-to-back discrimination can be achieved. A reduction of the field of vision by excluding critical angle of arrivals, where bias is largest, through putting a collimator in front of the array is currently investigated (results will not be included in this thesis). This is a principal choice when using an **ULA**, either correctly measuring and analysing only a part of the existing field or trying to register as many components as possible while taking the risk on distorted results.

While the bias with linear arrays stems from the lack of aperture in elevation, it is the changing aperture with elevation that causes the bias and spread with arrays with more than one spatial dimension, like the circular one (**UCA** $1 \times 1 \times 16$ ) used in these investigations, when not considered in the data model. This is an inherent effect too, but it can be avoided when using the full-polarimetric **2D** data model.

Another important result presented here is that ignoring the full polarisation characteristic of the antenna elements can produce serious artefacts too, both in terms of spreads and bias. Again, this is an inherent phenomenon. As with the other results, how these effects will manifest themselves depends on the particular measurement scenario and arrays.

Just as a contrast, it was shown that for the single path scenarios considered in this section, applying full-polarimetric **2D** data models renders very accurate estimates (shown for **UCA** $1 \times 1 \times 16$ ).

As mentioned earlier, in scenarios in which the elevational range of incoming or exiting waves is limited, without much cross-polarising scattering, the effects of using simplified data models do not degrade estimation accuracy seriously. These could be the less interesting scenarios, though, like an elevated base station in rural environments. On the other hand, for indoor scenarios, especially outside **LoS**, where rich scattering is to be expected with potentially many components out of the azimuthal plane ( $\vartheta = 90^\circ$ ), the use of full-polarimetric data models incorporating the elevational array characteristics is essential.

Furthermore, it has been shown that ignoring the curvature of the wave fronts is uncritical for outdoor measurements; the resulting systematic error is rather small. Especially for indoor scenarios and antenna arrays with a larger aperture it is not. Therefore, an estimation of the wave front curvature of each path should be considered for indoor scenarios. In an example it was shown, that such an algorithm, which is considering the curvature of the wave front in the estimation process, can greatly reduce the probability of estimating artificial path distributions. However, further investigations are necessary if one wants to apply this algorithm to various kinds of antenna arrays and measurements.

---

### 7.3 System Related Consequences

This section focuses on error sources related to the measurement system. In Section 2.3 several system properties that have an influence on the achievable estimation accuracy are discussed. In the following the discussion will be mainly related to the topic “Phase Noise” (Section 7.3.1). Only a brief discussion is related to the consequence of an unsuitable arranged and calibrated external LNA in the RF signal path. The aspect of receiver sensitivity will not be discussed here, as the consequences on the parameter estimation results can be described in terms of the CRLB as shown in Chapter 6.

#### 7.3.1 Consequence of Phase Noise on the DoD/DoA Estimation

Basically, the phase distribution over an antenna array for a certain direction of the incoming wave allows us to estimate their DoD/DoA. Therefore, knowing the consequences of phase noise on the parameter estimation are of major importance in evaluating any parameter estimation results. Only a few publications can be found related to this topic in combination with parameter estimation, which basically do not completely cover all relevant aspects [85, 86].

As described in Section 2.3.4, the effect of phase noise can be separated into two parts, the long term phase drift  $\varphi_{\text{pnL}}$  and the phase noise  $\varphi_{\text{pnS}}$ , which can be modeled as a (correlated/uncorrelated) Gaussian stationary process with zero mean and  $\sigma_{\text{pnS}}^2$  variance. For the measurement time of one snapshot  $t_s = 2 \cdot M_{\text{Rx}} \cdot M_{\text{Tx}} \cdot \tau_{\text{max}}$  the long term phase drift can be approximated by a linear function with the gradient  $\Delta\varphi_{\text{pnL}} \left[ \frac{\text{deg}}{\text{s}} \right]$ .

The consequences of the long term phase drift will be demonstrated for different array types of simulated and *practical* antenna arrays in Section 7.3.1.1. Even so the estimation accuracy is decreasing for larger  $\Delta\varphi_{\text{pnL}}$ , it will be shown in Section 7.3.1.2 that the impact of the phase noise on parameter estimation result is by far larger.

The impact of the phase noise is fundamentally different to the additive i.i.d. Gaussian measurement noise. In case of the additive measurement noise only the variance of the estimated parameters will increase with a worse SNR, but only noise power will remain after the estimation process. For the phase noise (multiplicative noise) not only an increased parameter variance is expected. The subtraction of the estimated array response from the observation correct in phase and magnitude is impossible, as the phase noise is of stochastic character. Opposed to the additive measurement noise, signal power will remain after subtraction of the estimated array response in the presence of phase noise. That means the resulting model accuracy is lower than the available  $\text{SNR}_{\text{IR}}$ . As demonstrated in the previous section for the other error sources, consequently also the effect of the phase noise will result in an estimation of artefacts, which will be presented in Section 7.3.1.3.

##### 7.3.1.1 Long Term Phase Drift

The consequences of the long term phase drift (random walk phase) on the parameter estimation results are basically dependent on the array type, number of elements, the switching scheme of the

antenna elements and the chosen impulse response length. The gradient of the phase change  $\Delta\phi_{\text{pnL}}$  itself depends on the quality of the synchronization between the Tx 10 MHz reference and the Rx 10 MHz reference (see Section 2.3.4). Note that the effect of a linear long term phase drift can not be distinguished from a Doppler shift. Consequently, the results are also valid for the case that the data and estimation model does not incorporate a Doppler shift over the antennas.

Obviously, it makes a difference if an antenna array is used as Tx or Rx antenna array, as the time between switching from one antenna element to the next antenna element of the array is  $2 \cdot M_{\text{Rx}} \cdot \tau_{\text{max}}$  or  $2 \cdot \tau_{\text{max}}$  respectively. The following investigations are carried out for an impulse response length of  $\tau_{\text{max}} = 3.2\mu\text{s}$  and Rx arrays only. Furthermore, the elements are switched corresponding to their geometrical arrangement. That means that always the closest antenna port (independent from its polarisation) will be switched next. Note that the results for a Tx antenna array or another impulse response length can be deduced from the Rx results. For example, the Tx phase gradient  $\Delta\phi_{\text{pnL,Tx}}$  corresponds to the phase gradient at Rx  $\Delta\phi_{\text{pnL,Rx}}$  multiplied with the number of Rx antennas. Herewith, the phase gradient at the Tx side is defined as:

$$\Delta\phi_{\text{pnL,Tx}} = M_{\text{Rx}} \cdot \Delta\phi_{\text{pnL,Rx}}. \quad (7.23)$$

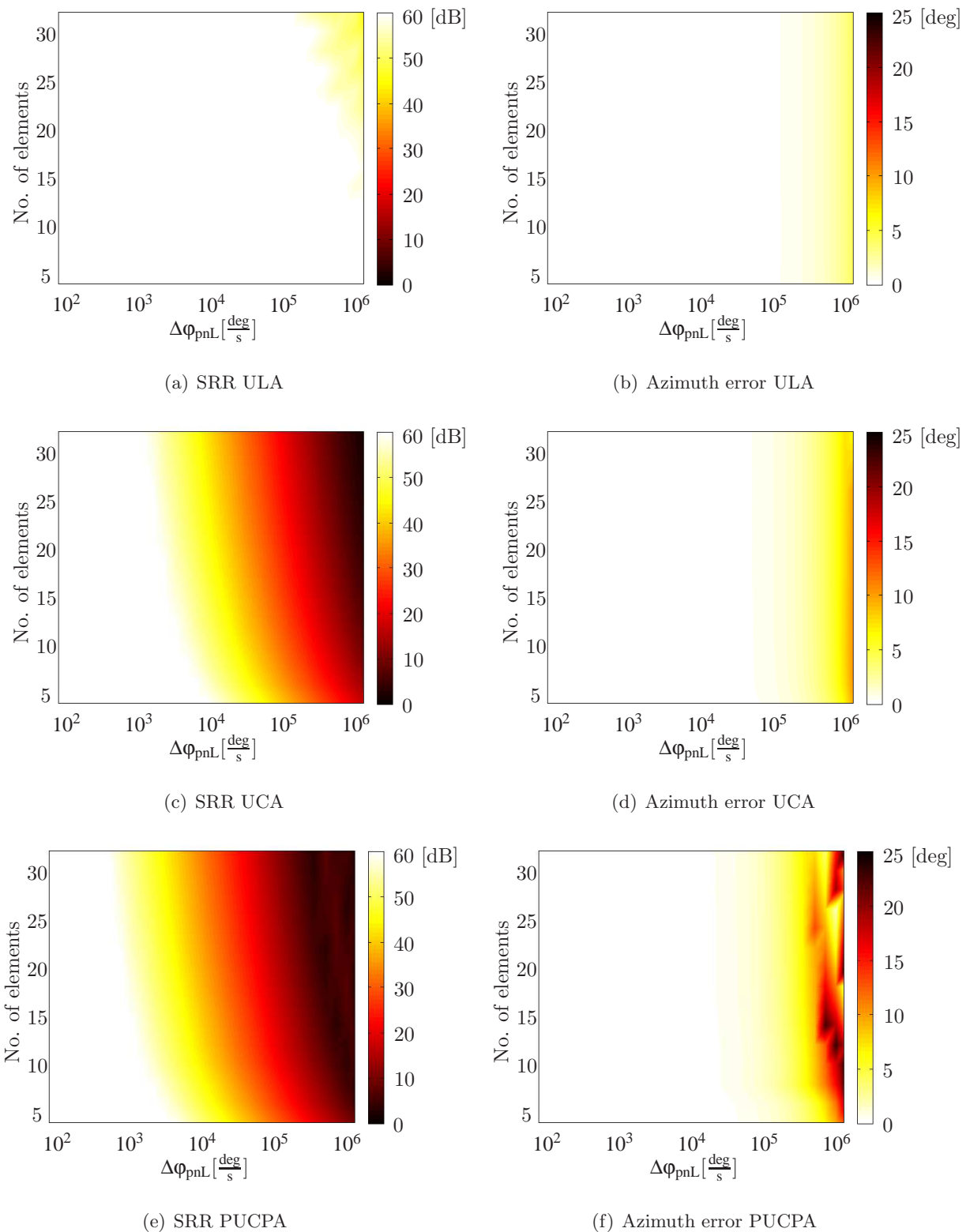
**Simulated antenna arrays:** The impact of long term phase drift for three different simulated antenna arrays by means of a **ULA**, a **UCA** and a **PUCPA** are presented dependent on the number of elements and the phase gradient  $\Delta\phi_{\text{pnL,Rx}}$  from top to bottom in Fig. 7.26. In the simulation only a single path was received from the direction  $\varphi = 0^\circ$  and  $\vartheta = 90^\circ$ , as the ideal arrays are almost uniform in azimuth. From left to right the estimation results of the single path estimation in terms of the achievable **SRR** and azimuth error are shown. Note that for the **ULA** and **UCA** omnidirectional antennas are assumed. In case of the **PUCPA** polarimetric patch antennas are used, each antenna has two output ports with the designated polarisation horizontal and vertical respectively. Herewith, the **PUCPA** with 24 elements has  $M_{\text{Rx}} = 48$  output ports in comparison to only  $M_{\text{Rx}} = 24$  output ports of the **UCA** with the same array size.

The **ULA** shows the best performance, that means even for a large phase drift and large number of elements the azimuth error is still low and the signal power, which can be modelled by a single path (shown with **SRR**) is in most cases better than 50 dB. The reason for that can be found in the linear phase over the antenna elements (see also eqn. (7.15)). Consequently, a slightly different estimated azimuth angle (see also the azimuth error in Fig. 7.26(b)) will match the array response in the presence of a linear long term phase drift. Note that changing the switching scheme of the antennas the result will be different, as the phase distribution is not necessarily linear over the antenna elements.

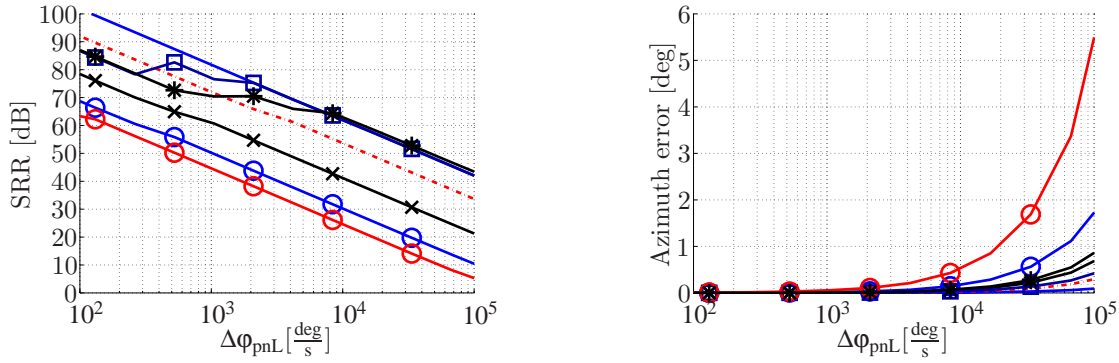
For the **UCA** and **PUCPA** it can be observed, that even though the azimuth error is still low, the **SRR** is already large. The reason for that is again the phase distribution over the antenna elements, which is sinusoidal in case of circular arrays (see also Fig. 7.14). Therefore, the **UCA** and **PUCPA** model can not approximate a linear phase drift over the antenna elements by a slightly deviated azimuth angle. Consequently, the **SRR** will decrease for larger phase gradients  $\Delta\phi_{\text{pnL,Rx}}$ . Furthermore, the **SRR** is decreasing for a larger number of elements as the total snapshot time  $t_s$  is

increasing. As the PUCPA has two times more output ports considering the same array size (number of elements), the results are comparable to an UCA with the double number of elements. Only the azimuth error is varying more for the PUCPA, as directional polarimetric radiation patterns were used in simulation.

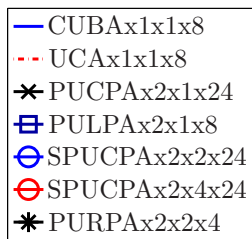
**Practical antenna arrays:** A set of *practical* antenna arrays of different type and number of elements is investigated (Fig. 7.27) in the following. Again a single path is received from the direction  $\varphi = 0^\circ$  and  $\vartheta = 90^\circ$ . The legend in Fig. 7.31(c) specifies the antenna arrays used. The CUBAx1x1x8 is an exception, as its angular resolution is based on the directional information of the radiation pattern, which should not include a phase difference between elements. All other arrays basically take gain from the phase differences between the elements to resolve the direction. The impact on the estimation result can be clearly seen by comparing the 8 element CUBA with the 8 element UCA. As the CUBA does not rely on the phase information the SRR is better in presence of the same long term phase drift (Fig. 7.27(a)). Again it can be observed, that the impact of the phase drift on the linear and planar arrays is smaller than for circular arrays of the same size (number of elements) in terms of SRR as well as azimuth error (Fig. 7.27(b)). The degradation of the accuracy with increasing number of elements seen for the 3 arrays with same diameter (24 elements at one ring) from PUCPax2x1x24 (1 ring) to SPUCPax2x4x24 (4 rings) definitely shows, that the impact of the phase drift can not be neglected, especially in the presence of larger phase gradients. For example in case of the SPUCPax2x4x24 ( $M_{Rx} = 192$ ) the consequences can not be neglected for phase gradients larger than  $10^3 \left[ \frac{\text{deg}}{\text{s}} \right]$ .



**Fig. 7.26:** Consequences of long term phase drift  $\Delta\phi_{pnL}$  in terms of **SRR** (left) and azimuth error (right) as function of the No. of elements in case of single path excitation and estimation for the simulated antenna arrays **ULA**, **UCA** and **PUCPA** from top to bottom



(a) SRR for a set of practical antenna arrays (b) Azimuth error for a set of practical antenna arrays



(c) Legend

**Fig. 7.27:** Consequences of long term phase drift for a set of practical antenna arrays (c) expressed as SRR (a) and azimuth error (b) in case of single path excitation and estimation

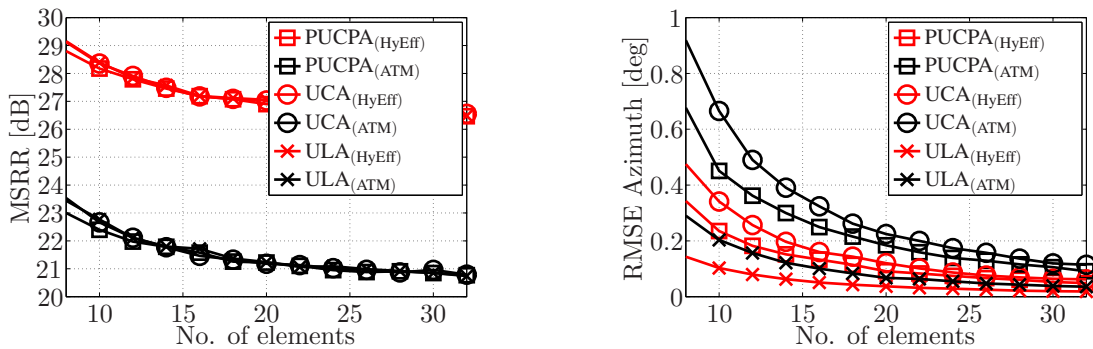
### 7.3.1.2 Phase Noise

The consequences of phase noise will be discussed for simulated and *practical* antenna arrays. Mostly the investigations will be related to the measurement systems used. The corresponding system properties such as standard deviation  $\sigma_{pn,S}$  and phase correlation (estimated covariance matrix of phase noise process) of the phase noise are taken from the analysis in Section 2.3.4. Again the simulations assume a single path excitation only, the dependencies are discussed with respect to one parameter only, whereas all other parameters remain constant. The following dependencies from top to bottom will be considered:

- Array type and size in case of uncorrelated phase noise ( $\varphi = 0^\circ$ ,  $\vartheta = 90^\circ$ , ATM,HyEff system)
- Array type and size, where the consequences of correlated and uncorrelated phase noise are compared ( $\varphi = 0^\circ$ ,  $\vartheta = 90^\circ$ , HyEff system)
- Phase noise standard deviation  $\sigma_{pn,S}$  ( $\varphi = 0^\circ$ ,  $\vartheta = 90^\circ$ )
- Azimuth direction of the true path ( $\vartheta = 90^\circ$ , HyEff system)
- Co-elevation direction of the true path ( $\varphi = 0^\circ$ , HyEff system)

If no *practical* antenna arrays are available to show the phase noise consequences dependent on a certain parameter, then simulated arrays (**ULA**, **UCA** and **PUCPA**) are used. Otherwise a set of *practical* antennas are used. As the phase noise is a stochastic process and expectation values are needed, 1000 independent realisations are generated and estimated. The estimation results are consequently analysed in terms of Mean SRR (**MSRR**), Root Mean Square Error (**RMSE**) of the estimated azimuth and co-elevation angle.

**Array Size and Type, consequences of Uncorrelated and Correlated Phase Noise:** First, only the consequences of uncorrelated phase noise will be discussed, the standard deviations of the ATM and HyEff systems are considered. The results are shown in Fig. 7.28. Analysing the mean **SRR** (Fig. 7.28(a)) almost no differences can be found between the arrays used. However, with increasing number of elements (array size) the **SRR** is decreasing, but with a difference of only 1 dB for a doubling of the elements. By far more critical is the decreasing **SRR** for a larger standard deviation of the phase noise, which can be seen by comparing the results of the ATM system (black,  $\sigma_{\text{pns}} = 5.69^\circ$ ) and HyEff system (red,  $\sigma_{\text{pns}} = 2.94^\circ$ ). The **SRR** for the ATM is around 6 dB lower than in the case of the HyEff, which can be related to a two times larger standard deviation of the ATM phase noise respectively. Herewith, the model error in case of the ATM is even larger than the error caused by some of the antenna related systematic errors (see Section 7.2). For the **RMSE** of the azimuth (Fig. 7.28(b)), it can be concluded that with increasing array size the error is decreasing. This is similar to the effect of a decreasing **CRLB** of the azimuth angle with larger antenna arrays (see Appendix D). Again it can be seen, that also in case of the phase noise the consequences on the **ULA** azimuth estimation error are smaller than for the other array types, which is basically related to the phase distribution over the antenna array. Furthermore, the azimuth **RMSE** of the **PUCPA** is smaller than the one of the **UCA**, as it has actually the double number of ports compared to the **UCA** of the same size. As an estimated covariance matrix of the phase noise process is known



(a) Mean **SRR** in presence of uncorrelated phase noise for the ATM (black) and HyEff (red) system

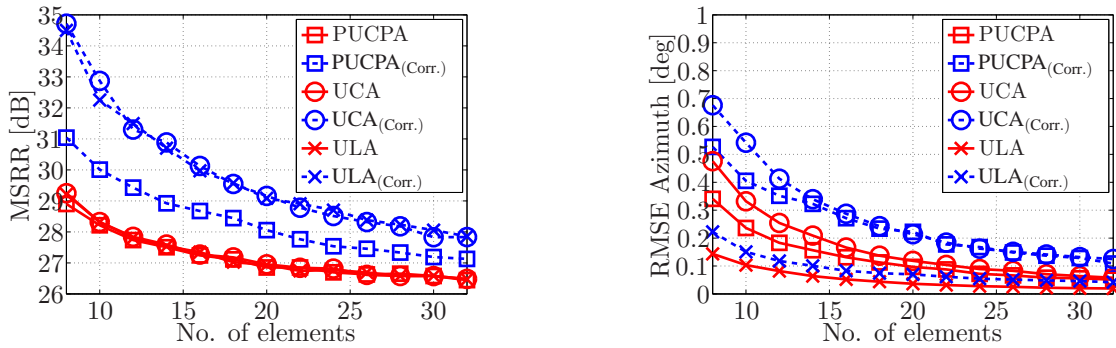
(b) **RMSE** azimuth in presence of uncorrelated phase noise for the ATM (black) and HyEff (red) system

**Fig. 7.28:** Consequences of phase noise (uncorrelated) on the estimation results for the simulated antenna arrays **ULA**, **UCA**, **PUCPA** for single path excitation and estimation: **SRR** (left) and azimuth error (right) as function of the number of elements.

for both systems used (see Section 2.3.4 and Appendix A.1 eqn. (A.5)), in the following the same analysis as for the uncorrelated phase noise is performed for correlated phase noise with same



phase noise standard deviation. The discussion is limited to the HyEff system, as comparable results were found for the ATM system. In Fig. 7.29 the consequences of correlated (blue) and uncorrelated (black) phase noise are shown. The effect of the correlation results in a slightly larger model accuracy (MSRR) for all array types with the disadvantage of an increased azimuth RMSE. This means that the correlated phase noise matches the array response for a different angle than the true one and consequently the model accuracy is increasing with the disadvantage of a biased angular estimation result. In [86] it was shown, that the effect of the correlation can be reduced by correcting for the known phase correlation. That means, that the RMSE of the angular parameters could be improved. However, it was not discussed, that this will result in a lower model accuracy (MSRR), which will result in the estimation of artefacts. Therefore, one needs to decide if a small bias in the angular estimates can be accepted to avoid the estimation of artefacts. However, it is obvious that the effect of the phase correlation becomes minor for a larger number of elements.



(a) Mean SRR in presence of correlated (blue) and uncorrelated phase noise (red) (b) RMSE azimuth in presence of correlated (blue) and uncorrelated phase noise (red)

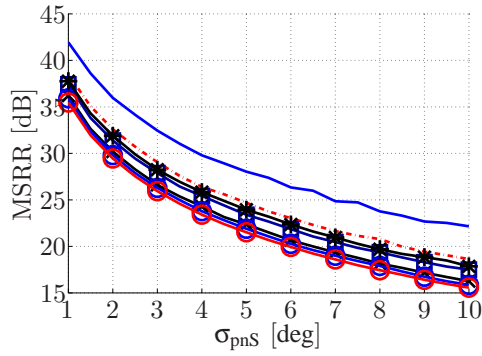
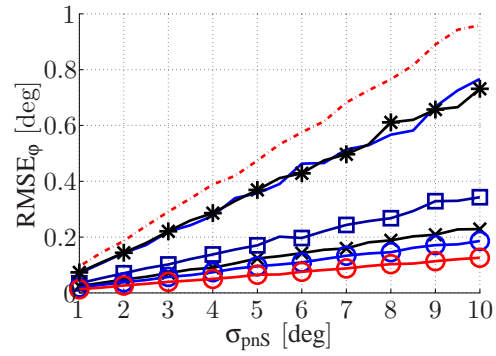
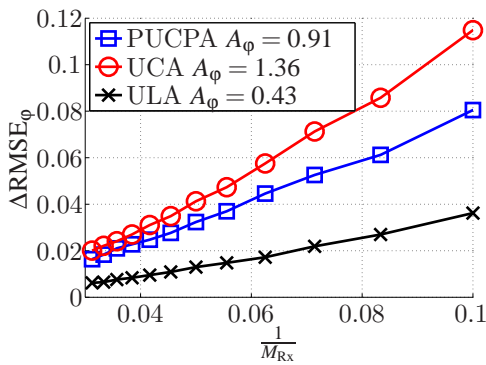
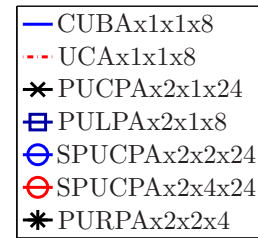
**Fig. 7.29:** Consequences of correlated phase noise in comparison to uncorrelated phase noise on the mean SRR (a) and RMSE of the azimuth (b) as function of the number of elements for different antenna types (HyEff system, single path excitation and estimation)

**Phase Noise Standard Deviation:** In this paragraph the consequences of phase noise as function of phase noise standard deviation will be discussed. Here, uncorrelated phase noise will be assumed, as the phase correlation is only given for the measurement systems used. Thus the phase correlation is not available for different standard deviations. A set of *practical* arrays are analysed (see legend in Fig. 7.30(d)). In terms of the mean SRR in Fig. 7.30(a) almost no difference can be found for different antenna arrays. However, if the phase noise standard deviation is doubled the model accuracy is decreased by around 6 dB. Assuming that for small phase noise angles  $\phi_{pns}$  the following approximation rules:  $e^{j\phi_{pns}} \approx 1 + j \cdot \phi_{pns}$ , this general behaviour dependent on the phase noise standard deviation for the mean SRR becomes clear. Thus, a rough estimate of the MSRR in the presence of uncorrelated phase noise is given by ( $\sigma_{pns}$  in [rad]):

$$MSRR \approx \frac{1}{|\sigma_{pns}|^2}. \tag{7.24}$$

Note that this approximation fits best for the antenna arrays, which take gain from the phase



(a) Mean **SRR** as function of the standard deviation of uncorrelated phase noise(b) **RMSE** azimuth as function of the standard deviation of uncorrelated phase noise(c) Dependence of  $\Delta \text{RMSE}_\varphi$  on  $1/M_{\text{Rx}}$ 

(d) Legend for (a) and (b)

**Fig. 7.30:** Consequences of uncorrelated phase noise on the estimation results mean **SRR** (a) and azimuth **RMSE** (b) for single path excitation and estimation for a set of practical antennas as function of the standard deviation of phase noise,  $\Delta \text{RMSE}_\varphi$  as function of  $1/M_{\text{Rx}}$  (c) ( $\varphi = 0^\circ$ ,  $\vartheta = 90^\circ$ , simulated antenna arrays)

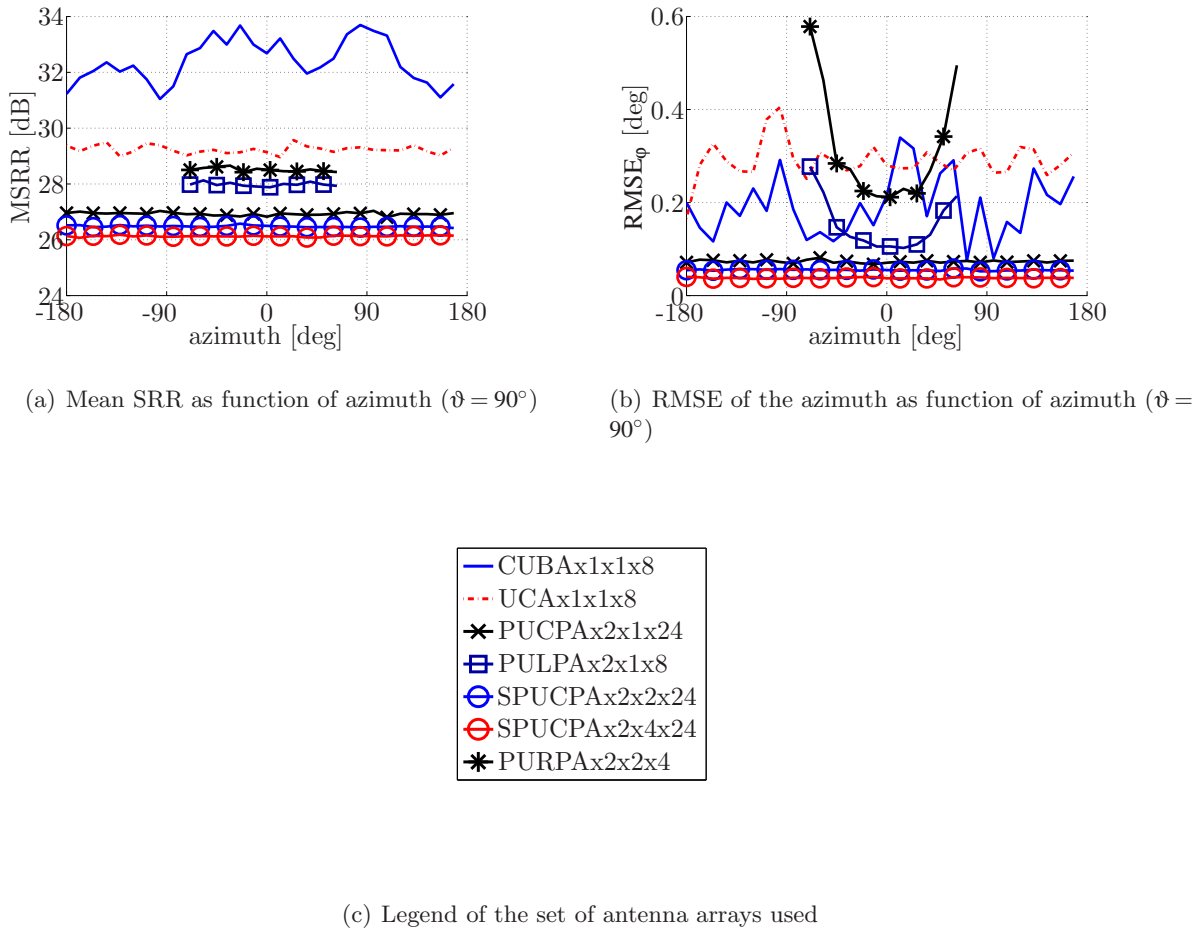
differences between the elements to resolve the **DoD/DoA**. In case of the **CUBAx1x1x8**, in which the directional information is related to the shape of the radiation pattern only this approximation underestimates the **MSRR**. The **RMSE** of the azimuth is proportional to the phase noise standard deviation  $\sigma_{\text{pnS}}$ , whereas the gradient of the **RMSE** is dependent on the antenna array used. The gradient is lower for arrays with a larger number of elements. It is found that the gradient  $\Delta \text{RMSE}_\varphi$  is reciprocally proportional to the number of elements  $M_{\text{Rx}}$ . An approximation for the azimuth **RMSE** is given by:

$$\text{RMSE}_\varphi(\sigma_{\text{pnS}}) \approx \frac{A_\varphi}{M_{\text{Rx}}} \cdot \sigma_{\text{pnS}}, \quad (7.25)$$

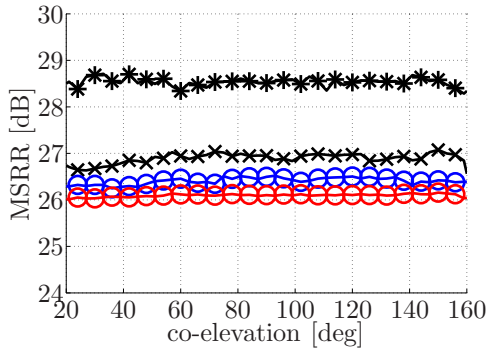
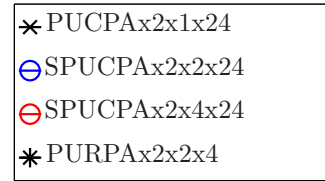
$A_\varphi$  is an array dependent constant. The found relation is shown for the simulated antenna arrays (**ULA**, **UCA** and **PCUPA**) in Fig. 7.30(c)

**Azimuth and Co-elevation of the True Path:** As the previous results are related to a fixed azimuth and co-elevation angle, in the following the dependence on the direction of arrival of the

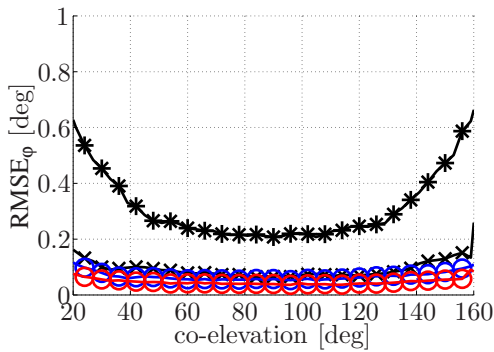
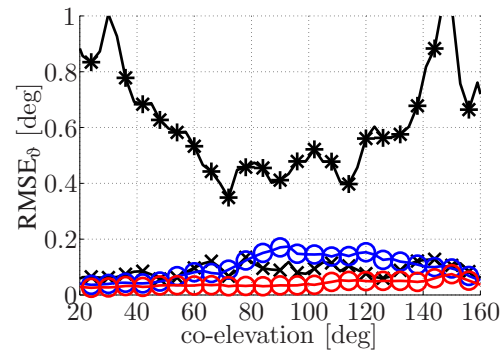
true path will be discussed. The results for the azimuth and co-elevation are shown in Fig. 7.31 and Fig. 7.32 respectively, uncorrelated phase noise with the phase noise standard deviation of the HyEff system was assumed. For the azimuth and co-elevation small variations for all parameters can be found, especially for the antenna arrays with a larger number of elements. The differences in the shape of the radiation pattern for DoA estimation is less important than the phase distribution over the antenna array, which is rather uniform for the larger antenna arrays. Furthermore, a slightly increased azimuth RMSE can be observed for the co-elevation angles towards the poles of the spherical coordinate system, whereas the MSRR remains almost constant. For antenna arrays with a smaller number of elements, the parameters MSRR, RMSE of the azimuth and co-elevation show a stronger variation dependent on the azimuth and co-elevation angle of the true path. This is related to the fact that for smaller arrays not only the phase information is important for the DoA estimation. The radiation pattern shape plays a more important role than in case of the larger arrays. As uniform radiation pattern shapes are not given for most of the arrays, this results in a stronger angular dependence of the estimation result.



**Fig. 7.31:** Consequences of uncorrelated phase noise on the estimation results mean SRR (a) and RMSE azimuth (b) for single path excitation and estimation for a set of practical antennas as function of the azimuth of the true path (HyEff system,  $\vartheta = 90^\circ$ )

(a) Mean SRR as function of co-elevation ( $\varphi = 0^\circ$ )

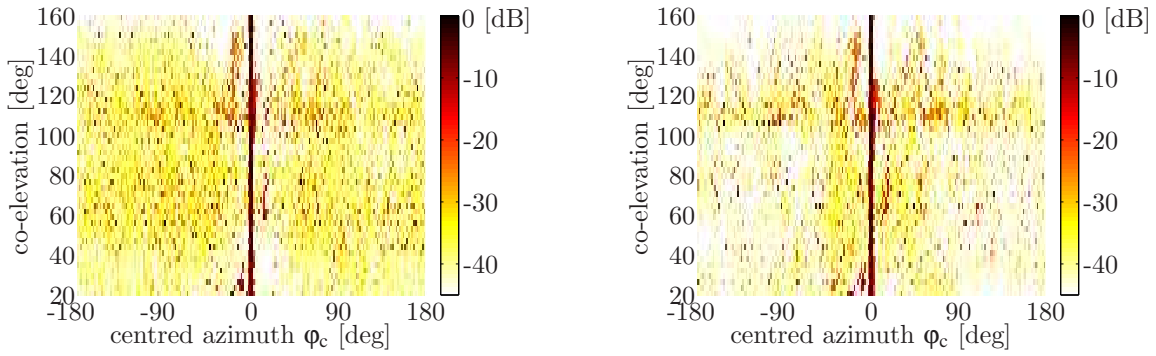
(b) Legend of the set of arrays used

(c) RMSE of the azimuth as function of co-elevation ( $\vartheta = 0^\circ$ )(d) RMSE of the co-elevation as function of co-elevation ( $\vartheta = 0^\circ$ )

**Fig. 7.32:** Consequences of uncorrelated phase noise on the estimation results mean SRR (a), azimuth RMSE (c) and co-elevation RMSE (d) for single path excitation and estimation for a set of practical antennas as function of the co-elevation of the true path (HyEff system,  $\varphi = 0^\circ$ )

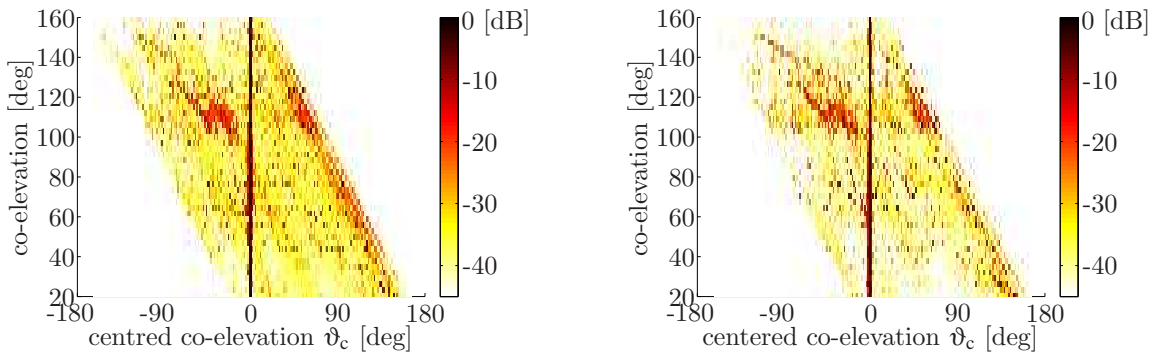
### 7.3.1.3 Estimation of Artefacts as Consequence of Phase Noise

The consequences of uncorrelated phase noise and correlated phase noise including a long term phase drift on the estimated mean angular power distributions will be demonstrated for the *practical* antenna array UCAX1x1x6. Again only the single path excitation is considered, the maximum number of path to estimate is set to  $K_{\max} = 10$ . For the correlated Fig. 7.33 (left) and uncorrelated phase noise Fig. 7.33 (right) the properties of the ATM system are assumed in the simulation. Additionally, a long term phase gradient of  $\Delta\varphi_{\text{pnl}} = 700 \left[ \frac{\text{deg}}{\text{s}} \right]$  is assumed in case of the correlated phase noise simulation. For both cases it can be observed that the power of the estimated artefacts is increasing towards the poles of the spherical coordinate system. On one hand this is related to the smaller phase differences between the antenna elements towards the poles and on the other hand it is related to the ambiguity in the estimation of the parameter co-elevation for one ring circular arrays. The latter one becomes especially apparent for the estimation of more than one path, whereas it can not be observed for the single path estimation (see also previous section). Comparing the results for correlated and uncorrelated phase noise it can be shown, that the power of the artefacts is slightly lower (2 to 3 dB) than in case of the correlated phase noise. Reconsidering the fact that the MSRR is slightly larger for the single estimated path for the correlated phase noise,



(a) Mean power distribution azimuth assuming uncorrelated phase noise  $\sigma_{pnS} = 5.69^\circ$

(b) Mean power distribution azimuth assuming correlated phase noise  $\sigma_{pnS} = 5.69^\circ$  and long term phase drift  $\Delta\phi_{pnL} = 700 \left[ \frac{\text{deg}}{\text{s}} \right]$



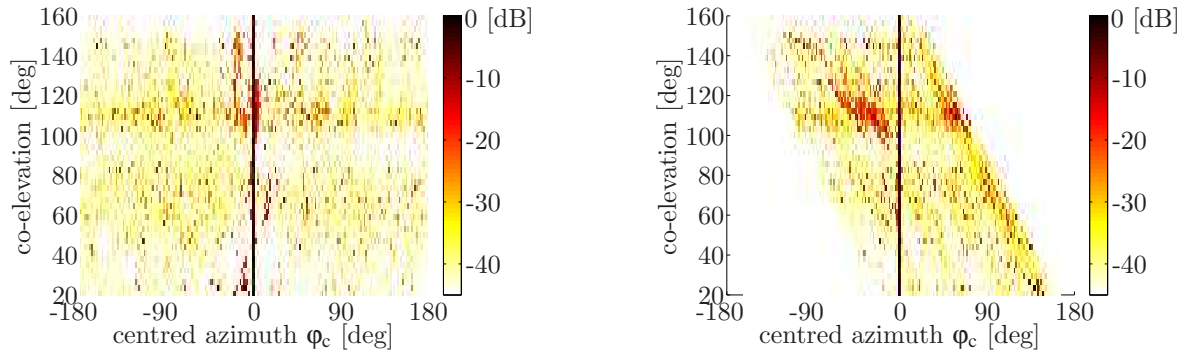
(c) Mean power distribution co-elevation assuming uncorrelated phase noise  $\sigma_{pnS} = 5.69^\circ$

(d) Mean power distribution co-elevation assuming correlated phase noise  $\sigma_{pnS} = 5.69^\circ$  and long term phase drift  $\Delta\phi_{pnL} = 700 \left[ \frac{\text{deg}}{\text{s}} \right]$

**Fig. 7.33:** Consequences of uncorrelated phase noise (left) and correlated phase noise including long term phase drift (right) on the mean estimated angular power distributions for azimuth (top) and co-elevation (bottom) as function of the co-elevation of the true path (ATM system)

as described in the previous section, this result is feasible. As the phase correlation and the phase drift is a deterministic effect, the resulting power distribution of the artefacts shows a concentration around certain azimuth angles, whereas in the uncorrelated case the power of the artefacts is almost uniformly distributed.

For the HyEff system with a lower phase noise standard deviation of  $\sigma_{pnS} = 2.94^\circ$  of the uncorrelated phase it is apparent in Fig. 7.34, that the power of the estimated artefacts is at least 6 dB lower (see also eqn. (7.24) in the previous section).



(a) Mean power distribution azimuth assuming uncorrelated phase noise  $\sigma_{\text{pnS}} = 2.94^\circ$

(b) Mean power distribution co-elevation assuming uncorrelated phase noise  $\sigma_{\text{pnS}} = 2.94^\circ$

**Fig. 7.34:** Consequences of uncorrelated phase noise on the mean estimated angular power distributions for azimuth (a) and co-elevation (b) as function of the co-elevation of the true path (HyEff system)

### 7.3.2 Consequence of an Unsuitable Calibrated External LNA

This section is an exception with respect to the analysed error sources. Basically, the resulting estimation errors as consequence of the previous described error sources were discussed with respect to the angular domain. As the consequences of an unsuitable calibrated LNA in the RF signal path are biggest in the delay domain, only the error of estimated delays of the propagation paths will be discussed. The following brief discussion is important in the practical analysis of measurements and the corresponding parameter estimation results, as an unsuitable calibration of an external LNA is a consistently and often made mistake during measurement campaigns. In the following a measurement is used, which was carried out at the Tokyo Institute of Technology during my time as visiting researcher in the Takada Laboratory. The measurement was performed in a micro-cell environment in the campus of the Tokyo Institute of Technology. At the Tx and Rx side the PURPAX2x2x4 and SPUCPAX2x2x24 was employed respectively. The impulse response length was chosen to  $\tau_{\text{max}} = 3.2 \mu\text{s}$ . The back-to-back calibration of the ATM system including the external LNA was carried out as described in Section 2.3.5. Note that for the ATM system only one AGC step is calibrated and consequently during the measurement time of one snapshot the AGC is fixed (see discussion in Section 2.3.2). The characteristic of the external LNA (which is included in the SPUCPAX2x2x24) used in this measurement can be found in Fig. 2.13. With the described setup, the external LNA and the ATM system was calibrated for a input power of around 0 dBm. For the conventional raw data processing, this vector valued frequency response  $\mathbf{y}_{\text{Calib}}$  of the external LNA  $\mathbf{y}_{\text{LNA}}(0 \text{ dBm})$  multiplied with the frequency responses of the other RF parts  $\mathbf{y}_{\text{Sys}}$  will be used for deconvolution with the measured impulse response, which corresponds to the following frequency domain operation:

$$\mathbf{H}^{[M_f \times M_{\text{Rx}} \cdot M_{\text{Tx}}]} = \text{diag}\{\mathbf{y}_{\text{Calib}}\}^{-1} \cdot \mathbf{H}_{\text{Meas}}. \quad (7.26)$$

The path loss of the estimated specular paths using eqn. (7.26) for the correction of the measured channel matrix  $\mathbf{H}_{\text{Meas}}$  are shown in the top row of Fig. 7.35 as function of the measurement snapshot

and normalised delay. It can be seen, that a large number of strong multipath clusters are located at normalised delays larger than 0.4. Furthermore, the analysis of those clusters has shown, that the angular distributions of the clusters with a normalised delay larger than 0.4 exactly match the angular distribution of the cluster around the strongest delay bin. The reason for this unusual channel characteristic is identified by the unsuitable calibrated external LNA. From the measurements and link budget estimation it was found that the total power impinging at the receive array was around -47 dBm, instead of the input power during the back-to-back calibration with 0 dBm. That means that  $\mathbf{H}$  (eqn. (7.26)) is distorted by:

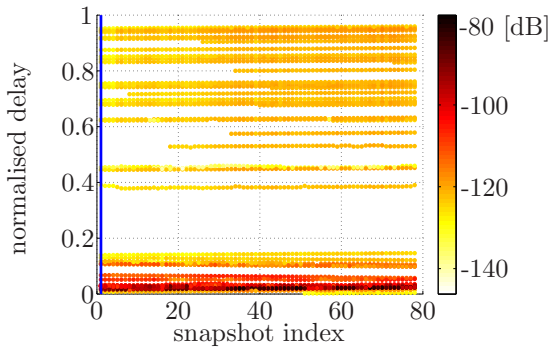
$$\mathbf{y}_{f,\text{Err}} = \frac{\mathbf{y}_{\text{LNA}}(-47 \text{ dBm})}{\mathbf{y}_{\text{LNA}}(0 \text{ dBm})}, \quad (7.27)$$

which corresponds to a convolution of the desired impulse response with the Fourier transform of  $\mathbf{y}_{f,\text{Err}}$ . In Fig. 7.35(b) the Fourier transform  $\mathbf{y}_{d,\text{Err}}$  of  $\mathbf{y}_{f,\text{Err}}$  normalised to the strongest path in the impulse response is plotted in the estimation results (blue solid line). It can be seen that most of the estimated clusters are located at the side lobes of the error impulse response  $\mathbf{y}_{d,\text{Err}}$ . Because of this, the angular distribution for those corresponding clusters matches the angular distribution of the cluster around the strongest delay bin. In the following the parameter estimation is repeated based on the corrected channel response:

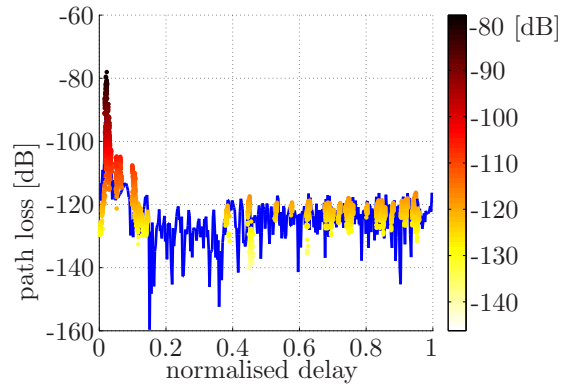
$$\mathbf{H}_{\text{Corr}}^{[M_f \times M_{\text{Rx}} \cdot M_{\text{Tx}}]} = \text{diag}\{\mathbf{y}_{f,\text{Err}}\}^{-1} \cdot \text{diag}\{\mathbf{y}_{\text{Calib}}\}^{-1} \cdot \mathbf{H}_{\text{Meas}}. \quad (7.28)$$

for comparison. The results of this estimation in terms of the specular paths are shown in the second row of Fig. 7.35. The clusters seen in the uncorrected case disappear. Furthermore, the angular distributions of the remaining clusters do not match the distribution of the cluster around the strongest delay bin. Comparing the results of the estimated parameters of the DMC for the corrected and uncorrected channel response it can be seen that more power is modelled in the DMC, as the estimated  $\alpha_1$  is around 3 dB to 4 dB larger in the uncorrected case. Furthermore, the coherency bandwidth of the DMC, which is reciprocally proportional to delay spread of the DMC, is larger in the uncorrected case.

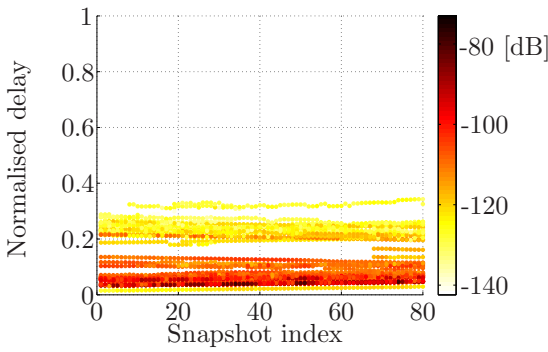
From the previous results it can be concluded, that an unsuitable calibrated LNA leads to physically meaningless estimation results in terms of the SC and DMC. As consequence, the usage of an unsuitable calibrated external LNA and system should be avoided. Note that the proposed correction is not practical, as an exact estimation of the input power at the LNA is impossible in most cases.



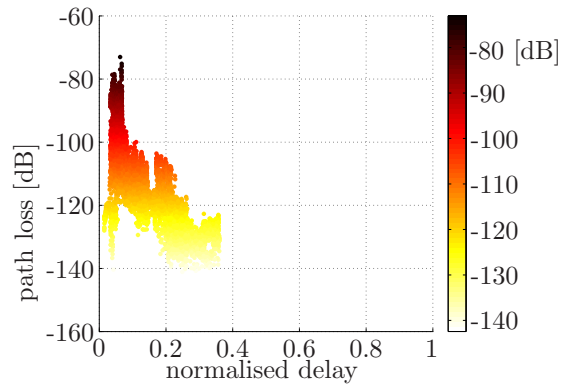
(a) Estimated path loss for the uncorrected channel response  $\mathbf{H}$  (unsuitable calibrated LNA)



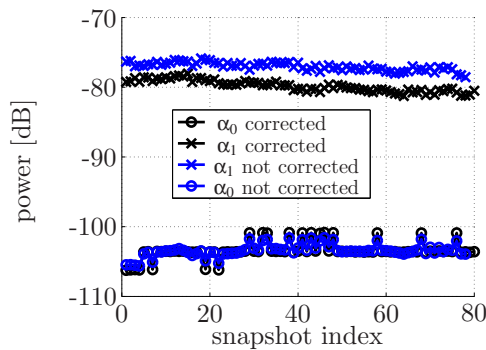
(b) Lateral view of the estimated path loss for the uncorrected channel response  $\mathbf{H}$  (unsuitable calibrated LNA) and impulse response  $\mathbf{y}_{d,Err}$  of the error term (blue solid line)



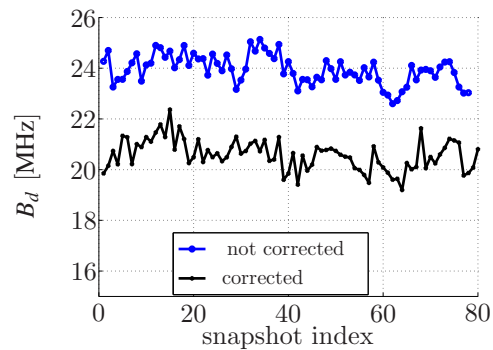
(c) Estimated path loss for the corrected channel response  $\mathbf{H}_{Corr}$



(d) Lateral view of the estimated path loss for the corrected channel response  $\mathbf{H}_{Corr}$



(e) Estimated parameters  $\alpha_0$  and  $\alpha_1$  of the DMC for the corrected and uncorrected case



(f) Estimated coherency bandwidth  $B_d$  of the DMC for the corrected and uncorrected case

**Fig. 7.35:** Consequences of an unsuitable calibrated LNA and system on the parameter estimation results for the SCs in the delay domain (a)(b) in comparison to the corrected calibration (c)(d). In (e)(f) the estimated parameters of the DMCs are compared for both cases.



### 7.3.3 Concluding Remarks on System Related Consequences

It could be shown that the effect of the long term phase drift can not be neglected especially for circular antenna arrays with a large number of elements. For small circular antenna arrays, linear and planar ones the consequences of the long term phase drift are minor.

For the phase noise, a general expression for the model error expressed as mean **SRR** was found dependent on the phase noise standard deviation. Also phase noise results in the estimation of artefacts, which are almost uniformly distributed. The power of the artefacts is related to the achievable model accuracy dependent on the phase noise standard deviation. If an accuracy better than 25 dB is wanted, a system with a phase noise standard deviation  $\sigma_{\text{pnS}}$  smaller than  $3^\circ$  is required. A reduction of the phase noise standard deviation can be only achieved by calculating an average channel response over a larger number of static measured responses. This procedure is applied for the calibration measurements, but it is inconvenient for measurements in a time variant channel.

A measurement system including external **RF** components such as **LNAs** need to be fully calibrated with respect to to the full range of expected power input levels and for the frequency band used. Ignoring this step may lead to misinterpretations of channel characteristics.

## 7.4 Conclusions Chapter 7 and Array Error Chart

The point made here is that estimation of resolvable discrete scatterer distributions will result in the estimation of artefacts if the appropriate data models for the antenna arrays and well calibrated measurement systems are not used. In channel modelling, the angular spread is an important parameter for determining the correlation matrix, which defines the correlation between the output signals of the different antenna elements of an antenna array. Artificial spreads, as appearing from parameter estimations based on incomplete data models and/or large phase noise, portray on one hand a channel with larger spread (lower correlation) than in reality and on the other hand could well give an impression of clustered discrete components where a single strong one is actually received. Furthermore, estimation bias is unavoidable for some arrays (e.g. linear arrays). It is concluded that channel parameter estimation with imperfect data models gives rise to potentially large apparent bias and angular spreads.

Recently, the approach of clustering multi-paths components, for channel modelling became very popular. It is not ruled out that clusters of scatterers published in propagation studies are partly artefacts resulting from estimations based on incomplete data models. Several publications can be found trying to find clusters based on estimation results, while incomplete data models were used [67, 70, 71]. Furthermore, some estimation algorithms are especially developed to fit distribution of paths around a centroid ([132–135]), which may be questionable if appropriate data models are not used.

The results shown can not be directly applied to other antenna arrays of same type, as the mechanical and electrical design may differ. Nevertheless, trends became apparent and let us conclude that also for other antenna arrays than the ones discussed, the considerations with respect to

---



the different error sources are necessary. The first questions should always be:

**Does the antenna array cover all spatial dimensions?**

and if not:

**How can it be avoided to receive any signal from missing dimensions?**

The second question should be:

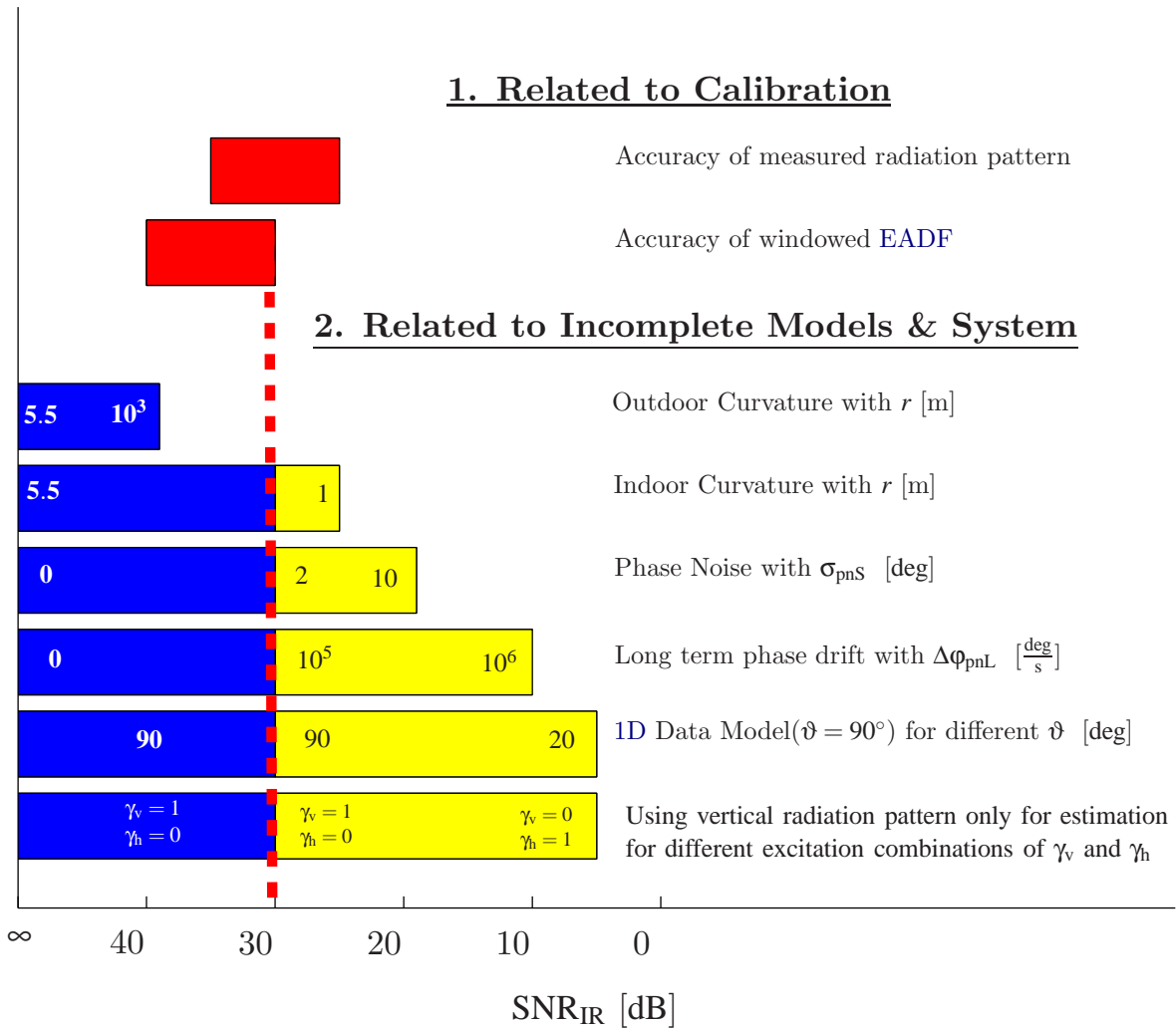
**Is it necessary to use the full polarimetric 2D (azimuth, co-elevation) array data model?**

For the polarisation characteristics, this question can be already answered. The polarisation characteristics need to be considered in all cases, except when the antenna has a very high XPD (30 or higher) in the directions of the incoming waves. Ignoring the elevation characteristics can be acceptable, if it can be assured, that the incoming waves only arrive from the co-elevation range, which is used for the data model used during estimation.

Finally, if we need to decide if an antenna array can be used in a certain measurement environment, then it is important to have an overview of the consequences of the different error sources. Therefore, an array error chart should be generated for each antenna array that will be used in measurements. In Fig. 7.36 the UCAX1x1x6 is used as an example for the array error chart. The chart shows which error source becomes important for a certain impulse response signal to noise ratio  $\text{SNR}_{\text{IR}}$ . The bars show the range of maximum achievable model accuracy dependent on a certain error source.

First, the bars in red colours are related to the maximum achievable model accuracy when deriving the array data model from calibration measurements. A difference is made between the accuracy of the measured radiation patterns and the proposed EADF antenna array data model. The consequences of the parasitic reflections are reduced by using the windowed EADF.

Second, the errors related to the usage of incomplete antenna array data models and errors related to the system property phase noise are shown. Each bar is divided in a yellow and a blue part, which corresponds to the practically and theoretically achievable model accuracy respectively. The practical achievable model accuracy based on the calibration measurements defines the boundary. For the UCAX1x1x16 the boundary is set to 30 dB, as this is the minimum achievable model accuracy when using the windowed EADFs (calculated from calibration measurements). That means, that the blue parts specify the theoretical expected behaviour if a Windowed Effective Aperture Distribution Function (WEADF) accuracy better than 30 dB based on calibration measurements could be achieved. For some error source, the consequences can be related to a certain parameter. Therefore, each bar contains the values for these parameters at the boundaries of the bar. Using this chart it will be easier to plan measurement campaigns by avoiding setups that lead to measurement results, which hold the potential risk of a misinterpretation of the channel due to ignored model errors and biases.



**Fig. 7.36:** UCAx1x16 error chart showing in which SNR<sub>IR</sub> range a certain error source can not be neglected. The red parts are related to the maximum achievable accuracy of the array data model deduced from calibration. The yellow parts specify the practical achievable model accuracy limited by the minimum achievable model accuracy of the windowed EADF with 30 dB. Consequently, the blue parts specify the theoretical achievable values assuming an accuracy of the windowed EADF larger than 30 dB could be achieved based on calibration measurements.

## 8. OVERALL LIMITATIONS OF EXPERIMENTAL CHANNEL CHARACTERISATION

This chapter deals with the overall consequences of *practical* measurement systems, *practical* antenna arrays, and unavoidable model errors on *Experimental Channel Characterisation* in realistic and more complex environments than the simple *single* or *coherent two paths scenario* (already discussed in Chapter 6). The investigations are based on observations from different propagation scenarios obtained from ray-tracing calculations and measurements. The ray-tracing based analysis is applied for the verification of the estimated parameters of the **SC**. Estimating also the **DMC** in the ray-tracing scenario will show if the **DMC** are related to unresolved **SC** or partially to model error. As the modelling of distributed diffuse scattering in ray-tracing is still in its infancy, measurement examples are chosen to investigate under which circumstances the **DMC** are related to model error or to the physical propagation conditions in the measured scenario. The relevance of the **DMC** under different propagation conditions will be clearly shown.

In Section 8.1 metrics are defined for the comparison between the “true” channel (*reference*) and the estimated channel. The ray-tracing and measurement based analysis are dealt in Section 8.2 and Section 8.3, respectively.

### 8.1 Definition of Metrics

The possibilities of an error analysis will differ depending on whether *Experimental Channel Characterisation* is based on ray-tracing calculations or measurements. In case of the ray-tracer, the “true” channel is known and metrics for a comparison can be directly defined based on the parameters of the **SC**. In case of measurements, only the recorded observations are known and can be used for comparison. That means only antenna dependent metrics can be applied for the measurement based analysis.

The metrics for the comparison between the *reference MIMO* channel and the estimated **MIMO** channel can be categorised in antenna independent metrics:

- Angular power spectrum
- Environment Characterisation Metric (**ECM**) [136])

and antenna dependent metrics:

- **MIMO** channel capacity [137–139]
-

- Normalised Parallel Channel Gain (NPCG) [140].

Note that the first category is related to antenna independent description of the channel only in terms of the SC. The second category is related to the spatial diversity of the MIMO channel applying a application specific antenna array.

**Definition 8.1.1.** The abbreviation **Ref**, used as superscript or subscript, denotes parameters / observations that correspond to the *reference* MIMO channel (ray-tracer / measurement).

**Definition 8.1.2.** The abbreviation **Set** denotes the estimated parameters or generated observations for a certain analysis setup that will be compared with the parameters / observations of **Ref**.

All equations and metrics which are used for comparison are defined with the abbreviation **Ref** and **Set**. As different estimation and analysis setups will be applied, the abbreviation **Set** will be replaced by the notation of the chosen setup in the final analysis in Sections 8.2 and 8.3.

A further antenna dependent metric that will be used for the validation of the estimation results and not for comparison of the *reference* and the estimated channel is introduced in the following. The metric can not be directly assigned to the metrics that will be defined in the Sections 8.1.1 and 8.1.2 and therefore it is defined here.

**Estimated SNR<sub>IR</sub> of the SC and DMC:** The SNR<sub>IR,SC</sub> and SNR<sub>IR,DMC</sub> that will be defined in the following is mainly used to analyse the relevance of the DMC in the presence of model error. This means, the ratio between the SNR<sub>IR,SC</sub> and SNR<sub>IR,DMC</sub> indicates if the estimated DMC are a feature of the radio channel or if they are related to model error.

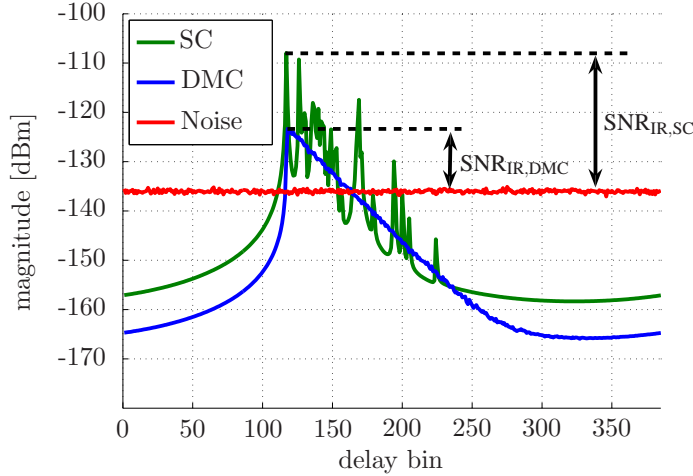
The SNR<sub>IR,SC</sub>/SNR<sub>IR,DMC</sub> is defined as the ratio between the mean peak power over the estimated impulse responses of the SC/DMC and the mean estimated noise power  $\alpha_0$ . For the estimated SC, the SNR<sub>IR,SC</sub> is calculated from band limited antenna dependent estimation result of all paths  $\mathbf{s}(\theta_{SC})$  (see eqn. 5.12). For the estimated DMC, the SNR<sub>IR,DMC</sub> is calculated as the ratio between the antenna dependent estimated peak power of the DMC  $\alpha_1$  and the estimated mean noise power  $\alpha_0$ . The SNR<sub>IR,SC</sub> and SNR<sub>IR,DMC</sub> are illustrated in Fig. 8.1 for an example.

### 8.1.1 Antenna Independent Metrics

**Angular Power Spectrum of the SC:** The angular power spectrum is calculated as function of the Rx measurement position and the azimuth angle  $\varphi$ . The bin for the measurement position covers a range of 1 m, whereas in the angular domain the bin width of  $2^\circ$  is chosen. The power of each bin  $C$  is given by the incoherent summation of the powers over all polarisations and all  $K_C$  paths corresponding to the bin:

$$P_C = \sum_{k_C=1}^{K_C} |\gamma_{hh,k_C}|^2 + |\gamma_{hv,k_C}|^2 + |\gamma_{vh,k_C}|^2 + |\gamma_{vv,k_C}|^2. \quad (8.1)$$

The angular power spectrum will be mainly used for a general comparison between the “true” and estimated channel.



**Fig. 8.1:** Illustration of the  $\text{SNR}_{\text{IR}}$  of the SC and DMC

**Environment Characterisation Metric (ECM) of the SC:** For the ECM proposed in [136] the parameters: power of the polarimetric path weights, TDoA, DoD, and DoA of all  $K$  paths at a measurement position are considered. The metric can be interpreted as the “fingerprint” of a certain propagation environment.

The ECM is calculated at every measurement position. The complete description of each path  $k$  in terms of  $\theta_k$  will be considered. As the metric has to cope with path parameters in different units (angular and delay), it is essential to transform the parameter matrix by proper scaling of its elements. For every path  $k$ , the angular data is transformed into coordinates on the unit sphere for both, Tx and Rx. For angles of arrival the transformation is given as:

$$\begin{bmatrix} x_{\text{Rx},k} \\ y_{\text{Rx},k} \\ z_{\text{Rx},k} \end{bmatrix} = \frac{1}{2} \begin{bmatrix} \cos(\varphi_{\text{Rx},k}) \cdot \sin(\vartheta_{\text{Rx},k}) \\ \sin(\varphi_{\text{Rx},k}) \cdot \sin(\vartheta_{\text{Rx},k}) \\ \cos(\vartheta_{\text{Rx},k}) \end{bmatrix}, \quad (8.2)$$

for angles at the Tx it reads similarly. The scaling is done such that the maximum Euclidean distance between two paths is limited to 1. Also in case of delay  $\tau_k$  the normalised value  $\tau'_k$  is applied (normalised to maximum excess delay). Every path is now described by seven (dimensionless) parameters collected in

$$\boldsymbol{\pi}_k = [x_{\text{Rx},k} \ y_{\text{Rx},k} \ z_{\text{Rx},k} \ x_{\text{Tx},k} \ y_{\text{Tx},k} \ z_{\text{Tx},k} \ \tau'_k]^T \quad (8.3)$$

and its total power of the polarimetric path weights:

$$\gamma_k^2 = |\gamma_{\text{hh},k}|^2 + |\gamma_{\text{hv},k}|^2 + |\gamma_{\text{vh},k}|^2 + |\gamma_{\text{vv},k}|^2. \quad (8.4)$$

The mean parameter vector is then given as:

$$\bar{\boldsymbol{\pi}} = \frac{\sum_{k=1}^K \gamma_k^2 \cdot \boldsymbol{\pi}_k}{\sum_{k=1}^K \gamma_k^2}. \quad (8.5)$$

The **ECM** is defined as the covariance matrix of the path parameter vector  $\boldsymbol{\pi}$ , so that:

$$\mathbf{C}_\pi = \frac{\sum_{k=1}^K \gamma_k^2 \cdot (\boldsymbol{\pi}_k - \bar{\boldsymbol{\pi}})(\boldsymbol{\pi}_k - \bar{\boldsymbol{\pi}})^T}{\sum_{k=1}^K \gamma_k^2}. \quad (8.6)$$

As discussed in [136] the metric shows the following properties:

- The main diagonal contains the directional spreads of the single components ( $x/y/z$ ) at **Tx** and **Rx** and the (normalised) rms delay spread.
- The Singular Values (**SV**) of  $\mathbf{C}_\pi$  can be interpreted as “fingerprint” of the scenario.
- The trace  $\text{tr}\{\mathbf{C}_\pi\}$  is the sum of the directional spreads at **Tx** and **Rx** plus the (normalised) delay spread. Note that the trace is dominated by the *large SVs*.
- The determinant  $\det\{\mathbf{C}_\pi\}$  has similar importance as detailed in [141, 142]. It describes the volume spanned in the parameter space. Since the value is dominated by the *small* singular values, it provides information about the most compact domain.

To quantify the difference between the “true” channel (**Ref**) and the estimated channel (**Set**), the **ECMs**  $\mathbf{C}_\pi^{(\text{Ref})}$  and  $\mathbf{C}_\pi^{(\text{Set})}$  are calculated. In [136] the mismatch between both was defined as the deviation between the singular values in logarithmic scale:

$$\mathcal{E} = \frac{1}{D} \sum_{d=1}^D |\log_{10}(\sigma_{d,\text{Ref}}) - \log_{10}(\sigma_{d,\text{Set}})|, \quad (8.7)$$

where  $\sigma_{d,\text{Ref}}$  and  $\sigma_{d,\text{Set}}$  denote the value of the respective singular value of the **ECM**, and  $D$  is the number of non-zero singular values. From signal theory and from analysis in various environments it was found that the definition (8.7) is not appropriate to describe the mismatch between two channels. Therefore, the following **ECM** mismatch definition will be used:

$$\mathcal{E}_{\text{ECM}} = \sqrt{\frac{1}{D} \sum_{d=1}^D \frac{(\sigma_{d,\text{Ref}} - \sigma_{d,\text{Set}})^2}{\sigma_{d,\text{Ref}}^2}}. \quad (8.8)$$

### 8.1.2 Antenna Dependent Metrics

The antenna dependent band limited observation  $\mathbf{x}_{\text{Ref}}$  of the *reference* **MIMO** channel (ray-tracer / measurement) and the observation  $\mathbf{x}_{\text{Set}}$  generated on the basis of the parameter estimation results of the estimation setup **Set** will be compared applying the following metrics. The diversity metrics **MIMO** channel capacity and **NPCG** are calculated based on the channel matrix  $\mathbf{H}^{[M_{\text{Rx}} \times M_{\text{Tx}}]}(m_f, m_t)$  which is obtained from the generated or measured observation vector  $\mathbf{x}^{[M_f \cdot M_{\text{Tx}} \cdot M_{\text{Rx}} \times 1]}$  (see eqn. (5.14)) for the snapshot  $m_t$  that corresponds to a certain **Rx** measurement position.

For the purpose of comparison, in Section 8.1.2.1 the relative error between the *reference* channel **Ref** and the estimated channel **Set** in terms of the diversity metrics is defined. Based on this relative error a mean error and its standard deviation for a snapshot range of  $m_t$  is calculated.

**MIMO Channel Capacity** The channel capacity, as described in [137], is the upper bound on the amount of transformation that can be reliably transmitted over a noisy communication channel. The averaged instantaneous MIMO capacity ([35, 138, 139]) of a frequency selective channel can be defined as the mean capacity over all  $M_f$  frequency bins:

$$C_{\text{Norm}}(m_t) = \frac{1}{M_f} \sum_{m_f=1}^{M_f} \log_2 \left( \det \left( \mathbf{I}_{M_{\text{Rx}} \times M_{\text{Rx}}} + \frac{\rho}{\chi_{\text{Norm}}^2 \cdot M_{\text{Tx}}} \mathbf{H}(m_f, m_t) \cdot \mathbf{H}(m_f, m_t)^{\text{H}} \right) \right) \left[ \frac{\text{bit}}{\text{s} \cdot \text{Hz}} \right], \quad (8.9)$$

where  $\rho$  is the mean Application SNR (Appl. SNR) and  $\chi_{\text{Norm}}$  is a normalisation factor. With this factor the channel matrix is normalised to the mean power over all frequencies, Rx antennas and Tx antennas. The corresponding normalisation factor:

$$\chi_{\text{SelfNorm}} = \sqrt{\frac{\sum_{m_f=1}^{M_f} \|\mathbf{H}(m_f, m_t)\|_{\text{F}}^2}{M_f \cdot M_{\text{Tx}} \cdot M_{\text{Rx}}}} \quad (8.10)$$

will be indicated with the subscript ‘‘Selfnorm’’ throughout this Chapter. This normalisation will be used for comparison in case of the ray-tracing based analysis.

The equations (8.9) and (8.10) are only valid for noise free channel matrices  $\mathbf{H}$ . If these equations are applied to measured channel matrices, then measurement noise power is taken as signal power. To achieve that the Appl. SNR  $\rho$  in eqn. (8.9) is only related to signal power in the channel matrices  $\mathbf{H}$  the normalisation factor  $\chi_{\text{SignalNorm}}$ :

$$\chi_{\text{SignalNorm}} = \sqrt{\frac{\sum_{m_f=1}^M \|\mathbf{H}(m_f, m_t)\|_{\text{F}}^2}{M_f \cdot M_{\text{Tx}} \cdot M_{\text{Rx}}} - \alpha_0} \quad (8.11)$$

will be applied for measurements. Again,  $\alpha_0$  corresponds to the estimated mean noise power of the measurement. Analysing eqn. (8.11) it is clear that the channel matrix is normalised to the mean received signal power, which includes the power of the SC and the DMC.

Please keep in mind that the Appl. SNR is the SNR we assume for the capacity calculation (eqn. (8.9)) employing arbitrary application antenna arrays. Do not mix up the Appl. SNR with the SNR of the measurement that is performed for the *Experimental Channel Characterisation*!

**Normalised Parallel Channel Gain:** This metric characterises the MIMO channel with respect to the singular value distribution in terms of power. The NPCG can be also interpreted as an effective number of spatial sub channels (eigenmodes). In contrast to the channel capacity  $C(m_t)$  it describes the diversity of the channel independent of Appl. SNR. The normalised parallel channel gain [140] is defined as:

$$\text{NPCG}(m_t) = \frac{1}{\sigma_{\text{max}}^2(m_t)} \cdot \sum_{i=1}^{\min\{M_{\text{Rx}}, M_{\text{Tx}}\}} \sigma_i^2(m_t), \quad (8.12)$$

where  $\sigma_i(m_t)$  is the  $i$ -th singular value and  $\sigma_{\max}(m_t)$  is the strongest (in terms of power) singular value of the channel matrix  $\mathbf{H}^{[M_{\text{Rx}} \times M_{\text{Tx}}]}$ .

### 8.1.2.1 Relative Error of the MIMO Channel Diversity Metrics

The relative error between the metric dependent on the *reference* channel matrix  $\mathbf{H}_{\text{Ref}}(m_t)$  (ray-tracer/measurement) and the metric dependent on the channel matrix that is generated based on the estimated parameters of the setup *Set*  $\mathbf{H}_{\text{Set}}(m_t)$  in terms of the chosen metric  $\zeta$  ( $C$  or NPCG) is defined as:

$$\varepsilon_{\zeta, \text{Norm}}(m_t) = 100 \cdot \frac{\zeta_{\text{Norm}}(\mathbf{H}_{\text{Set}}(m_t)) - \zeta_{\text{Norm}}(\mathbf{H}_{\text{Ref}}(m_t))}{\zeta_{\text{Norm}}(\mathbf{H}_{\text{Ref}}(m_t))} \quad [\%]. \quad (8.13)$$

The mean relative error and standard deviation of the relative error for a measurement route between the measurement position  $m_{t1}$  and  $m_{t1} + \Delta m_t$  are defined as:

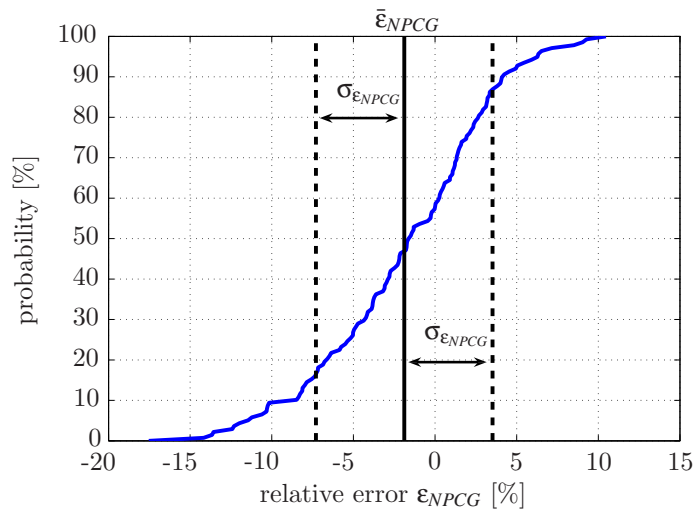
$$\bar{\varepsilon}_{\zeta} = \frac{1}{\Delta m_t} \sum_{m_t=m_{t1}}^{m_{t1}+\Delta m_t} \varepsilon_{\zeta}(m_t) \quad [\%] \quad (8.14)$$

and

$$\sigma_{\varepsilon_{\zeta}} = \sqrt{\frac{1}{\Delta m_t} \sum_{m_t=m_{t1}}^{m_{t1}+\Delta m_t} (\varepsilon_{\zeta}(m_t) - \bar{\varepsilon}_{\zeta})^2} \quad [\%]. \quad (8.15)$$

Note that the generated channel (*Set*) overestimates in average the “true” channel in terms of the metric  $\zeta$  if  $\bar{\varepsilon}_{\zeta}$  is positive, whereas it underestimates if  $\bar{\varepsilon}_{\zeta}$  is negative.

In Fig. 8.2 the Cumulative Distribution Function (CDF) of the relative error in terms of NPCG for exemplary measurement route and example estimation setup is shown. The mean value of the relative error and its standard deviation are highlighted.



**Fig. 8.2:** CDF of relative error in terms of NPCG for an example measurement route



## 8.2 Error Analysis Based on Ray-tracing

This Section deals in detail with the impact of the overall model error on the estimation results of the **SC** and with the relevance of the estimated **DMC**. By applying different estimation setups, it will be shown if the **DMC** are unresolved **SC** only or if they partially compensate for model error.

Realistic observations are calculated based on the ray-tracing *reference* and undistorted array data models of *practical* measurement antenna arrays at **Tx** and **Rx**. At one hand, white Gaussian measurement noise is considered as the only source of error (indicated by the abbreviation **NoDist**). This assumption is commonly made when parameter estimation algorithms are discussed. At the other hand, all unavoidable error sources discussed in Chapter 7 are incorporated in the observation (additive noise, phase noise, phase drift) and estimation data model (distorted array data models). These setups are indicated by the abbreviation **FullDist**. With this approach the conditions are similar to a real world measurement and analysis. Applying a joint **SC** and **DMC** estimation in both cases, **NoDist** and **FullDist** respectively, it will be clearly shown if the **DMC** result from unresolved **SC** only or if they are related to model error. As the relevance of the **DMC** depends on the overall model accuracy and the maximum  $\text{SNR}_{\text{IR}}$  of the **SC**, the investigations will be performed for two cases:

1. overall model accuracy lower than the maximum  $\text{SNR}_{\text{IR}}$
2. overall model accuracy higher than the maximum  $\text{SNR}_{\text{IR}}$ .

Moreover, all results will be analysed in comparison to the results where only **SC** are estimated, since most parameter estimation algorithms do not incorporate the **DMC** estimation.

Section 8.2.1 briefly reviews the applied state of the art ray-tracer developed at the **IHE** Karlsruhe [40]. In Section 8.2.2 the analysis procedure is discussed in detail. The consequences of an overall model accuracy lower and higher than the maximum  $\text{SNR}_{\text{IR}}$  are presented in Section 8.2.3 and Section 8.2.4 respectively.

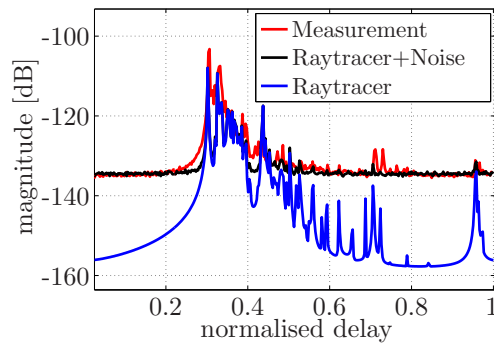
### 8.2.1 Description of the 3D Ray-tracer

As with measurements a *reference* for direct comparison between the “true” channel parameters and the estimated parameters is not given, a state of the art ray-tracer (in international standards) developed at the **IHE** Karlsruhe [40] will be used in Section 8.2. With the ray-tracing results a *reference* is given, which can be used for comparison with estimation results of the **RIMAX** parameter estimation algorithm. Realistic observations for the channel parameter estimation are generated on the basis of the ray-tracing results.

The three dimensional (**3D**) ray-tracing model consists of two major parts: a realistic model of the propagation environment and a model to calculate the multi-path wave propagation between the transmitter and the receiver [40]. A digital model of a district of Karlsruhe city, Germany, as environment data for ray-tracing is used (Fig. 8.3(a)). The digital model includes buildings, trees and the pavement. Buildings are generated by means of a vector data set that describes their exact



(a) 3D environment of Karlsruhe city showing the paths calculated by the raytracer



(b) Generated IR (Raytracer) vs. measured IR

**Fig. 8.3:** 3D ray-tracer environment showing the detected paths for one measurement position (a) and corresponding generated IR compared with the measured IR (b)

position and size. Each building is modeled as a box with a certain roof-top type (e.g. flat roof, pitched roof, hipped roof). It is assumed that on average all buildings have constitutive parameters of dry concrete ( $\epsilon_r = 5 - j0.1$ ,  $\mu_r = 1$ ). For accurate wave propagation modelling it is essential to include huge trees into the model. Only the tree crown is considered, the tree trunk is neglected. The crown is modelled as a box, with an average height of 3 m above ground. The exact position and size of the trees is determined from a morphographic data set. For the street floor, concrete with a surface roughness of  $s = 1$  mm is assumed ( $\epsilon_r = 5 - j0.1$ ,  $\mu_r = 1$ ) [143].

A ray-optical wave propagation tool is used to calculate the channel between the transmitter and the receiver. It distinguishes between different multi-path components. Each path may consecutively experience several different propagation phenomena. The propagation phenomena taken into account in the channel model are single reflections, combinations of multiple reflections and multiple diffractions, and single scattering (diffuse). The modified Fresnel reflection coefficients, which account for slightly rough surfaces, are used to model the reflections [144]. In order to trace pure reflection paths, the method of image transmitters (image theory) is implemented [145]. Diffraction is described by the UTD and the corresponding heuristic coefficients for lossy wedge diffraction [146]. Moreover, the UTD slope diffraction coefficients according to [147] are used to enhance the accuracy, especially for multiple diffractions. Since the proposed propagation model supports full 3D diffraction, Fermat's principle is used to determine the diffracted ray paths [144]. For mixed paths, image theory and Fermat's principle are combined.

Real objects such as buildings or trees have no perfectly flat surface. Buildings for example, exhibit a variety of irregularities, e.g. windows, balconies, eaves gutters, etc. If the wave-length is in the order of the dimensions of these irregularities, an incident wave gives rise to several scattering contributions in all directions. In reality, the resulting multipath components can only be distinguished up to a certain degree, i.e. diffuse scattering will cause that several components/paths interfere with each other.

Diffuse scattering from buildings as well as from tree crowns is taken into account in the 3D ray-

tracing model. To describe scattering from an object, the surface of the object is divided into small squared tiles. Depending on the energy, which is incident on the surface of the object, each tile gives rise to a Lambertian scattering source [43, 45]. The amount of scattered energy per tile is derived from measured normalised radar cross sections. The corresponding values for co- and cross-polarisation of buildings and trees depend on the frequency. As only single scattering is taken into account, the scattering paths are defined by the position of the transmitter and the receiver as well as of the position of the central point of the tiles, into which the surface of the building or the tree is subdivided. A detailed description of the implemented scattering approach and values for co- and cross-polarisation is given in [40].

For the simulations that will be presented in Section 8.2, the number of diffractions is limited to two per path and combinations of reflections and diffraction to five interactions in total. Additionally, the power ratio between the strongest and the weakest path is limited to 50 dB. This results in total number of paths between 500 and 6000 with the parameter vector  $\theta_{\text{SC,Ref}}$ . The large number of paths is related the attempt to model the diffuse scattering in the environment, which is a superposition of a large number of weak (in terms of power) paths.

For comparison, the impulse response generated based on the ray-tracing results and the measured impulse response for the measurement position shown in Fig. 8.3(a) are compared in Fig. 8.3(b). It can be seen that an agreement between the impulse responses exists in terms of power, although in some delay regions a larger received energy is measured. A possible cause for this behaviour may be related to diffuse scattering, which is not completely modeled by the ray-tracer.

### 8.2.2 Ray-tracing Based Analysis Procedure

For better understanding, Fig. 8.4 illustrates the procedure for the ray-tracing based error analysis that will be described in the following. The upper part of the block diagram contains the observation generation and estimation for different setups. The lower part is related to error analysis in terms of:

1. antenna independent metrics
2. antenna dependent metrics (MBPCM approach with application antenna array).

The analysis procedure begins with the generation of undistorted observations from the calculated specular components of the ray-tracer  $\theta_{\text{SC,Ref}}$ . Undistorted array data models (EADFs) of measurement antenna arrays at Tx and Rx are applied. Based on this observations two estimation setups are considered:

**Definition 8.2.1. NoDist:** only *i.i.d.* Gaussian noise is added to the undistorted observations and undistorted array data models are applied for estimation.

**Definition 8.2.2. FullDist:** *i.i.d.* Gaussian noise, phase noise and phase drift affected observations are generated. Distorted antenna array data models (windowed EADFs from antenna array

---

calibration (see Section 7.2.1.4)) are applied for estimation.

For both setups, **SC** only and **SC+DMC** are estimated, which results in a total number of four setups *Set* that are indicated with the following abbreviations:

1. **SC(NoDist)**  $\Rightarrow$  never available from measurements (**SC** estimation only)
2. **SC+DMC(NoDist)**  $\Rightarrow$  never available from measurements (joint **SC** and **DMC** estimation).  
If the estimated  $\text{SNR}_{\text{IR,DMC}}$  is larger than zero, then the **DMC** are related to unresolved **SC**.
3. **SC(FullDist)**  $\Rightarrow$  comparable to measurements (**SC** estimation only).
4. **SC+DMC(FullDist)**  $\Rightarrow$  comparable to measurements (joint **SC** and **DMC** estimation).  
If the estimated  $\text{SNR}_{\text{IR,DMC}}$  is larger than the  $\text{SNR}_{\text{IR,DMC}}$  of the **SC+DMC(NoDist)** setup, then the **DMC** are mainly related to model error.

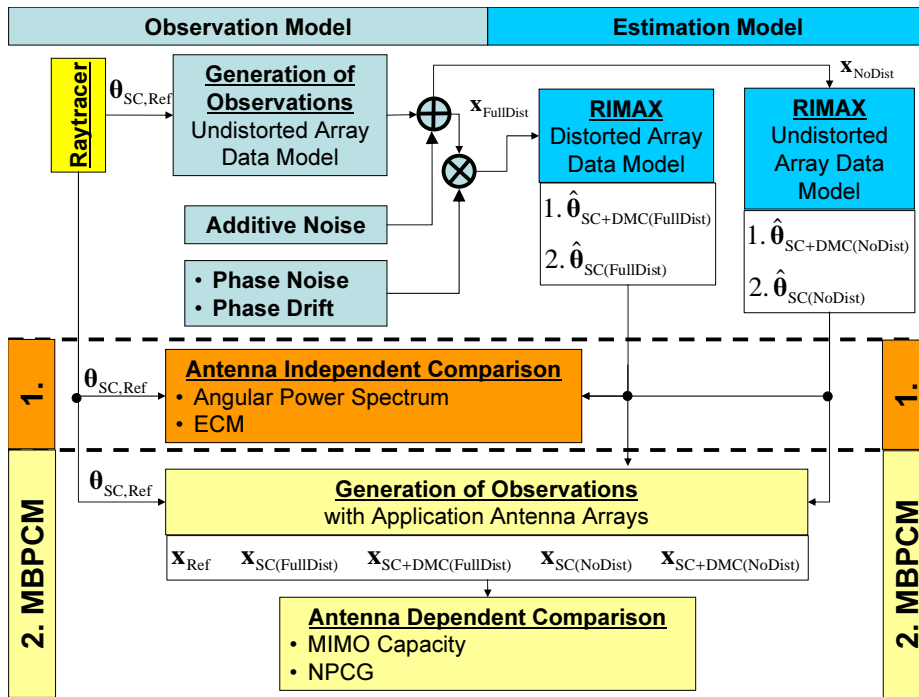


Fig. 8.4: Block diagram for the ray-tracing based error analysis

For these estimation setups the **EADF**s of the *practical* antenna array **PULPAx2x1x8** will be employed at **Tx** side. At the **Rx** side a simulated **SPUCPAx2x2x24** is applied. Undistorted **EADF**s and distorted but windowed **EADF**s are generated for the **Rx** array only (see Section 7.2.1.3 and 7.2.1.4). A summary of the settings for the four estimation setups in terms of observation and estimation data model is given in Table 8.1. It is also considered that in case of the **PULPAx2x1x8** the observations are generated with the **2D EADF**s, whereas for the estimation only the **1D EADF**s (azimuth cut with constant co-elevation  $\vartheta = 90^\circ$ ) can be applied. For the error analysis of the previous described estimation setups the metrics described in Section 8.1 will be applied.

First, the relevance of the estimated **DMC** is analysed comparing the estimated  $\text{SNR}_{\text{IR,DMC}}$  of the

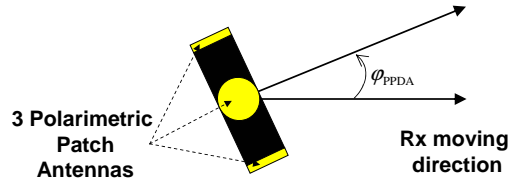
Tab. 8.1: Observation model vs. Estimation model

Setup Abbreviation	Observation model	Estimation model
SC(NoDist)	<ul style="list-style-type: none"> <li>additive measurement noise (HyEff system)</li> <li>using <b>undistorted 2D EADFs</b> at Tx/Rx</li> </ul>	<ul style="list-style-type: none"> <li>estimation of <b>SC</b> only</li> <li>using <b>undistorted 1D EADF</b> at Tx</li> <li>using <b>undistorted 2D EADF</b> at Rx</li> </ul>
SC+DMC(NoDist)	<ul style="list-style-type: none"> <li>additive measurement noise (HyEff system)</li> <li>using <b>undistorted 2D EADFs</b> at Tx/Rx</li> </ul>	<ul style="list-style-type: none"> <li>estimation of <b>SC+DMC</b></li> <li>using <b>undistorted 1D EADFs</b> at Tx</li> <li>using <b>undistorted 2D EADFs</b> at Rx</li> </ul>
SC(FullDist)	<ul style="list-style-type: none"> <li>additive measurement noise (HyEff system)</li> <li>phase noise (Hyeff system)</li> <li>phase drift <math>700 \left[ \frac{\text{deg}}{\text{s}} \right]</math></li> <li>using <b>undistorted 2D EADFs</b> at Tx/Rx</li> </ul>	<ul style="list-style-type: none"> <li>estimation of <b>SC</b> only</li> <li>using <b>undistorted 1D EADFs</b> at Tx</li> <li>using <b>distorted 2D EADFs</b> at Rx</li> </ul>
SC+DMC(FullDist)	<ul style="list-style-type: none"> <li>additive measurement noise (HyEff system)</li> <li>phase noise (Hyeff system)</li> <li>phase drift <math>700 \left[ \frac{\text{deg}}{\text{s}} \right]</math></li> <li>using <b>undistorted 2D EADFs</b> at Tx/Rx</li> </ul>	<ul style="list-style-type: none"> <li>estimation of <b>SC+DMC</b></li> <li>using <b>undistorted 1D EADFs</b> at Tx</li> <li>using <b>distorted 2D EADFs</b> at Rx</li> </ul>

setup **SC+DMC(NoDist)** and the setup **SC+DMC(FullDist)**.

Second, the parameters of the specular components calculated from the ray-tracer  $\theta_{\text{SC,Ref}}$  and the estimated parameters  $\hat{\theta}_{\text{Set}}$  can be directly compared in terms of the antenna independent metrics angular power spectrum and **ECM** (see Section 8.1).

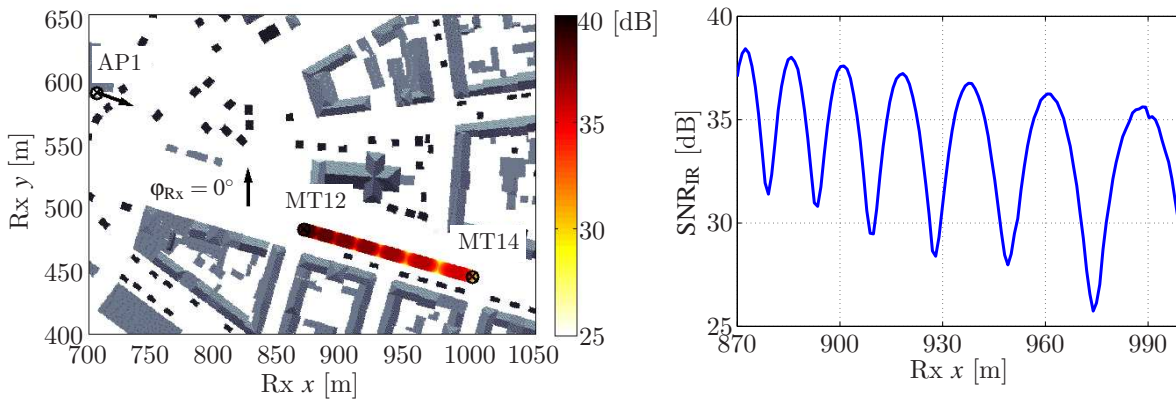
Third, the antenna dependent metrics **MIMO** capacity and **NPCG** are calculated on basis of generated observations dependent on the estimated parameters  $\hat{\theta}_{\text{Set}}$  and the observation generated from the *reference* parameter vector  $\theta_{\text{SC,Ref}}$ . Thus, the relative error of the **MIMO** channel diversity metrics (see Section 8.1.2.1) will be analysed. The observations are generated for a  $6 \times 6$  **MIMO** system. At the **Tx** side a subset of three adjacent dual polarised antenna elements of the measurement antenna array **PULPAx2x2x8** will be used, at the **Rx** side the application antenna array Polarimetric Personal Digital Assistant (**PPDA**) (see Fig. 2.15) with three dual polarised patch antennas will be employed. As the results in terms of the antenna dependent metrics depends on the alignment of the **PPDA**, the **PPDA** will be rotated in azimuth about  $\phi_{\text{PPDA}}$  in  $10^\circ$  steps related to the moving direction. For better understanding see Fig. 8.5.



**Fig. 8.5:** Alignment  $\varphi_{PPDA}$  of the application antenna array **PPDA** related to the Rx moving direction

### 8.2.3 Consequences of an Overall Model Accuracy Lower than the Maximum SNR in the CIR

In the following simulations the digital environment data of Karlsruhe city is used. The **Tx** array **PULPAx2x1x8** is placed at a height of 38 m above street level at the position **AP1**, shown in Fig. 8.6(a). In the figure, the zero direction of the **Tx** array is indicated by an arrow, which is pointing towards the tower of the church. A down tilt of  $9^\circ$  in co-elevation is applied at **Tx**. The **Rx** array **SPUCPASim2x2x24** is placed at a height of 2 m above street level and was moving between **MT12** and **MT14**. The zero direction of the antenna array in azimuth is aligned to the moving direction. Nevertheless, if estimated angular parameters are discussed in the following, the parameters are given in the global coordinate system, in which the zero azimuth direction  $\varphi_{Rx} = 0^\circ$  of Fig. 8.6(a) is parallel to the direction of the unit vector of the y-axis. By applying the system parameters of the HyEff system and the chosen antenna arrays the maximum  $SNR_{IR}$  in the impulse response is given in Fig. 8.6(b). Additionally, the colour of the line between Rx position **MT12** and **MT14** indicates the  $SNR_{IR}$  for the corresponding position. Strong fading processes can be observed in the  $SNR_{IR}$  that are mainly caused by the superposition of the **LoS** path and two or three other strong paths with small delay differences. The  $SNR_{IR}$  is varying between 25 dB and almost 40 dB, which is higher than the achievable overall model accuracy during estimation, which is between 25 dB and 30 dB (corresponds to the estimation setups **SC(FullDist)** and **SC+DMC(FullDist)** only, see Section 8.2.2 and Table 8.1).



(a) Simulation route MT12 to MT14, in which case the colour indicates the  $SNR_{IR}$  at each position.

(b)  $SNR_{IR}$  vs. the Rx x position

**Fig. 8.6:** Simulation route and  $SNR_{IR}$  for positions between MT12 and MT14.



### 8.2.3.1 Relevance of the Estimated DMC

The relevance of the estimated **DMC** can be easily answered comparing the  $\text{SNR}_{\text{IR}}$  of the **DMC** between the estimation setups **SC+DMC(NoDist)** and **SC+DMC(FullDist)**.

**Theorem 8.2.3.** *In case of **SC+DMC(NoDist)**, the  $\text{SNR}_{\text{IR}}$  of the estimated **DMC** expresses the maximum  $\text{SNR}_{\text{IR}}$  of unresolved **SC**. This means that for an  $\text{SNR}_{\text{IR,DMC}}$  around zero the estimated **DMC** define additive Gaussian measurement noise only, whereas for a  $\text{SNR}_{\text{IR,DMC}}$  larger than zero the **DMC** are a feature of the radio channel.*

**Theorem 8.2.4.** *If the  $\text{SNR}_{\text{IR,DMC}}$  in case of the **SC+DMC(FullDist)** setup is larger than the  $\text{SNR}_{\text{IR,DMC}}$  of **SC+DMC(NoDist)** at the same **Rx** position, then the **DMC** of the estimation setup **SC+DMC(FullDist)** are partially related to model error. Consequently, they do not describe the propagation in the radio channel.*

Let us now analyse the  $\text{SNR}_{\text{IR}}$  illustrated in Fig. 8.7 for the **SC** and **DMC** in case of **SC+DMC(NoDist)** (indicated by blue lines) and **SC+DMC(FullDist)** ((indicated by black lines)). The  $\text{SNR}_{\text{IR,SC}}$  of the estimated **SC** of both estimation setups are almost overlapping. It can be seen that the  $\text{SNR}_{\text{IR,DMC}}$  in case of the **SC+DMC(NoDist)** setup is always around zero dB with only a few exceptions. This means that almost all received **SC** were resolved. For **SC+DMC(FullDist)**, the  $\text{SNR}_{\text{IR,DMC}}$  is approximately 5 dB to 20 dB higher. Thus, most of the estimated **DMC** power is related to model error only.

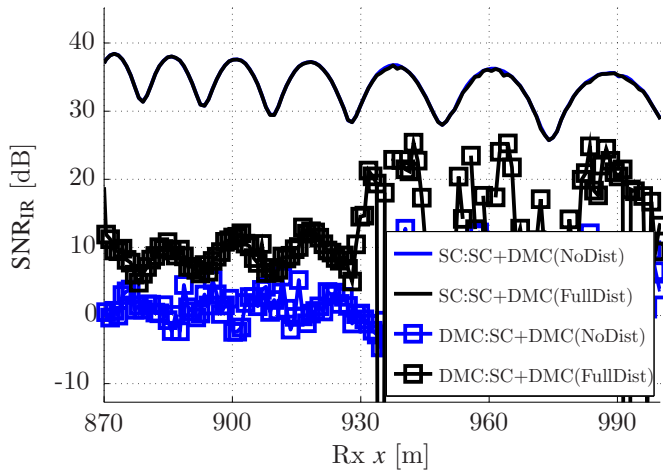
From Fig. 8.7 it can be observed that a correlation between a high  $\text{SNR}_{\text{IR,SC}}$  and a high  $\text{SNR}_{\text{IR,DMC}}$  exist for the **SC+DMC(FullDist)** setup. The ratio between the  $\text{SNR}_{\text{IR,SC}}$  and  $\text{SNR}_{\text{IR,DMC}}$  is smaller or equal to the overall model accuracy of about 25 dB to 30 dB. It can be conclude that the **DMC** in case of **SC+DMC(FullDist)** are mainly related to model error if the  $\text{SNR}_{\text{IR,SC}}$  is larger than the overall model accuracy.

### 8.2.3.2 Angular Power Spectrum of the SC

For the following comparison, the *reference* and the estimated azimuth power spectra only at the receiver are considered. This is reasonable as the impact of model error are most significant in the parameter dimension  $\phi_{\text{Rx}}$ , because a distorted array data model is applied at the **Rx** for the estimation setups **SC(FullDist)** and **SC+DMC(FullDist)** (see Table 8.1).

In Fig. 8.8 the angular spectra as function of the Rx  $x$  position are shown for the calculated paths of the ray-tracer (*reference*) and the four different estimation setups described in Table 8.1. The spectra are clipped 50 dB below the maximum, as the ray-tracing calculations were limited to 50 dB between the strongest and the weakest path. Comparing the estimated angular power spectra of the four estimation setups with the *reference* spectrum, the estimated artefacts around the “true” paths give information about the quality of the discussed estimation setups. With narrower spreads around the “true” paths the estimation result is said to be “better”. The following points can be noticed from Fig. 8.8:

- Estimating **SC** and **DMC** in case of **NoDist** and **FullDist** gives better results than estimating **SC** only.

(a) SNR<sub>IR</sub>SCandDMCMT1214.fig

**Fig. 8.7:** Estimated SNR<sub>IR</sub> of SC and DMC for the measurement route MT12 to MT14 in case of the estimation setups SC+DMC(NoDist) (denoted by colour blue) and SC+DMC(FullDist) (denoted by colour black)

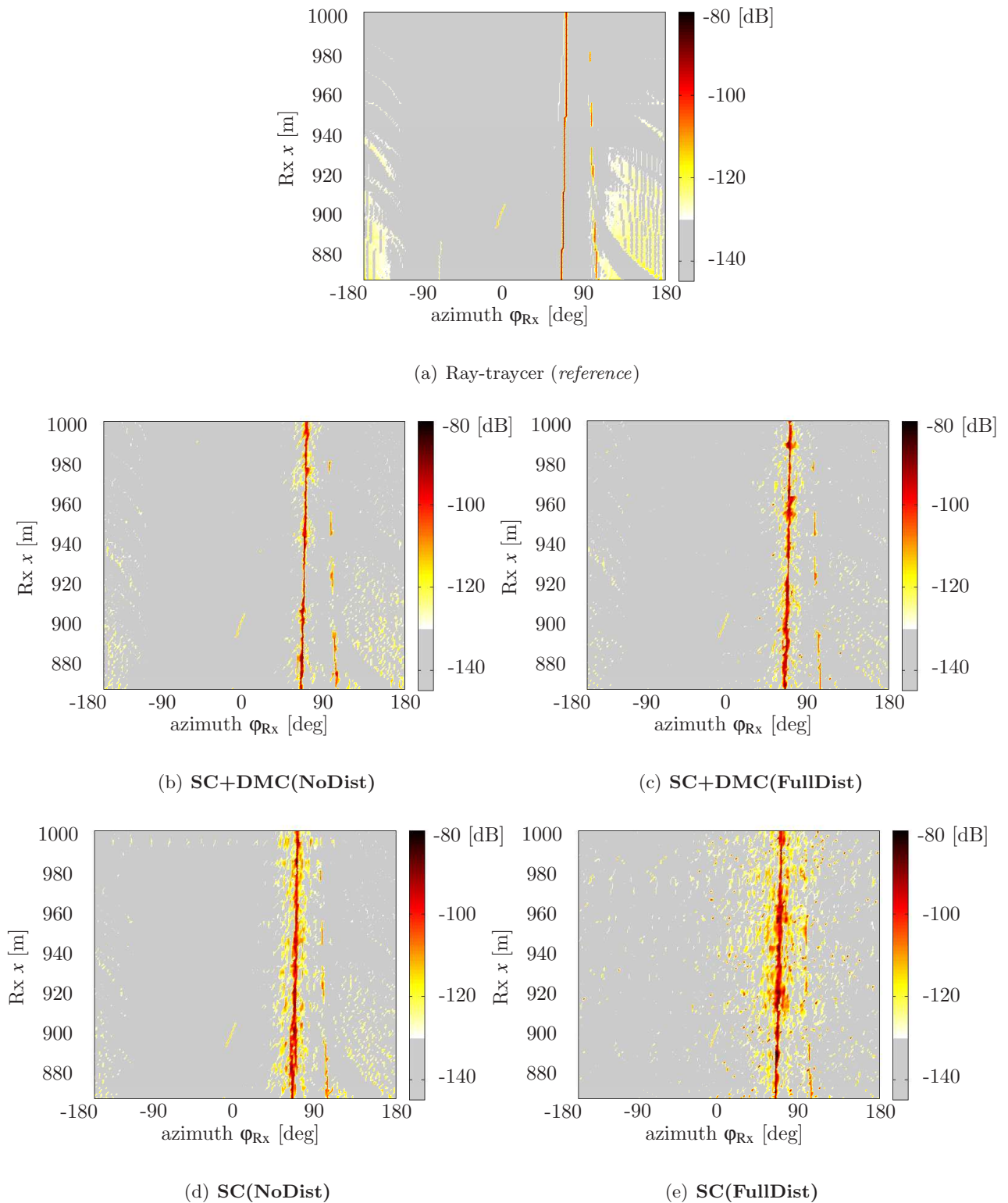
- Especially in case of **FullDist** the consequences of the model errors are expected to be largest, but the joint estimation of SC and DMC improves the estimation results drastically compared to SC only estimation. Consequently, in case of SC+DMC(FullDist) the artefacts due to model error as seen for SC(FullDist) are compensated by the estimated DMC (see Section 8.2.3.1). This means, the estimated DMC are not a feature of the radio channel.
- The artificial spreads that can be observed in case of **NoDist** are caused by the additive i.i.d. Gaussian noise only and can be described by the estimated CRLBs of the estimated parameters (reconsider Chapter 6).
- The artificial spreads that can be observed in case of **FullDist** are caused by array model error, phase noise and drift of the system, and additive i.i.d. Gaussian noise. These artificial spreads can not be completely described by the CRLBs of the estimated path parameters, as the CRLB are calculated for a model which is only 25 dB accurate.

The estimation results of SC+DMC(FullDist) shown in Fig. 8.8(c) are the best result we can achieve in a real measurement. From the above discussion and from the discussion in Section 8.2.3.1 we can conclude again that the estimated DMC of the SC+DMC(FullDist) setup are not a feature of the radio channel if the maximum SNR<sub>IR</sub> is higher than the overall model accuracy (here between 25 dB and 30 dB). In this case the estimated DMC are mainly related to model error.

### 8.2.3.3 ECM Mismatch of the SC

In Fig. 8.9 the ECM mismatch (see Section 8.1.1) between the estimation results and the ray-tracer *reference* is shown in dB. Negative or small values of the ECM mismatch in dB indicate a good





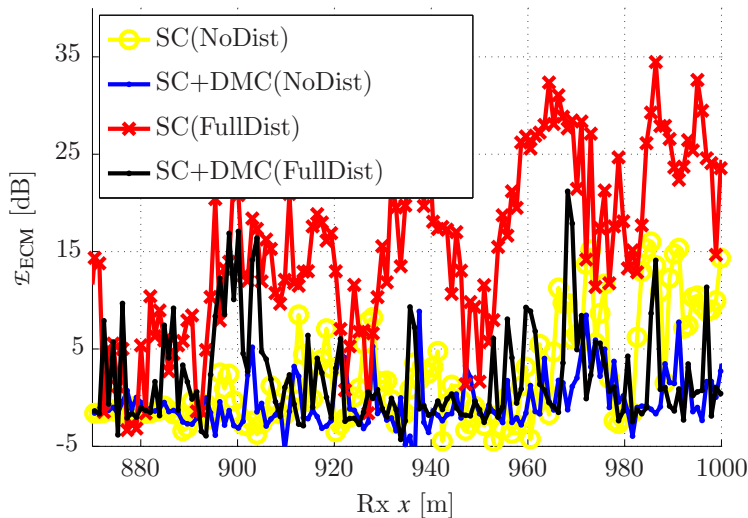
**Fig. 8.8:** Rx azimuth power spectra as a function of Rx x, for the ray-tracer (*reference*)(a) and the estimated spectra for the setups described in Table 8.1 estimating SC+DMC (b)(c) and SC only (d)(e).

agreement between the “true” propagation paths and the estimated, whereas large values indicate that the estimation results can not approximate the “true” propagation paths.

The following points can be noticed from Fig.8.9:

- As already seen in the previous section, the estimation results from the joint estimation of **SC** and **DMC**, show best agreement but here in terms of the **ECM** mismatch (small values in dB).
- For the estimation setup **SC(FullDist)** the **ECM** mismatch is largest. Especially in the regions with a  $\text{SNR}_{\text{IR,SC}}$  larger than the overall model accuracy the **ECM** mismatch is drastically increasing.
- When incorporating the **DMC** estimation in case of **FullDist**, the results are comparable to the **SC+DMC(NoDist)** case.

From the **ECM** mismatch, the same conclusions can be drawn as in the previous section analysing the estimated angular power spectra. First, estimation of **DMC** improves the estimates of the **SC**. Second, it can be concluded (indirectly) that the estimated **DMC** are related to model error if the maximum  $\text{SNR}_{\text{IR}}$  is larger than the overall model accuracy. Notice, contrary to the angular power spectrum, the **ECM** mismatch has the advantage that the mismatch over all parameter dimensions is described.



**Fig. 8.9:** **ECM** mismatch  $\mathcal{E}_{\text{ECM}}$  between the **SC** parameters of the ray-tracer (*reference*) and the parameters of the estimated **SC** of the four different estimation setups.

#### 8.2.3.4 MIMO Capacity Error

Again, the *reference* for comparison are the generated observations based on the calculated parameters of the ray-tracer. For the generation of the observations based on the four estimation setups,

only the estimated **SC** are considered, the estimated **DMC** are ignored. This is reasonable, as they are mainly related to model error in the case **SC+DMC(FullDist)** (see previous sections). In the case **SC+DMC(NoDist)** the estimated **DMC** are negligible as they are mainly related to additive **i.i.d.** Gaussian noise (see Fig. 8.7). This means, they do not contribute to the received signal energy.

In Fig. 8.10 the mean relative capacity error and its standard deviation are shown (equations (8.14) and (8.15)). The variation of the mean error and its standard deviation for a certain estimation setup (indicated by a unique colour) is related to the different alignments  $\phi_{\text{PPDA}}$  of the application antenna array **PPDA** as shown in Fig. 8.5.

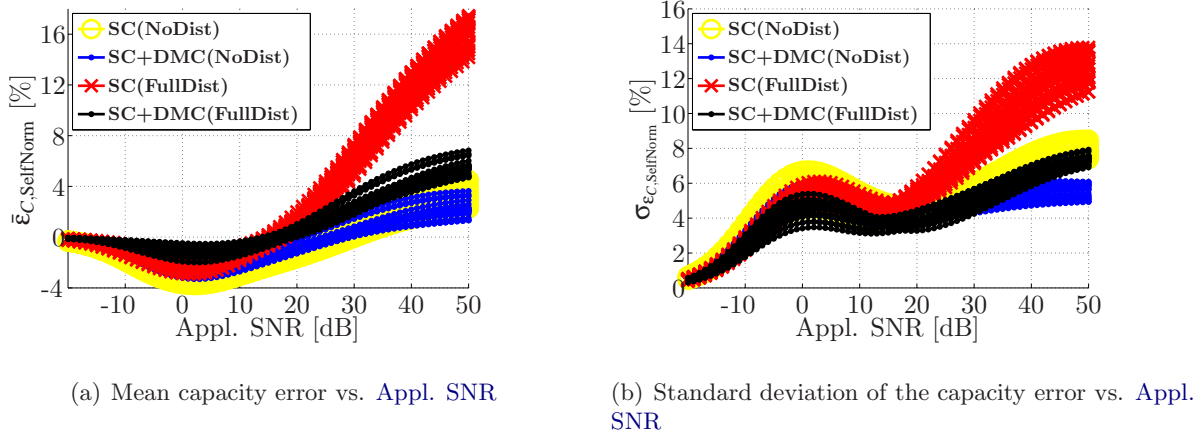
The following points can be noticed from Fig. 8.10:

- The **NoDist** estimation results give us best agreement in terms of the **MIMO** capacity when comparing the *reference* and estimated channel. The mean capacity error varies only around  $\pm 4\%$ .
- From the mean capacity error it can be seen that especially in case of **SC(FullDist)** the capacities are overestimated for **Appl. SNRs** larger than 20 dB. This behaviour is related to the overall model accuracy for the **FullDist** estimation setups that is not better than 25 dB to 30 dB.
- In case of **FullDist** and the joint estimation of **SC** and **DMC** (**SC+DMC(FullDist)**), the **DMC** compensate for the model error. This means that the mean capacity error can be reduced in case of **SC+DMC(FullDist)**. But this is only the case if the estimated **DMC** will be ignored when generating observations based on the estimation results! Considering the estimated **DMC** would consequently result in a larger capacity error.
- From the standard deviation of the capacity error a similar behaviour as for the mean capacity error can be observed. The standard deviation is especially increasing for **Appl. SNRs** larger than 20 dB and for the **FullDist** estimation setups.

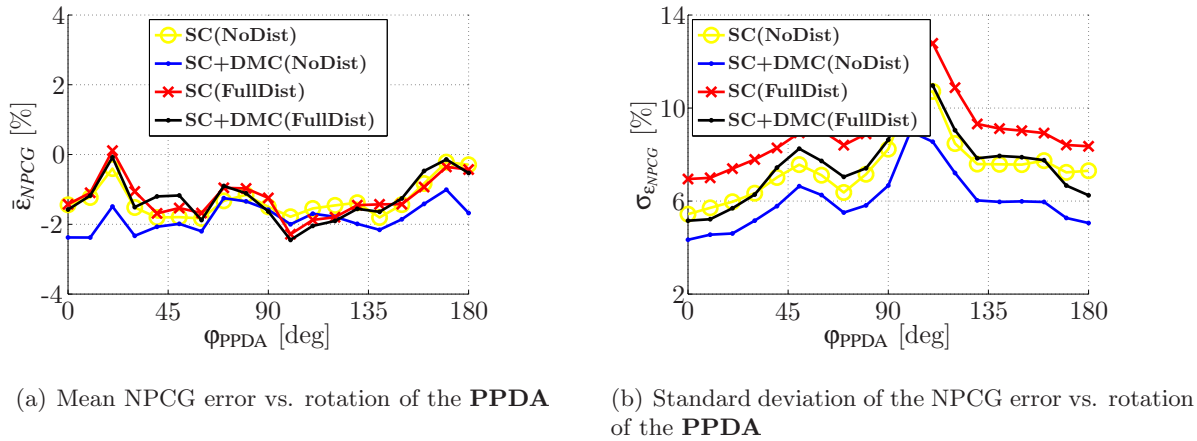
### 8.2.3.5 NPCG Error

In Fig. 8.11 the mean relative NPCG error and its standard deviation are shown as a function of the alignment  $\phi_{\text{PPDA}}$  of the application antenna array **PPDA**. It can be seen that the mean error of the **NPCG** is almost equal for all four estimation setups and small (around -2%). As opposed to the mean value of the **NPCG** error, the standard deviation of the relative **NPCG** error is strongly dependent on the alignment  $\phi_{\text{PPDA}}$  of the application antenna array **PPDA**. Reconsidering the angular power spectra shown in Section 8.2.3.2, it is understandable that larger standard deviations of the relative **NPCG** error can be expected if the main beam of one of the patch antennas of the application antenna array **PPDA** is pointing towards the estimated artefacts.

From the standard deviation of the relative **NPCG** error similar conclusions as in the previous sections can be drawn. The results of **SC(FullDist)** are worst, the standard deviation can be reduced if the results of the **SC+DMC(FullDist)** setup are applied.



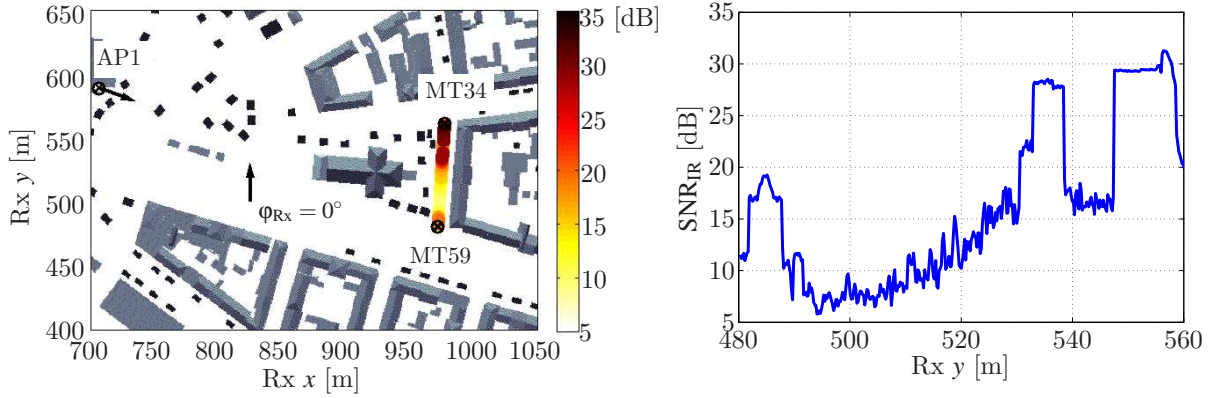
**Fig. 8.10:** Error in terms of capacity for the route MT12 to MT14 as a function of the Appl. SNR. The variation of the plots of each estimation setup (indicated by colour) is caused by the different alignments of the Rx application antenna array PPDA.



**Fig. 8.11:** Error in terms of NPCG for the route MT12 to MT14

### 8.2.4 Consequences of an Overall Model Accuracy Higher than the Maximum SNR in the CIR

The same simulation setup as in Section 8.2.3 is applied, but the Rx array SPUCPASim2x2x24 was moving between MT59 and MT34 (see Fig. 8.12(a)). By applying the system parameters of the HyEff system and the chosen antenna arrays the maximum  $SNR_{IR}$  of the impulse responses is given in Fig. 8.12(b). Again, the colour of the line between Rx position MT59 and MT34 indicates the  $SNR_{IR}$  for the corresponding position. The scenario is dominated by Non Line of Sight (NLoS) condition, whereas in the beginning and end of the measurement route the condition is LoS and Obstructed Line of Sight (OLOs). In the NLoS region the  $SNR_{IR}$  is below 20 dB, which is lower than the achievable overall model accuracy during estimation, which is approximately 25 dB to 30 dB. Therefore, the analysis results will be presented for this region only (Rx  $y = 490$  m to  $y = 530$  m). However, the angular power spectra will be illustrated for the entire simulation route.



(a) Simulation route MT59 to MT34, in which case the colour indicates the  $\text{SNR}_{\text{IR}}$  at each position.

(b)  $\text{SNR}_{\text{IR}}$  vs. the Rx y position

**Fig. 8.12:** Simulation route and  $\text{SNR}_{\text{IR}}$  for positions between MT59 and MT34.

#### 8.2.4.1 Relevance of the Estimated DMC

From the discussion in Section 8.2.3.1 (Theorem 8.2.3 and 8.2.4) the meaning of the  $\text{SNR}_{\text{IR,SC}}$  /  $\text{SNR}_{\text{IR,DMC}}$  in terms of the relevance of the estimated DMC is already known. Again, the estimation of DMC in case of **SC+DMC(NoDist)** can be only caused by unresolved SC. In the case of **SC+DMC(FullDist)** and a model accuracy higher than the  $\text{SNR}_{\text{IR,SC}}$  we expect that contrary to the previous section the DMC are related to unresolved SC only.

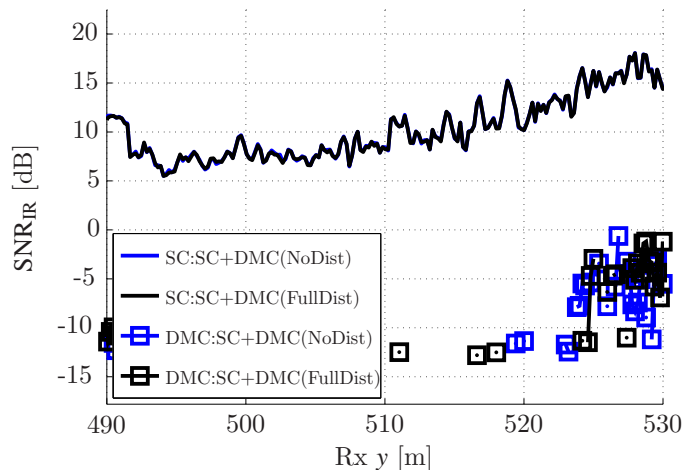
**Theorem 8.2.5.** *If all SC can be resolved then the DMC estimation is not possible. The remaining impulse response after subtraction of the estimated SC contains measurement noise only. Thus, the DMC estimation is based on noise power only and the estimated  $\text{SNR}_{\text{IR,DMC}}$  in dB can be negative.*

In Fig. 8.13 mostly negative  $\text{SNR}_{\text{IR,DMC}}$  in dB can be observed for both measurement setups **SC+DMC(NoDist)** and **SC+DMC(FullDist)** respectively. At some measurement positions the DMC estimation was impossible and no values are plotted. The  $\text{SNR}_{\text{IR,SC}}$  is lower than the overall model accuracy and consequently model error will not contribute to the estimated DMC. Additionally, in both cases all SC above noise can be estimated but the estimated parameters of paths with less power will have a larger variance (maximum  $\text{SNR}_{\text{IR,SC}}$  is only between 10 dB and 20 dB). Again, the  $\text{SNR}_{\text{IR,SC}}$  of the estimated SC of both estimation setups are almost overlapping.

#### 8.2.4.2 Angular Power Spectrum of the SC

Again, the angular power spectra only at Rx will be analysed. In Fig. 8.14 the angular spectra as a function of the Rx y position are shown for the calculated paths of the ray-tracer (*reference*) and the four different estimation setups described in Table 8.1. Again, the results are clipped 50 dB below the maximum in the spectrum, as the ray-tracing calculations were limited to 50 dB between the strongest and the weakest path.

The following points can be noticed from Fig. 8.14:

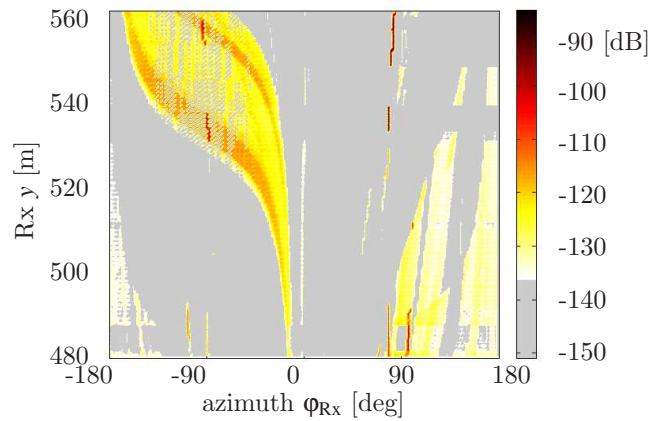
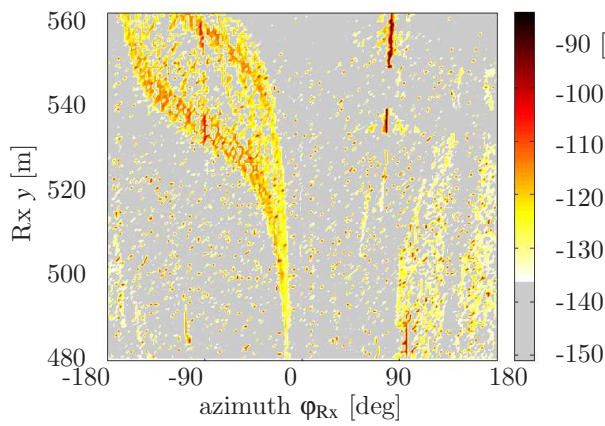


**Fig. 8.13:** Estimated  $\text{SNR}_{\text{IR}}$  of **SC** and **DMC** for the measurement route **MT59** to **MT34** in case of the estimation setups **SC+DMC(NoDist)** (denoted by colour blue) and **SC+DMC(FullDist)** (denoted by colour black)

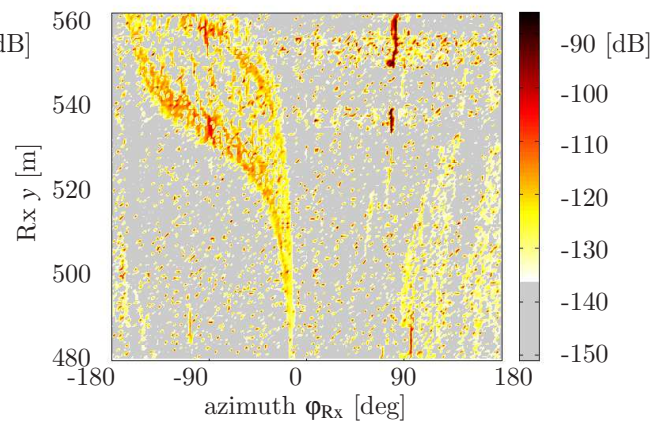
- In the regions with a maximum  $\text{SNR}_{\text{IR}}$  larger than the overall model accuracy the same conclusions can be drawn as in the previous Section 8.2.3 (e.g.  $\text{Rx y}$  positions between 550 m and 560 m).
- In the **NLoS** region with maximum  $\text{SNR}_{\text{IR}}$ s lower than 25 dB, the four different estimation setups give us similar results.
- In the **NLoS** region weak artefacts (in terms of power) are estimated. Comparing the angular power spectra of the ray-tracer with the estimation results of the four setups, it can be seen that these artefacts are mainly estimated in the directions where no power can be observed in the angular power spectrum of the ray-tracer.
- However, most of the strong paths in the **NLoS** region are estimated in the same directions where a concentration of paths can be found in the angular power spectrum of the ray-tracer. Here, the variance of the estimates is mainly caused by additive **i.i.d.** Gaussian noise and not because of model error. The overall model accuracy is higher than the maximum  $\text{SNR}_{\text{IR}}$ . Consequently, the estimated **CRLBs** are a reliable estimate for the variance of the estimated parameters.

In summary, with a maximum  $\text{SNR}_{\text{IR}}$  lower than the overall model accuracy, similar results are achieved by the **NoDist** and **FullDist** setups. This means, model mismatch has no impact on the estimation results in this case. However, the variance of the estimated parameters, which is related to additive **i.i.d.** Gaussian noise only is increasing. To this end, the variances can be described by the estimated **CRLBs**, as the used model is accurate enough.

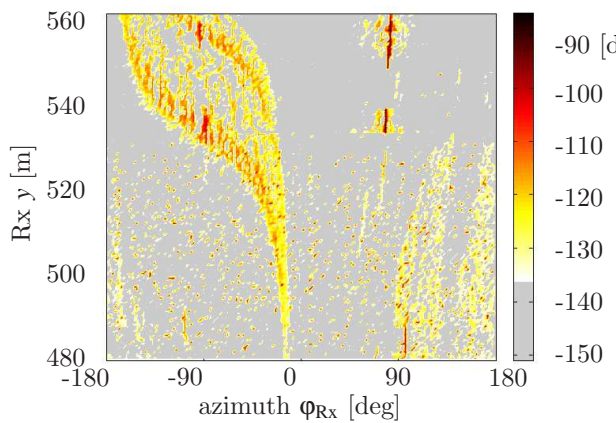


(a) Ray-tracer (*reference*)

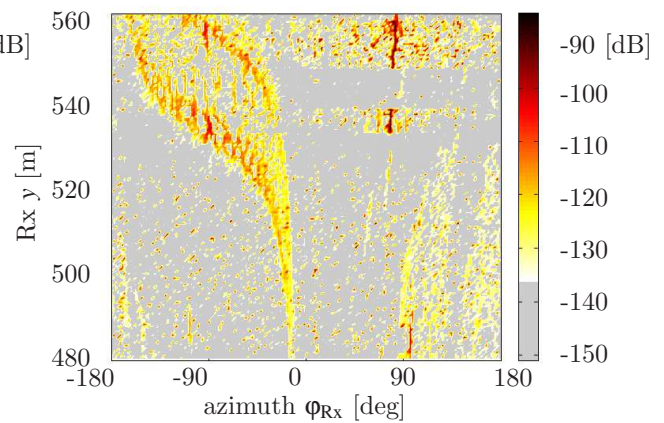
(b) SC+DMC(NoDist)



(c) SC+DMC(FullDist)



(d) SC(NoDist)

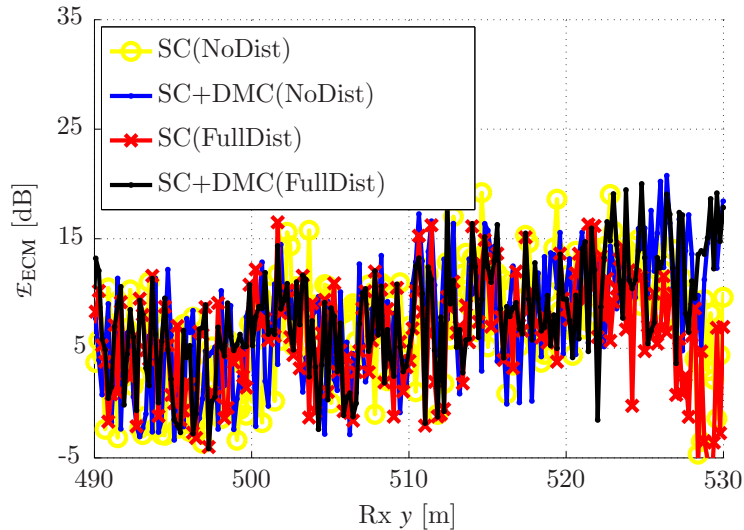


(e) SC(FullDist)

**Fig. 8.14:** Rx azimuth power spectra as a function of Rx  $x$ , for the ray-tracer (*reference*) (a) and the estimated spectra for the setups described in Table 8.1 estimating SC+DMC (b)(c) and SC only (d)(e)

### 8.2.4.3 ECM Mismatch of the SC

Also in case of the ECM mismatch the differences between the four estimation setups are negligible in the NLoS region. Nevertheless, it can be observed in Fig. 8.15 that the absolute values of the mismatch are larger compared to regions with a higher maximum  $\text{SNR}_{\text{IR}}$  as shown in Section 8.2.3.3. From the previous sections and the discussion here, it can be indirectly concluded that the calculated ECM mismatch is only related to additive i.i.d. Gaussian noise and not to model error.



**Fig. 8.15:** ECM mismatch  $\mathcal{E}_{\text{ECM}}$  between SC parameters of the ray-tracer (*reference*) and the parameters of the estimated SC of the four different estimation setups ( $\text{SNR}_{\text{IR}}$  lower than 20 dB).

### 8.2.4.4 MIMO Capacity Error

Again, the *reference* capacity values are based on the SC parameters of the ray-tracer. For calculation of the capacities of the four estimation setups, only the estimated SC are considered, while the estimated DMC are ignored. This is reasonable, as they are related to additive measurement noise only (see previous sections).

In Fig. 8.16 the mean relative capacity error and its standard deviation are shown (equations (8.14) and (8.15)). The variation of the mean error and its standard deviation for a certain estimation setup (indicated by a unique colour) is related to the different alignments  $\Phi_{\text{PPDA}}$  of the application antenna array PPDA as shown in Fig. 8.5.

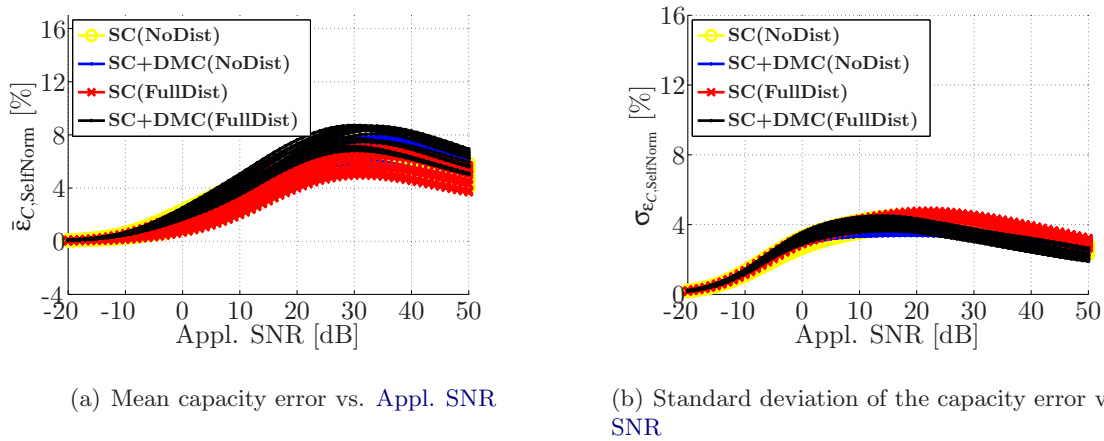
The following points can be noticed from Fig. 8.16:

- The mean capacity error is similar for all four estimation setups. The capacities are overestimated upto 8 %.
- With increasing Appl. SNR the mean capacity error is increasing and the maximum error is reached around 30 dB Appl. SNR. The increasing mean capacity is related to the limited measurement SNR that results in a higher parameter variance of the weak paths.



- For Appl. SNRs larger than 30 dB the error decreases. This behaviour is related to the limited dynamic range of the ray-tracer with 50 dB. With higher Appl. SNRs the absolute error between the capacity  $C_{\text{Ref}}$  and the capacity for a certain estimation setup  $C_{\text{Set}}$  remains constant, but the capacity  $C_{\text{Ref}}$  increases. Consequently, the relative error (eqn. (8.1.2.1)) decreases.
- The standard deviation of the capacity error shows a similar characteristic for the four different estimation setups.
- Compared to Section 8.2.3.4 the standard deviation of the capacity error is lower with a maximum of 4 %.

As the SC model accuracy of all four estimation setups was larger than the maximum  $\text{SNR}_{\text{IR}}$  in the impulse responses, the capacity errors are related to the additive Gaussian measurement noise only.

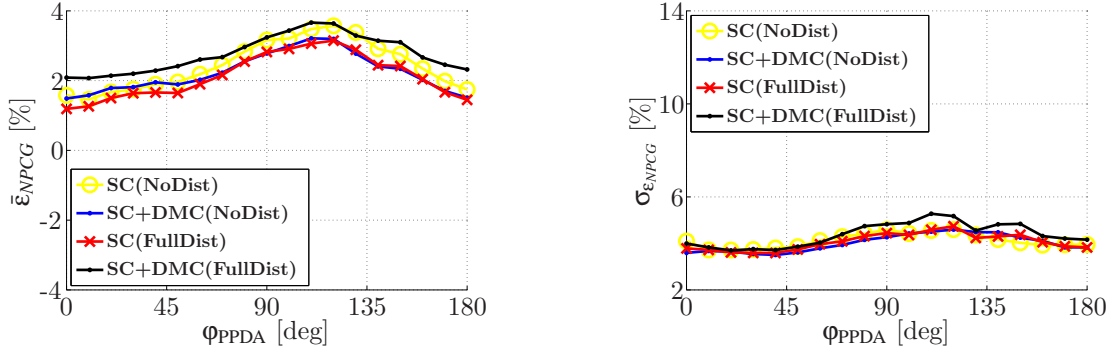


**Fig. 8.16:** Error in terms of capacity for the route MT59 to MT34 as a function of Appl. SNR. The variation of the plots of each estimation setup (indicated by colour) is caused by the different alignments of the Rx application antenna array PPDA.

#### 8.2.4.5 NPCG Error

In Fig. 8.17 the mean relative NPCG error and its standard deviation are shown as function of the alignment  $\phi_{\text{PPDA}}$  of the application antenna array PPDA.

Also the NPCG is overestimated in average for all four estimation setups, but the standard deviation of the NPCG error is much smaller compared to Section 8.2.3.5. For the directions between  $\phi_{\text{PPDA}} = 90^\circ$  and  $\phi_{\text{PPDA}} = 135^\circ$  the mean NPCG error and its standard deviation are increasing due to the concentration of weak paths with large parameter variances. Again, the variances of the estimated parameters for these directions are only related to the additive Gaussian measurement noise.

(a) Mean NPCG error vs. rotation of the **PPDA**(b) Standard deviation of the NPCG error vs. rotation of the **PPDA****Fig. 8.17:** Error in terms of NPCG for the route MT59 to MT34

### 8.3 Error Analysis Based on Measurements

As aforementioned, a good agreement between the **SC** estimated from measurements and calculated by the **IHE** ray-tracer could be found in [34]. However, from the ray-tracing based estimation results in Section 8.2 the **DMC** could be mostly identified as model error and not as a feature of the radio channel. This is obviously evidence of underestimation of diffuse scattering in ray-tracing. Contrary to the ray-tracing results, we found from measurements in different kind of scenarios that the **DMC** contribute up to 80 % to the total received signal energy [14]. Therefore, in this section the model error analysis is performed for measurements considering both the **SC** and **DMC**. The focus of this section is the differentiation between estimated **DMC** caused by model error and **DMC** as a feature of the radio channel.

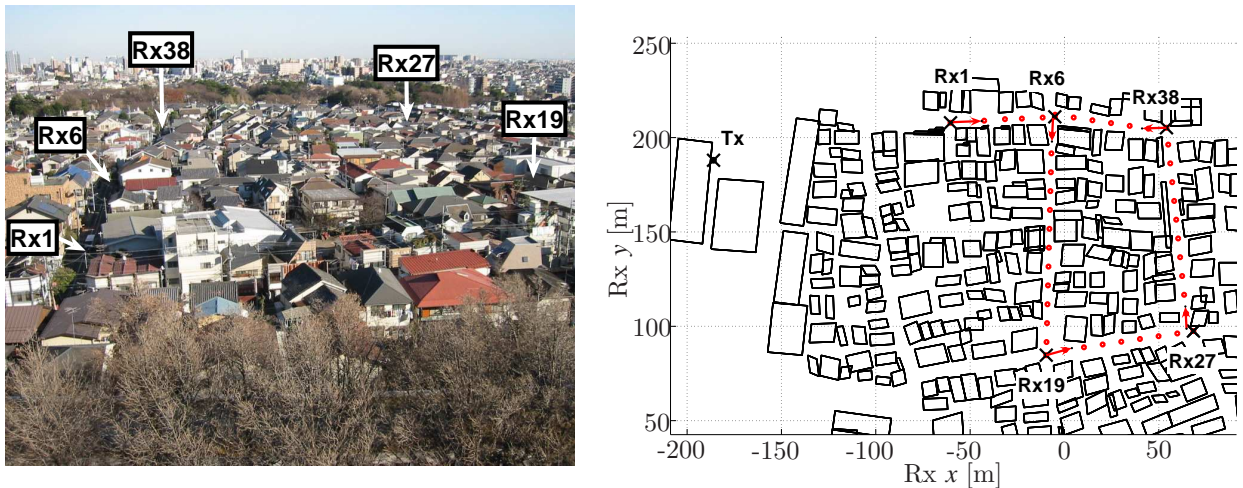
The measurements<sup>1</sup> (see [3, 4]), which were carried out in Tokyo during my time as visiting researcher at the Tokyo Institute of technology, are described in Section 8.3.1. In Section 8.3.2 the analysis procedure is discussed in detail. The consequences of an overall model accuracy lower and higher than the maximum  $\text{SNR}_{\text{IR}}$  are presented in Section 8.3.3.

#### 8.3.1 Description of the Measurement

The full polarimetric double directional channel measurements are performed in a macro-cell environment in Tokyo (see [4]). The ATM system described in Section 2.3 with a centre frequency of 4.5 GHz and a signal bandwidth of 120 MHz was used. The transmit antenna array, the  $2 \times 4$  polarimetric uniform rectangular patch array PURPA $_{2 \times 2 \times 4}$  was placed over roof-top at a 10 floor high building ( $\approx 35$  m). The picture of Fig. 8.18(a) is taken from the Tx position in the zero azimuth direction of the antenna array. The receive antenna array, the  $2 \times 24$  stacked polarimetric uniform circular patch array SPUCPA $_{2 \times 2 \times 24}$  was placed at a cart around 1.6 m above the ground. The buildings in the surrounding residential area are between two and three floors high. In Fig. 8.18(b)

<sup>1</sup> This measurement was supported by the National Institute of Information and Communications Technology (NICT) of Japan. Furthermore, I would like to thanks the members of the Takada Laboratory for the support during measurements.

the significant positions of the measurement route like corners are labelled with crosses. The propagation conditions vary between pure LoS, mixed NLoS and OLoS and pure NLoS. Around 1700 snapshots were recorded along the 490 m long measurement route. Each snapshot consists of 1536 complex impulse responses with a maximum excess delay of  $3.2 \mu\text{s}$ .



(a) Picture taken from Tx in the direction of Rx6 macro cell

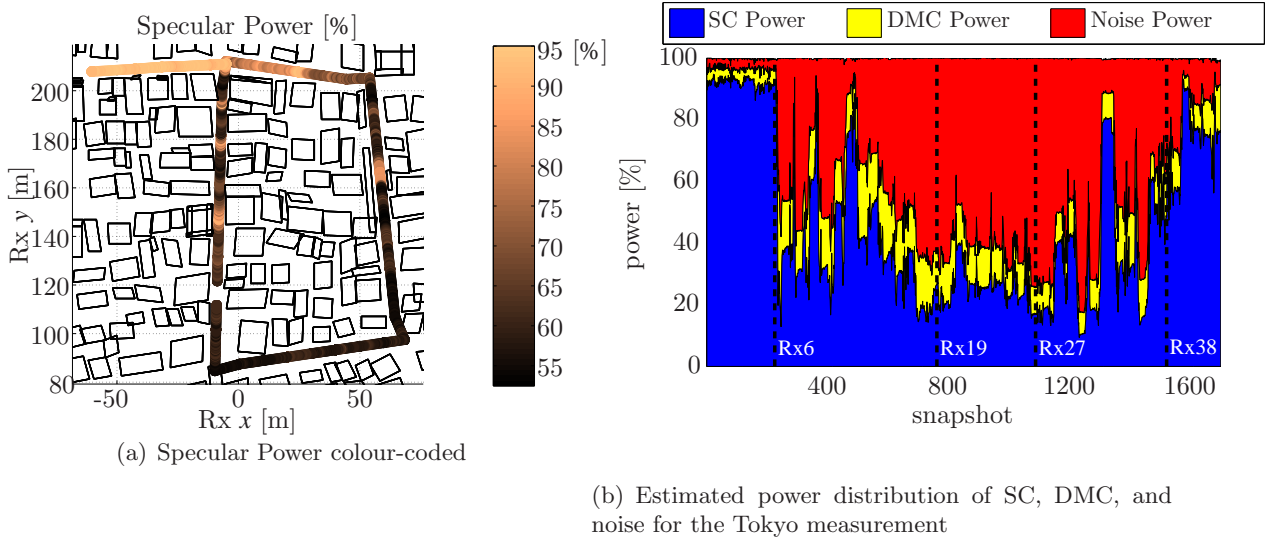
(b) Map of the measurement scenario, Rx moving direction indicated by red arrows.

**Fig. 8.18:** Measurement scenario

Before we start with the measurement based analysis, let us characterise the measurement positions in terms of their propagation conditions. Additionally, the estimation results from the joint estimation of SC and DMC are discussed, whereas only the power contribution of estimated SC, estimated DMC, and measurement noise to the total power will be discussed for a general classification of the measurements. The portion of SC power of the total received signal power in percentage is shown in Fig. 8.19(a), whereas the remaining percentage corresponds to the signal power of the DMC. Figure 8.19(b) shows the contribution of the total received power in terms of SC, DMC, and noise power. The dashed lines indicate the measurement positions that are also shown in Fig. 8.18(b).

- In the LoS case, moving from position Rx1 to Rx6 (see Fig. 8.18(b)), the total specular power represents around 95 % of the total received signal power.
- The measurements between position Rx6 and Rx19 are mostly NLoS with a total SC power of around 55 % to 65 %. However, at some positions, the specular power increases to 80 %, which is mainly caused by strong single bounce scattering and OLoS. In the parallel street between position Rx27 and Rx38, we observe similar behaviour.
- In the street between position Rx19 and Rx27, the portion of SC is almost constant (around 55 %). All measurements here were taken under NLoS conditions. Furthermore, strong single bounce reflections and OLoS are rare.

- The measurements between Rx38 and Rx6 are dominated by strong single bounce scattering and OLoS around the corner of Rx6. The total SC power is between 65 % to 85 %.



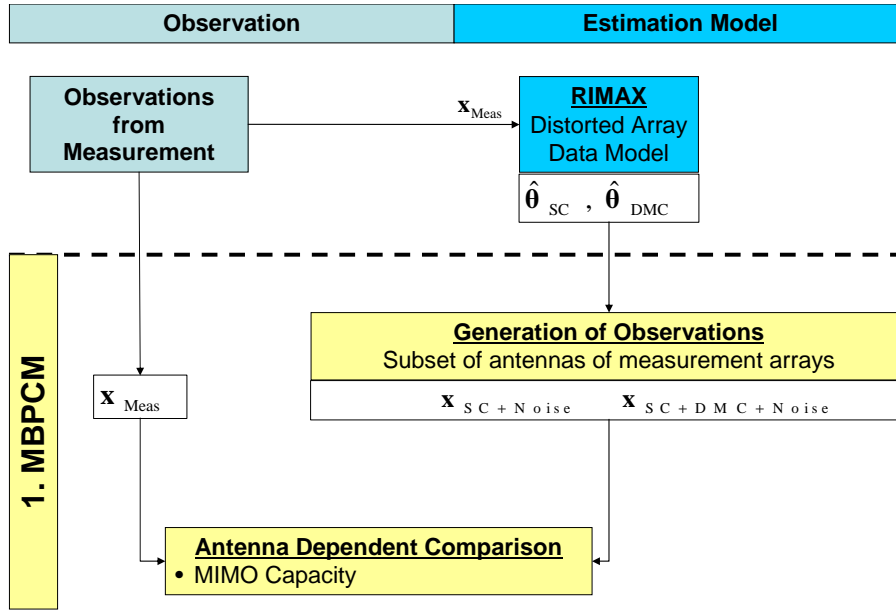
**Fig. 8.19:** Portion of SC power dependent on the measurement position (a) and estimated power distribution w.r.t. SC, DMC and noise over the entire measurement route (b)

### 8.3.2 Measurement Based Analysis Procedure

For better understanding, Fig. 8.20 illustrates the procedure for the measurement based error analysis that will be described in the following. From the measured observations the parameters  $\hat{\theta}_{\text{SC}}$  and  $\hat{\theta}_{\text{DMC}}$  are jointly estimated applying the antenna array data model derived from calibration measurements (distorted array data model with model accuracy between 20 dB to 30 dB).

Note that the SC only estimation is not performed for the measurement. One reason is that “real” DMC as part of the propagation are expected. Another reason is that from the ray-tracing results discussed in the previous section it became clear that the joint estimation of SC and DMC gives us the most reliable results.

Furthermore, the antenna independent metrics angular power spectrum and ECM mismatch (see Section 8.1.1) will not be considered for the following analysis. They are not appropriate for measurements, as the “true” parameters of the channel  $\theta_{\text{SC,Ref}}$  are not available in complex measurement environment. Only the measured observation  $\mathbf{x}_{\text{Meas}}$  can be compared with the generated observations calculated based on the parameter estimation results  $\hat{\theta}_{\text{SC}}$  and  $\hat{\theta}_{\text{DMC}}$ . For the comparison with measurements, observations based on the estimated parameters have to be generated with artificial additive measurement noise.



**Fig. 8.20:** Block diagram of the analysis procedure in case of measurements

From the estimation results two different observations will be generated:

1. observations of the **SC** superposed with artificial additive measurement noise (indicated by **SC+Noise**)
2. observations of the **SC** superposed with the generated observations of the **DMC** and artificial measurement noise (indicated by **SC+DMC+Noise**).

The generated observations are given as:

$$\mathbf{x}_{\text{SC+Noise}} = \mathbf{s}(\hat{\boldsymbol{\theta}}_{\text{SC}}) + \mathbf{n} \quad (8.16)$$

$$\mathbf{x}_{\text{SC+DMC+Noise}} = \mathbf{s}(\hat{\boldsymbol{\theta}}_{\text{SC}}) + \mathbf{d}(\hat{\boldsymbol{\theta}}_{\text{DMC}}) + \mathbf{n}. \quad (8.17)$$

The artificial measurement noise  $\mathbf{n}$  is defined as described in eqn. (E.3) setting  $\boldsymbol{\sigma}$  to the square root of the mean estimated noise power  $\alpha_0$ .

While the generation of the observation  $\mathbf{s}(\hat{\boldsymbol{\theta}}_{\text{SC}})$  for the estimated **SC** was already explained in Section 5.1 with the equations (5.4) and (5.12), the generation of the **DMC** based on the estimated parameters  $\hat{\boldsymbol{\theta}}_{\text{DMC}}$  will be explained in the following. The observation  $\mathbf{d}(\hat{\boldsymbol{\theta}}_{\text{DMC}})$  of the **DMC** is modelled as a stochastic process with the covariance matrix  $\mathbf{R}_f$  (see Section 5.1.2 and [62]), which is calculated using the sampled version of the covariance function defined in eqn. (5.13) with:

$$\kappa(\hat{\boldsymbol{\theta}}_{\text{DMC}}) = \frac{\alpha_1}{M_f} \begin{bmatrix} \frac{1}{\beta_d} & \frac{e^{-j2\pi\tau'_d}}{\beta_d + j2\pi\frac{1}{M_f}} & \dots & \frac{e^{-j2\pi\tau'_d(M_f-1)}}{\beta_d + j2\pi\frac{(M_f-1)}{M_f}} \end{bmatrix}^T \quad (8.18)$$

This gives us the covariance matrix of the **DMC** process as follows:

$$\mathbf{R}_f = \text{toep}(\kappa(\hat{\theta}_{\text{DMC}}), \kappa(\hat{\theta}_{\text{DMC}})^H). \quad (8.19)$$

The generation is carried out in the frequency domain. For each antenna channel  $i$  a random vector (i.i.d. Gaussian process in real and imaginary part) is created with:

$$\mathbf{z}_i \in \mathbb{C}^{M_f \times 1} \sim \mathcal{N}_{\mathbb{C}}(\mathbf{0}, \mathbf{I}), i = 1 \dots M_{\text{Tx}} \cdot M_{\text{Rx}}. \quad (8.20)$$

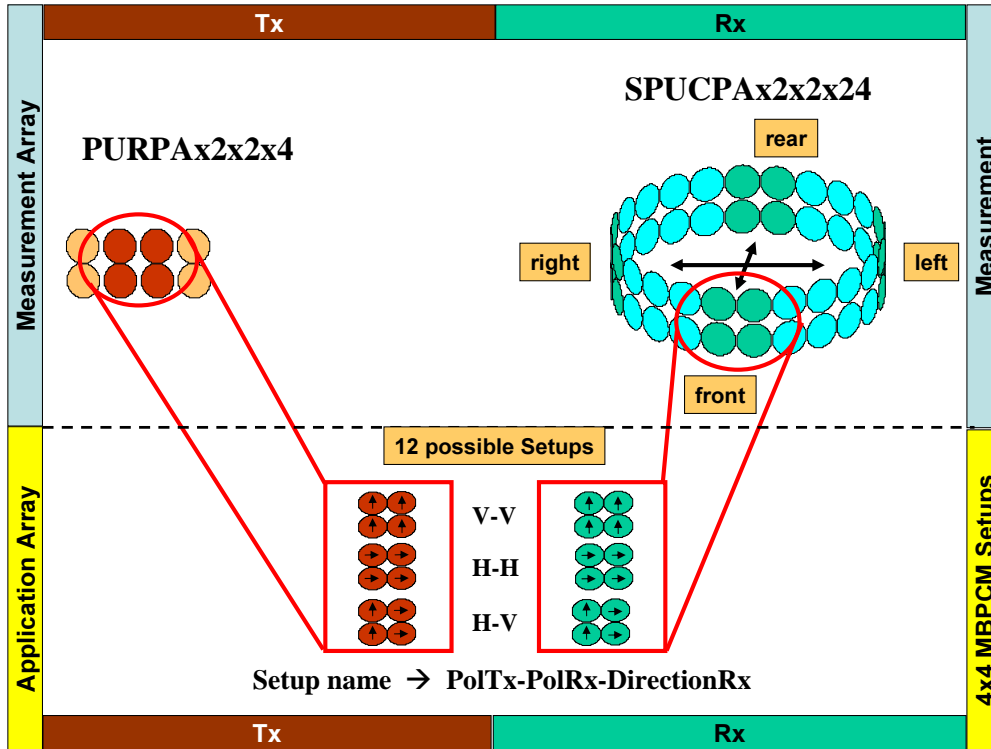
Applying the transformation matrix  $\mathbf{L}$  to the random vector  $\mathbf{z}_i$  of the  $i$ -th channel a single realisation of the **DMC** is calculated:

$$\mathbf{d}_i(\hat{\theta}_{\text{DMC}}) = \mathbf{L}(\hat{\theta}_{\text{DMC}}) \cdot \mathbf{z}_i \quad (8.21)$$

The matrix  $\mathbf{L}$  is obtained by the Cholesky decomposition of  $\mathbf{R}_f = \mathbf{L} \cdot \mathbf{L}^H$ . Finally, the observation of the **DMC** for the  $M_{\text{Rx}} \cdot M_{\text{Tx}}$  antenna channels is generated with:

$$\mathbf{d}(\hat{\theta}_{\text{DMC}}) = [\mathbf{d}_1^T \dots \mathbf{d}_{M_{\text{Rx}} \cdot M_{\text{Tx}}}^T]^T. \quad (8.22)$$

All observations are generated for a  $4 \times 4$  subset of the measurement antenna arrays at **Tx** and **Rx** as shown in Fig. 8.21. In total 12 subsets are considered with 3 different polarisation combinations



**Fig. 8.21:** Antenna subset selection from the measurement antenna array for the capacity calculations using a  $4 \times 4$  **MIMO** system

between **Tx** and **Rx** (H-H,V-V,H-V) and four directions at the **Rx** side (front, rear, left, and right) related to the **Rx** moving direction shown in Fig. 8.18(b)).

For the error analysis, the capacities of the observations  $\mathbf{x}_{\text{SC+DMC+Noise}}$  and  $\mathbf{x}_{\text{SC+Noise}}$  are compared

with the capacities of the measured channel  $\mathbf{x}_{\text{Meas}}$ . The capacities are calculated for Appl. SNRs between -10 dB and 20 dB. The mean capacity error (see Section 8.1.2.1) between the measurements (*reference*) and the generated observations  $\mathbf{x}_{\text{SC+DMC+Noise}}$  and  $\mathbf{x}_{\text{SC+Noise}}$  will be analysed.

**Some remarks to the defined capacity error in the presence of measurement noise:** It should be noted that the defined capacity error between the noisy generated observations and the measured observation is more reliable for Appl. SNRs that are lower than the mean measurement  $\text{SNR}_{\text{FR}}$  at a single frequency bin. For an Appl. SNR higher than the mean measurement  $\text{SNR}_{\text{FR}}$ , the relative capacity error will always decrease. The influence of the singular values of the measured and generated channel matrices  $\mathbf{H}$  that are related to measurement noise becomes larger when calculating the capacities for a higher Appl. SNR. The singular values that are related to measurement noise from the measured observation are “compared” with the singular values related to the artificial measurement noise of the generated observations. As the generated measurement noise can be perfectly modelled, the capacity error between the two noisy observations will decrease for Appl. SNRs higher than the measurement  $\text{SNR}_{\text{FR}}$ ! This means, in the presence of model error the maximum mean capacity error can be found at the Appl. SNR equal to the measurement  $\text{SNR}_{\text{FR}}$ . Nevertheless, it depends on the characteristic of the model error if such a maximum can be found. However, it always needs to be considered that the defined relative capacity error for Appl. SNRs higher than the measurement  $\text{SNR}_{\text{FR}}$  becomes less reliable.

### 8.3.3 Consequences of an Overall Model Accuracy Lower or Higher than the SNR in the CIR

Conform to the ray-tracing based analysis, the measurement based analysis will be performed for measurement positions with a  $\text{SNR}_{\text{IR,SC}}$  higher than the available model accuracy (Rx1 to Rx6) and for measurement positions with a  $\text{SNR}_{\text{IR,SC}}$  smaller than the available model accuracy (Rx19 to Rx27). The overall model accuracy of the estimation model for these measurements is mainly limited by phase noise ( $\sigma_{\text{pns}} = 5.69^\circ$ ) of the ATM system. From the approximation equation (7.24) the expected mean model accuracy is around 20 dB. The model accuracy of the antenna array data model (EADFs) is between 20 dB and 30 dB.

#### 8.3.3.1 Relevance of the Estimated DMC

With the ray-tracing based analysis it was shown that with a  $\text{SNR}_{\text{IR,SC}}$  larger than the overall model accuracy, the DMC are mainly related to model error (Section 8.2.3.1). For a  $\text{SNR}_{\text{IR,SC}}$  lower than the overall model accuracy, the DMC can be assumed as feature of the radio channel (Section 8.2.4.1). Note that these conclusions could be drawn since results from estimation with distorted and undistorted data models were available.

For a measurement, we can only assume that in case of a  $\text{SNR}_{\text{IR,SC}}$  equal to or lower than the overall model accuracy the DMC are related to propagation in the radio channel. In case of the measurement route Rx19 to Rx27, the  $\text{SNR}_{\text{IR,SC}}$  is almost equal to the overall model accuracy of 20 dB, but contrary to the ray-tracing results ( $\text{SNR}_{\text{IR,DMC}} \approx 0$  dB) the  $\text{SNR}_{\text{IR,DMC}}$  is around



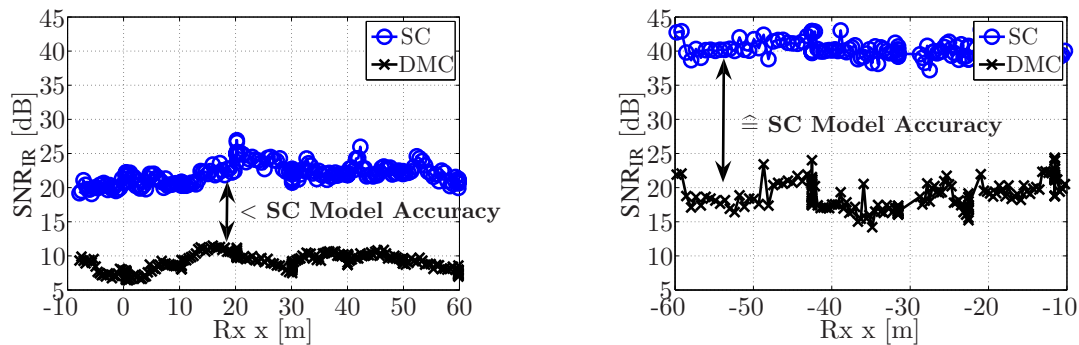
10 dB (see Fig. 8.22(a)). This means, that **DMC** in terms of unresolved **SC** and distributed diffuse scattering as part of the propagation exist.

If the  $\text{SNR}_{\text{IR,SC}}$  is higher than the overall model accuracy, a differentiation has to be made between two cases:

1. the ratio between the  $\text{SNR}_{\text{IR,SC}}$  and the  $\text{SNR}_{\text{IR,DMC}}$  matches the overall model accuracy
2. the ratio between the  $\text{SNR}_{\text{IR,SC}}$  and  $\text{SNR}_{\text{IR,DMC}}$  is lower than the overall model accuracy.

In the first case, the estimated **DMC** are mainly related to model error. But in the second case, the **DMC** may also be related to the propagation in the radio channel!

Figure 8.22(b) illustrates the  $\text{SNR}_{\text{IR,SC}}$  and the  $\text{SNR}_{\text{IR,DMC}}$  for measurements Rx1 to Rx6 with a  $\text{SNR}_{\text{IR,SC}}$  higher than the overall model accuracy. From the figure it can be seen that the ratio between  $\text{SNR}_{\text{IR,SC}}$  and  $\text{SNR}_{\text{IR,DMC}}$  is always around 20 dB. This ratio is as large as the expected model accuracy of the **SC**. Consequently, it can be assumed that most of the **DMC** power is related to model error.



(a)  $\text{SNR}_{\text{IR}}$  of the SC and DMC for the measurement route Rx19 to Rx27

(b)  $\text{SNR}_{\text{IR}}$  of the SC and DMC for the measurement route Rx1 to Rx6

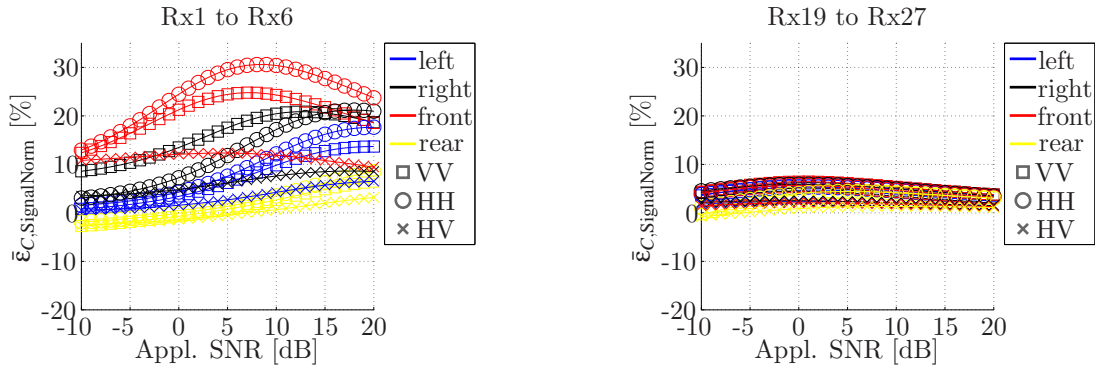
**Fig. 8.22:** Comparison of the  $\text{SNR}_{\text{IR}}$  of the SC and DMC for a measurement in case of  $\text{SNR}_{\text{IR}}$  of the SC that is lower (a) and higher (b) than the overall model accuracy of the SC ( $\approx 20$  dB)

### 8.3.3.2 MIMO Capacity Error

In the previous section it was concluded that the **DMC** are only relevant for the measurement route Rx19 to Rx27 ( $\text{SNR}_{\text{IR,SC}}$  lower than model accuracy), whereas for the measurement route Rx1 to Rx6 ( $\text{SNR}_{\text{IR,SC}}$  higher than model accuracy) the **DMC** are not related to propagation in the radio channel. Nevertheless, let us first discuss the mean capacity error (Fig. 8.23(a) and Fig. 8.23(b)) and its standard deviation (Fig. 8.23(c) and Fig. 8.23(d)) for the generated observations  $\mathbf{x}_{\text{SC+DMC+Noise}}$  that include the **DMC** for both measurement routes. The following points can be noticed from Fig. 8.23:

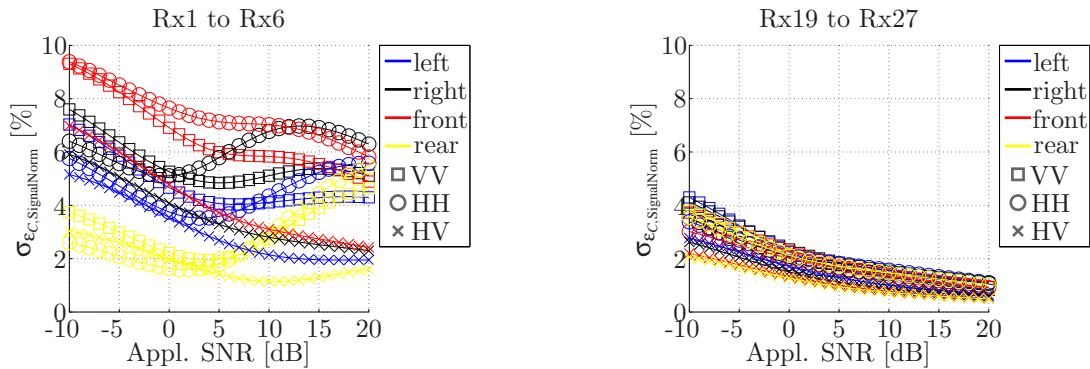
- For the measurement route Rx1 to Rx6 the capacity is up to 30 % overestimated in average. The overestimation is related to the generated **DMC**. The **DMC** characterise mainly model errors and are not a feature of the radio channel.

- In case of Rx19 to Rx27 the average capacity overestimation does not exceed 8 %. The slightly overestimated capacities are basically related to the assumption that the **DMC** are uniformly distributed in the angular domain. This assumption is not always fulfilled in real propagation environments.
- Also from the standard deviation of the capacity error it can be seen that the generated observations **SC+DMC+Noise** match the measured observation in terms of capacity better for the measurement route Rx19 to Rx27 than for the measurement route Rx1 to Rx6.



(a) Mean capacity error vs. Appl. SNR ( $\text{SNR}_{\text{IR}}$  of the SC larger than the model accuracy of the SC)

(b) Mean capacity error vs. Appl. SNR ( $\text{SNR}_{\text{IR}}$  of the SC smaller than the model accuracy of the SC)



(c) Standard deviation of the capacity error vs. Appl. SNR ( $\text{SNR}_{\text{IR}}$  of the SC larger than the model accuracy of the SC)

(d) Standard deviation of the capacity error vs. Appl. SNR ( $\text{SNR}_{\text{IR}}$  of the SC smaller than the model accuracy of the SC)

**Fig. 8.23:** Mean capacity error (top) and its standard deviation (bottom) of the generated observations **SC+DMC+Noise** for the measurement route Rx1 to Rx6 (left) and Rx19 to Rx27 (right) as a function of the Appl. SNR for different alignments of the Rx application antenna subset (color) and different polarisation combinations between Tx and Rx (marker).

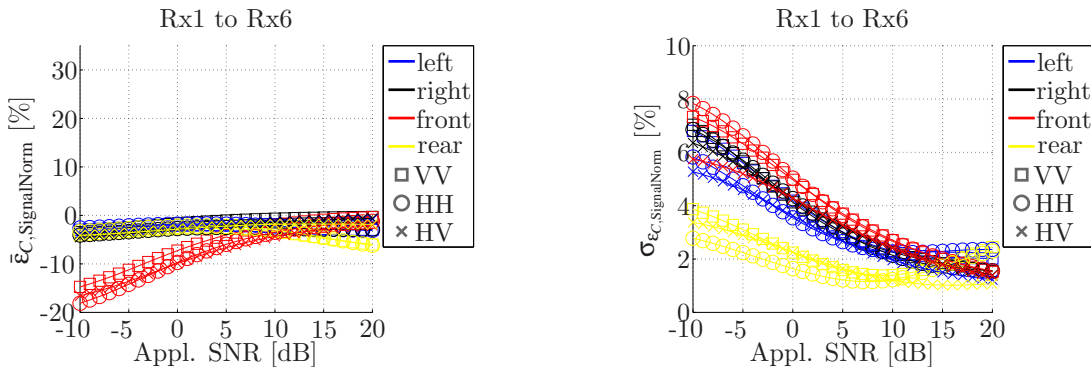
Again, it can be concluded that for the route Rx19 to Rx27, the estimated **DMC** are mostly related to the propagation. Consequently, they need to be considered for the generation of a realistic observation based on estimation results. However, in case of route Rx1 to Rx6, the **DMC** are mainly related to model error.

If the **DMC** for the measurement route Rx1 to Rx6 are mainly related to model error then we can expect that the generated observations  $\mathbf{x}_{\text{SC+Noise}}$  without the **DMC** will have a lower capacity

error. In Fig. 8.24 the mean capacity error and its standard deviation are shown for the **SC+Noise** observations. The following points can be noticed from the figures:

- For the left, right, and rear subsets the capacity error is almost negligible when using the **SC+Noise** model. In these directions most of the specular power is received and the estimated **DMC** correspond mainly to model error.
- As the **DMC** estimation results are strongly affected by the model error caused in the left, right, and rear directions, weak **SC** in the front direction could not be resolved. Consequently, the generated **SC** observations are less reliable for the front direction and the mean capacity error of the **SC+Noise** observations is larger than for the other directions.

Again, the estimated **DMC** should not be considered as characteristic of the radio channel for the measurement route Rx1 to Rx6 with a  $\text{SNR}_{\text{IR,SC}}$  higher than the overall model accuracy. The **SC+Noise** observations give more reliable results than the **SC+DMC+Noise** observations, while the only exception are the results of the front direction. However, such exceptions will always demand a careful analysis of the estimation results. This means in the case of a  $\text{SNR}_{\text{IR,SC}}$  that is higher than the overall model accuracy, a critical analysis of the results is required, whereas in the case of a  $\text{SNR}_{\text{IR,SC}}$  lower than the overall model accuracy, a generation of the observations including **SC** and **DMC** is most reliable.



(a) Mean capacity error vs. application SNR ( $\text{SNR}_{\text{IR}}$  of the SC larger than the model accuracy of the SC)

(b) Standard deviation of the capacity error vs. Appl. SNR ( $\text{SNR}_{\text{IR}}$  of the SC larger than the model accuracy of the SC)

**Fig. 8.24:** Mean capacity error (left) and its standard deviation (right) of the generated observations **SC+Noise** for the measurement route Rx1 to Rx6 as a function of the Appl. SNR for different alignments of the Rx application antenna subset (color) and different polarisation combinations between Tx and Rx (marker).

## 8.4 Conclusion Chapter 8

In this chapter three crucial questions are answered:

1. Can we improve the reliability of the **SC** if we incorporate the **DMC** estimation in the estimation algorithm?
2. How reliable are the estimated **SC** in complex propagation environments in the presence of model error?
3. Under which conditions the estimated **DMC** are related to model error or to propagation in the radio channel?

The answers to these questions were found based on ray-tracing and measurement based analysis.

### Ray-tracing

With the ray-tracing based analysis, it was shown that in case of a  $\text{SNR}_{\text{IR,SC}}$  higher than the overall model accuracy, the error of all discussed metrics is increasing when not estimating the **DMC**. It was shown that the estimated **DMC** for a  $\text{SNR}_{\text{IR,SC}}$  higher than the overall model accuracy are mainly related to model error and should be discarded when generating observations for simulations with application specific antennas.

In case of a  $\text{SNR}_{\text{IR,SC}}$  lower than the overall model accuracy, the error of the generated observations in terms of the discussed metrics is similar for **SC** only estimation and joint estimation of **SC** and **DMC**. The error is only related to the additive Gaussian measurement noise.

The relevance of the estimated **DMC** as part of the propagation in terms of unresolved **SC** or distributed diffuse scattering could not be shown based on the ray-tracing analysis. The ray-tracer used can not completely describe the “real” propagation and a further analysis with measurements was necessary.

### Measurements

Also with measurements it was shown that with a  $\text{SNR}_{\text{IR,SC}}$  higher than the overall model accuracy, the estimated **DMC** are mainly related to model error.

As opposed to ray-tracing the relevance of the estimated **DMC** was clearly shown in case of a  $\text{SNR}_{\text{IR,SC}}$  lower than the overall model accuracy. In this case, the estimated **DMC** are related to the propagation in the radio channel. Consequently, the estimated **DMC** have to be considered when generating observations for simulations with application-specific antennas or when geometry based channel models are parametrised with the results of *Experimental Channel Characterisation*.

The results based on measurements also show that **DMC** are indeed a feature of the radio channel, contrary to the ray-tracing results. This is obviously evidence that ray-tracing still underestimates the contribution of diffuse scattering to the propagation in the radio channel.



## 9. CONCLUSIONS AND FUTURE PROSPECTS

The points that are addressed in this thesis refer to the overall limitations of *Experimental Channel Characterisation*. Although, some limitations have been discussed in literature before, most of them were ignored, neglected, or simply overlooked. Additionally, it is often assumed that certain sources of error can be neglected or that the propagation in the radio channel follows certain constraints. However, in this work it is clearly shown that in reality such assumptions are mostly inappropriate. In this context, the error sources ranging from measurement system impairments to antenna array calibration errors to limitations of the radio channel model as applied by *high-resolution* parameter estimation procedures, were investigated. First, the consequence of each error source separately was analysed and finally the overall consequences of all unavoidable errors were demonstrated. From our investigations, it can be concluded that the necessity to consider a certain error source is strongly dependent on the system configuration, the employed antenna arrays, and on their data models. It is emphasised that generalisations can not be made. The entire measurement system has to be analysed to determine which error source dominates in that specific configuration. The most important contributions of this thesis are summarised as follows:

- The measured radiation patterns of any *practical* antenna array as well as their derivatives were efficiently and accurately modelled by a novel analytic description, the so called Effective Aperture Distribution Function (EADF).
- For full-polarimetric two-dimensional calibration of *practical* antenna arrays with Multiple-Input Multiple-Output (MIMO) channel sounders, an accurate calibration procedure for the system frequency responses was proposed. This includes the frequency dependent calibration of the polarimetric reference horn antenna, of all RF cables, of the AGC dependent frequency responses of the measurement system, and of the RF multiplexers at the transmitter and receiver side.
- A gradient based Maximum Likelihood (ML) estimator was developed to correct the measured radiation patterns for phase offsets occurring during the antenna array calibration measurement.
- Sources for model mismatch such as:
  - systematic error in antenna array calibration caused by parasitic reflections
  - ignoring elevation and/or polarisation characteristics of the antenna elements
  - phase noise and phase drift during propagation measurements

were identified and examined with respect to their impact.

---

- Model mismatch causes the estimation of biased and/or artificially spread angular parameters of the Specular Components (SC) and increases the amount of power that is estimated for the Dense Multipath Components (DMC).
- In case of an adequate model accuracy of the derived EADFs, any practical antenna array can be evaluated in terms of the directional resolution limits with a novel, powerful framework proposed in this thesis. The framework allows the analytic calculation of the Cramér-Rao Lower Bound of the DoD/DoA parameters in arbitrary test scenarios based on measured radiation patterns as described by their corresponding EADFs.
- Generally, the estimation of DMC improves the reliability of the parameter estimation results for the SC in the presence of non-resolved scattering and/or model errors.
- However, the estimated DMC can only be interpreted as feature of the radio channel if the accuracy of the data model is larger than the maximum Signal-to-Noise ratio of the impulse response.
- Finally, it is emphasised that the relevance and reliability of the estimated SC and DMC have to be taken into account when using the results of *Experimental Channel Characterisation* for channel modelling.

## Future Prospects

1. Further improvements of *Experimental Channel Characterisation* can be achieved by reducing the model mismatch.

On one hand, the model of the radio channel applied for parameter estimation can be improved, especially with respect to the DMC. Up to now, the DMC are assumed to be uniformly distributed in the angular domain, but an angular dependence is more realistic. Models for the angular distribution of the DMC have been proposed already elsewhere, but further measurements are required to verify whether the model assumptions are valid in reality. Furthermore, such directional models of the DMC may also help to suppress direction dependent model errors during the estimation of the SC. With this approach, the estimation of the SC could be further improved. However, still such estimated direction dependent DMC could be related to model errors instead of being a feature of the radio channel.

On the other hand, the error sources related to the measurement system can be reduced. For example, the consequence of phase noise and/or drift can be reduced by an improved design of the Local Oscillators, the frequency references, and by improving the synchronisation between Tx and Rx. Additionally, novel designs of the antenna positioning system may help to reduce the amount of parasitic reflections.

2. The results of our ray-tracing based analyses show that the modelling of diffuse scattering in ray-tracing is still in its infancy and further research is required. The MIMO capacity especially in Non Line of Sight (NLoS) is likely to be underestimated without diffuse scattering being modelled.



# Appendices

---



## Appendix A

# CHANNEL MEASUREMENT

### A.1 Estimation of the Phase Noise Properties of the MIMO Sounders Used

Here measurements are performed to obtain the phase noise standard deviation  $\sigma_{\text{pnS}}$  and the corresponding phase noise covariance matrix  $\Sigma$  for the ATM and HyEff channel sounders. A common reference signal is used. Nevertheless, it can be seen in Fig. A.1(a) and Fig. A.1(b) for ATM and HyEff system respectively, that the measured data is still affected by a long term phase drift. Therefore, it is necessary to estimate the long term phase drifts  $\varphi_{\text{pnL}}$  for both systems in order to obtain an estimation of the phase noise  $\varphi_{\text{pnS}}$ . To estimate the long term phase drift, a moving average filter with a length  $w$  is used. The estimated long term phase drift for a given  $w$  is  $\hat{\varphi}_{\text{pnL}}(w, t)$ . Under the assumption that  $\varphi_{\text{pnS}}$  is normal distributed, the best estimate of  $\varphi_{\text{pnL}}(t)$  is given for a smoothing window length  $w$ , in which case the ideal normal distribution fits best the distribution of:

$$\hat{\varphi}_{\text{pnS}}(w, t) = \varphi_{\text{pn}}(t) - \hat{\varphi}_{\text{pnL}}(w, t). \quad (\text{A.1})$$

Therefore, the Frobenius norm  $\text{Resnorm}(w)$  of the residual between the probability density of the best fit normal distribution  $p_{\text{pnBF}}(\hat{\varphi}_{\text{pnS}}(w))$  and the estimated distribution  $\hat{p}_{\text{pn}}(\hat{\varphi}_{\text{pnS}}(w))$ :

$$\text{Resnorm}(w) = \left\| p_{\text{pnBF}}(\hat{\varphi}_{\text{pnS}}(w)) - \hat{p}_{\text{pn}}(\hat{\varphi}_{\text{pnS}}(w)) \right\|_{\text{F}} \quad (\text{A.2})$$

is calculated (See Fig. A.1(c) and Fig. A.1(d)). Herewith, the best estimate of the long term phase drift and the phase noise is given by:

$$\begin{aligned} \hat{w} &= \arg \min_w \{ \text{Resnorm}(w) \} \\ \hat{\varphi}_{\text{pnS}}(t) &= \hat{\varphi}_{\text{pnS}}(\hat{w}, t) \\ \hat{\varphi}_{\text{pnL}}(t) &= \hat{\varphi}_{\text{pnL}}(\hat{w}, t) \end{aligned} \quad (\text{A.3})$$

The estimated phase noise  $\hat{\varphi}_{\text{pnS}}$  and its distributions for the optimum  $w$  are shown in third and fourth row of Fig. A.1 respectively. Finally, the ATM system has a phase noise standard deviation  $\hat{\sigma}_{\text{pnS}}$  of  $5.69^\circ$ , where the HyEff system has a lower phase noise standard deviation with  $\hat{\sigma}_{\text{pnS}} = 2.94^\circ$ .

For simulations in chapter 7 the realistic correlated phase noise need to be modelled, therefore the Auto Correlation Function (ACF) (e.g. in Fig. 2.11(b)) or the covariance matrix of the phase noise process is estimated from the estimated phase noise  $\hat{\varphi}_{\text{pnS}}$ . The phase noise vector for a correlation

length  $t_s$  and interval  $i$  is given by:

$$\Phi_i = [\hat{\phi}_{\text{pnS}}((i-1) \cdot t_s) \quad \hat{\phi}_{\text{pnS}}((i-1) \cdot t_s + (2 \cdot \tau_{\text{max}})) \quad \cdots \quad \hat{\phi}_{\text{pnS}}(i \cdot t_s)]^T. \quad (\text{A.4})$$

Consequently, the estimated covariance matrix is defined as:

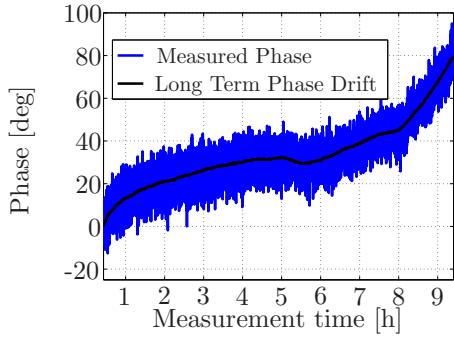
$$\Sigma(t_s) = \frac{\sum_{i=1}^I [\Phi_i \cdot \Phi_i^H]}{I \cdot \hat{\sigma}_{\text{pnS}}^2} \quad (\text{A.5})$$

## A.2 Correction for the Switched Reference Attenuator in the AGC dependent back-to-back Calibration

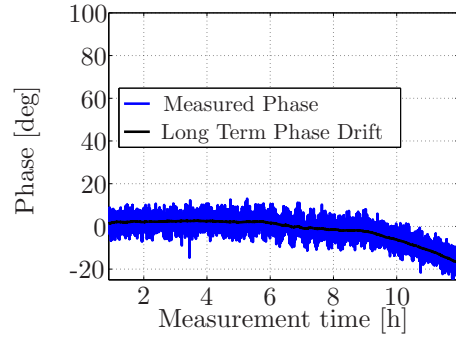
The switched reference attenuator consists of 9 blocks with different attenuations (0, 1, 2, 4, 4, 10, 20, 40, 40 dB), which will be cascaded to achieve a certain attenuation. The corresponding frequency responses normalised to the nominal attenuation are shown in Fig. 2.8(a); Fig. 2.8(b) shows the phase offset of each attenuation block. That means each measured system frequency response from the Automatic Gain Control (AGC) dependent back-to-back calibration contains an additional phase offset due to the set attenuation of the switched reference attenuator. Therefore, it is necessary to correct the measured system frequency responses of each AGC level for the corresponding frequency responses of the switched reference attenuator. The attenuation set at the switched reference attenuator to measure a certain AGC level are known from the AGC dependent back-to-back calibration.

In the following the achievable accuracy by using the AGC dependent back-to-back calibration incorporating the correction for the switched reference attenuator will be demonstrated in comparison to the uncorrected case. Therefore, a measurement is performed in which the back-to-back calibration setup in Fig. 2.6 is used. The transmit power is attenuated from 10 dB to 90 dB in 1 dB steps. After recording the data the corrected and uncorrected measurements are compared in terms of the magnitude (Fig. A.2(a)) and the phase (Fig. A.2(b)) of the maximum in the impulse responses. The magnitude is normalised to the square root of the input power. It can be seen that in case of the correction the phase error is almost constant, the standard deviation being around  $2.56^\circ$ . This variation is related to the phase noise, which will be discussed in Section 2.3.4. The mean value of around  $-10^\circ$  is a constant phase offset for all input levels, which has no effect on the channel characterisation. The magnitude error is almost 0 dB, only for attenuation levels below 20 dB a higher error can be observed. Below 20 dB attenuation the receiver amplifiers are used in its non-linear region, which results in an increased magnitude error. In case of the uncorrected data the phase is strongly varying w.r.t. to the attenuation level, the magnitude error only having a constant offset. Consequently, if we do not correct for the phase offsets of the switched reference attenuator, a reliable Direction of Departure (DoD) and Direction of Arrival (DoA) estimation is impossible.

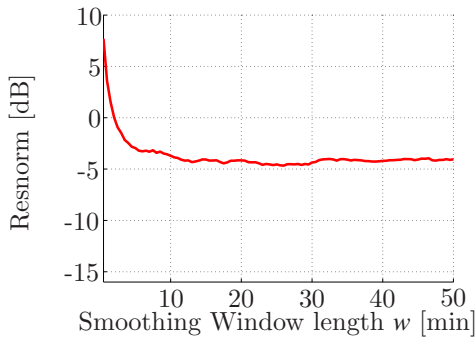
Note that in case of the AGC dependent back-to-back calibration it is necessary to use a common frequency rubidium reference for the Transmitter (Tx) and Receiver (Rx), as the time to calibrate



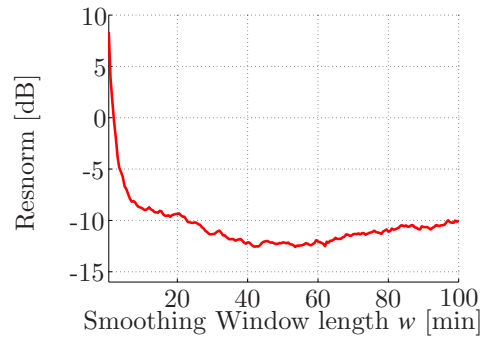
(a) Measured Phase and estimated Long term phase drift ( $w = 26$  min, ATM)



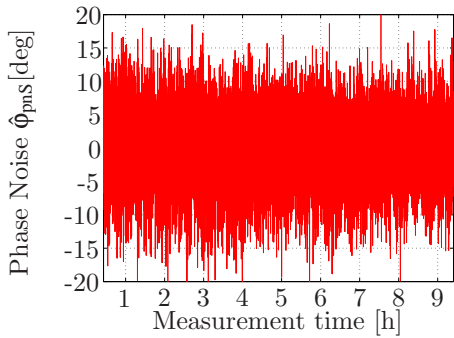
(b) Measured Phase and estimated Long term phase drift ( $w = 54$  min, HyEff)



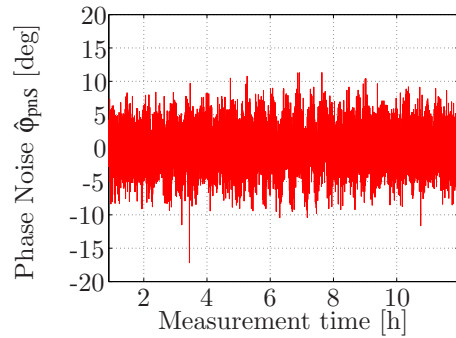
(c) Residual after comparing the estimated and ideal normal distribution (ATM)



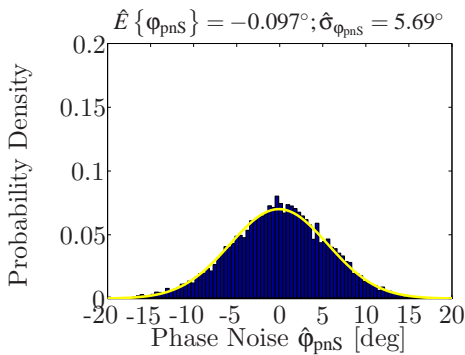
(d) Residual after comparing the estimated and ideal normal distribution (HyEff)



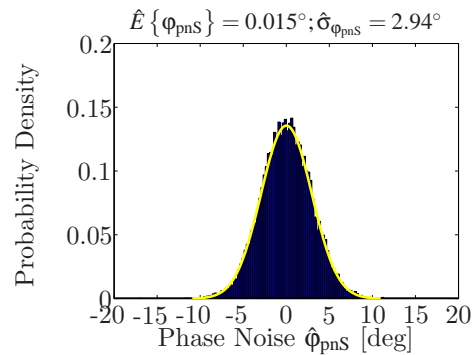
(e) Phase noise  $\hat{\phi}_{pns}$  ( $w = 26$  min, ATM)



(f) Phase noise  $\hat{\phi}_{pns}$  ( $w = 54$  min, HyEff)



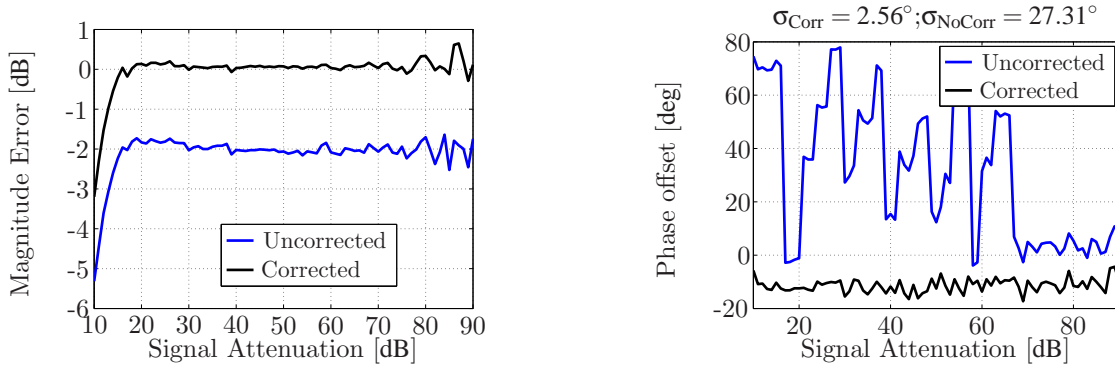
(g) Ideal normal (yellow) and estimated distribution ( $w = 26$  min) of the phase noise (ATM)



(h) Ideal normal (yellow) and estimated distribution ( $w = 54$  min) of the phase noise (HyEff)

**Fig. A.1:** Phase noise estimation for the ATM (left) and HyEff (right) system

all AGC levels drastically increases. If two rubidium references are used, the measured frequency responses of each AGC level would be affected by a not negligible phase offset, which corresponds to the phase drift between the two references.



(a) Magnitude dependent on the Tx power attenuation level

(b) Phase offset dependent on the Tx power attenuation level

**Fig. A.2:** Magnitude and phase offset dependent on the Tx power attenuation level for the corrected and uncorrected data

## Appendix B

# ANTENNA ARRAY DATA MODEL

## B.1 Efficient Antenna Array Data Format

In the following an efficient antenna array data format for a joint computation of the  $M$  radiation patterns and its derivatives dependent on a set of angle pairs (azimuth, co-elevation) and for both polarisations is proposed. First, a compressed implementation of the **EADF** is described in Subsection B.1.1. Second, an efficient matrix notation is found for the joint calculation of all radiation patterns using the compressed versions of the **EADF** (Subsection B.1.2).

### B.1.1 Compressed EADF for Single Antenna Element

The following formulation allows an efficient calculation of the continuous function of the radiation patterns and its derivatives dependent on the azimuth and co-elevation angle. As the complex exponentials (3.25)(3.26) are symmetric, the complexity can be reduced by a factor two. Therefore, the following matrices of the  $m$ th antenna  $\mathbf{G}_{\mathbf{K}1}^{[(L_\vartheta-1)/2+1] \times [(L_\varphi-1)/2+1]}(m)$  to  $\mathbf{G}_{\mathbf{K}4}^{[(L_\vartheta-1)/2+1] \times [(L_\varphi-1)/2+1]}(m)$  are calculated:

$$\mathbf{G}_{\mathbf{K}1}(m) = \begin{bmatrix} \mathbf{I}^{[\frac{L_\vartheta-1}{2} \times \frac{L_\vartheta-1}{2}]} & \mathbf{0}^{[\frac{L_\vartheta-1}{2} \times 1]} & \mathbf{\Pi}^{[\frac{L_\vartheta-1}{2} \times \frac{L_\vartheta-1}{2}]} \\ 0 & 1 & 0 \end{bmatrix} \cdot \mathbf{G}_m \cdot \begin{bmatrix} \mathbf{I}^{[\frac{L_\varphi-1}{2} \times \frac{L_\varphi-1}{2}]} & 0 \\ \mathbf{0}^{[1 \times \frac{L_\varphi-1}{2}]} & 1 \\ \mathbf{\Pi}^{[\frac{L_\varphi-1}{2} \times \frac{L_\varphi-1}{2}]} & 0 \end{bmatrix} \quad (\text{B.1})$$

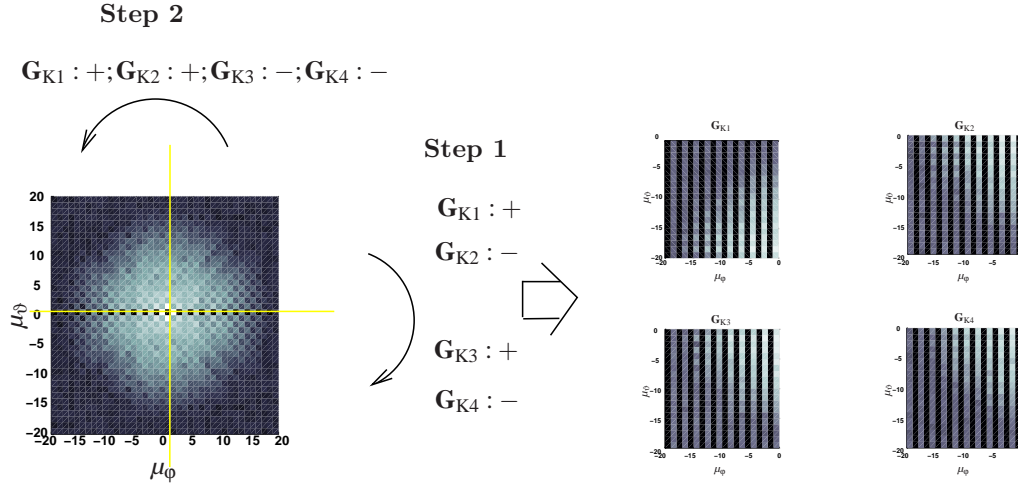
$$\mathbf{G}_{\mathbf{K}2}(m) = \begin{bmatrix} \mathbf{I} & 0 & -\mathbf{\Pi} \\ 0 & 1 & 0 \end{bmatrix} \cdot \mathbf{G}_m \cdot \begin{bmatrix} \mathbf{I} & 0 \\ 0 & 1 \\ \mathbf{\Pi} & 0 \end{bmatrix} \quad (\text{B.2})$$

$$\mathbf{G}_{\mathbf{K}3}(m) = \begin{bmatrix} \mathbf{I} & 0 & \mathbf{\Pi} \\ 0 & 1 & 0 \end{bmatrix} \cdot \mathbf{G}_m \cdot \begin{bmatrix} \mathbf{I} & 0 \\ 0 & 1 \\ -\mathbf{\Pi} & 0 \end{bmatrix} \quad (\text{B.3})$$



$$\mathbf{G}_{K4}(m) = \begin{bmatrix} \mathbf{I} & 0 & -\Pi \\ 0 & 1 & 0 \end{bmatrix} \cdot \mathbf{G}_m \cdot \begin{bmatrix} \mathbf{I} & 0 \\ 0 & 1 \\ -\Pi & 0 \end{bmatrix} \quad (\text{B.4})$$

Figure B.1 illustrates the calculation of these matrices. The arrows indicate the direction of the mathematical operation, which is indicated for each matrix  $\mathbf{G}_{Kx}(m)$  separately.



**Fig. B.1:** Illustration of the calculation of  $\mathbf{G}_{K1}$  to  $\mathbf{G}_{K4}$

With the reduced definitions of

$$\mu_{\vartheta}^T = \begin{bmatrix} \frac{-L_{\vartheta}-1}{2} & \dots & 0 \end{bmatrix} \quad (\text{B.5})$$

$$\mu_{\varphi}^T = \begin{bmatrix} \frac{-L_{\varphi}-1}{2} & \dots & 0 \end{bmatrix} \quad (\text{B.6})$$

, the radiation patterns and derivatives are defined with.

$$\begin{aligned} b(\varphi, \vartheta) = & \Re \{ \mathbf{d}_{\vartheta} \} \cdot \mathbf{G}_{K1} \cdot \Re \{ \mathbf{d}_{\varphi} \} + j \cdot \Im \{ \mathbf{d}_{\vartheta} \} \cdot \mathbf{G}_{K2} \cdot \Re \{ \mathbf{d}_{\varphi} \} \\ & + j \cdot \Re \{ \mathbf{d}_{\vartheta} \} \cdot \mathbf{G}_{K3} \cdot \Im \{ \mathbf{d}_{\varphi} \} - \Im \{ \mathbf{d}_{\vartheta} \} \cdot \mathbf{G}_{K4} \cdot \Im \{ \mathbf{d}_{\varphi} \} \end{aligned} \quad (\text{B.7})$$

$$\begin{aligned} \frac{\partial b(\varphi, \vartheta)}{\partial \vartheta} = & j \cdot \Re \{ \mathbf{d}_{\vartheta} \} \cdot \text{diag} \{ \mu_{\vartheta}^T \} \cdot \mathbf{G}_{K2} \cdot \Re \{ \mathbf{d}_{\varphi} \} - \Im \{ \mathbf{d}_{\vartheta} \} \cdot \text{diag} \{ \mu_{\vartheta}^T \} \cdot \mathbf{G}_{K1} \cdot \Re \{ \mathbf{d}_{\varphi} \} \\ & - \Re \{ \mathbf{d}_{\vartheta} \} \cdot \text{diag} \{ \mu_{\vartheta}^T \} \cdot \mathbf{G}_{K4} \cdot \Im \{ \mathbf{d}_{\varphi} \} - j \cdot \Im \{ \mathbf{d}_{\vartheta} \} \cdot \text{diag} \{ \mu_{\vartheta}^T \} \cdot \mathbf{G}_{K3} \cdot \Im \{ \mathbf{d}_{\varphi} \} \end{aligned} \quad (\text{B.8})$$

$$\begin{aligned} \frac{\partial b(\varphi, \vartheta)}{\partial \varphi} = & j \cdot \Re \{ \mathbf{d}_{\vartheta} \} \cdot \mathbf{G}_{K3} \cdot \text{diag} \{ \mu_{\varphi}^T \} \cdot \Re \{ \mathbf{d}_{\varphi} \} - \Im \{ \mathbf{d}_{\vartheta} \} \cdot \mathbf{G}_{K4} \cdot \text{diag} \{ \mu_{\varphi}^T \} \cdot \Re \{ \mathbf{d}_{\varphi} \} \\ & - \Re \{ \mathbf{d}_{\vartheta} \} \cdot \mathbf{G}_{K1} \cdot \text{diag} \{ \mu_{\varphi}^T \} \cdot \Im \{ \mathbf{d}_{\varphi} \} - j \cdot \Im \{ \mathbf{d}_{\vartheta} \} \cdot \mathbf{G}_{K2} \cdot \text{diag} \{ \mu_{\varphi}^T \} \cdot \Im \{ \mathbf{d}_{\varphi} \} \end{aligned} \quad (\text{B.9})$$

Using this set of equations the number of real-valued multiplications is reduced to  $2 \cdot (L_{\vartheta} \cdot L_{\varphi} + 2 \cdot L_{\varphi})$ . It is obvious from Fig. B.1 that every second column of matrices  $\mathbf{G}_{K1}$  to  $\mathbf{G}_{K4}$  is filled with zeros. Due to the periodification of  $\tilde{\mathbf{B}}$  to  $\tilde{\mathbf{B}}_p$  redundant data is added. Therefore, a further complexity reduction is achievable. This reduction is only applicable in the azimuth aperture direction, therefore,  $\mu_{\varphi}$  is

written in two parts with an odd part

$$\boldsymbol{\mu}_{\varphi\text{u}}^{\text{T}} = \left[ \begin{array}{ccc} \frac{-L_{\varphi}-1}{2} & \dots(2)\dots & 0 \end{array} \right]^{\left[1 \times \frac{L_{\varphi}-1}{4} + 1\right]} \quad (\text{B.10})$$

and an even part

$$\boldsymbol{\mu}_{\varphi\text{g}}^{\text{T}} = \left[ \begin{array}{ccc} \frac{-L_{\varphi}-1}{2} + 1 & \dots(2)\dots & -1 \end{array} \right]^{\left[1 \times \frac{L_{\varphi}-1}{4}\right]}. \quad (\text{B.11})$$

Using these definitions the radiation pattern is calculated like follows:

$$\begin{aligned} \text{b}(\vartheta, \varphi) = & \Re\{\mathbf{d}_{\vartheta}\} \cdot \mathbf{G}_{\text{K1}} \cdot \mathbf{J}_{\text{g}} \cdot \Re\{\mathbf{d}_{\varphi\text{g}}\} + \text{j} \cdot \Im\{\mathbf{d}_{\vartheta}\} \cdot \mathbf{G}_{\text{K2}} \cdot \mathbf{J}_{\text{u}} \cdot \Re\{\mathbf{d}_{\varphi\text{u}}\} \\ & + \text{j} \cdot \Re\{\mathbf{d}_{\vartheta}\} \cdot \mathbf{G}_{\text{K3}} \cdot \mathbf{J}_{\text{g}} \cdot \Im\{\mathbf{d}_{\varphi\text{g}}\} - \Im\{\mathbf{d}_{\vartheta}\} \cdot \mathbf{G}_{\text{K4}} \cdot \mathbf{J}_{\text{u}} \cdot \Im\{\mathbf{d}_{\varphi\text{u}}\}, \end{aligned} \quad (\text{B.12})$$

where the matrix  $\mathbf{J}_{\text{g}}^{\left[\frac{L_{\varphi}-1}{2} + 1 \times \frac{L_{\varphi}-1}{4}\right]}$  is a selection matrix that selects the data of the odd columns and  $\mathbf{J}_{\text{u}}^{\left[\frac{L_{\varphi}-1}{2} + 1 \times \frac{L_{\varphi}-1}{4} + 1\right]}$  selects the data of the even columns (see appendix E equations (E.5) and (E.6)). Consequently, the derivatives are defined as:

$$\begin{aligned} \frac{\partial \text{b}(\vartheta, \varphi)}{\partial \vartheta} = & \text{j} \cdot \Re\{\mathbf{d}_{\vartheta}\} \cdot \text{diag}\{\boldsymbol{\mu}_{\vartheta}^{\text{T}}\} \cdot \mathbf{G}_{\text{K2}} \cdot \mathbf{J}_{\text{u}} \cdot \Re\{\mathbf{d}_{\varphi\text{u}}\} - \Im\{\mathbf{d}_{\vartheta}\} \cdot \text{diag}\{\boldsymbol{\mu}_{\vartheta}^{\text{T}}\} \cdot \mathbf{G}_{\text{K1}} \cdot \mathbf{J}_{\text{g}} \cdot \Re\{\mathbf{d}_{\varphi\text{g}}\} \\ & - \Re\{\mathbf{d}_{\vartheta}\} \cdot \text{diag}\{\boldsymbol{\mu}_{\vartheta}^{\text{T}}\} \cdot \mathbf{G}_{\text{K4}} \cdot \mathbf{J}_{\text{u}} \cdot \Im\{\mathbf{d}_{\varphi\text{u}}\} - \text{j} \cdot \Im\{\mathbf{d}_{\vartheta}\} \cdot \text{diag}\{\boldsymbol{\mu}_{\vartheta}^{\text{T}}\} \cdot \mathbf{G}_{\text{K3}} \cdot \mathbf{J}_{\text{g}} \cdot \Im\{\mathbf{d}_{\varphi\text{g}}\} \end{aligned} \quad (\text{B.13})$$

$$\begin{aligned} \frac{\partial \text{b}(\vartheta, \varphi)}{\partial \varphi} = & \text{j} \cdot \Re\{\mathbf{d}_{\vartheta}\} \cdot \mathbf{G}_{\text{K3}} \cdot \mathbf{J}_{\text{g}} \cdot \text{diag}\{\boldsymbol{\mu}_{\varphi\text{g}}^{\text{T}}\} \cdot \Re\{\mathbf{d}_{\varphi\text{g}}\} - \Im\{\mathbf{d}_{\vartheta}\} \cdot \mathbf{G}_{\text{K4}} \cdot \mathbf{J}_{\text{u}} \cdot \text{diag}\{\boldsymbol{\mu}_{\varphi\text{u}}^{\text{T}}\} \cdot \Re\{\mathbf{d}_{\varphi\text{u}}\} \\ & - \Re\{\mathbf{d}_{\vartheta}\} \cdot \mathbf{G}_{\text{K1}} \cdot \mathbf{J}_{\text{g}} \cdot \text{diag}\{\boldsymbol{\mu}_{\varphi\text{g}}^{\text{T}}\} \cdot \Im\{\mathbf{d}_{\varphi\text{g}}\} - \text{j} \cdot \Im\{\mathbf{d}_{\vartheta}\} \cdot \mathbf{G}_{\text{K2}} \cdot \mathbf{J}_{\text{u}} \cdot \text{diag}\{\boldsymbol{\mu}_{\varphi\text{u}}^{\text{T}}\} \cdot \Im\{\mathbf{d}_{\varphi\text{u}}\} \end{aligned} \quad (\text{B.14})$$

Using these compressed version of the EADF the complexity for calculation of the radiation pattern or their derivatives dependent on one angle pair  $\varphi, \vartheta$  is  $(L_{\vartheta} \cdot L_{\varphi} + 2L_{\varphi})$ . This means an approximately improvement of a factor of 8 compared to the original version.

### B.1.2 Efficient Matrix Notation for Joint Description of All Antenna Elements

As the antenna elements in an antenna array have comparable designs and consequently similar radiation patterns and, in most cases, a similar distance to the centre of the antenna array, the size  $L_{\vartheta}$  and  $L_{\varphi}$  can be chosen for all antenna elements at once. Several optimised libraries are available for the mathematical operation of matrix-matrix multiplication [148]. Consequently, it is preferable to combine all EADFs of all antennas and polarisations into one matrix for a joint calculation of radiation patterns. The matrices with the even number of samples in azimuth:

$$\mathbf{G}_{\text{K1g}}^q = \mathbf{G}_{\text{K1}} \cdot \mathbf{J}_{\text{g}} \quad (\text{B.15})$$

and

$$\mathbf{G}_{\text{K3g}}^q = \text{j} \cdot \mathbf{G}_{\text{K3}} \cdot \mathbf{J}_{\text{g}} \quad (\text{B.16})$$

of all  $M$  antennas and for the polarization  $q$  equal to horizontal (h) or vertical (v) are combined in one matrix  $\Gamma_{13}$ . Accordingly the matrices with the odd number of samples in the azimuth aperture:

$$\mathbf{G}_{\mathbf{K}2_u}^q = \mathbf{j} \cdot \mathbf{G}_{\mathbf{K}2} \cdot \mathbf{J}_u \quad (\text{B.17})$$

and

$$\mathbf{G}_{\mathbf{K}4_u}^q = -\mathbf{G}_{\mathbf{K}4} \cdot \mathbf{J}_u \quad (\text{B.18})$$

are combined in  $\Gamma_{24}$ . To avoid unnecessary multiplications in case of back transformation into the angular domain, the multiplication with  $-1$  or the complex  $\mathbf{j}$  are already included in these matrices. Figure B.2 illustrates the structure of the described matrices. To calculate the radiation patterns for  $P$  angle pairs:

$$\boldsymbol{\varphi} = \begin{bmatrix} \varphi_1 & \cdots & \varphi_P \end{bmatrix} \quad (\text{B.19})$$

and

$$\boldsymbol{\vartheta}' = \begin{bmatrix} \vartheta'_1 & \cdots & \vartheta'_P \end{bmatrix}, \quad (\text{B.20})$$

the back transformation matrix for elevation:

$$\mathbf{D}_{\mathbf{b}\vartheta} = \begin{bmatrix} \mathbf{d}_{\vartheta}(\vartheta'_1) \\ \vdots \\ \mathbf{d}_{\vartheta}(\vartheta'_P) \end{bmatrix} \quad (\text{B.21})$$

and both matrices for azimuth:

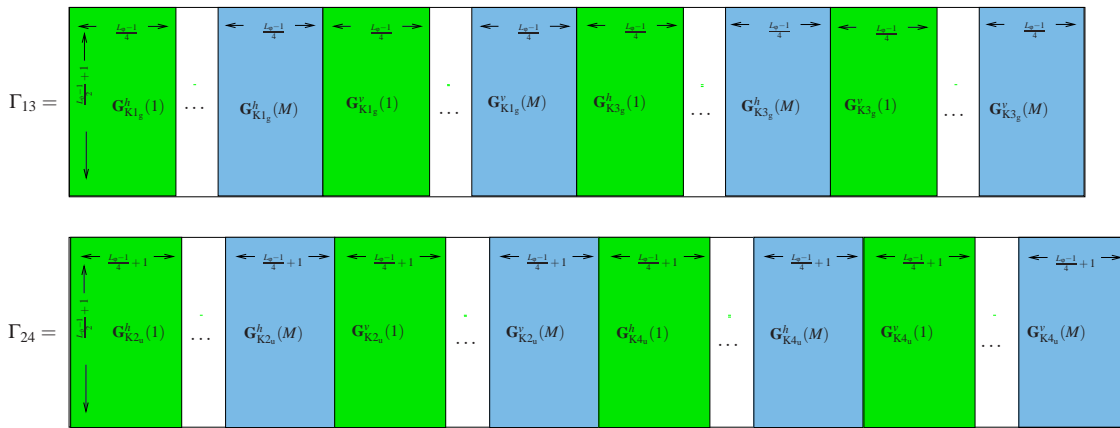
$$\mathbf{D}_{\mathbf{b}g\varphi} = \begin{bmatrix} \mathbf{d}_{\varphi}(\mu_{\varphi g}, \varphi_1) & \cdots & \mathbf{d}_{\varphi}(\mu_{\varphi g}, \varphi_P) \end{bmatrix} \quad (\text{B.22})$$

$$\mathbf{D}_{\mathbf{b}u\varphi} = \begin{bmatrix} \mathbf{d}_{\varphi}(\mu_{\varphi u}, \varphi_1) & \cdots & \mathbf{d}_{\varphi}(\mu_{\varphi u}, \varphi_P) \end{bmatrix} \quad (\text{B.23})$$

are calculated. The final calculation of the radiation pattern is done in two steps. In the first step  $\Gamma_{13}$  is multiplied with the real part of  $\mathbf{D}_{\mathbf{b}\vartheta}$  from the left side, while  $\Gamma_{24}$  is multiplied with the imaginary part of  $\mathbf{D}_{\mathbf{b}\vartheta}$ . The  $P$  rows of each resulting matrix need to be reshaped to the size  $[\frac{L_{\varphi}-1}{4} \times 4 \cdot M]$  or  $[\frac{L_{\varphi}-1}{4} + 1 \times 4 \cdot M]$ . In the second step the azimuth back transformation is done by multiplying the first half of the corresponding matrix with the real part of the corresponding column  $p$  of  $\mathbf{D}_{\mathbf{b}g\varphi}$  or  $\mathbf{D}_{\mathbf{b}u\varphi}$ , while the second half is multiplied with the imaginary part of the corresponding column  $p$  of  $\mathbf{D}_{\mathbf{b}g\varphi}$  or  $\mathbf{D}_{\mathbf{b}u\varphi}$ . The results of these vector matrix multiplications are added according to equation (B.12). Finally we get a complex matrix of size  $[2 \cdot M \times P]$ , where the first  $M$  entries of each column depend on the radiation pattern with respect to the horizontal excitation, while the second  $M$  entries depend on the vertical polarization. The column  $p$  corresponds to the radiation

patterns of all antenna elements and polarisations with respect to the angle pair  $\vartheta_p$  and  $\phi_p$ .

In case that only an azimuth cut (constant co-elevation) or co-elevation cut (constant azimuth) of the radiation patterns is required, the calculation is reduced to one vector matrix multiplication and an additional matrix matrix multiplication. Consequently, the performance increases compared to the full case (arbitrary angle pairs in azimuth and co-elevation). Several estimation algorithms require a computation of the azimuth and co-elevation correlation function in the global search step. To reduce the computational complexity the maximum of this 2D correlation function is searched by using a coordinate wise approach (e.g. alternating search along azimuth cuts and co-elevation cuts). Estimation algorithms would profit from the described data model especially in this case.



**Fig. B.2:** Matrices  $\Gamma_{13}$  and  $\Gamma_{24}$  of antenna array data format



## Appendix C

# A GENERAL CHARACTERISATION OF THE ANTENNA ARRAYS USED

In this appendix the antenna arrays are classified by calculating basic antenna parameters like antenna gain, 3 dB beam width and cross polarisation discrimination (XPD). In this context, the parameters for a “mean antenna array element” are defined in C.1. A summary of these parameters for all antenna arrays used is given in C.2.

### C.1 Definition of Mean Antenna Array Element Parameters

#### C.1.1 Maximum Gain and Mean Gain of All Antennas

Let us define the maximum gain of the antenna array as follows:

$$\bar{g}_{\max,q,p} = 10 \cdot \log_{10} \left( \frac{1}{M_p} \sum_{m_p=1}^{M_p} \max_{\varphi, \vartheta} \left\{ |\mathbf{b}(\varphi, \vartheta, q, m_p)|^2 \right\} \right) \quad [\text{dBi}] \quad (\text{C.1})$$

where  $q$  and  $p$  are either horizontal or vertical. This means that  $m_p$  specifies all antenna ports with the preferred polarisation  $p$ . Furthermore, let us define a mean gain:

$$g(q, m) = \frac{\int_{\varphi_{\min}}^{\varphi_{\min} + \Delta\varphi} \int_{\vartheta_{\min}}^{\vartheta_{\min} + \Delta\vartheta} |\mathbf{b}(\varphi, \vartheta, q, m)|^2 \cdot \sin(\vartheta) d\vartheta d\varphi}{\int_{\varphi_{\min}}^{\varphi_{\min} + \Delta\varphi} \int_{\vartheta_{\min}}^{\vartheta_{\min} + \Delta\vartheta} 1 \sin(\vartheta) d\vartheta d\varphi} \quad (\text{C.2})$$

where  $\varphi_{\min} \dots \varphi_{\min} + \Delta\varphi$  and  $\vartheta_{\min} \dots \vartheta_{\min} + \Delta\vartheta$  specify the azimuth and co-elevation ranges of interest respectively. Since only a sampled version of the radiation pattern can be calculated, an approximation for this integral will be used. As already mentioned there are several grids on the sphere available to calculate the integral of a function on the sphere. Here a Chebyshev grid of order  $N$ :

$$\zeta^{(N)} = \left\{ (\vartheta_u, \varphi_n) : \vartheta_u = \frac{\pi u}{N-1}; \varphi_n = \frac{2\pi n}{N-1}; \right. \\ \left. u, n \in \mathbb{Z}; u \in [0, N-1]; n \in \left[-\frac{N-1}{2}, \frac{N-1}{2}\right] \right\} \quad (\text{C.3})$$

and consequently the Chebyshev quadrature with the weights in azimuth and co-elevation direction:

$$\begin{aligned} w_u^{(N)} &= \epsilon_u^{(N-1)} \frac{4\pi}{N-1} \sum_{s=0}^{(N-1)/2} \epsilon_u^{((N-1)/2)} \frac{2}{1-4s^2} \cos\left(\frac{us2\pi}{N-1}\right) \\ w_n^{(N)} &= \frac{1}{N-1} \end{aligned} \quad (\text{C.4})$$

with:

$$\epsilon_u^{(N)} = \begin{cases} 0.5 & \text{for } u = 0, N \\ 1 & \text{for } u = 1, 2, \dots, N-1 \end{cases} \quad (\text{C.5})$$

are used (See [149], [150]). Finally, the approximation of the mean gain of the  $m^{\text{th}}$  antenna is defined as follows:

$$g(q, m) \approx \frac{\frac{1}{N-1} \sum_{u=0}^N w_u^{(N)} \sum_{n=-(N-1)/2}^{(N-3)/2} w_n^N \cdot |\mathbf{b}(\boldsymbol{\varphi}_n, \vartheta_u, q, m)|^2}{\frac{1}{N-1} \sum_{u=0}^N w_u^{(N)} \sum_{n=-(N-1)/2}^{(N-3)/2} w_n^N \cdot 1} \quad (\text{C.6})$$

where the mean gain of the array is defined similar to eq. (C.1) as:

$$\bar{g}_{q,p} = 10 \cdot \log_{10} \left( \frac{1}{M_p} \sum_{m_p=1}^{M_p} g(q, m_p) \right) \quad [\text{dBi}]. \quad (\text{C.7})$$

### C.1.2 Mean XPD of All Antennas of the Array

Similar to [151] the mean XPD of all antennas is calculated using the definition of the mean gain as follows:

$$\text{XPD}_{A,p} = 10 \cdot \log_{10} \left( \frac{1}{M_p} \sum_{m_p=1}^{M_p} \frac{g(p, m_p)}{g(q, m_p)} \right) \quad [\text{dB}]. \quad (\text{C.8})$$

### C.1.3 3 dB beam width in azimuth and co-elevation

The definition of the 3 dB beam width is commonly used, therefore it is just noted that the mean of the 3 dB beam widths of all antennas in azimuth  $\bar{B}_{\varphi 3\text{dB},q,p}$  is calculated for a constant co-elevation of  $90^\circ$ . The mean 3 dB beam width w.r.t. the co-elevation is calculated for a constant azimuth, where the azimuth is chosen in the main beam direction of each antenna element.

## C.2 Overview of All Arrays

In Table C.1 the defined parameters are calculated for the antenna arrays used. In case of the mean gain and the XPD, the full azimuth and co-elevation range is chosen. The parameters which could not be calculated are marked with an x. Especially, the parameter list of the last four antenna arrays (columns) are incomplete, because the full polarimetric calibration in absolute gain and

phase dependent on azimuth and co-elevation is not available.

The derived minimum sampling grid  $N_{95}$  (See Section 3.5) is also listed, since it is directly related to the array aperture size and consequently to the array performance in terms of DoA estimation. In case of the last four antenna array columns  $N_{95}$  specifies the number of required samples in azimuth for a constant co-elevation of  $90^\circ$ .

**Tab. C.1:** Array Characterisation

Parameter / Array Type ↔↔↔↔↔↔ ↓↓↓↓↓	UCAx1x1x16 $p = h$ Port, $[p = v$ Port]	PUCPASIMx2x1x24 $p = h$ Port, $[p = v$ Port]	PUCPAx2x1x24 $p = h$ Port, $[p = v$ Port]	PULPAx2x1x8 $p = h$ Port, $[p = v$ Port]	SPUCPAx2x2x24 $p = h$ Port, $[p = v$ Port]	SPUCPAx2x4x24 $p = h$ Port, $[p = v$ Port]	PURPAx2x2x4 $p = h$ Port, $[p = v$ Port]	CUBAx1x1x8 $p = h$ Port, $[p = v$ Port]	UCAx1x1x8 $p = h$ Port, $[p = v$ Port]	PUCPAx2x1x8h $p = h$ Port, $[p = v$ Port]	PUCPAx2x1x8v $p = h$ Port, $[p = v$ Port]
$\bar{g}_{\max,h,p}$ [dBi]	x [-8]	-11 [-19]	-10 [-16]	-2 [-11]	-10 [-17]	-18 [-27]	0 [-10]	x [x]	x [x]	x [x]	x [x]
$\bar{g}_{\max,v,p}$ [dBi]	x [-2]	-17 [-10]	-15 [-9]	-13 [-2]	-20 [-11]	-27 [-18]	-11 [0]	x [x]	x [x]	x [x]	x [x]
$\bar{g}_{h,p}$ [dBi]	x [-14]	-17 [-25]	-17 [-26]	-11 [-21]	-18 [-27]	-26 [-35]	-7 [-19]	x [x]	x [x]	x [x]	x [x]
$\bar{g}_{v,p}$ [dBi]	x [-9]	-22 [-16]	-25 [-16]	-22 [-11]	-30 [-18]	-36 [-26]	-21 [-8]	x [x]	x [x]	x [x]	x [x]
$XPD_{A,p}$ [dB]	x [5]	6 [9]	8 [10]	11 [10]	13 [8]	10 [10]	14 [11]	x [x]	x [x]	x [x]	x [x]
$B_{\phi 3dB,h,p}$ [deg]	x [72]	108 [40]	112 [13]	97 [18]	85 [48]	90 [27]	93 [34]	x [x]	x [x]	54 [x]	x [x]
$B_{\phi 3dB,v,p}$ [deg]	x [125]	54 [57]	17 [83]	16 [106]	55 [121]	28 [112]	30 [100]	x [68]	x [58]	x [x]	x [66]
$B_{\theta 3dB,h,p}$ [deg]	x [53]	99 [109]	74 [18]	64 [34]	85 [39]	79 [40]	96 [38]	x [x]	x [x]	x [x]	x [x]
$B_{\theta 3dB,v,p}$ [deg]	x [63]	132 [82]	15 [54]	38 [40]	31 [62]	21 [60]	38 [87]	x [x]	x [x]	x [x]	x [x]
$N_{95}$	167	276	363	280	418	437	67	22	28	30	30





## Appendix D

# PERFORMANCE COMPARISON OF PRACTICAL ANTENNA ARRAYS

In the Chapter 6, the Cramér-Rao Lower Bound (CRLB) based antenna array performance evaluation framework was introduced and verified. Here the framework is used to compare the performance of antenna arrays, which are introduced in Section 2.4. Two types of scenarios are considered, the simple *Single path scenario* and *Coherent two path scenario* (D.1). There are two different questions to answer.

One could ask how do the antenna arrays perform in the case of the same mean  $\text{SNR}_{\text{IR}}$  in the impulse responses of all elements. In this case it is assumed that the Signal to Noise Ratio (SNR) at the array output connector is the same for all antenna arrays that are compared. The antenna array attenuation due to the multiplexers is herewith neglected and a transmit power control is necessary to achieve a constant receive power at the array output. The antenna arrays are compared in terms of the antenna element design and arrangement of the elements in the array. In the following the term *Constant SNR* is used for this case.

But one could also ask how do the arrays perform in case of constant transmit power, constant receiver sensitivity, including all losses in the antenna arrays and all losses of the cables used in a practical measurement. In this case the mean  $\text{SNR}_{\text{IR}}$  at the output connector of the antenna array is different for the discussed antenna arrays. Therefore, the antenna arrays are evaluated under real measurement conditions using a total transmit power of 27 dBm at 5.2 GHz in a bandwidth of 120 MHz and the Hyeff receiver with the specified mean noise power of -106.5 dBm at one frequency bin in case of an impulse response length of  $3.2\mu\text{s}$  (see section 2.3.3). In this case the term *Constant transmit power and receiver sensitivity* is used.

In case of the *Constant SNR* all antenna arrays are compared but only with respect to the performance in azimuth. Furthermore, the following arrays:

- **CUBAx1x1x8** (vertical excitation only)
  - **UCAx1x1x8** (vertical excitation only)
  - **PUCPAx2x1x8h** (horizontal ports for horizontal excitation only)
  - **PUCPAx2x1x8v** (vertical ports for vertical excitation only)
  - **UCAx1x1x16v** (vertical ports for vertical excitation only)
-

can be discussed with respect to one polarisation only, because the two dimensional (2D) antenna radiation patterns w.r.t. horizontal and vertical excitation were not available at the time for all antenna arrays.

In case of *Constant transmit power and receiver sensitivity* the results are presented with respect to a certain distance between transmitter and receiver. The whole link budget needs to be calculated; where an absolute antenna gain calibration is necessary. Since the absolute full polarimetric 2D calibrations are only available for the arrays:

- UCA<sub>x1x1x16</sub>
- PURPA<sub>x2x2x4</sub>
- PUCPA<sub>x2x1x24</sub>
- SPUCPA<sub>x2x2x24</sub>
- SPUCPA<sub>x4x2x24</sub>

the discussion is limited to these arrays.

## D.1 Settings for the Analysis

One or two coherent paths are considered. The total path weight power of the  $k^{\text{th}}$  path for the different cases is defined as follows.

Horizontal polarisation only:

$$|\gamma_{h,k}|^2 = a \quad (\text{D.1})$$

Vertical polarisation only:

$$|\gamma_{v,k}|^2 = a \quad (\text{D.2})$$

Horizontal and vertical polarisation:

$$|\gamma_{h,k}|^2 = |\gamma_{v,k}|^2 = \frac{a}{2}, \quad (\text{D.3})$$

where  $a = 1$  in the *Constant SNR* case. To adjust a certain  $\text{SNR}_{\text{IR}}$  [dB] in the *Constant SNR* case the standard deviation  $\sigma$  of the noise is set to:

$$\sigma_{\text{ConstSNR}} = \sqrt{\frac{(\gamma_{v,k} \cdot \mathbf{b}_v(\varphi_k) + \gamma_{h,k} \cdot \mathbf{b}_h(\varphi_k))^H \cdot (\gamma_{v,k} \cdot \mathbf{b}_v(\varphi_k) + \gamma_{h,k} \cdot \mathbf{b}_h(\varphi_k))}{10^{\frac{\text{SNR}_{\text{IR}}}{10}} \cdot M_{\text{Rx}}}}. \quad (\text{D.4})$$

In the case of *Constant transmit power and receiver sensitivity*,  $a$  is defined as:

$$a = \left( \frac{\lambda}{4\pi \cdot l} \right)^2 \cdot P_{\text{Tx}} \cdot a_{\text{RDL}} \cdot a_{\text{CL}} \quad (\text{D.5})$$

and the standard deviation  $\sigma$  is set to:

$$\sigma_{\text{ConstPTx}} = \sqrt{\frac{P_n}{M_f}}, \quad (\text{D.6})$$

where  $P_{\text{Tx}}$  is the total transmitted Tx power in the frequency band of 120 MHz around the center frequency 5.2 GHz,  $l$  is the path length,  $a_{\text{RDL}}$  is a power factor related to the loss due to reflection and diffraction,  $a_{\text{CL}}$  is a power factor related to the loss included by cables and connectors,  $P_n$  is the noise power (-106.5 dBm, see section 2.3.3) at one frequency bin and  $M_f$  is the number of frequency bins used. For notational convenience the CRLB results are shown as standard deviations, instead of  $\sqrt{\text{CRLB}(\varphi_1)}$  the notation  $\sigma(\varphi_1)$  is applied. Furthermore, the term "relative variance" of the path weights is introduced as:

$$\sigma_{\text{Rel}\gamma,k}^2 = \frac{\sigma(\Re_{\gamma_{v,k}})^2 + \sigma(\Im_{\gamma_{v,k}})^2 + \sigma(\Re_{\gamma_{h,k}})^2 + \sigma(\Im_{\gamma_{h,k}})^2}{|\gamma_{v,k}|^2 + |\gamma_{h,k}|^2}. \quad (\text{D.7})$$

Note that in all the following plots comparing the different arrays, the same marker style and colour is used throughout the whole Section for each array. Therefore, not every figure contains the legend with the corresponding marker and line styles.

## D.2 Constant SNR

In the *Constant SNR* case only the *Single path scenario* is considered to demonstrate the performance of the antenna arrays with respect to the arrangement of the antenna elements and their element design. All calculations are done for a constant co-elevation of  $90^\circ$ . The results are plotted in Fig. D.1; Fig. D.1(e) and Fig. D.1(f) being the corresponding legends to indicate the used antenna arrays. In the first analysis step the  $\text{SNR}_{\text{IR}}$  is set to 25 dB. The  $\text{SNR}_{\text{IR}}$  is kept constant for all azimuth angles by using equation (D.4) for the standard deviation of the noise. Consequently a smaller gain of all radiation patterns of the antenna array in a certain direction will not have any influence on the results. For example in the case of the **PULPAx2x1x8** the same total power is received in every direction even when the angle of incidence is outside the 3 dB beam width of the antenna elements. In the Fig. D.1(a) the standard deviation  $\sigma(\varphi_1)$  is plotted for all antenna arrays with respect to the azimuth direction of the single path. It is obvious that with an increasing aperture size of the antenna arrays the standard deviation becomes smaller.

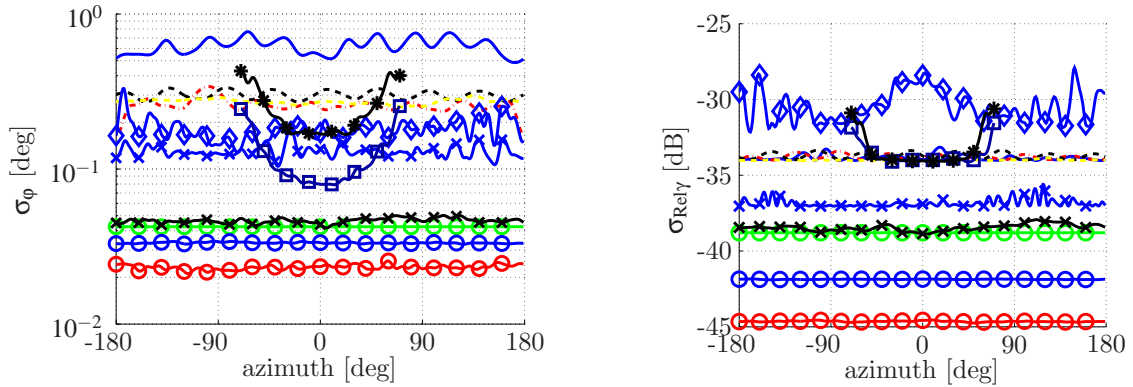
- The **CUBA1x1x1x8** has the worst performance, since its aperture size is the smallest. It is followed by the 8 element circular arrays, here the elements of all the three 8 element arrays are arranged at a radius of  $0.6533 \lambda$ , which corresponds to a distance between adjacent elements of  $0.5 \lambda$ .
- Since the **PURPAx2x2x4** has almost the same aperture size of around  $2\lambda$  in the broad side direction as the **UCAx1x1x16**, the performance is comparable. Due to a decreasing aperture size of the **PURPAx2x2x4**, for azimuth directions higher or lower than  $0^\circ$  the performance becomes worse for that directions, which is the same as for the **PULPAx2x1x8**.

- Comparing the  $\mathbf{UCAx1x1x16v}$ , calculating the **CRLB** considering only the vertical radiation patterns, with the  $\mathbf{UCAx1x1x16}$ , in which case both polarisations are used, it becomes obvious that the  $\mathbf{UCAx1x1x16}$  has a worse performance since the horizontal path weight has a higher variance for certain directions. This alternating behaviour is related to the **XPD** of the single antennas. The **XPD** is high in the antennas main beam direction (see Section C), which means that the elements can not receive any horizontal power. Consequently the variances of the horizontal path weights are worse exactly for those directions, while it has a better variance in the direction between two main beams of adjacent antenna elements.
- Even if the  $\mathbf{PULPAx2x1x8}$  and the  $\mathbf{PUCPAx2x1x24}$  have the same aperture size of approximately  $3.5\lambda$ , the circular array performs better due to the higher number of elements and consequently a higher **SNR** gain.
- Also the performance improvement from the one ring, to the two ring and the four ring **SPUCPA** is related to the increasing **SNR** gain with respect to the total number of elements.
- The simulated  $\mathbf{PUCPASIMx2x1x24}$  has a slightly better performance than the practical antenna array  $\mathbf{PUCPAx2x1x24}$ . The small discrepancy between the simulation and the practical antenna array is basically related to the simulation conditions, while the effects of the complete construction and the multiplexer design are neglected. Furthermore, only 6 adjacent elements are considered during simulation. This means that coupling effects between the remaining elements are neglected, which apparently leads to a slightly better performance of the simulated antenna array.

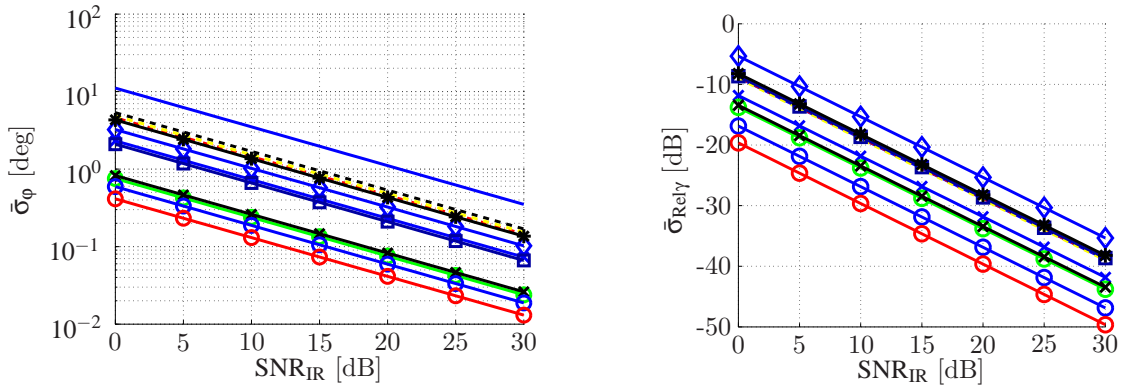
In Fig. D.1(b) the relative variances of the path weights are shown. Basically the **SNR** gain due to the increasing number of elements can be observed. Figure D.1(c) illustrates the mean standard deviation of the azimuth angle  $\bar{\sigma}(\varphi_1)$  dependent on the  $\text{SNR}_{\text{IR}}$ . The mean standard deviation is taken over the valid azimuth range, which is the full azimuth range of  $\pm 180^\circ$  in the case of the circular arrays and about  $\pm 70^\circ$  in case of the planar arrays. The mean relative variance of the path weights  $\bar{\sigma}_{\text{Rely}}$  is shown in Fig. D.1(d).

### D.3 Constant transmit power and receiver sensitivity

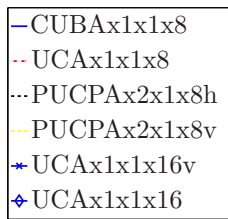
The purpose of this analysis is to evaluate the performance of the antenna arrays under real world conditions, which are comparable to measurements with the HyEff system. As mentioned above, the transmit power  $P_{\text{Tx}}$  is constant with 27 dBm, transmitting the same amount of power in the vertical and horizontal polarisation. An isotropic **Tx** antenna with 0 dBi gain for vertical and horizontal polarisation is applied. The **Rx** array and the **Tx** antenna is connected using cables, which have an attenuation of 3.6 dB and 6 dB respectively. Consequently, the term  $10 \cdot \log_{10}(a_{\text{CL}})$  is 9.6 dB. The loss due to reflection and diffraction of the path is  $10 \cdot \log_{10}(a_{\text{RDL}}) = 20$  dB, which can be related to a double bounce reflection. This approximation is based on [152] matching a path under **NLoS** condition. Using these settings and equations (D.3), (D.5) the power of the horizontal and vertical path weights are calculated. In case of the *Single path scenario* equally phased path weights in vertical and horizontal polarisation are applied. In case of the *Coherent*



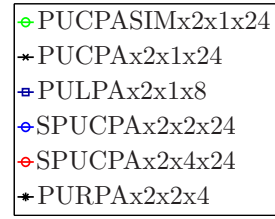
(a) Standard deviation of the azimuth ( $25 \text{ dB SNR}_{\text{IR}}$ ) (b) Relative variance of the path weights ( $25 \text{ dB SNR}_{\text{IR}}$ )



(c) Mean azimuth standard deviation dependent on  $\text{SNR}_{\text{IR}}$  (d) Mean relative variance of the path weights dependent on  $\text{SNR}_{\text{IR}}$



(e) Legend of arrays used part I



(f) Legend of arrays used part II

**Fig. D.1:** Array comparison w.r.t. the azimuth standard deviation and relative variance of the path weights for a single path dependent on its  $\text{SNR}_{\text{IR}}$  (constant  $\text{SNR}_{\text{IR}}$  at each azimuth, constant co-elevation of  $90^\circ$ )

*two path scenario* different phase constellations between the path weights of the two path will be considered to analyse the arrays under worst and best case conditions, which is basically related to a constructive and destructive superposition of the two paths (see Section 6.2.2). Equivalent to the Hoeff system (see Section 2.3) system the impulse response length is set to  $3.2\mu\text{s}$ , which is related to a number of  $M_f = 385$  frequency samples. The standard deviation of the noise is set to  $\sigma_{\text{ConstPTx}}$  using equation (D.6).

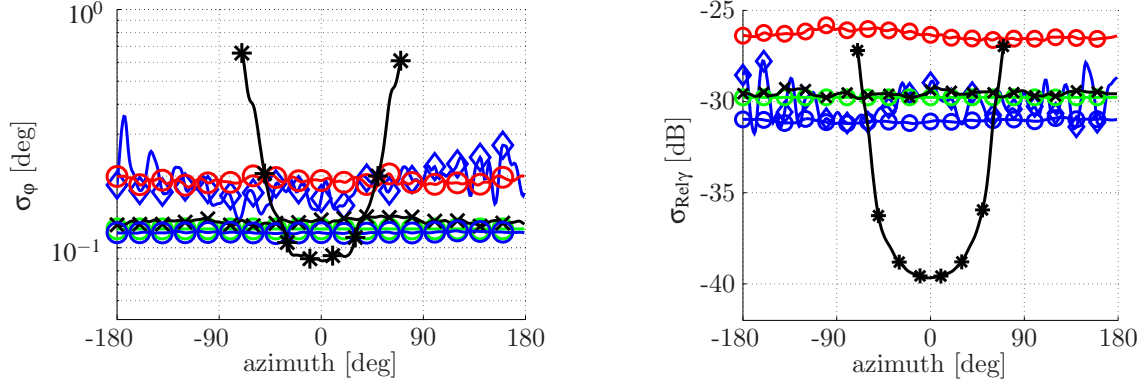
The following analysis is done separately for the case of a constant co-elevation of  $90^\circ$  w.r.t. to the azimuth and for a constant azimuth of  $0^\circ$  w.r.t. to the co-elevation. As already shown, the method is actually capable of calculating the CRLBs with respect to all available parameters. Nevertheless, the number of analysed dimensions is limited to azimuth or co-elevation, to be able to interpret the graphs. The limitation to these two slices in azimuth and co-elevation is reasonable and sufficient to describe the array performance at least in case of the circular arrays. The behaviour of the circular arrays with respect to the azimuth angle varies only a little. Only in case of the planar arrays a worse performance can be expected for directions aside the broad side direction. For the *Single path scenario* and *Coherent two path scenario*, the discussion starts for a fixed path length of  $l = 300\text{m}$ . Finally the performance is shown in the range of 50 m to 950 m (corresponding to the chosen impulse response length).

### D.3.1 Single path scenario

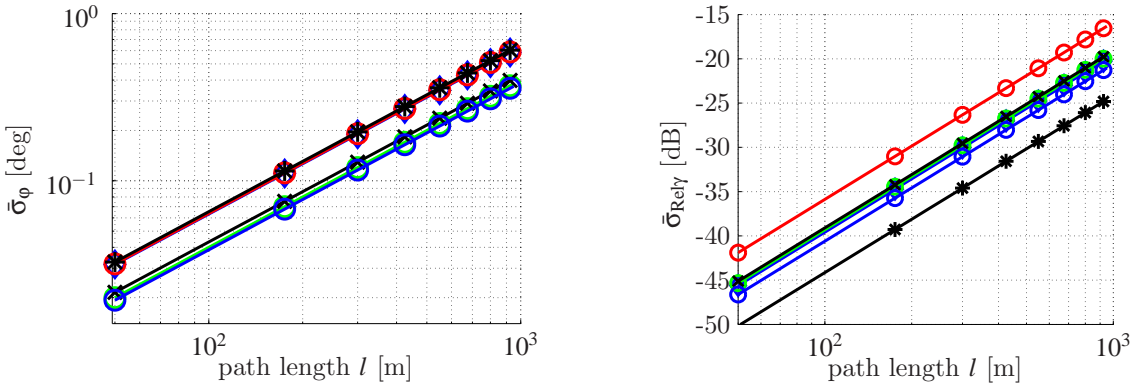
The results are shown in Fig. D.2 for the slice in azimuth and in Fig. D.3 for the elevation slice. From Fig. D.2(a) and Fig. D.2(b) for a constant path length of  $l = 300\text{m}$  and the slice in azimuth, it can be concluded:

- The difference in the performance of the antenna arrays with respect to the azimuth is less significant compared to the *Constant SNR* case. This can be basically related to the higher Multiplexer (MUX) attenuation in case of the antennas with a higher number of elements (please check the values of the MUX attenuation in the Figures 2.16, 2.14, 2.17 and also the mean gains of the arrays in table C.1). Especially in case of the **SPUCPAx2x4x24**, it becomes obvious that the MUX attenuation of ca. 23 dB leads to a worse performance in case of the azimuth variance and the relative variance of the path weights. Although, it has the highest number of elements, the performance is worse compared to the **PUCPAx2x2x24** with only one ring instead of four.
- All circular arrays perform with almost constant variances in the full azimuth range even without a Tx power control.
- The **PURPA2x2x4** has the best performance (considering the broad side direction), which is related to low MUX attenuation. However, in the range beside broad side the variances increase drastically compared to the *Constant SNR* case due to the decreasing gain of the antenna elements in these directions.
- As already observed in the *Constant SNR* case, the **PUCPASIMx2x2x24** has almost the same or a slightly better performance than the practical antenna array **PUCPAx2x2x24**.

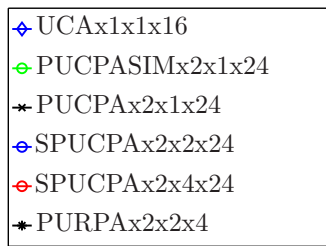
This results are reasonable as the known multiplexer attenuation of around 11.5 dB of the practical antenna array is also assumed in case of the simulated antenna array.



(a) Standard deviation of the azimuth (path length  $l = 300$  m) (b) Relative variance of the path weights (path length  $l = 300$  m)



(c) Mean azimuth standard deviation dependent on path length  $l$  (d) Mean relative variance of the path weights dependent on path length  $l$



(e) Legend of the arrays used

**Fig. D.2:** Array comparison w.r.t. the azimuth standard deviation and relative variance of the path weights for a single path with path length  $l$  (assuming constant transmit power, constant receiver sensitivity, an additional path loss of 20 dB due to reflection and diffraction and constant co-elevation of  $90^\circ$ )

For the slice in co-elevation the following can be concluded:

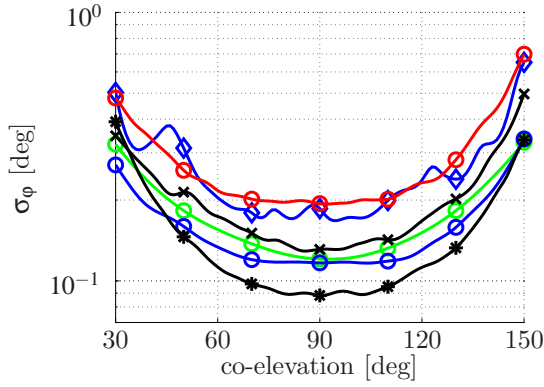
- The differences between the arrays in terms of the azimuth variance (see Fig. D.3(a)) remain almost constant for different co-elevation angles.



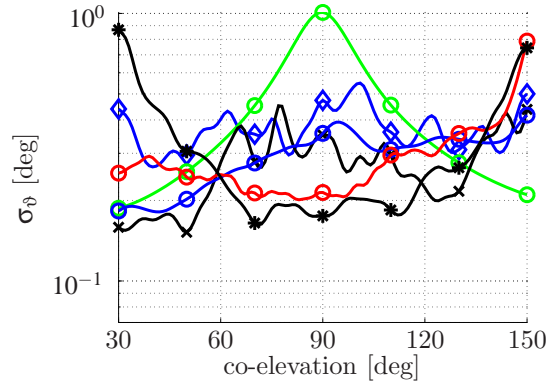
- However, due to the decreasing aperture size for the azimuth resolution towards the poles of the spherical coordinate system and the lower gain of the antenna elements in these directions, the azimuth variance and the relative variances of the path weights increases for all arrays.
- The co-elevation variance (see Fig. D.3(b)) varies more compared to the azimuth, since the array construction leads in most cases to a non uniform behaviour.
- Nevertheless, trends like a slightly worse variance can be observed towards  $90^\circ$  co-elevation in case of the one ring circular arrays, since the aperture size for the co-elevation resolution reaches the minimum in this case.
- In case of the **SPUCPA $_{x4x2x24}$**  the aperture size seen for the co-elevation resolution is almost constant. Therefore, the co-elevation variance is also almost constant.
- In case of the **PURPA $_{x2x2x4}$**  the performance gets worse towards the poles, due to a decrease in the aperture size.

In conclusion it seems that the performance of the arrays do not differ that much considering the results of the *Single path scenario* in the case of *Constant transmit power and receiver sensitivity*. Even by using a high sophisticated array with a big aperture size and large number of elements, almost the same or even worse performance compared to the arrays with a small aperture size can be observed. But performance degradation can be expected in the presence of more than one path.

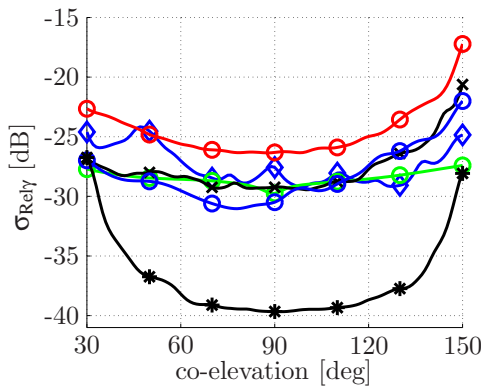
---



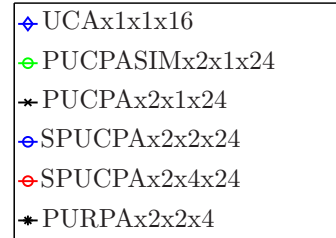
(a) Standard deviation of the azimuth (path length  $l = 300$  m)



(b) Standard deviation of the co-elevation (path length  $l = 300$  m)



(c) Relative variance of the path weights (path length  $l = 300$  m)



(d) Legend

**Fig. D.3:** Array comparison w.r.t. azimuth, co-elevation standard deviation and relative variance of the path weights for a single path for different co-elevations (assuming constant transmit power, constant receiver sensitivity, an additional path loss of 20 dB due to reflection and diffraction, path length  $l = 300$ m, and constant azimuth of  $0^\circ$ )

### D.3.2 Coherent two path scenario

As already mentioned the most severe problems arise if coherent wave-fronts are involved, which is often the case in real world measurements. Therefore, in the following the *Coherent two path scenario* is discussed. The necessary settings and parameters for comparison are defined in the next section and are explained based on an example.

#### D.3.2.1 Settings and Parameter Definition

As seen in Section 6.2.2 the parameter variance strongly depends on the phase constellation between the two coherent paths. Therefore, the phases of the horizontal and vertical path weights of the second path  $k = 2$  are adjusted by the additional phase factors  $p_h$  and  $p_v$ . The complex path weights

of the second path are defined as follows:

$$\begin{aligned}\gamma_{h,2} &= p_h \cdot \gamma_{h,1} \\ \gamma_{v,2} &= p_v \cdot \gamma_{v,1}.\end{aligned}\tag{D.8}$$

To limit the number of analysis, 4 different path weight constellations are chosen:

- $p_h = 1, p_v = 1$  in the legends and discussion noted as path weight constellation **11** (worst case and equivalent to  $p_h = -1, p_v = -1$ )
- $p_h = -j, p_v = j$  noted as path weight constellation **-jj**
- $p_h = -1, p_v = 1$  noted as path weight constellation **-11**
- $p_h = j, p_v = j$  noted as path weight constellation **jj** (best case).

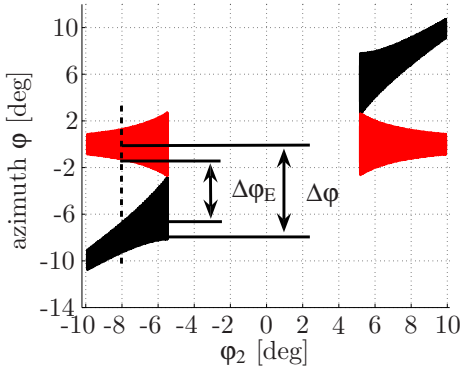
Exemplary the two antenna arrays **SPUCPAx2x4x24** and **UCAx1x1x16** are compared for all 4 path weight constellations (see Figures D.4, D.5. For the analysis of the *coherent two path scenario*, the parameters *maximum separation error in azimuth*  $E_{\Delta\varphi}$ , *maximum separation error in co-elevation*  $E_{\Delta\vartheta}$ , *minimum resolvable separation in azimuth*  $\Delta\varphi_{\min}$ , and *minimum resolvable separation in co-elevation*  $\Delta\vartheta_{\min}$  will be introduced. Basically, both paths have the same path length  $l$  and the direction of the path  $k = 1$  is always kept constant. The direction of path  $k = 2$  is varied in the range  $\pm 15^\circ$  around the azimuth angle of path 1 with  $\varphi_1 = 0^\circ$  for the analysis w.r.t. to the azimuth performance ( $\vartheta_1 = \vartheta_2 = 90^\circ$ ). For the analysis w.r.t. the co-elevation performance the co-elevation of path 2 is varied in the range of  $\pm 15^\circ$  around the co-elevation angle  $\vartheta_1$ , with the azimuth angles of both paths kept constant with  $\varphi_1 = \varphi_2 = 0^\circ$ . In the Figures D.4(a) and D.4(b) the confidence intervals of both paths w.r.t. to  $\varphi_2$  in case of constant co-elevation are plotted, the confidence intervals being derived from the calculated **CRLBs** of the corresponding parameters. Note that only the regions are plotted, where the two confidence intervals are not overlapping. The minimum distance between the two intervals are defined as  $\Delta\varphi_E$  and  $\Delta\vartheta_E$ . The true distance between the two path is defined as  $\Delta\varphi$  and  $\Delta\vartheta$ . As an example, the two parameters are shown in Fig. D.4(a) for a azimuth angle  $\varphi_2 = -8^\circ$ . Based on these parameters let us define the *maximum separation error in azimuth*:

$$E_{\Delta\varphi}(\varphi_2) = 100 \cdot \frac{(\Delta\varphi(\varphi_2) - \Delta\varphi_E(\varphi_2))}{\Delta\varphi(\varphi_2)} \quad [\%]\tag{D.9}$$

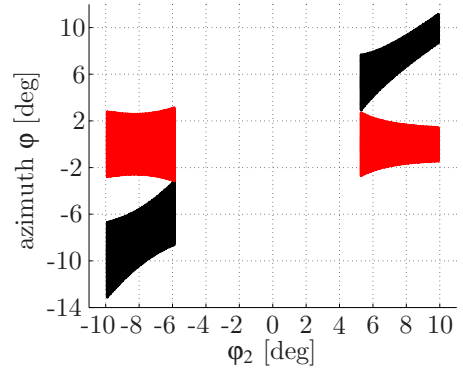
and in co-elevation

$$E_{\Delta\vartheta}(\vartheta_2) = 100 \cdot \frac{(\Delta\vartheta(\vartheta_2) - \Delta\vartheta_E(\vartheta_2))}{\Delta\vartheta(\vartheta_2)} \quad [\%].\tag{D.10}$$

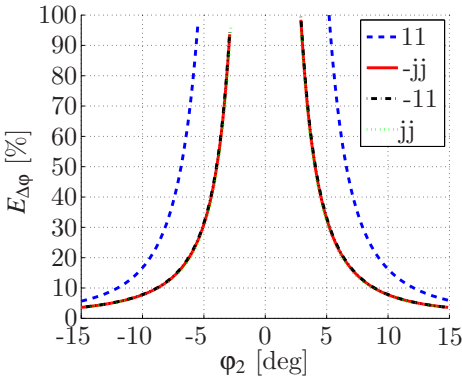
The minimum resolvable distance  $\Delta\varphi_{\min}$  and  $\Delta\vartheta_{\min}$  is reached for  $\Delta\varphi_E = 0^\circ$  and  $\Delta\vartheta_E = 0^\circ$ . Furthermore, the mean relative variance of the path weights  $\bar{\sigma}_{\text{Rel}\gamma}$  are defined as the mean of the relative path weight variances of both paths. Comparing the azimuth results of the **SPUCPAx2x4x24** and the **UCAx1x1x16** it becomes obvious that:



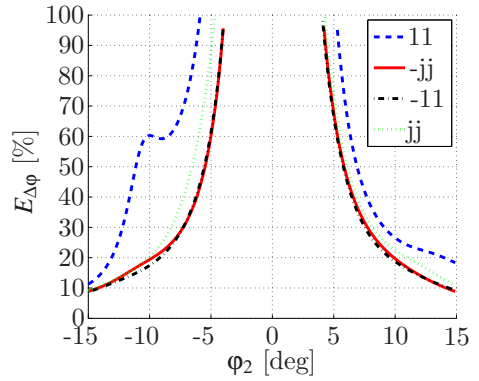
(a) Confidence interval of the paths in the worst case path weight constellation **11** (**SPUCPAx2x4x24**)



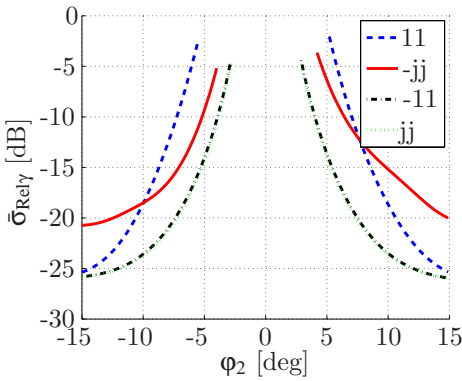
(b) Confidence interval of the paths in the worst case path weight constellation **11** (**UCAX1x1x16**)



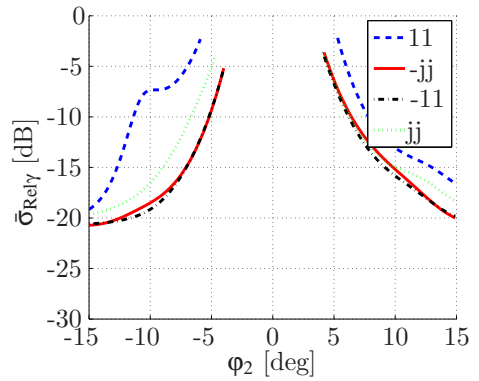
(c) *Maximum separation error in azimuth SPUC-PAx2x4x24*



(d) *Maximum separation error in azimuth UCAX1x1x16*

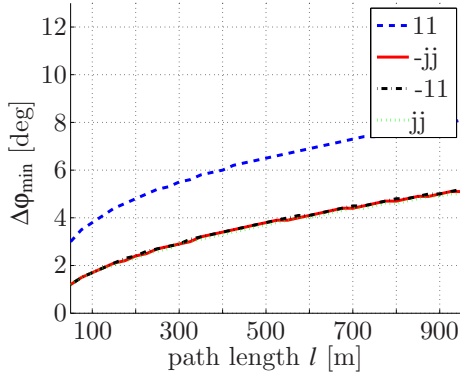


(e) Mean relative variance of the path weights **SPUC-PAx2x4x24**

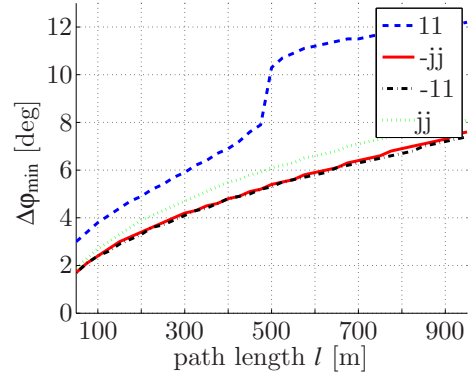


(f) Mean relative variance of the path weights **UCAX1x1x16**

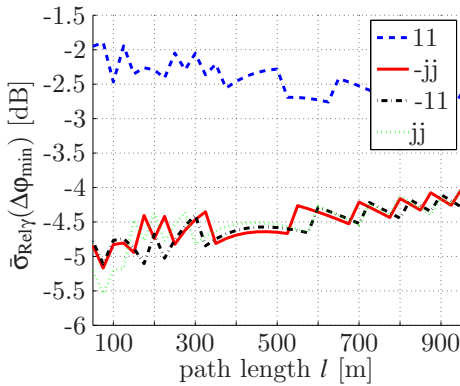
**Fig. D.4:** Performance comparison between the **SPUCPAx2x4x24** and **UCAX1x1x16** w.r.t. the azimuth resolution and relative variance of the path weights for two coherent paths for different azimuth angles of  $\varphi_2$  (assuming constant transmit power, constant receiver sensitivity, an additional path loss of 20 dB due to reflection and diffraction, path length  $l_1 = l_2 = 300$  m,  $\varphi_1 = 0^\circ$ , and constant co-elevation  $\vartheta_1 = \vartheta_2 = 90^\circ$ )



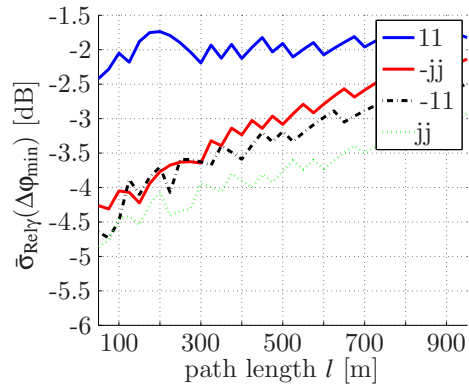
(a) Minimum resolvable separation in azimuth (SPUCP $\mathbf{x}2\mathbf{x}4\mathbf{x}24$ )



(b) Minimum resolvable separation in azimuth (UCA $\mathbf{x}1\mathbf{x}1\mathbf{x}16$ )



(c) Mean relative variance of the path weights at  $\Delta\phi_{\min}$  (SPUCP $\mathbf{x}2\mathbf{x}4\mathbf{x}24$ )



(d) Mean relative variance of the path weights at  $\Delta\phi_{\min}$  (UCA $\mathbf{x}1\mathbf{x}1\mathbf{x}16$ )

**Fig. D.5:** Performance comparison between SPUCP $\mathbf{x}2\mathbf{x}4\mathbf{x}24$  and UCA $\mathbf{x}1\mathbf{x}1\mathbf{x}16$  w.r.t. the *minimum resolvable separation in azimuth* and mean relative variance of the path weights for two coherent paths, for different path length  $l$  (assuming constant transmit power, constant receiver sensitivity, an additional path loss of 20 dB due to reflection and diffraction, and constant co-elevation  $\vartheta_1 = \vartheta_2 = 90^\circ$ )

- The confidence intervals of both paths are larger in case of the array with the smaller aperture size. Nevertheless, it seems that the minimum resolvable separation is almost the same for both arrays (Fig. D.4(a), D.4(b)).
- A crucial difference can be observed analysing the parameters *maximum separation error in azimuth* in the Figures D.4(c),D.4(d) and the mean relative variance in the Figures D.4(e), D.4(f). The parameters of the SPUCP $\mathbf{x}2\mathbf{x}4\mathbf{x}24$  converge faster against the values of well separated paths than the parameters of the UCA $\mathbf{x}1\mathbf{x}1\mathbf{x}16$ .
- Especially in the worst case path weight constellation **11** the degradation of the UCA $\mathbf{x}1\mathbf{x}1\mathbf{x}16$  is enormous. The error  $E_{\Delta\phi}$  is around 20 % to 50 % bigger and the mean relative variance is 5 dB to 10 dB worse than in the best case constellations (assuming same separation between the two paths). Furthermore, the array behaviour in the worst case is not homogenous for all

directions.

- The **SPUCPAx2x4x24** performs in the worst case almost as good as the **UCAx1x1x16** in the best case.

To get an understanding for the limitations on resolution not only for a fixed distance, the minimum resolvable separation and the corresponding mean relative variance are plotted with respect to the path length  $l$  in the range of 50 m to 950 m (Fig. D.5). As already mentioned above, both arrays can resolve paths with almost the same minimum separation  $\Delta\phi$ . In the best case path weight constellation, the difference in resolution capability between the two arrays is only around  $1^\circ$ . In the worst case, a performance degradation in case of the **UCAx1x1x16** can be observed w.r.t. to bigger path lengths, which is related to the non homogeneous behaviour of this array. But one important fact can be observed analysing the mean relative variance of the path weights. The values in the worst case with around -2 dB are almost the same for both arrays. Also in the best case, the differences between the two arrays are not that big.

### D.3.2.2 Azimuth Results for Constant Co-Elevation

All available antenna arrays will be evaluated with respect to the worst case path weight constellation **11**. The results are shown in Fig. D.6, whereby the following can be concluded:

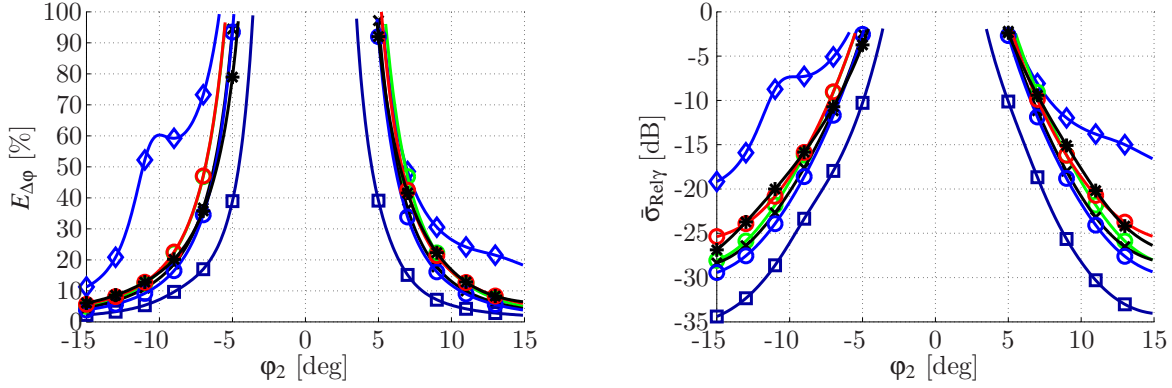
- In all four plots it becomes obvious that almost all arrays have the same performance with respect to the azimuth resolution of the two paths.
- There are only 2 exceptions:
  - The **UCAx1x1x16** has the worst performance due to its non-uniform behaviour and its small aperture size.
  - Also the **PULPAx2x2x8** performs best due to its big aperture in azimuth and the relatively small **MUX** attenuation.

Observing the mean relative variance of the path weights at the minimum resolvable azimuth separation  $\Delta\phi_{\min}$  in the Fig. D.6(d) it becomes again obvious that it is almost the same for all arrays and path lengths  $l$ . This leads us to an important question:

**Is there any relation between the *maximum separation error*  $E$  and the mean relative variance of the path weights, when comparing different arrays?**

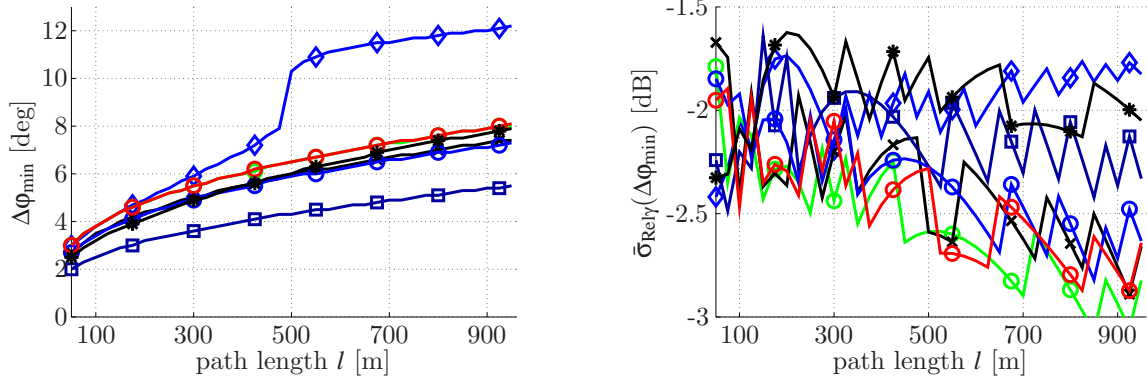
The answer to this question is especially important from the viewpoint of the parameter estimation, where in the RIMAX (RIMAX) algorithm the relative variance of the path weights with -3 dB is used to decide if a path is considered as reliable or not. Therefore, the *maximum separation error*  $E_{\Delta\phi}$  with respect to  $\bar{\sigma}_{\text{Rel}\gamma}$  is plotted for the best case in Fig. D.7(a) and for the worst case in Fig. D.7(b). Obviously there exists a relation between  $\bar{\sigma}_{\text{Rel}\gamma}$  and  $E_{\Delta\phi}$  independent from the antenna array. In the Fig. D.7(c) the results of all arrays (except the **UCAx1x1x16**) for the worst case are plotted blue. The results of the best case is plotted in black. In the Fig. D.7(d) different path weight constellations with  $p_v = p_h = e^{j\phi_p}$  are analysed. Surprisingly the error  $E_{\Delta\phi}$  in the best case

is around 10 % to 30 % bigger than in the worst case dependent on  $\bar{\sigma}_{\text{Rel}\gamma}$ . This means to assure an error  $E_{\Delta\phi}$  that is at least smaller than 90 % efforts a path drop level of at least -5 dB relative variance during the reliability check in the estimation algorithm. Note the shown relation between the error  $E_{\Delta\phi}$  and mean relative varinace  $\bar{\sigma}_{\text{Rel}\gamma}$  is independent of the path length  $l$ .



(a) Maximum separation in azimuth ( $l = 300$  m, path weight constellation worst case **11**)

(b) Mean relative variance of the path weights ( $l = 300$  m, path weight constellation worst case **11**)



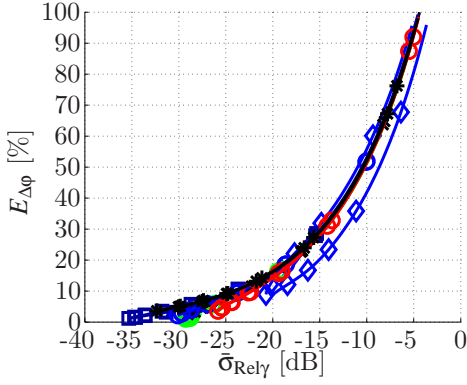
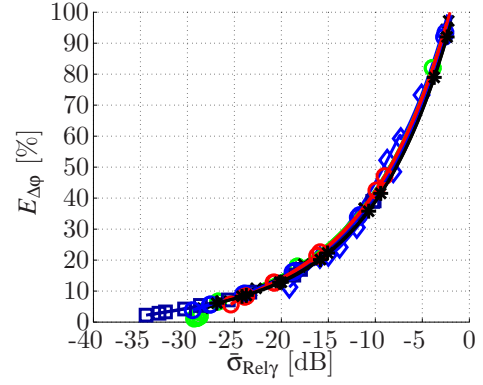
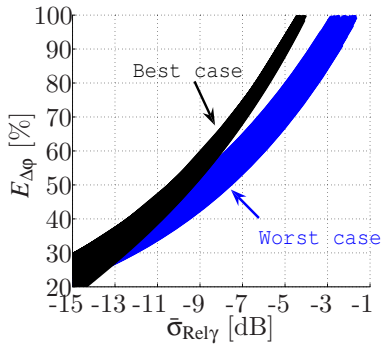
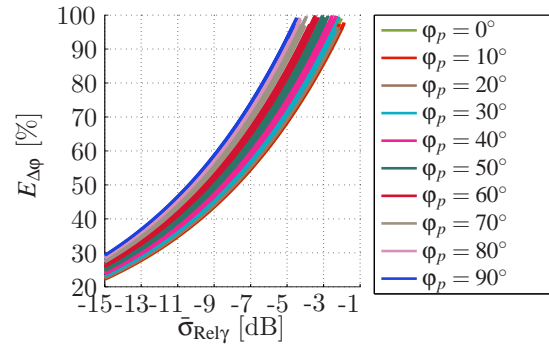
(c) Minimum resolvable separation in azimuth (path weight constellation worst case **11**)

(d) Mean relative variance of the path weights at  $\Delta\phi_{\text{min}}$  (path weight constellation worst case **11**)

- ◆ UCAX1x1x16
- ◇ PUCPASIMx2x1x24
- \* PUCPAx2x1x24
- PULPAx2x1x8
- SPUCPAx2x2x24
- ◇ SPUCPAx2x4x24
- \* PURPAx2x2x4

(e) Legend of the arrays used

**Fig. D.6:** Array comparison in terms of resolution capability in azimuth for fixed path lengths  $l = 300$  m (a)(b) and different path lengths in the worst case path weight constellation **11** (assuming constant transmit power, constant receiver sensitivity, an additional path loss of 20 dB due to reflection and diffraction and constant co-elevation  $\vartheta_1 = \vartheta_2 = 90^\circ$ )

(a) Relation between  $E_{\Delta\phi}$  and  $\bar{\sigma}_{\text{Rel}\gamma}$  in the best case in azimuth(b) Relation between  $E_{\Delta\phi}$  and  $\bar{\sigma}_{\text{Rel}\gamma}$  in the worst case in azimuth(c) Relation between  $E_{\Delta\phi}$  and  $\bar{\sigma}_{\text{Rel}\gamma}$  in the worst case (blue) and best case (black)(d) Relation between  $E_{\Delta\phi}$  and  $\bar{\sigma}_{\text{Rel}\gamma}$  for different phase constellations  $\phi_p$ 

**Fig. D.7:** Comparison of the relation between  $E_{\Delta\phi}$  and  $\bar{\sigma}_{\text{Rel}\gamma}$  for all arrays and for different path weight constellations

### D.3.2.3 Co-elevation Results for Constant Azimuth

As in case of the azimuth, the arrays have an almost uniform characteristic and constant aperture size (at least for all circular arrays), it was not necessary to evaluate the arrays at different azimuth angles  $\phi_1$ . This is not the case in the co-elevation dimension. Basically, the effective aperture size with respect to the co-elevation angle is changing. Furthermore, the gain of the antenna elements is decreasing towards the poles of the spherical coordinate system. Nevertheless, it is acceptable to choose a constant azimuth angle for the analysis with respect to the co-elevation performance. Consequently, the analysis is performed for different co-elevation angles  $\vartheta_1$ , where  $\vartheta_2$  is chosen in the range of  $\pm 15^\circ$  around  $\vartheta_1$  and the azimuth angles are set to  $\phi_1 = \phi_2 = 0^\circ$ .

In Fig. D.8 the results with respect to the co-elevation performance in terms of resolving two coherent paths are shown. The *maximum separation error*  $E_{\Delta\vartheta}$  and the mean relative variance  $\bar{\sigma}_{\text{Rel}\gamma}$  are shown for a co-elevation angle  $\vartheta_1 = 45^\circ$  (Fig. D.8(a),D.8(c)) and  $\vartheta_1 = 90^\circ$  (Fig. D.8(b),D.8(d)). The path length  $l$  is kept constant with 300 m. Furthermore, the minimum resolvable distance is plotted with respect to the co-elevation angle  $\vartheta_1$  for a constant path length of 300 m (Fig. D.8(e)) and with respect to path length  $l$  for constant co-elevation angle  $\vartheta_1 = 90^\circ$  (Fig. D.8(f)). From the

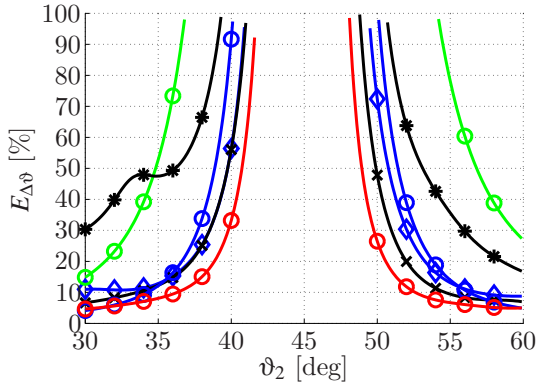


results, the following can be concluded:

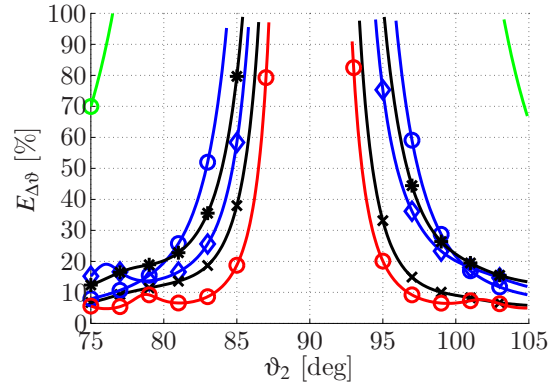
- Non-uniform behaviour of almost all arrays with respect to the co-elevation angle  $\vartheta_1$ . Especially the planar antenna array **PURPAx2x2x4** performs worse due to the decreasing effective aperture size towards the North Pole ( $\vartheta_1 = 0^\circ$ ). For co-elevation angles  $\vartheta_1$  bigger than  $90^\circ$ , all practical antenna arrays perform worse with respect to the minimum resolvable distance  $\Delta\vartheta_{\min}$ , since in all cases the multiplexers and mounting mechanism are located in the direction of  $\vartheta = 180^\circ$  (lower part of the array).
- The **SPUCPAx2x4x24** performs best and almost uniform in terms of the co-elevation resolution of two paths in the range between  $\vartheta_1 = 40^\circ$  and  $\vartheta_1 = 90^\circ$ .
- Obviously, the simulated **PUCPASIMx2x2x24** has the worst performance especially in the direction of  $\vartheta_1 = 90^\circ$ . All antenna radiation patterns are identical and symmetric with respect to the co-elevation. Due to this reason there is no additional information available to resolve co-elevation except the effective aperture size. Since the effective aperture size decreases towards  $\vartheta_1 = 90^\circ$ , the minimum resolvable separation in co-elevation increases.
- Analysing the minimum resolvable separation in co-elevation with respect to the path length  $l$ , it is obvious that the resolution performance is related to the seen aperture size and number of elements. Only the performance of the **SPUCPAx2x2x24** is rather hard to explain, one possibility is that the internal construction strongly differs from the **SPUCPAx4x2x24**. Unfortunately, the details of the internal construction are not available.

As already analysed in the case of the azimuth resolution also here the relation between the *maximum separation error* but with respect to the co-elevation error  $E_{\Delta\vartheta}$  and the mean relative variance of the path weights are discussed (Fig. D.9). Keeping a constant co-elevation  $\vartheta_1 = 90^\circ$  and changing the path length  $l$  between 50 m and 950 m leads to the results plotted in Fig. D.9(a). Different to the azimuth results (Fig. D.7(c)), it is hard to distinguish between the worst case path weight constellation **11** and the best case path weight constellation **jj**. Nevertheless, the boundaries for a certain error  $E$  in terms of the mean relative variance are the same. To get a final conclusion concerning the relationship of these two parameters, in Figures D.9(b) and D.9(c), the relation is shown with respect to the co-elevation  $\vartheta_1$  and again for the different phase constellations  $\varphi_p$ . From these analyses and from the analysis with respect to the azimuth, the following can be concluded:

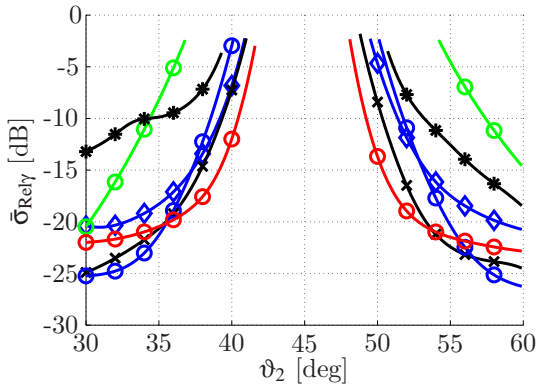
- The relation between  $E_{\Delta\varphi}$ ,  $E_{\Delta\vartheta}$  and the mean relative variance of the path weights is independent from the chosen antenna array in certain boundaries, where the boundaries are determined by the phase constellation between the path weights of the two paths.
- The boundaries in case of azimuth and co-elevation are the same.
- For a certain error  $E_{\Delta\varphi}$  or  $E_{\Delta\vartheta}$  the mean relative variance can be predicted with an accuracy of around  $\pm 2$  dB even without knowing the exact phase constellation.
- As a consequence, a fixed threshold level at a relative variance of -3 dB, which is used in the **RIMAX** algorithm to drop unreliable paths, can **not** be used to determine unresolvable



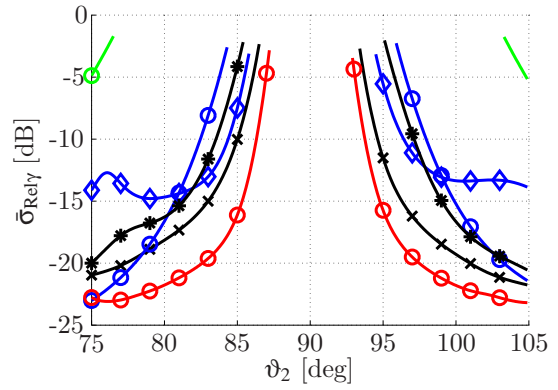
(a) Maximum separation error in co-elevation ( $l = 300$  m,  $\vartheta_1 = 45^\circ$ )



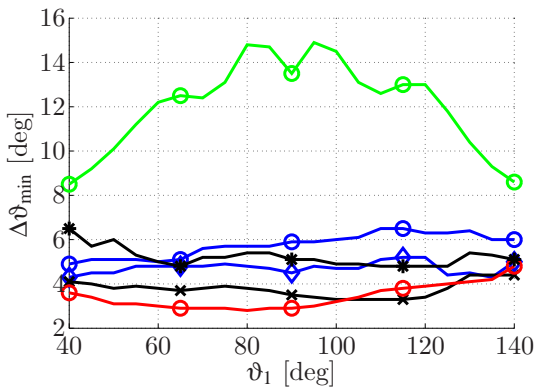
(b) Maximum separation error in co-elevation ( $l = 300$  m,  $\vartheta_1 = 90^\circ$ )



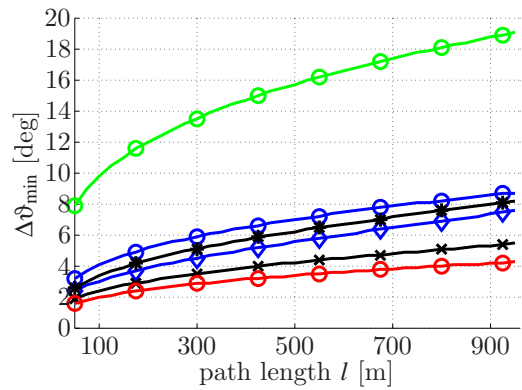
(c) Mean relative variance of the path weights ( $l = 300$  m,  $\vartheta_1 = 45^\circ$ )



(d) Mean relative variance of the path weights ( $l = 300$  m,  $\vartheta_1 = 90^\circ$ )

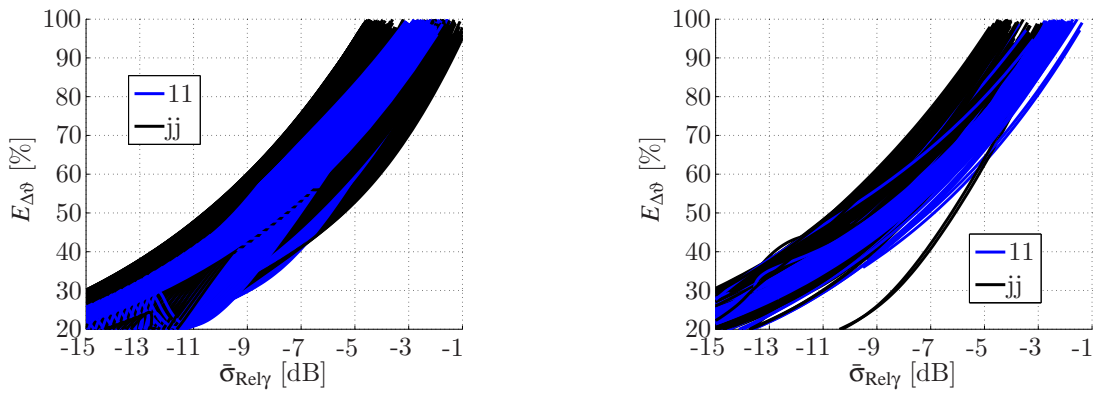


(e) Minimum resolvable separation  $\Delta\vartheta_{\min}$  w.r.t. co-elevation angle  $\vartheta_1$  ( $l = 300$  m)



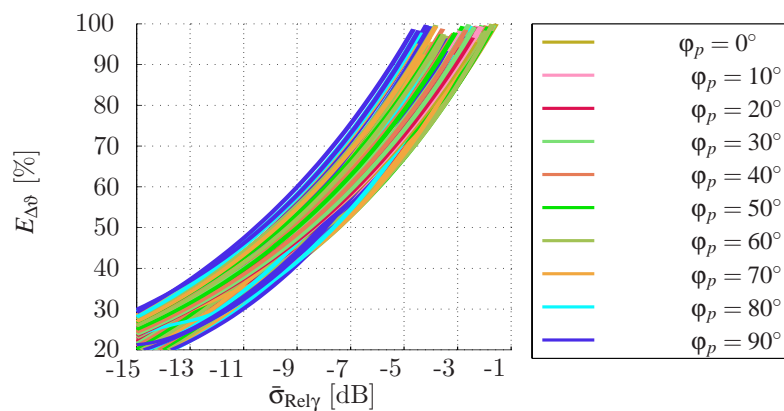
(f) Minimum resolvable separation  $\Delta\vartheta_{\min}$  w.r.t. the path length  $l$  ( $\vartheta_1 = 90^\circ$ )

**Fig. D.8:** Array comparison in terms of resolution capability in co-elevation w.r.t. co-elevation  $\vartheta_1$  and for different path length  $l$  (assuming worst case path weight constellation **11**, constant transmit power, constant receiver sensitivity, an additional path loss of 20 dB due to reflection and diffraction and constant azimuth  $\varphi_1 = \varphi_2 = 0^\circ$ )



(a) Relation between  $E_{\Delta\vartheta}$  and  $\bar{\sigma}_{\text{Rel}\gamma}$  changing the path length  $l$  from 50 m to 950m (all arrays,  $\vartheta_1 = \vartheta_2 = 90^\circ$ )

(b) Relation between  $E_{\Delta\vartheta}$  and  $\bar{\sigma}_{\text{Rel}\gamma}$  changing  $\vartheta_1$  from  $45^\circ$  to  $135^\circ$  (all arrays,  $l=300$  m)



(c) Relation between  $E_{\Delta\vartheta}$  and  $\bar{\sigma}_{\text{Rel}\gamma}$  for different phase constellations  $\varphi_p$  (all arrays,  $\vartheta_1 = 90^\circ$ ,  $l=300$  m)

**Fig. D.9:** Comparison of the relation between  $E_{\Delta\vartheta}$  and  $\bar{\sigma}_{\text{Rel}\gamma}$  changing path length  $l$  (a),  $\vartheta_1$  (b) and the path weight constellation (c)

paths. Either the phase constellations need to be considered in the dropping procedure or to assure a separation error of all paths better than 90 %, the threshold should be set to at least -6 dB.

## Appendix E

# GLOSSARY OF NOTATIONS, OPERATORS, MATRICES, SYMBOLS, AND ACRONYMS

### E.1 Notations

- All italic characters in equations denote variables.
- Small bold symbols and characters specify vectors or vector valued functions.
- Large bold symbols and characters specify matrices or matrix valued functions.
- Small or large normal roman symbols and characters specify functions.
- The subscript  $[M \times N]$  denotes the size of a matrix with  $M$  rows and  $N$  columns.
- Single or a set of Roman characters in the superscript or subscript indicate a description and do not refer to a variable e.g.  $G_{\text{Sys}}(f)$ , where Sys is a abbreviation for System.

### E.2 Mathematical operators

- $\text{vec}\{\mathbf{X}\}$  forms a column vector of the matrix  $\mathbf{X}$
  - $\text{diag}\{\mathbf{x}\}$  forms a diagonal matrix, in which the diagonal contains the values of the vector  $\mathbf{x}$
  - $\|\mathbf{X}\|_F / \|\mathbf{x}\|_F$  Frobenius norm of a matrix/vector  $\mathbf{X}/\mathbf{x}$
  - $\mathbf{X}^H$  denotes the hermitian of the matrix  $\mathbf{X}$
  - $\mathbf{X}^+$  denotes the pseudo inverse of the matrix  $\mathbf{X}$
  - $\mathbf{X} \circ \mathbf{Y}$  denotes the point wise multiplication of two matrices  $\mathbf{X}$  and  $\mathbf{Y}$ , where both matrices have the same size, also known as Schur product
  - $\mathbf{a} \otimes \mathbf{b}$  denotes the Kronecker product of two vectors  $\mathbf{a}$  and  $\mathbf{b}$
  - $\mathbf{A} \diamond \mathbf{B}$  denotes the column wise Kronecker product of two matrices  $\mathbf{A}$  and  $\mathbf{B}$ , known as Kathri-Rao product
  - $\mathbf{X} \circ \mathbf{Y}$  denotes the point wise multiplication of two matrices (Schur product)  $\mathbf{X}$  and  $\mathbf{Y}$ , where both matrices have the same size
-

- $\Re\{x\}$  is the real part of  $x$
- $\Im\{x\}$  is the imaginary part of  $x$
- $\text{toep}(\mathbf{a}, \mathbf{b})$  returns a toeplitz matrix with  $\mathbf{a}$  as its first column and  $\mathbf{b}$  as its first row

### E.3 Special matrices

In the following matrices are defined, which are used throughout this thesis.

#### E.3.1 Fourier matrix

The  $N \times N$  square matrix  $\mathbf{F}_N$  with entries given by:

$$F_{ik} = e^{2\pi \cdot j \cdot ik/N} = \omega^{ik} \quad (\text{E.1})$$

for  $i, k = 0, 1, 2, \dots, N-1$ , where  $j$  is the imaginary number  $j = \sqrt{-1}$ . Applying the normalisation  $1/\sqrt{N}$ , the Fourier matrix is defined as:

$$\mathbf{F}_N^{[N \times N]} = \frac{1}{\sqrt{N}} \begin{bmatrix} \omega^{0 \cdot 0} & \dots & \omega^{0 \cdot (N-1)} \\ \vdots & \ddots & \vdots \\ \omega^{(N-1) \cdot 0} & \dots & \omega^{(N-1) \cdot (N-1)} \end{bmatrix} \quad (\text{E.2})$$

where this normalisation is used to make  $\mathbf{F}_N$  unitary. Note, in publications different normalisations can be found. For example in case of Matlab<sup>TM</sup> the normalisation  $1/N$  is used for the transformation from frequency domain to time domain, where no normalisation is applied for the opposite direction.

#### E.3.2 Noise matrix or vector

The matrix  $\mathbf{N}$  and the vector  $\mathbf{n}$  represent the stationary measurement noise, where each element  $n$  is defined as:

$$n \sim N(0; \frac{\sigma^2}{2}) + j \cdot N(0; \frac{\sigma^2}{2}) \quad (\text{E.3})$$

where  $\sigma$  corresponds to the standard deviation.

#### E.3.3 Reflection and Selection matrices

Reflection matrix:

$$\mathbf{\Pi}^{[N \times N]} = \begin{bmatrix} 0 & 0 & 1 \\ 0 & \ddots & 0 \\ 1 & 0 & 0 \end{bmatrix} \quad (\text{E.4})$$

Example of a selection matrix which selects only the even columns of an example matrix with the size  $L_{\emptyset} \times 7$  matrix by right sight multiplication:

$$\mathbf{J}_g = \begin{bmatrix} 1 & 0 & 0 & 0 \\ 0 & 0 & 0 & 0 \\ 0 & 1 & 0 & 0 \\ 0 & 0 & 0 & 0 \\ 0 & 0 & 1 & 0 \\ 0 & 0 & 0 & 0 \\ 0 & 0 & 0 & 1 \end{bmatrix}^{[7 \times (7-1)/2+1]} \quad (\text{E.5})$$

Example of a selection matrix which selects only the odd columns of an example matrix with the size  $L_{\emptyset} \times 7$  matrix by right sight multiplication:

$$\mathbf{J}_u = \begin{bmatrix} 0 & 0 & 0 \\ 1 & 0 & 0 \\ 0 & 0 & 0 \\ 0 & 1 & 0 \\ 0 & 0 & 0 \\ 0 & 0 & 1 \\ 0 & 0 & 0 \end{bmatrix}^{[7 \times (7-1)/2]} \quad (\text{E.6})$$

### E.4 List of Frequently Used Symbols

Symbol	Range	Description	Chapter
$M_t$	$\mathbb{C}$	number of snapshots (measurement at a certain time stamp)	2-8
$M_f$	$\mathbb{C}$	number of frequency bins	2-8
$M_{\text{Tx}}$	$\mathbb{R}$	number of <b>Tx</b> antennas	2-8
$M_{\text{Rx}}$	$\mathbb{R}$	number of <b>Rx</b> antennas	2-8
$f$	$\mathbb{R}$	frequency	2-4
$B$	$\mathbb{R}$	measurement bandwidth	2-8
$t_s$	$\mathbb{R}$	total snapshot measurement time	2-8, A
$\tau_{\text{max}}$	$\mathbb{R}$	maximum excess time-delay	2-8
$H$	$\mathbb{C}$	channel frequency response	2-3
$\Phi_{\text{pn}}$	$\mathbb{R}$	overall phase noise	2,7,A
$\Phi_{\text{pnS}}$	$\mathbb{R}$	stochastic phase noise contribution	2,7,A
$\sigma_{\text{pnS}}$	$\mathbb{R}$	phase noise standard deviation	2,7,8,A
$\Phi_{\text{pnL}}$	$\mathbb{R}$	long term phase drift	2,7,A
$\Delta\Phi_{\text{pnL}}$	$\mathbb{R}$	phase gradient	2,7,8,A
$\lambda$	$\mathbb{R}$	wave length	3-8
$f_0$	$\mathbb{R}$	centre frequency	3-8
$G_{\text{Sys}}$	$\mathbb{C}$	system frequency response	3, 4
$\varphi$	$\mathbb{R}$	azimuth	3, 4
$\vartheta$	$\mathbb{R}$	co-elevation ( $\vartheta = 0^\circ \equiv$ north pole)	3, 4
$q$	$\mathbb{R}$	polarisation (horizontal ( $\vec{e}_\varphi$ ) or vertical ( $\vec{e}_\theta$ ))	3, 4
$m$	$\mathbb{R}$	$m$ -th antenna element of the array	3, 4
$\theta$	$\mathbb{R}$	elevation ( $\theta = 90^\circ \Rightarrow$ north pole, $\theta = -90^\circ \Rightarrow$ south pole)	3, 4
$b$	$\mathbb{C}$	radiation pattern function	3, 4
$\mathbf{b}_f$	$\mathbb{C}^{[M_f \times 1]}$	vector valued radiation pattern function (frequency domain)	3
$\mathbf{b}_d$	$\mathbb{C}^{[M_f \times 1]}$	vector valued radiation pattern function (delay domain)	3
$N_\varphi$	$\mathbb{R}$	number of samples in azimuth	3,4,B
$N_\vartheta$	$\mathbb{R}$	number of samples in co-elevation	3,4,B
$\Delta\varphi$	$\mathbb{R}$	measurement grid in azimuth	3, 4
$\Delta\vartheta$	$\mathbb{R}$	measurement grid in co-elevation ( $\vartheta = 0^\circ \equiv$ north pole)	3, 4
$\mathbf{B}$	$\mathbb{C}^{[N_\vartheta \times N_\varphi]}$	matrix of the narrow band radiation pattern	3,4,B
$\mathbf{B}_p$	$\mathbb{C}^{[N'_\vartheta \times N_\varphi]}$	matrix of the periodic narrow band radiation pattern	3,4,B
$L_\varphi$	$\mathbb{R}$	number of relevant aperture samples azimuth aperture	3,4,6,B
$L_\vartheta$	$\mathbb{R}$	number of relevant aperture samples co-elevation aperture	3,4,B
$\mu_\varphi$	$\mathbb{R}$	vector for the selection of the $L_\varphi$ relevant azimuth aperture samples	3,4,6,B
$\mu_\vartheta$	$\mathbb{R}$	vector for the selection of the $L_\vartheta$ relevant co-elevation aperture samples	3,4,B
$\mathbf{D}_\vartheta$	$\mathbb{C}^{[N'_\vartheta \times L_\vartheta]}$	elevation transformation matrix (truncated Fourier matrix)	3,4,B
$\mathbf{D}_\varphi$	$\mathbb{C}^{[L_\varphi \times N_\varphi]}$	azimuth transformation matrix (truncated Fourier matrix)	3,4,B
$\mathbf{b}$	$\mathbb{C}^{[M_{\text{Rx}} \times 1]}$	vector valued function of $M_{\text{Rx}/\text{Tx}}$ radiation patterns	3,4,B
$\mathbf{G}$	$\mathbb{C}^{[L_\vartheta \times L_\varphi]}$	EADF matrix of one antenna element	3,4,B
$\Gamma$	$\mathbb{C}^{[M \times L_\vartheta \cdot L_\varphi]}$	EADF matrix of $M$ antennas	3,4,B
$\zeta^{N_{95}}$	$\mathbb{R}^{[N_{95} \times 2]}$	minimum sampling grid for antenna array radiation patterns with $N_{95}$ pairs of azimuth and co-elevation angles	3,5
$K$	$\mathbb{R}$	maximum number of paths	5-8
$k$	$\mathbb{R}$	path counter	5-8
$\tau_k$	$\mathbb{R}$	time delay of the $k$ -th path	5-8
$\varphi_{\text{Tx}/\text{Rx},k}$	$\mathbb{R}$	azimuth of Departure/Arrival of the $k$ -th path	5-8
$\vartheta_{\text{Tx}/\text{Rx},k}$	$\mathbb{R}$	co-elevation of Departure/Arrival of the $k$ -th path	5-8
$\gamma_{\text{hh},k}$	$\mathbb{C}$	complex path weight of the $k$ -th path h-h polarisation	5-8
$\gamma_{\text{hv},k}$	$\mathbb{C}$	complex path weight of the $k$ -th path h-v polarisation	5-8

Symbol	Range	Description	Chapter
$\gamma_{vh,k}$	$\mathbb{C}$	complex path weight of the $k$ -th path v-h polarisation	5-8
$\gamma_{vv,k}$	$\mathbb{C}$	complex path weight of the $k$ -th path v-v polarisation	5-8
$\theta_k$	$\mathbb{R}, \mathbb{C}$	condensed parameter vector of all parameters of the $k$ -th path	5-8
$\theta_{SC}$	$\mathbb{R}, \mathbb{C}$	condensed parameter vector of all parameters of all $K$ paths	5-8
$\alpha_0$	$\mathbb{R}$	mean estimated noise power	5-8
$\alpha_1$	$\mathbb{R}$	peak power in the <b>IR</b> of <b>DMC</b> process	5-8
$\tau_d$	$\mathbb{R}$	base delay of the <b>DMC</b> process	5-8
$B_d$	$\mathbb{R}$	coherency bandwidth of the <b>DMC</b> process	5-8
$\theta_{DMC}$	$\mathbb{R}, \mathbb{C}$	condensed parameter vector of all parameters of <b>DMC</b>	5-8
$\Psi(\tau)$	$\mathbb{R}$	expectation value of the <b>DMC</b> channel impulse responses	5
$\Psi(f)$	$\mathbb{C}$	power density function of the <b>DMC</b> in the frequency domain	5,8
$\mathbf{s}(\theta_{SC})$	$\mathbb{C}^{[M \times 1]}$	observable channel response of the <b>SC</b> with $M = M_t \cdot M_f \cdot M_{R_x} \cdot M_{T_x}$	5-8
$\mathbf{d}(\theta_{DMC})$	$\mathbb{C}^{[M \times 1]}$	observable channel response of the <b>DMC</b> with $M = M_t \cdot M_f \cdot M_{R_x} \cdot M_{T_x}$	5-8
$\mathbf{x}$	$\mathbb{C}^{[M \times 1]}$	observation including <b>SC</b> , <b>DMC</b> and measurement noise with $M = M_t \cdot M_f \cdot M_{R_x} \cdot M_{T_x}$	5-8
$\mathbf{G}_{xy}$	$\mathbb{C}^{[L \times L]}$	linear projector matrix for the transmit polarisation $x$ and receive polarisation $y$ (describes the measurement system response with the total aperture size $L$ )	5
$\mu_k^{(i)}$	$\mathbb{R}$	parameter of $i$ -th parameter dimension and $k$ -th path ( <b>SC</b> )	5
$\mu_k$	$\mathbb{R}^{[1 \times R]}$	parameter vector of the $k$ -th path containing $R$ parameters ( <b>SC</b> )	5
$\mathbf{a}(\mu_k^{(i)})$	$\mathbb{C}^{[L_i \times 1]}$	complex exponentials for the $i$ -th parameter dimension and $k$ -th path with $L_i$ corresponding samples ( <b>SC</b> )	5
$\mathbf{B}_d$	$\mathbb{C}^{[M_d \times M_{pol}]}$	basis functions of the $d$ -th data dimension (e.g. Doppler $M_d = M_t$ ; $M_{pol} = 1$ samples, polarimetric <b>Rx</b> array $M_d = M_{R_x}$ ; $M_{pol} = 2$ , etc.)	5
$\mathbf{R}_f$	$\mathbb{C}^{[M_f \times M_f]}$	covariance matrix of the <b>DMC</b> process	5,8
$c(\mu_k)$	$\mathbb{C}$	multidimensional correlation function with respect to the $k$ -th path	5
$\mathbf{D}$	$\mathbb{C}^{[M_{R_x} \times L]}$	Jacobian matrix (first order derivatives) for $L$ parameters	6
$\mathbf{J}$	$\mathbb{C}^{[L \times L]}$	Hessian matrix (approximation of the second order derivatives) for $L$ parameters	6
$\varphi_c$	$\mathbb{R}$	centred azimuth (azimuth deviation from the true path)	7
$\vartheta_c$	$\mathbb{R}$	centred co-elevation (co-elevation deviation from the true path)	7
$\mathbf{H}$	$\mathbb{C}^{[M_{R_x} \times M_{T_x}]}$	MIMO channel matrix at one frequency bin	8
$\mathcal{E}_{ECM}$	$\mathbb{R}$	Environment Characterisation Metric mismatch ( <b>ECM</b> mismatch)	8
$C_{Norm}$	$\mathbb{R}$	MIMO channel capacity applying a certain normalisation	8
$\chi_{Norm}$	$\mathbb{R}$	normalisation factor for the capacity calculation ( <b>ECM</b> mismatch)	8
$\rho$	$\mathbb{R}$	application <b>SNR</b> for the capacity calculation	8
$\epsilon_{\zeta, Norm}$	$\mathbb{R}$	relative error of a diversity metric $\zeta$ for a certain normalisation	8
$\bar{\epsilon}_{\zeta}$	$\mathbb{R}$	mean relative error of a diversity metric $\zeta$	8
$\sigma_{\epsilon_{\zeta}}$	$\mathbb{R}$	standard deviation of the relative error $\epsilon_{\zeta, Norm}$	8



## E.5 Acronyms

<b>1D</b>	one-dimensional
<b>2D</b>	two dimensional
<b>3D</b>	three dimensional
<b>3G</b>	third generation
<b>ACF</b>	Auto Correlation Function
<b>AGC</b>	Automatic Gain Control
<b>Appl. SNR</b>	Application SNR <b>SNR</b> that is assume for the capacity calculation, do not mix up with the measurement <b>SNR</b> !
<b>BRI</b>	University of Bristol - Department of Electrical and Electronic Engineering
<b>BS</b>	Base Station
<b>CDF</b>	Cumulative Distribution Function
<b>CEADF</b>	Complete Effective Aperture Distribution Function
<b>CIR</b>	Complex Impulse Response
<b>CRLB</b>	Cramér-Rao Lower Bound
<b>CUBA</b>	Circular Uniform Beam Array
<b>CW</b>	Continuous Wave
<b>DFT</b>	Discrete Fourier Transformation
<b>DMC</b>	Dense Multipath Components
<b>DoA</b>	Direction of Arrival
<b>DoD</b>	Direction of Departure
<b>EADF</b>	Effective Aperture Distribution Function
<b>ECM</b>	Environment Characterisation Metric
<b>EM</b>	Expectation Maximisation
<b>ESPRIT</b>	Estimation of Signal Parameters via Rotational Invariance Techniques
<b>FDTD</b>	Finite-Difference Time-Domain
<b>FFT</b>	Fast Fourier Transformation
<b>FIM</b>	Fisher Information Matrix
<b>GBSCM</b>	Geometry-Based Stochastic Channel Models
<b>IHE</b>	University of Karlsruhe - Institut für Höchstfrequenztechnik und Elektronik
<b>i.i.d.</b>	independent and identically distributed
<b>IR</b>	Impulse Response
<b>IRK</b>	IRK-Dresden
<b>LO</b>	Local Oscillator
<b>LoS</b>	Line of Sight
<b>LNA</b>	Low Noise Amplifier
<b>MBPCM</b>	Measurement Based Parametric Channel Modelling
<b>MCSSS</b>	Multi-Carrier Spread Spectrum Signal
<b>MIMO</b>	Multiple-Input Multiple-Output
<b>ML</b>	Maximum Likelihood
<b>MS</b>	Mobile Station
<b>MSRR</b>	Mean SRR
<b>MUSIC</b>	Multiple Signal Classification
<b>MUX</b>	Multiplexer
<b>N95</b>	N95 (minimum sampling grid in the angular domain)
<b>NLoS</b>	Non Line of Sight
<b>NPCG</b>	Normalised Parallel Channel Gain
<b>NWA</b>	Network Analyser
<b>OFDM</b>	Orthogonal Frequency Division Multiplex
<b>OLoS</b>	Obstructed Line of Sight
<b>PA</b>	Power Amplifier
<b>PRBS</b>	Pseudo Random Bit Sequence
<b>pdp</b>	power delay profile
<b>PIN</b>	Positive Intrinsic Negative

---

---

<b>PPDA</b>	Polarimetric Personal Digital Assistant
<b>PLL</b>	Phase Locked Loop
<b>pn</b>	phase noise
<b>PUCPA</b>	Polarimetric Uniform Circular Patch Array
<b>RF</b>	Radio Frequency
<b>RFT</b>	Radio Frequency Tuner
<b>RIMAX</b>	RIMAX (Gradient based ML Parameter estimation algorithm)
<b>r.m.s.</b>	root mean square
<b>RMSE</b>	Root Mean Square Error
<b>Rx</b>	Receiver
<b>SC</b>	Specular Components
<b>SAGE</b>	Space Alternating Generalized Expectation Maximisation
<b>SIC</b>	Serial Interference Cancellation
<b>SISO</b>	Single-Input Single-Output
<b>SNR</b>	Signal to Noise Ratio
<b>SRR</b>	Signal to Remainder Ratio
<b>SV</b>	Singular Values
<b>TDoA</b>	Time Delay of Arrival
<b>TUI</b>	Ilmenau University of Technology
<b>Tx</b>	Transmitter
<b>UCA</b>	Uniform Circular Array
<b>UCPA</b>	Uniform Circular Patch Array
<b>ULA</b>	Uniform Linear Array
<b>URA</b>	Uniform Rectangular Array
<b>UTD</b>	Uniform Geometrical Theory of Diffraction
<b>UWB</b>	Ultra Wide-Band
<b>VSH</b>	Vector Spherical Harmonics
<b>WEADF</b>	Windowed Effective Aperture Distribution Function
<b>XPD</b>	cross polarisation discrimination (property of antenna!)

---



## BIBLIOGRAPHY

### Own References

- [1] Thoma R., Hampicke D., Landmann M., Richter A., and Sommerkorn G., "Measurement-based Channel Modelling (MBPCM)," in *Proceedings of the International Conference on Electromagnetics in Advanced Applications (ICEAA03)*, Torino, Italy, September 2003.
  - [2] Thoma R., Landmann M., and Richter A., "RIMAX-a maximum likelihood framework channel parameter estimation in multidimensional channel sounding," in *Proc. 2004 Int. Symp. on Antennas and Propag.*, Sendai, Japan, August 2004 (**Received Best Paper Award**), pp. 53–56.
  - [3] Landmann M., Sivasondhivat K., Takada J.-I., Ida I., and Thoma R., "Polarization Behavior of Discrete Multipath and Diffuse Scattering in Urban Environments at 4.5 GHz," in *EURASIP Journal on Wireless Communications and Networking, Special Issue on Space-Time Channel Modeling for Wireless Communications and Networking*, vol. 2007, 2007, pp. Article ID 57980, 16 pages, doi:10.1155/2007/57980.
  - [4] Landmann M., Kaeske M., Thoma R., Takada J., and Ida I., "Measurement Based Parametric Channel Modeling Considering Diffuse Scattering and Specular Components," in *International Symposium on Antennas and Propagation*, Niigata, Japan, August 2007 (**Received Best Paper Award**).
  - [5] Landmann M., "Untersuchung von zirkularen Antennenarrays für Channel-Sounder-Anwendungen," Master's thesis, TU Ilmenau, 2001.
  - [6] Thoma R., Hampicke D., Landmann M., Sommerkorn G., and Richter A., "MIMO measurement for double-directional channel modelling," in *MIMO: Communications Systems from Concept to Implementations (Ref. No. 2001/175)*, IEE Seminar on, Dec. 2001, pp. 1/1–1/7.
  - [7] Hampicke D., Schneider C., Landmann M., Richter A., Sommerkorn G., and Thoma R., "Measurement-based simulation of mobile radio channels with multiple antennas using a directional parametric data model," in *Vehicular Technology Conference, 2001. VTC 2001 Fall. IEEE VTS 54th*, vol. 2, 7-11 Oct. 2001, pp. 1073–1077.
  - [8] Landmann M., Richter A., and Thoma R., "Estimation Of Multidimensional Polarimetric Channel Model Parameters," in *COST 273 Temporary Document TD(02) 132*, Lisbon, Portugal, September 2002.
  - [9] Tan C. M., Landmann M., Richter A., Pesik L., Beach M., Schneider C., Thoma R., and Nix A., "On the Application of Circular Arrays in Direction Finding Part II: Experimental evaluation on SAGE with different circular arrays," in *1st Annual COST 273 Workshop*, Espoo, Finland, May 2002.
  - [10] Hampicke D., Landmann M., Schneider C., Sommerkorn G., Thoma T., Fugen T., Maurer J., and Wiesbeck W., "MIMO capacities for different antenna array structures based on double
-

- directional wide-band channel measurements,” in *Vehicular Technology Conference, 2002. Proceedings. VTC 2002-Fall. 2002 IEEE 56th*, vol. 1, Sept. 2002, pp. 180–184.
- [11] Thoma R., Landmann M., Sommerkorn G., and Richter A., “Multidimensional high-resolution channel sounding in mobile radio,” in *Instrumentation and Measurement Technology Conference, 2004. IMTC 04. Proceedings of the 21st IEEE*, vol. 1, 18-20 May 2004, pp. 257–262.
- [12] Richter A., Schneider C., Landmann M., and T., “Parameter Estimation Results of Specular and Dense Multipath Components in Micro-Cell Scenarios,” in *The 7th Intl. Symp. On Wireless Personal Multimedia Communications WPMC 2004 7*, Abano Terme, Italy, Sept. 2004.
- [13] Thoma R., Landmann M., Richter A., and Trautwein U., “Multidimensional High-Resolution Channel Sounding,” in *Smart Antennas in Europe State of the Art, EURASIP Book Series on SP & C*, Kaiser T., Ed. Hindawi Publishing Corporation, 2005, vol. 3.
- [14] Kotterman W., Landmann M., Sommerkorn G., and Thoma R., “On diffuse and non-resolved multipath components in directional channel characterisation,” in *XXVIIIth General Assembly of URSI*, New Delhi, India, October 2005.
- [15] Ching G., Ghorraishi M., Landmann M., Lertsirisopon N., Takada J., Samedá I., Imai I., and Sakamoto H., “Directional Measurements Inside Tunnel,” in *Proceedings of IEICE Society Conference*, Sapporo, Japan, Sept. 2005, pp. B–1–23.
- [16] Ching G., Ghorraishi M., Landmann M., Lertsirisopon N., Takada J., Samedá I., Imai I., and Sakamoto H., “Wideband Directional Measurements in an Arched Tunnel to Determine the Spread Parameters,” in *Proceedings of IEICE Antennas Propagation Technical Meeting*, Chiba, Japan, Nov. 2005, pp. AP2005–111.
- [17] Sivasondhivat K., Takada J.-I., Landmann M., Ida I., and Oishi Y., “Street dependency propagation at MS based on urban macrocellular measurement,” in *1st European Conference on Antennas & Propagation (EuCAP 2006)*, Nice, France, Nov. 2006.
- [18] Landmann M., Kotterman W., and Thoma R., “On The Influence of Incomplete Data Models on Estimated Angular Distributions In Channel Characterisation,” in *The Second European Conference on Antennas and Propagation (EuCAP 2007)*, 2007 (**Received Best Paper Award**).
- [19] Narandzic M., Landmann M., Schneider C., and Thoma R. S., “Influence of Extraction Procedures on Estimated Wideband MIMO Channel Parameters,” in *Mobile and Wireless Communications Summit, 2007. 16th IST*, 1-5 July 2007, pp. 1–5.
- [20] Ching G. S., Ghorraishi M., Landmann M., Lertsirisopon N., Takada J., Imai T., Samedá I., and Sakamoto H., “Wideband polarimetric directional propagation channel analysis inside an arched tunnel,” *accepted on IEEE Trans. Antennas Propag.*, 2008.
- [21] Del Galdo G., Lotze J., Landmann M., Haardt M., and Thoma R., “VecSHARP: Vector Spherical Harmonics-based Antenna Radiation Pattern Descriptor,” *IEEE TRANSACTIONS ON ANTENNAS AND PROPAGATION*, vol. ?, pp. 1–25, 2008 (submitted).
- [22] Narandzic M., Kaeske M., Schneider C., Milojevic M., Landmann M., Sommerkorn G., and Thoma R., “3D-Antenna Array Model for IST-WINNER Channel Simulations,” in *Vehicular Technology Conference, 2007. VTC2007-Spring. IEEE 65th*, 22-25 April 2007, pp. 319–323.
-

- 
- [23] Landmann M., Richter A., and Thoma R., "Performance Evaluation of Real Antenna Arrays for High-Resolution DoA Estimation in Channel Sounding - Part 1: Channel Parameter Resolution Limits," in *COST 273 Temporary Document*, Prague, Czech Republic, September 2003.
- [24] Sommerkorn G., Landmann M., Richter A., and Thoma R., "Performance Evaluation of Real Antenna Arrays for High-Resolution DoA Estimation in Channel Sounding - Part 2: Experimental ULA Measurement Results," in *COST 273 Temporary Document*, Prague, Czech Republic, September 2003.
- [25] Landmann M. and Del Galdo G., "Efficient Antenna Description for MIMO Channel Modelling and Estimation," in *Millenium Conference on Antennas & Propagation AP*, Amsterdam, The Netherlands, September 2004.
- [26] Landmann M., Richter A., and Thoma R., "Performance Evaluation of Antenna Arrays for High-Resolution DoA Estimation in Channel Sounding," in *International Symposium on Antennas and Propagation*, Sendai, Japan, August 2004 (**Received Young Scientist Travel Grant**).
- [27] Landmann M., Richter A., and Thoma R., "DoA Resolution Limits in MIMO Channel Sounding," in *International Symposium on Antennas and Propagation and USNC/URSI National Radio Science Meeting*, Monterey CA, USA, June 2004.
- [28] Landmann M. and Thoma R., "Resolution Limits and Antenna Array Calibration of Real Arrays," in *Mobile Broadband Multimedia Networks: Techniques, Models and Tools for 4G Techniques*, COST 273, Correia L., Ed. Academic Press, 2006, pp. 165–167.
- [29] Landmann M. and Thoma R., "Estimation of phase drift during calibration measurements for efficient beam pattern modelling," in *NEWCOM-ACORN Workshop*, Wien, Austria, September 2006.
- [30] Richter A., Landmann M., and Thoma R., "A Gradient Based Method for Maximum Likelihood Channel Parameter Estimation from Multidimensional Channel Sounding Measurement," in *Proc. XXVIIIth URSI General Assembly*, Maastricht, NL, August 2002.
- [31] Richter A., Landmann M., and Thoma R., "Maximum likelihood channel parameter estimation from multidimensional channel sounding measurements," in *Vehicular Technology Conference, 2003. VTC 2003-Spring. The 57th IEEE Semiannual*, vol. 2, April 2003, pp. 1056–1060.
- [32] Landmann M. and Takada J.-I., "On the Plane Wave Assumption in Indoor Channel Modelling," in *IEICE Society Conference*, Sapporo, Japan, September 2005, p. 1.
- [33] Landmann M., Kotterman W., and Thoma R., "On the Influence of Incomplete Data Models on Estimated Angular Distributions in Channel Characterisation," in *3rd MCM - Duisburg, COST 2100 Temporary Document TD(07) 321*. Duisburg, Germany: COST 2100, September 2007.
- [34] Fuegen T., Knoerzer S., Landmann M., Thoma R., and Wiesbeck W., "A 3-D Ray Tracing Model For Macrocell Urban Environments and its Verification with Measurements," in *The Second European Conference on Antennas and Propagation (EuCAP 2007)*, 2007.
-

### References by Other Authors

- [35] Foschini G. and Gans M., "On limits of wireless personal communications in a fading environment when using multiple antennas," in *Wireless Personal Communications*, vol. 6, March 1998, pp. 335–1311.
- [36] Erceg V., Fortune S., Ling J., Rustako A., and Valenzuela R., "Comparisons of a computer-based propagation prediction tool with experimental data collected in urban microcellular environments," *Selected Areas in Communications, IEEE Journal on*, vol. 15, no. 4, pp. 677–684, May 1997.
- [37] Liang G. and Bertoni H., "A new approach to 3-D ray tracing for propagation prediction in cities," *Antennas and Propagation, IEEE Transactions on*, vol. 46, no. 6, pp. 853–863, June 1998.
- [38] Seong-Cheol K., Guarino B., Willis T., Erceg V., Fortune S., Valenzuela R., Thomas L., Ling J., and Moore J., "Radio propagation measurements and prediction using three-dimensional ray tracing in urban environments at 908 MHz and 1.9 GHz," *Vehicular Technology, IEEE Transactions on*, vol. 48, no. 3, pp. 931–946, May 1999.
- [39] Maurer J., Fügen T., and Wiesbeck W., "A Ray-Optical Channel Model for Vehicle-to-Vehicle Communications," *P. Russer, M Mongiardo (eds.), Proceedings in Physics: Fields, Networks, Computational Methods, and Systems in Modern Electrodynamics*, pp. 243–254, December 2004.
- [40] Fügen T., Maurer J., Kayser T., and Wiesbeck W., "Capability of 3D Ray Tracing for Defining Parameter Sets for the Specification of Future Mobile Communications Systems," *IEEE Transactions on Antennas and Propagation, Special issue on Wireless Communications*, vol. 54, no. 11, pp. 3125–3137, Nov. 2006.
- [41] Takada J., Jiye F., Houtao Z., and Kobayashi T., "Spatio-temporal channel characterization in a suburban non line-of-sight microcellular environment," *Selected Areas in Communications, IEEE Journal on*, vol. 20, pp. 532–538, 2002.
- [42] Pongsilamanee P. and Bertoni H., "Specular and nonspecular scattering from building facades," *Antennas and Propagation, IEEE Transactions on*, vol. 52, pp. 1879–1889, 2004.
- [43] Degli-Esposti V., Guiducci D., de'Marsi A., Azzi P., and Fuschini F., "An advanced field prediction model including diffuse scattering," *Antennas and Propagation, IEEE Transactions on*, vol. 52, no. 7, pp. 1717–1728, July 2004.
- [44] Maurer J., "Strahlenoptisches Kanalmodell für die Fahrzeug-Fahrzeug-Funkkommunikation," Ph.D. dissertation, Univ. Karlsruhe, Juli 2005.
- [45] Degli-Esposti V., Fuschini F., Vitucci E., and Falciasecca G., "Measurement and Modelling of Scattering From Buildings," *IEEE Transactions on Antennas and Propagation*, vol. 52, no. 1, pp. 143–153, January 2007.
- [46] Molisch A., "A Generic Model for MIMO Wireless Propagation Channels in Macro- and Microcells," in *IEEE Trans. Signal Proc.*, vol. 52, January 2004, pp. 61–71.
- [47] Correia L. M., *Wireless Flexible Personalised Communications COST 259*. New York: John Wiley and Sons, 2001.
- [48] Correia L., *Mobile Broadband Multimedia Networks: Techniques, Models and Tools for 4g. Techniques, Models and Tools for 4G*, Correia L., Ed. London: Academic Press, 2006.
-



- [49] “3rd Generation Partnership Project,” Tech. Rep. 3GPP TR 25.996 V.6.1.0, September 2003. [Online]. Available: <http://www.3gpp.org>
- [50] “WINNER II interim channel models,” Tech. Rep. IST-4-027756 WINNER D1.1.1. [Online]. Available: <https://www.ist-winner.org>
- [51] Steinbauer M., Molisch A., and Bonek E., “The Double-Directional Radio Channel,” in *Antennas and Propagation Magazine*, vol. 45, August 2001, pp. 51–63.
- [52] Kalliola K., Laitinen H., Vainikainen P., Toeltsch M., Laurila J., and Bonek E., “3-D double-directional radio channel characterization for urban macrocellular applications,” *Antennas and Propagation, IEEE Transactions on*, vol. 51, no. 11, pp. 3122–3133, Nov. 2003.
- [53] “The world of channelsounding,” MEDAV GmbH, Tech. Rep. [Online]. Available: <http://www.channelsounder.de>
- [54] “EB Propsound CS,” Elektrobit, Automaatitietie 1 (PL 45), 90461 Oulunsalo, Finland, Tech. Rep. [Online]. Available: <http://www.propsim.net>
- [55] Del Galdo G., “Geometry-based channel modeling for multi-user MIMO systems and applications,” Ph.D. dissertation, Ilmenau University of Technology, Ilmenau, Germany, 2007, ISBN: 978-3-938843-27-7, available to download at <http://www.delgaldo.com>.
- [56] Viberg M. and Krim H., “Two decades of statistical array processing,” in *Signals, Systems & Computers, 1997. Conference Record of the Thirty-First Asilomar Conference on*, vol. 1, 2-5 Nov. 1997, pp. 775–777vol.1.
- [57] Richter A., Hampicke D., Sommerkorn G., and Thoma R., “MIMO measurement and joint M-D parameter estimation of mobile radio channels,” *Vehicular Technology Conference, 2001. VTC 2001 Spring. IEEE VTS 53rd*, vol. 1, pp. 214–218, May 2001.
- [58] Haardt M., “Efficient One-, Two-, and Multidimensional High-Resolution Array Signal Processing,” Ph.D. dissertation, TU Muenchen, March 1997.
- [59] Barabell A., “Improving the resolution performance of eigenstructure-based direction-finding algorithms,” in *Acoustics, Speech, and Signal Processing, IEEE International Conference on ICASSP '83.*, vol. 8, Apr 1983, pp. 336–339.
- [60] Fleury B., Tschudin M., Heddergott R., Dahlhaus D., and Ingeman Pedersen K., “Channel parameter estimation in mobile radio environments using the SAGE algorithm,” in *Selected Areas in Communications, IEEE Journal on Publication Date: March 1999*, vol. 17, March 1999, pp. 434–450.
- [61] Haneda K., Takada J., and Kobayashi T., “Experimental evaluation of a SAGE algorithm for ultra wideband channel sounding in an anechoic chamber,” in *Ultra Wideband Systems, 2004. Joint with Conference on Ultrawideband Systems and Technologies. Joint UWBST & IWUWBS. 2004 International Workshop on*, 18-21 May 2004, pp. 66–70.
- [62] Richter A., “On the Estimation of Radio Channel Parameters: Models and Algorithms (RIMAX),” Ph.D. dissertation, TU-Ilmenau, Ilmenau, Germany, May 2005. [Online]. Available: <http://www.db-thueringen.de/servlets/DerivateServlet/Derivate-7407/ilm1-2005000111.pdf>
- [63] Tschudin M., Brunner C., Kurpjuhn T., Haardt M., and Nossek J., “Comparison between unitary ESPRIT and SAGE for 3-D channel sounding,” in *Vehicular Technology Conference, 1999 IEEE 49th*, vol. 2, 16-20 May 1999, pp. 1324–1329vol.2.
-



- 
- [64] Roemer F. and Haardt M., "Efficient 1-D and 2-D DOA Estimation for Non-Circular Sources with Hexagonal Shaped Espar Arrays," in *Acoustics, Speech and Signal Processing, 2006. ICASSP 2006 Proceedings. 2006 IEEE International Conference on*, vol. 4, 14-19 May 2006, pp. IV–IV.
- [65] Bonek E. and Steinbaner M., "Double-directional channel measurements," *Antennas and Propagation, 2001. Eleventh International Conference on (IEE Conf. Publ. No. 480)*, vol. 1, pp. 226–230, April 2001.
- [66] Pal A., Tan C., and Beach M., "Comparison of MIMO channels from multipath parameter extraction and direct channel measurements," *Personal, Indoor and Mobile Radio Communications, 2004. PIMRC 2004. 15th IEEE International Symposium*, vol. 3, pp. 1574–1578, September 2004.
- [67] Czink N., Bonek E., Xuefeng Y., and Fleury B., "Cluster Angular Spreads in a MIMO Indoor Propagation Environment," *Personal, Indoor and Mobile Radio Communications, 2005. PIMRC 2005. IEEE 16th International Symposium*, vol. 1, pp. 664 – 668, September 2005.
- [68] Skentos N., Kanatas A., and Constantinou P., "MIMO channel characterization results from short range rooftop to rooftop wideband measurements," *Wireless And Mobile Computing, Networking And Communications, 2005. (WiMob'2005), IEEE International Conference*, vol. 1, pp. 137–144, August 2005.
- [69] Salmi J., Richter A., and Koivunen V., "Enhanced Tracking of Radio Propagation Path Parameters using State Space Modeling," in *European Signal Processing Conference EUSIPCO 2006*, 2006.
- [70] Wyne S., Czink N., Karedal J., Almers P., Tufvesson F., and Molisch A., "A Cluster-based Analysis of Outdoor-to-Indoor Office MIMO Measurements at 5.2 GHz," in *Vehicular Technology Conference, 2006. VTC-2006 Fall. 2006 IEEE 64th*, Montreal, QC, Canada, September 2006, pp. 1–5.
- [71] Czink N., Xuefeng Y., OZcelik H., Herdin M., Bonek E., and Fleury Bernard H., "Cluster Characteristics in a MIMO Indoor Propagation Environment," *Wireless Communications, IEEE Transactions on*, vol. 6, pp. 1465–1475, April 2007.
- [72] Medbo J., Riback M., Asplund H., and Berg J., "MIMO channel characteristics in a small macrocell measured at 5.25 GHz and 200 MHz bandwidth," *Vehicular Technology Conference, 2005. VTC-2005-Fall. 2005 IEEE 62nd*, vol. 1, pp. 372–376, September 2005.
- [73] Salmi J., Richter A., Enescu M., Vainikainen P., and Koivunen V., "Propagation Parameter Tracking using Variable State Dimension Kalman Filter," *Vehicular Technology Conference, 2006. VTC 2006-Spring. IEEE 63rd*, vol. 6, pp. 2757–2761, 2006.
- [74] Sommerkorn G., Hampicke D., Klukas R., Richter A., Schneider A., and Thoma R., "Reduction of DoA Estimation Errors Caused by Antenna Array Imperfections," in *29th European Microwave Conference*, Munich, Germany, October 1999.
- [75] Sommerkorn G., Hampicke D., Richter A., Schneider A., and Thoma R., "Measurement and Modeling Error Influence to Antenna Array Calibration and its Affect to ESPRIT-Based DoA-Estimation," in *Millenium Conference on Antennas and Propagation AP*, Davos, Switzerland, April 2000.
- [76] Sommerkorn G., Hampicke D., Klukas R., Richter A., Schneider A., and Thoma R., "Uniform Rectangular Antenna Array Calibration Issues for 2-D ESPRIT Application," in *4th European Personal Mobile Communications Conference EPMCC*, Vienna, Austria, February 2001.
-

- [77] Del Galdo G. and Lotze J., "The ilmpop channel modelling environment," Ilmenau University of Technology, Communications Research Laboratory, 2006. [Online]. Available: <http://tu-ilmenau.de/ilmpop>
- [78] Parsons J. D., *The Mobile Radio Propagation Channel*. Chichester: John Wiley & Sons, 2000.
- [79] Sachs J. and Peyerl P., "Ein neues Breitbandmeßverfahren für das Basisband," in *IEEE Workshop on Short-Range Radar*, July 1999.
- [80] Zetik R. and et a., "Ultra-Wideband Real-Time Channel Sounder and Directional Channel Parameter Estimation," in *2004 URSI Intl. Symp. On Electromagnetic Theory*, Pisa, Italy, May 2004.
- [81] Pintelon R. and Schoukens J., "System Identification-A Frequency Domain Approach," in *IEEE Press*, Piscataway , NJ, 2001.
- [82] Abouda A., El-Sallabi H., and Haeggman S., "Reducing Impact of Phase Noise on Accuracy of Measured MIMO Channel Capacity," in *Vehicular Technology Conference VTC 2006-Spring*, Dublin, Ireland, April 2007.
- [83] Baum D. S. and Boelcskei H., "Impact of Phase Noise on MIMO Channel Measurement Accuracy," in *Vehicular Technology Conference, 2004. VTC2004-Fall. 2004 IEEE 60th*, vol. 3, September 2004, pp. 1614–1618.
- [84] Rutman J., "Characterization of phase and frequency instabilities in precision frequency: Fifteen years of progress," in *Proc. of the IEEE*, vol. 66, May 1978, pp. 1048–1075.
- [85] Almers P., Wyne S., Tufvesson F., and Molisch A., "Effect of Random Walk Phase Noise on MIMO Measurements," in *Vehicular Technology Conference VTC 2005-Spring*, vol. 1, no. 10, June 2005, pp. 141–145.
- [86] Yin X., Ylitalo J., and Fleury B., "Phase Noise Mitigation in Channel Parameter Estimation for TDM Switched MIMO Channel Sounding," in *2007 Asilomar conference on Signals, Systems and Computers*, 2007.
- [87] Klukas R., "Microwave engineering and Antenna Development," IRK-Dresden, Dresden, Germany, Tech. Rep., 2001. [Online]. Available: <http://www.irk-dresden.de>
- [88] Demmerle F. and Wiesbeck W., "A biconical multibeam antenna for space-division multiple access," in *IEEE Transactions on Antenna and Propagations*, vol. 46, June 1998, pp. 782–787.
- [89] Fleury B., Dahlhaus D., Heddergott R., and Tschudin M., "Wideband angle of arrival estimation using the SAGE algorithm," in *Proc. IEEE Fourth Int. Symp. spread Spectrum techniques and Applications (ISSSTA '96)*, Mainz, Germany, September 1996, pp. 79–85.
- [90] Haardt M., Thoma R., and Richter A., "Multidimensional High-Resolution Parameter Estimation with Applications to Channel Sounding," in *High-Resolution and Robust Signal Processing*, Yingbo Hua et. a., Ed. New York, USA: Marcel Dekker, 2003, pp. 253–337.
- [91] Wuellen C. and Laikov D., "A FORTRAN code to generate lebedev grids up to order  $l = 131$ ," Computational Chemistry List, ltd., 2000. [Online]. Available: <http://server.ccl.net/ccs/software/SOURCES/FORTRAN/Lebedev-Laikov-Grids/index.shtml>
- [92] Lebedev V. I., "Quadratures on A Sphere," *Zh. vßchisl. Mar. mat. Fiz.*, vol. 16, pp. 293–306, 1976.
-

- 
- [93] Hansen J. E., *Spherical Near-Field Antenna Measurements*, ser. Numerical Analysis. London, UK: Peter Peregrinus, 1988, p. 387 p.
- [94] Friis H. T., "A note on a simple transmission formula," *Proc. of the IRE*, vol. 41, pp. 254–256, May 1946.
- [95] Belloni F., Richter A., and Koivunen V., "Avoiding Bias in Circular Arrays Using Optimal Beampattern Shaping and EADF," in *Signals, Systems and Computers, 2005. Conference Record of the Thirty-Ninth Asilomar Conference on*, October 28 - November 1, 2005, pp. 1390–1393.
- [96] Belloni F., Richter A., and Koivunen V., "Performance of Root-MUSIC Algorithm using Real-World Arrays," in *European Signal Processing Conference (EUSIPCO)*, Florence, Italy, September 4 – 8 2006.
- [97] Belloni F., Richter A., and Koivunen V., "Extension of root-MUSIC to non-ULA Array Configurations," *Acoustics, Speech and Signal Processing, 2006. ICASSP 2006 Proceedings. 2006 IEEE International Conference on*, vol. 4, pp. IV–897 – IV–900, 2006.
- [98] Balanis C., *Near Field/Far Field Methods*, ser. Numerical Analysis. John Wiley & Sons, INC, 1997, pp. 852–858.
- [99] *Electromagnetic Modeling of Composite Metallic and Dielectric Structures*. [Online]. Available: <http://www.wipl-d.com/quicktour/customers.php>
- [100] More J., "The Levenberg-Marquardt Algorithm: Implementation and Theory," ser. Numerical Analysis. Springer Verlag, 1977, pp. 105–116.
- [101] Vaughan R. and Andersen J., "Channel Propagation and Antennas for Mobile Communications," *IEE electromagnetic waves series London*, no. 50, 2003.
- [102] Fessler J. and Hero A., "Space Alternating Generalized Expectation Maximization Algorithm," in *IEEE Trans. on Signal Processing*, vol. 42, October 1994, pp. 664–2677.
- [103] Ziskind I. and Wax M., "Maximum Likelihood Localization of Multiple Sources by Alternating Projection," in *IEEE Trans. Acoustics, Speech, and Signal Processing*, vol. 36, October 1988, pp. 1553–1560.
- [104] Andersen J., Nielsen J., Bauch G., and Herdin M., "The Large Office Environment - Measurement and Modeling of the Wideband Radio Channel," in *Personal, Indoor and Mobile Radio Communications, 2006 IEEE 17th International Symposium on*, Sept. 2006, pp. 1–5.
- [105] Scharf L., *Statistical Signal Processing: detection, estimation, and time series analysis*. New York, USA: Addison-Wesley, 1991.
- [106] Stoica P. and Nehorai T., "Performance Study of Conditional and Unconditional Direction-of-Arrival Estimation," in *IEEE Trans. On ASSP*, vol. 38, October 1990.
- [107] Stoica P. and Nehorai A., "MUSIC, maximum likelihood, and Cramer-Rao bound: further results and comparisons," in *Acoustics, Speech, and Signal Processing [see also IEEE Transactions on Signal Processing]*, *IEEE Transactions on Publication Date: Dec 1990*, vol. 38, December 1990, pp. 2140–2150.
- [108] Hongbin L., Stoica P., and Jian L., "Computationally efficient maximum likelihood estimation of structured covariance matrices," in *IEEE Transactions on Signal Processing*, [see also *Acoustics, Speech, and Signal Processing*], vol. 47, May 1999, pp. 1314–1323.
-

- [109] Heddergott R., "Implementierung und Untersuchung eines Verfahrens zur hochauflösenden Schätzung von Parametern aus breitbandigen Funkanalmessungen," Nachdiplomarbeit Lfd.Nr:48, ETH Zurich, 1999.
- [110] Richter A. and Thoma R., "Angle Estimation With Circular Uniform Beam Arrays Using the CUBA ESPRIT," in *Millenium Conference on Antennas & Propagation AP*, Davos, Switzerland, April 2000.
- [111] Lanne M., Lundgren A., and Viberg M., "Optimized Beamforming Calibration in the Presence of Array Imperfections," in *Acoustics, Speech and Signal Processing, 2007. ICASSP 2007. IEEE International Conference on*, vol. 2, 15-20 April 2007, pp. II-973-II-976.
- [112] Lundgren A., "Weighted Regression with Application to Array Calibration," Ph.D. dissertation, CHALMERS UNIVERSITY OF TECHNOLOGY, Goeteborg, 2007.
- [113] Youming L. and Er M., "Theoretical analyses of gain and phase error calibration with optimal implementation for linear equispaced array," *Signal Processing, IEEE Transactions on [see also Acoustics, Speech, and Signal Processing, IEEE Transactions on]*, vol. 54, no. 2, pp. 712-723, Feb. 2006.
- [114] Lin M. and Yang L., "Blind Calibration and DOA Estimation With Uniform Circular Arrays in the Presence of Mutual Coupling," *Antennas and Wireless Propagation Letters*, vol. 5, pp. 315-318, December 2006.
- [115] Tuan D.-H. and Russer P., "An analysis of wideband direction-of-arrival estimation for closely-spaced sources in the presence of array model errors," *Microwave and Wireless Components Letters, IEEE [see also IEEE Microwave and Guided Wave Letters]*, vol. 13, no. 8, pp. 314-316, Aug. 2003.
- [116] "Pyramiden-Absorber DATENBLATT 390-1, Noppen-Absorber DATENBLATT 390-7," Emc-Technik & Consulting, Tech. Rep., 2007. [Online]. Available: <http://www.emc-technik.de/>
- [117] Zhongfu Y., Li X., and Xu X., "DOA Estimation With Circular Array via Spatial Averaging Algorithm," *Antennas and Wireless Propagation Letters*, vol. 6, pp. 74-76, December 2007.
- [118] Roald G. and Hendrik R., "A Hybrid UCA-RARE/Root-MUSIC Approach for 2-D Direction of Arrival Estimation in Uniform Circular Arrays in the Presence of Mutual Coupling," *IEEE Transactions on Antennas and Propagation*, vol. 55, pp. 841 - 849, March 2007.
- [119] Belloni F. and Koivunen V., "Beamspace Transform for UCA: Error Analysis and Bias Reduction," in *Signal Processing, IEEE Transactions on [see also Acoustics, Speech, and Signal Processing, IEEE Transactions on]*, vol. 54, August 2006, pp. 3078-3089.
- [120] Liu H.-S. and Xiao X.-C., "The study of DOA estimation error caused by sensors position error of planar array," *2006 6th International Conference on ITS Telecommunications Proceedings*, pp. 405-407, June 2006.
- [121] Qiaowei Y., Qiang C., and Sawaya K., "Accurate DOA estimation using array antenna with arbitrary geometry," *Antennas and Propagation, IEEE Transactions*, vol. 53, pp. 1352-1357, April 2005.
- [122] Gao D.-Y., Wang B.-H., and Guo Y., "Comments on Blind Calibration and DOA Estimation With Uniform Circular Arrays in the Presence of Mutual Coupling," *Antennas and Wireless Propagation Letters*, vol. 5, pp. 566-568, December 2006.
-

- 
- [123] Wu B., "Realization and Simulation of DOA estimation using MUSIC Algorithm with Uniform Circular Arrays," *Environmental Electromagnetics, The 2006 4th Asia-Pacific Conference*, pp. 908–912, August 2006.
- [124] Fang-Ming H. and Xian-Da Z., "An ESPRIT-like algorithm for coherent DOA estimation," *Antennas and Wireless Propagation Letters*, vol. 4, pp. 443–446, 2005.
- [125] Krzysztofik W. and Fafara M., "Comparison & examination the methods of direction-of-arrival estimation," *Antennas and Propagation Society International Symposium, 2005 IEEE*, vol. 4A, pp. 154–157, July 2005.
- [126] Obeidat B., Yimin Z., and Amin M., "Performance analysis of DOA estimation using dual-polarized antenna arrays," *Signal Processing and Information Technology, 2005. Proceedings of the Fifth IEEE International Symposium*, pp. 423–428, December 2005.
- [127] Maurice K., Yvo de J., and Matti H., "MOBILE HIGH-RESOLUTION DIRECTION FINDING OF MULTIPATH RADIOWAVES IN AZIMUTH AND ELEVATION," in *Proceedings of SPS-DARTS 2005 (the 2005 The first annual IEEE BENELUX/DSP Valley Signal Processing Symposium)*, April 2005.
- [128] Wyne S., Almers P., Eriksson G., Karedal J., Tufvesson F., and Molisch A., "Outdoor to Indoor Office MIMO Measurements at 5.2 GHz," *Vehicular Technology Conference VTC2004-Fall*, vol. 1, pp. 101 – 105, September 2004.
- [129] Medbo J. and Berg J.-E., "Spatio-temporal channel characteristics at 5 GHz in a typical office environment," *Vehicular Technology Conference, 2001. VTC 2001 Fall. IEEE VTS 54th*, vol. 3, pp. 1256–1260, 2001.
- [130] Fuhl J., Rossi J.-P., and Bonek E., "High-resolution 3-D direction-of-arrival determination for urban mobile radio," *IEEE Transactions on Antennas and Propagation*, vol. 45, pp. 672–682, 1997.
- [131] Jeng-Shiann J. and Ingram M., "Distributed source model for short-range MIMO," in *Vehicular Technology Conference, 2003. VTC 2003-Fall. 2003 IEEE 58th*, vol. 1, pp. 6–9 Oct. 2003, pp. 357–362 Vol.1.
- [132] Sivasondhivat K. and Takada J.-I., "An Application of Extended Array Mode Vector to ISI-SAGE," in *International Symposium on Antennas and Propagation (ISAP 2004)*, Sendai, Japan, Aug. 2004.
- [133] Xuefeng Y. and Fleury B., "Nominal direction estimation for slightly distributed scatterers using the SAGE algorithm," *Antennas and Propagation Society International Symposium, 2005 IEEE*, vol. 3B, pp. 418–421, 2005.
- [134] Sivasondhivat K. and Takada J.-I., "Investigation of Performance Improvement of EAMVs in Diffuse Scattering Channels," in *2005 IEICE General Conference*, 2005.
- [135] Ribeiro C., Richter A., Koivunen V., and Thomae R., "Recent Advances in Modeling and Estimation of Local and Distributed Scattering of Mobile Radio Channels," in *XXVIIIth URSI General Assembly 2005*, New Delhi, India, October 2005.
- [136] Czink N., Del Galdo G., Yin X., Bonek E., and Ylitalo J., "A Novel Environment Characterization Metric for Clustered MIMO Channels Used to Validate a SAGE Parameter Estimator," *Wireless Personal Communications Journal*, 2007.
- [137] Shannon C. E., "A mathematical theory of communication," *Bell System Technical Journal*, vol. vol. 27, pp. 379–423 and 623–656, 1948.
-



- 
- [138] Paulraj A., Nabar R., and Gore D., *Introduction to Space-Time Wireless Communications*. Cambridge University Press, 2003.
- [139] Haykin S., *Communications Systems*. Wiley-VCH, 2000.
- [140] Eggers P., “Dual directional channel formalism and descriptions relevant for Tx-Rx diversity and MIMO,” in *COST 273 Temporary Document TD(03)044*, 2003.
- [141] Pal A., Beach M., and Nix A., “A quantification of 3-D directional spread from small-scale fading analysis,” in *COST 273 Post-Project Meeting*, Lisbon, Portugal, Nov. 2005.
- [142] Pal A., Beach M., and Nix A., “A Novel Quantification of 3D Directional Spread from Small-Scale Fading Analysis,” in *Communications, 2006 IEEE International Conference on*, vol. 4, June 2006, pp. 1699–1704.
- [143] Schneider R., “Modellierung der Wellenausbreitung für ein bildgebendes Kfz-Radar, (in German),” Ph.D. dissertation, 1998.
- [144] Balanis C., *Advanced Engineering Electromagnetics*. New York: John Wiley & Sons, 1989.
- [145] Maurer J., Drumm O., Didascalou D., and Wiesbeck W., “A novel approach in the determination of visible surfaces in 3D vector geometries for ray-optical wave propagation modelling,” in *Vehicular Technology Conference Proceedings, 2000. VTC 2000-Spring Tokyo. 2000 IEEE 51st*, vol. 3, 15-18 May 2000, pp. 1651–1655vol.3.
- [146] Luebbers R., “Finite Conductivity Uniform GTD Versus Knife Edge Diffraction in Prediction of Propagation Path Loss,” vol. 32, no. 1, pp. 70–76, Jan. 1984.
- [147] Luebbers R., “Comparison of Lossy Wedge Diffraction Coefficients with Application to Mixed Path Propagation Loss Prediction,” *IEEE Transactions on Antennas and Propagation*, vol. 36, pp. 1031–1034, July 1988.
- [148] “Automatically tuned linear algebra software (atlas),” Sourceforge, 2006. [Online]. Available: <http://math-atlas.sourceforge.net/>
- [149] Sprengel F., “Can We Use the Known Fast Spherical Fourier Transforms in Numerical Meteorology?” GMD-Forschungszentrum Informationstechnik GmbH, Tech. Rep., 2001.
- [150] Lotze J., “Efficient Polarimetric Antenna Radiation Pattern Modeling,” Master’s thesis, TU Ilmenau, 2006.
- [151] Kalliola K., Sulonen K., Laitinen H., and et. a., “Angular power distribution and mean effective gain of mobile antenna in different propagation environments,” in *IEEE Transactions on Vehicular Technology*, vol. 51, September 2002.
- [152] Rappaport T. S., *Wireless Communications*. Prentice Hall Professional Technical Reference, 1996, pp. 79–83.
-



# THESES TO “LIMITATIONS OF EXPERIMENTAL CHANNEL CHARACTERISATION”

1. Propagation measurements give us an antenna dependent description of the radio channel, whereas the aim of *Experimental Channel Characterisation* is the antenna independent description of the channel.
2. The parameter estimation framework **RIMAX** has the potential to give us an antenna independent description of the radio channel by applying an estimation model that combines a simplified model of the radio channel comprising Specular Components (**SC**) and Dense Multipath Components (**DMC**) with a model of the measurement system including the employed antenna arrays.
3. The measured radiation patterns of any antenna array as well as its derivatives can be efficiently and accurately modelled by the novel Effective Aperture Distribution Function (**EADF**) approach that is essentially a two dimensional (**2D**) Fourier transformation of the periodic radiation patterns.
4. For full polarimetric **2D** calibration of practical antenna arrays with Multiple-Input Multiple-Output (**MIMO**) channel sounders, accurate calibration procedures for the system frequency responses are required. This includes the frequency dependent calibration of the polarimetric reference horn antenna, all Radio Frequency (**RF**) cables, the **AGC** dependent frequency responses of the measurement system, **RF** multiplexers at the transmitter side, and the receiver side.
5. The measured radiation patterns have to be corrected for a phase offset occurring during calibration measurement. A novel gradient based Maximum Likelihood (**ML**) estimator, which is suitable for this task has been developed.
6. A model of the measurement system including the employed antenna arrays that perfectly matches reality does not exist.
7. Consequences of model mismatch can be: the estimation of biased and/or artificially spread angular parameters of the **SC** and the estimation of **DMC** that are partially related to model error.



8. Model mismatch can be caused by:
  - systematic error in antenna array calibration caused by parasitic reflections
  - ignoring elevation and/or polarisation characteristics of the antenna elements
  - phase noise and phase drift during propagation measurements.
9. In case of an adequate model accuracy of the derived **EADFs**, any practical antenna array can be evaluated in terms of the directional resolution limits with the novel, powerful framework proposed. The framework allows the analytic calculation of the Cramér-Rao Lower Bound of the **DoD/DoA** parameters of multiple propagation paths applying measured radiation patterns described by its corresponding **EADFs**.
10. The estimation of **DMC** improves the reliability of the **SC** parameter estimation results in the presence of distributed diffuse scattering and/or model error.
11. The estimated **DMC** can only be interpreted as feature of the radio channel if the accuracy of the estimation model is larger than the maximum Signal-to-Noise ratio of the Complex Impulse Response (**CIR**).
12. The relevance and reliability of the estimated **SC** and **DMC** has to be taken into account when using the results of *Experimental Channel Characterisation* for channel modelling.